10/3-30-94 OSTI

SANDIA REPORT

SAND93–1899 • UC–~~610~~
Unlimited Release
Printed February 1994

MELCOR 1.8.2 Assessment: Surry PWR TMLB' (with a DCH Study)

L. N. Kmetyk, R. K. Cole Jr., R. C. Smith, R. M. Summers, S. L. Thompson

Prepared by
Sandia National Laboratories
Albuquerque, New Mexico 87185 and Livermore, California 94550
for the United States Department of Energy
under Contract DE-AC04-94AL85000

Issued by Sandia National Laboratories, operated for the United States Department of Energy by Sandia Corporation.

Available to DOE and DOE contractors from
Office of Scientific and Technical Information
PO Box 62
Oak Ridge, TN 37831

Prices available from (615) 576-8401, FTS 626-8401

Available to the public from
National Technical Information Service
US Department of Commerce
5285 Port Royal Rd
Springfield, VA 22161

NTIS price codes
Printed copy: A14
Microfiche copy: A01

Distribution
Category UC-610

SAND93-1899
Unlimited Release
Printed February 1994

MELCOR 1.8.2 Assessment: Surry PWR TMLB' (with a DCH Study)

L. N. Kmetyk, R. K. Cole Jr.,
R. C. Smith, R. M. Summers, S. L. Thompson
Thermal/Hydraulic Analysis Department
Sandia National Laboratories
Albuquerque, NM 87185

Abstract

MELCOR is a fully integrated, engineering-level computer code, being developed at Sandia National Laboratories for the USNRC. This code models the entire spectrum of severe accident phenomena in a unified framework for both BWRs and PWRs. As part of an ongoing assessment program, the MELCOR computer code has been used to analyze a station blackout transient in Surry, a three-loop Westinghouse PWR.

Basecase results obtained with MELCOR 1.8.2 are presented, and compared to earlier results for the same transient calculated using MELCOR 1.8.1. The effects of new models added in MELCOR 1.8.2 (in particular, hydrodynamic interfacial momentum exchange, core debris radial relocation and core material eutectics, CORSOR-Booth fission product release, high-pressure melt ejection and direct containment heating) are investigated individually in sensitivity studies. The progress in reducing numeric effects in MELCOR 1.8.2, compared to MELCOR 1.8.1, is evaluated in both machine-dependency and time-step studies; some remaining sources of numeric dependencies (valve cycling, material relocation and hydrogen burn) are identified.

Contents

List of Figures

List of Tables

1 Introduction

MELCOR [1] is a fully integrated, engineering-level computer code, being developed at Sandia National Laboratories for the U. S. Nuclear Regulatory Commission (USNRC), that models the progression of severe accidents in light water reactor (LWR) nuclear power plants. The entire spectrum of severe accident phenomena, including reactor coolant system and containment thermal/hydraulic response, core heatup, degradation and relocation, and fission product release and transport, is treated in MELCOR in a unified framework for both boiling water reactors (BWRs) and pressurized water reactors (PWRs).

The MELCOR computer code has been developed to the point that it is now being successfully applied in severe accident analyses. Some limited technical assessment activities were performed early in the MELCOR development process [2]; more recently, a more extensive, systematic program of verification and validation has been underway. To this end, a number of assessment calculations have been and are being done [3-10]. One of these assessment activities is analysis of a TMLB' station blackout sequence in the Surry plant, a 3-loop Westinghouse PWR. This report documents the results of those analyses.

As part of the MELCOR Peer Review process [11], Sandia performed and presented a demonstration calculation of a Surry station blackout (TMLB') accident with MELCOR. This was the first fully integrated PWR severe accident calculation performed with the code (since the earlier TMI analysis only included in-vessel phenomena). That calculation was done using the release version of MELCOR 1.8.1. (MELCOR 1.8.1 calculations of a Surry TMLB' station blackout also have been performed by the UK AEA, as documented in [12].) The Surry TMLB' calculation has been rerun with the release version of MELCOR 1.8.2, allowing direct comparison of predicted results for the same problem. That analysis also has been used as a standard test problem to investigate problems identified by the Peer Review (*e.g.*, lack of pressurizer draining prior to vessel breach) and to evaluate the impact on the results of model improvements and extensions (for example, adding the CORSOR-Booth fission product release model) and of new models (such as radial debris relocation, material eutectics interactions, and high pressure melt ejection (HPME) and associated direct containment heating (DCH)).

MELCOR version 1.8NM (the version released as MELCOR 1.8.2 in April 1993) was used for almost all of the calculations described in this report; the analyses for the sensitivity study on the new direct containment heating model used version 1.8NN, which included a number of corrections and enhancements to that model developed as a result of our IET direct containment heating experiments assessment analyses [10]. (Those code changes between the release version and version 1.8NN are discussed briefly in Section 6.5.)

The Surry plant is described very briefly in Section 2. Section 3 summarizes the input used for these MELCOR assessment analyses. The results of our reference calculation with MELCOR 1.8.2 are given in Section 4, and compared to earlier results for the same

transient calculated using MELCOR 1.8.1 in Section 5. Sensitivity studies on the effects of the new models added in MELCOR 1.8.2 (in particular, hydrodynamic interfacial momentum exchange, core debris radial relocation and core material eutectics, CORSOR-Booth fission product release, and high-pressure melt ejection and direct containment heating) are presented in Section 6. Section 7 contains the results of our time step and machine dependency sensitivity studies, as well as results from numeric sensitivity studies concentrating on valve cycling and on hydrogen burn. Comparison with results obtained by other codes is done in Section 8. Section 9 presents the conclusions of this MELCOR plant transient assessment study.

(Unlike our usual practice in previous MELCOR assessment reports [3-10], a listing of the input used for the Surry TMLB' reference calculation is not given in an appendix, because some of the input values include proprietary information. A listing of the input can be obtained from the author or the MELCOR development staff, with NRC approval.)

2 Plant Description

The MELCOR analyses described in this report were based on the Surry Power Station, Unit 1. Operated by the Virginia Electric Power Company, it is located on the James River in southeastern Virginia, about 16 kilometers (10 miles) south of Williamsburg, Virginia. Two units are located on the site, with Unit 2 essentially identical to Unit 1.

The nuclear reactor of Surry Unit 1 is a 2441MWt pressurized water reactor (PWR) designed and built by Westinghouse. The Reactor Coolant System (RCS) is a three loop design, with a reactor coolant pump (RCP) and a U-tube steam generator (SG) in each loop. In addition, Loop C contains the primary system pressurizer. Under normal operating conditions, the RCS operates at ~15.5MPa (155bar or 2,250psia), with a core inlet coolant temperature of 557K (543°F) and a core exit coolant temperature of 593K (608°F). The RCS coolant flow rate during normal operation is 12,688kg/s (27,972lb/s).

The reactor vessel (see Figure 2.1) contains the core, core barrel, core support structures, and control rod and instrumentation component structures. Water from the SGs is pumped through the cold legs by the RCPs to the reactor vessel (RV) inlet nozzles, transiting the downcomer and RV lower plenum prior to passing through the lower core support plate and entering the core. Moving upward through the core, the coolant flows out the top and exits the RV via the outlet nozzles, flowing through the hot legs into the steam generators again. The reactor core is made up of 32,028 Zircaloy-4 clad fuel rods containing sintered UO_2 distributed in 157 fuel assemblies. The core active height is 3.66m (12ft). RCS overpressure control is assured by three safety valves set to open at a nominal pressure of 17.2MPa (172.4bar or 2,500psia). Capacity of each safety valve is 36.3kg/s (80lb/s). Two Power Operated Relief Valves (PORVs) are available, set to relieve RCS pressure when it reaches 162bar (2,350psia). PORV nominal relief capacity is 22.6kg/s (49.7lb/s).

Safety grade emergency systems are designed to protect the RCS in the event of an accident. Should normal feedwater flow be lost, the auxiliary feedwater system (AFWS) is available to provide coolant to the steam generator secondaries. The AFWS has three pumps: two are driven by electric motors; the third is driven by a steam turbine. The AFWS takes suction from the condensate storage tank (CST). The Emergency Core Cooling System (ECCS) is a suite of systems designed to deliver coolant water to the reactor vessel in the event of a loss of coolant accident (LOCA). The ECCS provides makeup water during small break accidents when the RCS remains at a relative high pressure via three High Pressure Injection System (HPIS) pumps. These pumps serve as charging pumps under normal operating conditions. For larger breaks in the RCS, the Low Pressure Injection System (LPIS) is available to provide high volume, low pressure coolant flow to the RCS. Both the HPIS and the LPIS can function in a recirculation mode as well as in an injection mode; in the recirculation mode they take suction from the containment sump. Surry also has three passive accumulators to provide immediate, high flow, low pressure injection to the RV in the case of large breaks in the RCS.

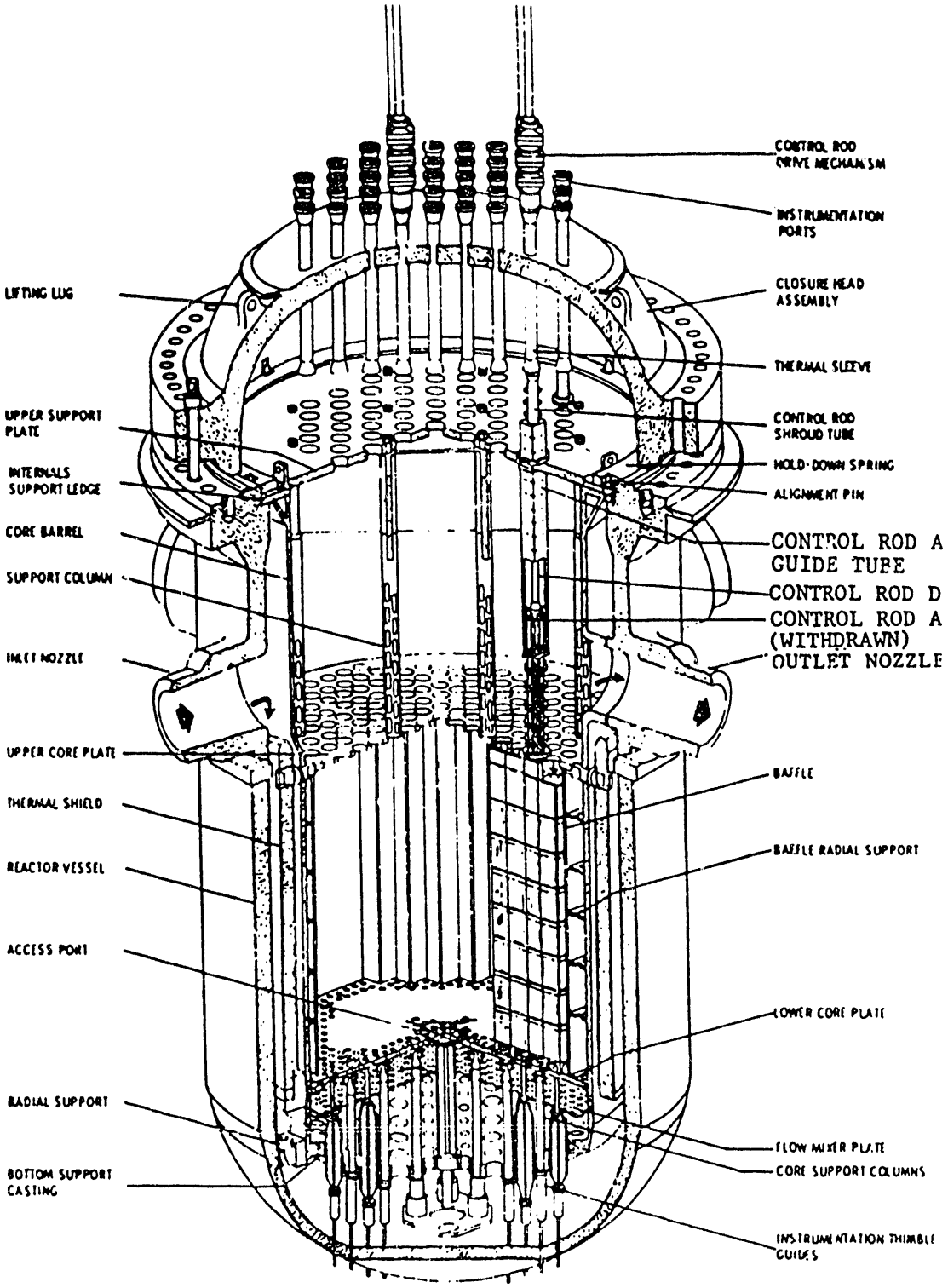

Figure 2.1. Surry Reactor Vessel

The Surry containment, designed and built by Stone and Webster, is a reinforced concrete cylinder with a hemispherical dome. Figure 2.2 shows a cross section of the containment. The cylindrical portion of the containment sits on a basemat that is 3.05m (10ft) thick. The wall of the cylinder is about 1.3m (4.3ft) thick. The dome thickness is about 0.8m (2.6ft). A welded steel liner forms the pressure boundary. Containment volume is 50,971m^3 (1,800,000ft^3), and the design pressure is 4.1bar (45psig, 59.7psia). Due to safety factors in design and construction, most estimates of the failure pressure are between two and three times the design pressure. For the MELCOR analyses, a containment failure pressure of 9.7bar (126psig, 140.7psia) was used, identical to the mean value used for the calculations done for the Surry plant in support of NUREG-1150 [13] and reported in the supporting document [14].

During normal operation, the interior of the containment is maintained at about 70kPa (0.7bar or 10psia). Normal containment cooling is by fan coolers. These are not safety grade, and they are partially submerged if the containment sump is full of water. Emergency containment heat removal is accomplished by the spray systems. The containment spray injection system (CSIS) has two trains, each with one pump which takes suction from the RWST. There are two containment spray recirculation systems (CSRS), each with two trains. Each of the six containment spray trains is independent of the other spray systems, except that each requires electrical power for the pumps. Each containment spray recirculation train includes a heat exchanger that is cooled by the service water system and a pump that takes suction directly from the containment sump. One system has its pumps located inside the containment and the other has its pumps located outside the containment.

There is no connection between the containment sump and the reactor cavity at a low elevation in the Surry containment. Water from a pipe break in containment will flow to the sump. The reactor cavity will remain dry unless the containment sprays operate.

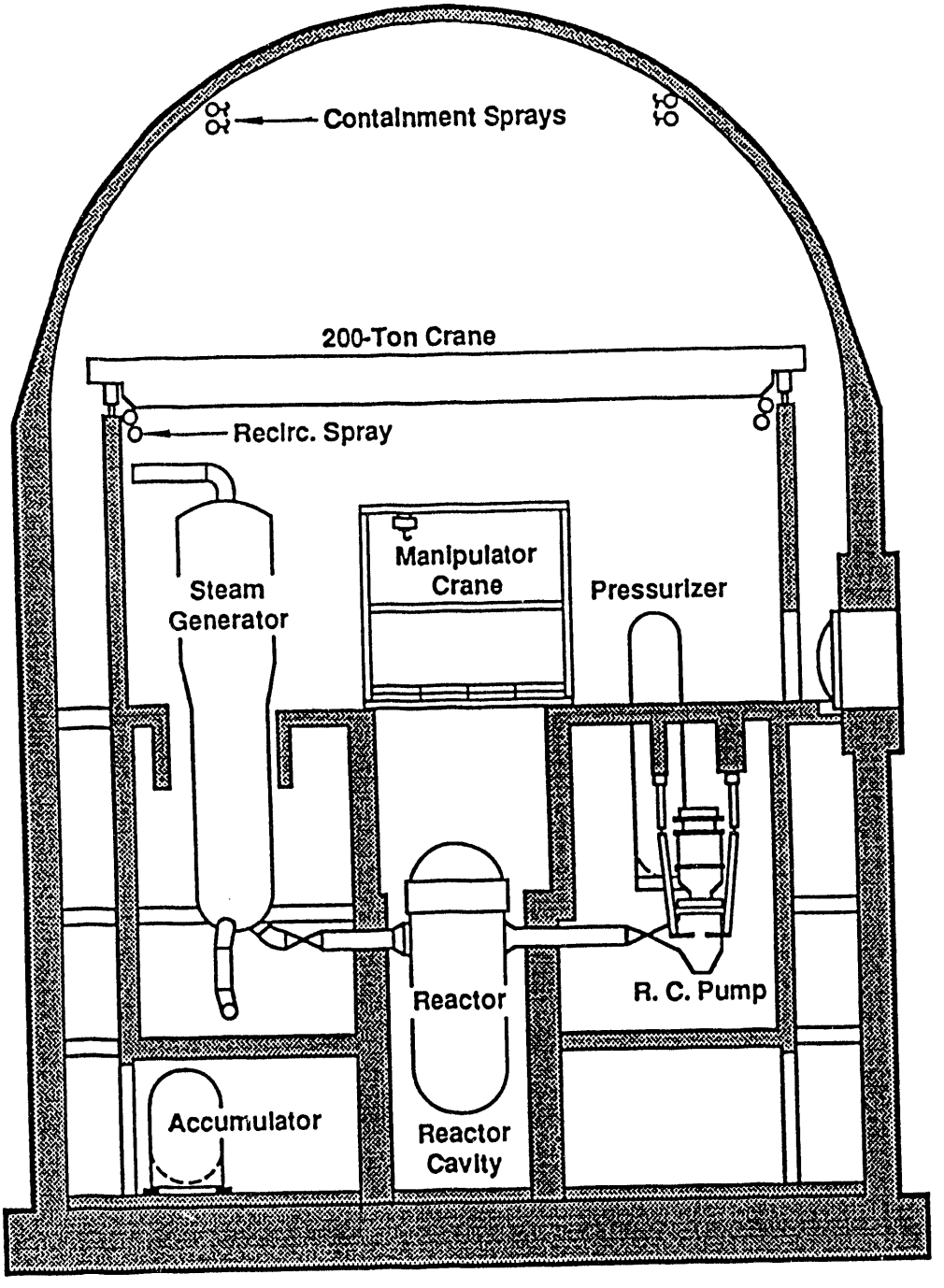

Figure 2.2. Surry Containment

3 MELCOR Computer Model

Our MELCOR Surry model was developed from a MELCOR input deck originally received from the Idaho National Engineering Laboratory (INEL) [15, 16, 17], which in turn was based on a SCDAP/RELAP5 input deck developed by INEL [18].

The MELCOR Surry model for these calculations has 21 control volumes (6 for the reactor vessel and internals, 4 for the primary system loops, 4 for the steam generator secondaries, 6 for the containment, and 1 for the environment); 33 flow paths (13 internal to the RCS, 7 associated with the steam generator secondary side, 10 internal to the containment, and 3 connecting the RCS to containment); and 88 heat structures (64 for the RCS and 24 for the containment). Figures 3.1 and 3.2 give a graphic representation of the basic nodalization used for the primary system and for the containment, respectively, of the Surry plant.

All control volumes were specified to use nonequilibrium thermodynamics and were specified to be vertical volumes; all heat structures used the steady-state temperature-gradient self-initialization option. Detailed volume-altitude tables and junction flow segments were used to correctly represent subcomponents in and between the major components modelled.

The vessel was represented by six control volumes: four for the downcomer, lower and upper plenum, and upper head and two for the parallel core and core bypass regions. In the intact loop piping, one control volume was used for the hot leg, steam generator (SG) inlet plenum and the uphill side of the U-tubes; a second control volume was used for the downhill side of the U-tubes, the steam generator outlet plenum, and the downhill leg and half of the horizontal section of the pump loop seal; and a third control volume represented the remaining horizontal section and the uphill leg of the branching pump loop seal, together with the parallel primary coolant pumps and the cold leg. This division, at lowest and highest points in the piping, was intended to allow resolution of the various vertical differentials driving natural circulation flow.

The steam generator secondary system was modelled using four control volumes: one each for the boiler and downcomer, and two time-independent volumes providing the steady-state outlet pressure boundary and an ambient-environment collection volume for the relief valve flow paths. The feedwater was sourced directly into the downcomer using control and tabular functions to specify mass and energy addition as functions of time. The outlet flow path used valve input to represent the main steam isolation valve (MSIV) closure. Two more outlet flow paths, communicating with an ambient-environment volume rather than the steady-state pressure-control volume, were included to model relief valves, with hysteresis control functions used to govern opening and closing at the desired pressure setpoints.

The pressurizer and its surge line were modelled as a single, separate control volume (set to be time-independent during steady-state initialization calculations, and then reset to be a normal control volume at the start of the transient). The PORV and SRV were represented by valved flow paths from the top of the pressurizer to the containment, with

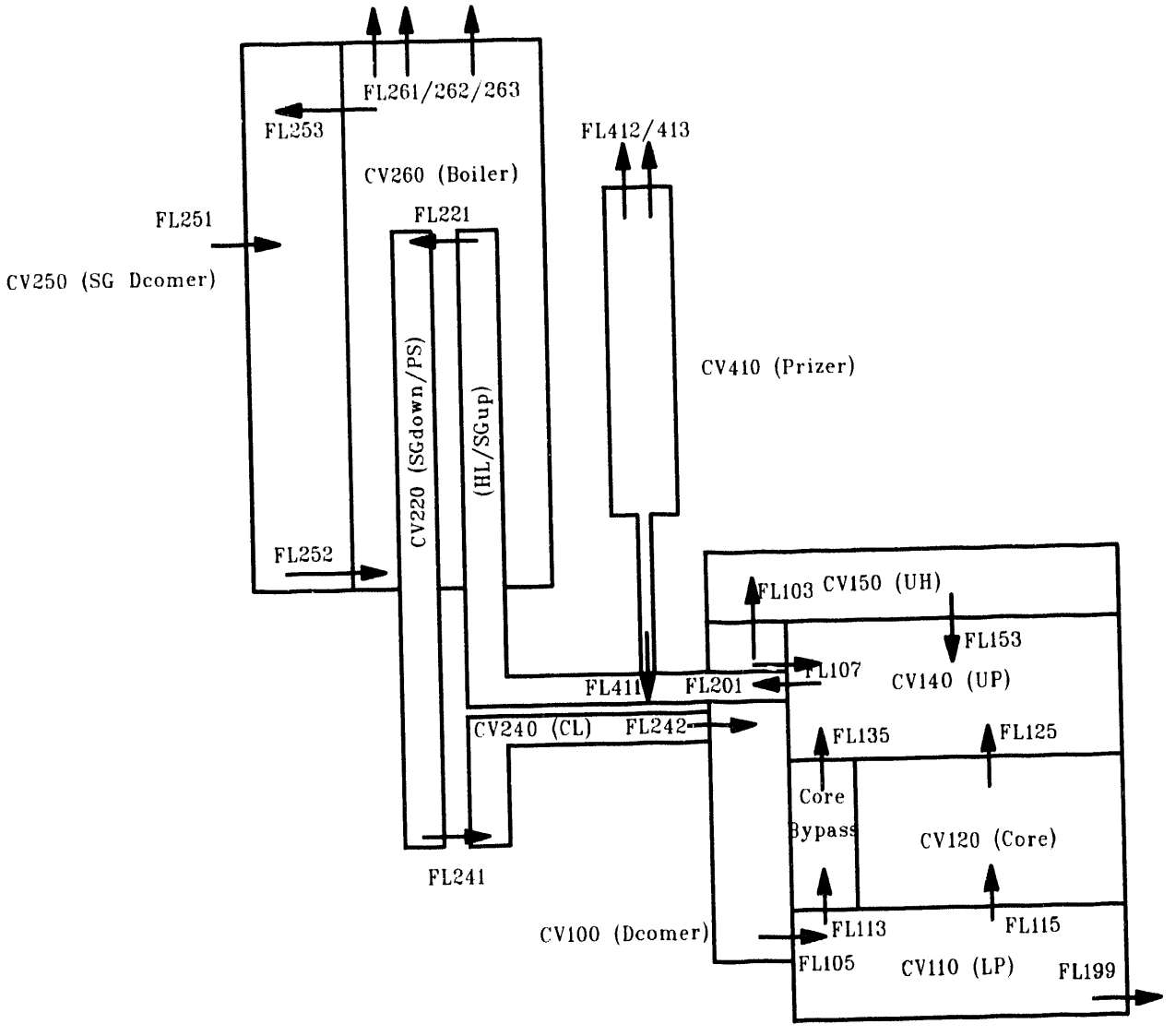

Figure 3.1. Reference MELCOR CVH/FL Input Model for Surry Primary System

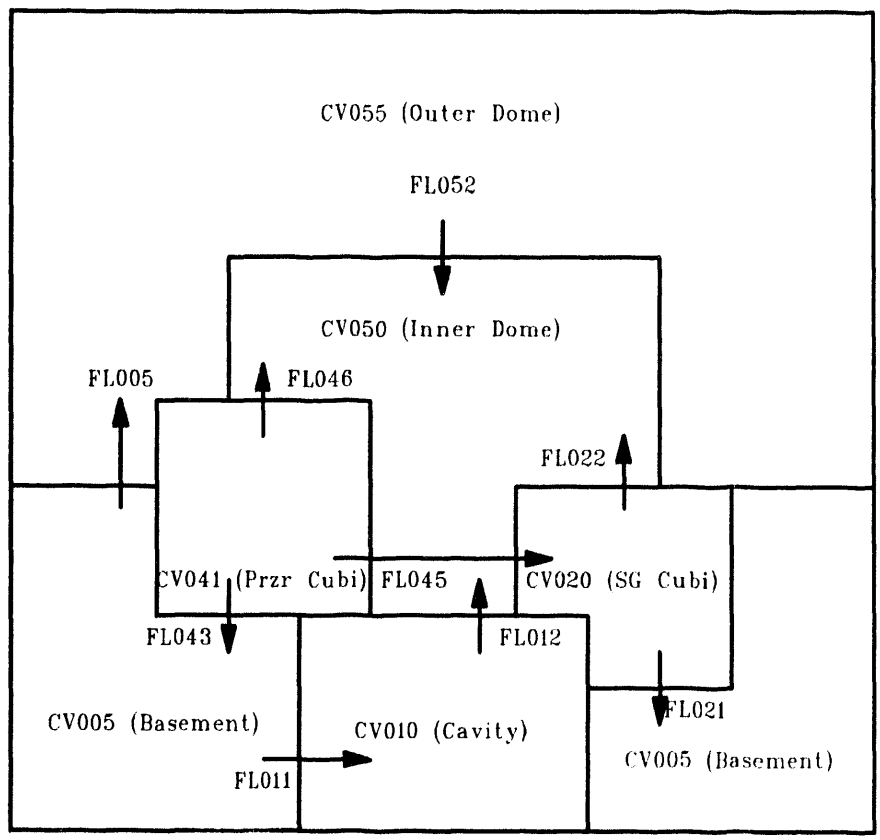

Figure 3.2. Reference MELCOR CVH/FL Input Model for Surry Containment

hysteresis control functions used to govern opening and closing at the desired pressure setpoints.

Junctions were defined to be either normal vertical flow paths or normal horizontal flow paths as determined by the system geometry. SPARC bubble rise physics was not turned on at the junctions (the default). All area changes were explicitly modelled using flow path segments, and loss coefficients for all elbows, bends, plenum inlets and outlets, etc., derived from the basic facility geometry using standard formulae [19, 20] were input. Flow path opening heights were based on pipe diameters for horizontal junctions, while the opening heights used on vertical flow paths (primarily within the vessel) were generally set to small values (*e.g.*, ~5-15cm).

The heat structures were generally specified to use the "internal" set of heat transfer coefficient correlations on the inside of most heat structures, with the heated equivalent diameter input as the characteristic length; on their outside surface, most of the heat structures were specified to use the "external" set of heat transfer coefficient correlations with the heat structure length or height input as the characteristic length. The critical pool and atmosphere fractions were set to 0.01 and 0.99 respectively, for most of the heat structure surfaces, to ensure very little artificial limiting of heat transfer; they were set equal, to 1.0, for the outside surface of piping and vessel wall heat structures, where the air-filled, time-specified control volume representing the environment was used as the heat structure outside boundary volume. Radiation heat transfer between structure and atmosphere was not modelled (except within the core).

The reactor core nodalization, a separate model from the control volumes listed above, consisted of 39 core cells divided into 3 radial rings and 13 axial levels. Axial levels 4 through 13 made up the active core region, while levels 1 through 3 modelled the lower plenum, including the core support plate in level 3. Figure 3.3 illustrates the reactor core nodalization used in all our Surry TMLB' calculations.

Default view factor values were used in the core for ring-to-ring radial radiation heat transfer, level-to-level axial radiation heat transfer, for radiation heat transfer between fuel rod cladding and other structure (*e.g.*, control rods) and for radiation heat transfer between core components and a liquid pool (if present); because there is no canister in a PWR, there is no separate radiative exchange between canister wall and fuel rod cladding or between other structure and the adjacent canister wall. The COR package in MELCOR allows also structure-to-structure radiation heat transfer to a boundary heat structure, but only in the outer ring.

The core material eutectic interaction model was enabled though input, with no change to default property values, and the core debris radial relocation model for both molten and for particulate debris was enabled by default. The core plate and bottom head penetration failure temperatures, and the falling debris and lower head penetration heat transfer coefficients were all set to their default values in the MELCOR reference calculation.

The cavity was specified to have an internal depth and radius of 1.00 and 4.28m, respectively; the concrete was 1.302m thick on the sides and 3.04m thick below the cavity.

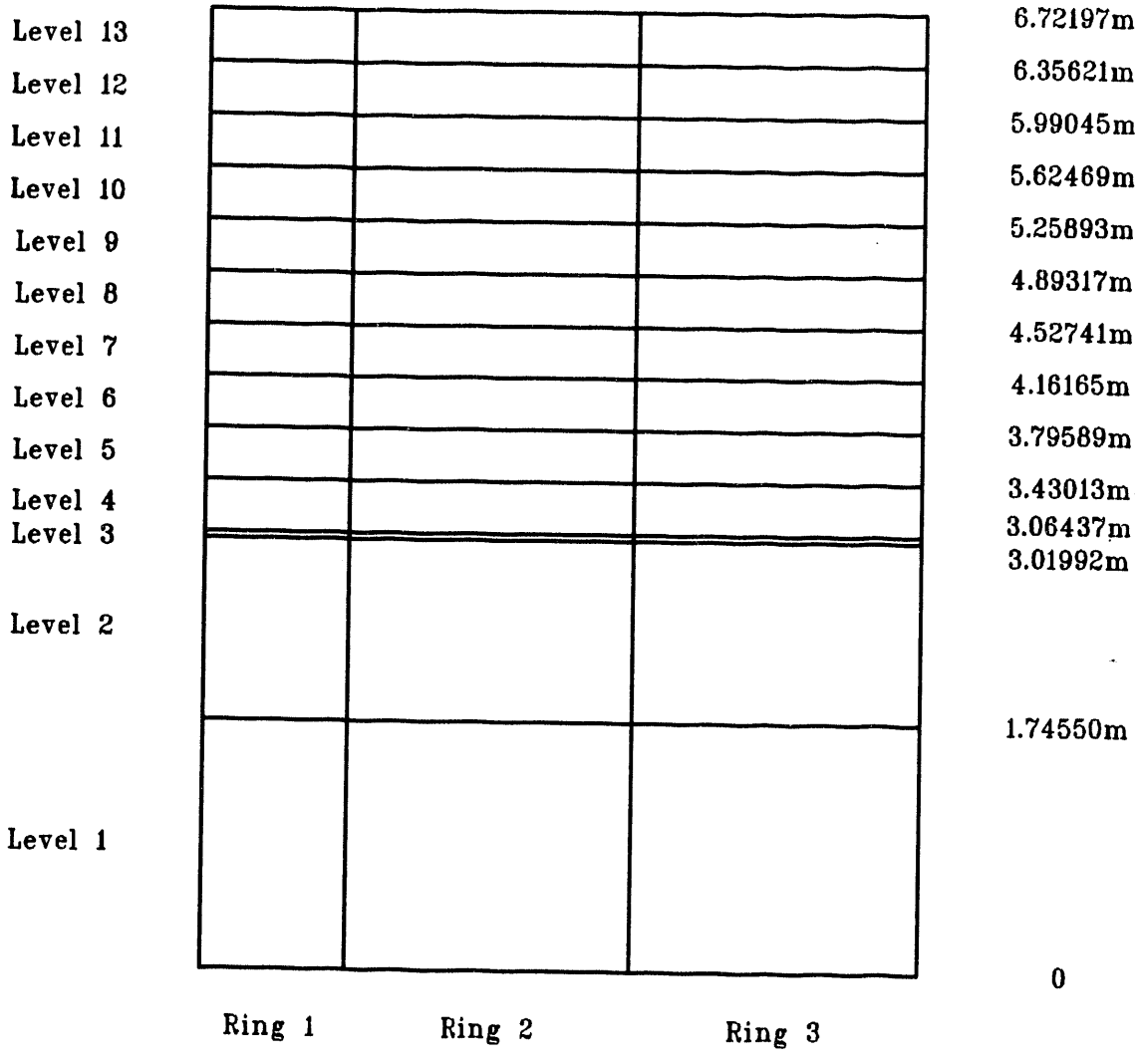

Figure 3.3. Reference MELCOR COR Input Model for Surry Core

Default limestone-aggregate/common-sand concrete was specified, with no modification to default composition or properties.

The default classes in the MELCOR RN and DCH packages were used. Table 3.1 presents a list of the MELCOR fission product material classes, including the total radioactive mass inventory of each class initially present; a small fraction of these were specified to be in the gap rather than in the fuel. Most of our calculations were done using the CORSOR fission product release model; Section 6.4 presents results using the alternative CORSOR-M and CORSOR-Booth release model options. These analyses were done specifying two MAEROS components, one for fog (the water droplets in the atmosphere) and another for all other aerosols, and the default number of and diameter bounds of aerosol distribution size bins.

A large number of control functions (278) were used to track the source term release and subsequent distribution, to determine timing and flow of various systems, and to adjust valves and pumps as required. In particular, control functions were used to track the total and radioactive masses of each class 1) released from the intact fuel and/or debris in the vessel (either in the core, the bypass or in the lower plenum), 2) released from the debris in the cavity, 3) remaining in the primary system (*i.e.*, the reactor vessel), 4) in the containment, and 5) in the environment. Those control functions provided time-dependent source term release and distribution data for subsequent postprocessing in a form more convenient for analysis and evaluation.

The density, specific heat and thermal conductivity properties needed to model the inconel steam generator U-tubes, carbon steel and piping insulation were specified in the MELCOR deck.

Most of the Surry TMLB' calculations presented in this report were run on an IBM RISC-6000 Model 550 workstation; the differences in results found running the reference calculation on other hardware platforms are summarized in Section 7.1. The user-input maximum time step in the final, reference calculation was 10s throughout the transient period analyzed. The effect of reducing the maximum allowed time step is described in Section 7.2.

As part of the MELCOR Peer Review process [11], Sandia performed and presented a demonstration calculation of the Surry station blackout (TMLB') accident with the release version of MELCOR 1.8.1. As part of this overall assessment, that calculation has been rerun with the release version of MELCOR 1.8.2, allowing direct comparison of predicted results for the same problem, with results described in Section 5. No input changes were required between running with the release versions of MELCOR 1.8.1 and 1.8.2. A small number of input changes were made in the basecase MELCOR 1.8.2 model to take advantage of new models and/or upgraded models included using step functions in valve area-*vs*-time tables, and enabling the new eutectics model (not used as the default); the new debris radial relocation model is enabled by default. However, note that other input changes made for the reference analysis discussed in detail in Section 4 and for various other sensitivity studies, especially specifying high-pressure melt ejection debris distribution and direct containment heating interactions, were not used in the MELCOR 1.8.2 calculation used in the 1.8.2 *vs* 1.8.1 comparison.

Table 3.1. Radionuclide Classes and Initial Inventories

Class	Class Name	Representative Element	Member Elements	Initial Radionuclide Mass (kg)
1	Noble Gases	Xe	He, Ne, Ar, Kr, Xe, Rn,H, N	244.83
2	Alkali Metals	Cs	Li, Na, K, Rb, Cs, Fr, Cu	136.45
3	Alkaline Earths	Ba	Be, Mg, Ca, Sr, Ba, Ra, Es, Fm	107.40
4	Halogens	I	F, Cl, Br, I, At	10.545
5	Chalcogens	Te	O, S, Se, Te, Po	21.481
6	Platinoids	Ru	Ru, Rh, Pd, Re, Os, Ir, Pt, Au, Ni	151.10
7	Early Transition Elements	Mo	V, Cr, Fe, Co, Mn, Nb, Mo, Tc, Ta, W	178.19
8	Tetravalents	Ce	Ti, Zr, Hf, Ce, Th, Pa, Np, Pu, C	314.40
9	Trivalents	La	Al, Sc, Y, La, Ac, Pr, Nd, Pm, Sm, Eu, Gd, Tb Dy, Ho, Er, Tm, Yb, Lu, Am, Cm, Bk, Cf	291.70
10	Uranium	U	U	61,025
11	More Volatile Main Group	Cd	Cd, Hg, Zn, As, Sb, Pb, Tl, Bi	0.7135
12	Less Volatile Main Group	Sn	Ga, Ge, In, Sn, Ag	4.0521
13	Boron	B	B, Si, P	0
14	Water	H_2O	H_2O	
15	Concrete			

Most of our Surry TMLB' calculations included input to model HPME/DCH, taking advantage of the new model added in MELCOR 1.8.2. The reference case input specified 73% of the HPME debris to end up in various containment control volume atmospheres, where it could then result in direct containment heating (60% in the cavity volume, 10% in the basement volume, and 3% in the inner dome volume). Of the remaining HPME debris most (18%) was specified to settle directly into the cavity (with no direct containment heating along the way), and 2%, 5% and 2% were specified to adhere directly onto various heat structures in the cavity, basement and dome, respectively. Several other calculations were done with different debris distributions, as summarized in Section 6.5.2, including one in which all the debris was specified to go directly to the cavity during HPME as well as in LPME. The debris distributions in these sensitivity study analyses were selected to cover three basic potential patterns: most of the HPME debris to remain in the cavity, most of the HPME debris to be blown into the containment dome, and most of the HPME debris to be trapped in some subcompartment(s). (Any debris subsequently lost from the vessel, during low-pressure melt ejection, simply fell directly into the cavity in all cases.)

The effect of high-pressure melt ejection and direct containment heating was not extremely pronounced in our reference calculation, because only ~10-15% of the total available core material was predicted to be ejected during the high-pressure melt ejection phase in our reference Surry TMLB' calculation. In addition, sensitivity study calculations were done in which ~60% of the available core material was predicted to be ejected during the high-pressure melt ejection phase; this was not to represent "correct" values for HPME mass, but simply to allow an evaluation of DCH behavior in calculations with significant amounts of high-pressure melt ejection, with results presented in Section 6.5.1.

In the reference case, the characteristic interaction times for airborne-debris oxidation and heat transfer were set to 0.1s in all control volumes, while the characteristic settling time for airborne debris was set to 1s; the characteristic interaction time for oxidation of deposited debris was set to 600s for all heat structures. These time constants represent a relatively rapid and brief DCH transient in the containment atmosphere and slow residual oxidation of debris on structures. As a sensitivity study presented in Section 6.5.3, calculations were run with characteristic interaction times for airborne-debris oxidation and heat transfer set to 0.5s in all control volumes, while the characteristic settling time for airborne debris was set to 5s in the dome and 2s in the other containment control volumes; the characteristic interaction time for oxidation of deposited debris was kept at 600s for all heat structures. These time constants allow more time for DCH interactions to occur, and are probably more reasonable values for plant analyses, based upon previous MELCOR DCH assessment analyses and results [10].

4 Reference Calculation Results

The TMLB' accident sequence assumes all electrical power to the plant has been lost. The resultant pump failure and subsequent loss of secondary feedwater to the steam generators result in the dryout of the secondary side. Most of the emergency cooling systems are unavailable due to the loss of electrical power. Deprived of its heat sink, the primary system begins to heat up and overpressurize. As water and steam are ejected through the pressurizer relief valve, the loss of primary system coolant inventory leads to core uncovery and elevated core temperatures. Without recovery of the cooling systems, the sequence rapidly progresses through core degradation, relocation and vessel failure.

The MELCOR calculation began with the reactor operating at full power. The electrical power failure was assumed to occur at time t=0, at which time the control rods were dropped into the reactor. Table 4.1 summarizes the main sequence of events predicted to occur in the reference calculation.

4.1 Primary System Thermal/Hydraulics

After the loss of power in the station blackout, the coolant pumps coasted down from full power to zero power in about five minutes, as visible in the primary system coolant flow rate presented in Figure 4.1.1. (Note that this figure, in giving the hot-leg flow, actually gives the total flow around the entire primary system, because the three loops were lumped into a single, equivalent, loop in our MELCOR input model.) However, primary system coolant flow, driven by natural circulation, continued at a much reduced rate (~5% of the steady-state, full-power flow rate) after this time. Therefore, the heat being generated by the core continued to be transferred to the steam generators, even after loss of pumped flow. This natural circulation around the primary system loop was finally ended at about 8000s (2.2hr) by increased voiding of the primary system after loss of the secondary heat sink, as discussed below.

With continued heat transfer from the primary system and with no SG feedwater or auxiliary feedwater supply available to replenish the secondary system, the secondary coolant inventory started to boil off. Because the MSIV was closed, the secondary side pressure quickly rose to the SG relief valve setpoint, and the heat being transferred from the primary was removed with the steam vented out the relief valve. Figures 4.1.2 and 4.1.3 show the rapid cycling of that relief valve. Dryout of the secondary side occurred at about 5000s (1.4hr), as illustrated by the steam generator secondary-side liquid levels in Figure 4.1.4.

After the loss of the secondary-side heat sink, the primary system pressure and temperature began to rise, as shown in Figure 4.1.5 for several control volumes in the primary system. The pressures predicted in all primary system control volumes were virtually identical. The primary system pressure initially dropped as decay heat was transferred to the secondary system and removed by vented steam. Note that, although it took ~5000s (1.4hr) to dry out the SG secondary, the primary system pressure began to rise

Table 4.1. Timing of Key Events - MELCOR 1.8.2 Reference Calculation

Event	Time
Loss of Electrical Power	0
Pump Coastdown Complete	~300s (5min)
SG Secondary SRV First Open	0
SG Secondary Side Dried Out	~5000s (1.4hr)
Pressurizer PORV First Open	~5250s (1.5hr)
TAF (Top-of-Active-Fuel) Core Uncovery	~7200s (2hr)
Natural Circulation Stopped	~7850s (2.2hr)
Start of Zr Oxidation/H_2 Production	~10,000s (2.8hr)
Gap Release	
Ring 1	10,235.0s (2.84hr)
Ring 2	10,334.4s (2.87hr)
Ring 3	10,667.9s (2.96hr)
Core Support Plate Fails	
Ring 1	11,177.9s (3.10hr)
Ring 2	11,906.3s (3.31hr)
Ring 3	13,062.9s (3.63hr)
Lower Head Penetration Fails	
Ring 1	11,219.3s (3.12hr)
Ring 2	13,029.5s (3.62hr)
Ring 3	13,842.3s (3.85hr)
Start of Debris Ejection to Cavity	11,219.3s (3.12hr)
HPME/DCH Starts	11,219.3s (3.12hr)
HPME/DCH Ends	11,251.7s (3.13hr)
Intermittent H_2 Deflagrations Start in Cavity	12,863.2s (3.57hr)
Intermittent H_2 Deflagrations Stop in Cavity	13,766.2s (3.82hr)
CORCON Layer Flip	~24,000s (6.7hr)
Cavity Dried Out	~28,200s (7.8hr)
Intermittent H_2 Deflagrations Start in Cavity	32,970.0s (9.16hr)
Intermittent H_2 Deflagrations Stop in Cavity	44,778.9s (12.44hr)
Calculation Ended	90,000.0s (25hr)

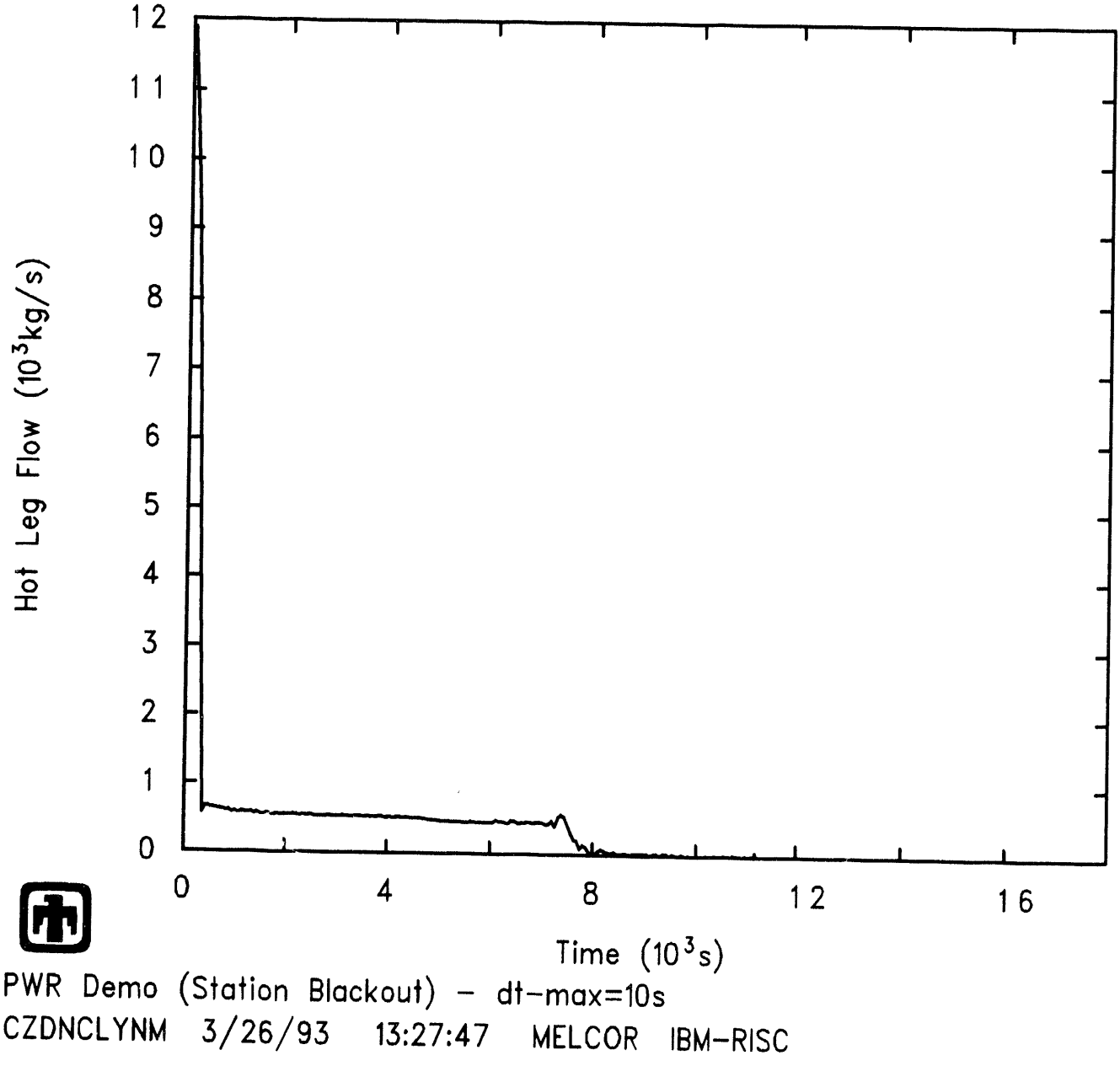

Figure 4.1.1. Primary Coolant System Mass Flow Rate - MELCOR 1.8.2 Reference Calculation

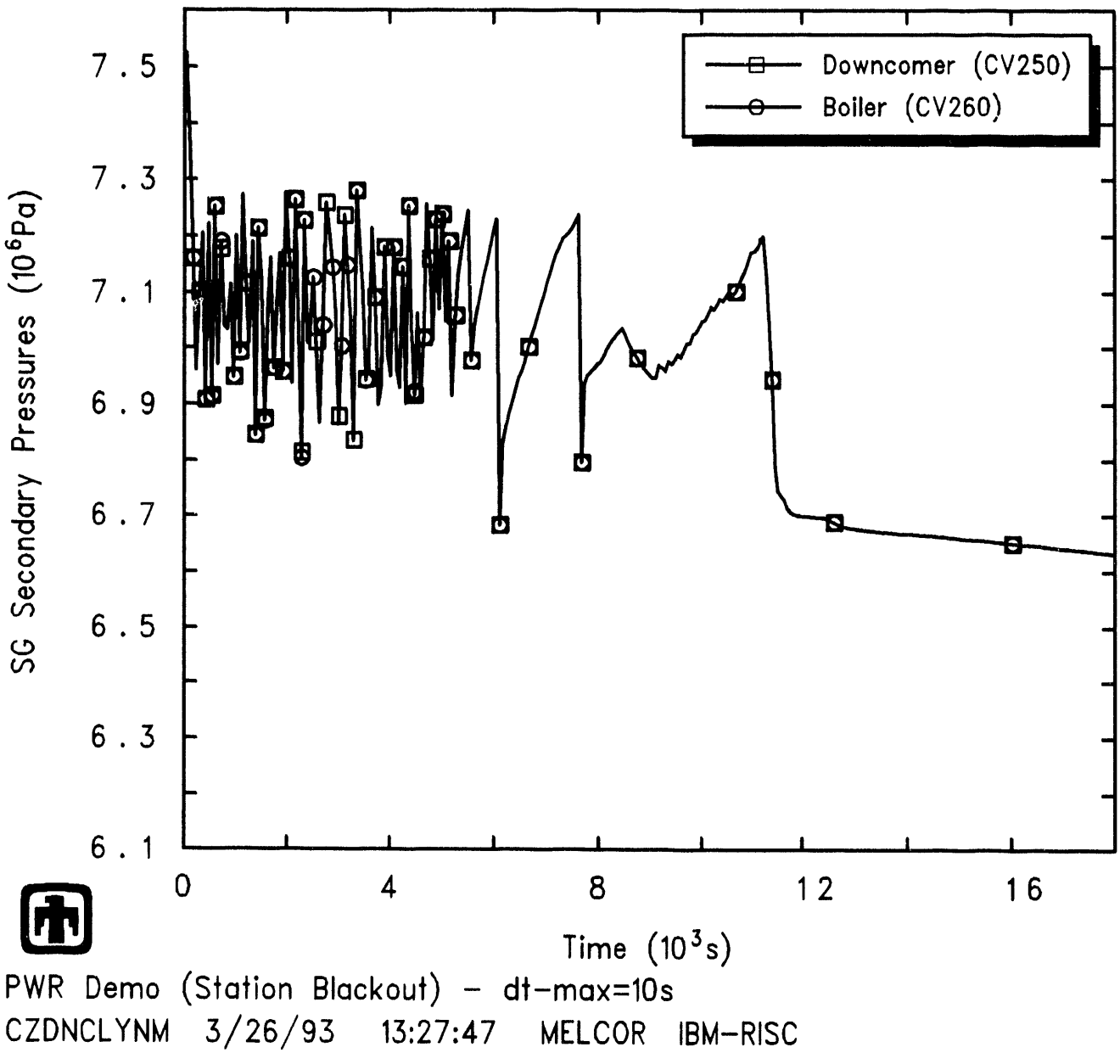

Figure 4.1.2. SG Secondary-Side Pressure - MELCOR 1.8.2 Reference Calculation

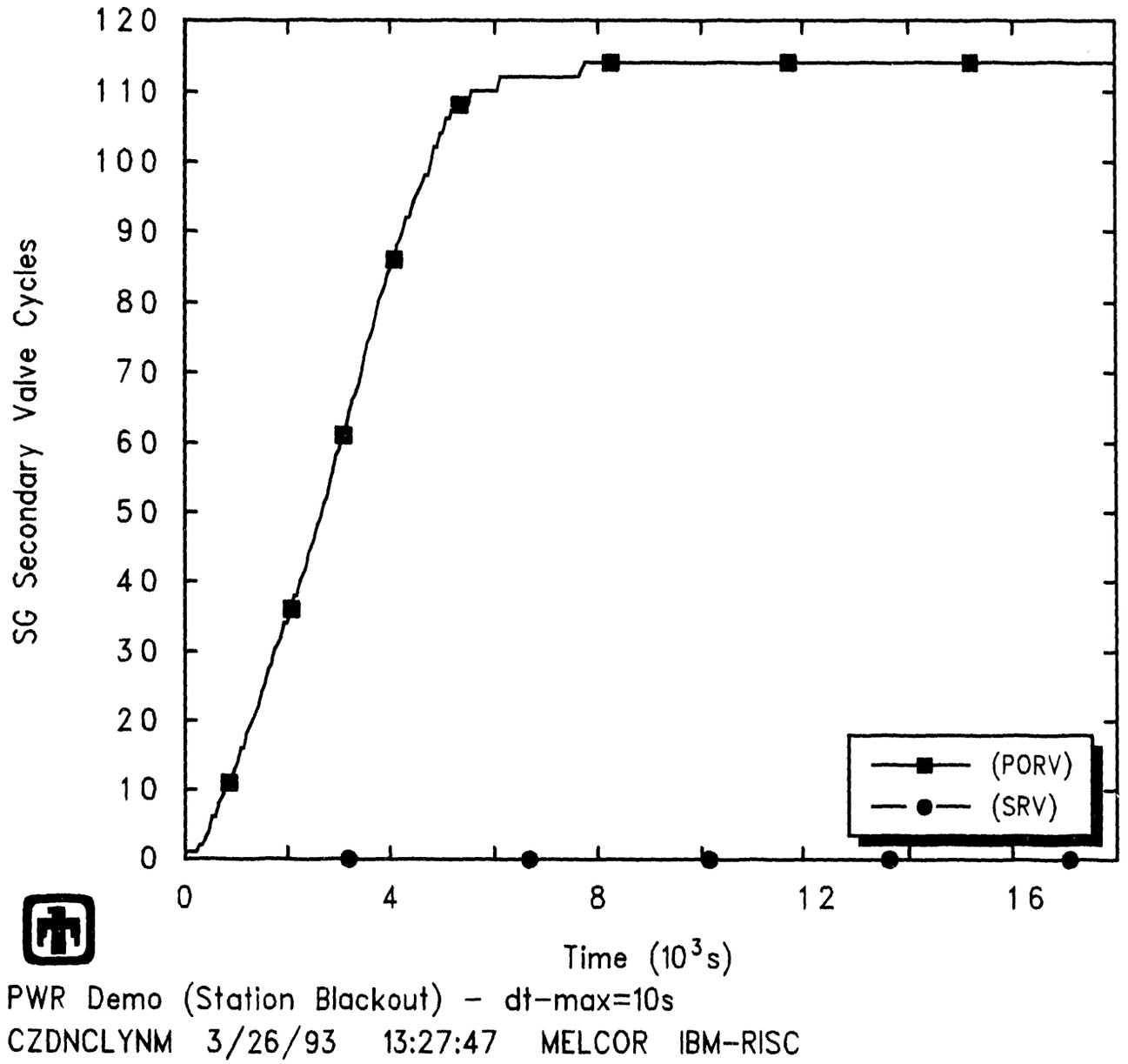

Figure 4.1.3. SG Secondary-Side Relief Valve Cycling - MELCOR 1.8.2 Reference Calculation

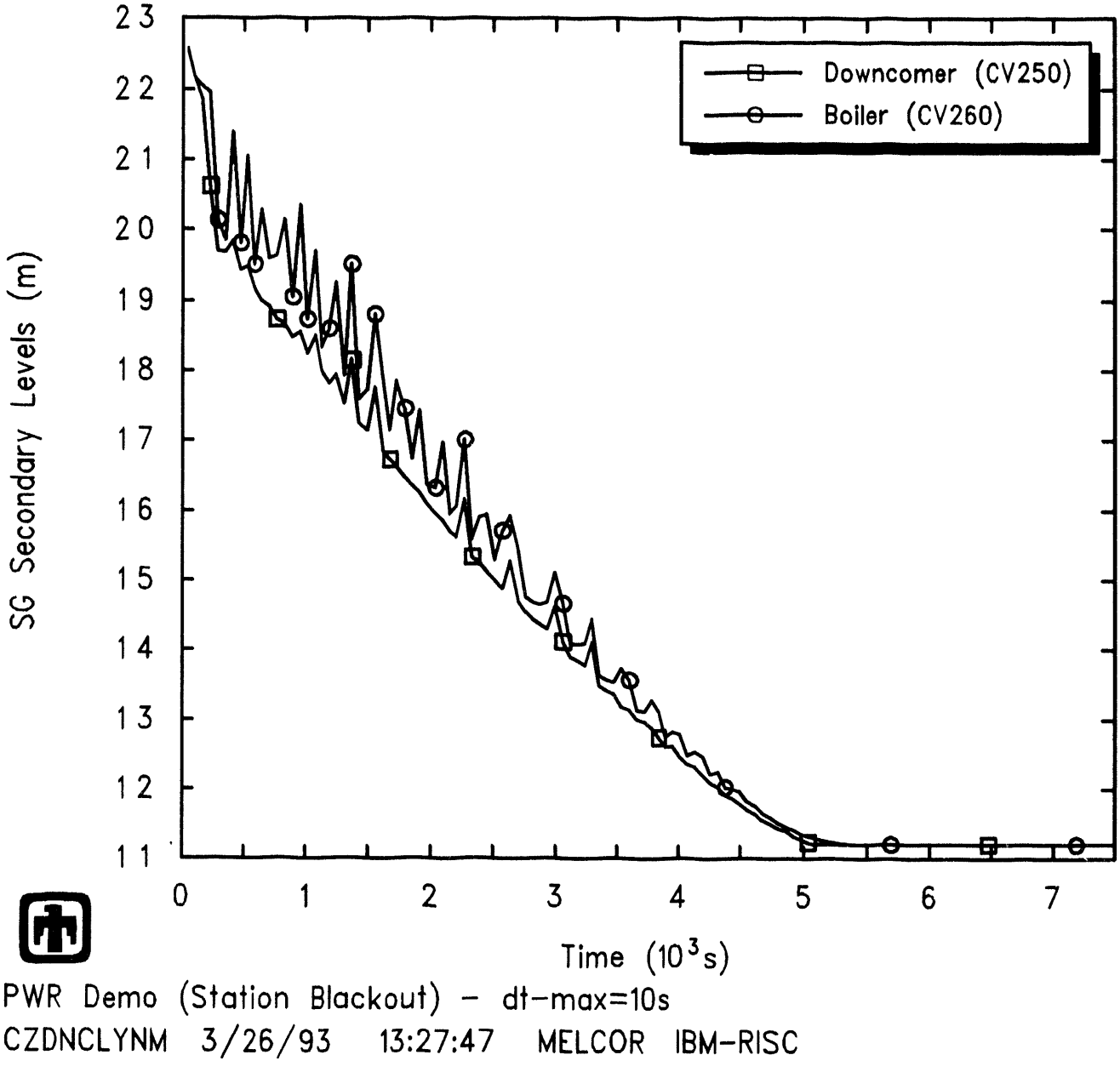

Figure 4.1.4. SG Secondary-Side Liquid Levels - MELCOR 1.8.2 Reference Calculation

at ~4000s (1.1hr), when the secondary system could no longer remove the decay heat quickly enough. At 5750s (1.6hr) the primary coolant pressure was sufficiently high to cause the PORV to open.

The water level in the pressurizer had been steadily increasing since secondary coolant boiloff, as illustrated in Figure 4.1.6. At about 5250s (1.46hr) the primary coolant pressure was sufficiently high to cause the PORV to open. As predicted earlier in the transient sequence for energy removal through the SG secondary-side relief valve, the pressurizer PORV cycled rapidly and often, as shown in Figure 4.1.7. Figure 4.1.8 presents the integral flow of liquid and vapor through the PORV calculated during this period, illustrating the discharge of primary coolant mass into the containment. Between around 6000s (1.7hr) and 8200s (2.3hr) water was ejected through the PORV. The increased voidage of the primary system due to the rapid loss of inventory during this liquid outflow (about 75% of the total primary system inventory lost out the PORV) brought the natural circulation around the primary system loop to an end at about 8000s (2.2hr), as shown in Figure 4.1.1. Although the pressurizer liquid level began to drop again after about 8200s (2.3hr), the pressurizer still had substantial liquid in it when vessel breach and RCS depressurization occurred at 11,200s (3.11hr).

Temperatures in several control volumes in the primary system are given in Figure 4.1.9. At early times, the calculated temperatures varied slightly in the various control volumes, with generally higher temperatures in the core, upper plenum, hot leg and pressurizer control volumes, as would be expected given heat generation in the core and removal first through the SG secondary and later through the pressurizer PORV. After the natural circulation flow stopped at about 8000s (2.2hr), the upper plenum began to heat up rapidly and substantially, until vessel failure was predicted to occur.

4.2 Core Damage

The loss of primary coolant though the PORV led to a progressive uncovery of the upper plenum and core. The liquid levels in the various control volumes representing the reactor vessel are given in Figure 4.2.1, showing the continuous level drop in the vessel; Figure 4.2.2 presents a closeup of the core elevations only. The top of the core was first uncovered at 7200s (2hr), after which time cooling of the core was reduced. The uncovery of the uppermost core elevations began even though the upper plenum still had substantial liquid (~45%) present. However, there was no substantial heatup of the core until after the upper plenum was void and a significant fraction (~30%) of the active-fuel length had been uncovered, after ~9000s (2.5hr). By 11,300s (3.14hr) the water level had fallen sufficiently to uncover the core completely.

After core uncovery, rapid temperature increases occurred in the uncovered regions (at around 0.5K/s for the inner two rings and about 0.33K/s for the outer ring). Figures 4.2.3 through 4.2.5 show the clad temperatures in the ten core axial levels modelled in the small, high-powered inner ring (with ~15% of the core area/volume), in the relatively large, middle ring (with ~60% of the total core area and volume), and in the low-powered

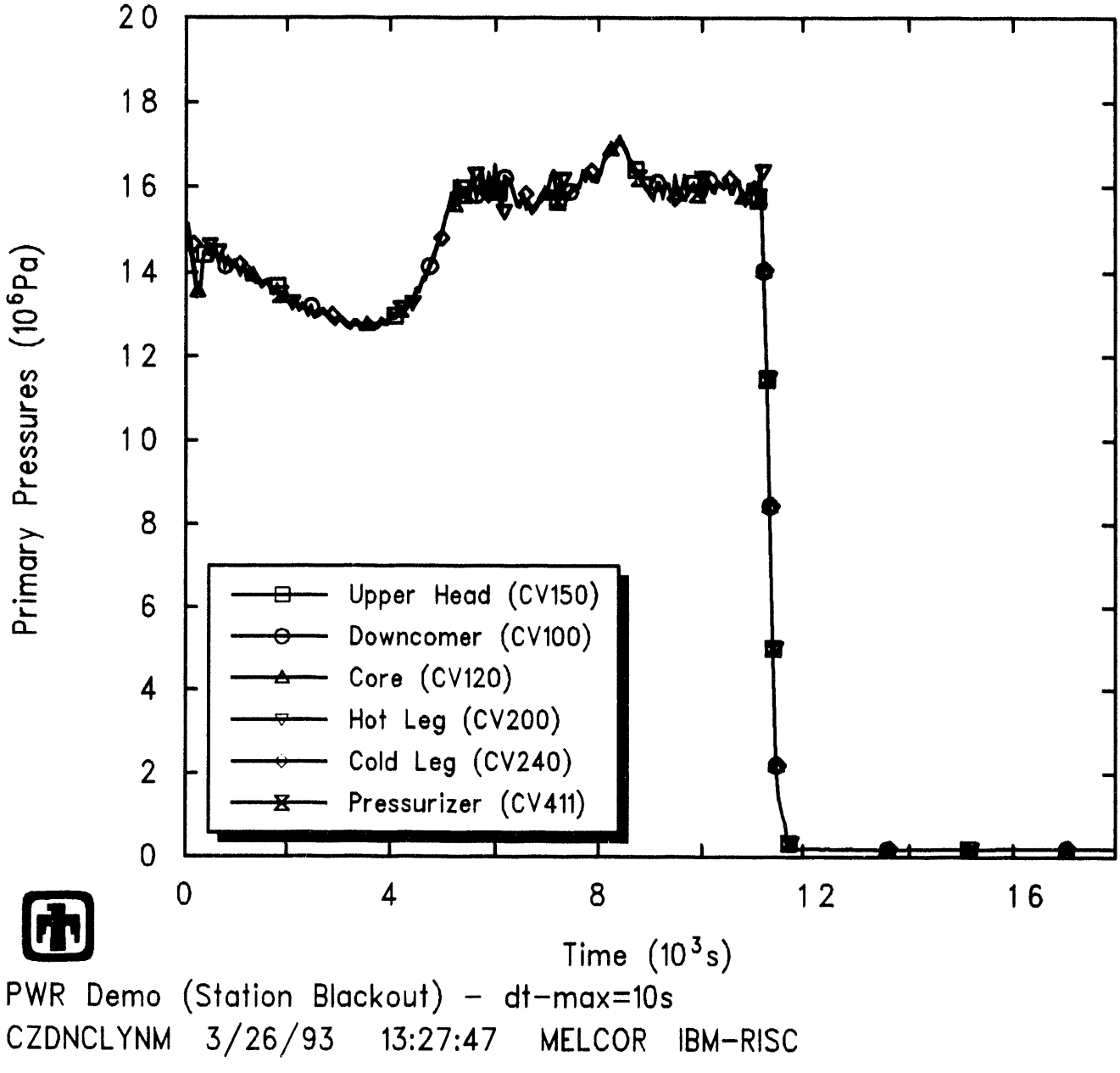

Figure 4.1.5. Primary System Pressure - MELCOR 1.8.2 Reference Calculation

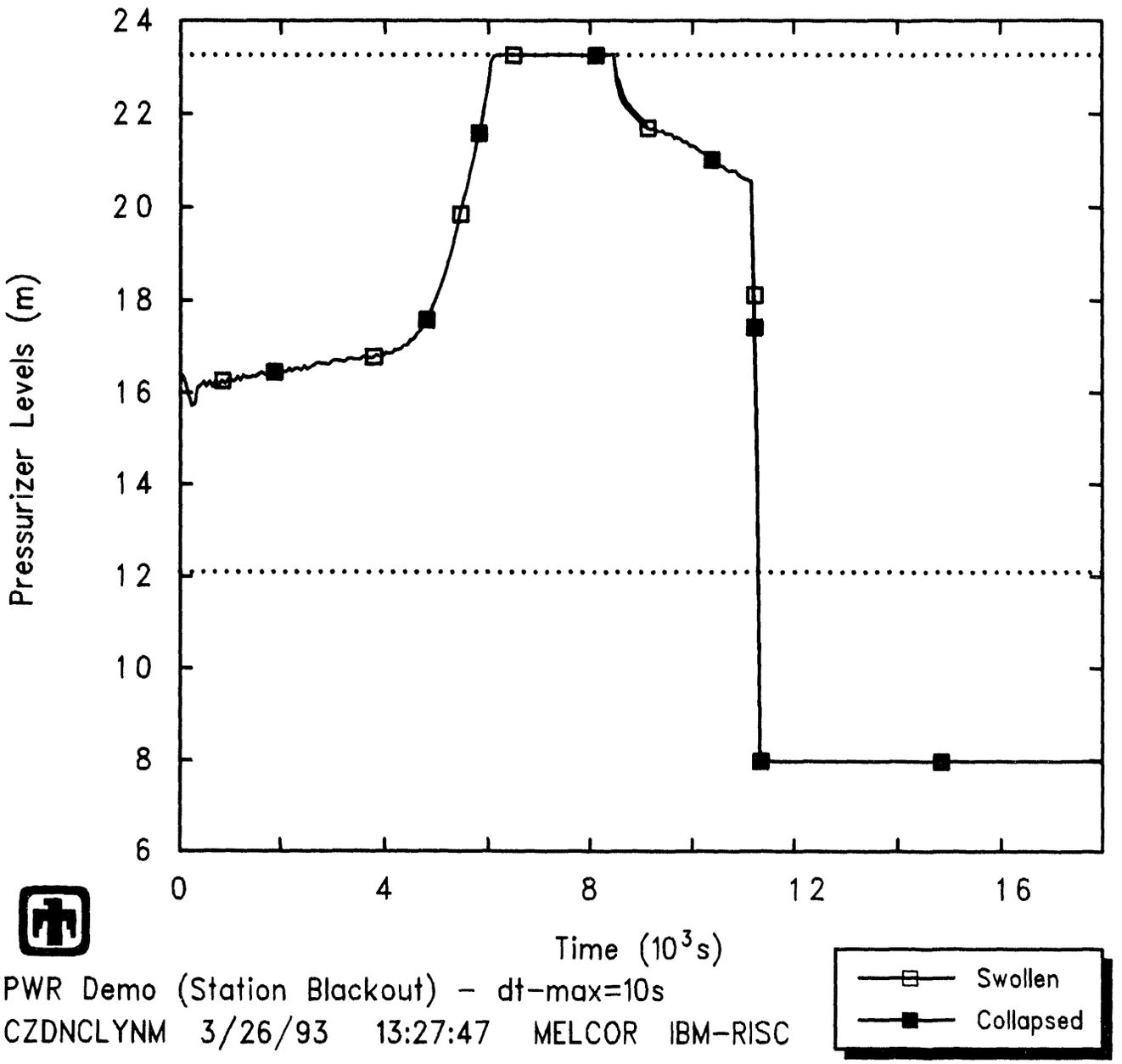

Figure 4.1.6. Pressurizer Liquid Level – MELCOR 1.8.2 Reference Calculation

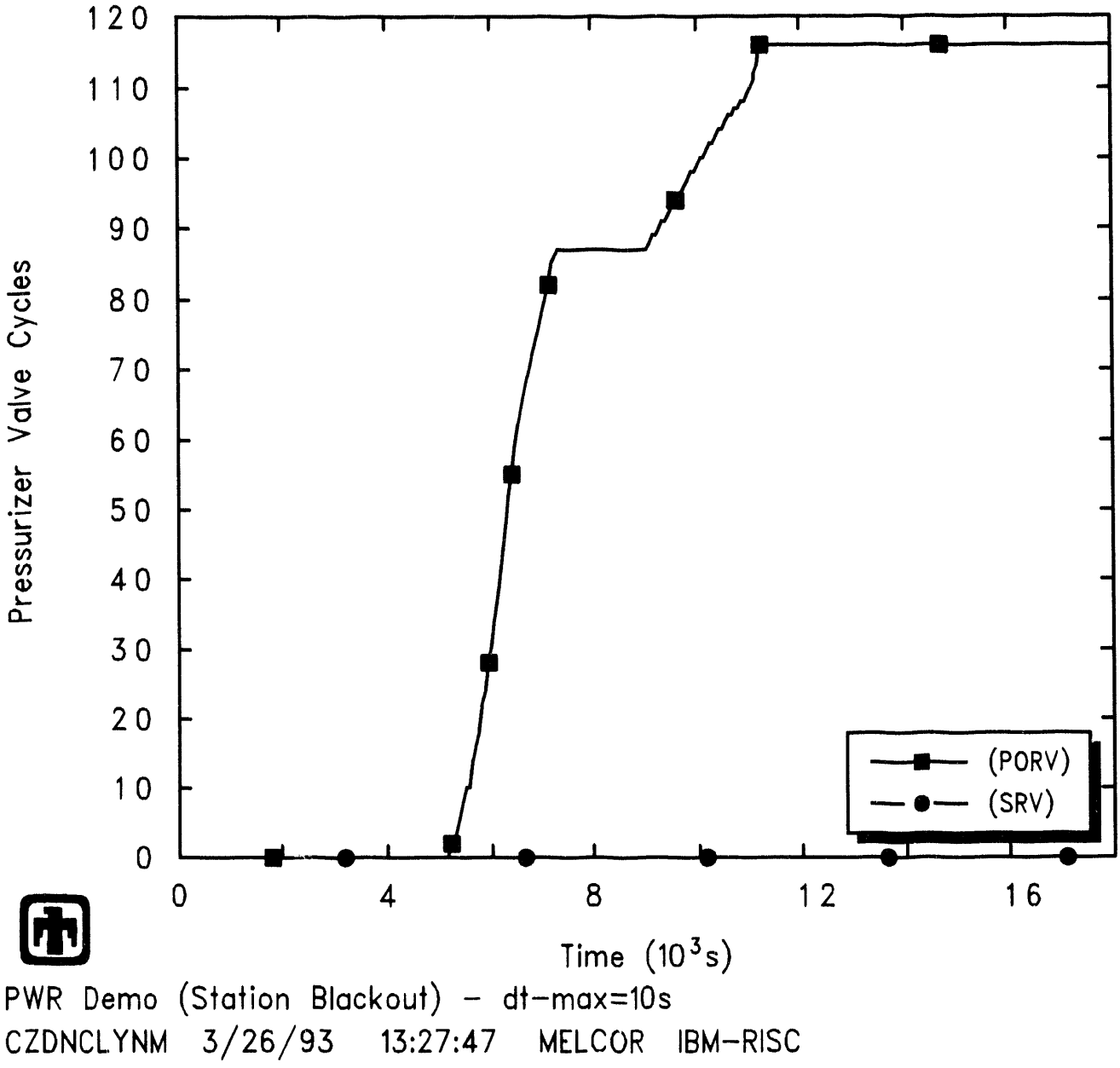

Figure 4.1.7. Pressurizer PORV Cycling - MELCOR 1.8.2 Reference Calculation

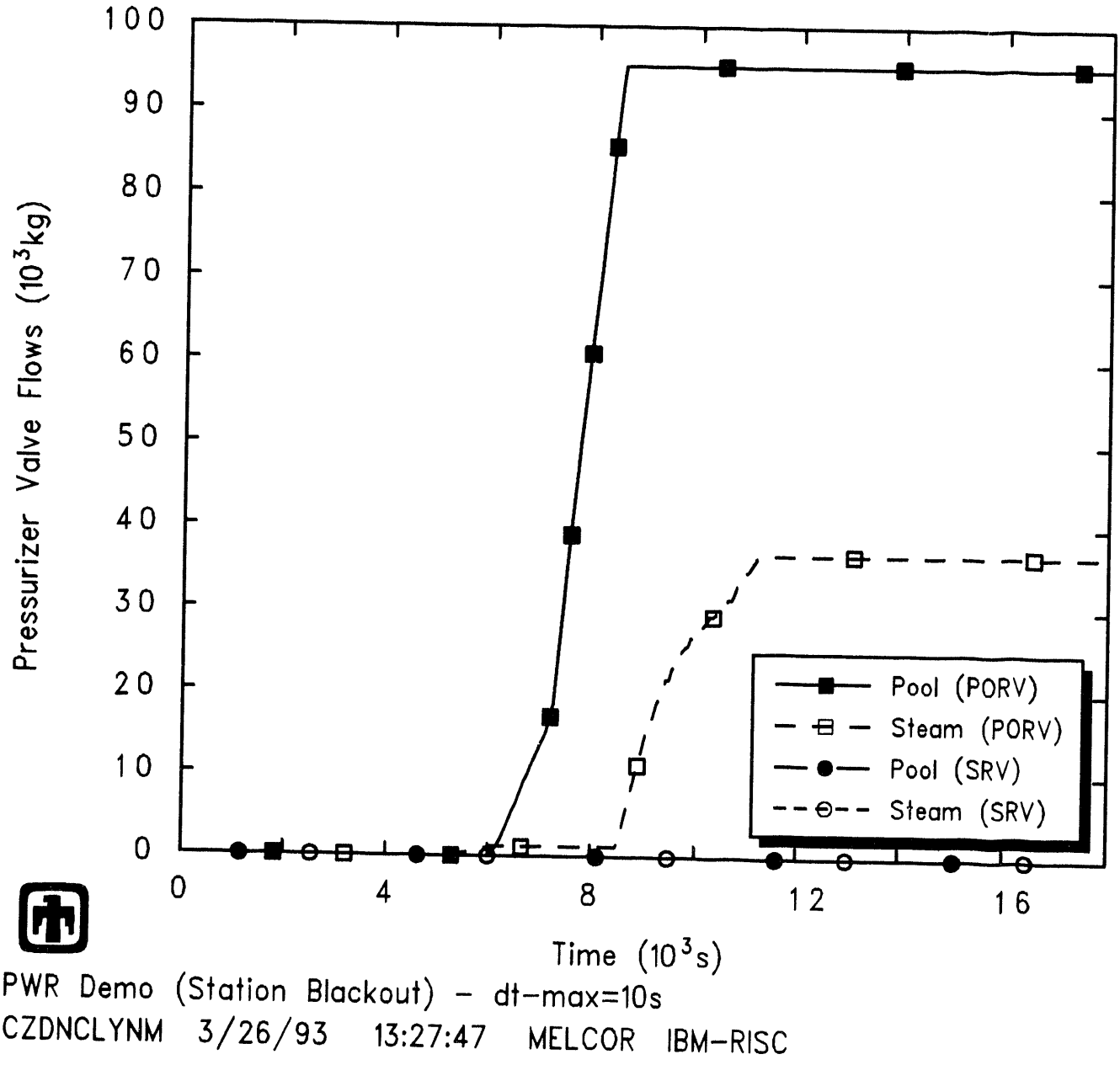

Figure 4.1.8. Pressurizer PORV Integral Flows - MELCOR 1.8.2 Reference Calculation

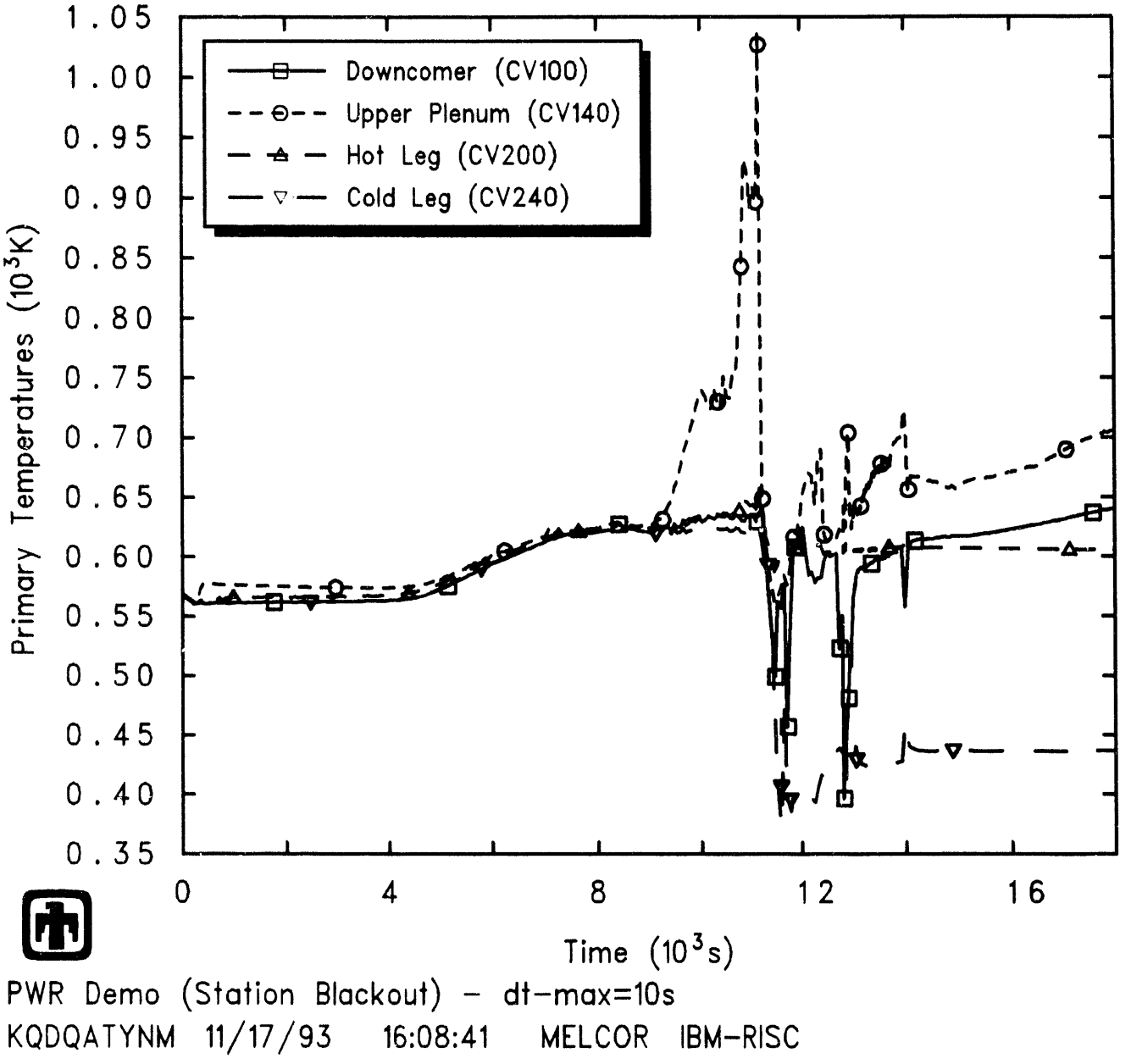

Figure 4.1.9. Primary System Temperatures - MELCOR 1.8.2 Reference Calculation

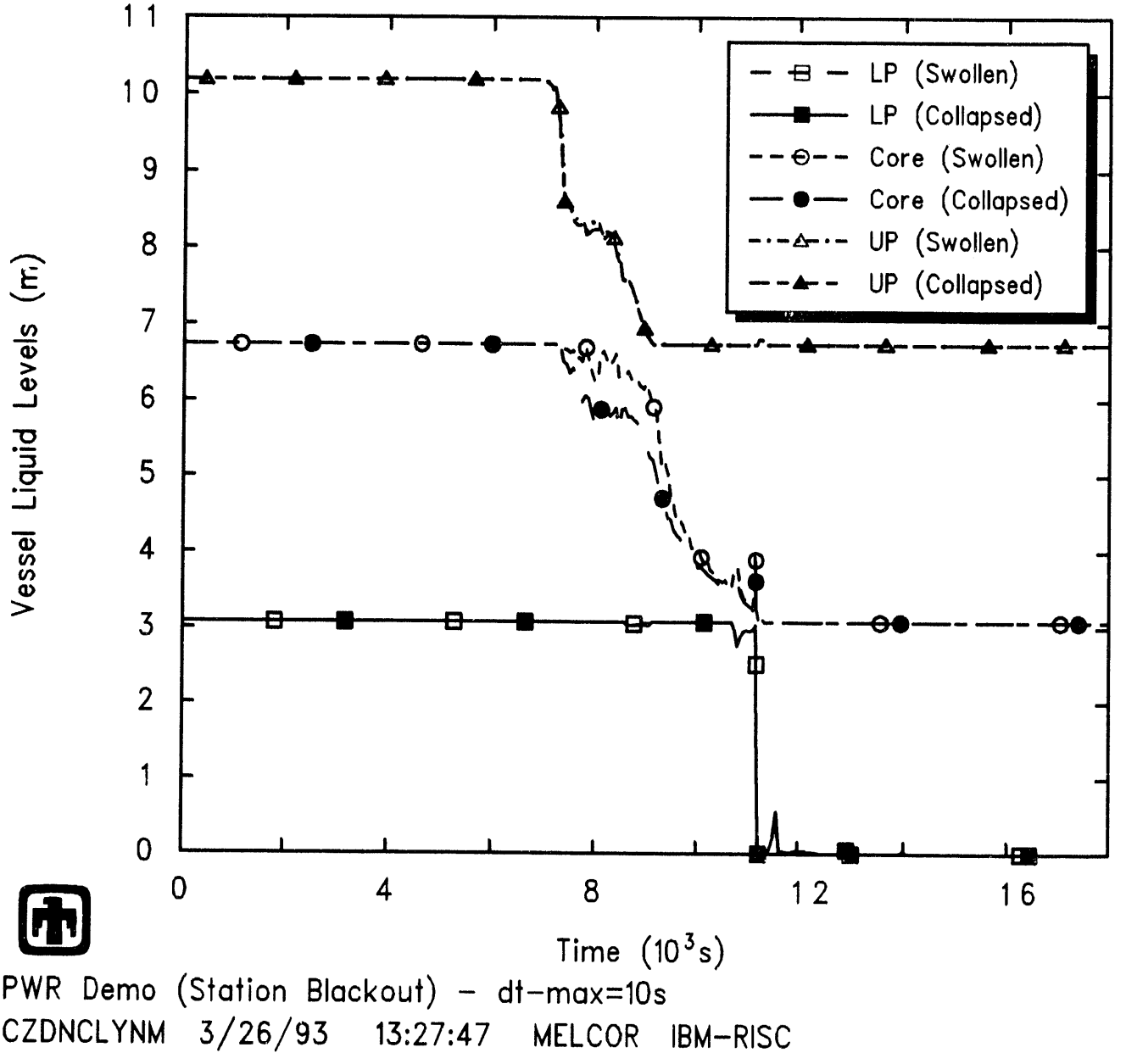

Figure 4.2.1. Vessel Liquid Levels - MELCOR 1.8.2 Reference Calculation

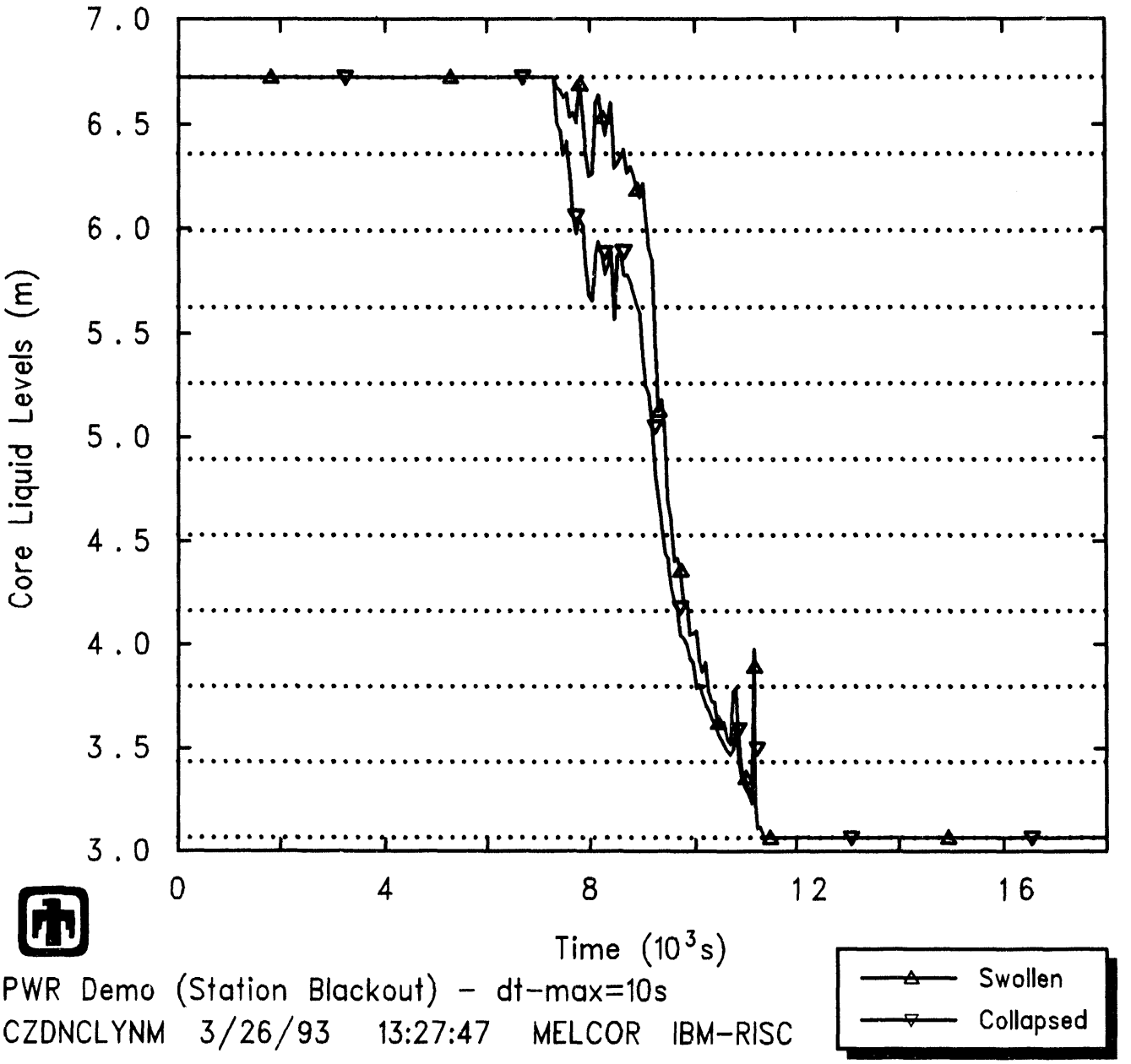

Figure 4.2.2. Core Liquid Levels – MELCOR 1.8.2 Reference Calculation

outer ring (with ~25% of the core area/volume). The upper axial levels heated up first because they were uncovered first; the inner two rings heated up faster because of their higher peaking factors.

The material in the innermost, highest-powered ring heated up without interruption through material melt and relocation to core plate heatup and failure. When the core plate first failed (at 11,178s or 3.10hr in the first ring), the falling debris fell into a water pool in the lower plenum. Although most of that water was ejected to the cavity through the almost-immediate lower head penetration failure, some of the water was boiled off by the hot core debris. The steam generated flowed upward through the core and temporarily significantly increased the steam cooling of the material remaining in the core region. This is visible in the temperature declines after about 11,200s (3.11hr) in Figures 4.2.4 and 4.2.5. Most of the intact material left in the core was cooled to <1000K before the interrupted heatup was resumed. This delayed the failure of the core plate in the other two rings, and delayed relocation of core material debris from these rings to the lower plenum and then to the cavity.

Zircaloy oxidation occurred beginning at around 10,000s, as indicated by the in-vessel production of hydrogen illustrated in Figure 4.2.6. No other noncondensable gases were generated in the core.

Core support plate temperatures are presented in Figure 4.2.7. The core support plate in the inner ring failed totally at 11,178s (3.10hr), allowing particulate debris to fall through into the lower plenum. Figures 4.2.8 and 4.2.9 present the temperature and mass of debris in the first core axial level, the lowest lower plenum level. The lower head surface and penetration temperatures are presented in Figure 4.2.10. The temperature of the lower head penetration in the inner ring quickly rose well above the weld failure temperature of 1273K. The weld failed and vessel breach occurred at 11,219s (3.12hr). The core support plate and vessel penetrations in rings 2 and 3 failed later, with a much longer delay (~1000s) between core plate and penetration failure. This was largely a result of the new debris radial relocation model allowing debris formed in the second and third rings to move laterally to the first, failed ring and fall through the failed core plate and lower head penetration in the first ring.

The calculated core state at vessel failure (*i.e.*, at 11,219.3s or 3.12hr) is illustrated in Figure 4.2.11. The various materials in the MELCOR "fuel/clad" component just prior to vessel failure, both any intact materials remaining in their original position and candled, refrozen conglomerate debris materials, are shown in the upper plot for the three radial rings in the MELCOR Surry core model the lower plot depicts the materials calculated to be in the "particulate debris" component in the three core rings at the same time. The various materials in the MELCOR "other-structure" component just prior to vessel failure are not shown; that plot is dominated by the structural steel still in place in the lower plenum. (Refer to [1] for an explanation of these MELCOR components, if necessary.) The "elevation" used as the ordinate in Figure 4.2.11 is the same as the core level elevations shown in Figure 3.3, with the core support plate at ≥3m, the lower plenum between 0 and ~3m, and the active fuel region from ≥3m to ~6.722m. The fraction of each core cell occupied by any given material is shown. However, although

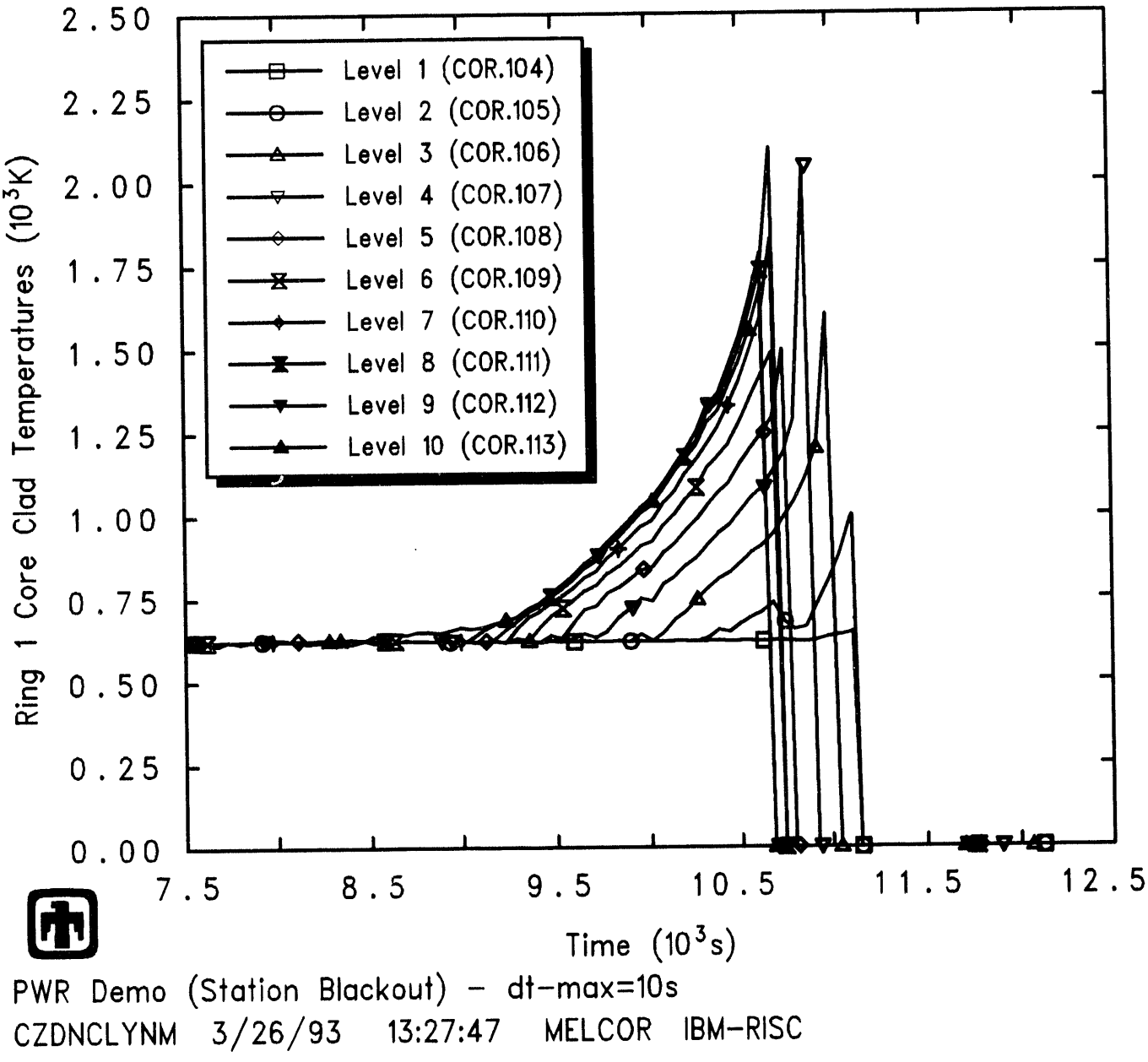

Figure 4.2.3. Core Ring 1 Clad Temperatures – MELCOR 1.8.2 Reference Calculation

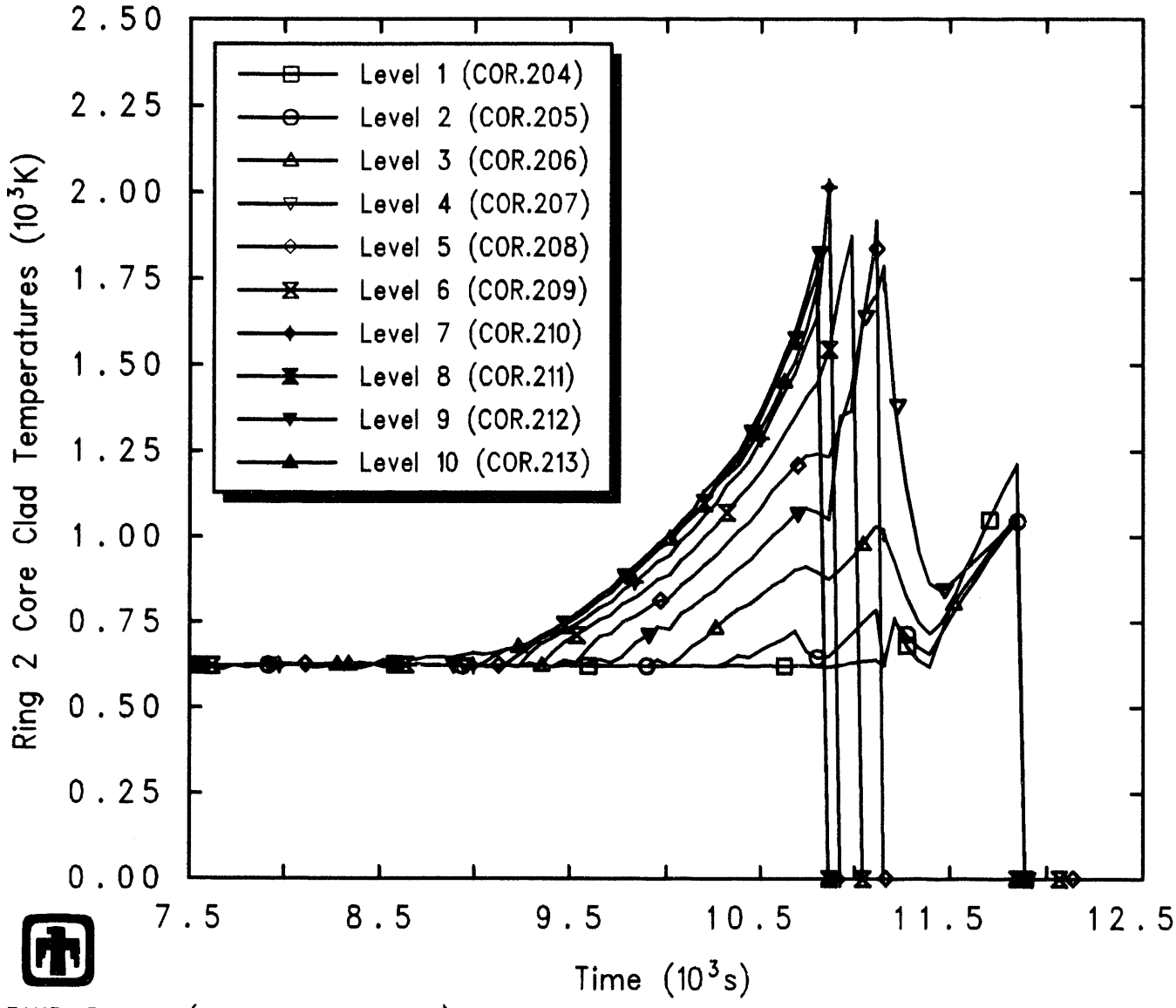

Figure 4.2.4. Core Ring 2 Clad Temperatures - MELCOR 1.8.2 Reference Calculation

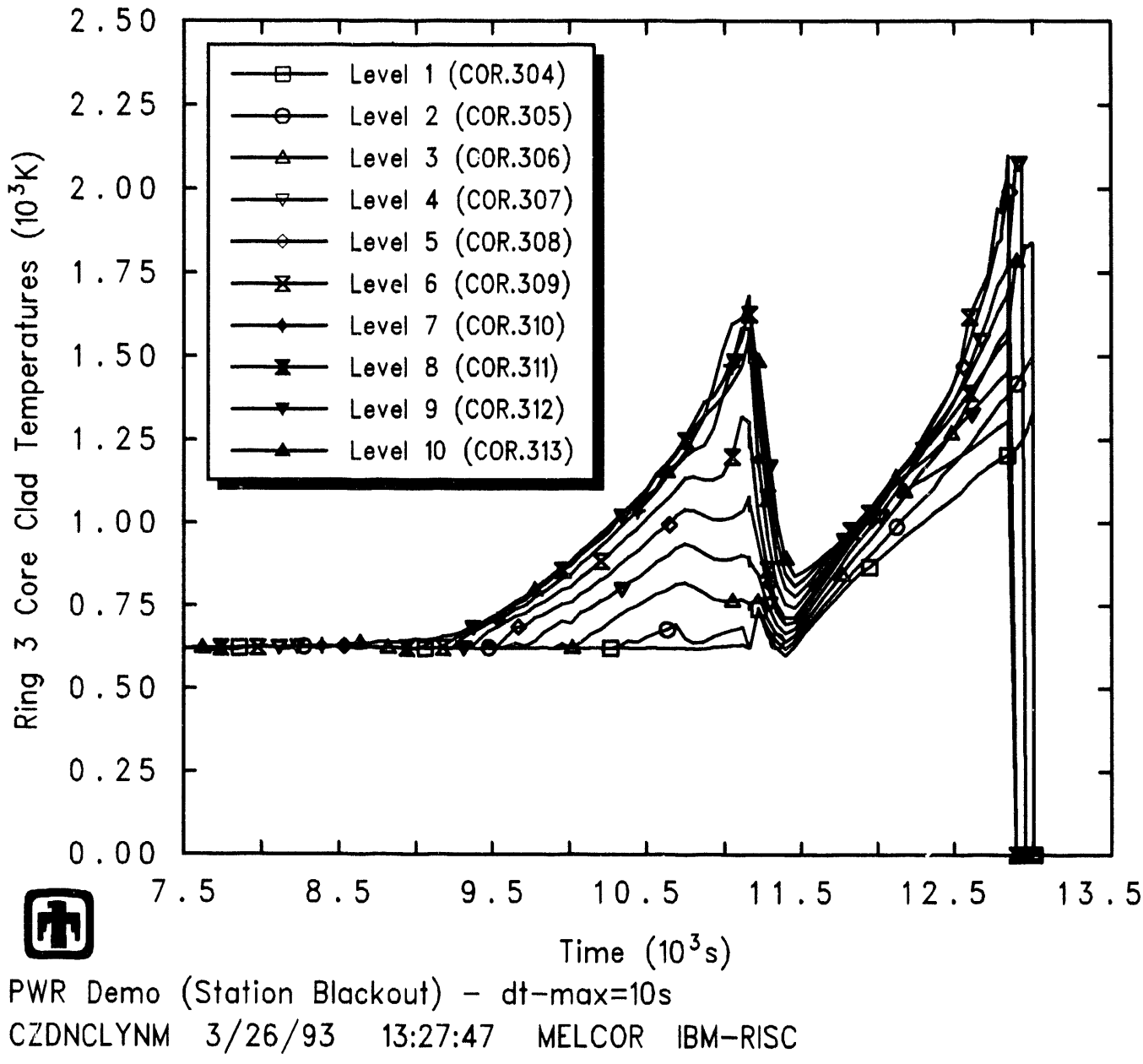

Figure 4.2.5. Core Ring 3 Clad Temperatures – MELCOR 1.8.2 Reference Calculation

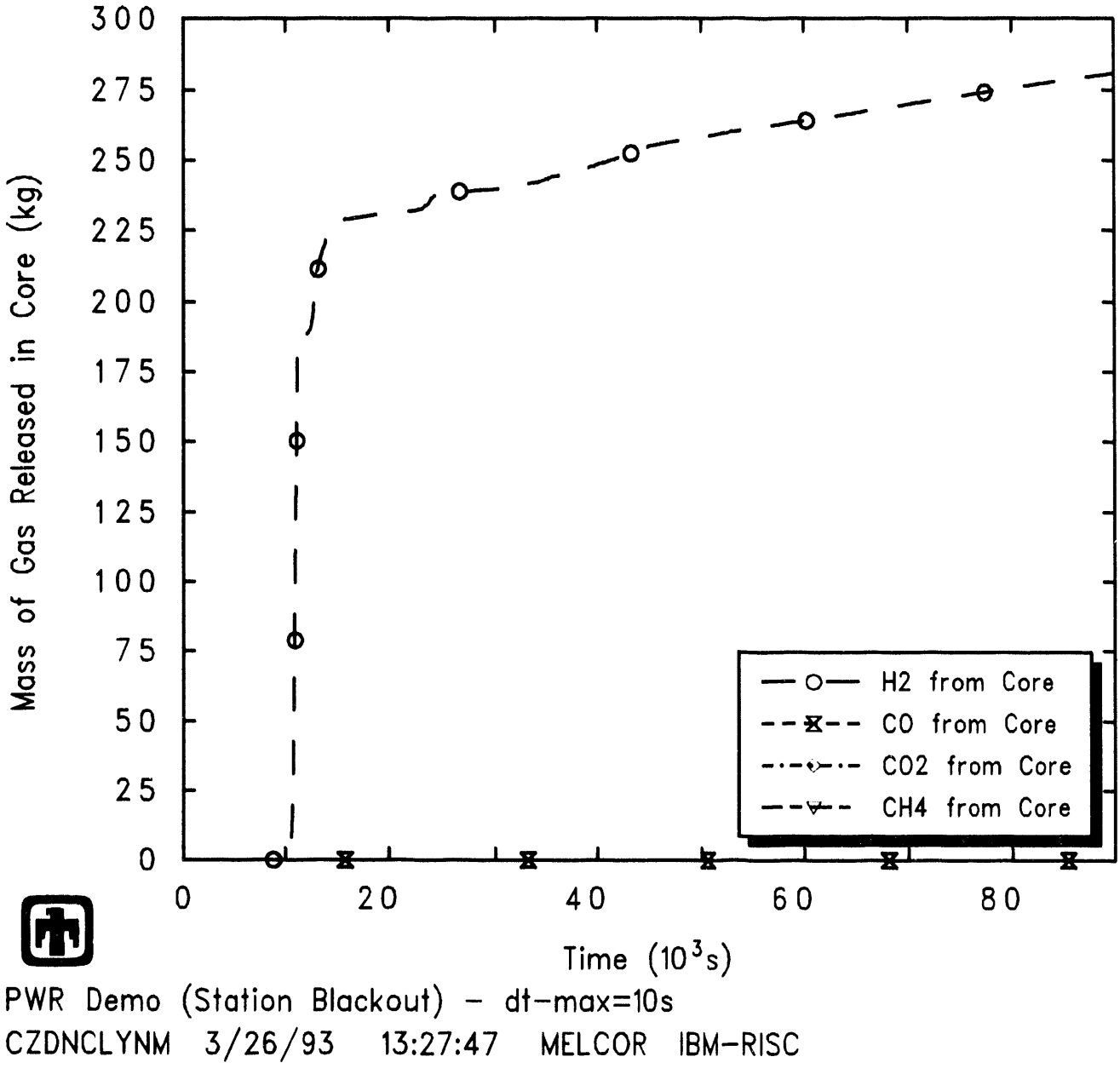

Figure 4.2.6. In-Vessel Hydrogen Production – MELCOR 1.8.2 Reference Calculation

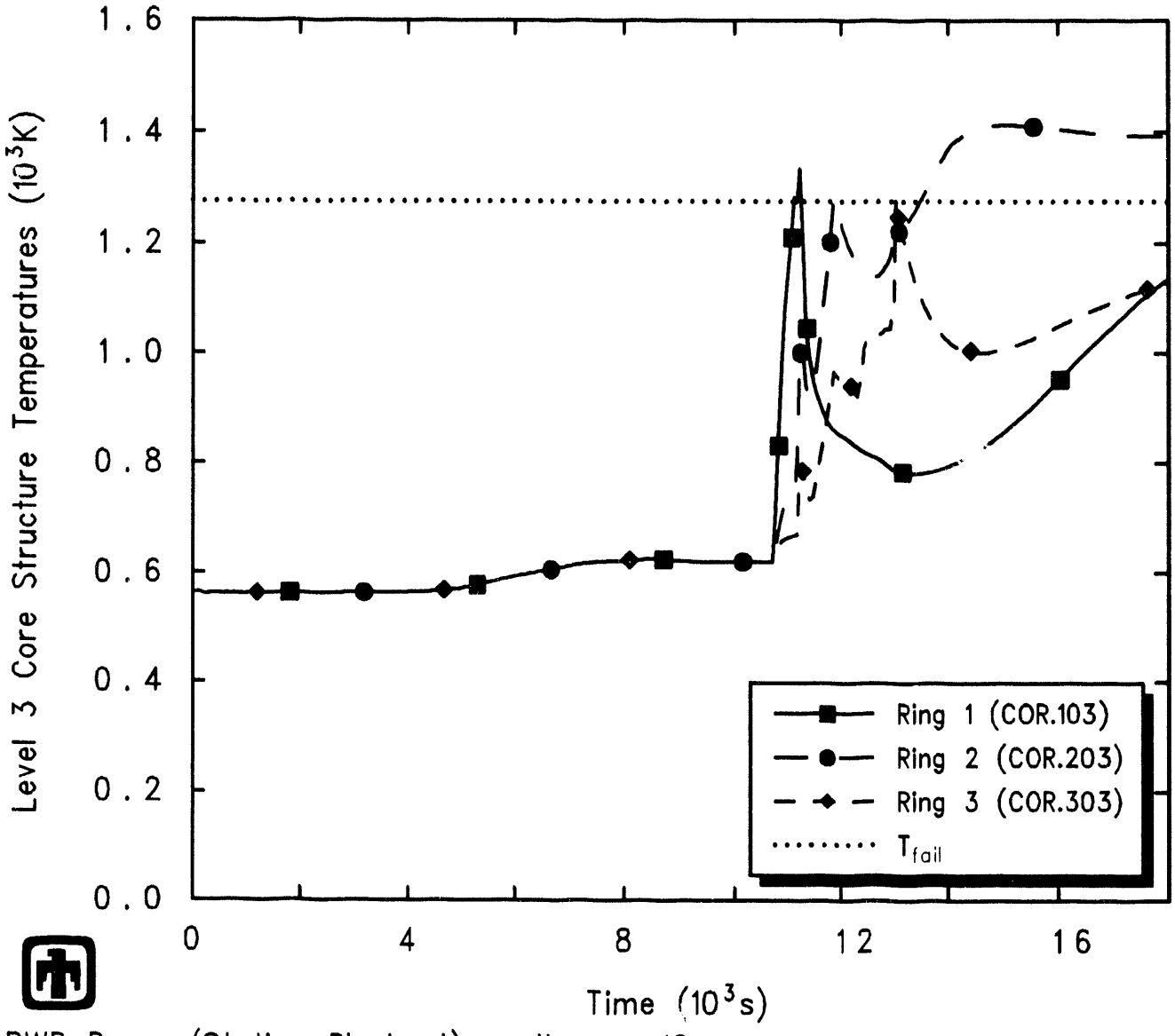

Figure 4.2.7. Core Support Plate Temperatures – MELCOR 1.8.2 Reference Calculation

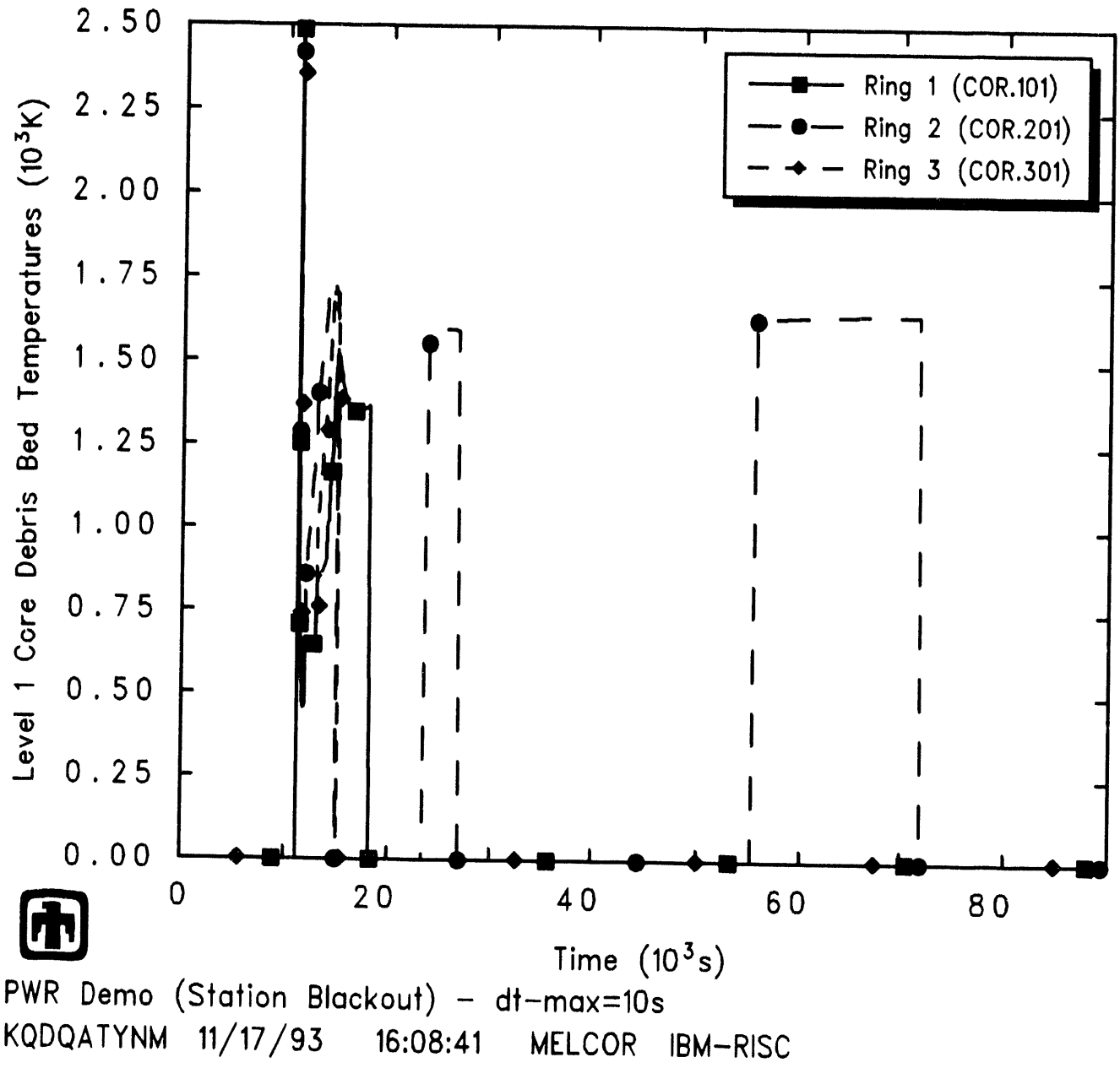

Figure 4.2.8. Lower Plenum Core Debris Temperatures – MELCOR 1.8.2 Reference Calculation

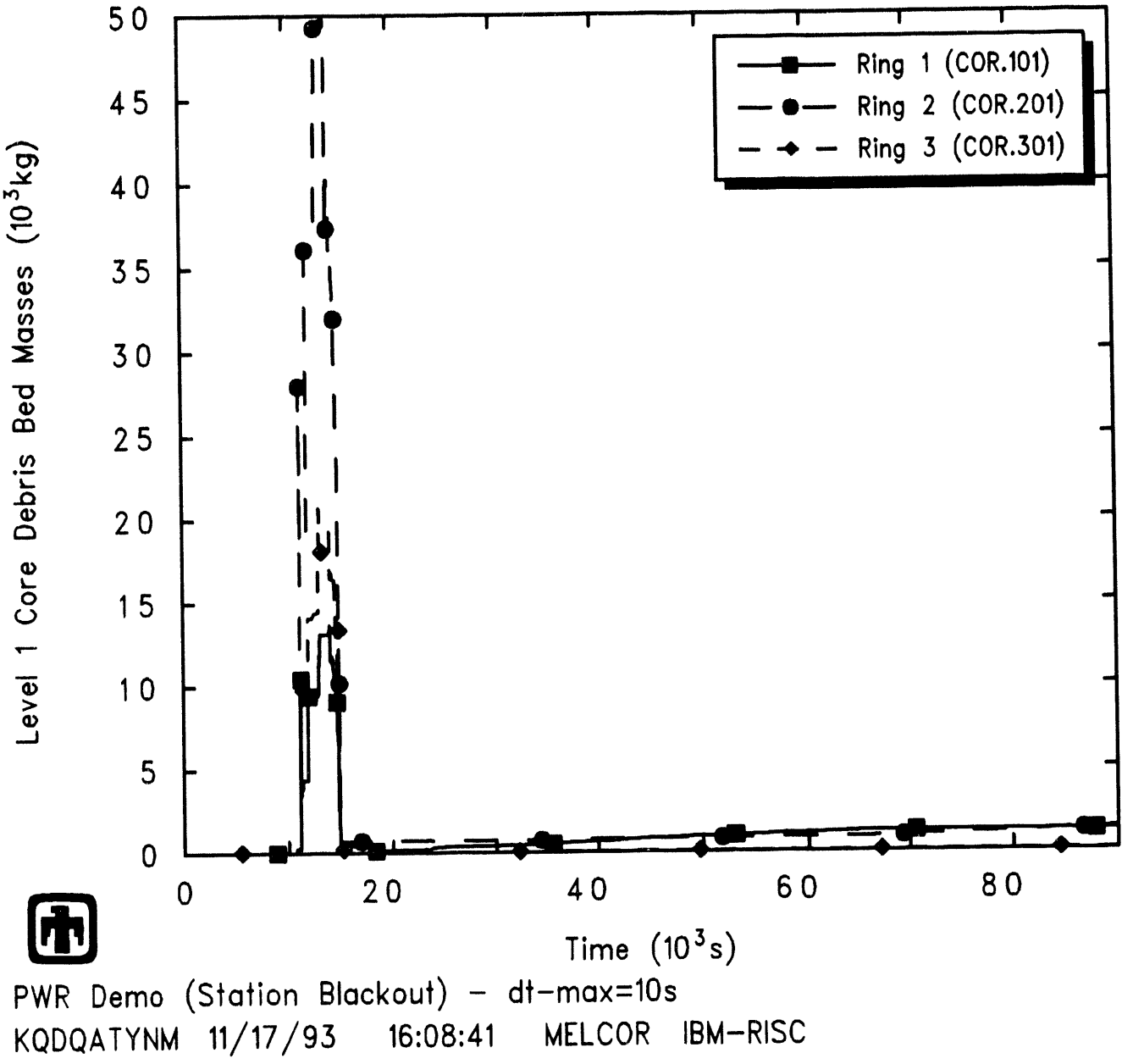

Figure 4.2.9. Lower Plenum Core Debris Masses – MELCOR 1.8.2 Reference Calculation

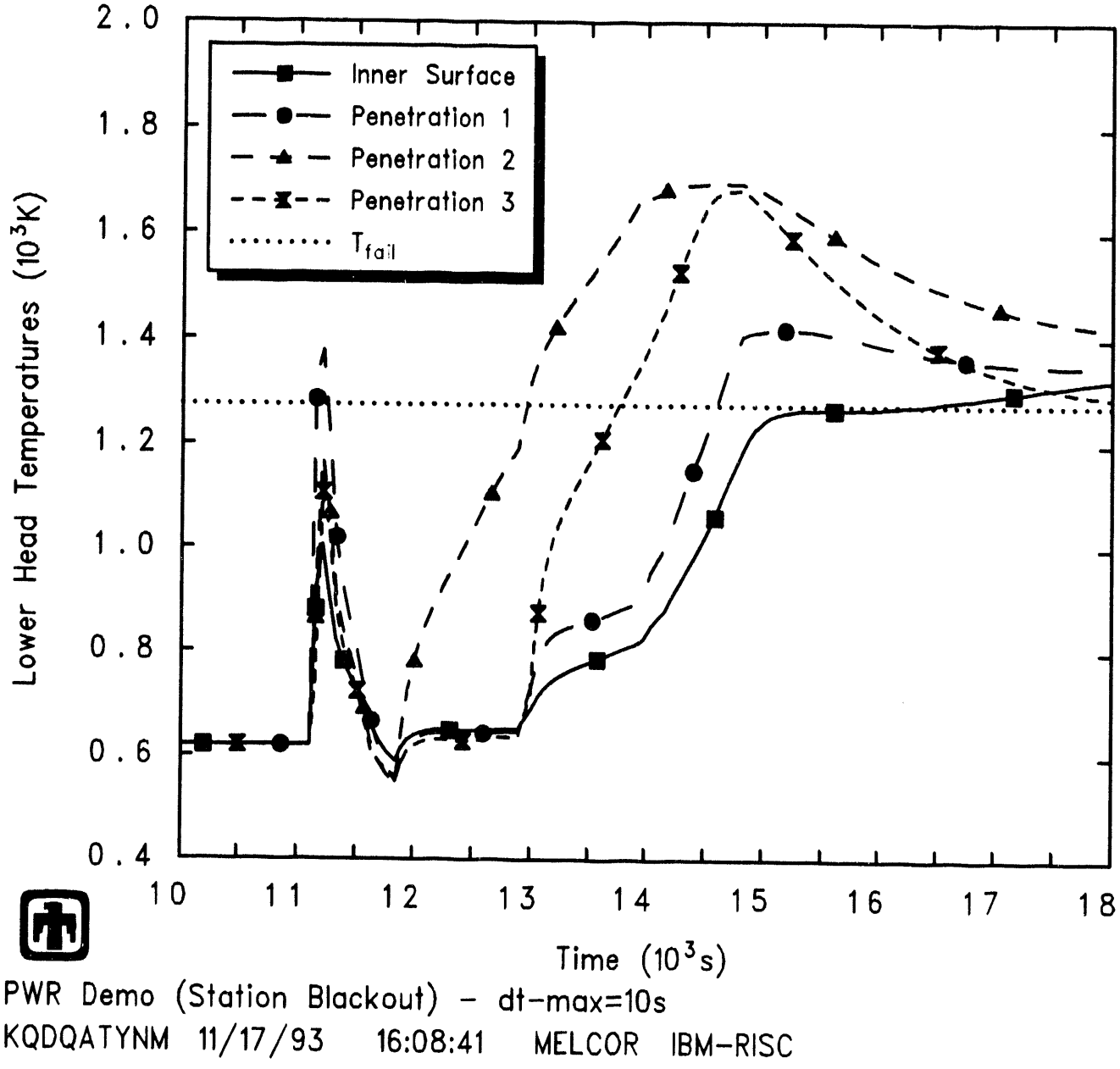

Figure 4.2.10. Lower Head Penetration Temperatures - MELCOR 1.8.2 Reference Calculation

each ring is shown as equal, recall that the core cells are not equal in the three rings modelled; the innermost, high-powered ring includes ~15% of the core, the middle ring contains ~60% of the core, and the outermost, low-power ring includes the remaining ~25% of the core.

The innermost ring had no intact structure in the active fuel region at all at the time of vessel failure, but there is a substantial debris bed visible in the lower plenum. About half of the intact material remained in the active fuel region in the second ring, with those intact materials together with the core plate supporting a small amount of particulate debris in the active fuel region in the middle ring; in addition, a substantial debris bed was found in the lower plenum in the second ring as well as in the first ring. Almost all of the intact material remained in place in the active fuel region in the third ring; there was very little particulate debris retained in the active fuel region in the third ring, but again a substantial debris bed in the lower plenum.

Table 4.2.1 summarizes the state of the various materials in the core active fuel region, core plate and lower plenum at the time a lower head penetration first fails (*i.e.*, at vessel breach). Masses of intact components and of debris components are given for each region. The fraction of debris molten in each region was estimated from the average debris temperature, which in this case resulted in assuming that Zircaloy, steel, steel oxide and control rod poison in the debris are molten and that UO_2 and ZrO_2 in the debris are solid (*i.e.*, neglecting eutectics mixtures; this assumption is forced by the MELCOR output available to the analyst). Also given is the fraction of material relocated. This is generally larger than the fraction molten because material can melt and relocate, and then subsequently refreeze or quench; also, UO_2 fuel usually relocates as a solid, after clad collapse but before fuel melt.

Figure 4.2.12 shows the total masses of core materials (UO_2, Zircaloy and zirc oxide, stainless steel and steel oxide, and control rod poison) remaining in the vessel. Debris ejection began immediately after lower head failure, and it took on the order of 5000s to transfer the majority of the core material from the vessel to the cavity. All the UO_2 was transferred to the cavity, as was most of the unoxidized zircaloy, the oxides and the control rod poison; however, much of the structural steel in the lower plenum was predicted to remain unmelted and in place even after vessel breach.

At vessel failure, the pressure of the primary system fell very rapidly, causing the accumulators to deliver 88m^3 of borated water to the core almost instantaneously. That water flowed through the vessel breach into the cavity, together with any water in the lower plenum not flashed by contact with the hot debris.

4.3 Cavity Response

The mass of core debris in the cavity, the mass of ablated concrete, the mass of gas produced, and the total mass of debris (including core debris together with ablated and reacted concrete) are presented in Figure 4.3.1. Before about 24,000s (6.7hr), the debris in the cavity was primarily debris ejected from the vessel; after ~24,000s (6.7hr)

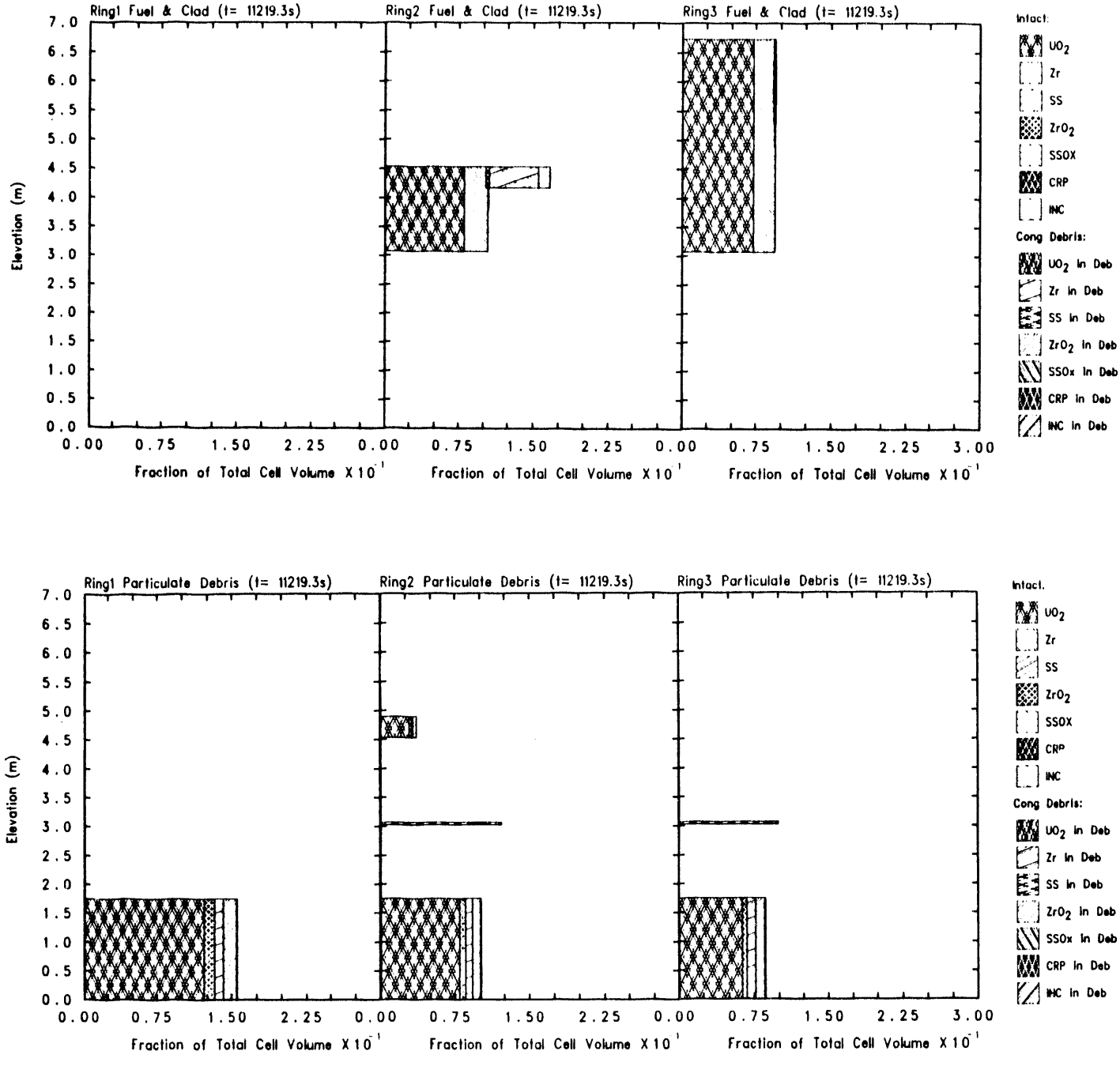

Figure 4.2.11. Core Fuel/Clad (top) and Particulate Debris (bottom) Component Materials at Vessel Failure – MELCOR 1.8.2 Reference Calculation

Table 4.2.1. Core State at Vessel Failure MELCOR 1.8.2 Reference Calculation

	Intact	Debris
Active Fuel Region Masses (kg)		
UO_2	38,250	1,759
Zircaloy	9,445	56
Zirc Oxide	694	217
Steel	267	0
Steel Oxide	35	0
CRP	1,672	0
Total	50,362	2,032
Core Plate Masses (kg)		
UO_2		953
Zircaloy		51
Zirc Oxide		98
Steel	1,815	4
Steel Oxide		12
CRP		0
Total	1,815	1,118
Lower Plenum Masses (kg)		
UO_2		39,751
Zircaloy		2,450
Zirc Oxide		4,486
Steel	32,655	96
Steel Oxide	6	78
CRP		334
Total	32,661	47,195
Average Debris Temperature (K)		
Active Fuel Region		~2570
Core Plate		~2290
Lower Plenum		~2450
Fraction Debris Molten		
Active Fuel Region		~4%
Core Plate		~6%
Lower Plenum		~6%
Fraction Material Relocated	~50%	
Fraction Oxidized	Zircaloy	Steel
	~30%	~0.3%

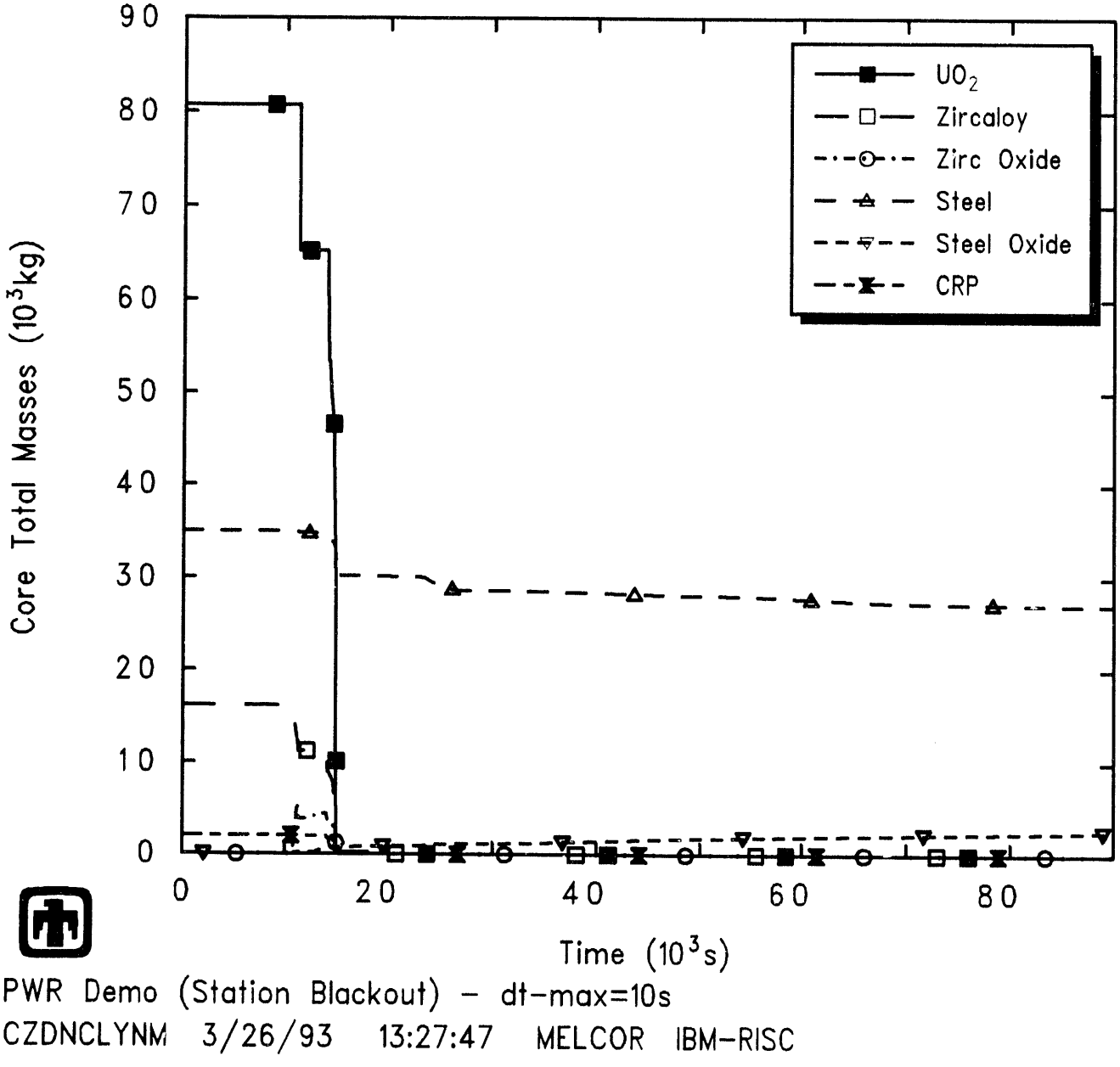

Figure 4.2.12. Total Core Masses - MELCOR 1.8.2 Reference Calculation

significant core-concrete interaction began and substantial masses of ablated and reacted concrete were added to the total cavity debris.

Figure 4.3.2 shows the thicknesses of the light oxide, metallic and heavy oxide debris layers in the cavity. At around 24,000s (6.7hr) a CORCON layer flip occurred, switching from an initial configuration with a metallic debris layer above a heavy oxide layer to a later configuration with a light oxide layer above a metallic debris layer. This layer flip occurred when enough concrete had been ablated (with its resultant low-density silicate oxides) to dilute the high-density zirc oxide and steel oxide debris to an average density value less than the metallic debris density.

Figure 4.3.3 presents the cavity debris layer temperatures. The heat transfer from the cavity debris pool downward and outward to the concrete surface, and upward to the cavity volume atmosphere, are shown in Figure 4.3.4. The layer flip resulted in greatly increased heat transfer from the melt to the concrete, for a short period of time. Figure 4.3.5 gives the maximum cavity depth and radius. The relocation of the metallic layer to the bottom of the cavity caused an increase in the rate of ablation vertically downward and halted further radial ablation. The heat generated by chemical reactions within the cavity also increased dramatically at this point.

As soon as significant core-concrete interaction began, so did production of carbon dioxide and water vapor; reduction of these gases by the molten metal also gave rise to carbon monoxide and hydrogen. Figure 4.3.6 illustrates the production of various gases in the cavity due to core-concrete interaction. While H_2O, CO and CO_2 were all generated in the cavity through various chemical reactions, most (~80%) of the in-cavity gas produced was hydrogen, and the amount of hydrogen produced in the cavity during core-concrete interaction was substantially larger than the amount of hydrogen produced in-vessel (~98% and ~2%, respectively).

Hydrogen deflagrations were predicted to occur only in the cavity. Figure 4.3.7 shows the number of hydrogen burns in the cavity; a large number of deflagrations occurred in two distinct intervals, with a single burn occurring at an intermediate and widely-separated time. The effect of these on the concentration of flammable gases in the cavity is shown in Figure 4.3.8. The rapid fluctuations in cavity atmosphere composition in Figure 4.3.8, reflecting a large number hydrogen combustion events between ~33,000s (9.2hr) and ~45,000s (12.5hr), are also visible as increased oscillations in the cavity surface heat loss, presented in Figure 4.3.4.

Heat from the core debris also began to boil off the overlying water pool drained from the primary coolant system and the accumulators, as shown by the cavity liquid level in Figure 4.3.9. By about 30,000s (8.3hr) the water in the cavity had all boiled off.

4.4 Containment Thermal/Hydraulics

The atmospheric pressure for each of the control volumes making up the containment is shown in Figure 4.4.1. During normal operation, the Surry-1 containment is maintained at a pressure of 68.5kPa. After the station blackout initiation, the pressure climbed only

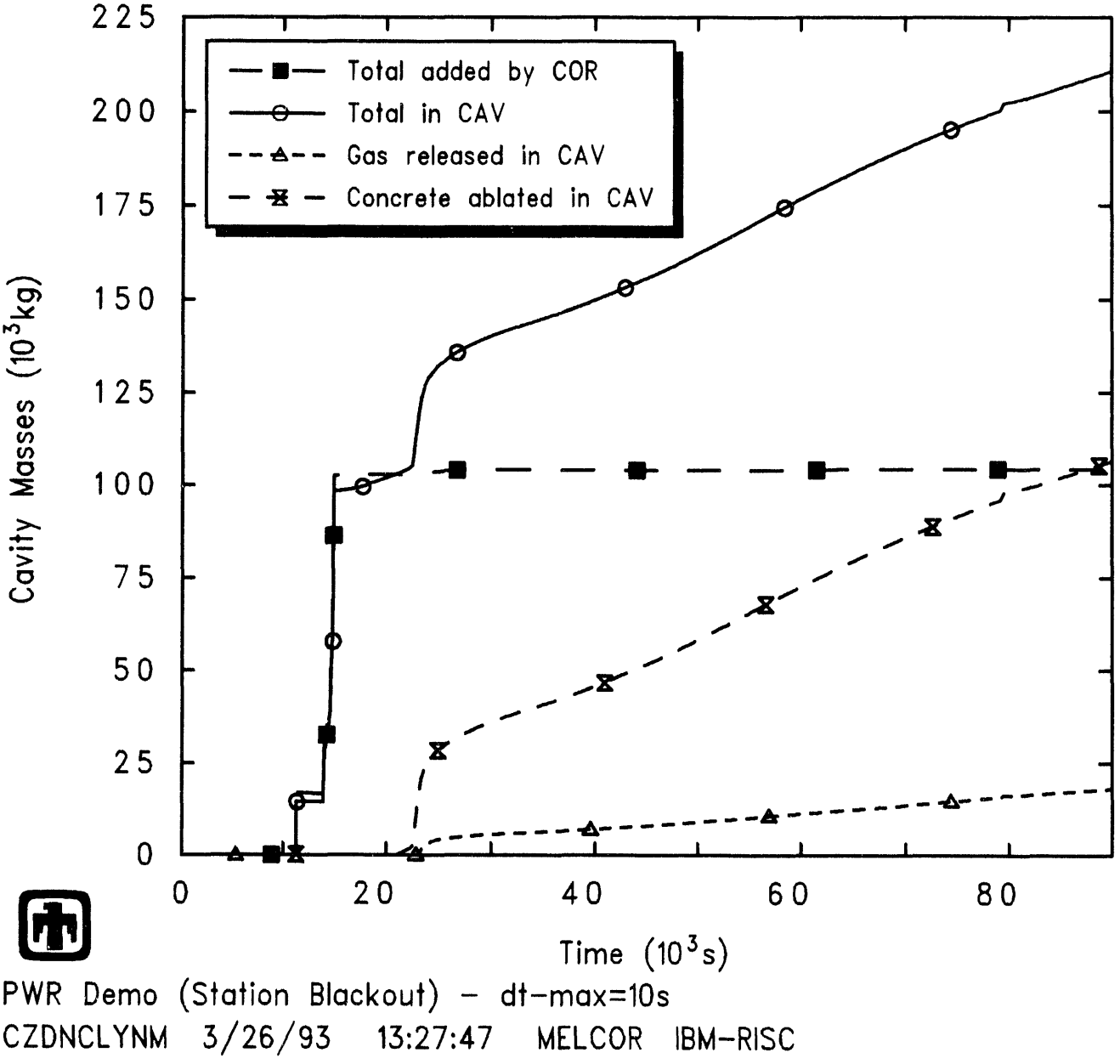

Figure 4.3.1. Total Cavity Masses - MELCOR 1.8.2 Reference Calculation

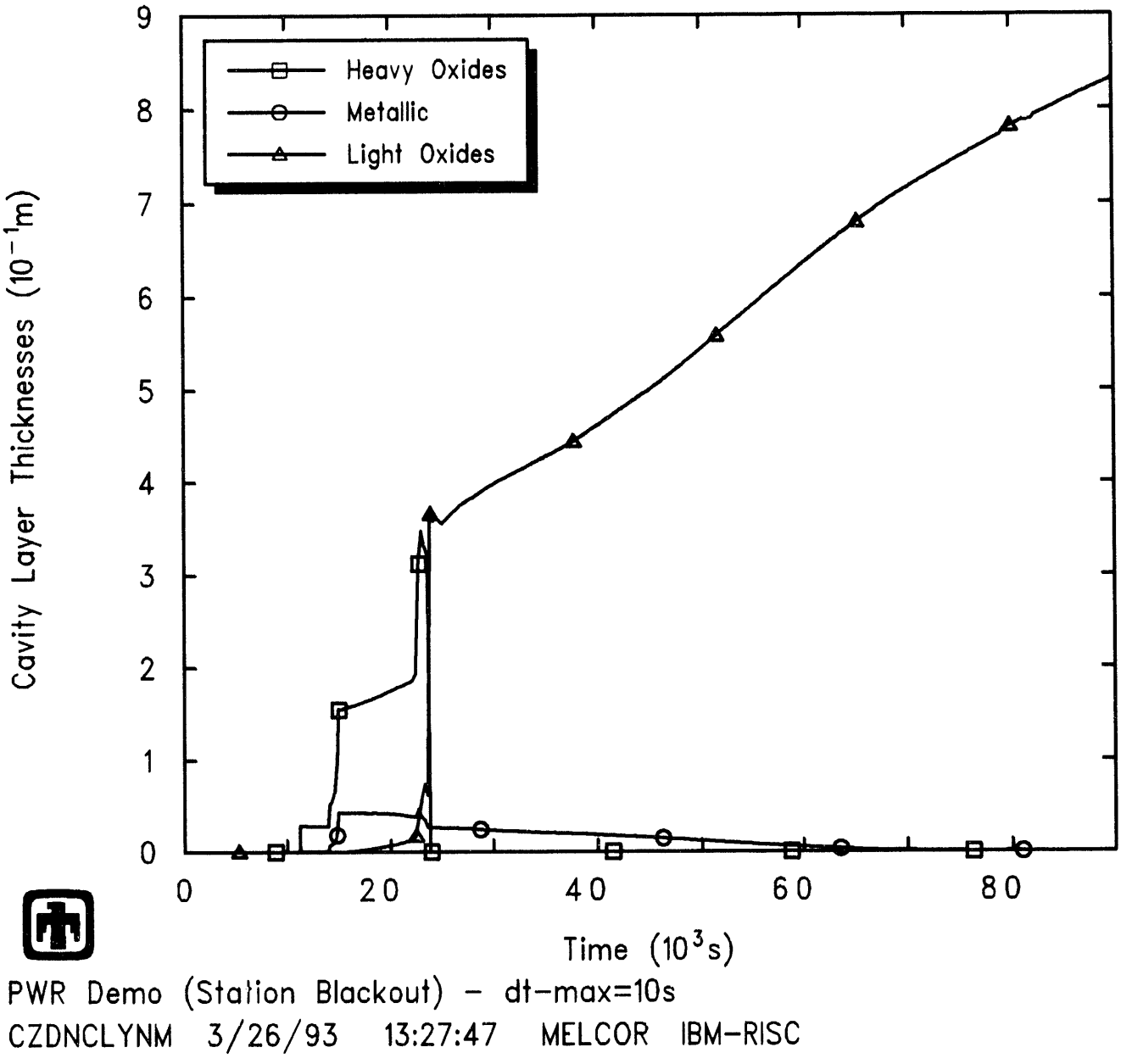

Figure 4.3.2. Cavity Layer Thicknesses - MELCOR 1.8.2 Reference Calculation

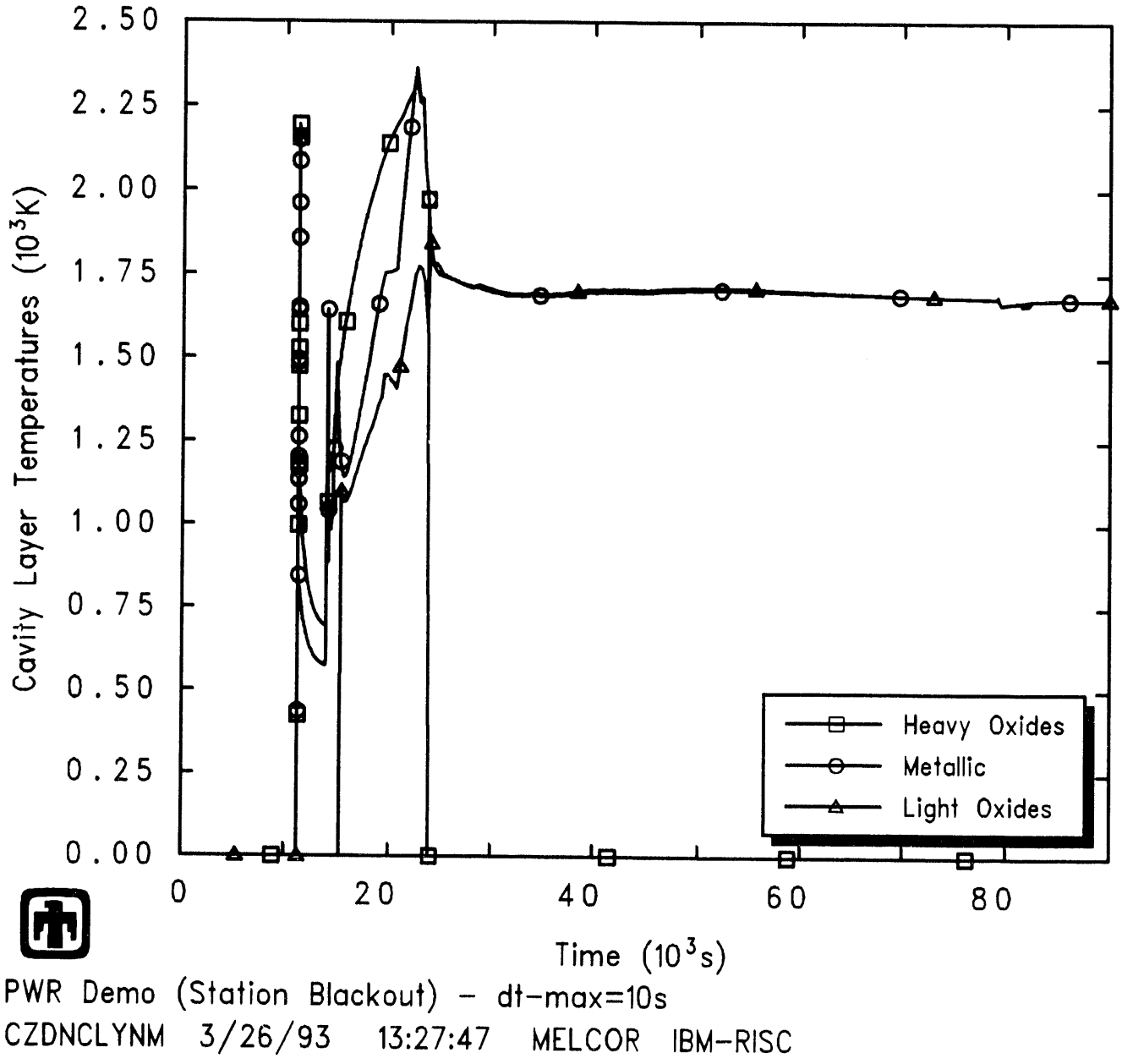

Figure 4.3.3. Cavity Layer Temperatures MELCOR 1.8.2 Reference Calculation

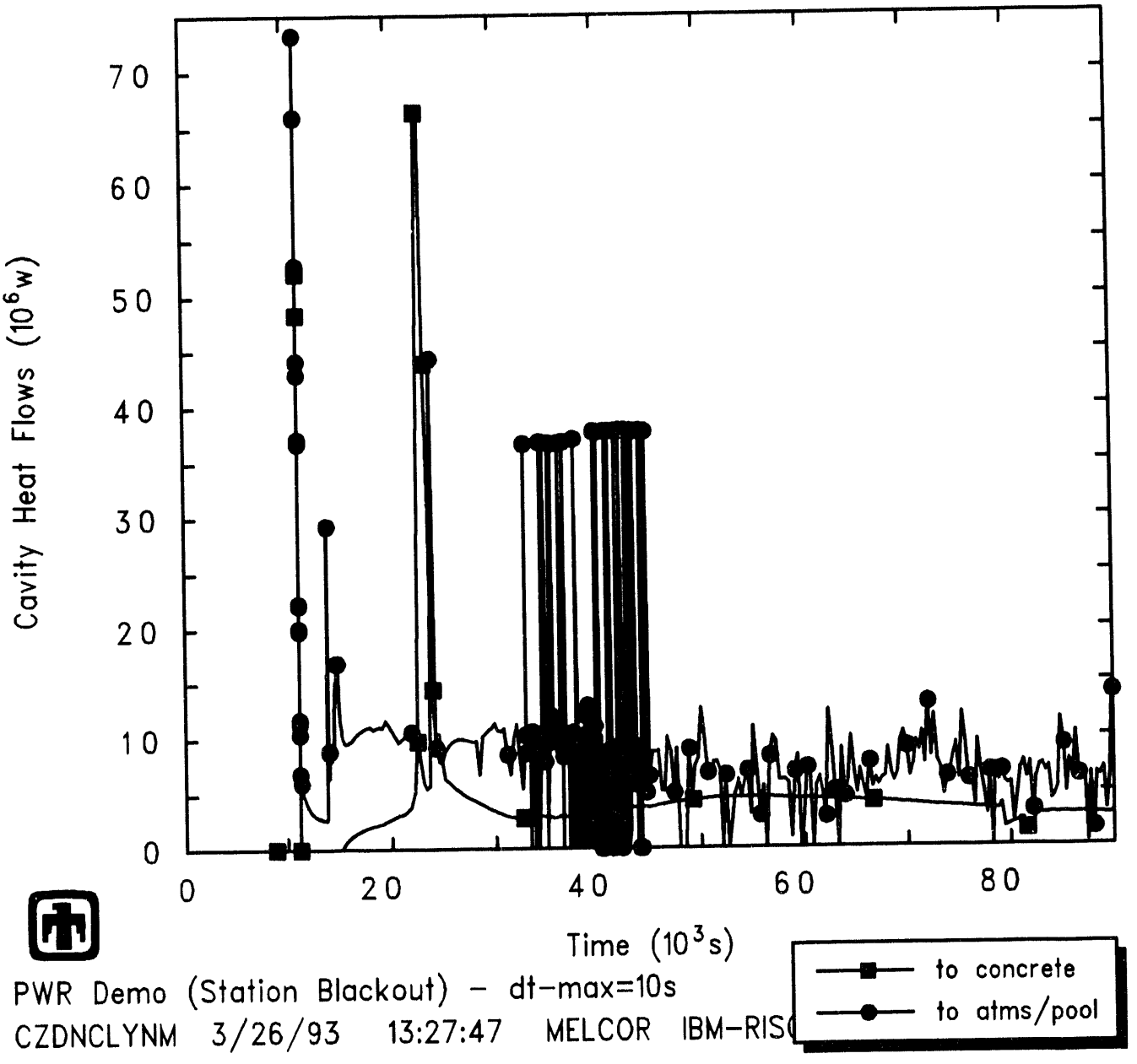

Figure 4.3.4. Cavity Heat Flows - MELCOR 1.8.2 Reference Calculation

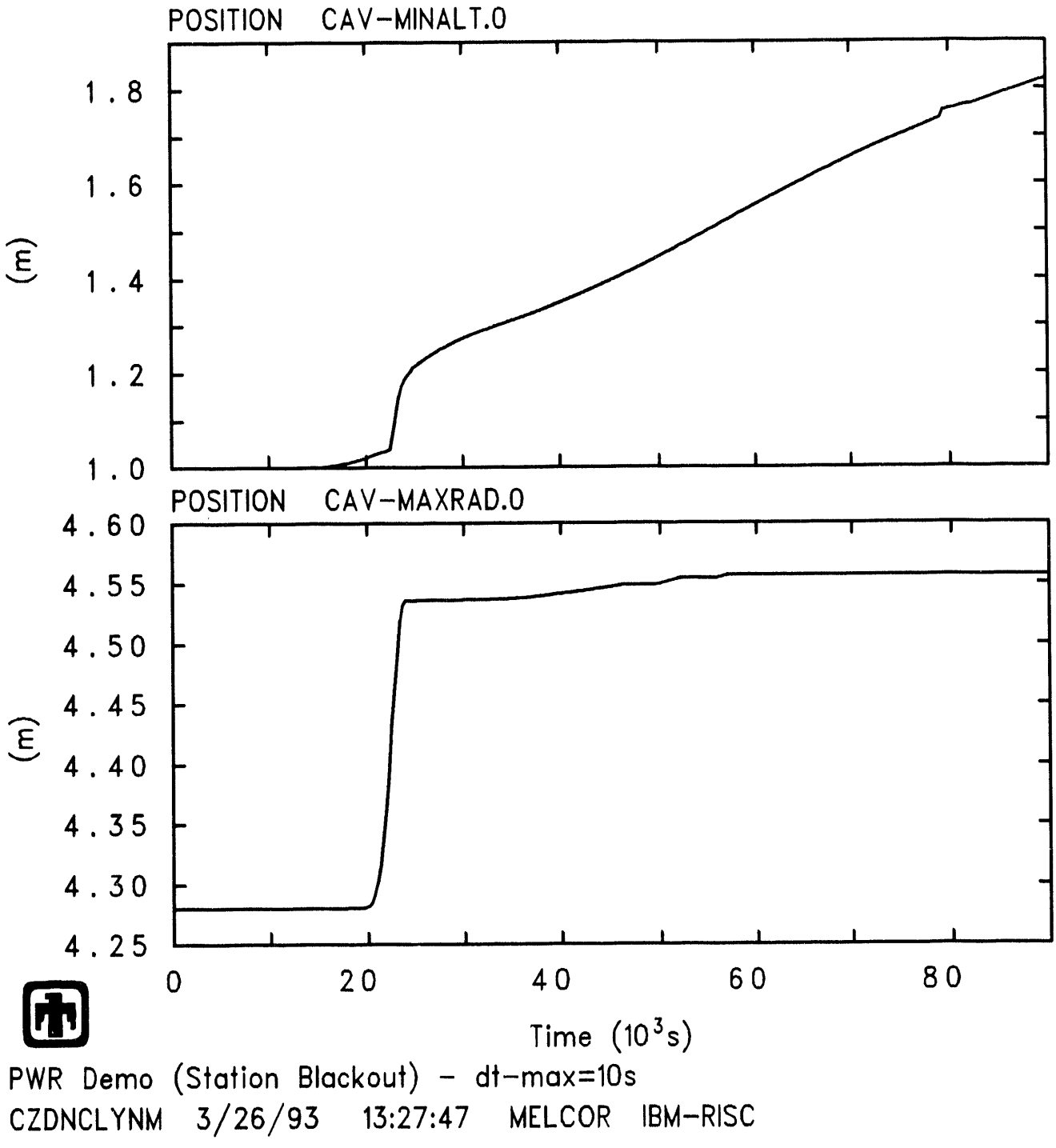

Figure 4.3.5. Cavity Maximum Depth (top) and Radius (bottom) - MELCOR 1.8.2 Reference Calculation

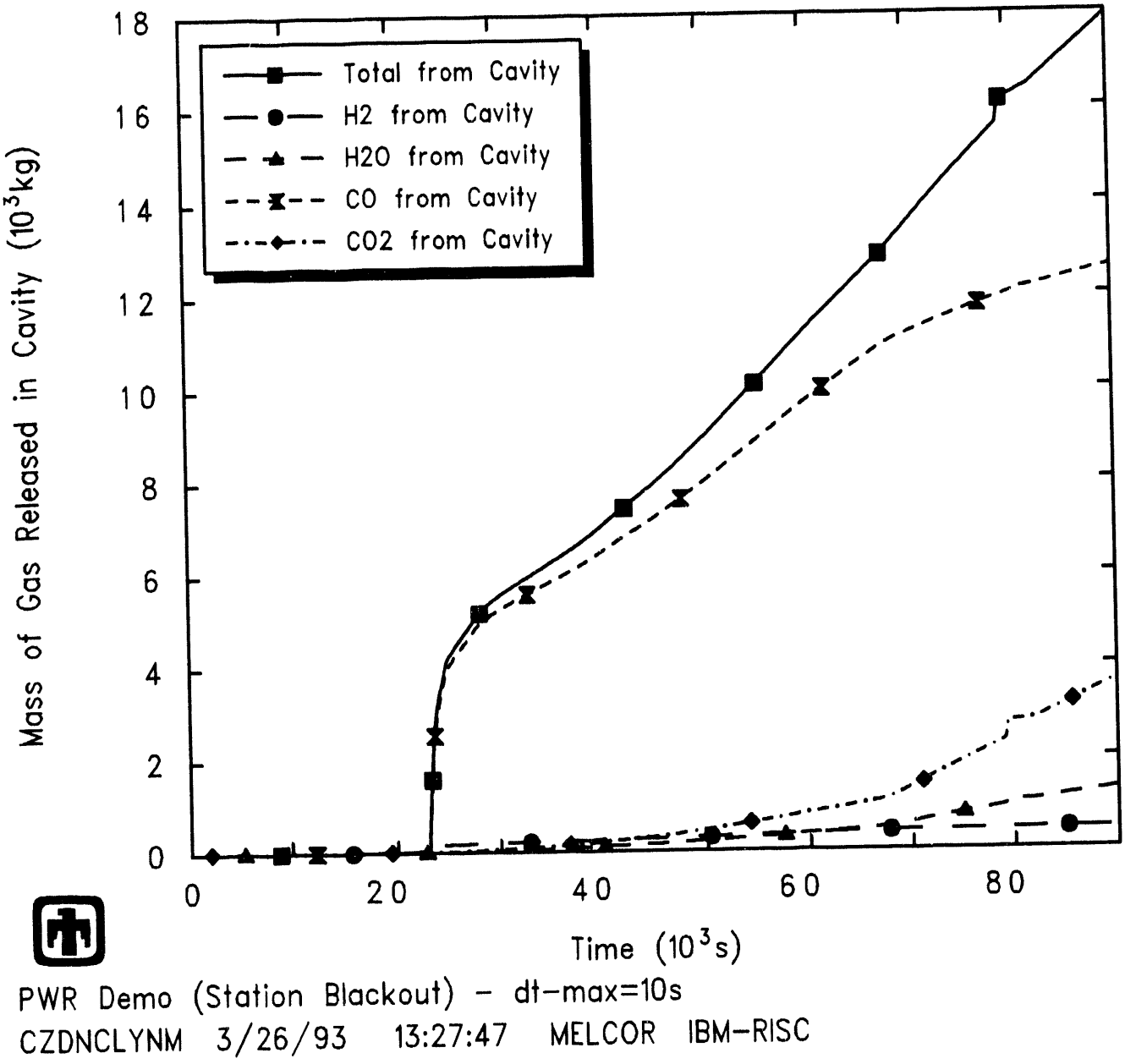

Figure 4.3.6. Cavity Gas Production – MELCOR 1.8.2 Reference Calculation

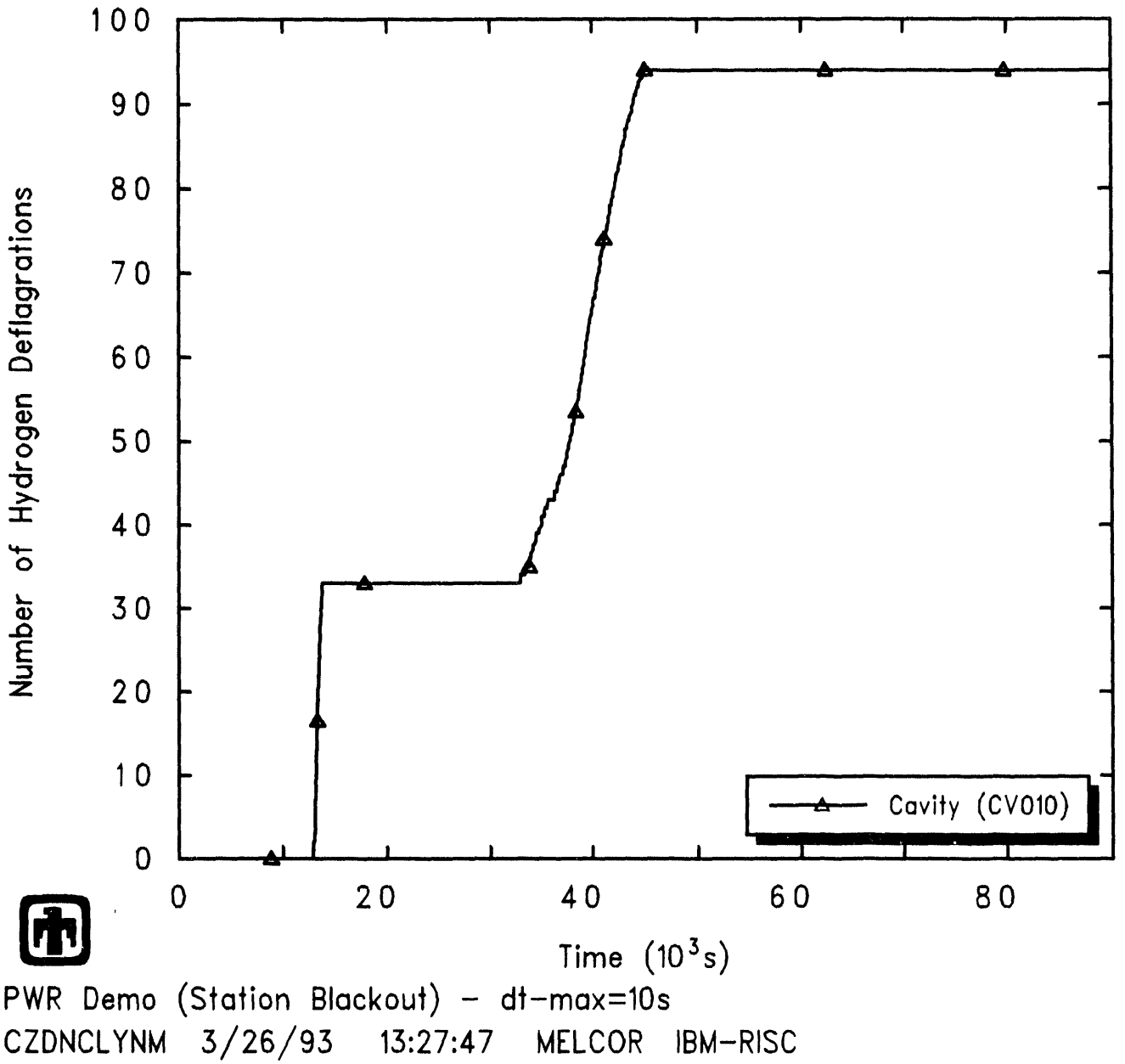

Figure 4.3.7. Cavity Hydrogen Deflagrations – MELCOR 1.8.2 Reference Calculation

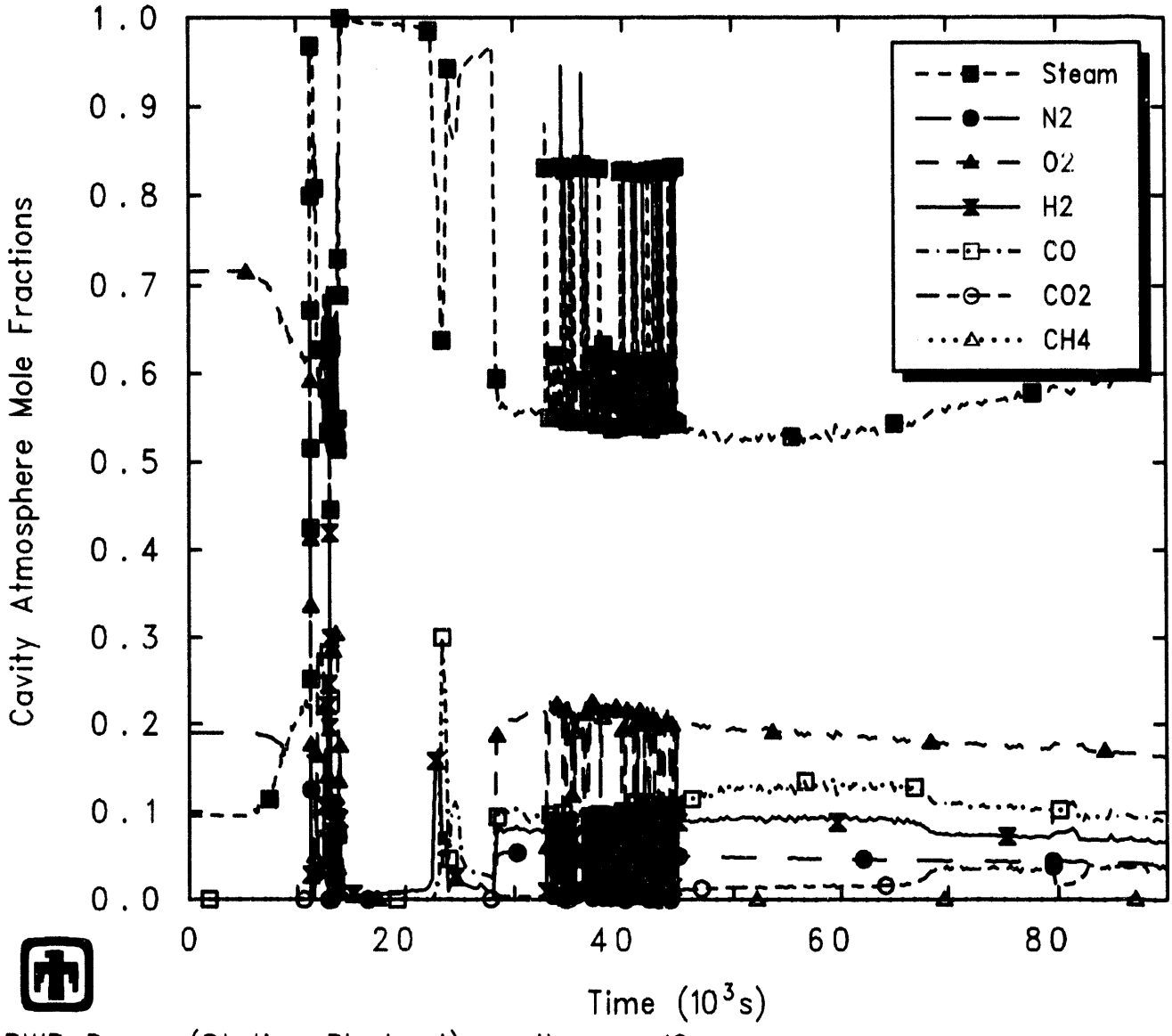

Figure 4.3.8. Cavity Atmosphere Mole Fractions – MELCOR 1.8.2 Reference Calculation

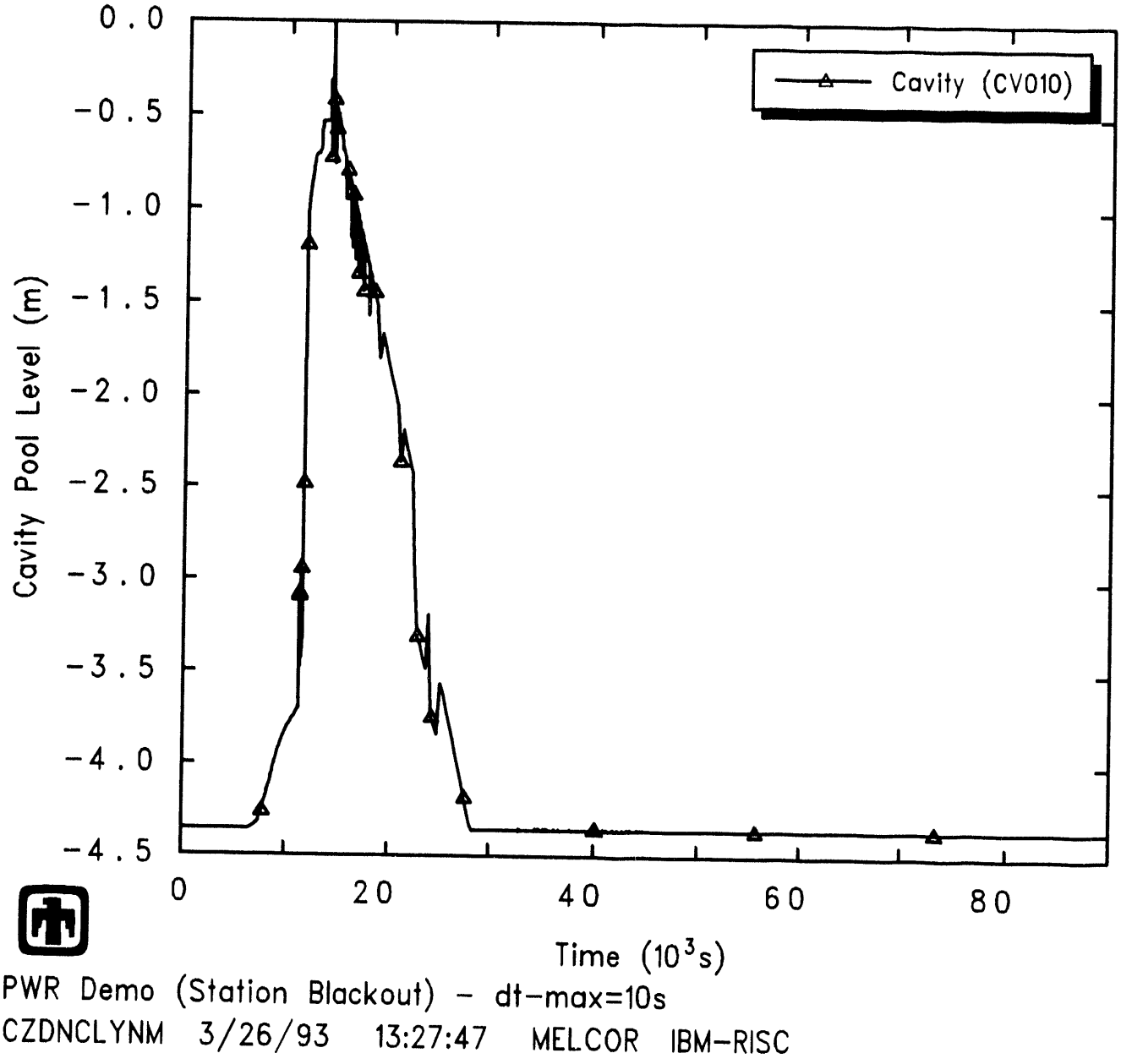

Figure 4.3.9. Cavity Liquid Level – MELCOR 1.8.2 Reference Calculation

very slightly, until the first opening of the PORV on the pressurizer. This caused a fairly rapid pressure rise, to around 140kPa, which soon dropped down to an average value of around 130kPa. When the vessel breach occurred, a pressure spike of 325kPa was predicted. However, the pressure quickly returned to around 175kPa and then began to climb slowly as the water in the cavity was boiled off. At ~24,000s (6.7hr) the increased ablation caused by the CORCON layer flip gave rise to a sudden increase in the rate of pressure rise, which soon subsided. After all the cavity water was boiled off (at ~30,000s or 8.3hr), the pressure increase became much slower, reaching a peak value of 400kPa at the end of the calculation (90,000s or 25hr). This was still very far from the containment failure pressure of 970kPa used in other MELCOR Surry analyses [21], which was taken to be identical to the mean value used for the calculations done for the Surry plant in support of NUREG-1150 [13] and documented in the supporting document [14].

The temperature behavior of the containment atmosphere was similar to that of the pressure, as illustrated in Figure 4.4.2. The initial temperature was 311K. The first temperature increase corresponded to the opening of the PORV at 5250s (1.5hr). The temperature spike at ~11,000s (3.1hr) was clearly due to the vessel breach, and reached about 1200K. The temperature spikes in the cavity atmosphere temperature around 13,000s (3.6hr) were caused by hydrogen burns in the cavity, as was the spike at ~28,500s (7.9hr) and the cluster of spikes between about 33,000s (9.2hr) and 45,000s (12.5hr), which are higher in magnitude and more frequent than at other times. The CORCON layer flip was responsible for the small disturbance at around 24,000s (6.7hr). When all the water in the cavity had boiled off (at ~30,000s or 8.3hr), the temperature of the cavity atmosphere jumped suddenly to that of the core debris materials, oscillating around 1700K. These fluctuations in cavity atmosphere temperature are reflected in oscillations in the cavity surface heat loss, presented in Figure 4.3.4. The rapid fluctuations in cavity atmosphere composition in Figure 4.3.8 and in the cavity surface heat loss presented in Figure 4.3.4, reflecting a large number hydrogen combustion events between ~33,000s (9.2hr) and ~45,000s (12.5hr), are also visible as increased oscillations in the cavity atmosphere temperature during that period. At the end of the calculation the containment atmosphere (excluding the cavity) had reached an average temperature of around 450K.

No hydrogen burns occurred in the containment outside the cavity during the calculation, owing to steam and/or CO_2 inerting in the other containment control volumes throughout the transient.

4.5 Fission Product Release, Transport and Deposition

Figures 4.5.1 through 4.5.12 show the fission product release predicted for the various MELCOR radionuclide classes (using the default class definitions, summarized in Table 3.1). In addition to total releases, in-vessel releases both from fuel in the core active fuel region and from fuel in debris fallen into the lower plenum are presented individually, as are ex-vessel releases from fuel ejected from the vessel into the cavity. All releases are normalized to the initial inventories present at the start of the transient. Only radioactive

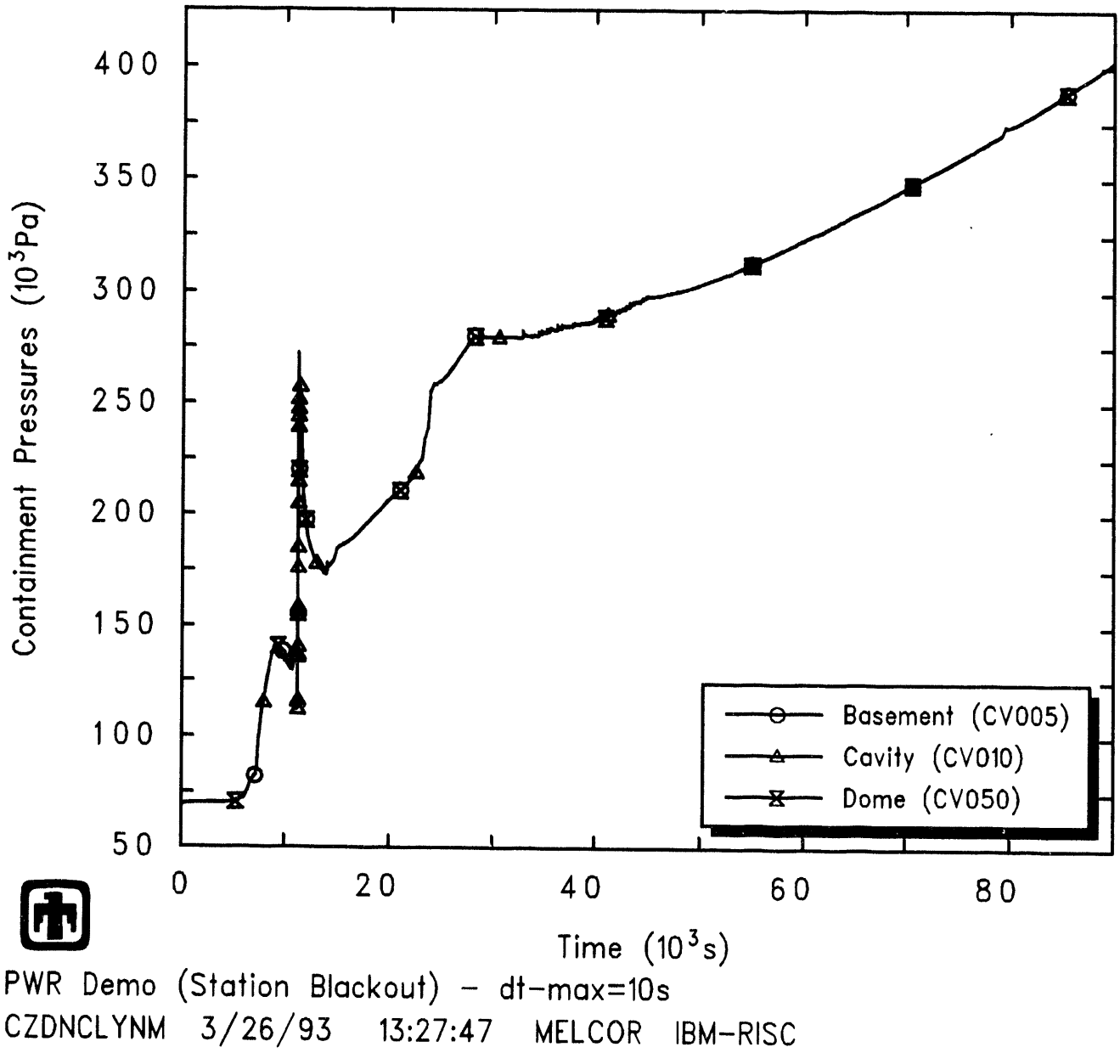

Figure 4.4.1. Containment System Pressure – MELCOR 1.8.2 Reference Calculation

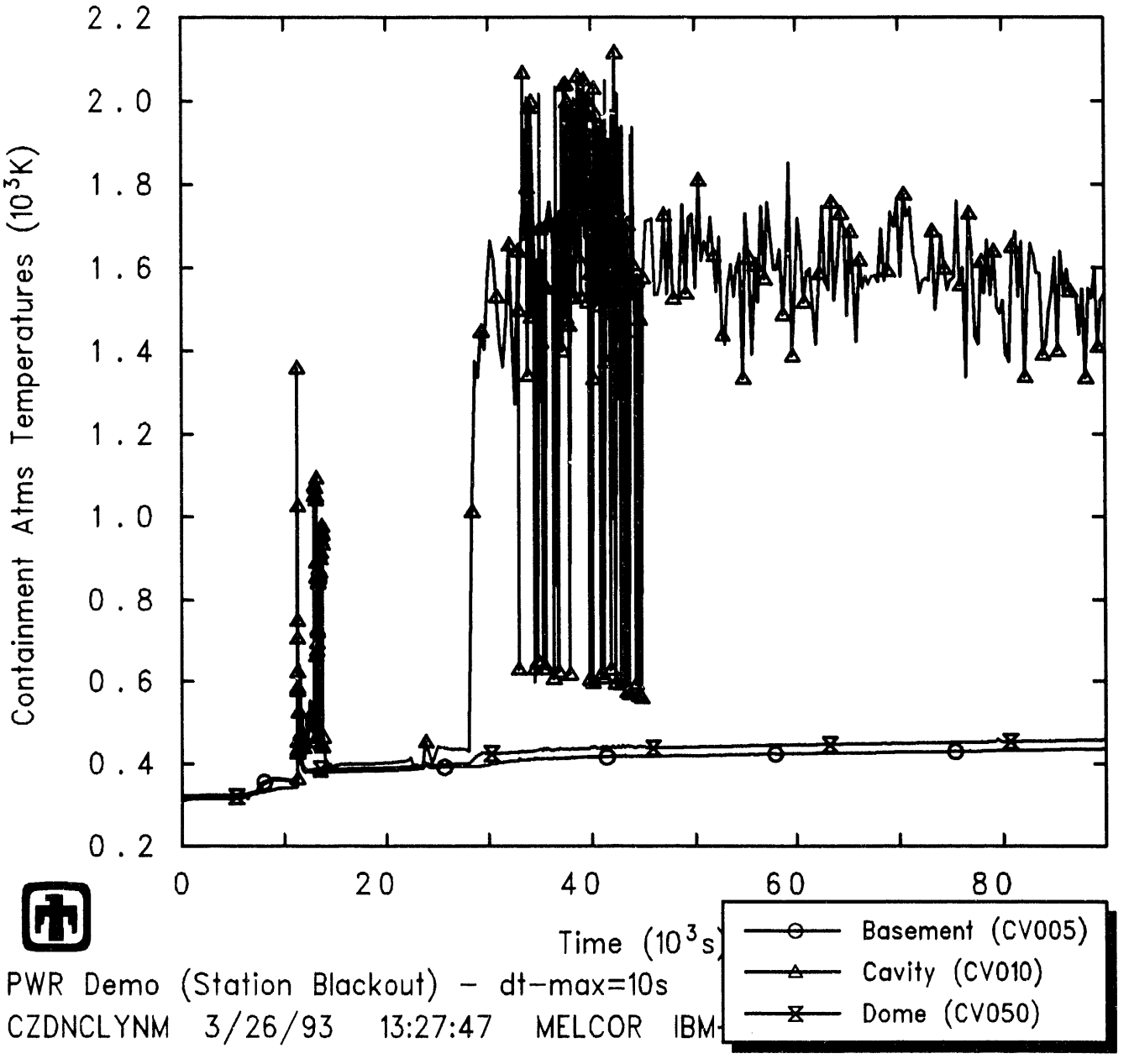

Figure 4.4.2. Containment System Temperatures - MELCOR 1.8.2 Reference Calculation

releases are included in this accounting, neglecting releases of nonradioactive materials, from structural steel, control rod poison or ablated concrete products.

The release of fission products from the fuel is summarized in Table 4.5.1. Fractional releases are given both in-vessel and in the cavity, and both final in-vessel releases and releases prior to vessel breach are presented. Note that a path to the containment was available and open when the first gap releases occurred in-vessel after ~10,000s (2.8hr); prior to reactor vessel lower head failure, fission products were transported from the primary system and into the containment via the PORV. At lower head penetration failure, molten corium was transferred in stages to the cavity, where further fission product release to the containment occurred.

Almost all of the Class 1 and Class 2 volatiles were released from the fuel by the end of the MELCOR calculation. About 60% of that release occurred in-vessel, with the remaining ~40% released ex-vessel in the cavity, as indicated in Figures 4.5.1 and 4.5.2, and in Table 4.5.1. Note that Table 4.5.1 shows a very similar release pattern for Class 4 (halogens like iodine, also volatiles) in-vessel, but no additional release in the cavity, as shown in Figure 4.5.4 and in Table 4.5.1. This is due to a coding problem in MELCOR: the VANESA code, which is used to calculate the ex-vessel release within MELCOR, considers iodine to be released as CsI; since there is no separate CsI class in these MELCOR calculations, MELCOR counts that CsI release to be a Class 2 (Cs) release (incidentally explaining why the total Class 2 release fraction shown in Table 4.5.1 is greater than 100%, which should be impossible). Based upon physical insight, the Class 4 release should closely resemble the Class 1 and 2 results. (Note that this problem does not occur if CsI in Class 16 is enabled by the user, as is normally done in many plant analyses. However, the default class mapping needs to be corrected.)

The release behavior predicted by MELCOR can be grouped into several subdivisions. Assuming the correct iodine behavior, ~100% of the Class 1, Class 2 and (corrected) Class 4 radionuclide inventories were released, about 50%/50% in-vessel and ex-vessel. The next major release fractions were of Te (~75%) and Ba (37%), both mostly predicted to occur in the cavity, illustrated in Figures 4.5.3 and 4.5.5. About 30% of the Cd and Sn radionuclide inventories were released, and about 5% of the Mo radionuclide inventory. (Note that these amounts consider only the release of radioactive forms of these classes, and not additional releases of nonradioactive aerosols from structural materials.) Finally, a total $\leq$1% of the initial inventories of the refractories (Ru, Ce, La and U) were released.

The release patterns became somewhat more varied as the release amount decreases. Most of the Class 9 (La) releases were predicted to occur in the cavity, as shown in Figure 4.5.9, similar to the behavior of Class 3 (Ba) and Class 5 (Te), illustrated in Figures 4.5.3 and 4.5.5. Almost all of the Class 6 (Ru) and Class 11 (Cd) releases were predicted to occur in-vessel, as shown in Figures 4.5.6 and 4.5.11. Class 7 (Mo), Class 8 (Ce), Class 10 (U) and Class 12 (Sn) had most of their releases predicted to occur in-vessel, but a significant fraction occurred in the cavity.

Most of the in-vessel radionuclide release was predicted to occur in a relatively small time window, during the core degradation from ~3hr to ~4hr. The ex-vessel release

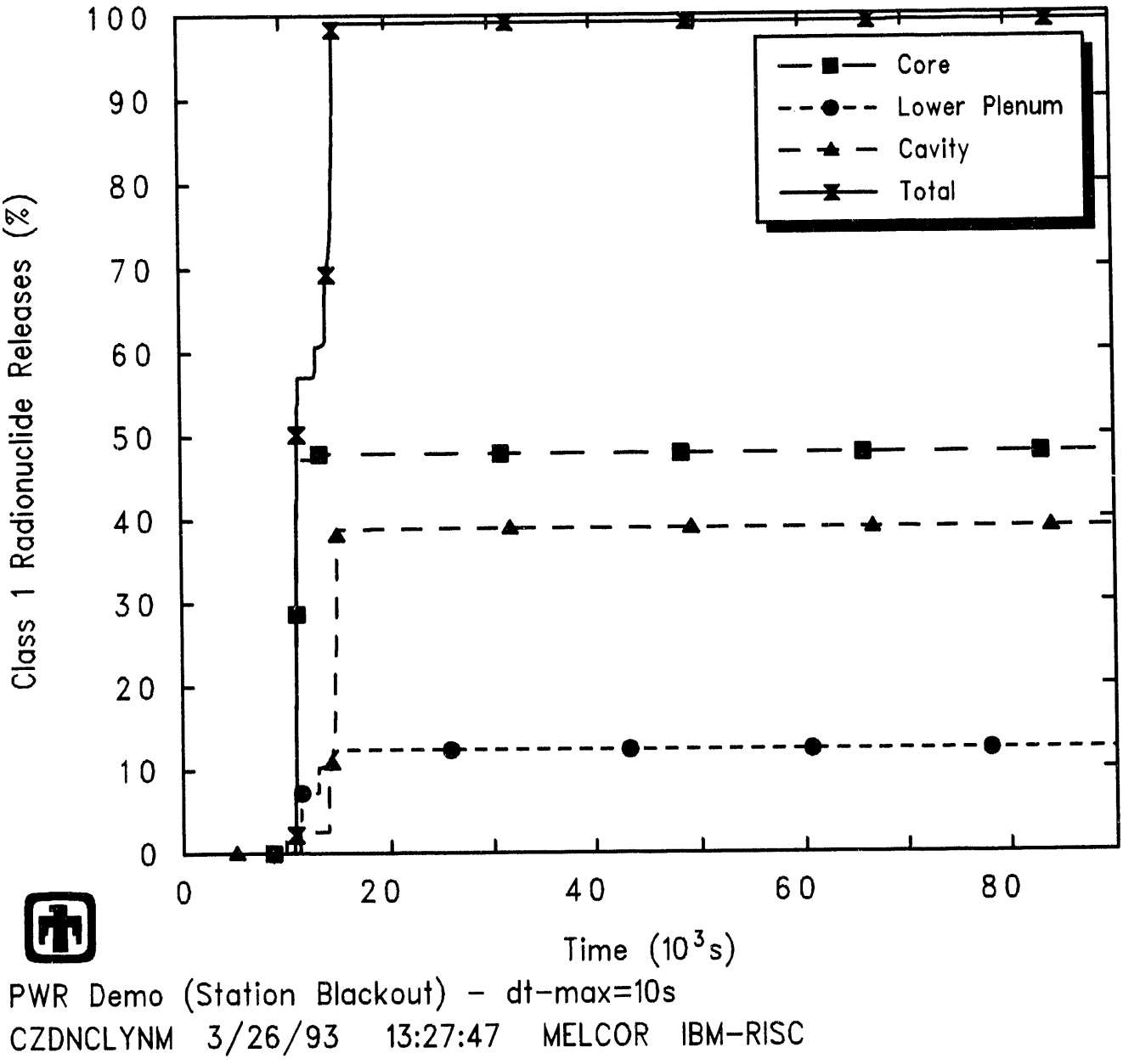

Figure 4.5.1. Class 1 (Xe) Noble Gases Fission Product Releases - MELCOR 1.8.2 Reference Calculation

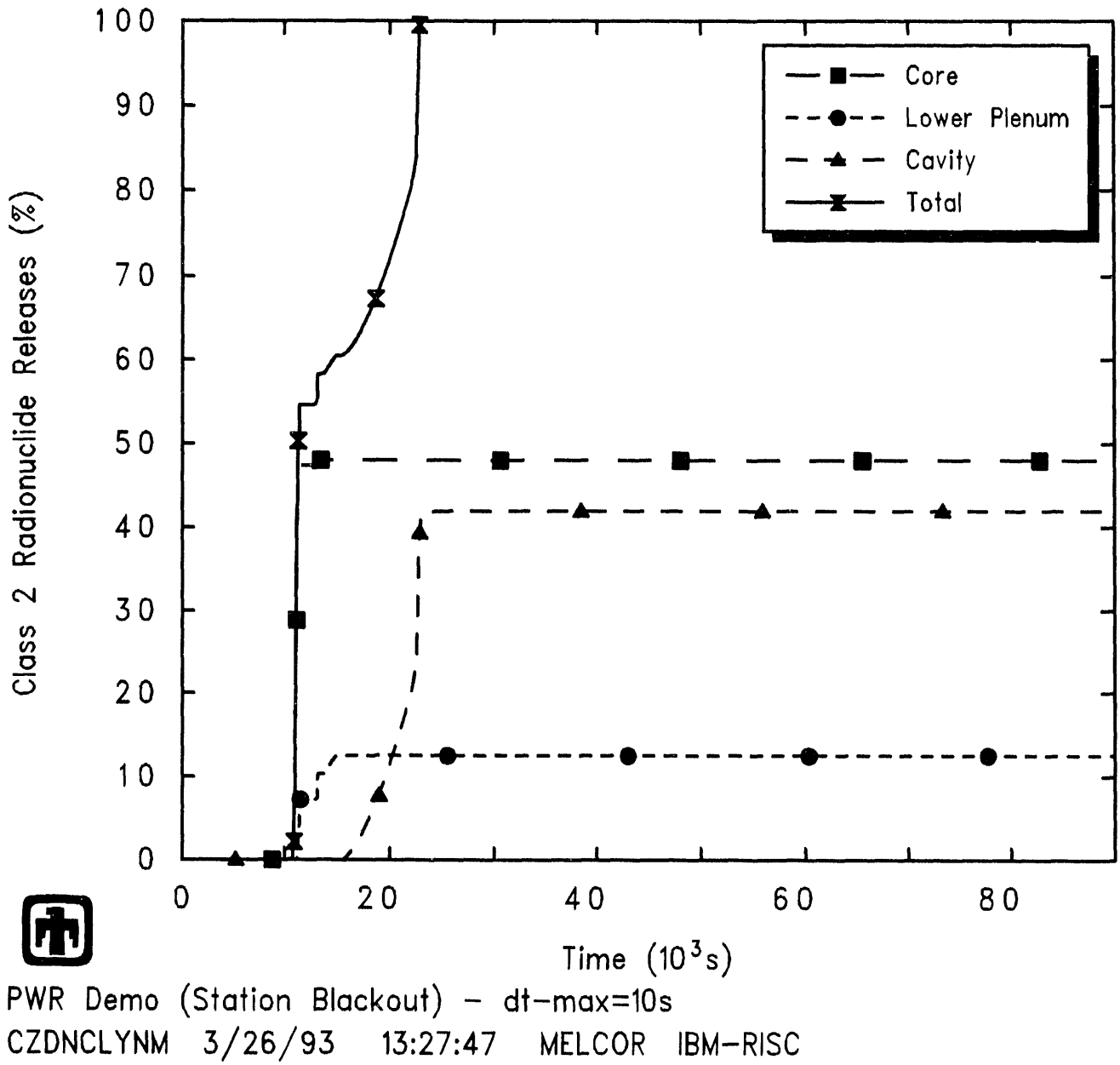

Figure 4.5.2. Class 2 (Cs) Alkali Metals Fission Product Releases – MELCOR 1.8.2 Reference Calculation

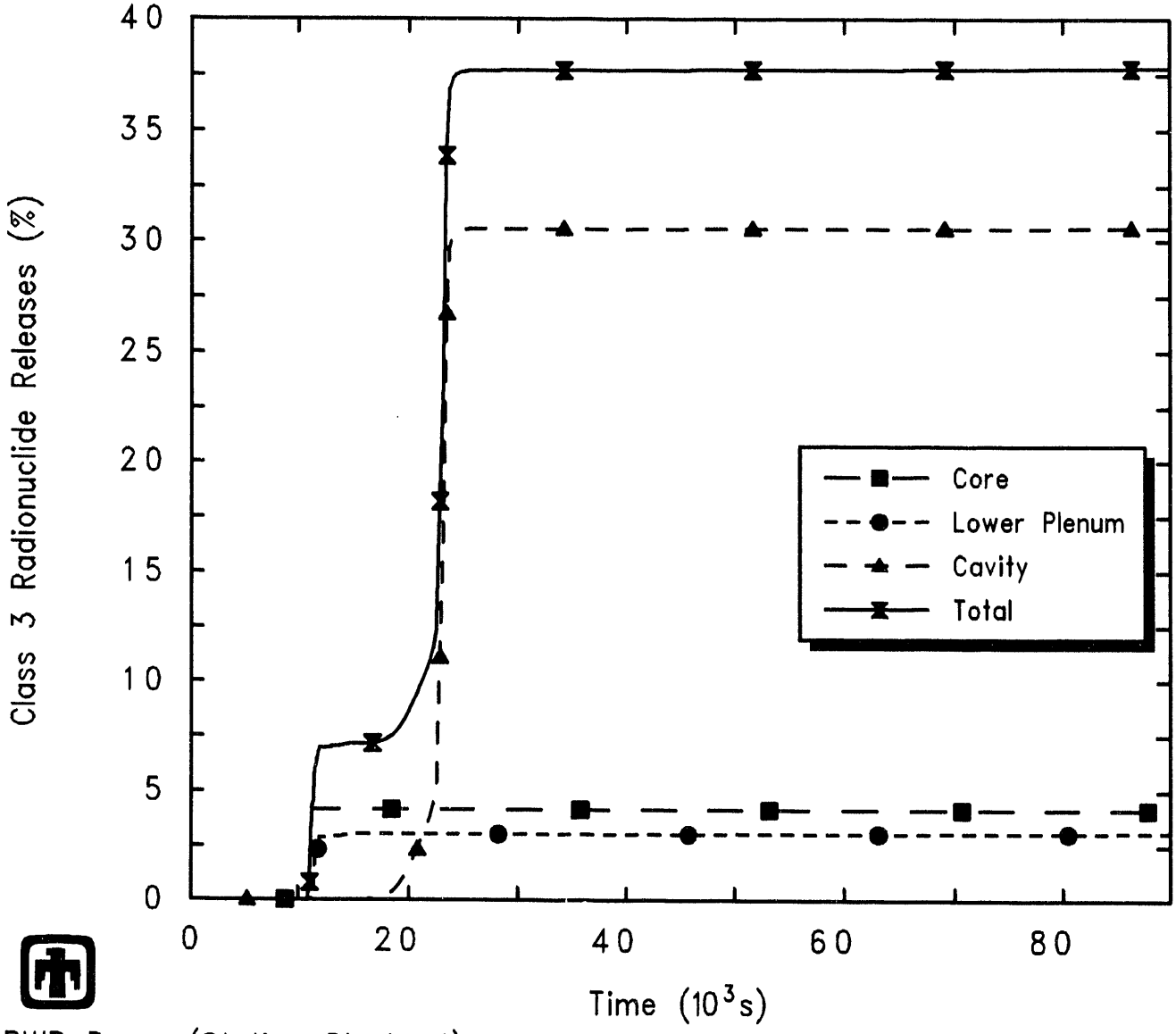

Figure 4.5.3. Class 3 (Ba) Alkaline Earths Fission Product Releases - MELCOR 1.8.2 Reference Calculation

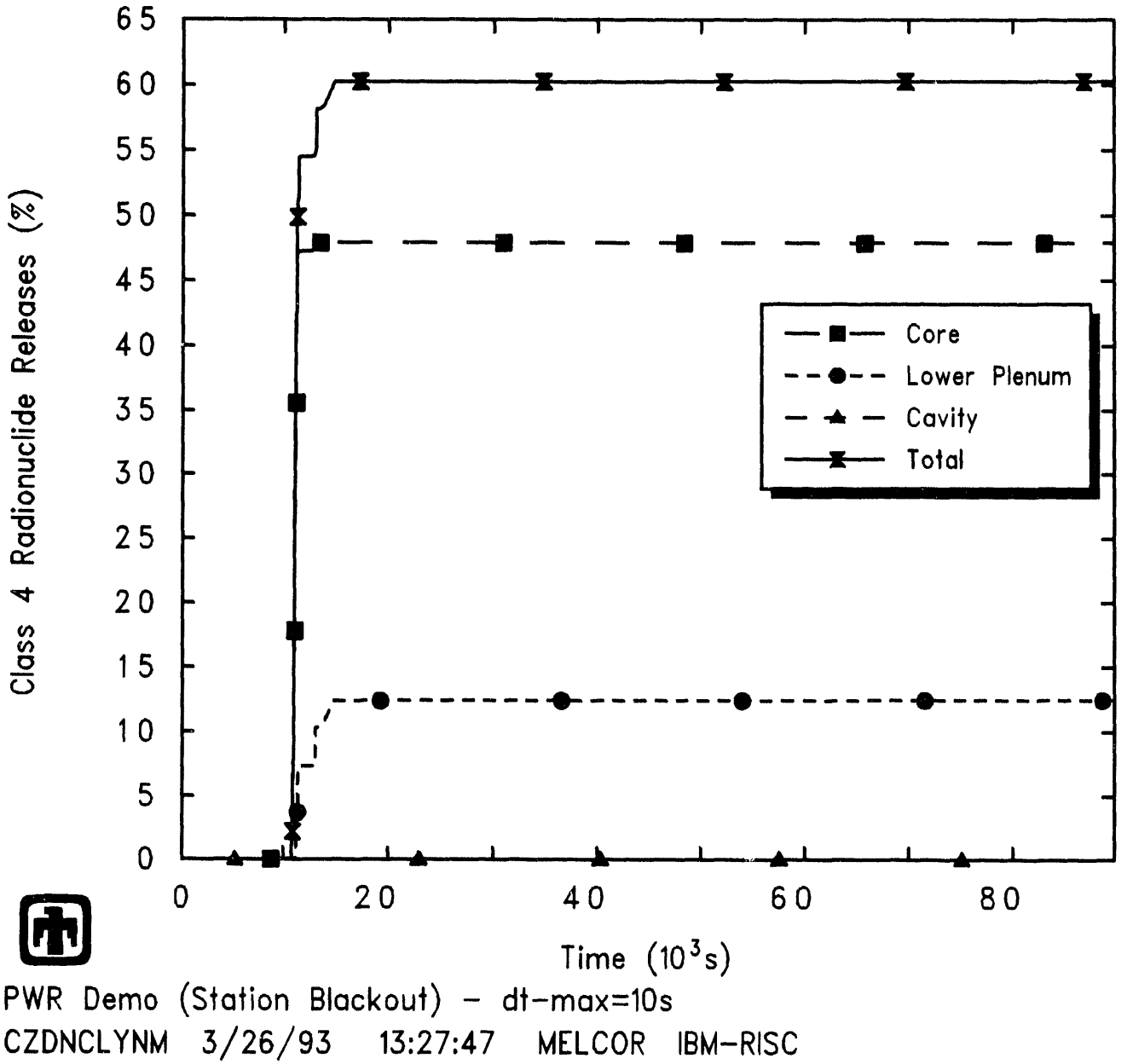

Figure 4.5.4. Class 4 (I) Halogens Fission Product Releases – MELCOR 1.8.2 Reference Calculation

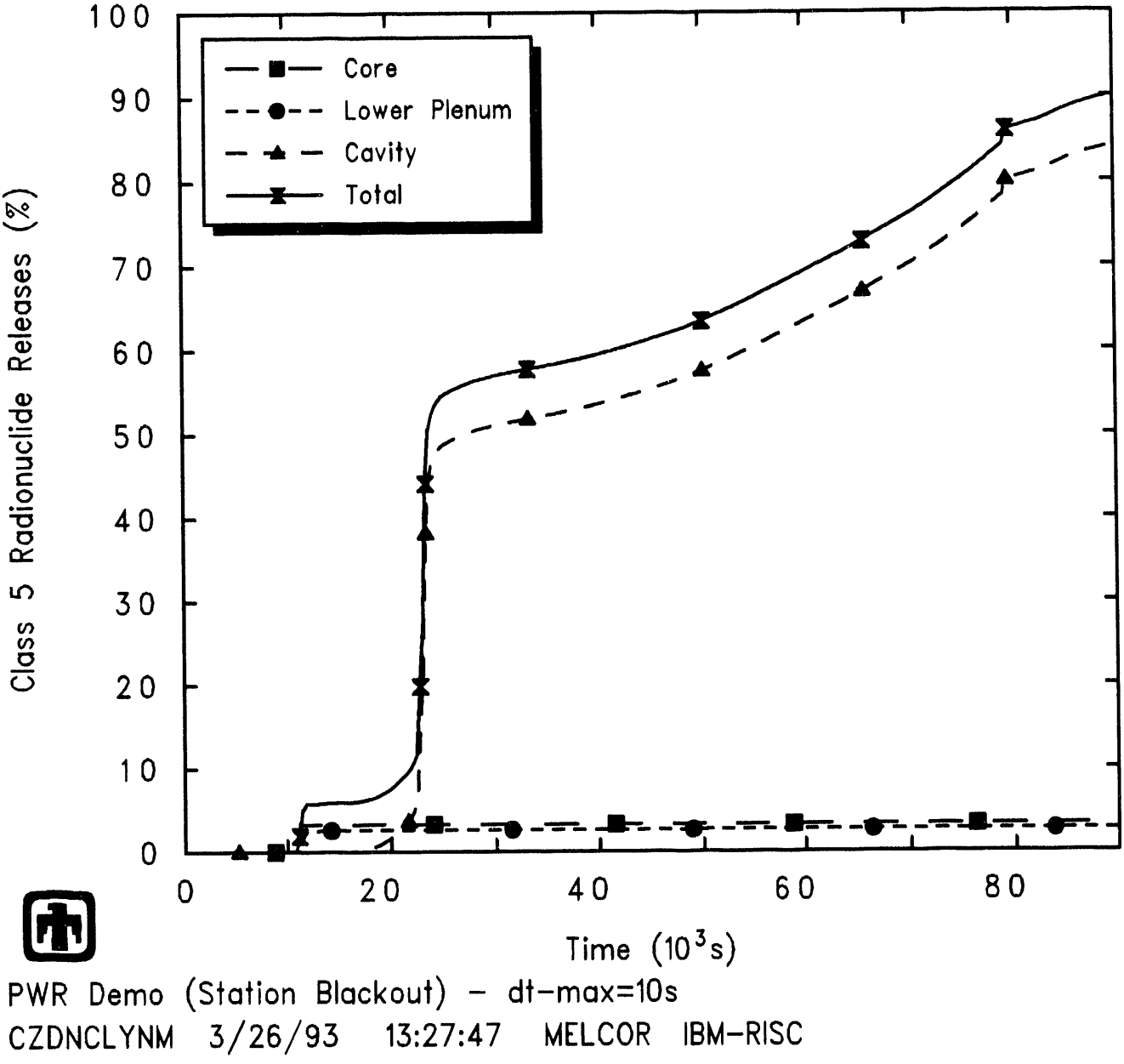

Figure 4.5.5. Class 5 (Te) Chalcogens Fission Product Releases – MELCOR 1.8.2 Reference Calculation

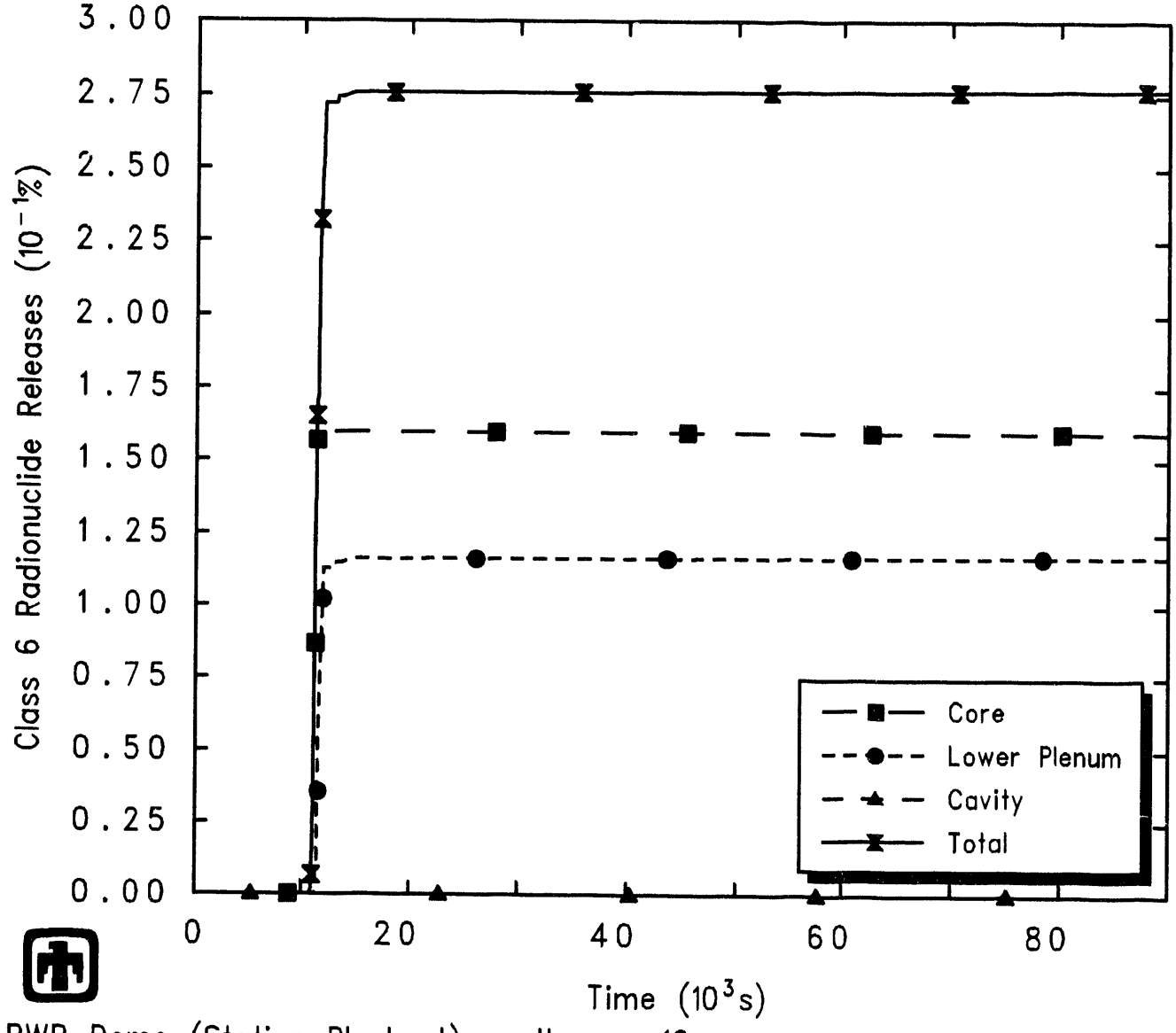

Figure 4.5.6. Class 6 (Ru) Platinoids Fission Product Releases - MELCOR 1.8.2 Reference Calculation

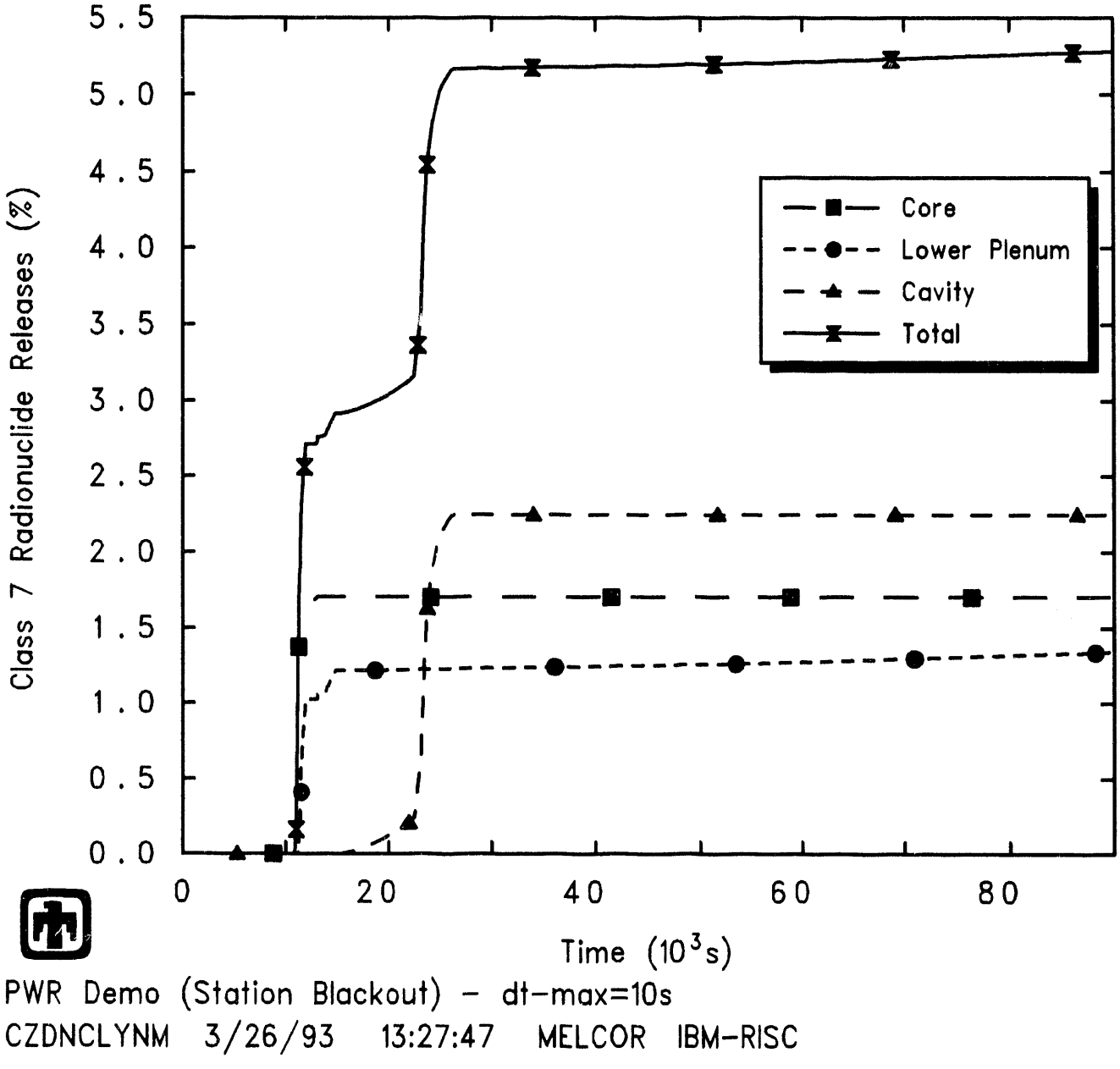

Figure 4.5.7. Class 7 (Mo) Early Transition Elements Fission Product Releases – MELCOR 1.8.2 Reference Calculation

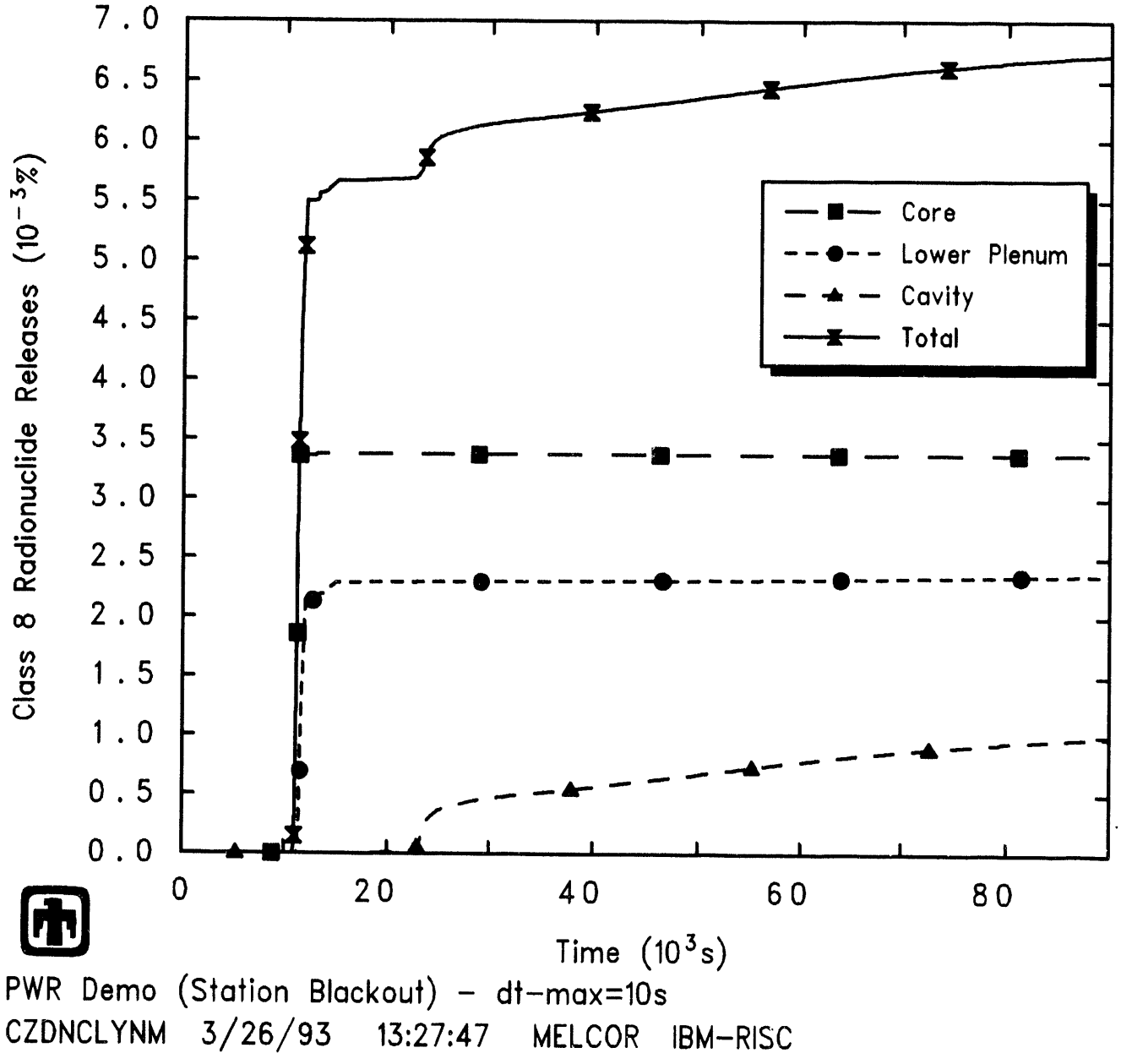

Figure 4.5.8. Class 8 (Ce) Tetravalents Fission Product Releases MELCOR 1.8.2 Reference Calculation

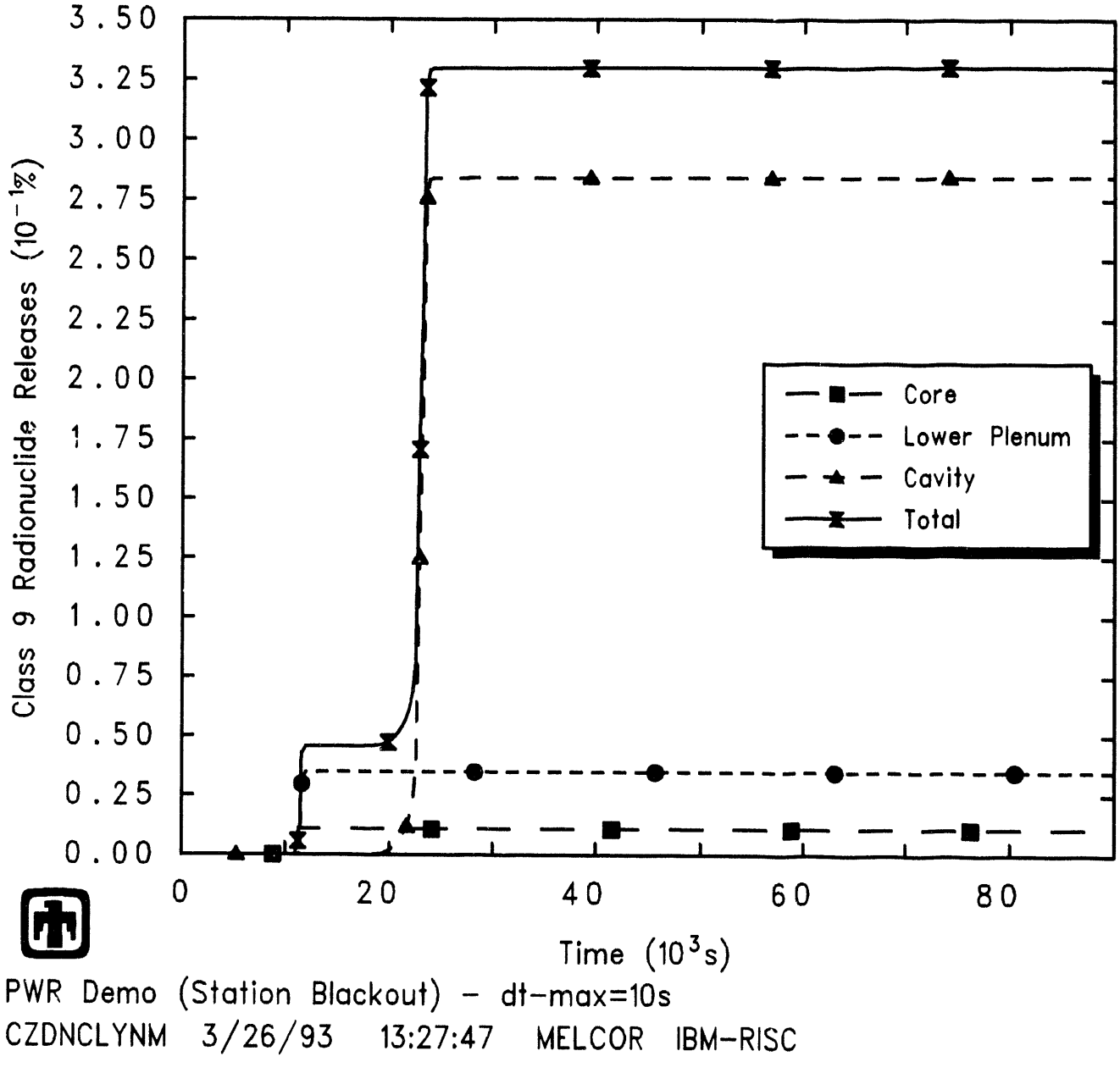

Figure 4.5.9. Class 9 (La) Trivalents Fission Product Releases - MELCOR 1.8.2 Reference Calculation

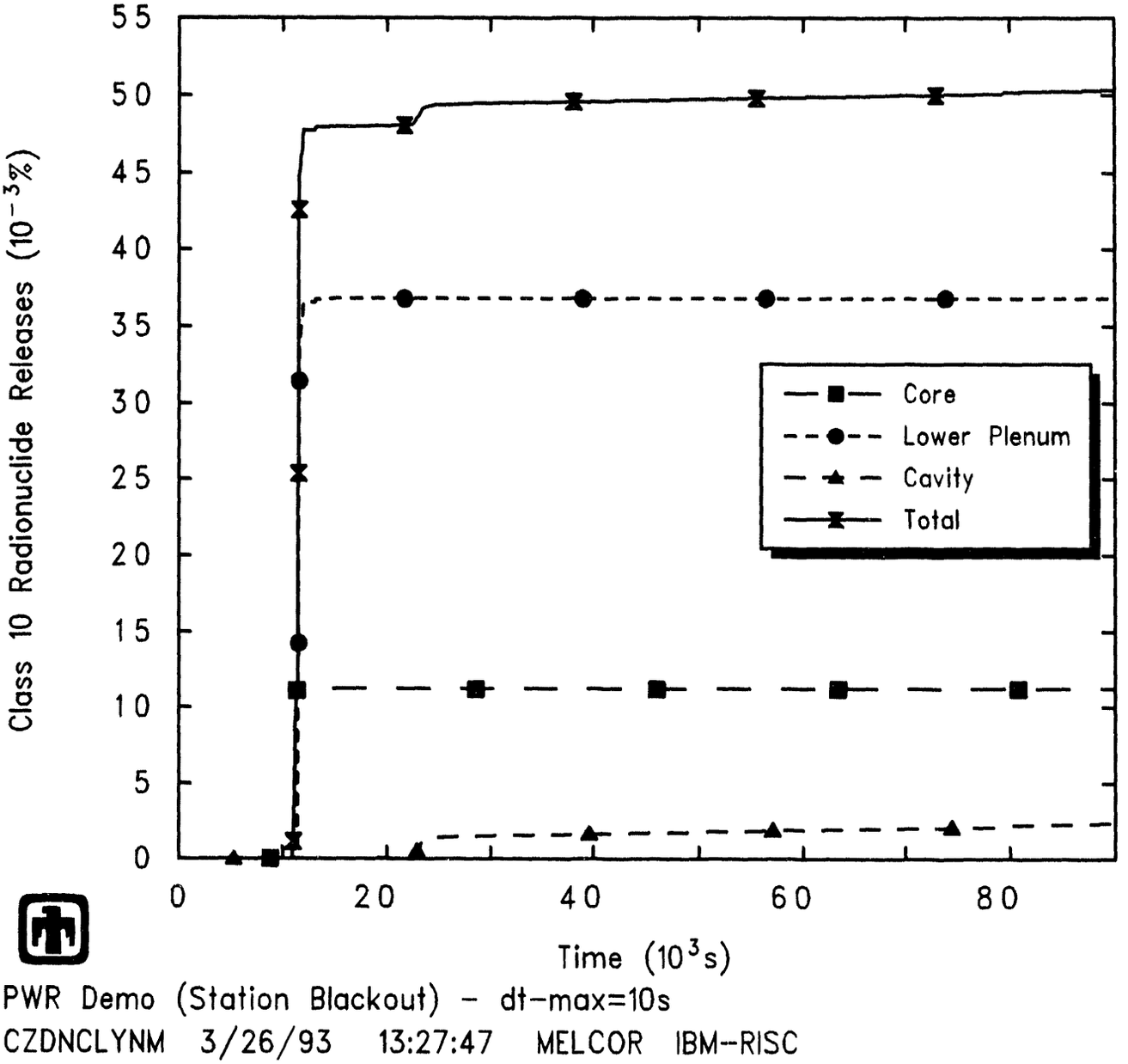

Figure 4.5.10. Class 10 (U) Uranium Fission Product Releases – MELCOR 1.8.2 Reference Calculation

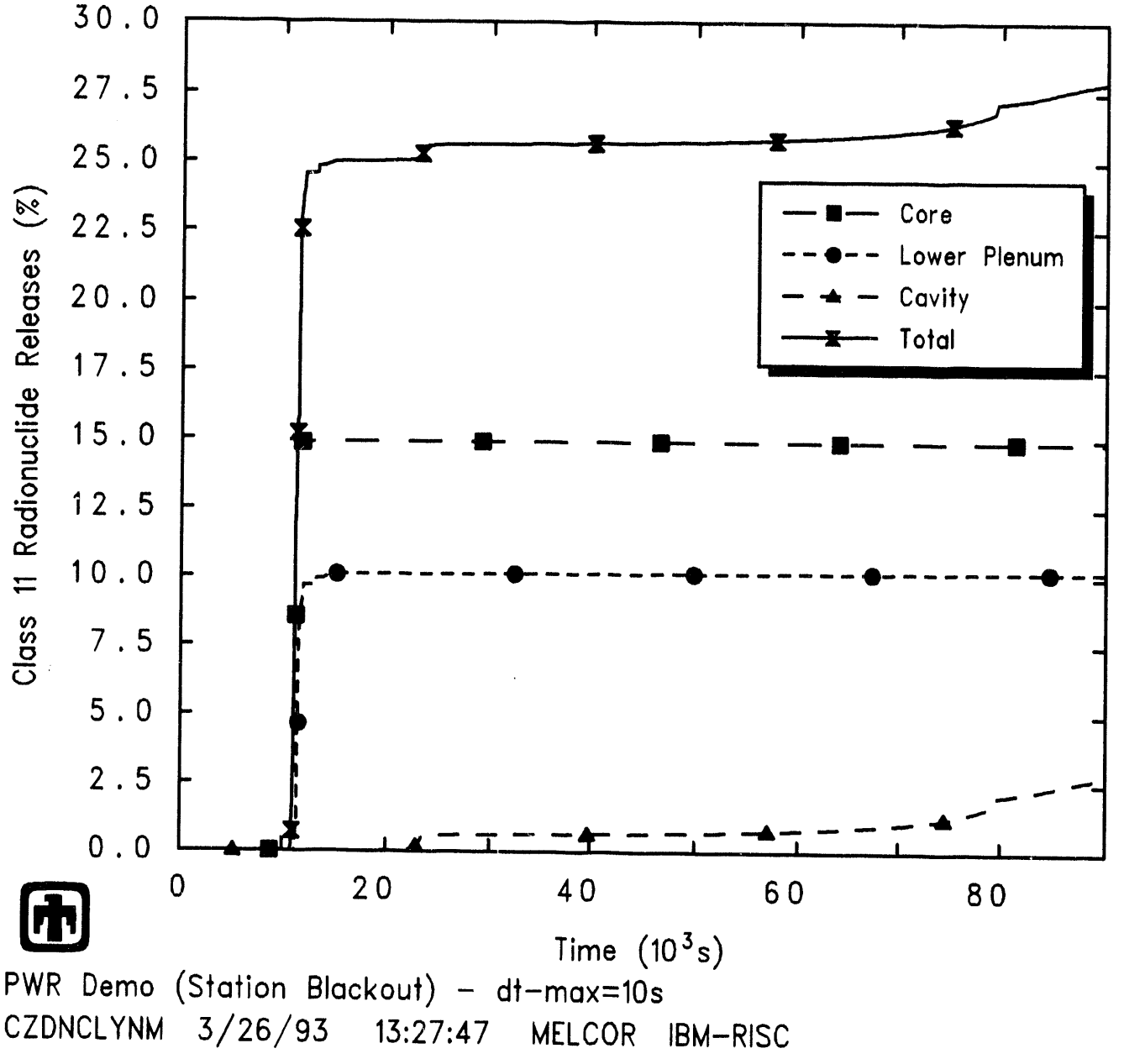

Figure 4.5.11. Class 11 (Cd) More Volatile Main Group Fission Product Releases - MELCOR 1.8.2 Reference Calculation

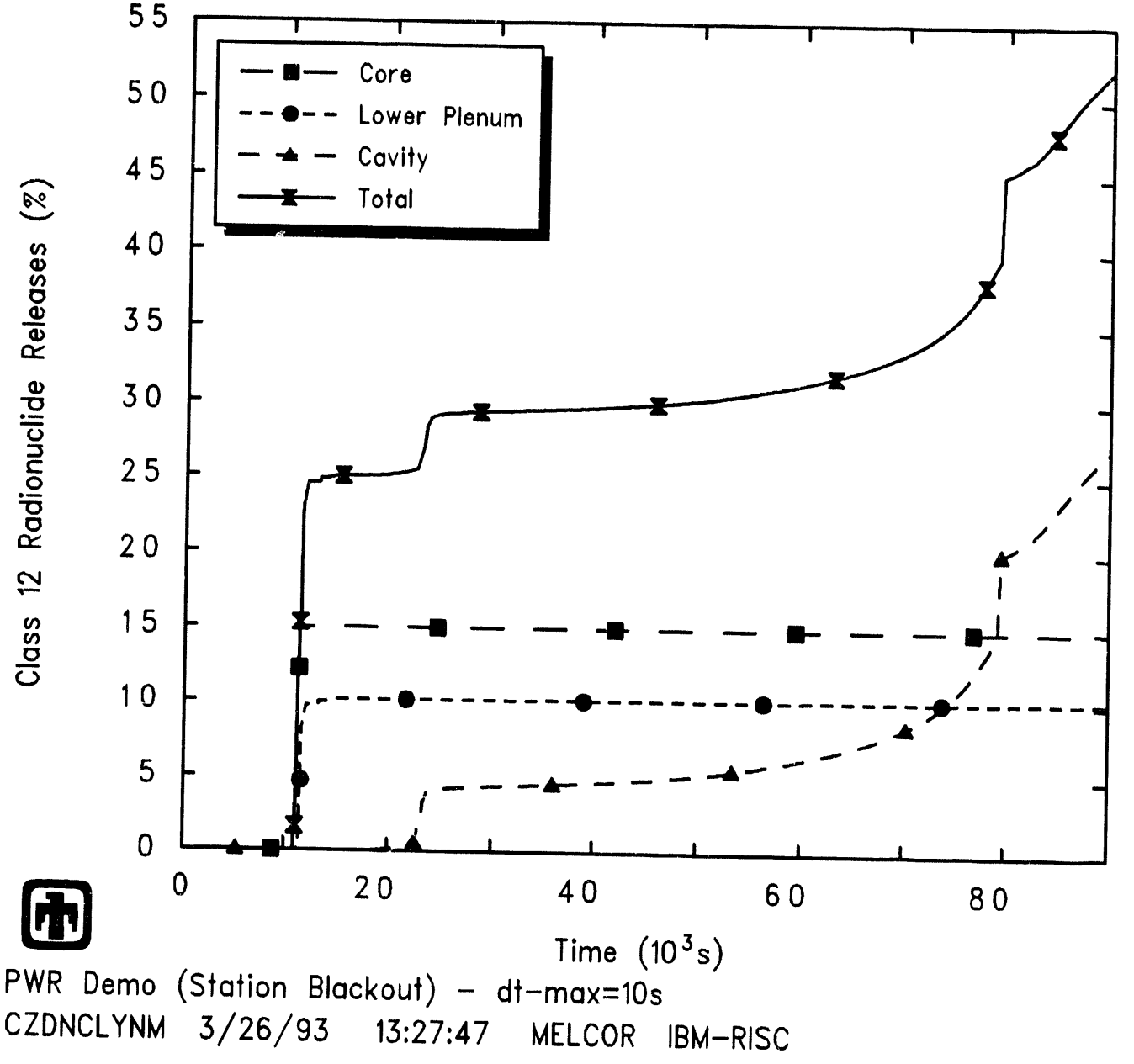

Figure 4.5.12. Class 12 (Sn) Less Volatile Main Group Fission Product Releases MELCOR 1.8.2 Reference Calculation

Table 4.5.1. Fission Product Release – MELCOR 1.8.2 Reference Calculation

Class	In-Vessel Release Before Vessel Failure	In-Vessel Release by 90,000s	In-Cavity Release by 90,000s	Total Release by 90,000s
	(% Initial Inventory)			
1 (Xe)	49.871	60.319	38.937	99.256
2 (Cs)	49.860	60.439	41.817	102.26
3 (Ba)	4.2391	7.2008	30.585	37.786
4 (I)	49.841	60.284	0	60.284
5 (Te)	3.3542	5.9839	84.122	90.106
6 (Ru)	0.1651	[illegible]65	4×10^{-6}	0.2765
7 (Mo)	1.7172	[illegible]6	2.2436	5.2802
8 (Ce)	0.0035	[illegible]057	0.0010	0.0067
9 (La)	0.0111	0.0458	0.2845	0.3303
10 (U)	0.0114	0.0480	0.0023	0.0503
11 (Cd)	15.199	25.093	2.7877	27.881
12 (Sn)	15.200	25.091	27.097	52.188

timing exhibited several distinct patterns. All of the Class 1 (Xe), Class 2 (Cs) and Class 4 (I) volatile-species inventories remaining in the fuel ejected to the cavity were released in the cavity within several hours, as were some of the remaining inventories of Class 3 (Ba), Class 7 (Mo) and Class 9 (La); none of those classes showed any visible release continuing in-cavity after ~6-7hr. Class 5 (Te) had substantial in-cavity release during the first few hours, but release then was predicted to continue, albeit at a slower rate, throughout the remainder of the transient period calculated (Figure 4.5.5. In contrast, Class 8 (Ce), Class 10 (U), Class 11 (Cd) and Class 12 (Sn) showed almost no in-cavity release during the first few hours, but release then was predicted to begin after ~6-7hr; the releases of Class 8 (Ce) and Class 10 (U) then continued at a nearly constant, slow rate through the remainder of the transient period calculated, but the releases of Class 11 (Cd) and Class 12 (Sn) were increasing at a growing rate near the end of the calculation. The increasing release of these radionuclides late in the transient is not real or physical, but instead represents driving the transient beyond the bounds of the VANESA code's assumptions and applicability.

(Note that the following discussion does not apply only to the implementation of the VANESA code in MELCOR, but to the VANESA code itself.)

The exponentially growing releases of several radionuclide species late in the TMLB' transient are a consequence of the disappearance of the metallic layer before the end of the transient, as indicated in Figure 4.3.2. The VANESA code [22], which is used to calculate ex-vessel releases in MELCOR, has no provision for a disappearing metallic layer. In contrast, the VANESA model was developed under the fundamental assumption that structural metals would always dominate the metallic component of the debris. VANESA calculations are not routinely run beyond 10 hours [23], and this assumption is justified for typical reactor debris during this time period. Furthermore, fission products are not simply associated with fuel (UO_2). Elements in an oxidized state, UO_2, oxidized structural metals and fission products assumed to be in an oxidic state form a single condensed oxide phase; elements in the metallic state, both unoxidized structural metals and fission products assumed to be metallic, form a condensed metallic phase. In VANESA, each fission product element is assumed to appear as a metal or as an oxide in the debris, and its assumed state does not change with time; fission products are assumed to be trace species, and are ignored in the oxygen mass balance. As concrete ablation progresses, concrete oxides are added to the oxide phase and melted rebar to the metal phase, and structural metals in the debris are oxidized and transferred to the oxide phase; however, unreleased fission products are not relocated in VANESA.

If a VANESA calculation is continued until the structural metals are largely or completely oxidized away, these assumptions are violated and two processes not included in VANESA modelling become significant:

1. As the structural metals are oxidized, "metallic" fission products become non-trace species in the cavity debris (and can compete successfully for available oxygen).

2. The oxidized "metallic" fission products become associated with the oxide phase, where they are still trace masses, rather than staying as the dominant components of the vanishing metal phase.

These conditions lie outside the range of applicability for the current VANESA model. Because (for ideal chemistry) the vapor pressure of a species over a mixture is proportional to its concentration in that mixture, the misapplication of the existing model to cases where the metallic phase is vanishing can significantly overestimate release rates of the "metallic" fission products.

In the assumed state of MELCOR radionuclides in VANESA, Te, Ru, Cd and Sn are all assumed to go into and remain in the metallic layer; Cs, Ba, La and U are all assumed to go into and remain in the oxide phase. Thus, as the metallic layer in the cavity disappears, the releases of radionuclide species associated with that layer (*i.e.*, Te, Ru, Cd and Sn) can begin growing exponentially. This is illustrated in Figures 4.5.11 and 4.5.12 for two of these radionuclide species. The effect is not pronounced for Te (as shown in Figure 4.5.5), because most of that species mass had been released prior to the metallic layer vanishing, and the effect is not pronounced for Ru (as seen in Figure 4.5.6) because so little of that refractory is released; however, the release of other species, such as Cd and Sn, is significantly in error. (The Class 7 fission product radionuclides, represented by Mo, and the Class 8 fission product radionuclides, represented by Ce, are associated with the nonradioactive structural Fe and Zr, respectively, and will therefore move from the metallic to the oxidic layer as oxidation progresses.)

As already noted, this problem is inherent in the VANESA formulation itself, not in MELCOR, but is more likely to be encountered with MELCOR 1.8.2 than with MELCOR 1.8.1 because of the increased likelihood of more retention of lower plenum structural steel in-vessel. Code users should check for this potential problem: if a vanishing metallic layer in CORCON is predicted, the time-dependent release of radionuclides in the cavity should be inspected and, if significant releases are occurring ex-vessel and increasing with time, the user sometimes can extrapolate the releases occurring prior to the metallic layer disappearing to estimate the degree of error. However, the problem is significant and needs to be addressed.

The total mass of fission products released from the fuel is shown in Figure 4.5.13. More than half the total release occurred during in-vessel core damage and melt ejection. The in-cavity release, consisting mainly of any volatile species remaining in the fuel ejected to the cavity, primarily occurred soon after vessel failure and melt ejection and before the CORCON layer flip at ~24,000s (6.7hr), with very little release at later times. Most of the fission products released were found in control volumes, in either atmosphere or pool, and about 50-70% of the fission products in the control volumes were vapors rather than aerosols (mostly because aerosols settled out and deposited onto heat structures more readily). The large increase in fission products deposited onto heat structures at ~30,000s (8.3hr), and the corresponding decrease in suspended aerosol mass, was due to boiloff of the cavity pool; once all the water was gone, the aerosols that had been in the cavity volume pool deposited onto the cavity structures. The decrease in fission products

deposited onto heat structures between >40,000s (11hr) and <50,000s (14hr), and the corresponding increase in suspended aerosol mass, was caused by increased removal of deposited radionuclides with draining condensate film runoff, beginning after the end of a series of hydrogen deflagrations in the cavity between ~33,000s (9.2hr) and ~45,000s (12.5hr). That decrease in fission products deposited onto heat structures and the corresponding increase in suspended aerosol mass, cannot be due to aerosol resuspension because the aerosol resuspension model is not active in the current version of MELCOR; that decrease in fission products deposited onto heat structures cannot be due to revaporization, because the fission product vapor mass in the atmosphere and/or pool remains constant. The suspended aerosol mass then dropped slowly through the remainder of the transient calculated as aerosols continued to settle out of the atmosphere and deposit onto structures.

Tables 4.5.2 and 4.5.3 give the distribution of the released radionuclides at the end of the calculation (*i.e.*, at 90,000s or 25hr). Table 4.5.2 provides an overview of how much of the radionuclides remained bound up in fuel in either the core or the cavity, and of how much of the released radionuclides were retained in the primary system *vs* how much of the radionuclides were transported to, or released in, containment. (Because the containment had not failed by the end of the calculation, and because no containment leakage was included in this model, there was no release to the environment calculated.) Table 4.5.3 gives a more detailed breakdown of the final distribution of the released radionuclides in both the primary system and in containment, noting aerosol and vapor forms present in the atmosphere and in the pools (*i.e.*, the water trapped in the loop seal in the primary system, and the water in the basement volume in containment), together with radionuclides deposited onto heat structure surfaces.

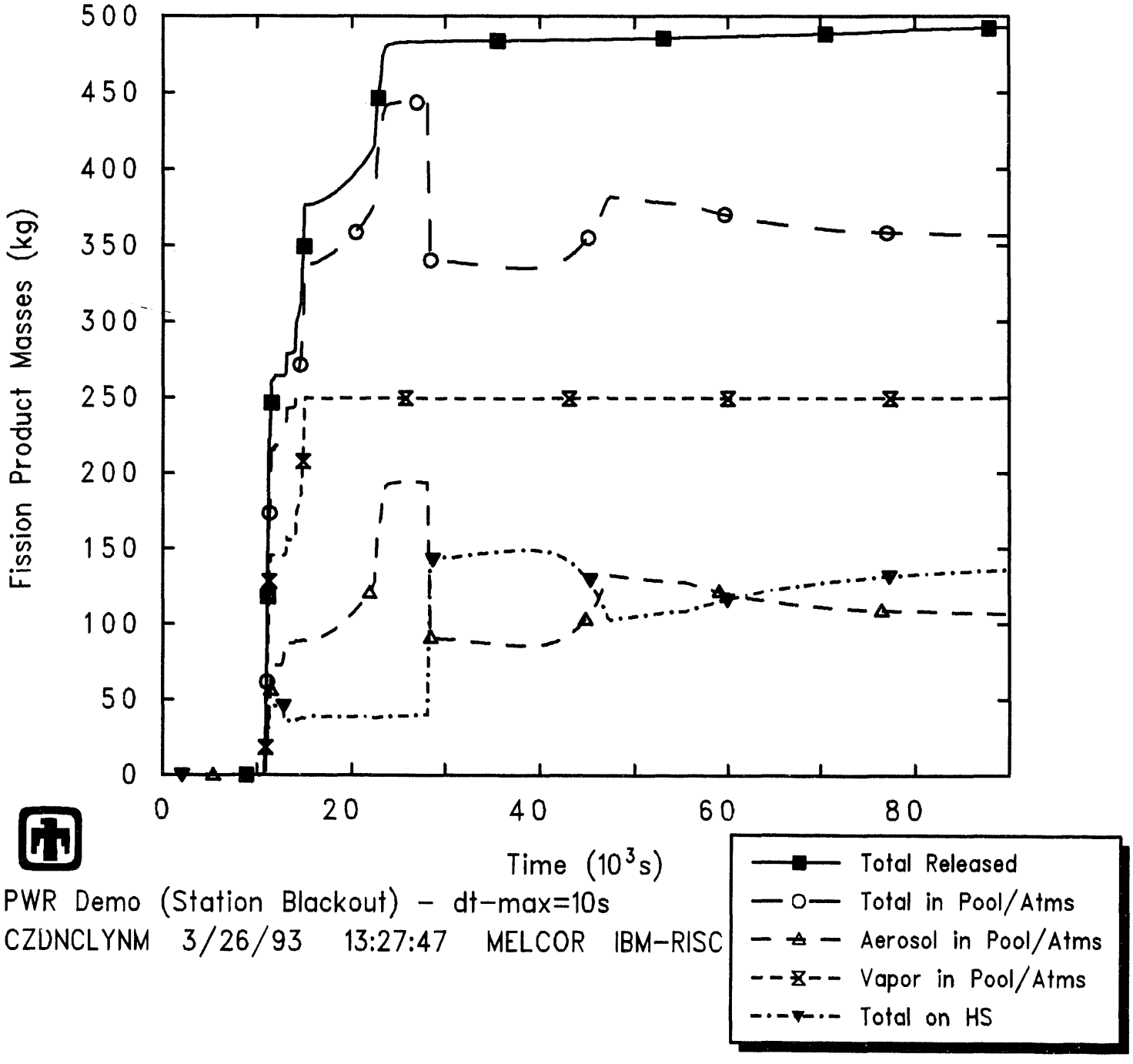

Figure 4.5.13. Released Fission Product Masses - MELCOR 1.8.2 Reference Calculation

Table 4.5.2. Final Fission Product Distribution – MELCOR 1.8.2 Reference Calculation

Class	Fission Product Distribution (% Initial Inventory)				(% Total Released)	
	Core	Cavity	Primary System	Containment	Primary System	Containment
1 (Xe)	0.04	0.0	0.30	99.7	0.30	99.7
2 (Cs)	0.03	0.0	19.8	80.2	19.8	80.2
3 (Ba)	3.56	57.2	2.42	36.8	6.17	93.8
4 (I)	0.06	0.0	0.44	99.5	0.44	99.5
5 (Te)	3.62	27.5	2.19	91.4	2.34	97.7
6 (Ru)	3.98	95.7	0.09	0.20	31.0	69.0
7 (Mo)	3.72	90.8	1.18	4.31	21.5	78.5
8 (Ce)	3.99	96.0	0.002	0.005	28.6	71.4
9 (La)	3.99	95.7	0.006	0.34	1.73	98.3
10 (U)	3.66	96.3	0.005	0.04	1.11	88.9
11 (Cd)	2.48	68.9	8.25	20.4	28.8	71.2
12 (Sn)	2.48	43.8	8.25	45.4	15.4	84.6

Table 4.5.3. Released Fission Product Distribution Details – MELCOR 1.8.2 Reference Calculation

Class	Fission Product Distribution (% Total Released)									
	Primary System					Containment				
	Aerosol		Vapor		Deposited	Aerosol		Vapor		Deposited
	Atms	Pool	Atms	Pool	on HS	Atms	Pool	Atms	Pool	on HS
1 (Xe)			0.30				99.7	0.0011		
2 (Cs)	0.007	0.005	0.075	10^{-6}	19.70	2.29	45.25	0.005	0.042	32.62
3 (Ba)	0.002	0.01			6.17	0.081	20.72			73.02
4 (I)			0.44				99.6			
5 (Te)	0.0002	0.003	0.003	2×10^{-9}	2.33	12.99	31.29	0.027	0.01	53.38
6 (Ru)	0.0036	0.064			31.05	0.08	44.63			24.17
7 (Mo)	0.024	0.029			21.44	0.096	30.76			47.64
8 (Ce)	0.010	0.055			28.44	0.93	39.00			31.59
9 (La)	0.0001	0.003			1.83	0.083	21.70			76.39
10 (U)	0.0008	0.023			11.80	0.42	62.69			24.88
11 (Cd)	0.004	0.022			28.65	2.51	41.11			27.68
12 (Sn)	0.003	0.012			15.36	14.08	26.36			44.21

5 MELCOR 1.8.2 *vs* 1.8.1

As part of the MELCOR Peer Review process [11], Sandia performed and presented a demonstration calculation of the Surry station blackout (TMLB') accident with MELCOR. This was the first fully-integrated PWR severe accident calculation performed with the code (since an earlier TMI analysis [24] only included in-vessel phenomena), and was done using the release version of MELCOR 1.8.1. That calculation has been rerun with the release version of MELCOR 1.8.2, allowing direct comparison of predicted results for the same problem, with results described in this section.

This analysis also has been used as a standard test problem to investigate problems identified by the Peer Review (*e.g.*, lack of pressurizer draining prior to vessel breach) and to evaluate the impact on the results of model improvements and extensions (for example, adding the CORSOR-Booth fission product release model) and of new models (such as radial debris relocation, material eutectics interactions, and direct containment heating due to high pressure melt ejection); the results of those studies are presented in Section 6.

No input changes were required between running with the release versions of MELCOR 1.8.1 and 1.8.2. However, as discussed in Section 3, a small number of input changes were made in the basecase MELCOR model to take advantage of new models and/or upgraded models.

For the 1.8.2 *vs* 1.8.1 comparison presented in this section, the reference 1.8.2 calculation discussed in detail in Section 4 was not used, because that analysis takes full advantage of new features available in MELCOR 1.8.2. Instead, a 1.8.2 calculation was done with minimal input changes. Minor input changes in the basecase MELCOR model that take advantage of some of the new models and/or upgraded models such as using step functions in valve area-*vs*-time tables and reducing surge-line flow-path interfacial momentum exchange length were retained. The new debris radial relocation model is enabled by default and was used in this 1.8.2 *vs* 1.8.1 comparison; the new core material eutectics interaction model, which is not used by default and which must be enabled through input, was not used in this 1.8.2 *vs* 1.8.1 comparison. Other input changes made for the reference analysis discussed in detail in Section 4 and for various other sensitivity studies, especially specifying high-pressure melt ejection debris distribution and direct containment heating interactions, also were not used in the MELCOR 1.8.2 calculation used in this comparison.

(Both the MELCOR 1.8.2 and the MELCOR 1.8.1 calculations compared in this section were run on a SUN Sparc2 workstation, unlike the MELCOR 1.8.2 reference calculation described in detail in Section 4, which was run on an IBM RISC-6000 Model 550 workstation.)

Table 5.1 summarizes the timings of various key events predicted by these two MELCOR versions. (Note that messages reporting core plate failure, added to the standard output in MELCOR 1.8.2, were not explicitly recorded by MELCOR 1.8.1 so that that information had to be estimated from the plot output.)

Table 5.1. Timing of Key Events – MELCOR 1.8.2 *vs* 1.8.1

Event	Time MELCOR 1.8.2	MELCOR 1.8.1
Gap Release		
Ring 1	10,226.4s (2.84hr)	9,998.9s (2.78hr)
Ring 2	10,336.4s (2.87hr)	10,095.6s (2.80hr)
Ring 3	10,666.4s (2.96hr)	10,418.9s (2.89hr)
Core Plate Fails		
Ring 1	11,663.2s (3.24hr)	11,260.9s (3.13hr)
Ring 2	12,754.4s (3.27hr)	11,961.7s (3.32hr)
Ring 3	12,246.4s (3.40hr)	13,970.5s (3.88hr)
LH Penetration Fails		
Ring 1	11,708.8s (3.25hr)	14,998.0s (4.17hr)
Ring 2	11,792.7s (3.28hr)	15,698.4s (4.36hr)
Ring 3	14,182.9s (3.94hr)	17,715.1s (4.92hr)
Debris to Cavity	11,786.6s (3.27hr)	15,021.4s (4.17hr)
Deflagrations Start	12,703.2s (3.53hr)	–
Deflagrations End	14,413.7s (4.00hr)	–
CORCON layer flip	~23,000s (6.4hr)	~27,000s (7.5hr)
Deflagrations Start	32,222.7s (8.95hr)	46,622.9s (12.95hr)
Deflagrations End	36,992.3s (10.28hr)	49,751.5s (13.82hr)

The results of the same transient run with MELCOR 1.8.1 and 1.8.2 show generally very similar early-time behavior. Figure 5.1 shows that the coolant inventory in the steam generator secondary was boiled off at the same rate in the two calculations. The predicted increase in pressurizer liquid level and the initial venting of primary-system inventory out the pressurizer was also very similar using the older and newer code versions, as indicated in Figure 5.2; the PORV opened at ~5250s (1.46hr) in the MELCOR 1.8.2 analysis, compared to an initial opening time of ~5350s (1.49hr) in the MELCOR 1.8.1 calculation. Note that the MELCOR 1.8.2 calculation showed slightly faster pressurizer draining just before vessel breach than did MELCOR 1.8.1, but substantial amounts of liquid remained in the pressurizer up to the time of vessel failure in both calculations. (Results of a sensitivity study on pressurizer draining are discussed in Section 6.1.)

Figure 5.3 gives swollen and collapsed liquid levels in the core. As with the steam generator secondary and pressurizer responses, the results from the same transient run with MELCOR 1.8.1 and 1.8.2 showed generally very similar behavior. There was also little difference in early core heatup, with initial clad failure and gap release in the three core rings in the MELCOR 1.8.1 calculation all ≤4min earlier than in the corresponding MELCOR 1.8.2 analysis.

While there was little difference in core uncovery and in the early core heatup and degradation, the vessel was calculated to fail ~1hr earlier by MELCOR 1.8.2 than by MELCOR 1.8.1. Lower core and lower plenum liquid levels are given in close-up view in Figure 5.4, and core support plate temperatures in the inner ring (the ring that fails the core plate first) are presented in Figure 5.5. Both code versions showed the liquid level dropping in the lower plenum while water was still present in the core control volume, in the lowest core active fuel level, but MELCOR 1.8.2 showed the liquid level dropping in the lower core slightly earlier. The core support plate began to heat up as soon as the lower plenum liquid level began to drop in the MELCOR 1.8.2 calculation, after which the core support plate continued to heat up almost linearly until reaching the 1273K failure criterion. In contrast, the MELCOR 1.8.1 calculation showed only intermittent core plate temperature excursions while the upper part of the lower plenum volume, that occupied by the core plate, was completely uncovered; sustained core plate heatup did not begin until the core control volume and therefore the lowest level of active fuel was uncovered, about 0.25hr after the core support plate was uncovered in the MELCOR 1.8.1 calculation (and about 0.35hr after the core support plate was uncovered in the corresponding MELCOR 1.8.2 calculation).

Initially, after heatup begins, the core support plate heated up more slowly in the MELCOR 1.8.1 calculation than in the MELCOR 1.8.2 calculation. Sensitivity study results in Section 6.2 show that this is probably due to using the new debris radial relocation model (enabled by default) in the MELCOR 1.8.2 analysis; with the debris radial relocation model, debris in the outer two rings moved sideways to the innermost high-powered ring, which was being degraded most rapidly, and thus there was more hot debris on the core plate in the innermost ring, increasing its heatup rate. Furthermore, in the MELCOR 1.8.1 calculation, the core support plate (in ring 1) did not fail when it reached 1273K, because the code logic in version 1.8.1 did not allow failure of a blocked

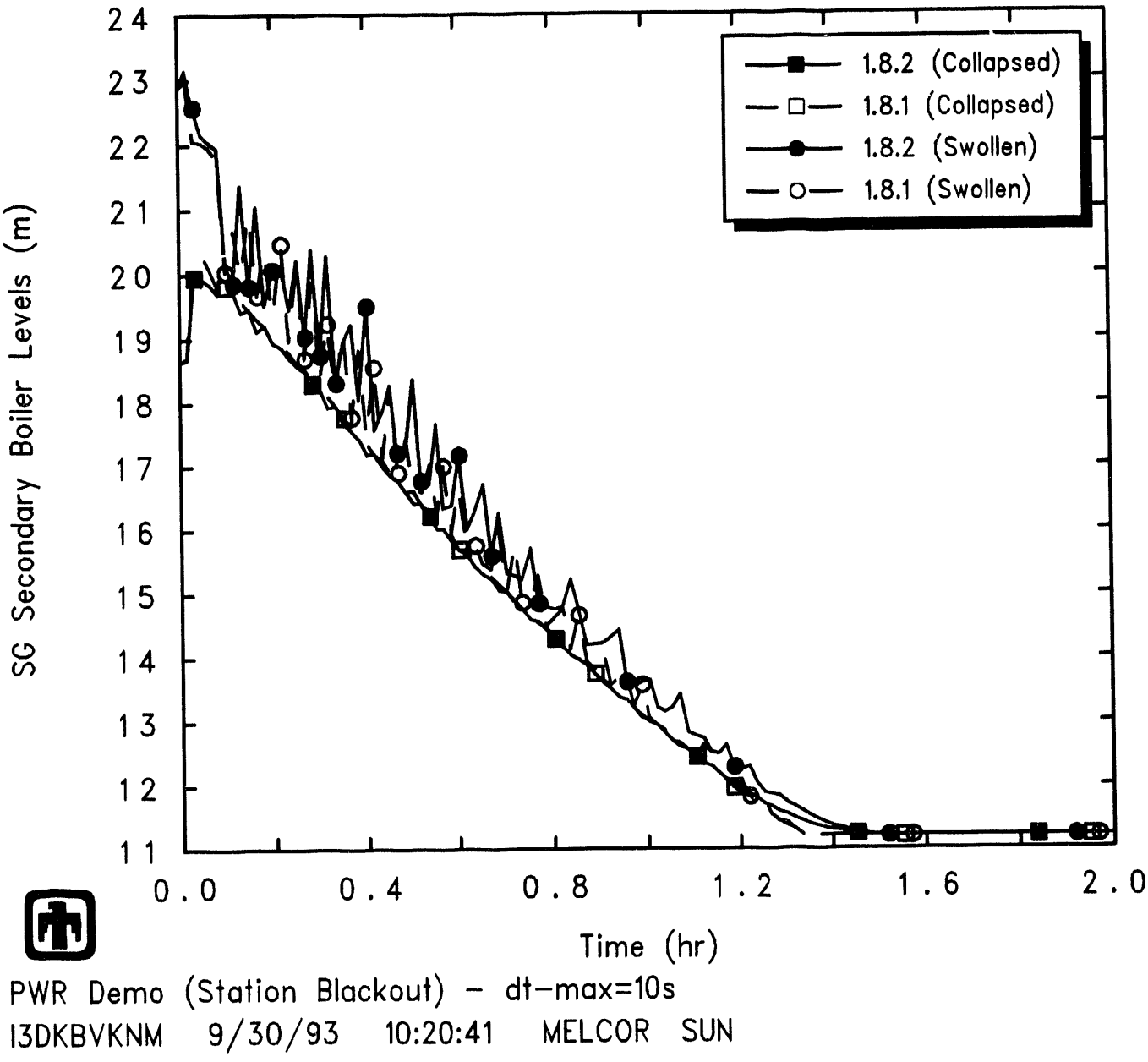

Figure 5.1. SG Secondary-Side Liquid Levels - MELCOR 1.8.2 *vs* 1.8.1

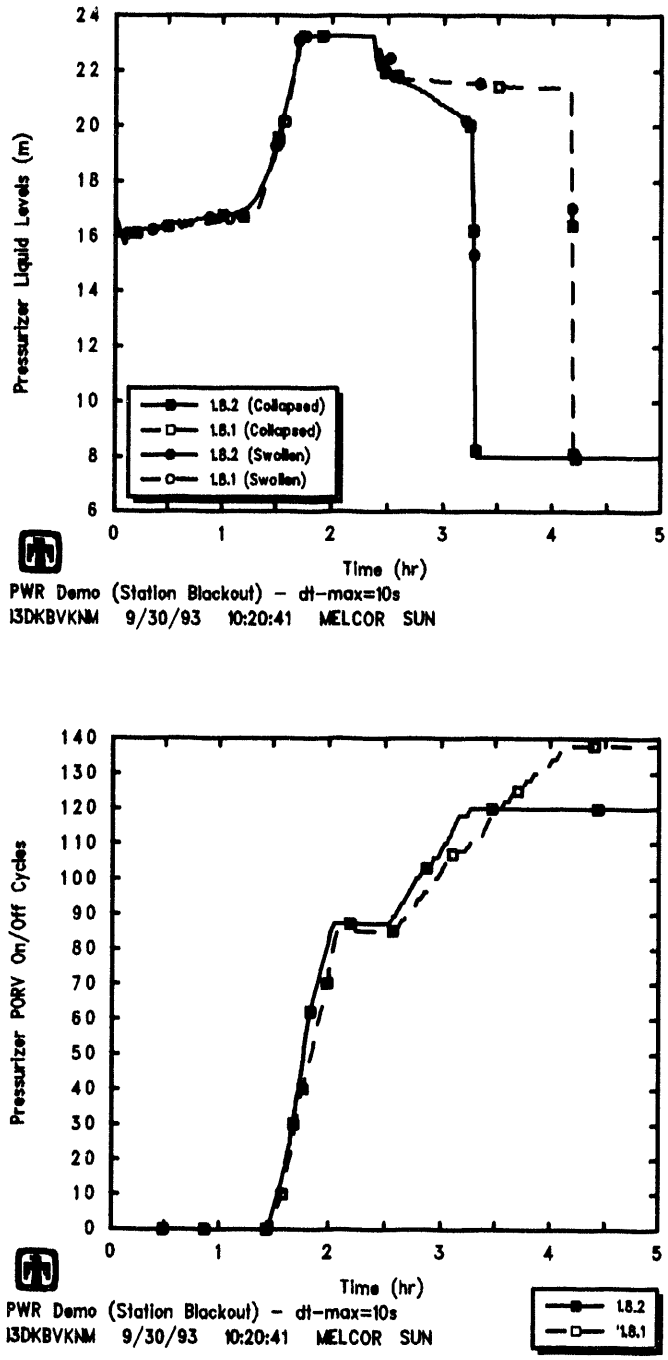

Figure 5.2. Pressurizer Liquid Levels (Top) and PORV Cycling (Bottom) -- MELCOR 1.8.2 *vs* 1.8.1

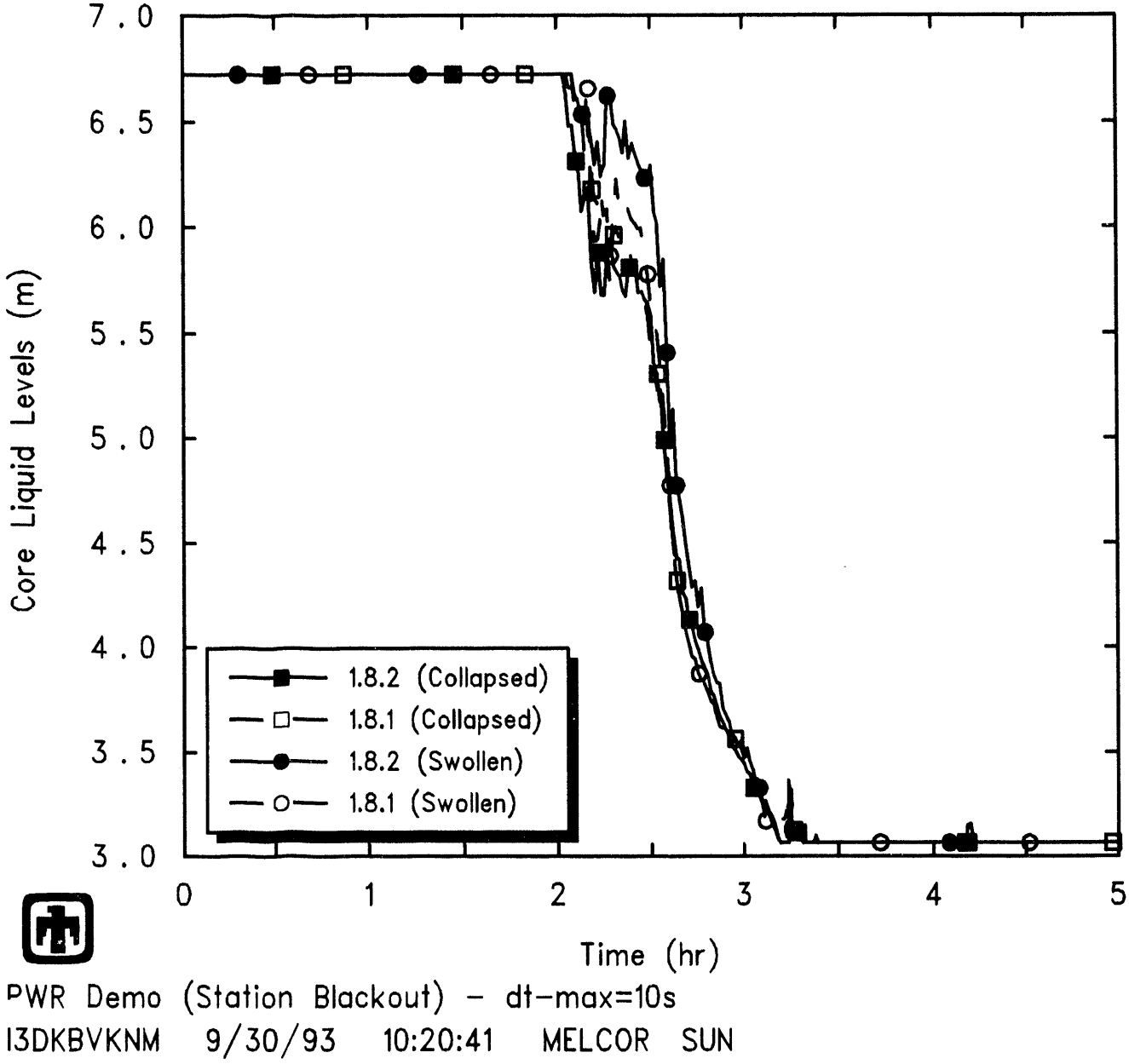

Figure 5.3. Core Liquid Levels - MELCOR 1.8.2 *vs* 1.8.1

component (as the core plate is at this time in ring 1) until the blockage material reached melt temperature. In both calculations, material fell into the lower plenum as particulate debris after core plate failure, and the lower head penetration (in ring 1) heated up to 1273K and fails within a few minutes after debris first fell into the lower plenum.

Table 5.2 summarizes the state of the various materials in the core active fuel region, core plate and lower plenum at the time a lower head penetration first fails (*i.e.*, at vessel breach), in the MELCOR 1.8.2 and MELCOR 1.8.1 calculations. Masses of intact components and of debris components are given for each region, together with average temperatures for the debris in the lower plenum, and fractions of zircaloy and steel oxidized by the time of vessel breach.

There is a very significant difference in the core state at the time of vessel failure in these two calculations. With a debris radial relocation model not available in MELCOR 1.8.1, there was much less debris in the lower plenum at the time a lower head penetration first failed; in particular, the amount of debris in the lower plenum corresponds quite well to the mass of material initially present in the active fuel region in the ring whose core plate failed just previously (*i.e.*, the first, inner, high-powered ring). In the MELCOR 1.8.2 calculation with the debris radial relocation model enabled, the mass of debris in the lower plenum at the time a lower head penetration first failed was much greater, about half the total mass initially present in the active fuel region. Also, in the MELCOR 1.8.2 calculation with the debris radial relocation model enabled, most of the material remaining in the active fuel region was "intact" (either still in its initial location or refrozen onto intact components). However, in the MELCOR 1.8.1 calculation with no debris radial relocation modelled, most of the material still in the active fuel region (*i.e.*, above the core support plate) was predicted to be particulate debris. This is the old problem of "stacking" of debris in separate columns, seen in many MELCOR 1.8.1 calculations; without the debris radial relocation model, debris in the outer two rings could not move sideways to the empty inner ring and move down to fall through the failed core plate in that innermost ring.

The primary system pressures predicted by MELCOR 1.8.2 and by MELCOR 1.8.1 were quite similar at early times, until the difference in vessel failure time caused a timing shift in primary system depressurization, as indicated in Figure 5.6; after vessel depressurization, the primary system pressure tracked the containment pressure, in both cases. Figure 5.7 gives the pressures calculated in the containment dome, using the two code versions. Except at late times in the cavity, the containment atmosphere was at saturation in both calculations, with similar agreement to the pressure behavior. There was very little change in calculated containment response, with the pressure spike at vessel breach shifted in time due to the different vessel failure times, but the same long-term pressure and temperature response predicted by both MELCOR 1.8.1 and 1.8.2. (Note that this direct comparison did not use the new direct containment heating model added in MELCOR 1.8.2, but even with that model enabled there was simply an increase in the containment pressure spike at vessel failure, and no other significant long-term differences in predicted system response, as discussed in more detail in Section 6.5.)

In both the MELCOR 1.8.2 and MELCOR 1.8.1 calculations, no hydrogen burns

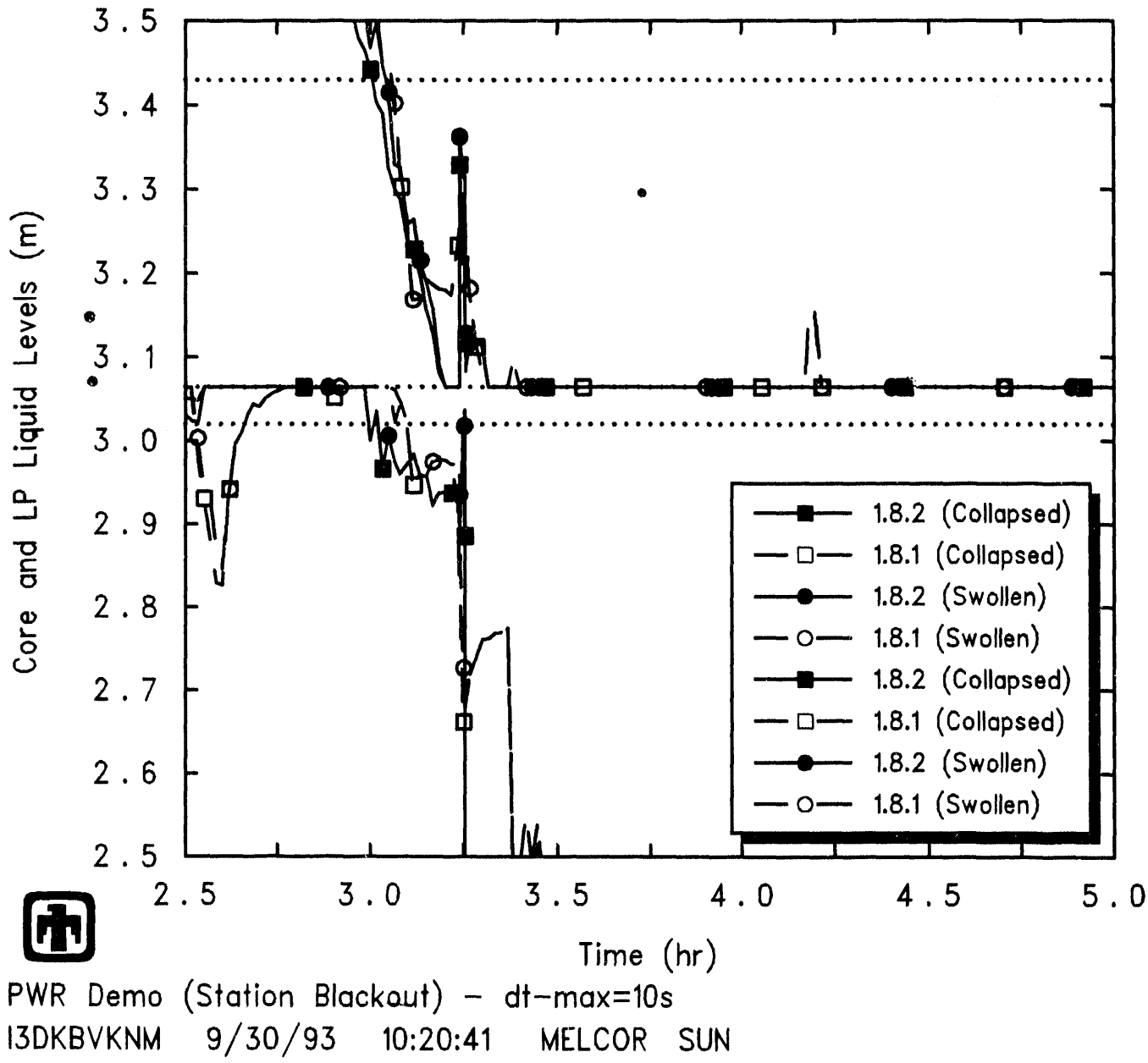

Figure 5.4. Lower Core and Lower Plenum Liquid Levels - MELCOR 1.8.2 *vs* 1.8.1

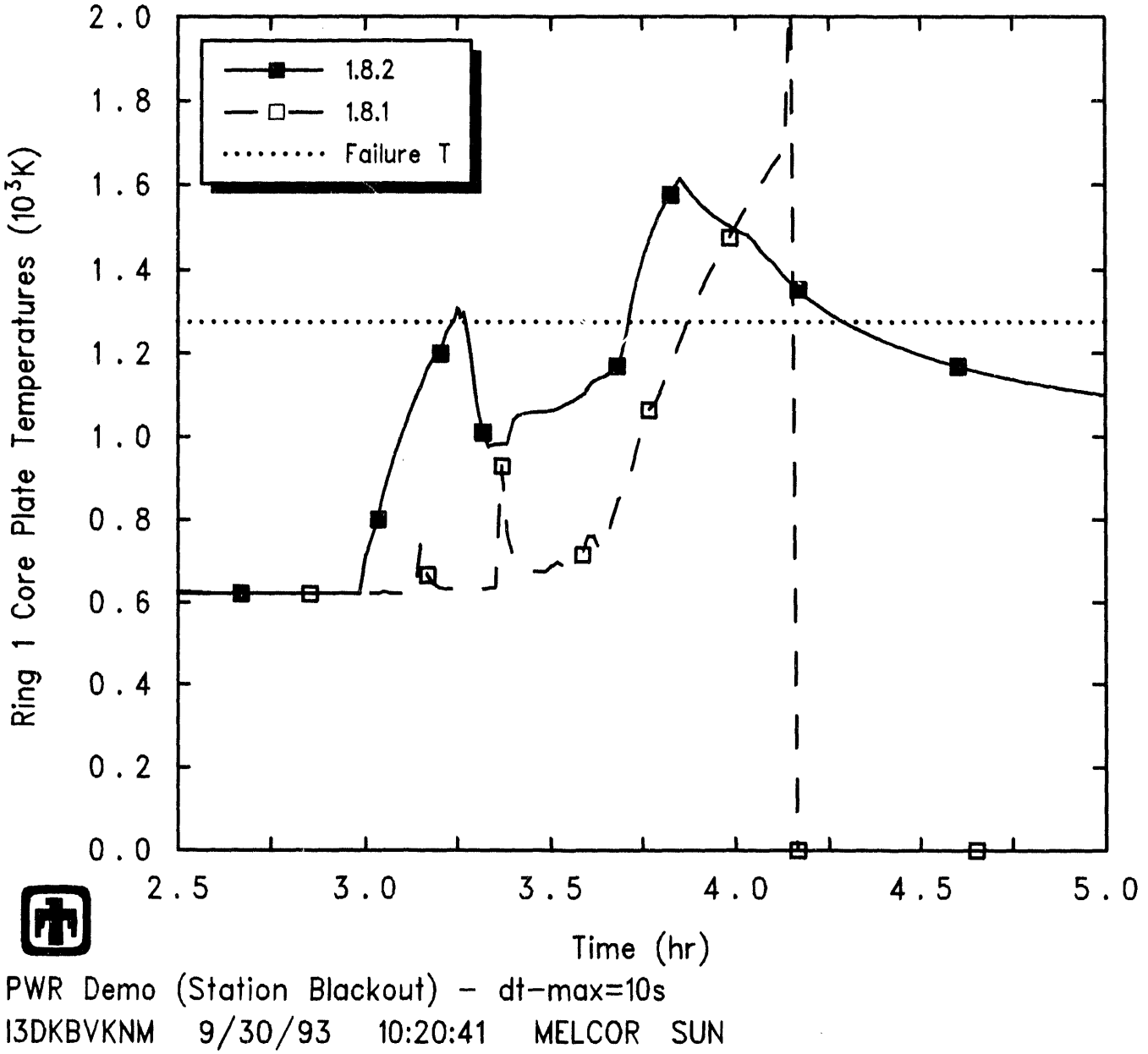

Figure 5.5. Core Support Plate Temperatures – MELCOR 1.8.2 *vs* 1.8.1

Table 5.2. Core State at Vessel Failure - MELCOR 1.8.2 *vs* 1.8.1

	MELCOR 1.8.2		MELCOR 1.8.1	
	Intact	Debris	Intact	Debris
Active Fuel Region Masses (kg)				
UO_2	11,430	6,748	5,553	62,196
Zircaloy	6,648	1,299	1,444	9,227
Zirc Oxide	2,249	729	280	3,296
Steel	1,485	20	298	18
Steel Oxide	65	24	95	11
CRP	993	340	884	
Total	22,870	9,160	11,074	74,748
Core Plate Masses (kg)				
UO_2		1,196		31
Zircaloy		165		153
Zirc Oxide		40		57
Steel	1,815	3	1,525	18
Steel Oxide				
CRP				754
Total	1,815	1,404	1,525	1,013
Lower Plenum Masses (kg)				
UO_2		62,268		12,853
Zircaloy		4,164		2,035
Zirc Oxide		2,126		707
Steel	32,675	175	32,990	
Steel Oxide	5	108	31	
CRP		672		368
Total	32,681	69,514	33,021	15,963
Average Debris Temperature (K)		~2175		~2850
Fraction Oxidized	Zircaloy ~24%	Steel ~0.4%	Zircaloy ~20%	Steel ~0.3%

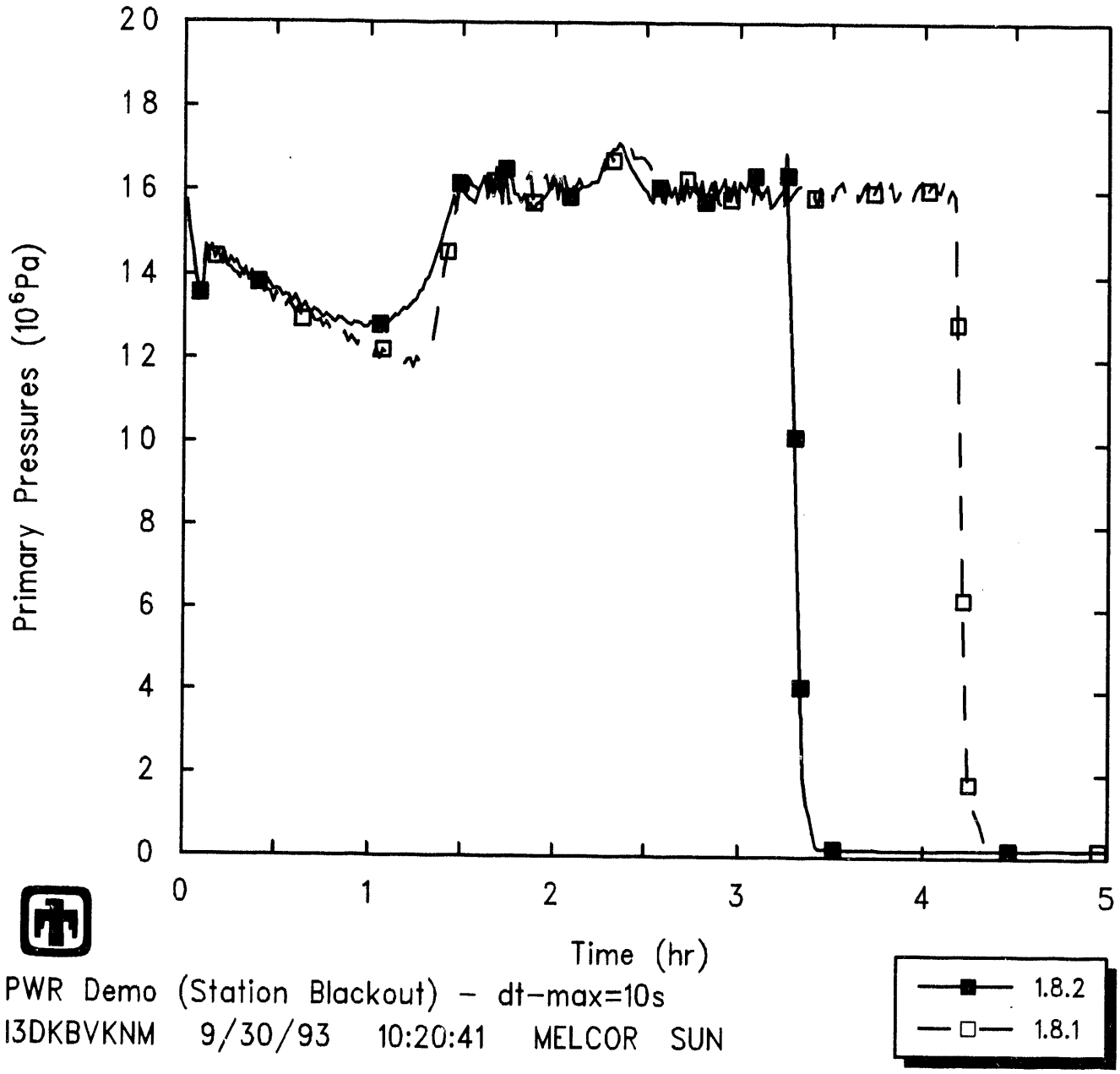

Figure 5.6. Primary System Pressure – MELCOR 1.8.2 *vs* 1.8.1

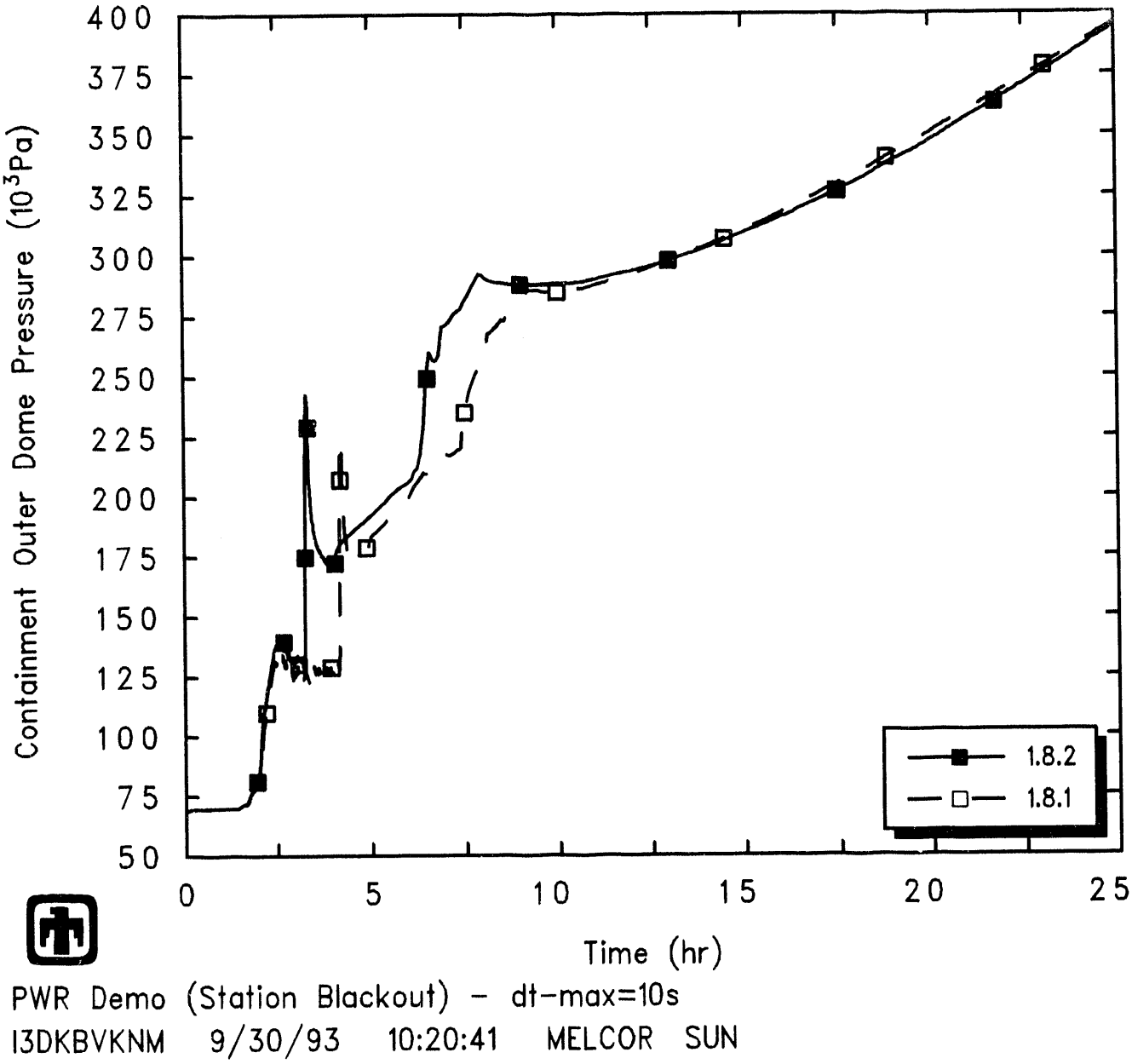

Figure 5.7. Containment System Pressures - MELCOR 1.8.2 *vs* 1.8.1

occurred in the containment outside the cavity during the calculation, owing to steam and/or carbon dioxide inerting in all other containment control volumes throughout the transient. The MELCOR 1.8.1 calculation predicted a series of hydrogen burns in the cavity beginning at 46,622.9s (12.95hr) and ending at 49,751.5s (13.82hr), as shown in Table 5.1 and in the upper plot in Figure 5.8. That plot also shows that the analysis using MELCOR 1.8.2 predicted two series of hydrogen burns, a relatively small, short series between 12,703.2s (3.53hr) and 14,413.7s (4.00hr) and a second, longer series between 32,222.7s (8.95hr) and 36,992.3s (10.28hr); the second series of burns probably corresponds qualitatively to the combustion predicted by MELCOR 1.8.1, given the accelerated sequence of events calculated by MELCOR 1.8.2. The amount of hydrogen burned also varied significantly in the two calculations, proportionally to the number of burns predicted, as illustrated in the lower plot in Figure 5.8. As will be discussed more in Section 7, this probably is largely a result of numerical effects in the burn package, in both the older and newer code versions.

More hydrogen was generated in-vessel in the MELCOR 1.8.2 analysis than in the MELCOR 1.8.1 analysis, but the total hydrogen generated (adding together in-vessel and in-cavity production) by the two code versions was within 5%, as shown in Figure 5.9.

Figure 5.10 shows the total masses of core materials (UO_2, Zircaloy and zirc oxide, and stainless steel and steel oxide) remaining in the vessel throughout the transient in the two calculations; the small amount of control rod poison material is not shown to avoid even more clutter in the plot. Debris ejection began almost immediately after lower head failure, earlier with MELCOR 1.8.2 than with MELCOR 1.8.1. All the UO_2 was transferred to the cavity, as was most of the unoxidized zircaloy, the oxides and the control rod poison, in both calculations; however, a small amount (~15%) of the structural steel in the lower plenum (and an associated small amount of oxidized steel) was predicted to remain unmelted and in place throughout the remaining transient period in the MELCOR 1.8.2 analysis, while all the steel and steel oxide was transferred to the cavity in the MELCOR 1.8.1 analysis, albeit over some time period after initial vessel breach.

The mass of core debris in the cavity, the mass of ablated concrete, and the resultant total mass of debris are presented in Figure 5.11. While the MELCOR 1.8.2 calculation had core debris entering the cavity earlier, due to the earlier vessel failure in that analysis, the MELCOR 1.8.1 calculation had more core debris eventually ejected to the cavity, and more concrete ablated later in the transient; the greater mass of core debris in the cavity in the MELCOR 1.8.1 analysis is a direct result of the greater retention of structural steel in the lower plenum in the MELCOR 1.8.2 calculation (as visible in Figure 5.10).

Figure 5.12 shows the thicknesses of the light oxide, metallic and heavy oxide debris layers in the cavity. A CORCON layer flip occurred at about 23,000s (6.4hr) in the MELCOR 1.8.2 calculation and at about 27,000s (7.5hr) in the MELCOR 1.8.1 calculation, with the delay primarily reflecting the difference in predicted vessel failure time in these two cases. This layer flip occurred when enough concrete had been ablated (with its resultant low-density silicate oxides) to dilute the high-density zirc oxide and steel oxide debris to an average density value less than the metallic debris density.

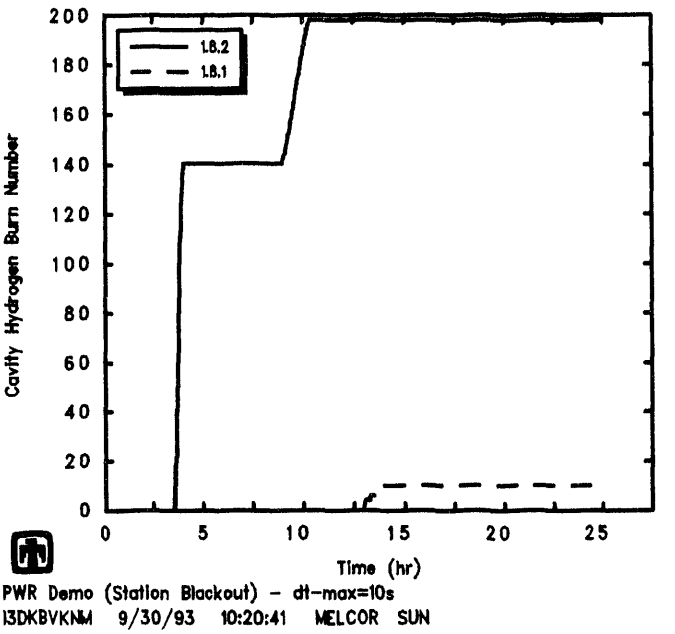

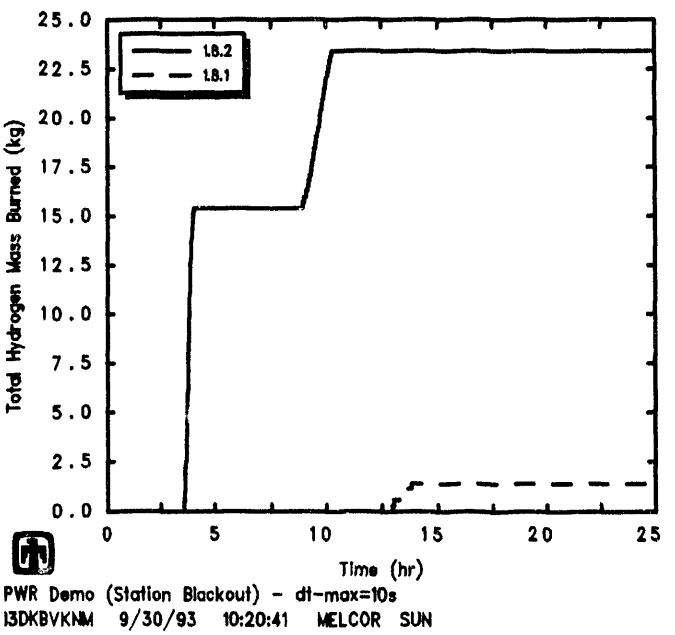

Figure 5.8. Number of (top) and Masses Burned in (bottom) Cavity Hydrogen Deflagrations - MELCOR 1.8.2 *vs* 1.8.1

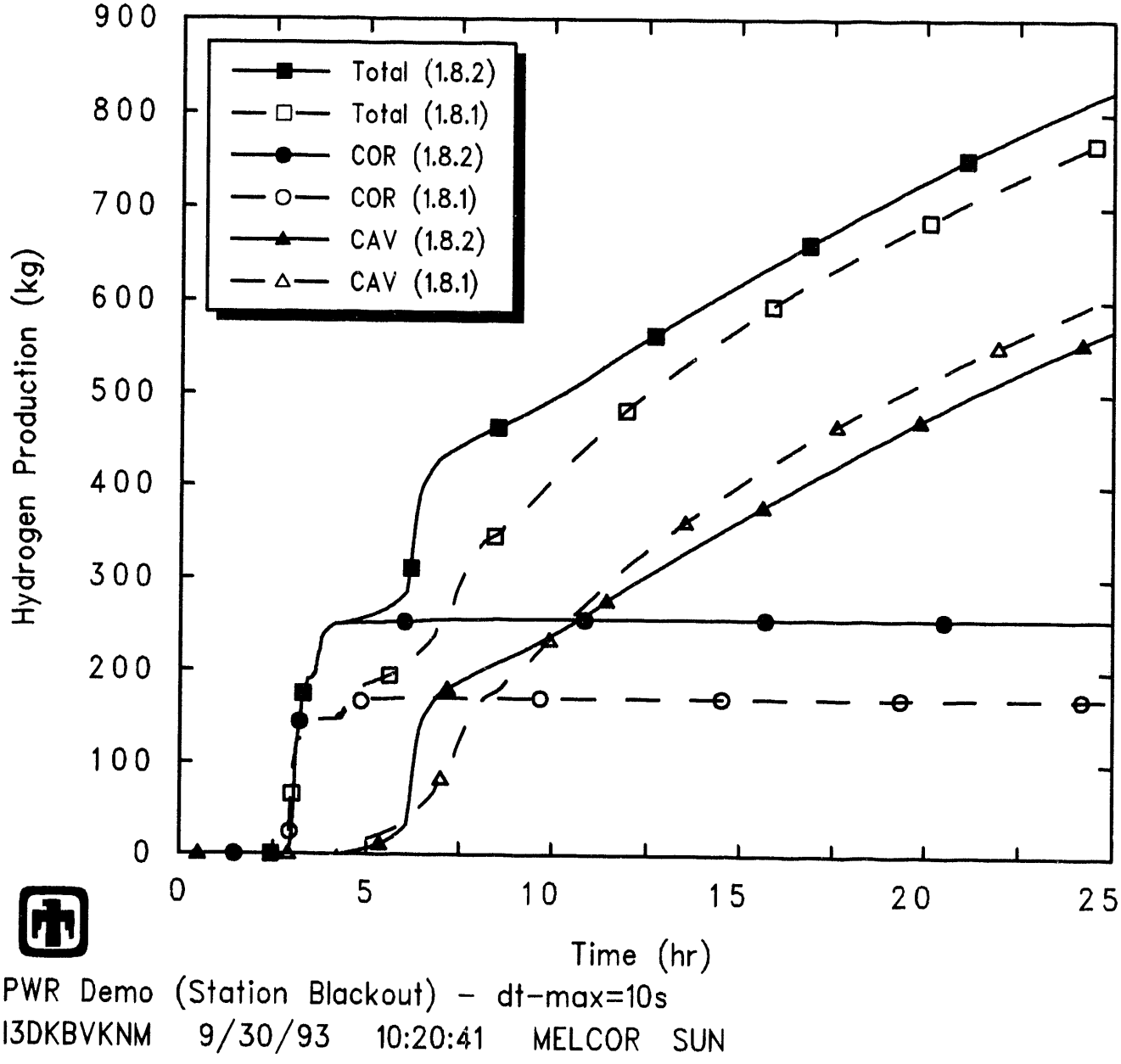

Figure 5.9. Hydrogen Production MELCOR 1.8.2 *vs* 1.8.1

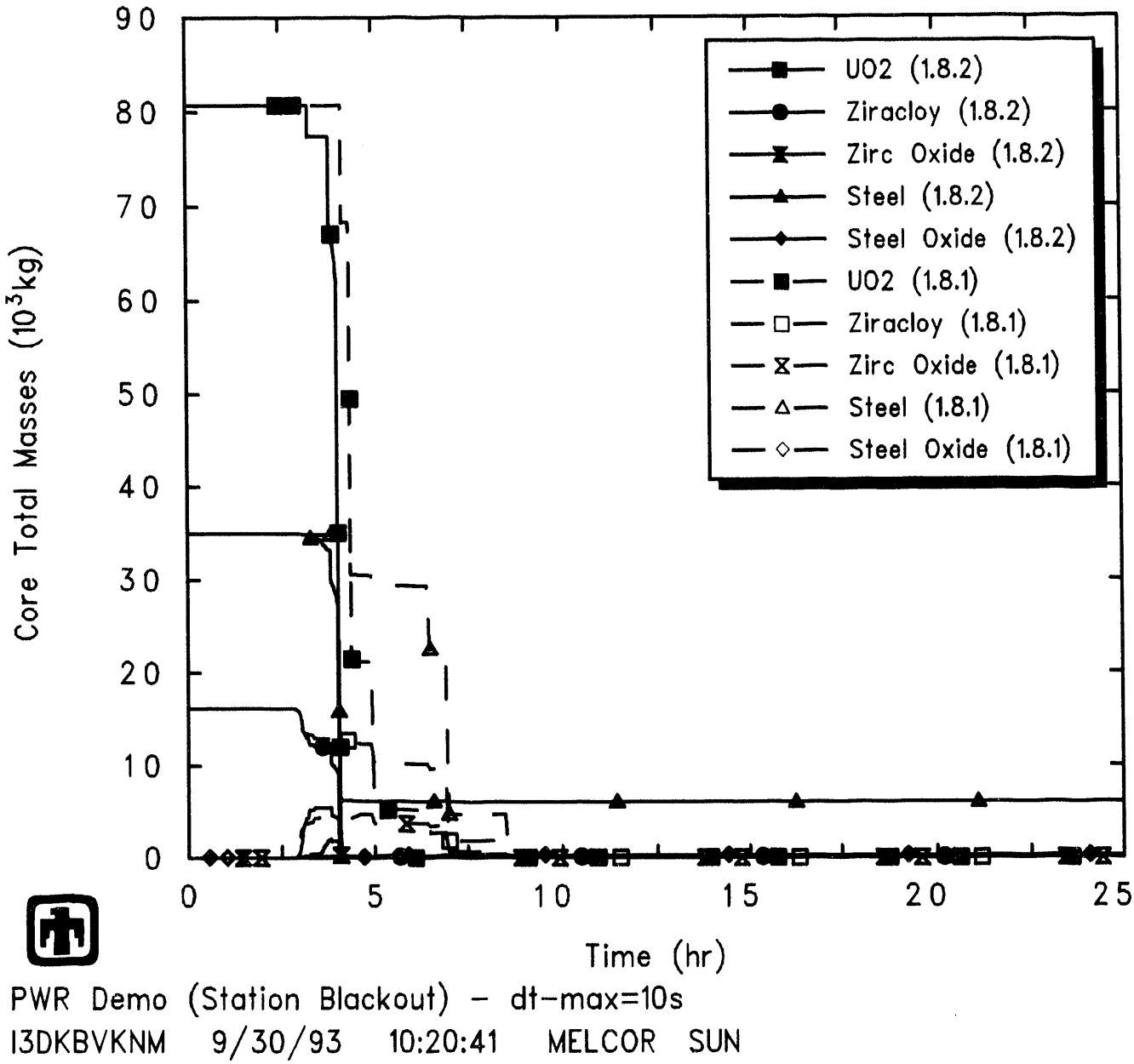

Figure 5.10. Total Core Masses - MELCOR 1.8.2 *vs* 1.8.1

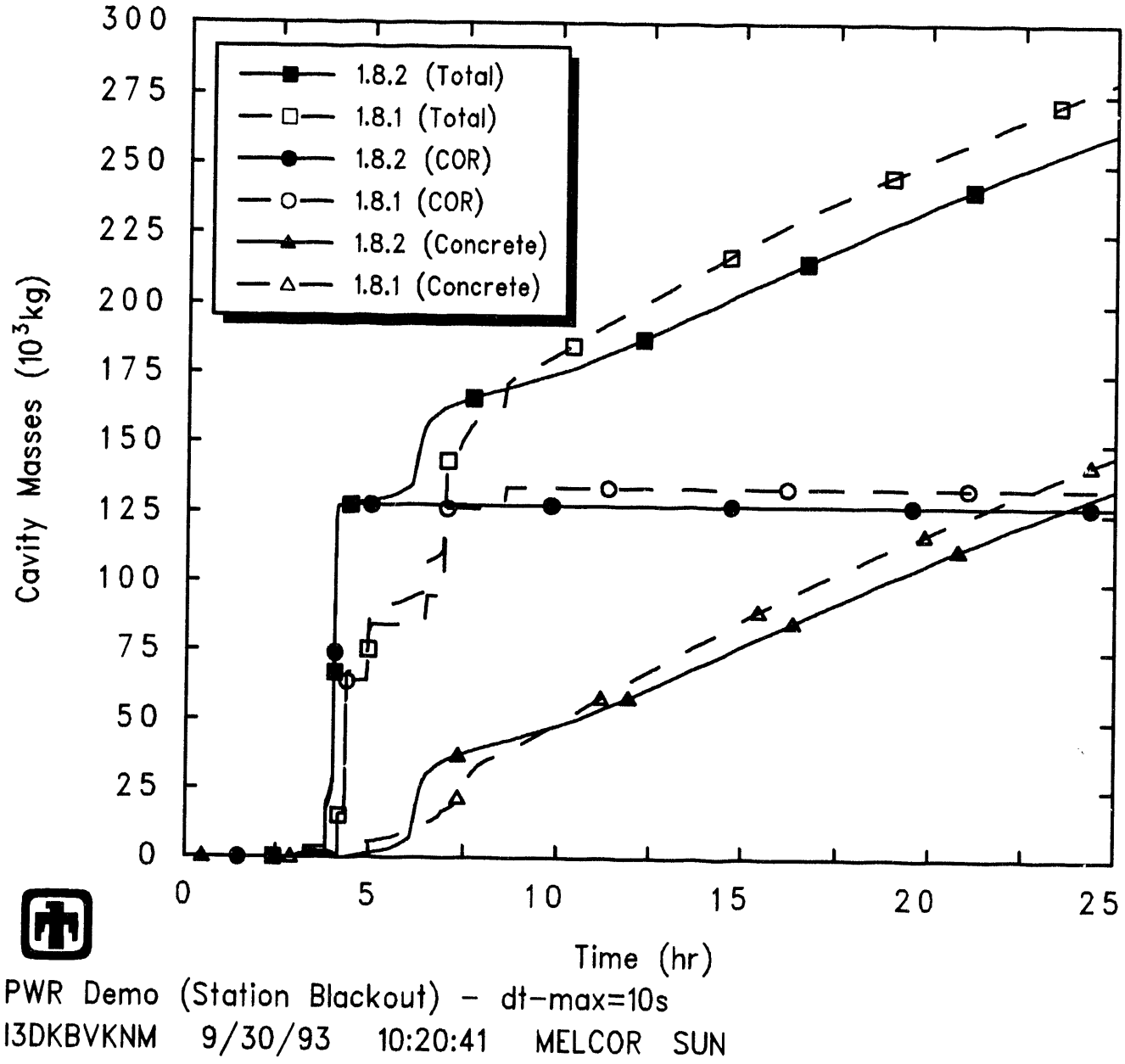

Figure 5.11. Cavity Masses - MELCOR 1.8.2 *vs* 1.8.1

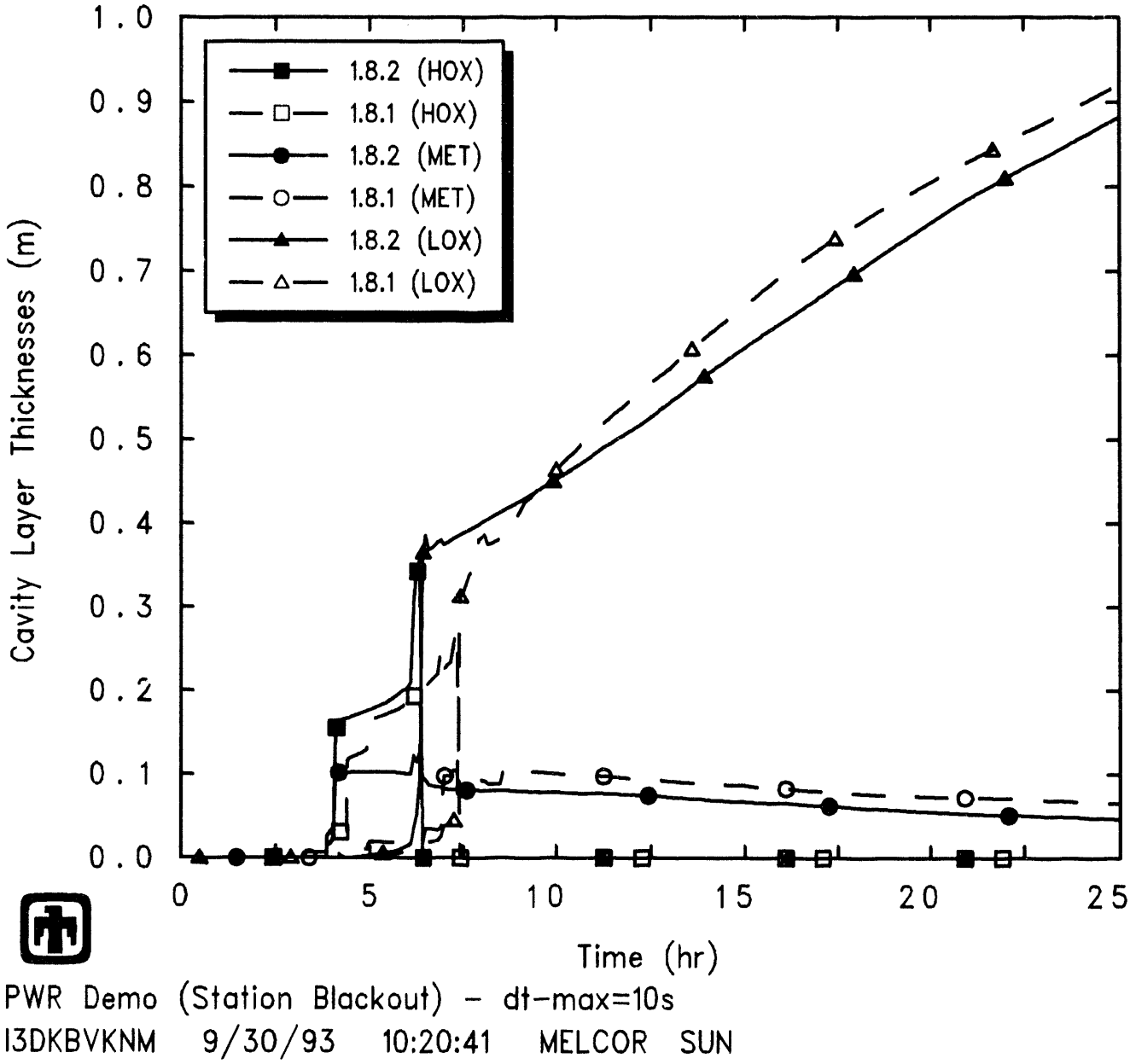

Figure 5.12. Cavity Layer Thicknesses – MELCOR 1.8.2 *vs* 1.8.1

Table 5.3. Fission Product Release – MELCOR 1.8.2 *vs* 1.8.1

Class	(% Initial Inventory) In-Vessel Release		In-Cavity Release		Total Release	
	1.8.2	1.8.1	1.8.2	1.8.1	1.8.2	1.8.1
1 (Xe)	63.517	94.099	36.458	5.8979	99.975	99.997
2 (Cs)	63.545	94.103	39.245	6.3444	102.79	100.45
3 (Ba)	3.1039	38.681	20.651	5.7530	23.755	44.434
4 (I)	63.500	94.094	0.0	0.0	63.500	94.094
5 (Te)	4.4007	34.786	43.727	36.651	48.128	71.438
6 (Ru)	0.0870	2.0211	6×10^{-7}	2×10^{-6}	0.0870	2.0211
7 (Mo)	2.3793	17.867	0.7352	1.0938	3.1145	18.960
8 (Ce)	0.0025	0.0393	0.0011	0.0013	0.0036	0.0406
9 (La)	0.0088	0.3024	0.1115	0.0391	0.1203	0.3415
10 (U)	0.0092	0.3023	0.0021	0.0018	0.0113	0.3041
11 (Cd)	10.224	69.257	0.2411	0.1659	10.465	69.422
12 (Sn)	10.225	69.255	2.5394	1.3662	12.764	70.621

There is little difference in the cavity layer temperatures calculated, ~1750K in both cases after layer flip was predicted to occur and steady cavity conditions became established. Figure 5.13 gives the maximum cavity depth and radius. The relocation of the metallic layer to the bottom of the cavity caused an increase in the rate of ablation vertically downward and temporarily halted further radial ablation in both MELCOR analyses; radial ablation continued later in both calculations, albeit more slowly and to a lesser degree than the axial ablation.

The release of fission products from the fuel by 90,000s is summarized in Table 5.3. Fractional releases are given both in-vessel and in the cavity, together with total releases. Both calculations used the CORSOR fission product release model option, with the S/V term included. (Note that Table 5.3 shows the same lack of any ex-vessel release for Class 4 in the MELCOR 1.8.1 analysis as in the MELCOR 1.8.2 analysis, due to the same class-mapping coding problem already discussed in Section 4.5.)

Overall, almost all of the Class 1, Class 2 and Class 4 volatiles were released from the fuel by the end of both MELCOR calculations. A much larger fraction of that release occurred in-vessel in the MELCOR 1.8.1 calculation than in the MELCOR 1.8.2 analysis. In fact, all the classes showed much higher in-vessel releases in the MELCOR 1.8.1 analysis than in the MELCOR 1.8.2 analysis. This is due primarily to the delay in core plate failure (and subsequent lower head penetration failure) in the MELCOR 1.8.1 run, for reasons already discussed above; the delay in core plate failure caused hot fuel, both intact and in debris, to be retained in the vessel for an extra ~1hr, as

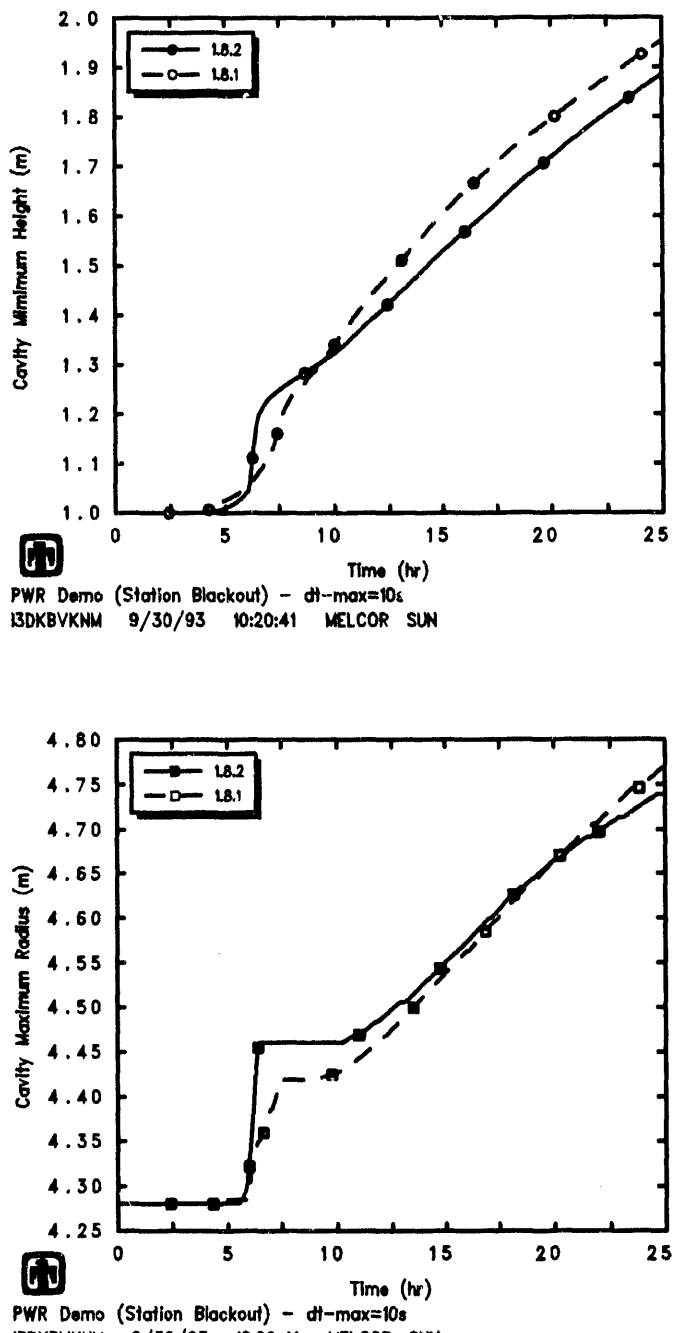

Figure 5.13. Cavity Maximum Depth (Top) and Radius (Bottom) - MELCOR 1.8.2 *vs* 1.8.1

shown respectively in Figures 5.14 and 5.15 for sample cells in the lower and upper core, significantly increasing the available time and maintaining sufficiently high temperatures for fission product release in-vessel.

The release behavior predicted by MELCOR can be grouped into several subdivisions, qualitatively similar in the MELCOR 1.8.2 and 1.8.1 calculations. Assuming the correct iodine behavior, ~100% of the Class 1, Class 2 and (corrected) Class 4 radionuclide inventories were released. The next major release fractions were of Te and Ba, Cd and Sn, all between ~10% and ~70%. Finally, a total $\leq$1-2% of the initial inventory of the refractories (Ru, Ce, La and U) were released with both the older and newer codes. (Note that these amounts generally consider only the release of radioactive forms of these classes, and not additional releases of nonradioactive aerosols from structural materials.)

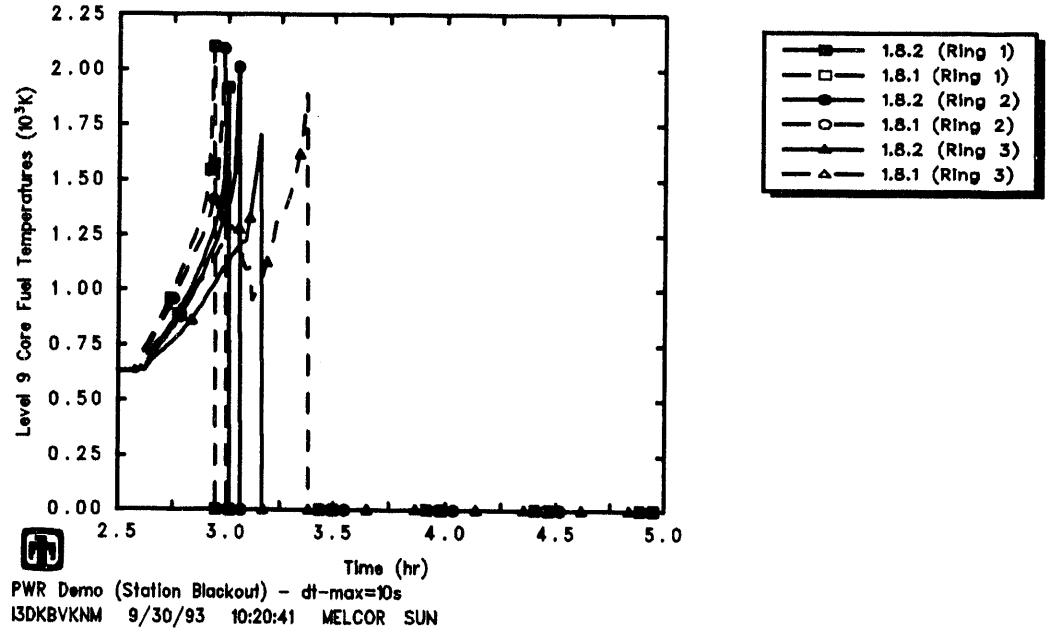

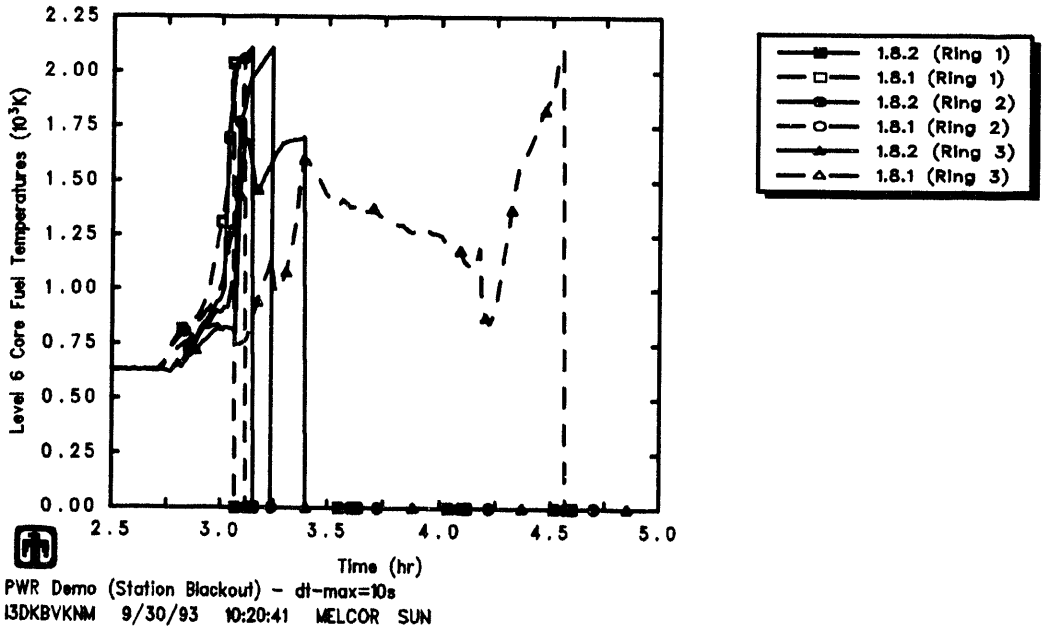

Figure 5.14. Upper (Top) and Lower (Bottom) Core Region Fuel Temperatures - MELCOR 1.8.2 *vs* 1.8.1

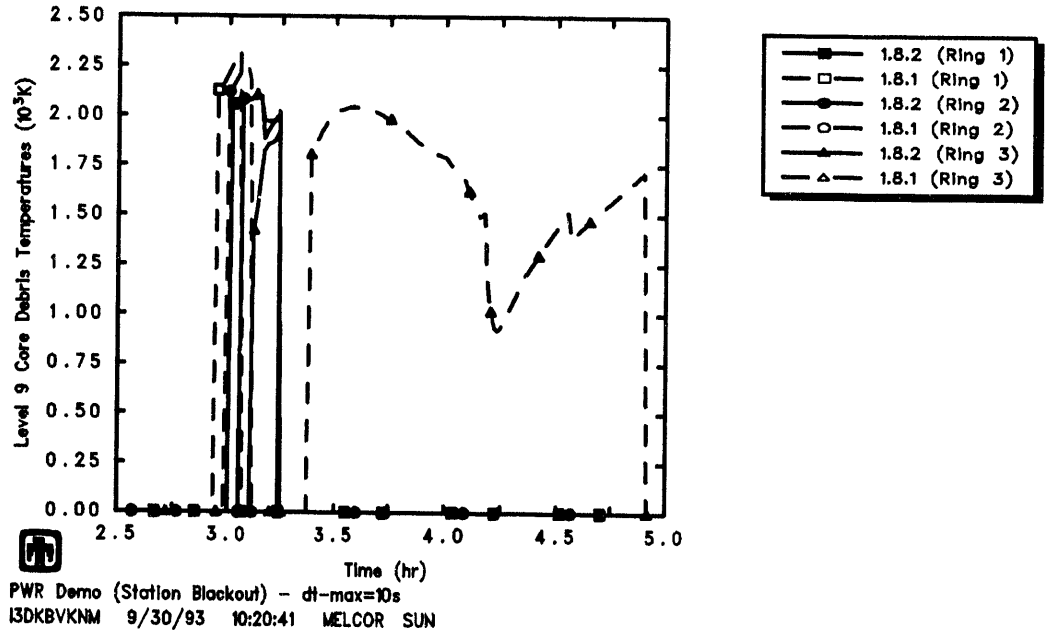

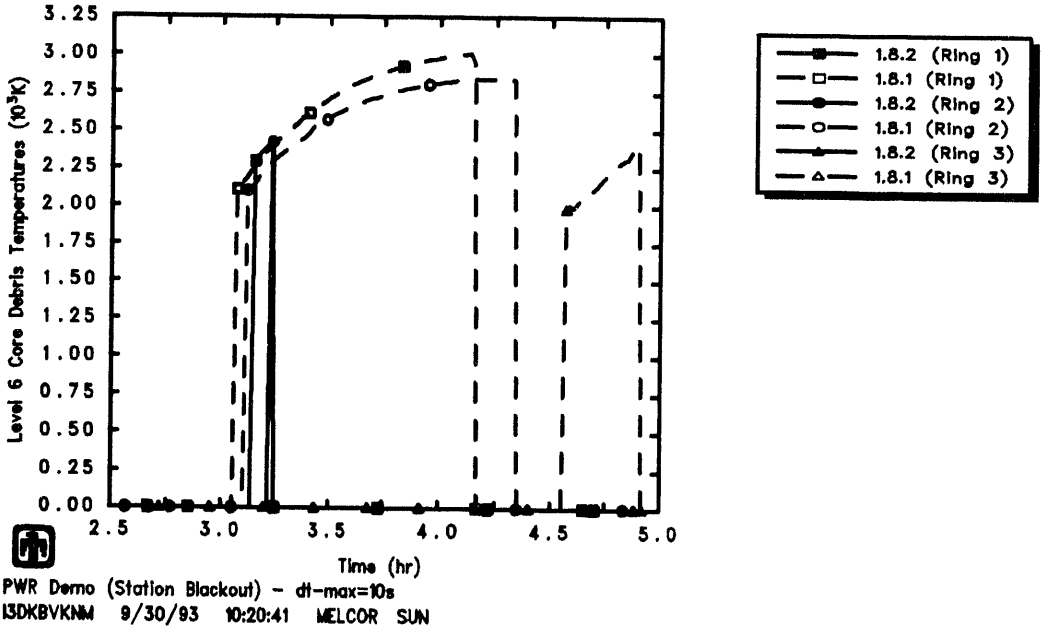

Figure 5.15. Upper (Top) and Lower (Bottom) Core Region Debris Temperatures MELCOR 1.8.2 *vs* 1.8.1

6 New Models

Sensitivity studies on the individual effects of new models added in MELCOR 1.8.2 (in particular, hydrodynamic interfacial momentum exchange, core debris radial relocation, core material eutectics, CORSOR-Booth fission product release, and high-pressure melt ejection and direct containment heating) are presented in this section.

6.1 Interfacial Momentum Exchange Length

During the MELCOR peer review [11], questions were raised concerning the failure of the pressurizer to drain until the time of vessel failure and subsequent primary system depressurization in the MELCOR 1.8.1 Surry TMLB' demonstration calculation; there was general agreement that this appeared to violate physical intuition, and might reflect a code problem.

Drainage of the pressurizer into a (partially) voided primary system at more or less constant pressure requires a countercurrent flow of steam and/or hydrogen into the pressurizer through the surge line to replace the liquid volume drained from it. In general, this process is controlled by a balance between buoyancy forces tending to force the gas to rise and the liquid to fall, and momentum-exchange or drag forces which tend to oppose the relative motion.

Most detailed thermal/hydraulic codes such as TRAC and RELAP5 contain explicit flow regime maps with mechanistic models for momentum exchange within each of a number of flow regimes; transition regions between regimes must also be constructed to assure continuity and, to some extent, smoothness in the overall model. The model in MELCOR 1.8.1 for the drag force (referred to as "interfacial momentum exchange") was simple, somewhat unconventional, and incompletely tested. The MELCOR team believed that a simple model could be developed that would reproduce experimentally-determined flooding curves while avoiding most of the complication and detail in the TRAC and RELAP5 models, and that such a simple model would be adequate for the intended applications of MELCOR.

Concern was expressed by members of the peer review committee that the failure of the pressurizer to drain was a result of the inadequacy of the momentum exchange model in MELCOR, leading to an incorrect two-phase countercurrent flow limit (CCFL). A task was included in the FY92-93 MELCOR development program to investigate and resolve the observed problems [25]. Since the release of MELCOR 1.8.1, two significant modifications have been made to the code that impact predictions of countercurrent flow. The first involves the momentum exchange model itself, and the second involves another MELCOR submodel.

As part of resolving cases of unphysical water levitation observed in some calculations (*e.g.*, in our LOFT LP-FP-2 MELCOR assessment analyses [6]), the way that the control volume form of the momentum exchange model was constructed from the original continuum form was changed. In MELCOR 1.8.1, it was assumed that the momentum exchange

force acted over the entire inertial length of a flow path. However, the buoyancy force acts only over the range of elevations encompassed by the junction openings associated with the flow path. If these distances are unequal, the calculated flooding curve will be affected. For flow paths such as the pressurizer surge line, the inertial length is frequently much longer than the range of elevations corresponding to the junction openings (*i.e.*, the elevation change in the surge line). Under the old modelling, the momentum exchange force opposing relative motion was then far too large compared to the buoyancy force driving phase separation, resulting in an excessive limitation on countercurrent flow. The default treatment in MELCOR was therefore modified to treat the momentum exchange length as a separate variable from the inertial length. A default momentum exchange length was taken as the range of elevations encompassed by junction openings for vertical flow paths, and as the inertial length for horizontal flow paths; user input could be used to override the default if desired. That code modification (update 1.8JQ) also included a change in the definition of the flow path void fraction for countercurrent flow; the new definition is consistent with the details of the continuum model, where the previous one was not. The effect is to substantially increase the maximum permitted countercurrent flow, particularly near the limits of the flooding curve.

Other changes were made under update 1.8LJ to prevent misapplication of the algorithm preventing phase depletion as a result of outflow of pool or atmosphere from a junction; the effect was that, under certain conditions, the calculated void fraction was occasionally being modified inappropriately, and could incorrectly preclude occurrence of countercurrent flow in a flow path. The code modification largely eliminated the problem.

A number of tests have been performed evaluating the current momentum exchange model, after including the corrections and enhancements summarized above. [25, 26] In addition, the Surry TMLB' analysis, which originally highlighted the pressurizer drainage problem, has been rerun with input appropriate to the new interfacial momentum exchange model in MELCOR, in a number of sensitivity study calculations with results decsribed in this subsection.

In the MELCOR input model for Surry, the pressurizer surge line flow path is modelled as a 10in-diameter horizontal flow path $\simeq$20m long, and there is an elevation change of $\simeq$4m from the hot leg to the bottom of the pressurizer. Thus the default interfacial momentum exchange length would be $\simeq$20m, as would have been the case with MELCOR 1.8.1. (Actually, due to a coding error in MELCOR 1.8.1, the square of that length, 400m, would have been used.) In the basecase input model, the momentum exchange length was set to $\sim$0.25m, equal to the surge line diameter; the momentum exchange length for the hot leg inlet, also specified as a horizontal flow path, also was reduced from a default length of $\sim$7.5m to $\sim$0.75m, the pipe diameter (because results of a test problem given in [25] indicated that the pressurizer drainage could be affected by CCFL in the upper-plenum/hot-leg flow path junction). These are the values used in the calculation whose results were described in detail in Section 4. Note that slightly more rapid pressurizer draining prior to vessel breach was predicted by MELCOR 1.8.2 with this input and the interfacial momentum exchange model changes compared to the MELCOR 1.8.1 basecase result as shown in Figure 5.2.

As a sensitivity study, the Surry station blackout transient was run with the user-input surge line flow path momentum exchange length further reduced by a factor of 10 (to ~2.5cm), with the user-input hot leg inlet flow path momentum exchange length further reduced by a factor of 10 (to ~7.5cm), with the user-input cold leg outlet flow path momentum exchange length similarly reduced to ~7.5cm (about 10% of the cold leg pipe diameter), and with the momentum exchange lengths in all three of these flow paths simultaneously reduced to these low values. (The momentum exchange length for the cold leg inlet was reduced in this sensitivity study because that flow path was also specified as a horizontal flow path, which would by default use a large momentum exchange length equal to to the pipe length.)

Figure 6.1.1 shows the collapsed liquid level in the pressurizer predicted in the MELCOR 1.8.2 and 1.8.1 basecase calculations and in these various momentum exchange length sensitivity study analyses; there is no significant swelling predicted in the pressurizer, so the swollen liquid levels appear the same. The pressurizer response predicted by SCDAP/RELAP5 for the same TMLB' accident sequence (Figure 4 in [18]) is included for comparison.

As already mentioned, there was a slight increase in the pressurizer drainage rate after ~2.5hr in the MELCOR 1.8.2 basecase calculation relative to the result from the MELCOR 1.8.1 analysis, although the pressurizer was still ~80% full of liquid when vessel breach was predicted to occur. The MELCOR results with reduced momentum exchange lengths for the hot leg inlet and cold leg outlet flow paths were generally quite similar to the 1.8.2 basecase calculation results, indicating that pressurizer draining behavior was not being significantly affected by CCFL in either the hot leg inlet or the cold leg outlet. There was a significant increase in pressurizer drainage if the interfacial momentum exchange length in the pressurizer surge line was further reduced, either individually or in conjunction with reductions in that parameter for other flow paths, with the pressurizer only ~30% liquid when vessel breach and primary depressurization occurred. (The small changes in timing of predicted vessel breach were largely due to changes in primary system inventory loss out the cycling PORV as the pressurizer draining was varied.)

Comparing these MELCOR results to corresponding SCDAP/RELAP5 results for the same accident, there is an initial timing shift visible in pressurizer filling and venting due to a higher initial liquid level. The subsequent pressurizer drainage rate from SCDAP/RELAP5 appears somewhat faster than the MELCOR 1.8.2 basecase result but somewhat slower than in the MELCOR sensitivity study analyses with the interfacial momentum exchange length in the pressurizer surge line further reduced. The pressurizer was still ~25% full of liquid when the SCDAP/RELAP5 calculation was terminated at 200min; the lower pressurizer water inventory in the SCDAP/RELAP5 analysis is due to drainage occurring over a longer period than in any of the MELCOR calculations.

The results of this sensitivity study indicate that the ability of the user to change the interfacial momentum exchange length through input added in MELCOR 1.8.2 obviously allows wide variation in countercurrent flow limits and associated pressurizer drainage rates, but the question of the "correct" value to use remains open.

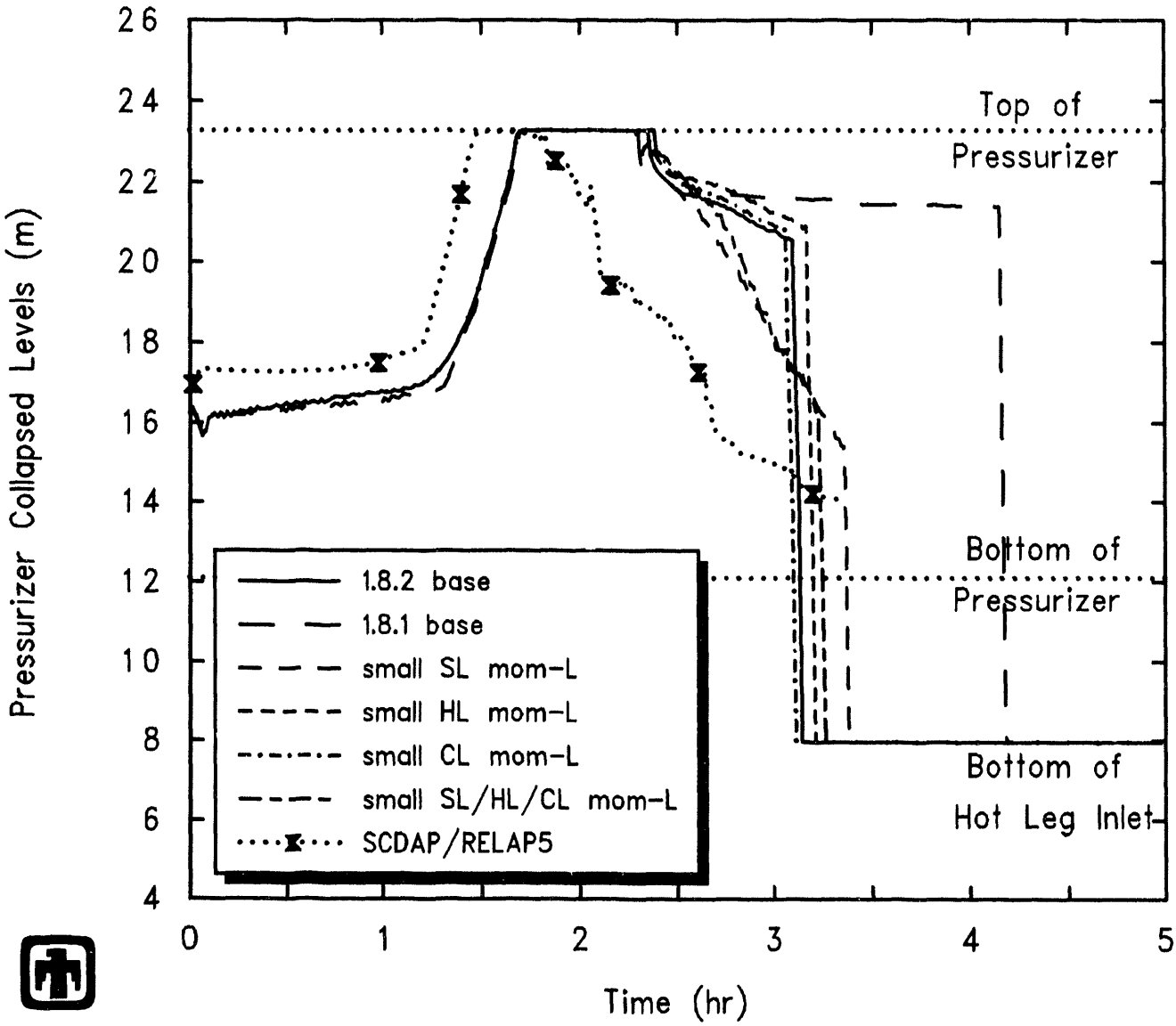

Figure 6.1.1. Pressurizer Liquid Levels - Interfacial Momentum Exchange Length Sensitivity Study

6.2 Core Debris Radial Relocation

Another code model added in MELCOR 1.8.2 is a debris radial relocation model [27]. This new model was added to relocate molten and/or particulate debris between rings (and axial levels), based upon hydrostatic head equilibration (*i.e.*, the tendency of gravity to establish a uniform pressure at any given depth in a stationary fluid). Exponential time constants (taken as 1s for molten debris relocation, and 3s for particulate debris relocation) control the rate of relocation. The model will first relocate molten material that still exists after any candling and refreezing to establish a uniform molten-liquid level across all rings for any given axial level; afterwards, solid particulate debris will be relocated to eliminate the artificial "stacking" of debris columns often observed in past calculations. Both molten and particulate debris radial relocation models are active by default with no new, additional user input needed; either or both can be disabled through user input, if desired.

The core debris radial relocation model underwent developmental testing on both BWR and PWR meltdown scenarios [27]. In general, the expected effect of the radial relocation model is to introduce more coherency between the behavior of the various core rings. The mobile material created by a temperature excursion in the innermost, high-power, ring soon spreads radially outward and triggers temperature excursions in those rings that could otherwise be delayed by hundreds of seconds. The mass of material ejected immediately following vessel failure also is expected to increase, because material can move into the ring in which the breach first occurs.

The new debris radial relocation interaction model generally had only a small effect on the overall results for the Surry TMLB' station blackout sequence, although it significantly affected details of core melt progression). Table 6.2.1 compares the timings of various key events predicted by MELCOR with and without the debris radial relocation model enabled. There was, of course, no effect on steam generator boiloff, pressurizer filling and venting, core uncovery, early core heatup or initial clad failure and gap release. However, there was a slightly faster core damage progression with the debris radial relocation model enabled; the sensitivity study results showed more coherent behavior among rings when the debris radial relocation model was enabled. Unexpectedly, the presence of the debris radial relocation model affected the code numerics (possibly the time step) sufficiently early that a slight difference was seen in the clad-failure/gap-release times predicted for the various rings, even before any debris had formed in the core and the debris radial relocation model was doing anything. Core plate and lower head failure occurred somewhat (~1000s) later with the debris radial relocation disabled. (Both the calculations being compared were run on an IBM RISC-6000 Model 550 workstation.)

The delay in core plate failure (and subsequent lower head penetration failure) caused hot fuel, both intact and in debris, to be retained in the vessel for an extra ~1000s, as shown respectively in Figures 6.2.1 and 6.2.2 for sample cells in the lower and upper core, significantly increasing the available time for fission product release and hydrogen production in-vessel.

The calculated core state at vessel failure (*i.e.*, at 11,219.3s or 3.12hr) for the calcu-

Table 6.2.1. Timing of Key Events – Core Debris Radial Relocation Sensitivity Study

Event	Time	
	With Debris Relocation	Without Debris Relocation
Gap Release		
Ring 1	10,235.0s (2.84hr)	10,230.6s (2.84hr)
Ring 2	10,334.4s (2.87hr)	10,320.6s (2.87hr)
Ring 3	10,667.9s (2.96hr)	10,660.6s (2.96hr)
Core Plate Fails		
Ring 1	11,177.9s (3.10hr)	12,114.3s (3.37hr)
Ring 2	11,906.3s (3.31hr)	12,929.5s (3.59hr)
Ring 3	13,062.9s (3.63hr)	12,795.7s (3.55hr)
LH Penetration Fails		
Ring 1	11,219.3s (3.12hr)	12,160.2s (3.38hr)
Ring 2	13,029.5s (3.62hr)	12,996.4s (3.61hr)
Ring 3	13,842.3s (3.85hr)	12,869.5s (3.57hr)
Debris to Cavity	11,219.3s (3.12hr)	12,160.2s (3.38hr)
HPME/DCH Starts	11,219.3s (3.12hr)	12,160.2s (3.38hr)
HPME/DCH Ends	11,251.7s (3.13hr)	12,167.3s (3.38hr)
Deflagrations Start	12,863.2s (3.57hr)	–
Deflagrations End	13,766.2s (3.82hr)	–
Deflagrations Start	–	29,180.1s (8.11hr)
Deflagrations End	–	29,181.7s (8.11hr)
Deflagrations Start	32,970.0s (9.16hr)	–
Deflagrations End	44,778.9s (12.44hr)	–

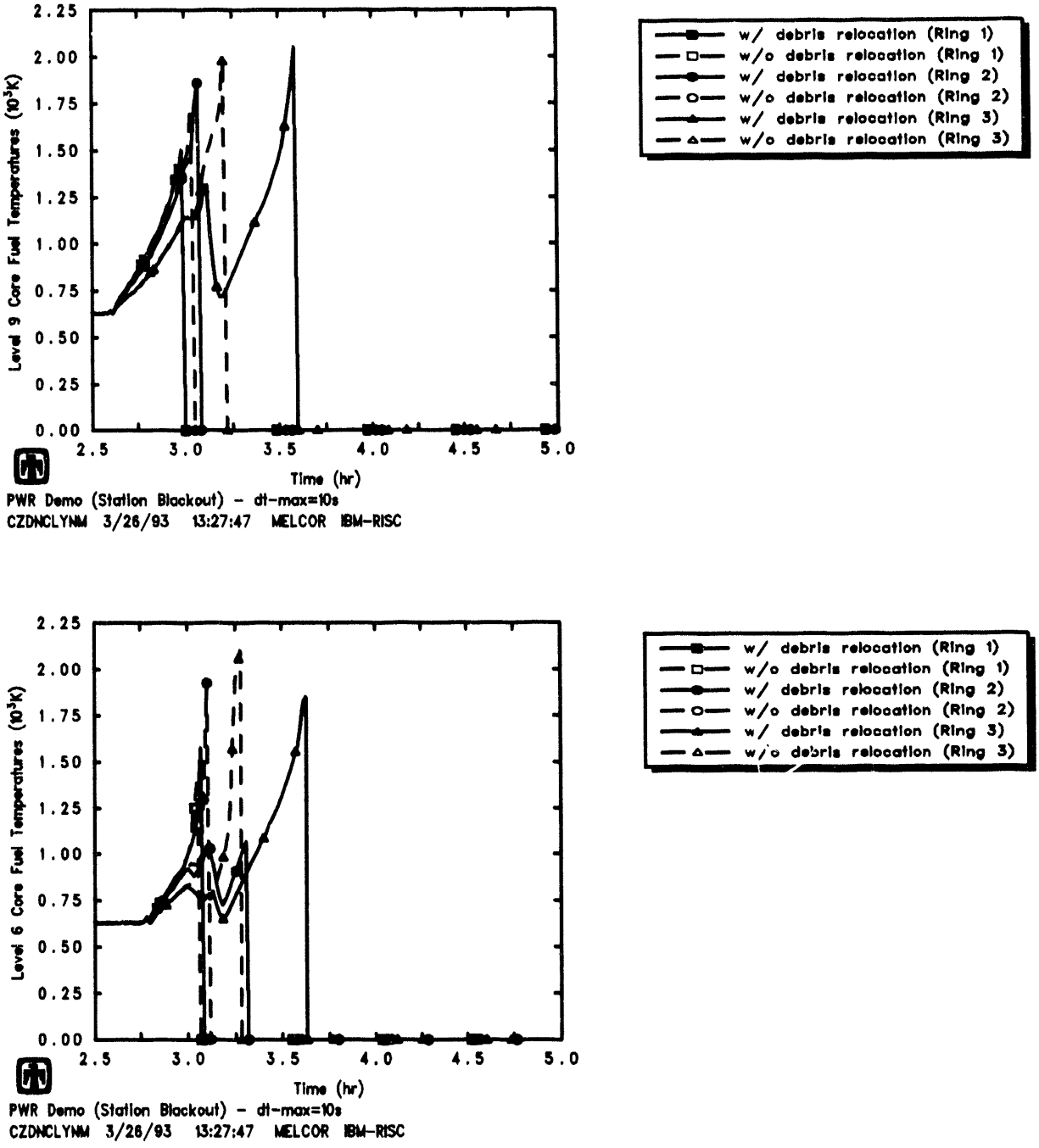

Figure 6.2.1. Upper (Top) and Lower (Bottom) Core Region Fuel Temperatures – Core Debris Radial Relocation Sensitivity Study

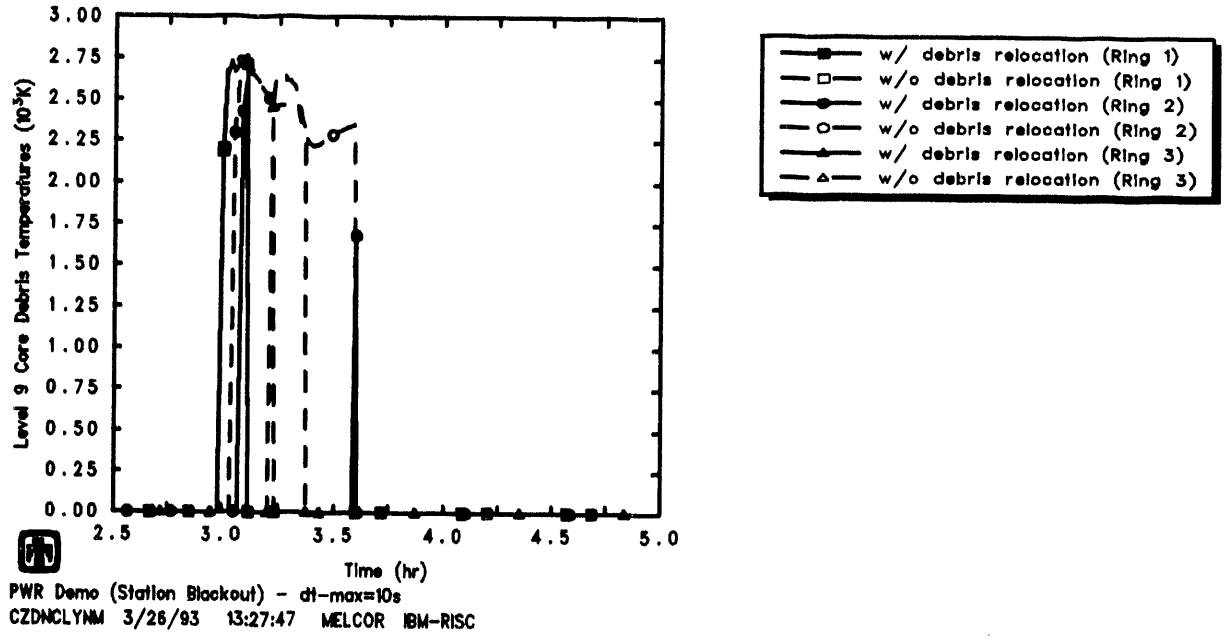

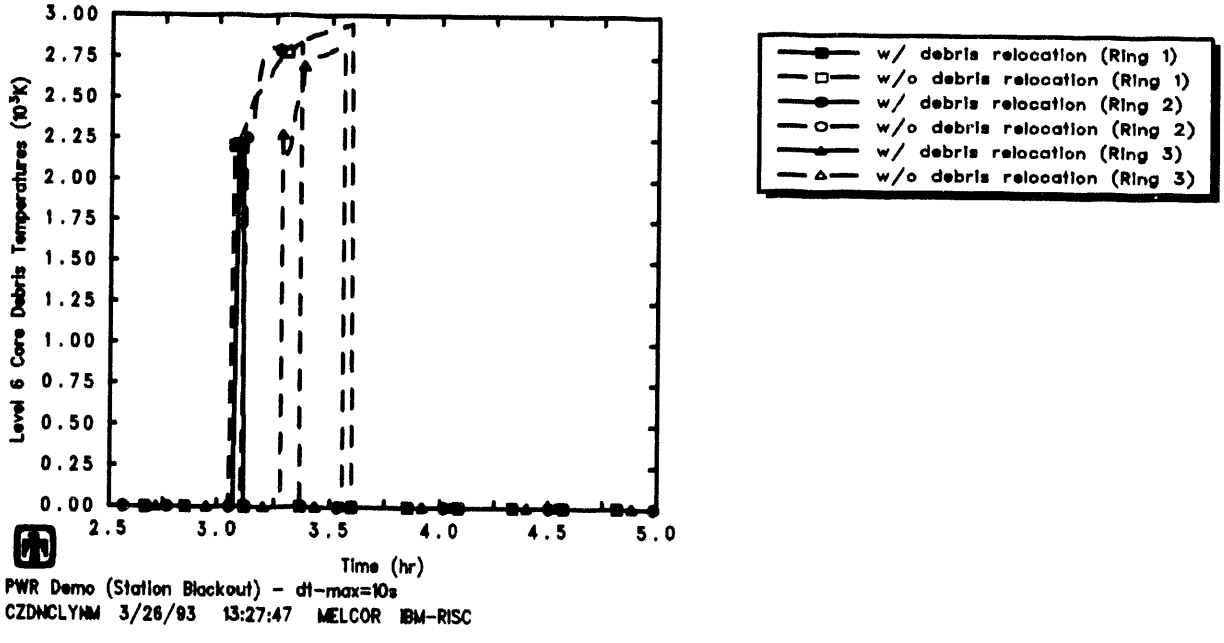

Figure 6.2.2. Upper (Top) and Lower (Bottom) Core Region Debris Temperatures Core Debris Radial Relocation Sensitivity Study

lation with the debris radial relocation model disabled is illustrated in Figure 6.2.3, for comparison to the reference calculation results with the debris radial relocation model enabled presented in Figure 4.2.11. The various materials in the MELCOR "fuel/clad" component just prior to vessel failure, both any intact materials remaining in their original position and candled, refrozen conglomerate debris materials, are shown in the upper plot for the three radial rings in the MELCOR Surry core model the lower plot depicts the materials calculated to be in the "particulate debris" component in the three core rings at the same time. The various materials in the MELCOR "other-structure" component just prior to vessel failure are not shown; that plot is dominated by the structural steel still in place in the lower plenum. (Refer to [1] for an explanation of these MELCOR components, if necessary.) The "elevation" used as the ordinate in Figure 4.2.11 is the same as the core level elevations shown in Figure 3.3, with the core support plate at $\geq$3m, the lower plenum between 0 and $\sim$3m, and the active fuel region from $\geq$3m to $\sim$6.722m. The fraction of each core cell occupied by any given material is shown. However, although each ring is shown as equal, recall that the core cells are not equal in the three rings modelled; the innermost, high-powered ring includes $\sim$15% of the core, the middle ring contains $\sim$60% of the core, and the outermost, low-power ring includes the remaining $\sim$25% of the core.

Table 6.2.2 summarizes the state of the various materials in the core active fuel region, core plate and lower plenum at the time a lower head penetration first failed (*i.e.*, at vessel breach), in the MELCOR 1.8.2 reference calculation and in the sensitivity study calculation with no debris radial relocation. Masses of intact components and of debris components are given for each region.

There is a very significant difference in the core state at the time of vessel failure in these two calculations. With the debris radial relocation model disabled, there was much less debris in the lower plenum at the time a lower head penetration first failed; in particular, the amount of debris in the lower plenum corresponds quite well to the mass of material initially present in the active fuel region in the ring whose core plate failed just previously (*i.e.*, the first, inner, high-powered ring). All the debris in the lower plenum was in the ring whose core plate just failed in the calculation with the debris radial relocation model disabled. In the reference calculation with the debris radial relocation model enabled, the mass of debris in the lower plenum at the time a lower head penetration first failed was much greater, about half the total mass initially present in the active fuel region, and that debris was found in all three radial rings even though the core plate had failed in only one ring. Also, in the reference calculation with the debris radial relocation model enabled, most of the material remaining in the active fuel region was "intact" (either still in its initial location or refrozen onto intact components). However, in the sensitivity study calculation with the debris radial relocation model disabled, almost all of the material still in the active fuel region (*i.e.*, in the second and third rings above the core support plate) was predicted to be particulate debris. This is the old problem of "stacking" of debris in separate columns, seen in MELCOR 1.8.1 calculations; without the debris radial relocation model, debris in the outer two rings cannot move sideways to the empty inner ring and fall through the failed core plate in

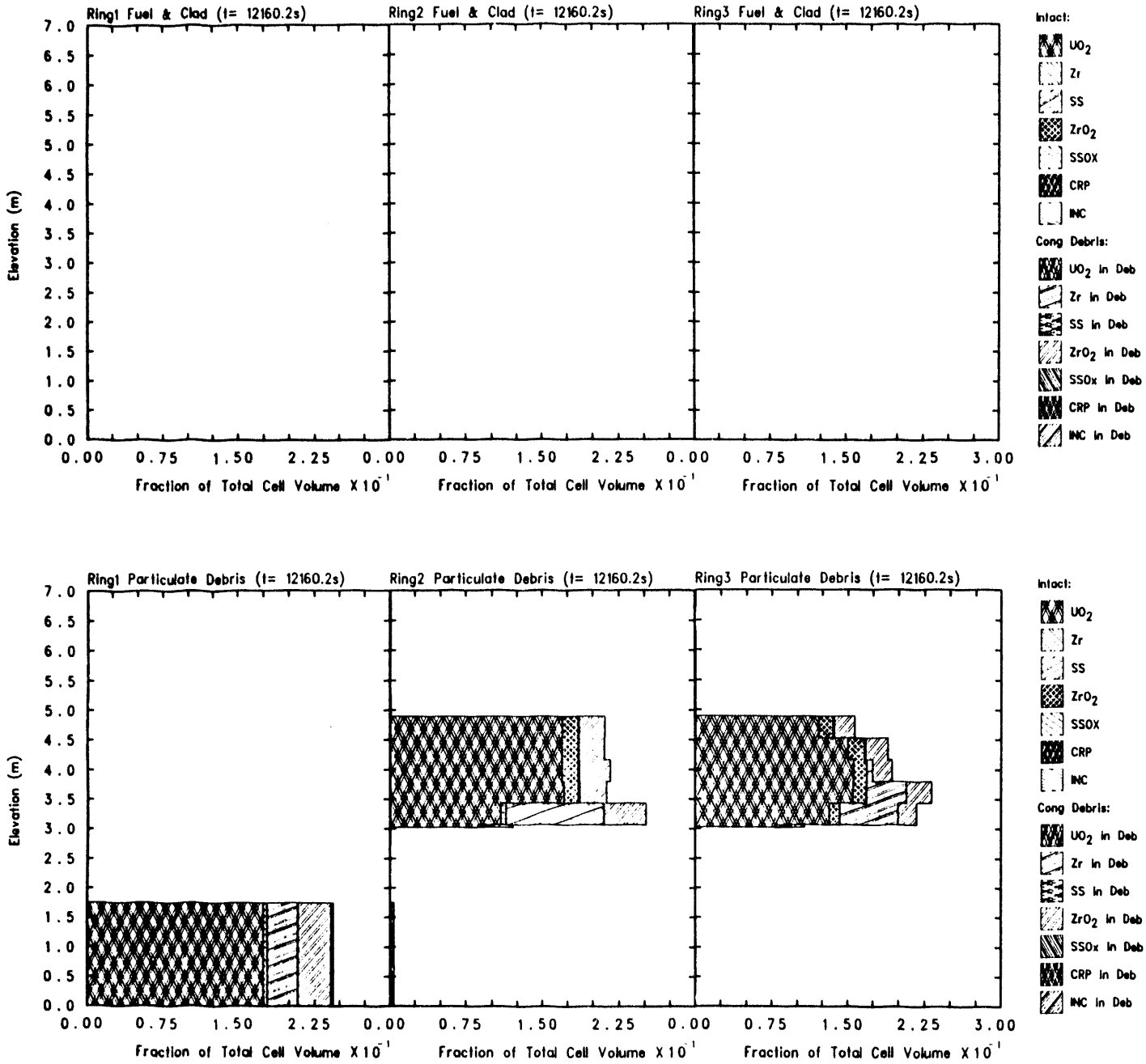

Figure 6.2.3. Core Fuel/Clad (top) and Particulate Debris (bottom) Component Materials at Vessel Failure with Debris Radial Relocation Model Disabled Core Debris Radial Relocation Sensitivity Study

Table 6.2.2. Core State at Vessel Failure – Core Debris Radial Relocation Sensitivity Study

	With Debris Relocation		Without Debris Relocation	
	Intact	Debris	Intact	Debris
Active Fuel Region Masses (kg)				
UO_2	38,250	1,759	0	52,437
Zircaloy	9,445	56	0	5,881
Zirc Oxide	694	217	0	10,187
Steel	267	0	37	4
Steel Oxide	34	0	3	1
CRP	1,672	0	257	0
Total	50,362	2,032	297	68,510
Core Plate Masses (kg)				
UO_2		953		242
Zircaloy		51		10
Zirc Oxide		98		18
Steel	1,815	4	1,563	18
Steel Oxide		12	1	26
CRP		0		104
Total	1,815	1,118	1,564	1,041
Lower Plenum Masses (kg)				
UO_2		39,751		12,876
Zircaloy		2,450		1,423
Zirc Oxide		4,486		1,548
Steel	32,655	96	31,480	48
Steel Oxide	6	78	15	34
CRP		334		1,672
Total	32,661	47,195	31,495	17,601
Average Debris Temperature (K)		~2450		~2400
Fraction Oxidized	Zircaloy ~30%	Steel ~0.4%	Zircaloy ~27%	Steel ~0.3%

Table 6.2.3. Fission Product Release - Core Debris Radial Relocation Sensitivity Study

Class	(% Initial Inventory) In-Vessel Release		In-Cavity Release		Total Release	
	With Debris	Without Relocation	With Debris	Without Relocation	With Debris	Without Relocation
1 (Xe)	63.517	95.033	36.458	4.7461	99.975	99.779
2 (Cs)	63.545	95.006	39.245	5.1110	102.79	100.12
3 (Ba)	3.1039	53.213	20.651	5.2456	23.755	58.458
4 (I)	63.500	95.038	0.0	0.0	63.500	95.038
5 (Te)	4.4007	45.685	43.727	17.774	48.128	63.459
6 (Ru)	0.0870	3.0891	$6\times10^{-7}s$	4×10^{-7}	0.0870	3.0891
7 (Mo)	2.3793	22.541	0.7352	0.3297	3.1145	22.870
8 (Ce)	0.0025	0.0571	0.0011	0.0010	0.0036	0.0581
9 (La)	0.0088	0.5740	0.1115	0.0686	0.1203	0.6426
10 (U)	0.0092	0.5976	0.0021	0.0015	0.0113	0.5992
11 (Cd)	10.224	84.034	0.2411	0.0182	10.465	84.052
12 (Sn)	10.225	84.021	2.5394	0.2065	12.764	84.227

that innermost ring.

The greater extent of core damage in the active fuel region was partly due to a longer heatup period resulting from the ~1000s later core plate and lower head penetration failure in the calculation without debris radial relocation (delayed because there was less debris above the core plate in the inner ring, since no debris relocated from the outer two rings, and thus the core plate heats up more slowly). The longer the material was held in-core (*i.e.*, above the core support plate), the higher the temperatures and the more damage and debris produced.

The release of fission products from the fuel by 90,000s (25hr)is summarized in Table 6.2.3. Fractional releases are given both in-vessel and in the cavity, together with total releases; these amounts consider only the release of radioactive forms of these classes, and not additional releases of nonradioactive aerosols from structural materials. (Note that Table 6.2.3 shows the same lack of any ex-vessel release for Class 4 in the analysis with no debris relocation as in the reference MELCOR 1.8.2 analysis, due to the same class-mapping coding problem already discussed in Section 4.5.)

The results in this table indicate that the fission product releases calculated by MELCOR 1.8.2 with the debris radial relocation model disabled were very similar to the fission product releases calculated by MELCOR 1.8.1 (given in Table 5.3), which would be expected since MELCOR 1.8.1 had no debris radial relocation model. Furthermore, the

results in Table 6.2.3 illustrate that most of the differences in the fission product releases calculated by MELCOR 1.8.2 and by 1.8.1 are primarily attributable to the effects of this one particular model, which strongly affects the details of core material degradation, relocation and ultimate ejection.

More hydrogen was generated in-vessel in the calculation with the debris radial relocation model disabled, due to the retention of high-temperature material in-vessel for a longer period of time; the hydrogen production in the cavity was similar in both calculations, so the total amount of hydrogen produced was $\geq$15% higher in the calculation with the debris radial relocation model disabled than in the reference calculation, as shown in Figure 6.2.4.

Figure 6.2.5 shows the total masses of core materials (UO_2, Zircaloy and zirc oxide, and stainless steel and steel oxide) remaining in the vessel in the two calculations; the relatively small amount of control rod poison material is not shown to avoid even more clutter in the plot.

Debris ejection began almost immediately after lower head failure, earlier with the debris radial relocation model enabled than without it; also, more material was initially ejected in the reference calculation with the debris radial relocation model enabled than in the sensitivity study calculation without it. However, there was a smaller delay between the initial, relatively small debris ejection and the later, substantially larger debris ejection in the sensitivity study calculation without the debris radial relocation model than in the reference calculation with it.

In both cases, all the UO_2 was transferred to the cavity, as was most of the unoxidized Zircaloy, the oxides and the control rod poison; however, a small amount ($\sim$15%) of the structural steel in the lower plenum (and an associated small amount of oxidized steel) was predicted to remain unmelted and in place throughout the remaining transient period in the MELCOR reference calculation with the debris radial relocation model enabled, while all the steel and steel oxide also was transferred to the cavity in the sensitivity study analysis with that model disabled, albeit over some time period after initial vessel breach. The behavior predicted by MELCOR 1.8.2 with the debris radial relocation model disabled is quite similar to the corresponding results of the MELCOR 1.8.1 reference calculation, shown in Figure 5.10; as with the discussion on fission product releases, this could be expected since MELCOR 1.8.1 had no debris radial relocation model.

The mass of core debris in the cavity, the mass of ablated concrete, and the resultant total mass of debris are presented in Figure 6.2.6. While the reference calculation with the debris radial relocation model enabled had core debris entering the cavity earlier, due to the earlier vessel failure in that analysis, the sensitivity study calculation with the debris radial relocation model disabled had more core debris eventually ejected to the cavity; the greater mass of core debris in the cavity in the sensitivity study analysis was a direct result of the greater retention of structural steel in the lower plenum in the reference calculation (as visible in Figure 6.2.5).

The different degrees of structural steel retention in the lower plenum did not sub-

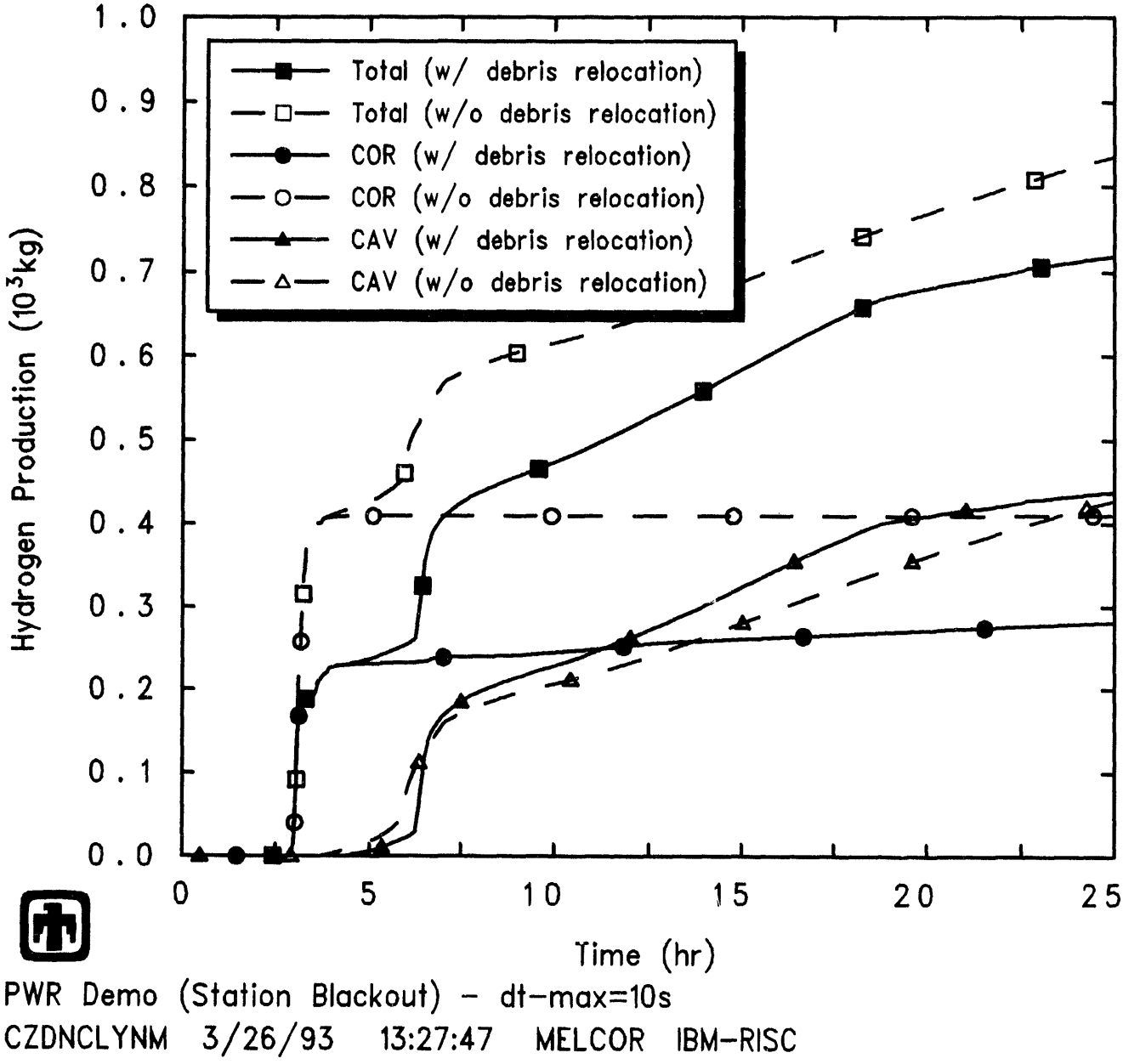

Figure 6.2.4. Hydrogen Production - Core Debris Radial Relocation Sensitivity Study

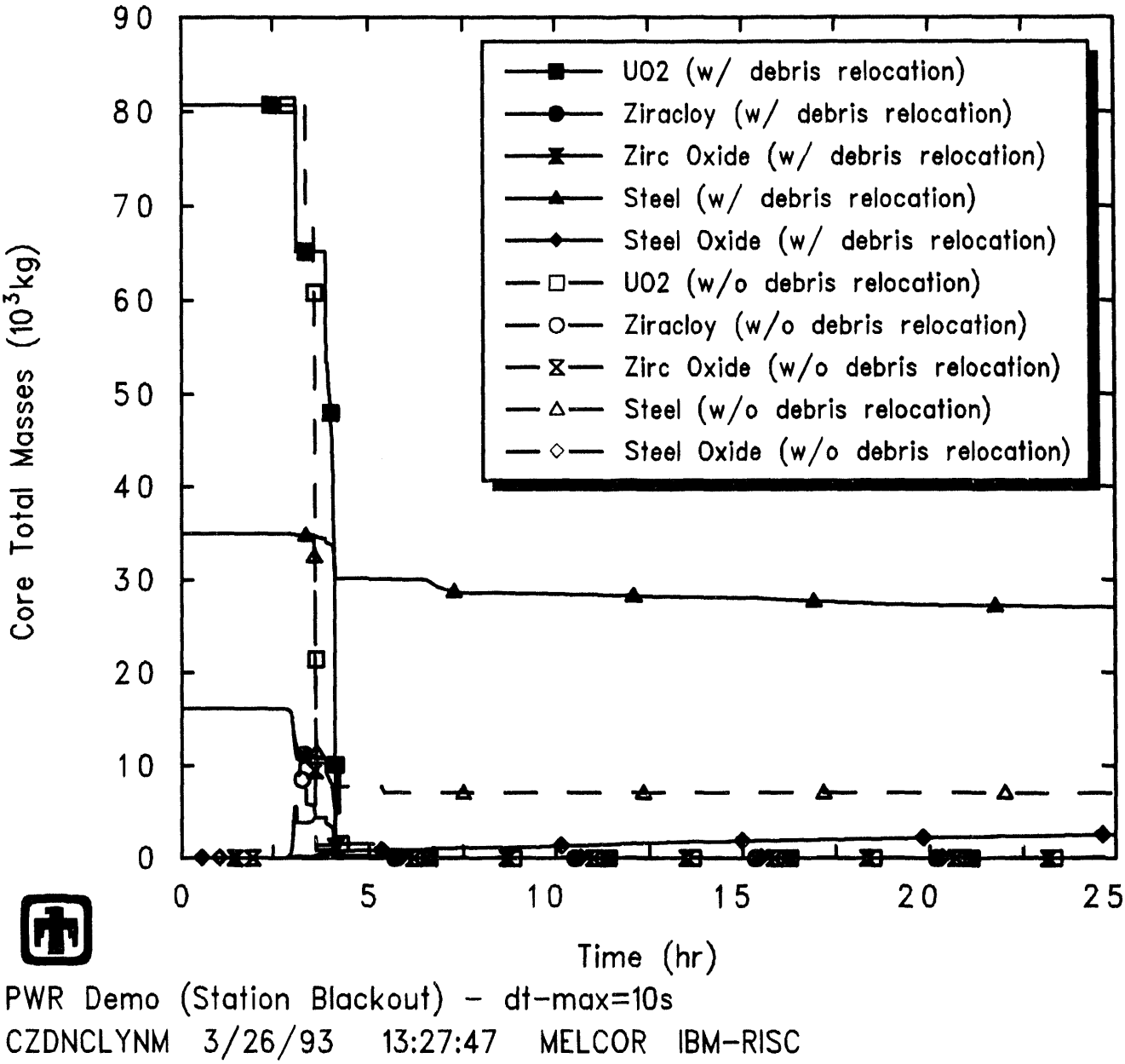

Figure 6.2.5. Total Core Masses – Core Debris Radial Relocation Sensitivity Study

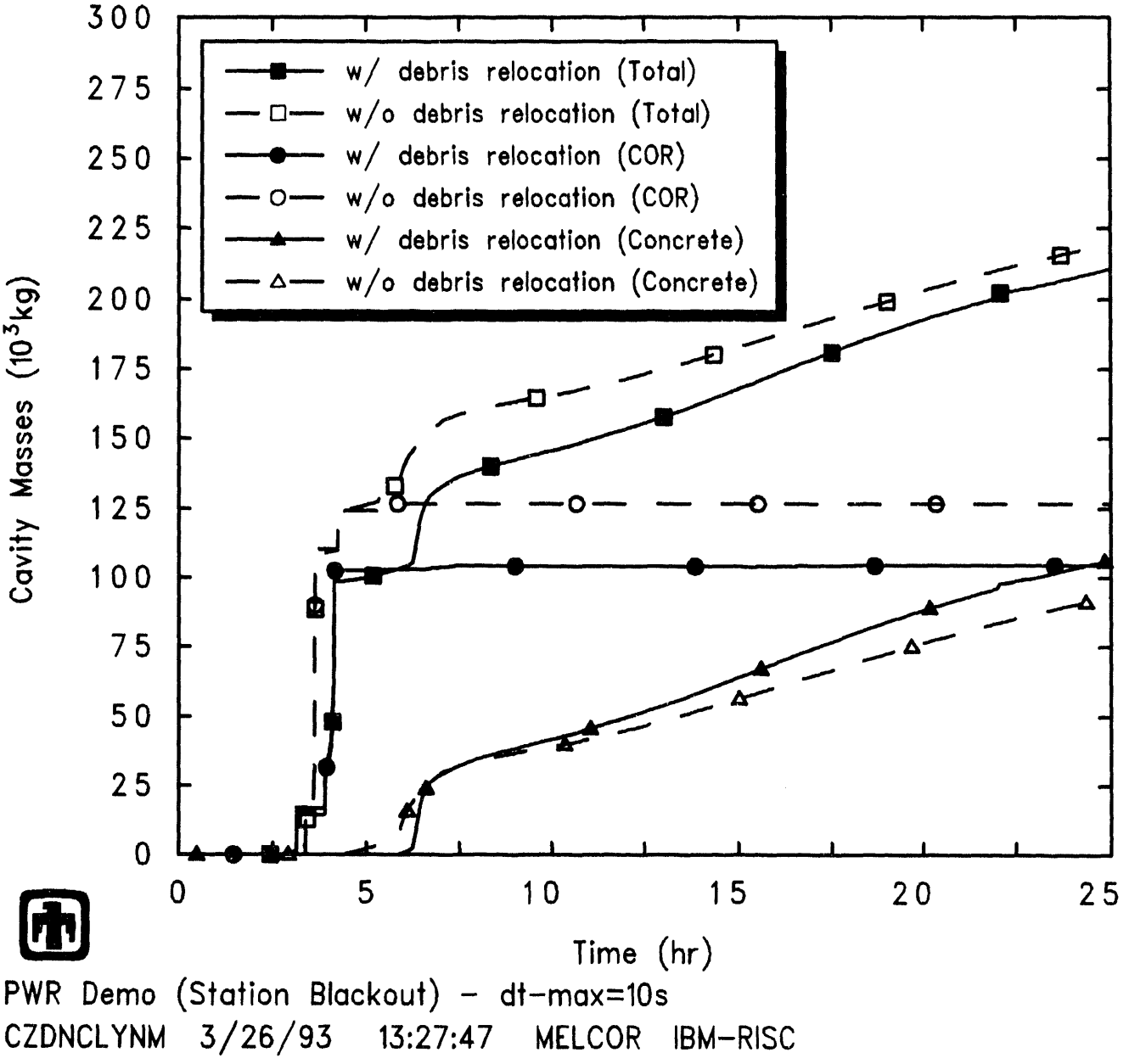

Figure 6.2.6. Cavity Masses - Core Debris Radial Relocation Sensitivity Study

stantially perturb the overall masses of core debris ejected to the cavity or the amount of concrete ablated in the cavity, because the steel mass was a small fraction of the overall core material mass. However, the increased retention of steel mass in the lower plenum in the reference calculation with the debris radial relocation model enabled resulted in a significantly smaller, thinner metallic layer in the cavity, which was completely oxidized by the end of the transient in this case, as indicated in Figure 6.2.7.

The disappearance of the metallic layer before the end of the transient had a significant and unanticipated effect on the ex-vessel source term (given in Table 6.2.3) for several radionuclide classes, as already discussed in Section 4.5. (Note that the problem discovered does not apply only to the implementation of the VANESA code in MELCOR, but also to the VANESA code itself.) As the metallic layer in the cavity went to zero, the releases of radionuclide species associated with that layer (*i.e.*, Te, Ru, Cd and Sn) began growing exponentially. This is illustrated in Figure 6.2.8 for several of these radionuclide species. The effect is not pronounced for Te, because most of that species mass had been released prior to the metallic layer vanishing; however, the release of other species, such as Cd and Sn, is significantly in error. There is not much effect on Ru, because very little of that species was released in any case at these temperatures.

As already noted, this problem is inherent in the VANESA formulation itself, not just in MELCOR, but is more likely to be encountered with MELCOR 1.8.2 than with MELCOR 1.8.1 because of the increased likelihood of more retention of lower plenum structural steel in-vessel.

6.3 Core Material Eutectics Interactions

In response to a high-priority code deficiency identified by the MELCOR peer review [11], the capability to model a variety of material eutectics also has been added in MELCOR 1.8.2, to improve the core package modelling of material interactions [28].

Severe accidents often generate conditions under which core materials begin to rapidly melt, oxidize or otherwise interact with one another. When molten materials mix or contact other solids, reactions can occur that produce new mixtures with properties which may or may not be like those of the reactants. Exact analysis of all the reactions and products that could conceivably occur may be impossible; however, to accurately describe the course of an accident, it is necessary to consider and effectively treat only those material interactions which could significantly affect the course of that accident. Reactions that lead to fuel relocation are potentially important because they could affect the source term in risk assessment; reactions that affect blockage formation are potentially important because blockages affect both material relocation and subsequent coolability; reactions that affect the reactor vessel integrity are obviously important.

Earlier versions of MELCOR treated each material melting as a separate process (with no consideration of independent, multicomponent phases), although there was coding for a specified fraction of solid material to be relocated by molten Zr or steel, to represent dissolution of UO_2 and/or ZrO_2 in melts. Rather than calculating melting, candling

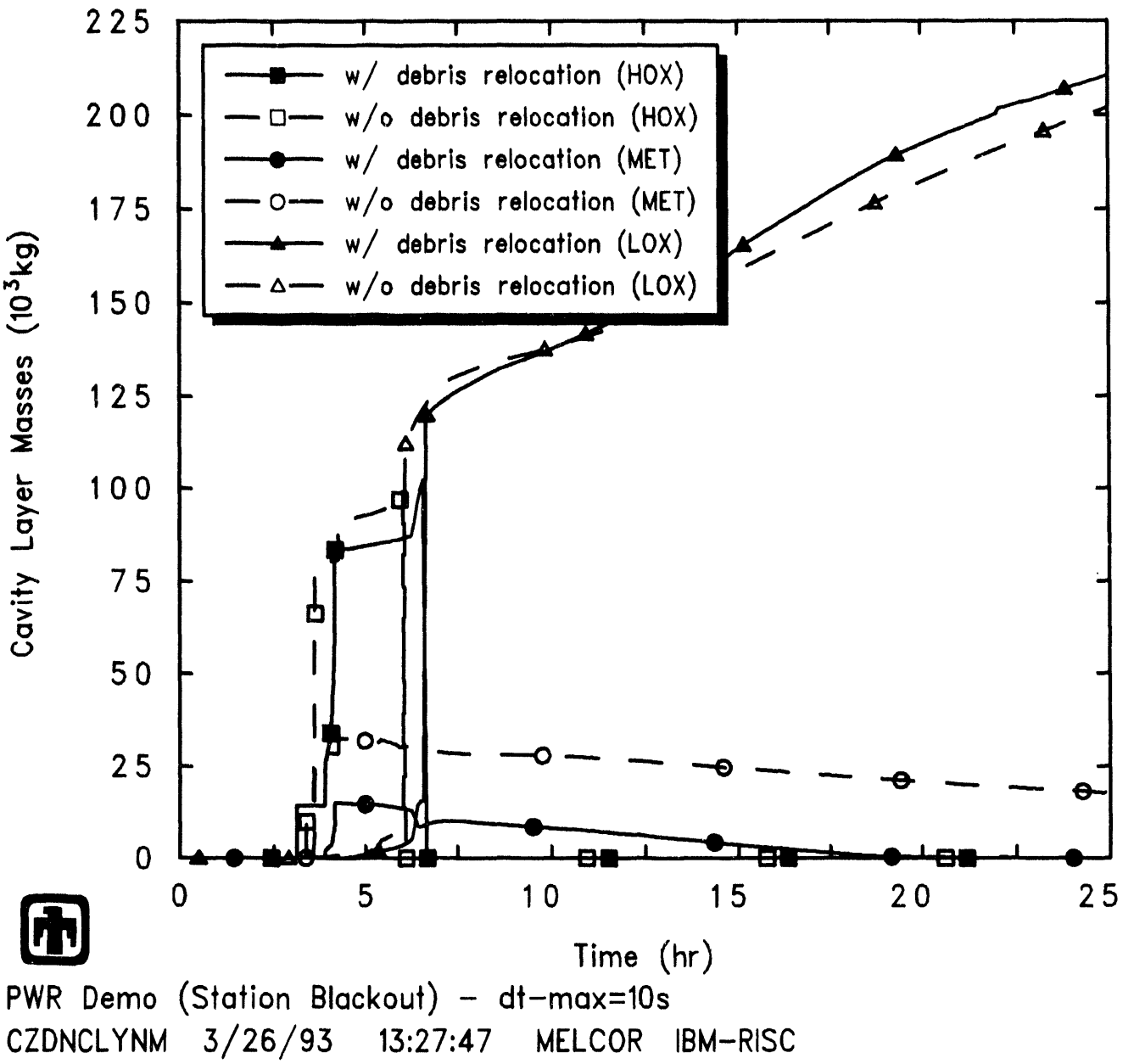

Figure 6.2.7. Cavity Layer Masses for Surry TMLB' - Core Debris Radial Relocation Sensitivity Study

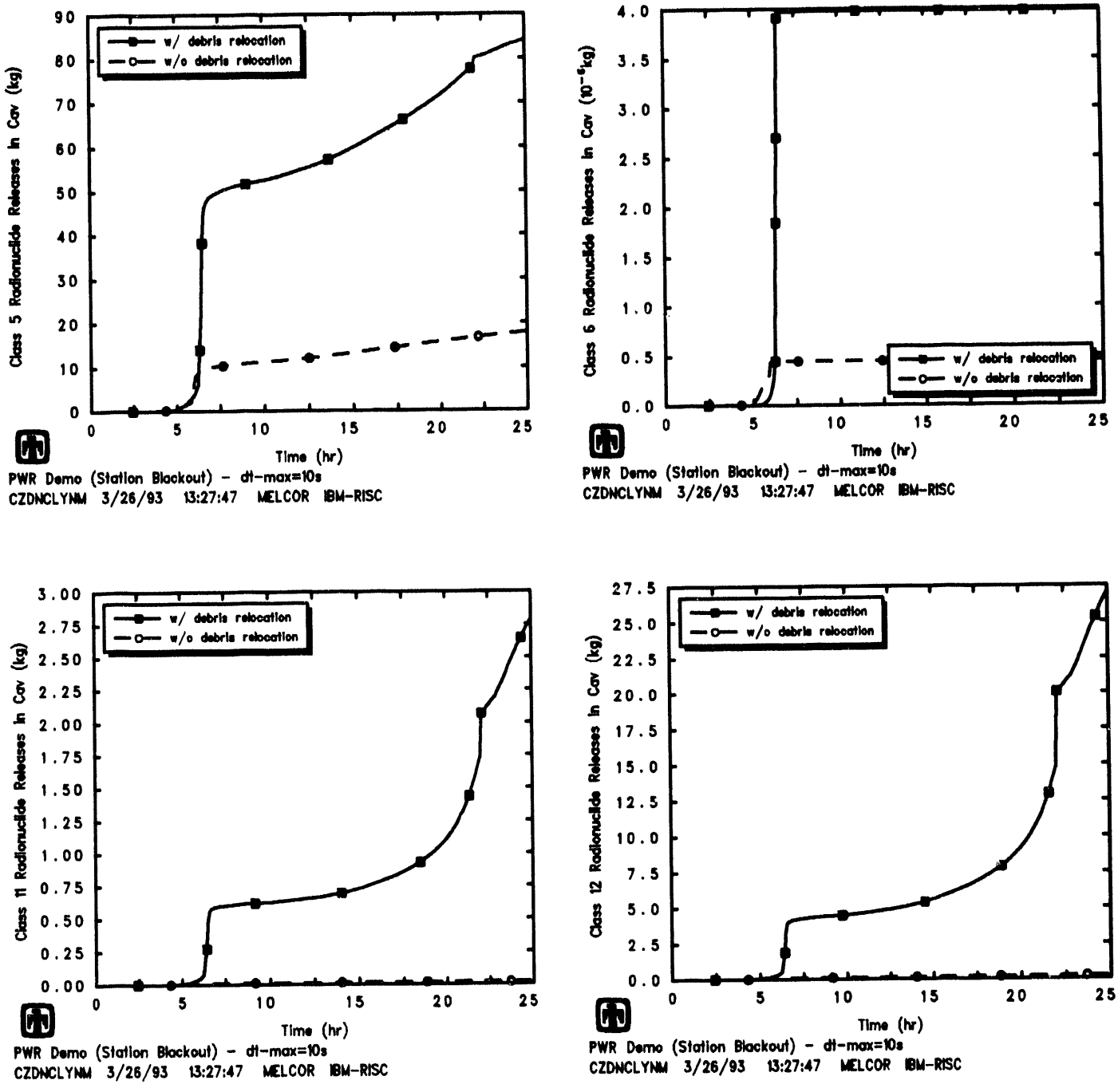

Figure 6.2.8. Ex-Vessel Class 5 (Te) Releases (upper left), Class 6 (Ru) Release (upper right), Class 11 (Cd) Releases (lower left) and Class 12 (Sn) Releases (lower right) for Surry TMLB' Core Debris Radial Relocation Sensitivity Study

and refreezing of individual materials in a given core component (*e.g.*, fuel/clad, canister, other structure) separately, the eutectics model deposits all molten materials in each component in the eutectic mixture for that component and then considers possible dissolution of solid material by the resultant mixture before calculating candling and refreezing of the liquid eutectic mixture.

Addition of liquid material to the eutectic mixture occurs either as single materials reach their normal melting point, or as solid material pairs undergo a eutectic reaction and enter the mixture when the temperature of the component in which they reside reaches the appropriate eutectic temperature. Three eutectic reactions are considered: 1) inconel grid spacers touching Zircaloy fuel cladding, 2) Zircaloy guide tubes touching steel control rod cladding, and 3) B_4C and the steel blade that contains that poison in a BWR control blade. The first two reactions become significant at ~1400K, while the third reaction becomes significant above 1500K.

For each component containing eutectic above the liquidus temperature, a hierarchical scheme is used to determine dissolution of solid material by the component eutectic, based upon the assumed configuration of intact materials and the availability of flow paths to the solid; Zircaloy-based mixtures are assumed to attack oxidic solids such as ZrO_2 and UO_2 preferentially, while B_4C attacks metal and the Ag-In-Cd in PWR control rods has an affinity for Zircaloy. For each solid attacked, the amount of dissolution is that required to achieve phase equilibrium, subject to prescribed dissolution rate limitations.

The primary effect of this material eutectic interactions model is a tendency to slow temperature excursions because of the formation of a relatively large heat sink associated with the heat of dissolution; the different materials also tend to relocate much more coherently than when melting and candling are done separately for each material.

The material eutectic interactions model has been tested both during development [28] and after implementation in the production code [9]. The eutectics model was enabled through user input in most of our MELCOR 1.8.2 Surry TMLB' analyses, as mentioned in Section 3, but a calculation was done with this new model disabled (the default state) as a sensitivity study.

Using the new material eutectic interactions model generally had only a small effect on the results for the Surry TMLB' station blackout sequence. Table 6.3.1 compares the timings of various key events predicted by MELCOR with and without the material eutectics model enabled. As would be expected, the calculations are identical early in the transient, before any significant material heatup, as evident from the identical clad-failure/gap-release times predicted for the inner two rings. Note, however, that the material eutectics model had then affected the core degradation process (and/or the time step) sufficiently that a slight difference is seen in the clad-failure/gap-release times predicted for the outer ring. Core plate and lower head failure occurred slightly ($\leq$4min) later if material eutectic interactions were neglected. (Both the calculations being compared were run on an IBM RISC-6000 Model 550 workstation.)

Table 6.3.2 summarizes the state of the various materials in the lower plenum when a lower head penetration first failed (*i.e.*, at vessel breach), in calculations with and

Table 6.3.1. Timing of Key Events - Material Eutectics Sensitivity Study

Event	Time With Eutectic Interactions	Time With No Eutectic Interactions
Gap Release		
Ring 1	10,235.0s (2.84hr)	10,235.0s (2.84hr)
Ring 2	10,334.4s (2.87hr)	10,334.4s (2.87hr)
Ring 3	10,667.9s (2.96hr)	10,664.4s (2.96hr)
Core Plate Fails		
Ring 1	11,177.9s (3.10hr)	11,624.3s (3.23hr)
Ring 2	11,906.3s (3.31hr)	12,192.4s (3.39hr)
Ring 3	13,062.9s (3.63hr)	12,172.8s (3.38hr)
LH Penetration Fails		
Ring 1	11,219.3s (3.12hr)	11,675.0s (3.24hr)
Ring 2	13,029.5s (3.62hr)	13,180.5s (3.66hr)
Ring 3	13,842.3s (3.85hr)	13,379.8s (3.72hr)
Debris to Cavity	11,219.3s (3.12hr)	11,685.0s (3.25hr)
HPME/DCH Starts	11,219.3s (3.12hr)	11,685.0s (3.25hr)
HPME/DCH Ends	11,251.7s (3.13hr)	11,730.1s (3.26hr)
Deflagrations Start	12,863.2s (3.57hr)	13,257.5s (3.68hr)
Deflagrations End	13,766.2s (3.82hr)	13,935.0s (3.87hr)
Deflagrations Start	32,970.0s (9.16hr)	34,954.9s (9.71hr)
Deflagrations End	44,778.9s (12.44hr)	40,308.9s (11.20hr)

without material eutectic interactions modelled, and gives the average temperature of the debris in the lower plenum, the fraction of core material relocated in or from the active fuel region, and the fractions of Zircaloy and steel oxidized by the time the vessel fails.

The biggest difference in plant response found was in the lower plenum structural response. Figure 6.3.1 shows the total masses of core materials (UO_2, Zircaloy and zirc oxide, stainless steel and steel oxide, and control rod poison) remaining in the vessel in these two calculations. Without the material eutectic interactions modelled, most (~80%) of the steel structure in the lower plenum melted and fell into the cavity; note that the behavior predicted by MELCOR 1.8.2 with the material eutectic interactions not modelled was very similar to the results previously obtained using MELCOR 1.8.1 (as discussed in Section 5). With the eutectics interaction model enabled, Zr and stainless steel debris in the lower plenum melted at lower temperatures and flowed to the cavity somewhat sooner, with less heating of the lower plenum steel structure due to the lower melt temperature and shorter residence time of the debris; thus, most (~70%) of the lower plenum structure remained in the vessel throughout the entire transient period analyzed.

The larger amount of stainless steel transferred to the cavity in the case without the eutectics interactions modelled resulted in a thicker metallic layer in CORCON existing for a longer time period, as shown in Figure 6.3.2.

Figure 6.3.3 illustrates that the total amount of hydrogen generated by the end of the problem was similar in both calculations. More hydrogen was generated in-vessel in the case with the material eutectic interactions modelled due to continued oxidation of the lower plenum steel structure remaining in the vessel; hydrogen generation in the cavity was similar during much of the transient in both cases, but the earlier disappearance of the metallic debris layer in the case with the eutectics interactions resulted in less hydrogen production in the cavity late in the transient, so the final overall hydrogen production was quite similar in both calculations.

Table 6.3.3 presents fractional fission product releases both in-vessel and in the cavity from the fuel by 90,000s (25hr), together with total releases. These amounts consider only the release of radioactive forms of these classes, and not additional releases of nonradioactive aerosols from structural materials. (Note that Table 6.3.3 also shows the same lack of any ex-vessel release for Class 4 in the analysis with no material eutectics interaction modelled as in the reference MELCOR 1.8.2 analysis, due to the same class-mapping coding problem already discussed in Section 4.5.)

The results in this table indicate that the fission product releases calculated by MELCOR 1.8.2 with the material eutectics model or without it are generally quite similar. When the material eutectics interaction model was not used, the in-vessel releases were slightly higher (probably because various materials had to reach their individual, higher melt temperatures in order to melt and relocate, rather than melting and relocating at somewhat lower eutectics-mixture melt temperatures); however, the ex-vessel releases are slightly lower when the material eutectics interaction model was not used, so the overall releases were very similar.

Table 6.3.2. Core State at Vessel Failure Material Eutectics Sensitivity Study

	With Eutectic Interactions		With No Eutectic Interactions	
	Intact	Debris	Intact	Debris
Active Fuel Region Masses (kg)				
UO_2	38,250	1,759	20,358	4,910
Zircaloy	9,415	56	8,632	746
Zirc Oxide	694	217	2,769	176
Steel	267	0	213	5
Steel Oxide	34	0	113	2
CRP	1,672	0	1,480	110
Total	50,362	2,032	33,565	5,949
Core Plate Masses (kg)				
UO_2		953		1,293
Zircaloy		51		168
Zirc Oxide		98		62
Steel	1,815	4	1,814	5
Steel Oxide		12	1	1
CRP		0		0
Total	1,815	1,118	1,815	1,528
Lower Plenum Masses (kg)				
UO_2		39,751		53,198
Zircaloy		2,450		3,375
Zirc Oxide		4,486		1,167
Steel	32,655	96	32,667	103
Steel Oxide	6	78	10	42
CRP		334		4162
Total	32,661	47,195	32,677	58,301
Fraction Oxidized	Zircaloy ~30%	Steel ~0.4%	Zircaloy ~20%	Steel ~0.4%

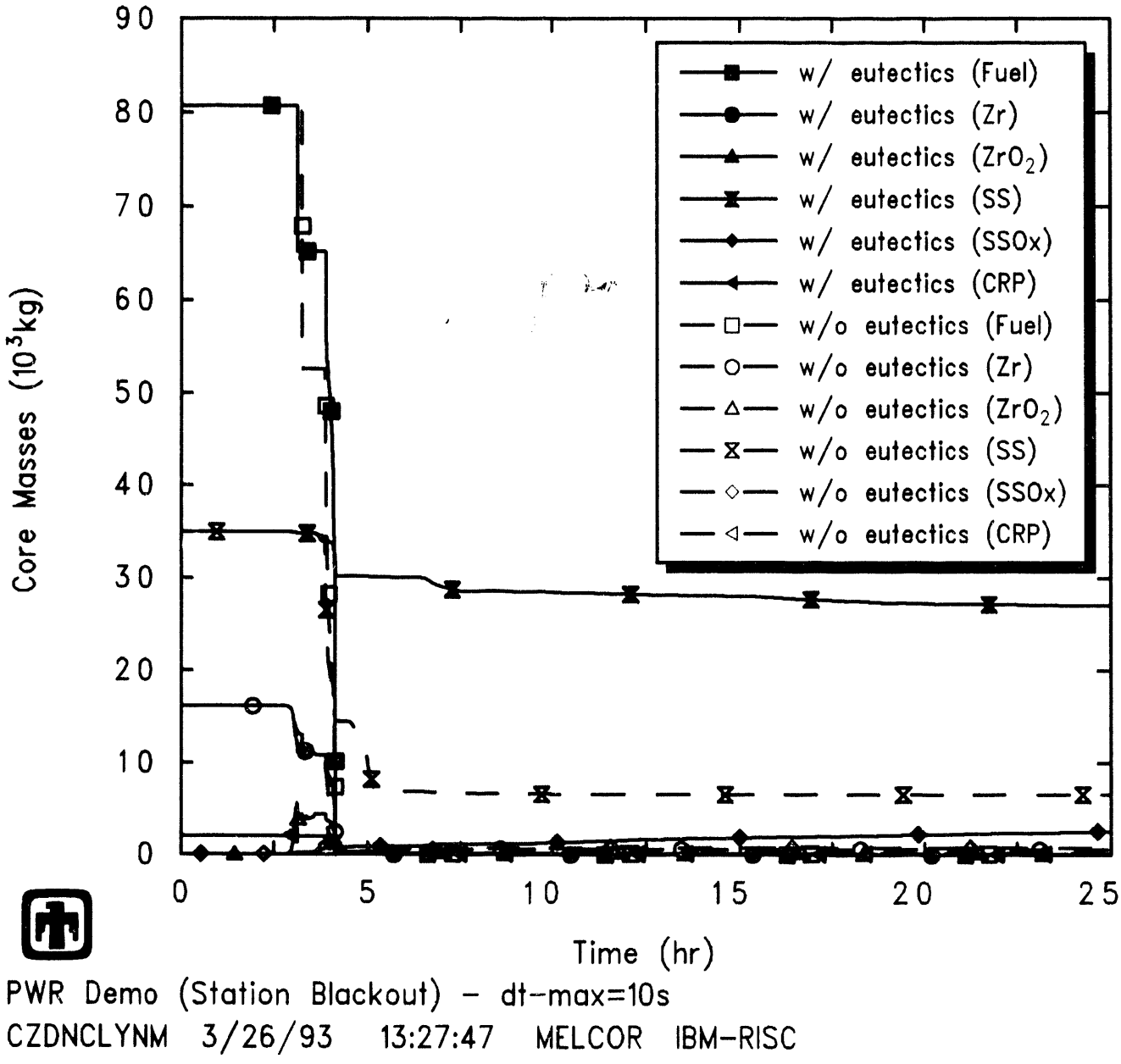

Figure 6.3.1. Total Core Masses Material Eutectics Sensitivity Study

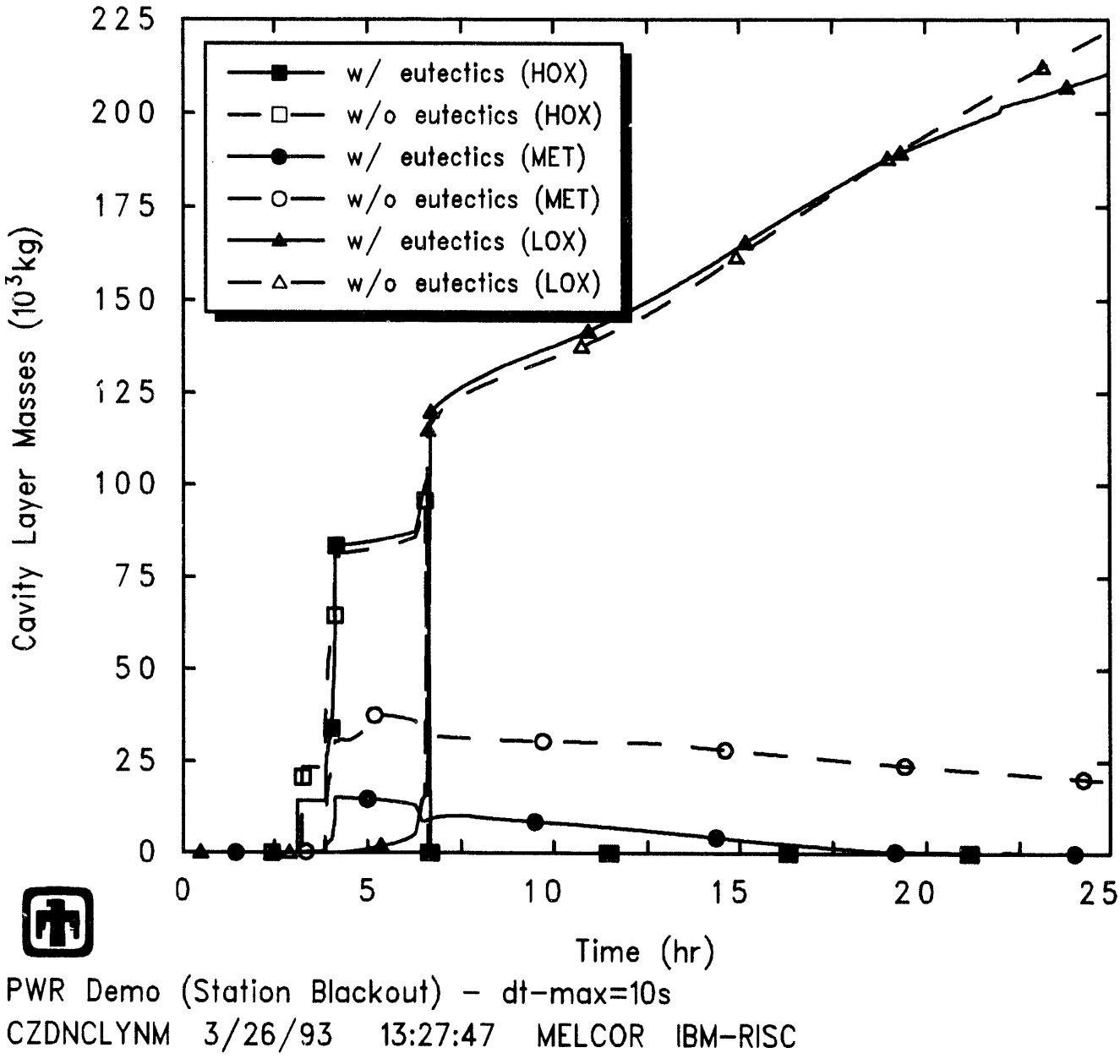

Figure 6.3.2. Cavity Layer Thicknesses – Material Eutectics Sensitivity Study

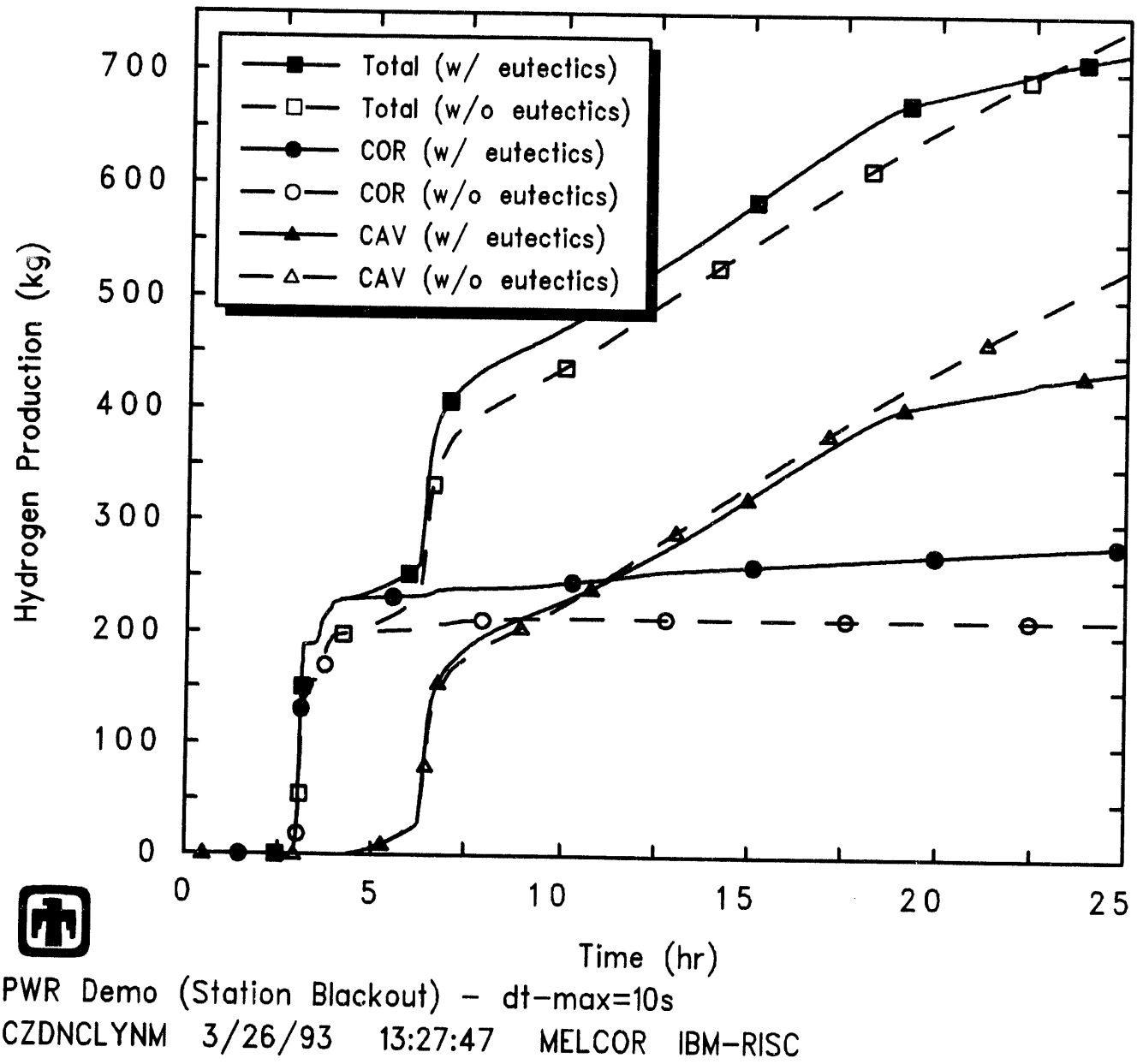

Figure 6.3.3. Hydrogen Production - Material Eutectics Sensitivity Study

Table 6.3.3. Fission Product Release - Material Eutectics Sensitivity Study

Class	(% Initial Inventory) In-Vessel Release		In-Cavity Release		Total Release	
	With Material	Without Eutectics	With Material	Without Eutectics	With Material	Without Eutectics
1 (Xe)	63.517	66.311	36.458	31.993	99.975	98.304
2 (Cs)	63.545	66.324	39.245	34.430	102.79	100.75
3 (Ba)	3.1039	3.8909	20.651	19.329	23.755	23.220
4 (I)	63.500	66.277	0.0	0.0	63.500	66.277
5 (Te)	4.4007	4.6483	43.727	38.323	48.128	42.971
6 (Ru)	0.0870	0.1156	6×10^{-7}	5×10^{-7}	0.0870	0.1156
7 (Mo)	2.3793	2.2519	0.7352	0.6942	3.1145	2.9461
8 (Ce)	0.0025	0.0027	0.0011	0.0010	0.0036	0.0037
9 (La)	0.0088	0.0455	0.1115	0.1046	0.1203	0.1502
10 (U)	0.0092	0.0515	0.0021	0.0019	0.0113	0.0534
11 (Cd)	10.224	17.068	0.2411	0.1861	10.465	17.254
12 (Sn)	10.225	17.068	2.5394	1.9286	12.764	18.997

6.4 CORSOR Options

A set of MELCOR Surry TMLB' assessment analyses were run with different release model options enabled in MELCOR, as a sensitivity study on fission product source term. These include the CORSOR and CORSOR-M models, each with and without a surface/volume correction term, and the new CORSOR-Booth model with low- and high-burnup coefficient sets, for a total of six possible variations. (Except in these source-term sensitivity study calculations, all the rest of our Surry TMLB' analyses were run using the CORSOR model including the surface/volume correction term.)

The CORSOR model is a simple correlational relationship based on data from early experiments [29]. Release of volatiles is assumed to be limited by diffusion, and all volatiles share the same release parameters, obtained by averaging experimental results; release of nonvolatiles is assumed to be limited by vaporization, and vapor pressures are scaled for consistency with experimental observations. The fractional release coefficients in CORSOR are simple exponentials, with constants selected for each species in specific temperature ranges based upon fitting experimental data. The fractional release coefficients used in CORSOR-M utilize an Arrhenius-type equation with constants representing empirical fits to experimental data.

The only substantial change in the utilization of the standalone CORSOR model in MELCOR is the (optional) use of a surface-volume (S/V) ratio to modify the calculated CORSOR and CORSOR-M release rates based on the ratio of the S/V ratios of the structure modelled to that of the typical experiments on which the coefficients are based. Other parameters possibly affecting release rates (such as pressure, atmospheric composition, fuel characteristics, chemistry, radiation environment, flow rates and the extent of fuel degradation) are not considered explicitly in either the CORSOR or CORSOR-M correlations.

The CORSOR code has been updated recently [30]. Time-dependent Cs release data from the larger data base currently available were used to fit parameters describing an effective diffusion coefficient in the new diffusion- and mass-transfer-based model; release rates of other species are then scaled to the Cs release rate. This model includes high- and low-burnup expressions, and also is a function of fuel grain size. This new CORSOR-Booth release model has been added to MELCOR in MELCOR 1.8.2 [31].

The final amounts of each class released by the end of the calculated transient period (90,000s or 25hr) in-vessel (in both the core active-fuel region and in the lower plenum), ex-vessel (in the cavity) and overall are given in Tables 6.4.1, 6.4.2 and 6.4.3, respectively, for analyses using CORSOR and CORSOR-M both with and without the surface/volume correction term, and for analyses using the low- and high-burnup CORSOR-Booth options (although obviously only the high-burnup version of the CORSOR-Booth model should apply to most plant analyses); these releases are expressed as percent of inventory initially present in the core. (Note that these amounts consider only the release of radioactive forms of these classes, and not additional releases of nonradioactive aerosols from structural materials.) There are a number of points to note about the results summarized in these tables.

Table 6.4.1. In-Vessel Source Terms – CORSOR Options Sensitivity Study

Class	Radionuclide Release (% Initial Inventory)					
	CORSOR	CORSOR (S/V)	CORSOR-M	CORSOR-M (S/V)	CORSOR-Booth high-burnup	CORSOR-Booth low-burnup
In-Core						
1 (Xe)	46.277	47.910	45.174	52.812	24.580	27.697
2 (Cs)	46.274	47.892	45.144	52.795	17.567	12.554
3 (Ba)	1.9813	4.1330	0.2312	0.4311	0.0761	0.0492
4 (I)	46.258	47.871	45.130	52.783	24.552	27.662
5 (Te)	1.6303	3.2899	44.793	52.465	9.0455	21.675
6 (Ru)	0.0725	0.1596	0.00006	0.0001	0.3217	0.4606
7 (Mo)	0.8373	1.6993	0.0	0.0	0.0225	0.0146
8 (Ce)	0.0015	0.0034	0.00001	0.00002	0.0008	0.0005
9 (La)	0.0056	0.0109	0.0	0.0	0.0050	0.0025
10 (U)	0.0056	0.0112	0.0033	0.0059	0.0024	0.0015
11 (Cd)	8.0196	14.898	0.0	0.0	10.608	7.4393
12 (Sn)	8.0206	14.896	1.2971	2.4876	10.609	7.4407
In LP						
1 (Xe)	20.328	12.409	11.579	20.426	22.509	22.105
2 (Cs)	20.373	12.547	11.579	20.432	18.351	18.505
3 (Ba)	5.3462	3.0679	0.5401	1.2951	0.1143	0.0986
4 (I)	20.341	12.413	11.588	20.436	22.513	22.115
5 (Te)	4.5250	2.6940	11.708	20.558	22.434	16.633
6 (Ru)	0.1823	0.1169	0.0004	0.0011	1.5136	1.5864
7 (Mo)	2.0899	1.3373	0.0	0.0	0.0344	0.0296
8 (Ce)	0.0033	0.0024	0.0002	0.0005	0.0011	0.0010
9 (La)	0.0790	0.0349	0.0	0.0	0.0034	0.0030
10 (U)	0.0819	0.0368	0.0202	0.0505	0.0036	0.0031
11 (Cd)	22.873	10.195	0.0	0.0	13.710	13.200
12 (Sn)	22.875	10.195	1.7707	3.8036	13.709	13.201

Table 6.4.2. Ex-Vessel Source Terms - CORSOR Options Sensitivity Study

Class	Radionuclide Release (% Initial Inventory)					
	CORSOR	CORSOR (S/V)	CORSOR-M	CORSOR-M (S/V)	CORSOR-Booth high-burnup	CORSOR-Booth low-burnup
1 (Xe)	33.382	38.937	42.029	25.683	49.626	49.136
2 (Cs)	35.932	41.817	45.305	27.673	63.597	71.117
3 (Ba)	21.256	30.585	30.157	29.273	28.546	22.122
4 (I)	0.0	0.0	0.0	0.0	0.0	0.0
5 (Te)	46.162	84.122	35.706	25.539	56.190	29.245
6 (Ru)	1×10^{-6}	4×10^{-6}	2×10^{-6}	2×10^{-6}	3×10^{-6}	8×10^{-7}
7 (Mo)	0.8525	2.2436	2.2908	2.2279	2.1269	0.8710
8 (Ce)	0.0011	0.0010	0.0009	0.0010	0.0010	0.0010
9 (La)	0.1508	0.2845	0.1732	0.1808	0.1980	0.1305
10 (U)	0.0021	0.0024	0.0018	0.0020	0.0020	0.0019
11 (Cd)	0.2363	2.7877	0.8048	2.4303	1.2353	0.1776
12 (Sn)	2.3571	27.097	7.6480	29.935	11.535	1.9773

Table 6.4.3. Total Source Terms - CORSOR Options Sensitivity Study

Class	Radionuclide Release (% Initial Inventory)					
	CORSOR	CORSOR (S/V)	CORSOR-M	CORSOR-M (S/V)	CORSOR-Booth high-burnup	CORSOR-Booth low-burnup
1 (Xe)	99.987	99.256	98.782	98.921	96.715	98.937
2 (Cs)	102.58	102.26	102.03	100.90	99.515	102.18
3 (Ba)	28.584	37.786	30.928	30.999	28.737	22.270
4 (I)	66.600	60.284	56.718	73.219	47.065	49.777
5 (Te)	52.317	90.106	92.208	98.562	87.669	67.553
6 (Ru)	0.2547	0.2765	0.0005	0.0012	1.8352	2.0470
7 (Mo)	3.7796	5.2802	2.2908	2.2279	2.1838	0.9152
8 (Ce)	0.0059	0.0067	0.0011	0.0015	0.0029	0.0025
9 (La)	0.2353	0.3303	0.1732	0.1808	0.2064	0.1360
10 (U)	0.0896	0.0503	0.0253	0.0584	0.0080	0.0065
11 (Cd)	31.129	27.881	0.8048	2.4303	25.553	20.817
12 (Sn)	33.252	52.188	10.716	36.226	35.853	22.619

In-vessel, using the CORSOR and CORSOR-M options resulted in similar releases of the Xe, Cs and I volatiles. The CORSOR expression and constants gave higher releases for many classes (Ba, Ru, Mo, Ce, La, Cd and Sn), while the CORSOR-M expression and constants produced significantly higher release of Te, with no release at all of Mo, La or Cd. The new CORSOR-Booth model predicted lower releases for the most volatile species (Xe, Cs and I), as well as for Ba, Te and U, than either of the older CORSOR options, while the releases of some other species were intermediate between the higher CORSOR and lower CORSOR-M predictions. The effects of using various CORSOR options are less evident in the total-release comparisons, because the later ex-vessel release somewhat compensate for in-vessel differences.

The overall release behavior predicted by MELCOR can be grouped into several subdivisions. Assuming the correct iodine behavior (as discussed below), ~100% of the Class 1, Class 2 and Class 4 radionuclide inventories were released, about 50%/50% in-vessel and ex-vessel. The next major release fractions were of Te (50-90%) and Ba (20-40%), both mostly predicted to occur primarily in the cavity. About 1-30% and 10-50% of the Cd and Sn radionuclide inventories, respectively, were released, and about 1-5% of the Mo radionuclide inventory; with the CORSOR and CORSOR-Booth options, the larger releases were in-vessel, while with the CORSOR-M option most of the release was ex-vessel. Finally, a total $\leq$1% of the initial inventories of the refractories (Ru, Ce, La and U) were released.

Using any of the CORSOR options, almost all of the Class 1 and Class 2 volatiles were predicted to be released from the fuel by the end of the MELCOR calculation. About $\geq$50% of that release occurred in-vessel, with the remaining $\leq$50% released ex-vessel in the cavity. Note that Tables 6.4.1, 6.4.2 and 6.4.3 show a very similar release pattern for Class 4 (halogens like iodine, also volatiles) in-vessel, but no additional release in the cavity. This is due to a coding problem in which the default radionuclide class mapping between MELCOR and the VANESA code, which is used to calculate the ex-vessel release within MELCOR. VANESA considers iodine to be released only as CsI. Since there is no separate CsI class in these MELCOR calculations, MELCOR assumes that CsI release to be a Class 2 (Cs) release (incidentally explaining why the total Class 2 release fraction shown in Table 4.5.1 is greater than 100%, which should be impossible). Based upon physical insight, the Class 4 release should closely resemble the Class 1 and 2 results. (This problem does not occur if CsI in Class 16 is enabled by the user, as is normally done in many plant analyses. However, the default class mapping needs to be corrected.)

The Class 5 release in-vessel appears surprisingly high, particularly in the analyses using CORSOR-M where its release matches the release of the volatiles. MELCOR includes a model for holdup of Te by unoxidized Zircaloy clad, in the form of ZrTe, which reduces the release by a factor of 1/40=0.025 if sufficient clad ($\geq$70%) remains unoxidized. There seemed to be enough unoxidized Zircaloy present during the core degradation process in these calculations to activate this hold-up model. However, inspection of the coding by the developers found that only intact Zircaloy in the clad component was used to calculate the degree of Te holdup; unoxidized Zircaloy present in either the particulate debris component or in conglomerate debris in any component (*e.g.*, Zircaloy candled and

refrozen onto clad or other structure) was not included in the holdup calculation. Because significant amounts of Zircaloy had relocated as either conglomerate or particulate debris, little holdup of Te as ZrTe was being predicted in these analyses. (Note that similar, unexpectedly high, Class 5 releases have been reported in other cases, *e.g.*, [32], probably due to the same cause.)

As expected, including the surface-to-volume (S/V) term increased the releases in-core in the analyses with CORSOR and CORSOR-M. However, note that the corresponding releases from fuel debris in the lower plenum were lower including the S/V term with the CORSOR option, but higher including the S/V term with the CORSOR-M option. This does not represent a direct result of using the S/V term, which only applies to intact fuel, but instead an indirect result of using different release options; different releases predicted using the different CORSOR options affected the time step used and the subsequent overall transient sequence (as already noted in our LOFT LP-FP-2 MELCOR assessment [6]).

Table 6.4.4 compares the timings of various key events predicted by MELCOR in this set of source-term sensitivity study calculations. The different initial gap release times calculated with the different CORSOR, CORSOR-M and CORSOR-Booth options indicate that some differences existed in these calculations even prior to clad failure, an unobvious result. The differences prior to clad failure and gap release were due to release of (nonradioactive, *i.e.*, structural) small masses for Classes 7, 9, 11 and 12; the amounts released were very small, but sufficient to affect the code time step, causing small but noticeable divergence of system response early in the transient. The differences were initially quite small, and generally did not result in significantly different transient behavior, but could potentially accumulate and increase until some important divergences occur. Also, the different releases of various radionuclides calculated using the various CORSOR options affected the local distribution of decay heating of fuel, debris, atmosphere and structures, which could further perturb the subsequent transient sequence.

In particular, note that in two cases (using CORSOR without the S/V term and using the low-burnup form of CORSOR-Booth) there was no high-pressure melt ejection of debris immediately following lower head penetration failure, but instead debris falling into the lower plenum water pool was sufficiently quenched that it remained in the lower plenum for ~2,000-3,000s before reheating sufficiently (to melt) that it could fall into the cavity.

These calculations all used the default debris ejection model in MELCOR, in which the masses of each material available for ejection are the total debris material masses, regardless of whether or how much they are melted. (In the other debris ejection option available, the masses of steel, Zircaloy and UO_2 available for ejection are simply the masses of these materials that are melted; the masses of steel oxide and control poison materials available for ejection are the masses of each of these materials multiplied by the steel melt fraction, based on an assumption of proportional mixing, and similarly the mass of ZrO_2 available for ejection is the ZrO_2 mass multiplied by the Zircaloy melt fraction. Additionally, the mass of UO_2 available for ejection is the Zircaloy melt fraction times the mass of UO_2 that could be relocated with the Zircaloy as calculated in the candling

Table 6.4.4. Timing of Key Events - CORSOR Options Sensitivity Study

Event	Time (s) CORSOR	CORSOR (S/V)	CORSOR-M	CORSOR-M (S/V)	CORSOR-Booth high-burnup	CORSOR-Booth low-burnup
Gap Release						
Ring 1	10,244.9	10,235.0	10,215.5	10,232.3	10,229.8	10,241.6
Ring 2	10,344.9	10,334.4	10,325.5	10,332.3	10,329.8	10,338.3
Ring 3	10,684.9	10,667.9	10,655.5	10,681.1	10,669.8	10,675.5
Core Plate Fails						
Ring 1	11,158.5	11,177.9	11,182.3	11,235.1	11,207.0	11 260.9
Ring 2	11,875.7	11,906.3	11,900.5	12,063.4	11,922.6	11,961.7
Ring 3	13,479.5	13,062.9	13,052.7	13,121.6	13,128.6	13,970.5
LH Penetration Fails						
Ring 1	11,220.9	11,219.3	11,225.5	11,278.7	11,253.1	11,308.7
Ring 2	11,250.9	13,029.5	13,013.0	13,304.9	13,161.4	11,349.7
Ring 3	11,262.8	13,842.3	13,795.4	13,943.6	13,791.8	11,366.5
Debris to Cavity	14,152.4	11,219.3	11,225.5	11,278.7	11,253.1	13,588.1
HPME/DCH Starts	-	11,219.3	11,225.5	11,278.7	11,253.1	-
HPME/DCH Ends	-	11,251.7	11,257.7	11,307.5	11,281.6	-
Deflagrations Start	12,857.0	12,863.2	12,785.5	12,770.8	12,597.9	12,763.6
Deflagrations End	14,069.5	13,766.2	13,951.2	13867.5	13,838.6	14,183.1
Deflagrations Start	-	-	29,351.3	-	-	-
Deflagrations End	-	-	29,353.0	-	-	-
Deflagrations Start	33,854.3	32,970.0	45,049.2	40,265.8	35,466.7	34,430.0
Deflagrations End	44,057.8	44,778.9	50,202.1	41,760.2	44,047.7	45,338.1

Table 6.4.5. Lower Plenum Debris Masses at Vessel Failure CORSOR Options Sensitivity Study

	Debris Mass in Lower Plenum (kg)					
	CORSOR	CORSOR (S/V)	CORSOR-M	CORSOR-M (S/V)	CORSOR-Booth high-burnup	CORSOR-Booth low-burnup
Total	10,235.2	9,991.0	10,596.1	17,476.3	17,853.3	12,733.2
Molten	359.5	434.4	455.9	575.1	1,926.2	382.3

model.) Regardless of which of these two options is used, in all these calculations the mass of debris to be ejected at vessel failure was being controlled by other constraints imposed. In particular, a total molten mass of 5000kg or a melt fraction of 0.1 (total mass melted divided by total debris mass) is necessary before debris ejection can begin. The latter constraint is implemented in the COR package as 0.1 times the volume of the core cell times 2000kg/m^3 (an assumed molten debris density), which in these cases corresponds to a threshold molten debris mass of 426.3kg needed for debris ejection to occur at first lower head penetration failure.

Table 6.4.5 presents the calculated total and molten debris masses in the lower plenum at the time of first lower head penetration failure in these source-term sensitivity study analyses. Note that the two cases with no HPME predicted (using CORSOR without the S/V term and using the low-burnup form of CORSOR-Booth) had molten debris masses 10-15% below this cutoff value, the reference calculation (using CORSOR with the S/V term) had a molten debris mass just 2% above this cutoff value, two other cases (using CORSOR-M without and with the S/V term) had molten debris masses 7% and 35% above this cutoff value, and one calculation (using the high-burnup form of CORSOR-Booth) had a molten debris mass substantially above this cutoff value.

The delay in debris ejection in the two cases without HPME at vessel failure explains why the releases in the lower plenum were larger in the calculation using the CORSOR model with no S/V term than with the S/V term, while the releases in the lower plenum were smaller in the calculation using the CORSOR-M model with no S/V term than with the S/V term; there was more debris in the lower plenum for a longer period of time to contribute to the in-vessel source term.

The delay in debris ejection in the two cases with no HPME at vessel failure also affected the melting and ejection of the structural steel mass in the lower plenum, as illustrated in Figure 6.4.1. With more debris in the lower plenum for a longer period of time to heat the structural material in the two cases with no HPME at vessel failure, most of the lower plenum steel was eventually melted and lost to the cavity; with less debris in the lower plenum for a shorter period of time to heat the structural material in the other four cases (with HPME at vessel failure), most of the lower plenum steel

remained in the lower plenum and little was melted and lost to the cavity. The different degrees of structural steel retention in the lower plenum did not substantially perturb the overall masses of core debris ejected to the cavity or the amount of concrete ablated in the cavity, because the steel mass was a small fraction of the overall core material mass. However, the increased retention of steel mass in the lower plenum in the four calculations with HPME at vessel failure resulted in a significantly smaller, thinner metallic layer in the cavity, which was completely oxidized by the end of the transient in those four cases, as indicated in Figure 6.4.2.

The disappearance of the metallic layer before the end of the transient in the four source-term sensitivity study calculations with HPME predicted at vessel breach had a significant and unanticipated effect on the ex-vessel source term (given in Table 6.4.2) for several radionuclide classes, discussed in more detail in Section 4.5. (Note that the problem is not in the implementation of the VANESA code in MELCOR, but also to the VANESA code itself.) As the metallic layer in the cavity disappeared, the releases of radionuclide species associated with that layer (*i.e.*, Te, Ru, Cd and Sn) began growing exponentially. This is illustrated in Figure 6.4.3 for several of these radionuclide species. The effect is not pronounced for Te, because most of that species mass had been released prior to the metallic layer vanishing, the effect is not pronounced for Ru, because very little of that species mass had been released at all; however, the release of other species, such as Cd and Sn, could be significantly in error.

As already noted, this problem is inherent in the VANESA formulation itself, not just in MELCOR, but is more likely to be encountered with MELCOR 1.8.2 than with MELCOR 1.8.1 because of the increased likelihood of more retention of lower plenum structural steel in-vessel.

(All these CORSOR options sensitivity study calculations were run on an IBM RISC-6000 Model 550 workstation.)

6.5 High Pressure Melt Ejection and Direct Containment Heating

One of the major severe accident phenomena identified as a missing model in MELCOR by the peer review [11] was high-pressure melt ejection and direct containment heating. A HPME/DCH model has been added to the fuel dispersal interactions (FDI) package in MELCOR 1.8.2 [33].

The FDI package in MELCOR calculates the behavior of debris in containment from the time it is ejected from a failed reactor pressure vessel until the time it is deposited in a cavity. Both low pressure melt ejection (LPME) from the reactor vessel and high pressure melt ejection (HPME) from the reactor vessel (leading to direct containment heating) now are modelled. If the velocity of the molten debris ejected from the reactor vessel exceeds a critical value (default to 10m/s), or if the user has invoked the stand-alone HPME option, then the fuel dispersal interactions will be treated by the high pressure model instead of the low pressure model. The parametric high pressure model requires

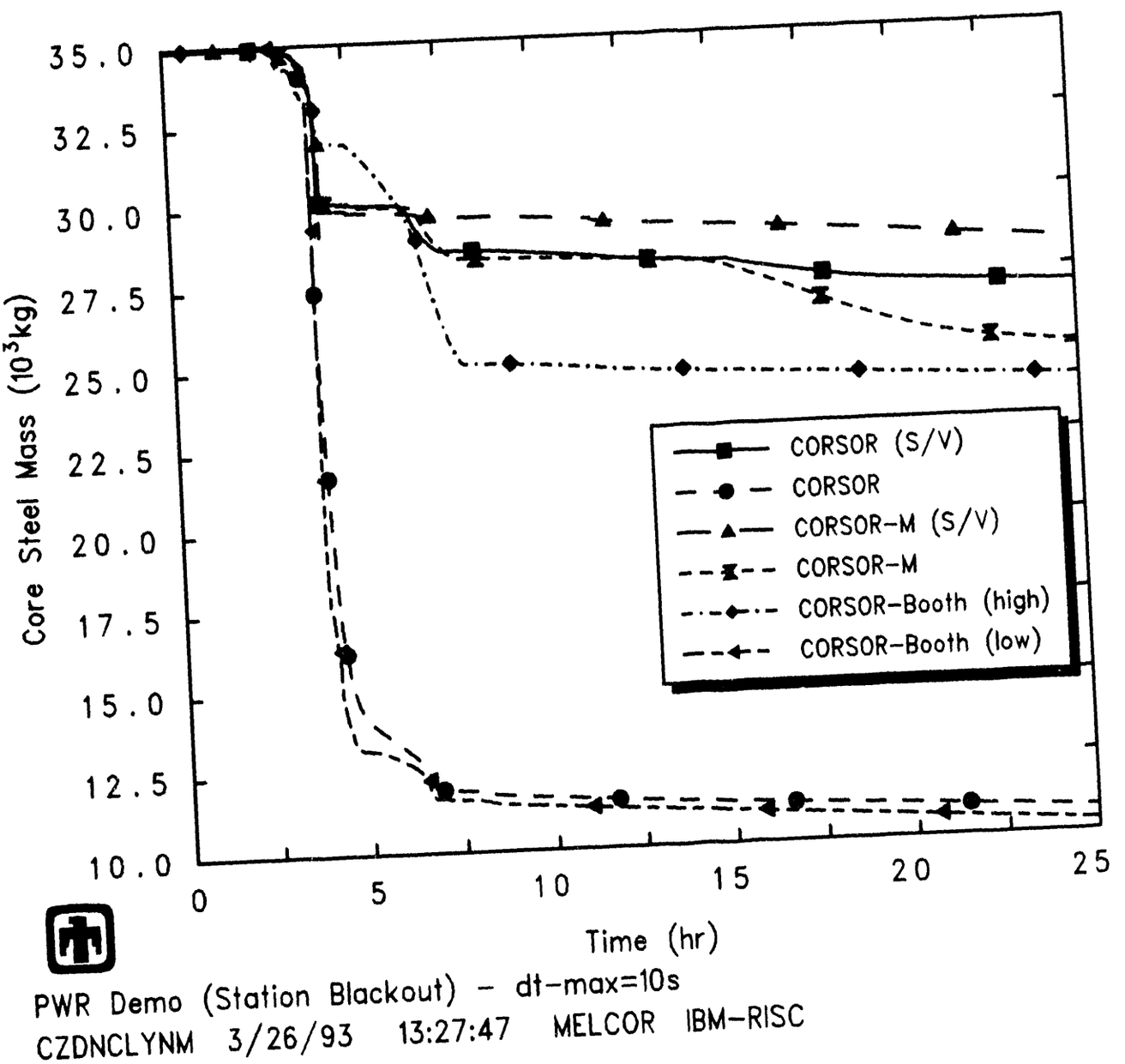

Figure 6.4.1. Core Steel Masses for Surry TMLB' - CORSOR Options Sensitivity Study

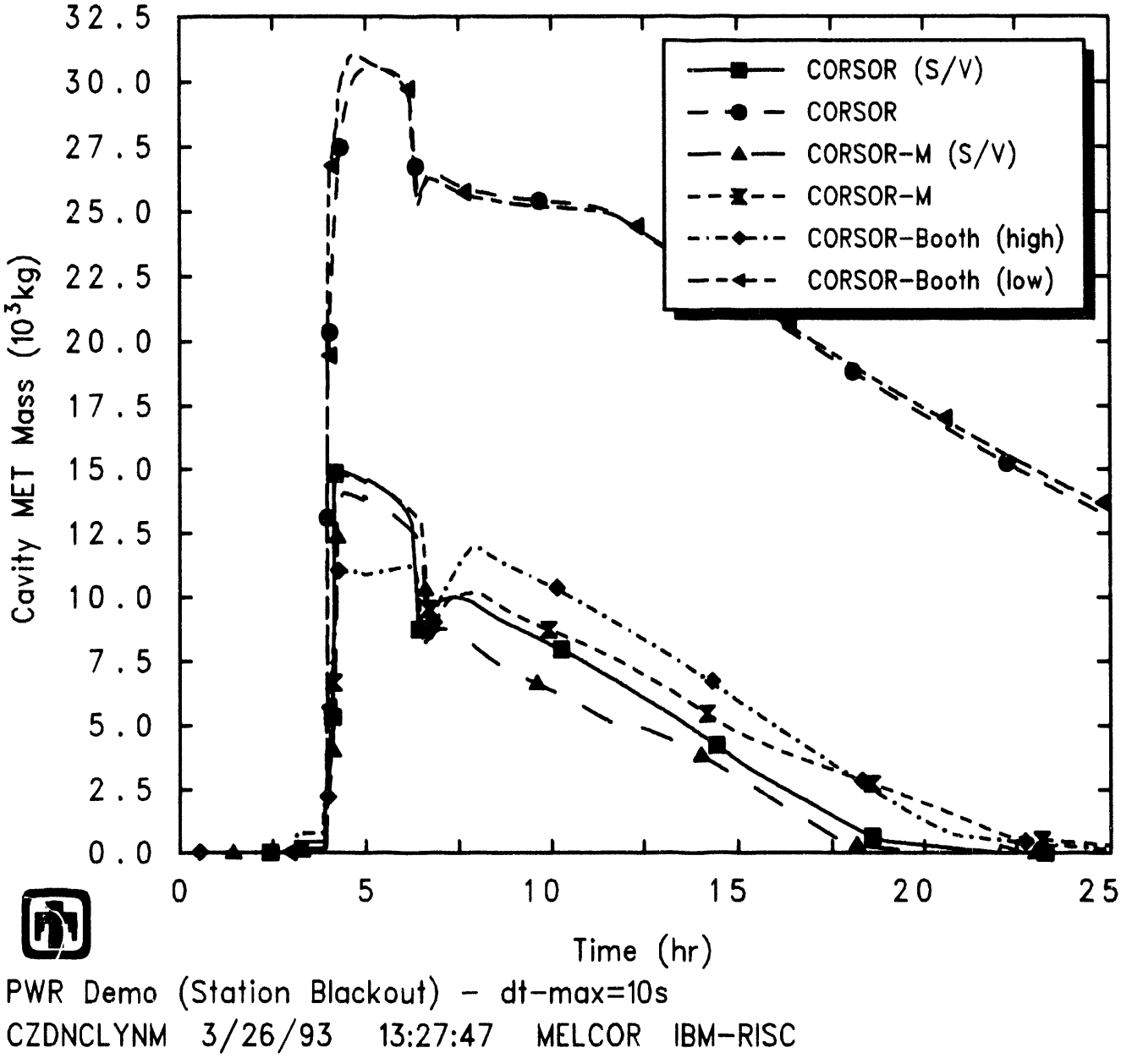

Figure 6.4.2. Cavity Metallic Layer Masses for Surry TMLB' CORSOR Options Sensitivity Study

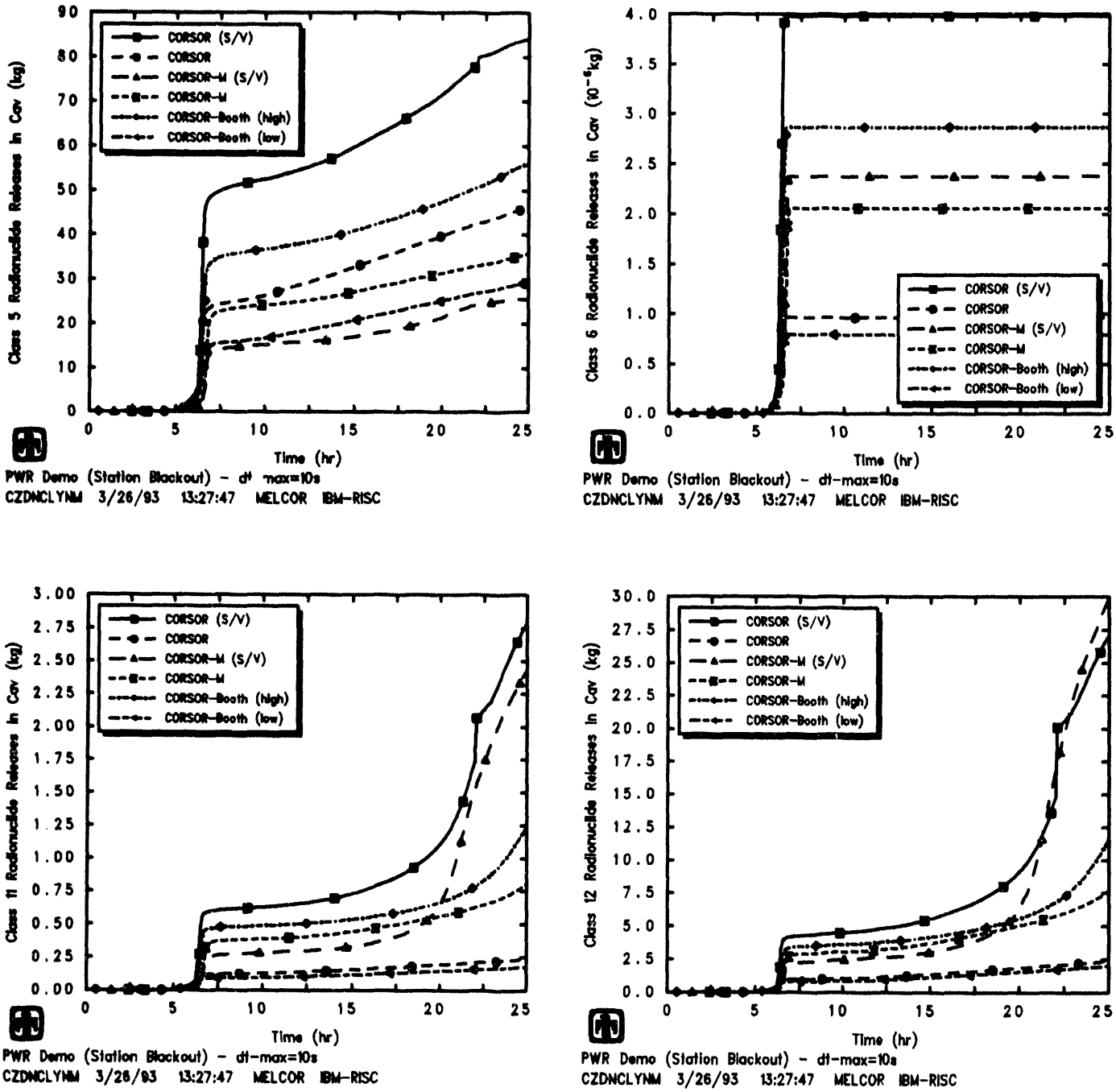

Figure 6.4.3. Ex-Vessel Class 5 (Te) Releases (upper left), Class 6 (Ru) Release (upper right), Class 11 (Cd) Releases (lower left) and Class 12 (Sn) Releases (lower right) for Surry TMLB' CORSOR Options Sensitivity Study

user input to control both the distribution of debris throughout the containment and the interaction of the hot debris with the containment atmosphere.

The HPME model does not include a mechanistic debris transport model; rather, the user specifies a set of debris destinations with a corresponding set of transport fractions that prescribe where the ejected debris is assumed to go. The debris destinations may include the atmosphere of any CVH control volume, the surface of any heat structure, and cavities defined by the CAV package; the sum of the transport fractions over all the specified control volume atmospheres, heat structure surfaces and cavities must equal one. Transport of the ejected debris to its assumed destinations occurs instantaneously with no interactions occurring between the point of ejection and the destination sites. As long as the HPME model is active (*i.e.*, as long as the ejection velocity exceeds the LPME/HPME transition velocity or if the user has invoked the stand-alone HPME model) the ejected debris will be partitioned among the destinations as specified by the transport fractions. When the ejection velocity falls below the LPME/HPME transition velocity for non-stand-alone applications, any debris subsequently ejected is passed to the LPME model, which uses LPME model input instead of the HPME transport model to determine the debris destination. However, debris that was transported to the HPME debris destinations before the model transition occurred will continue to be treated by the HPME model.

The processes modelled include oxidation of the metallic components of the debris in both steam and oxygen, surface deposition by debris trapping or airborne-debris settling and heat transfer to the atmosphere and heat structure surfaces. However, debris which is transported to cavity destinations is not treated further by the FDI package, but rather by the CAV package. As implemented in the HPME model, surface deposition of debris can occur in two distinct ways. Ejected debris which impacts structures prior to any significant interaction with the atmosphere is sourced directly to the destination surface via the user-specified transport fraction for that surface; this process is referred to as trapping in MELCOR. Alternatively, debris which interacts significantly with the atmosphere can be sourced to the appropriate control volume, in which a user-specified settling time constant will determine the rate of deposition to the specified settling destination (either a heat structure surface or a cavity); this process is referred to as settling in MELCOR. First order rate equations with user specified time constants for oxidation, heat transfer and settling are used to determine the rate of each process.

If the MELCOR Radionuclide (RN) package is active, then FDI will call RN1 anytime fuel is moved so that the associated radionuclides can be moved simultaneously. Furthermore, the decay heat associated with the radionuclides will be deposited in the appropriate location. However, there is no release of fission products calculated from airborne debris during the FDI/HPME/DCH interaction, or from debris deposited onto structures rather than into the cavity.

The simple direct containment heating model described above is not intended to predict all details of DCH events from first principles. To do so, nodalization requirements would be much greater than for normal MELCOR models. Rather, it is intended to allow

users to evaluate the overall effect of varying the relative rates of the most important processes controlling DCH loads.

For these PWR TMLB' HPME/DCH analyses, sensitivity studies have been done

1. varying the amount of debris ejected from the vessel during the high-pressure melt ejection process;

2. varying the relative amounts of debris deposited directly in the cavity, in the various containment volume atmospheres, and on various heat structures in the cavity, basement and containment dome during the HPME process (while any debris ejected later during low-pressure melt ejection is always deposited directly into the cavity);

3. varying the characteristic interaction times specified for oxidation, heat transfer and settling of airborne debris; and

4. enabling hydrogen combustion below the default mole fraction ignition limit in volumes during periods of HPME/DCH interactions.

These Surry TMLB' DCH analyses and sensitivity studies relied heavily on modelling insights and code improvements from the earlier MELCOR DCH assessment analyses of the IET experiments [10].

6.5.1 HPME Debris Mass

The reference PWR TMLB' calculation described in detail in Section 4, which included input enabling the new HPME/DCH model added in MELCOR 1.8.2 (as discussed in Section 3), showed a rapid, brief pressure and temperature spike in containment immediately upon high-pressure melt ejection and direct containment heating. The effect was not extremely pronounced, because only ~10-15% of the available core material was predicted to be ejected during the high-pressure melt ejection phase in our reference Surry TMLB' calculation.

The amount of melt in the lower plenum at vessel failure is a concatenation of early-time core damage, core plate failure criteria, falling debris heat transfer and possible quench in the lower plenum, and lower head penetration heat transfer and failure criteria. Further, as discussed in Section 6.4, the amount of material actually lost from the vessel at failure also depends on the relative amounts of molten and total debris in the lower plenum at vessel failure.

The core plate and bottom head penetration failure temperatures, and the falling debris and lower head penetration heat transfer coefficients were all set to their default values in these MELCOR Surry TMLB' calculations. Limited sensitivity studies were done varying some of these parameters, but there is little data available for these phenomena, either for evaluation of the MELCOR models' adequacy or for guidance on the values to use for the various input parameters controlling predicted response.

Instead, calculations were done in which the peaking factors used were adjusted until ~60% of the available core material was predicted to be ejected during the high-pressure melt ejection phase. In particular, the peaking factor of the innermost core radial ring (containing about 15% of the total core material) was lowered, while the peaking factor of the second, middle core radial ring (containing about 60% of the total core material) was increased until that ring failed first. This was not intended to represent "correct" values for core power peaking, but simply to allow a comparison of DCH behavior in otherwise similar calculations with different amounts of high-pressure melt ejection.

Several sets of calculations were done with ~15% and ~60% of the core material ejected at vessel failure. Calculations were done with no HPME/DCH modelled (*i.e.*, using the LPME model in the FDI package for both initial and subsequent debris ejection), with HPME modelled but no DCH (*i.e.*, with any HPME debris specified to go directly to the CORCON cavity, with no interaction with containment atmosphere and/or structures), and with HPME/DCH modelled (*i.e.*, with the initial HPME debris ejection specified as described in Section 3).

The atmospheric pressures predicted during the HPME period in the cavity and inner containment dome control volumes are shown in Figures 6.5.1.1 and 6.5.1.2, for calculations with ~15% and with ~60% of the total degraded core material coming out as HPME debris. Corresponding pressures calculated with the same debris ejection masses, but specified as HPME with no DCH or as LPME, are included to provide an indication of the magnitude of the HPME/DCH contribution to the pressurization. The pressures in the other containment control volumes were very similar to the pressures shown for the inner dome volume. (The differences in timing of vessel breach, HPME initiation and containment pressurization in these figures and in the rest of the figures in this subsection are due to delaying material retention in-vessel to create the larger, ~60% HPME debris mass.)

There was little or no difference in the calculations with only the LPME model used and with the HPME model used, but all the debris deposited directly into the cavity (*i.e.*, no DCH). There is a difference in modelling: with the LPME model used, debris falling into the cavity can interact with any water present in the cavity, with the resulting heat transfer contributing to debris cooling, while the HPME model assumes any water in the cavity is "blasted" up into the cavity atmosphere into fog droplets. In this sequence, there is little or no water in the cavity prior to vessel failure. Substantial amounts of water fall into the cavity after vessel breach, representing residual lower plenum water not vaporized by interaction with debris, and both accumulator water and remaining pressurizer water entering the primary system after vessel breach and primary system depressurization. Little if any of this water will be present in the cavity during the first 0.5min after vessel breach, the time scale of the HPME process. Therefore, the different assumptions about interaction with cavity water have little or no effect.

The long-term containment pressure history, for the containment dome, is presented in Figure 6.5.1.3; except for differences in the pressure spike in the cavity, the pressures in all containment volumes are the same. Very small differences are seen in the long-term containment response in the three calculations with ~15% initial debris ejection, with or

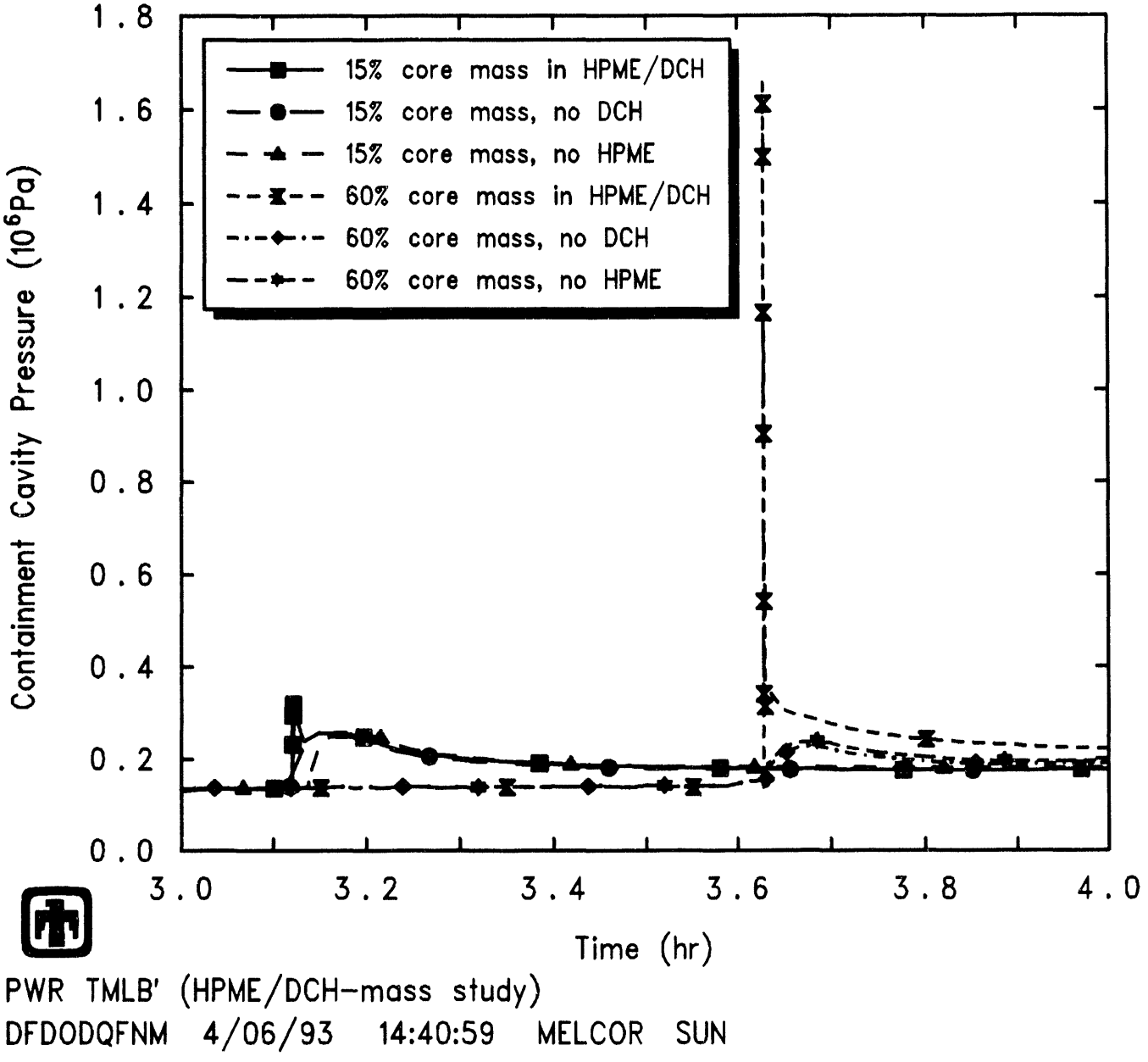

Figure 6.5.1.1. Cavity Pressure during HPME and DCH – HPME/DCH Debris Mass Sensitivity Study

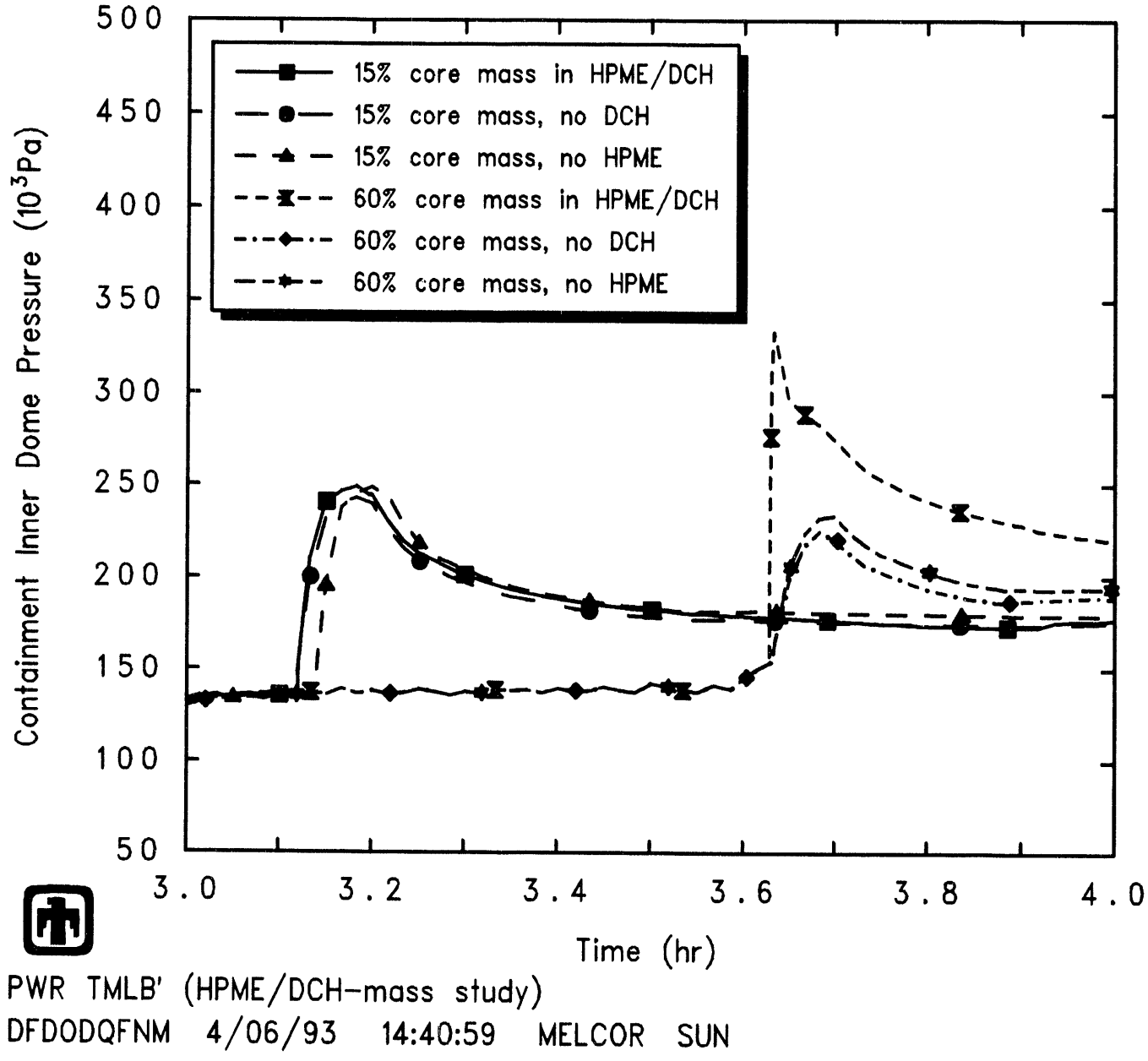

Figure 6.5.1.2. Containment Dome Pressure during HPME and DCH – HPME/DCH Debris Mass Sensitivity Study

without high-pressure melt ejection and direct containment heating, just as only small differences were seen in the short-term containment response in these three calculations in Figure 6.5.1.2.

The two calculations with ~60% initial debris ejection without direct containment heating, using either the LPME or the HPME model in the FDI package for the initial debris ejection, also gave very similar results; a small timing offset in the change in pressurization rate occurring when the cavity water is all boiled away was due to the different treatment of debris interaction with cavity water in these two models. The calculation using the HPME model, which "blasts" the cavity water into the atmosphere as fog, had slightly less water in the cavity at later times because some of that fog mass was carried by steam blowdown flow into other containment volumes before settling out; the slightly smaller amount of cavity water in that calculation allowed the cavity to boil dry, core-concrete interaction to begin, and the containment pressurization rate to decrease, all slightly earlier than in the calculation using only the LPME model.

There is a visible difference in the late-time containment pressurization predicted in the calculation with ~60% initial debris ejection and with both HPME and DCH modelled. Including both HPME and DCH in the Surry TMLB' analysis affected the amount of material in the cavity (because any debris specified to be transported to volumes and/or structures outside the cavity eventually settles onto heat structures outside the cavity). This also affected the time required to boil dry the cavity after which significant core-concrete interaction starts, the total amount of concrete ablated and the noncondensable gases generated, and the source term because release of fission products from airborne debris and from debris settled onto heat structures (instead of into the cavity) is neglected in the MELCOR model. These effects are discussed in more detail in the following subsection.

6.5.2 HPME Debris Distribution

Sensitivity studies also have been done varying the relative amounts of melt deposited directly in the cavity, in the various containment volume atmospheres, and on various heat structures in the cavity, basement and containment dome.

The reference calculation included input to model high-pressure melt ejection and direct containment heating, taking advantage of the new HPME/DCH model added in MELCOR 1.8.2. That input specified 60% of the debris ejected in high-pressure melt ejection to go to the cavity control volume atmosphere, 10% of the HPME debris to go to the basement control volume atmosphere, and 3% of the HPME debris to go to the inner dome control volume atmosphere; 18% was specified to fall directly into the cavity, and 2%, 5% and 2% were specified to go directly onto various heat structures in the cavity, basement and dome, respectively. This distribution was selected with two goals in mind: to specify some HPME debris to at least a few of each possible end site available in the MELCOR FDI/HPME/DCH model (*i.e.*, to the cavity itself, to control volume atmospheres, and directly to heat structure surfaces), and to include a relatively mild DCH interaction in the reference analysis.

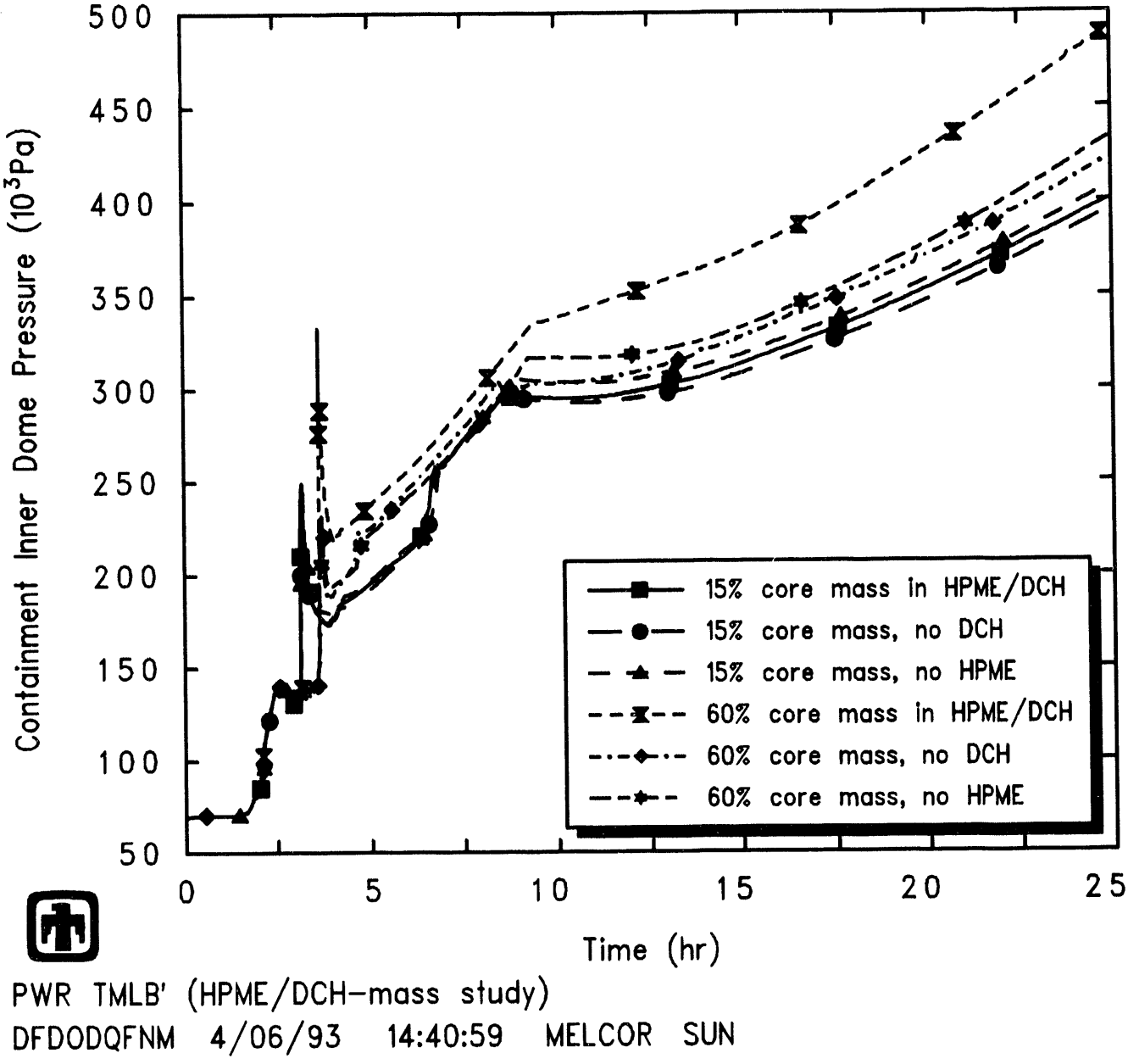

Figure 6.5.1.3. Containment Pressure - HPME/DCH Debris Mass Sensitivity Study

Several other calculations were done with different debris distributions, as summarized in Table 6.5.2.1, including one in which all the debris was specified to go directly to the cavity during HPME as well as in LPME. The debris distributions in these sensitivity study analyses were selected to cover three basic potential patterns: most of the HPME debris to remain in the cavity, most of the HPME debris to be blown into the containment dome, and most of the HPME debris to be trapped in some subcompartment(s). The last case was done using the only subcompartments available in the MELCOR Surry containment nodalization; other potential trapping sites such as the seal table room are not included separately in the MELCOR Surry containment model.

In most of these sensitivity study calculations, none of the HPME debris was specified to fall directly into the CORCON cavity or be deposited directly onto heat structures; all the HPME debris was specified to be deposited first somewhere in the containment atmosphere, and then to settle either into the cavity or onto floor heat structures. (Debris deposited in the cavity control volume atmosphere settles into the CORCON cavity; debris deposited in the other containment control volume atmospheres settles onto user-specified floor heat structures.) This is slightly more HPME debris deposited into the containment atmosphere than in the reference analysis, where most of the HPME debris (73%) was specified to be deposited first somewhere in the containment atmosphere; 18% of the HPME debris was specified to fall directly into the CORCON cavity and only 9% was specified to be deposited directly onto heat structures.

The atmospheric pressures predicted during the HPME period in the cavity and inner containment dome control volumes are shown in Figures 6.5.2.1 and 6.5.2.2, for calculations with the four debris distributions given in Table 6.5.2.1 as "Case *N*"; the pressures in the other containment control volumes were very similar to the pressures shown for the inner dome volume.

Depositing more debris directly into the cavity or onto heat structures reduces the magnitude of the pressure/temperature excursion in the atmosphere by bypassing the direct containment heating mechanisms; increasing the amount of debris deposited in the containment atmosphere increased the magnitude of the pressure/temperature excursion due to more debris oxidation and heat transfer. Further, varying the relative amounts of debris deposited into various containment control volume atmospheres changed the relative magnitude of the pressure/temperature excursion predicted: specifying more debris into the cavity atmosphere (a relatively small volume) resulted in a very large pressure and temperature spike in that local volume, but much smaller pressure/temperature excursions throughout the rest of containment before equilibration, while specifying more debris into the containment dome atmosphere (a relatively large volume) resulted in a significantly smaller local pressure and temperature spike, but a slightly larger global spike spread more uniformly throughout the containment. (Similarly, specifying more debris into subcompartments (also relatively small volumes) resulted in a very large pressure and temperature spike in those local volumes, but much smaller pressure/temperature excursions throughout the rest of containment, before equilibration.)

In particular, with 100% of the HPME debris deposited directly into the CORCON cavity, there was no direct containment heating and the pressures were very similar to

Table 6.5.2.1. Debris Distributions Assumed - HPME/DCH Debris Distribution Sensitivity Study

Location	Debris (% Ejected)				
	Reference	Case 1	Case 2	Case 3	Case 4
Cavity (CORCON)	18	100	0	0	0
Control Volume Atmosphere					
Basement	10	0	10	10	10
Cavity	60	0	75	15	10
SG Cubicle	0	0	0	50	0
Przr Cubicle	0	0	0	15	0
Inner Dome	3	0	10	5	75
Outer Dome	0	0	5	5	5
Control Volume Structures					
Basement	5	0	0	0	0
Cavity	2	0	0	0	0
SG Cubicle	0	0	0	0	0
Przr Cubicle	0	0	0	0	0
Inner Dome	2	0	0	0	0
Outer Dome	0	0	0	0	0

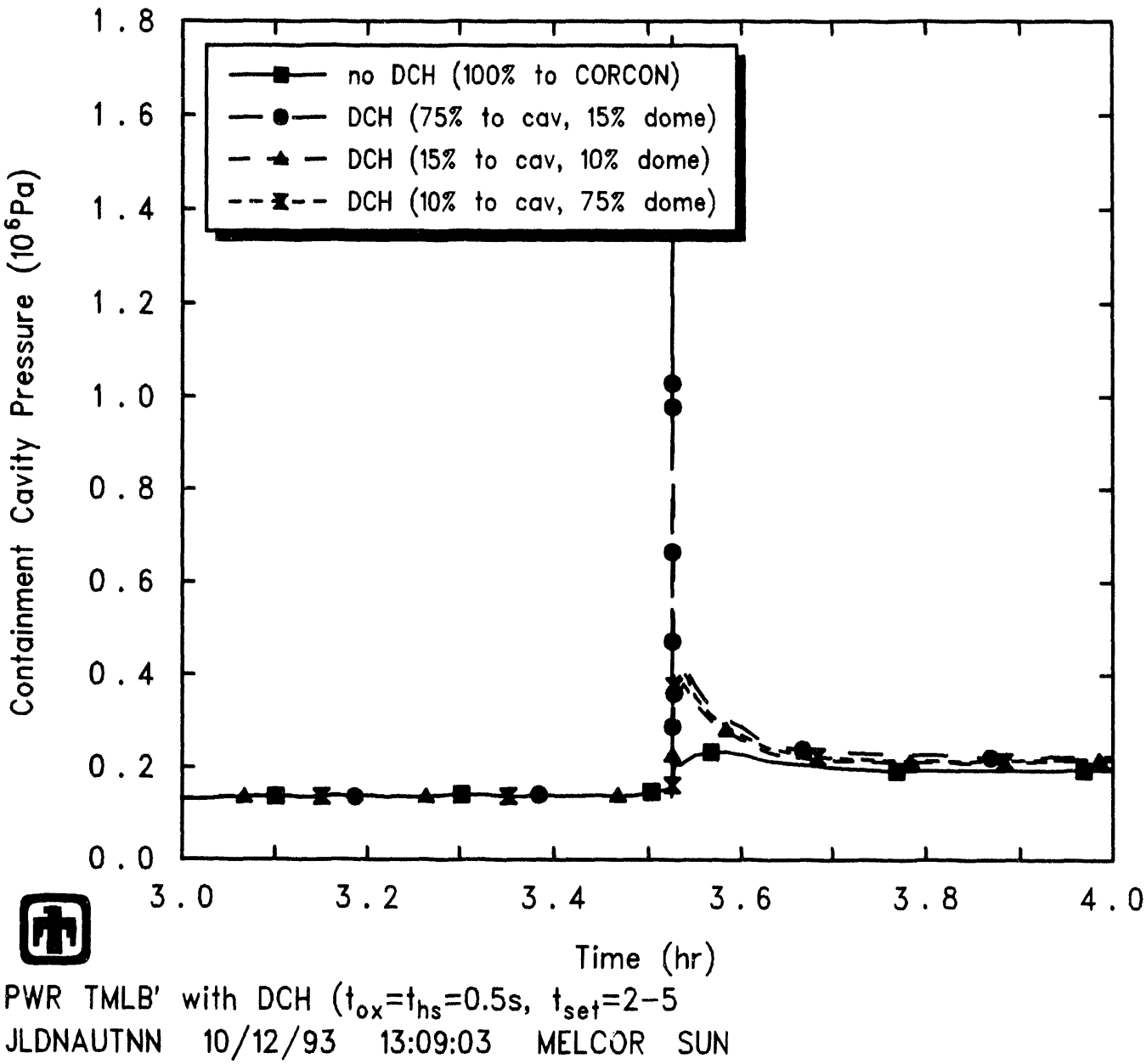

Figure 6.5.2.1. Cavity Pressure during HPME and DCH - HPME/DCH Debris Mass Sensitivity Study

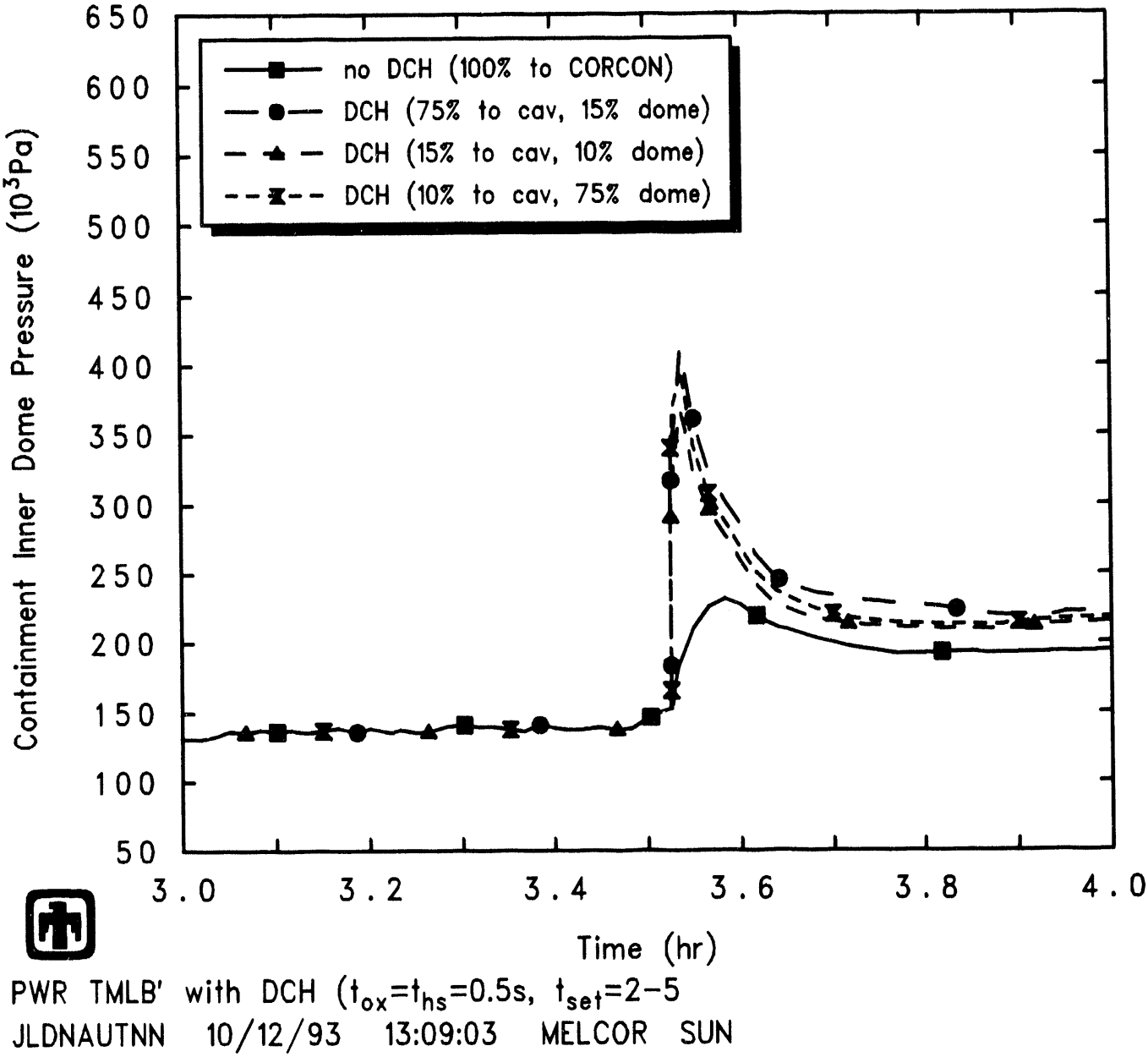

Figure 6.5.2.2. Containment Dome Pressure during HPME and DCH - HPME/DCH Debris Mass Sensitivity Study

those predicted using the original, LPME model (as shown in Figures 6.5.1.1 and 6.5.1.2). With most of the debris specified to go to the cavity atmosphere, a large spike in cavity pressure (and temperature) was calculated. However, in general, except for such local pressure (and temperature) spikes in those volumes to which most of the debris was specified to go, if a similar total fraction of debris iss specified to interact with the containment atmosphere (regardless of distribution within individual volumes) then a similar overall containment pressure (and temperature) response to direct containment heating is predicted.

The long-term containment pressure history is presented in Figure 6.5.2.3. The major division into two curves is due to the different debris distributions assumed. Lower late-time pressures were calculated for the two calculations with 100% and 75% of the HPME debris specified to go to the cavity; significantly higher late-time pressures were calculated for the two calculations with 15% and 10% of the HPME debris specified to go to the cavity. The two calculations with little debris deposited into the cavity took much longer to boil off the cavity water, as illustrated by the cavity water masses presented in Figure 6.5.2.4 for these sensitivity study calculations. While the debris decay heat was primarily being dissipated by boiling away the cavity water pool, the containment pressurized more rapidly. Later, after significant core-concrete interaction began, the debris decay heat was diverted to concrete decomposition and the containment pressurized more slowly.

Including DCH in the Surry TMLB' analysis thus affected the amount of material in the cavity (because some debris settled onto heat structures outside the cavity). The amount of concrete ablated was then affected both by how long before the cavity water was boiled away (after which significant core-concrete interaction begins), and by how much debris was in the cavity at late times to attack the concrete. Figures 6.5.2.5 and 6.5.2.6 present the mass of core debris in the cavity and the mass of ablated cavity concrete, respectively, for calculations with the four debris distributions given in Table 6.5.2.1 as "Case N". The more core debris in the cavity, the sooner the cavity water boiled away and the more concrete was ablated.

The differences in core debris mass in the cavity in Figure 6.5.2.5 are not as great as suggested by the curve labels and by the debris distributions in Table 6.5.2.1 because the DCH distribution specified only affects HPME debris; all debris ejected after the first ~30s goes through the LPME model directly to the cavity. Also, the debris source to the cavity was affected by different material retention in-vessel, shown in Figure 6.5.2.7 for these debris-distribution sensitivity study calculations. Small differences in time step histories in the HPME/DCH period due to the different debris distributions and resulting differences in containment response feed back to affect the subsequent core material loss and/or retention, sometimes substantially.

The final amounts of each radionuclide class released by the end of the calculated transient period (90,000s or 25hr) in-vessel (in both the core active-fuel region and in the lower plenum), ex-vessel (in the cavity) and overall are given in Tables 6.5.2.2, 6.5.2.3 and 6.5.2.4, respectively, for analyses run with different HPME debris distributions. These releases are expressed as percent of inventory initially present in the core, and

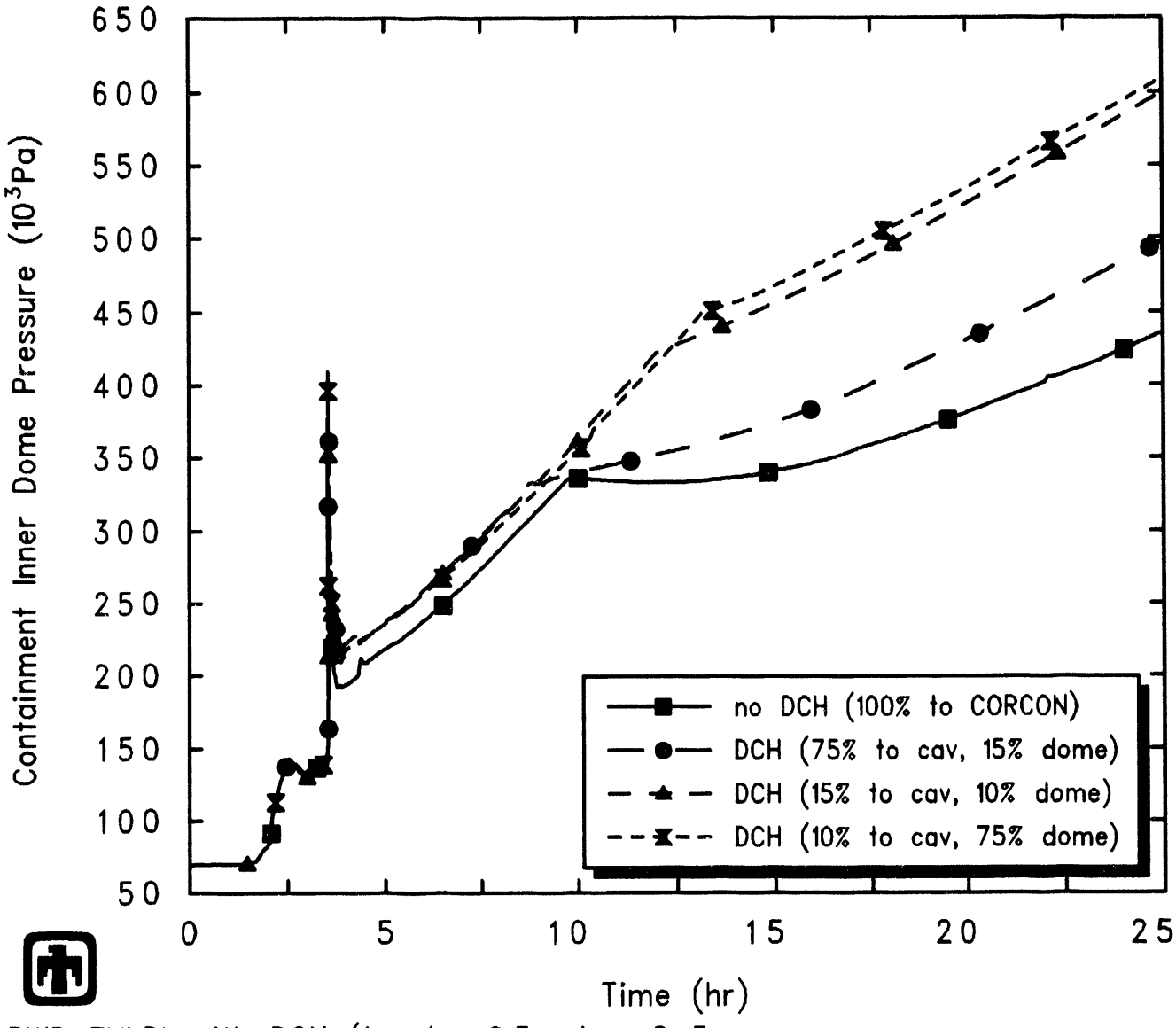

Figure 6.5.2.3. Containment Pressure HPME/DCH Debris Distribution Sensitivity Study

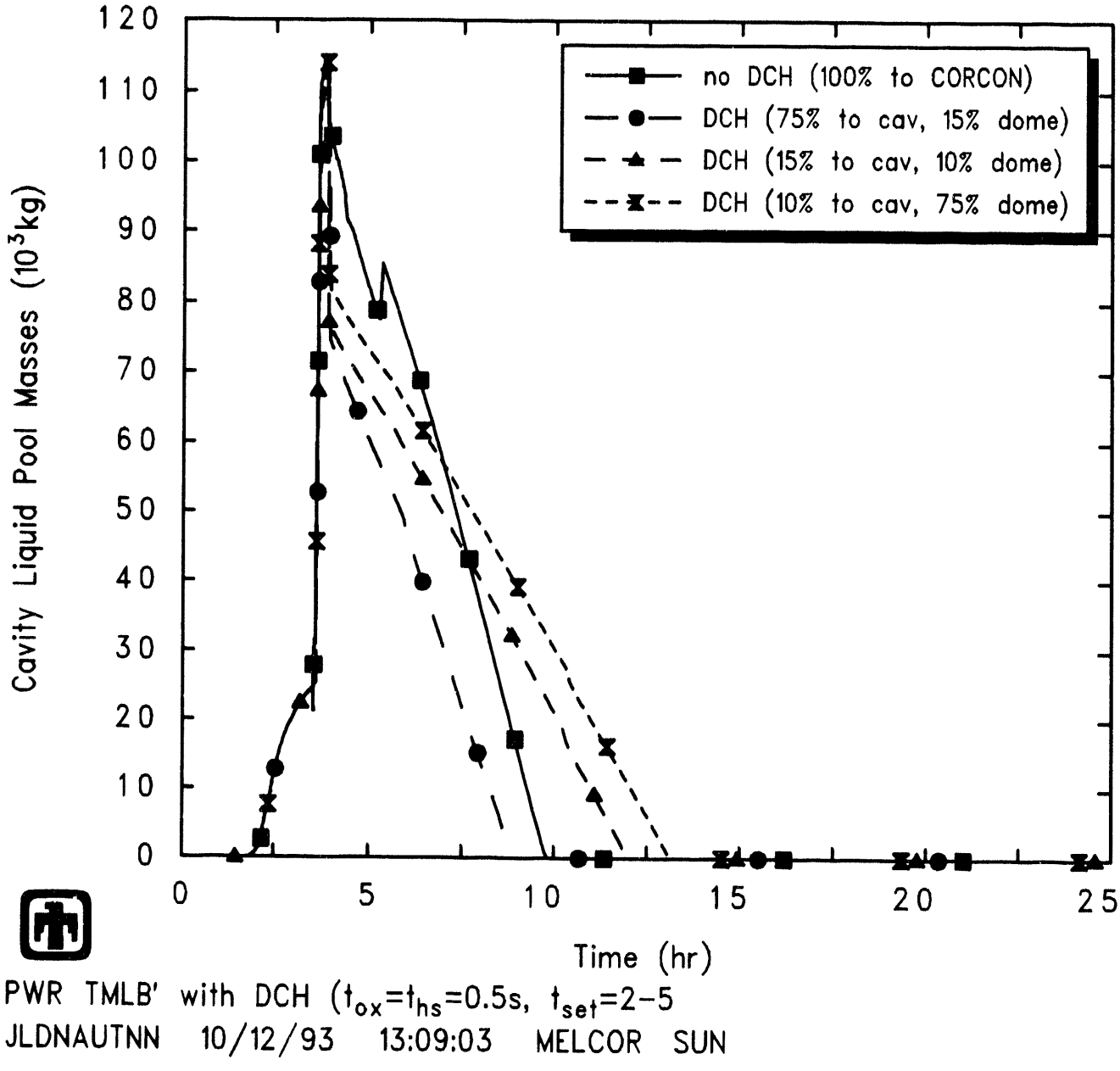

Figure 6.5.2.4. Cavity Water Mass - HPME/DCH Debris Distribution Sensitivity Study

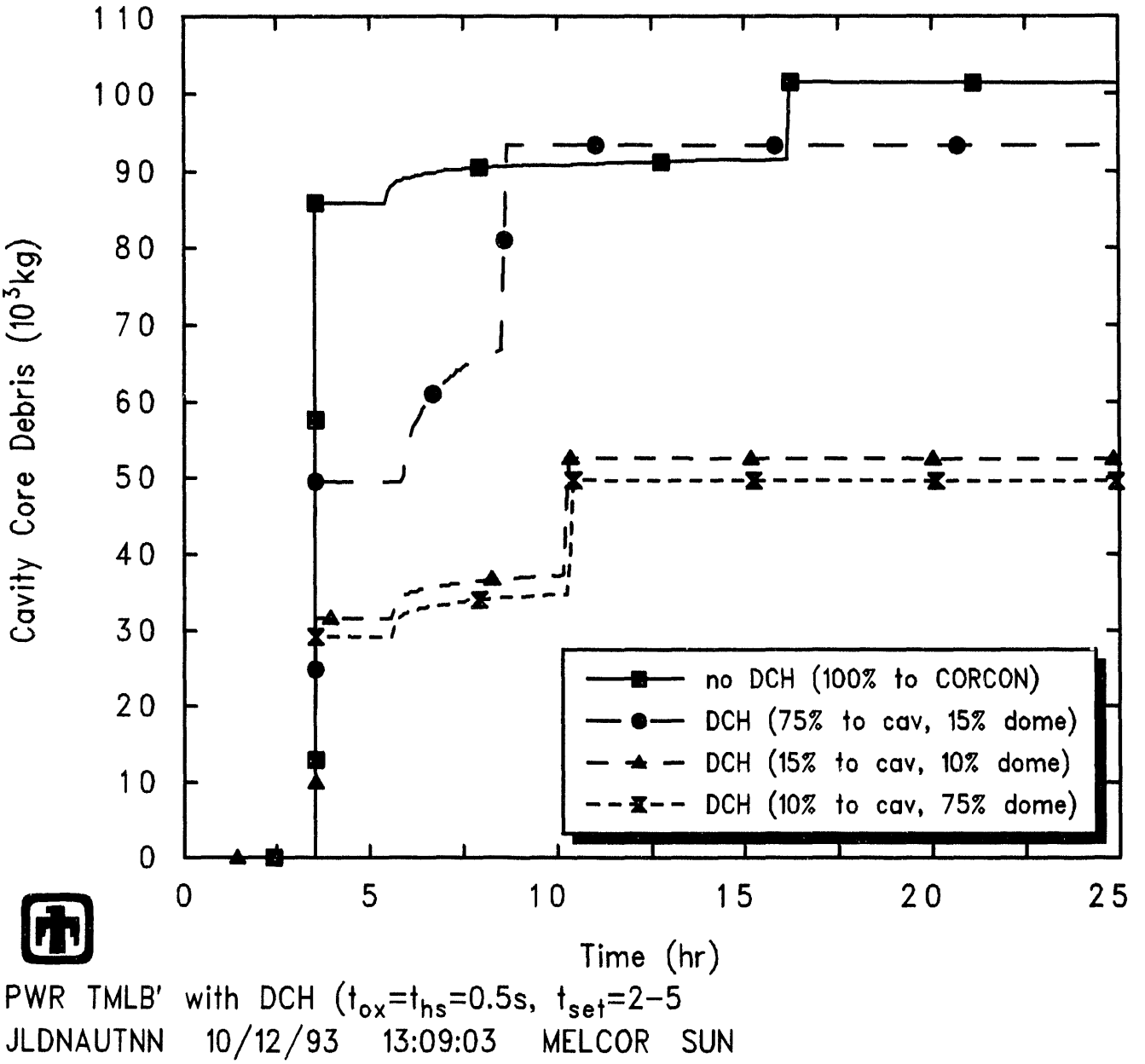

Figure 6.5.2.5. Cavity Core Debris Mass – HPME/DCH Debris Distribution Sensitivity Study

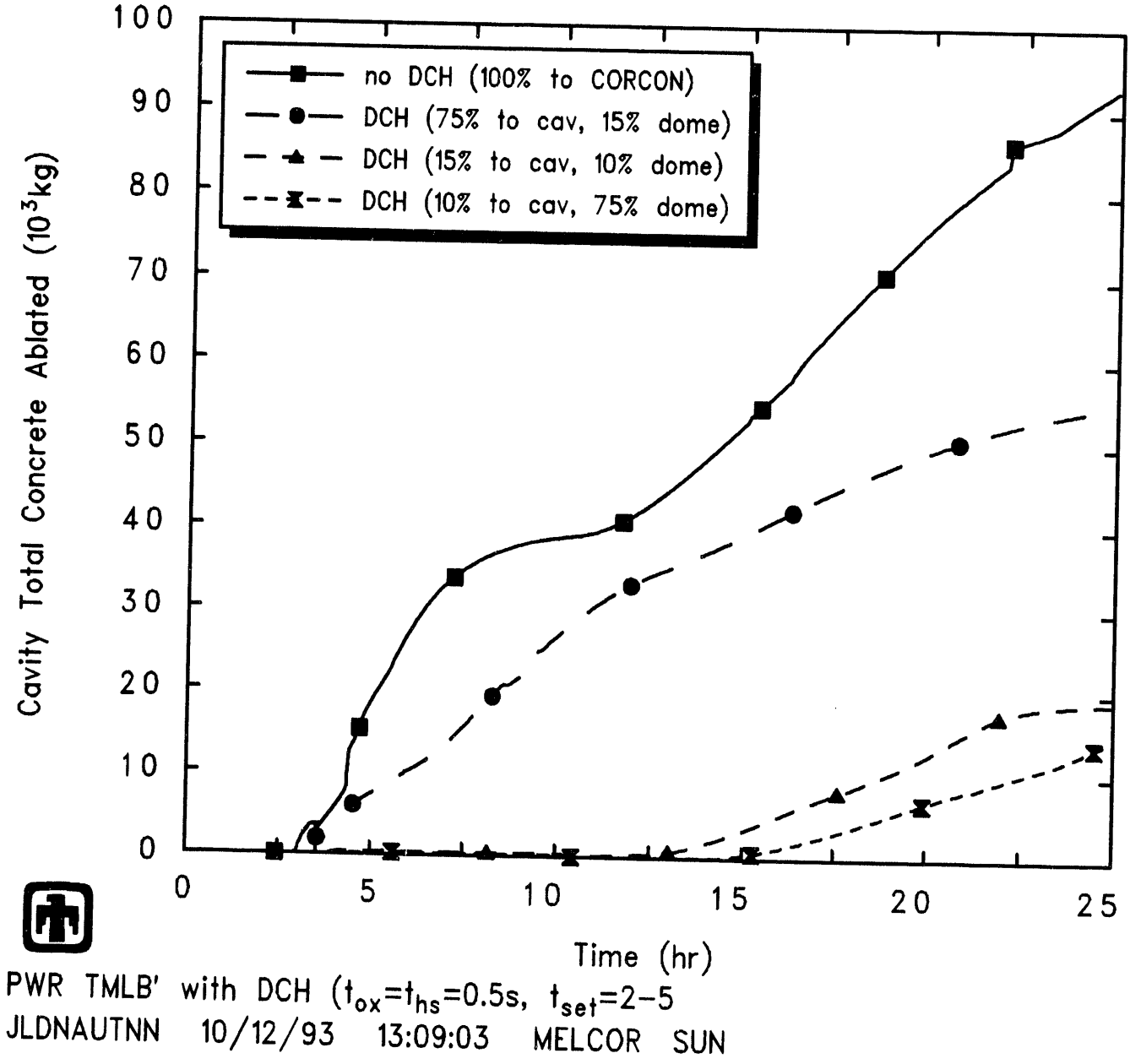

Figure 6.5.2.6. Cavity Concrete Mass Ablated – HPME/DCH Debris Distribution Sensitivity Study

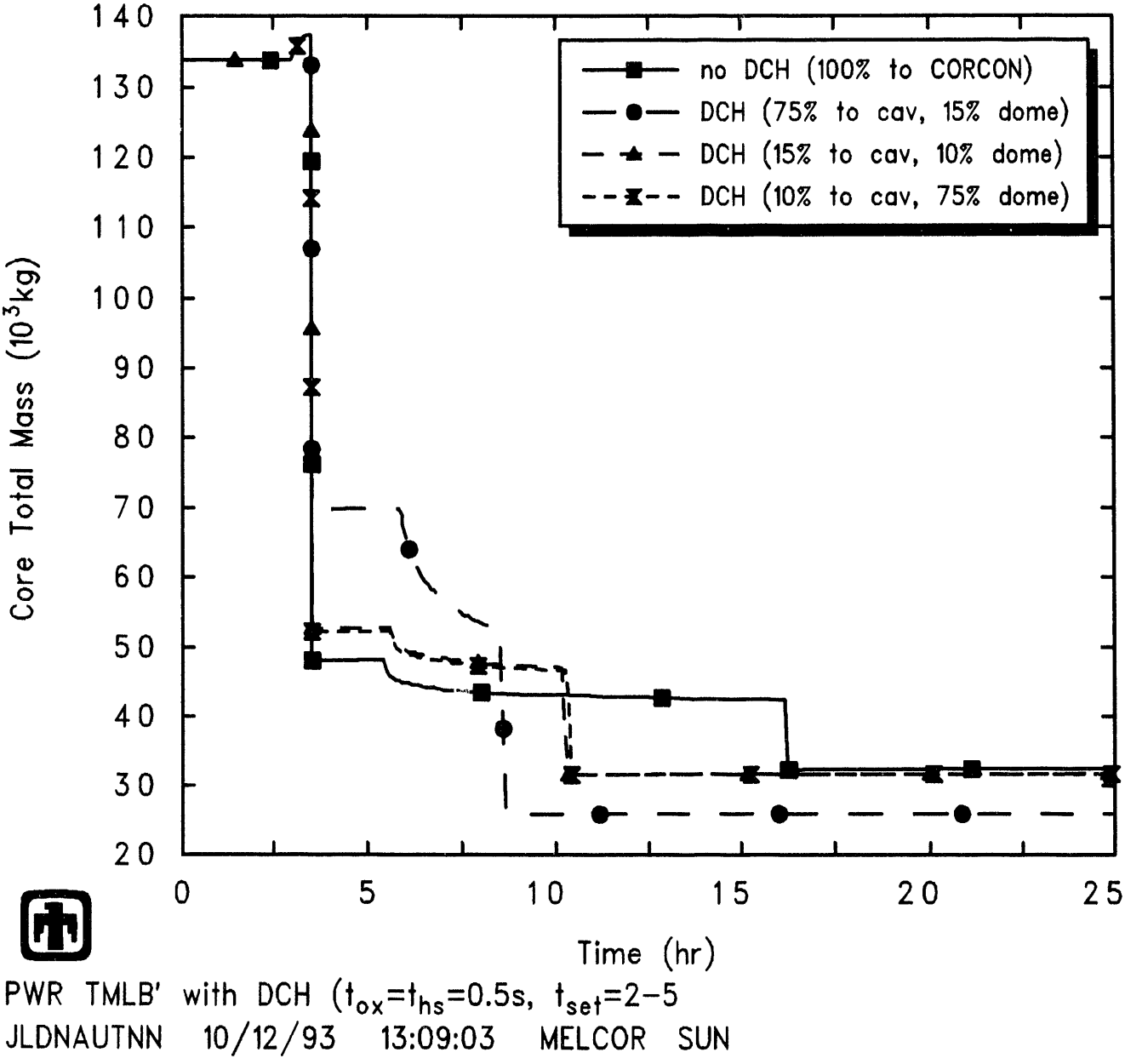

Figure 6.5.2.7. Total Core Mass – HPME/DCH Debris Distribution Sensitivity Study

consider only the release of radioactive forms of these classes, not additional releases of nonradioactive aerosols from structural materials.

The large in-vessel releases reflect the retention of the core material in the vessel for a longer period of time, as a result of forcing later vessel breach and more HPME debris (relative to the reference analysis discussed in detail in Section 4 and to most other sensitivity study calculations done). The in-vessel releases were virtually identical in all these cases; the releases in the active fuel region were exactly identical, while the releases in the lower plenum differred slightly (due primarily to time step differences caused by the different HPME/DCH scenarios resulting from the different HPME debris distributions assumed). Less radionuclides were released ex-vessel in those cases where a large fraction of the HPME debris was specified to go into non-cavity control volume atmospheres and/or heat structures; the differing amounts of material in the cavity (because some debris settled onto heat structures outside the cavity) affected the ex-vessel source term because release of fission products from airborne debris and from debris settled onto heat structures (instead of into the cavity) is neglected in the MELCOR model. This may or may not be a reasonable assumption. Debris dispersed throughout containment is quickly cooled and quenched, and fission product release is a strong function of temperature. However, the dispersal of debris into relatively small fragments during the HPME/DCH process, fragments which then undergo rapid oxidation, could conceivably facilitate fission product release from the greatly increased debris surface area.

6.5.3 Debris Characteristic Interaction Times

In the reference calculation, the characteristic interaction times for airborne-debris oxidation and heat transfer were set to 0.1s in all control volumes, while the characteristic settling time for airborne debris was set to 1s; the characteristic interaction time for oxidation of deposited debris was set to 600s for all heat structures. These time constants represent a relatively rapid DCH transient, based upon previous MELCOR DCH assessment analyses and results [10].

Another set of PWR TMLB' DCH calculations were run with characteristic interaction times for airborne-debris oxidation and heat transfer set to 0.5s in all control volumes, while the characteristic settling time for airborne debris was set to 5s in the dome and 2s in the other containment control volumes; the characteristic interaction time for oxidation of deposited debris was kept at 600s for all heat structures. These time constants allow more time for DCH interactions to occur, and are probably reasonable values for plant analyses, based upon previous MELCOR DCH assessment analyses and results [10].

The atmospheric pressures predicted during the HPME period in the cavity and inner containment dome control volumes are shown in Figures 6.5.3.1 and 6.5.3.2, for calculations with two different debris distributions assumed and with the two sets of debris characteristic interaction times just described; the pressures in the other containment control volumes were very similar to the pressures shown for the inner dome volume. (The small differences in timing of vessel breach, HPME initiation and containment

Table 6.5.2.2. In-Vessel Source Terms - Debris Distribution Sensitivity Study

Class	Radionuclide Release (% Initial Inventory) Case 1 (100% to cav)	Case 2 (75% to cav)	Case 3 (15% to cav)	Case 4 (10% to cav)
In-Core				
1 (Xe)	95.943	95.943	95.943	95.943
2 (Cs)	95.931	95.931	95.931	95.931
3 (Ba)	50.296	50.296	50.296	50.296
4 (I)	95.969	95.969	95.969	95.969
5 (Te)	42.447	42.447	42.447	42.447
6 (Ru)	2.6956	2.6956	2.6956	2.6956
7 (Mo)	19.855	19.855	19.855	19.855
8 (Ce)	0.0491	0.0491	0.0491	0.0491
9 (La)	0.5454	0.5454	0.5454	0.5454
10 (U)	0.5606	0.5606	0.5606	0.5606
11 (Cd)	86.278	86.278	86.278	86.278
12 (Sn)	86.277	86.277	86.277	86.277
In LP				
1 (Xe)	3.5159	3.3950	3.4669	3.5053
2 (Cs)	3.5258	3.4056	3.4752	3.5126
3 (Ba)	2.8807	2.9394	2.8528	2.8677
4 (I)	3.5173	3.3968	3.4689	3.5068
5 (Te)	2.7657	2.8160	2.7797	2.8221
6 (Ru)	0.1940	0.1997	0.1947	0.1945
7 (Mo)	2.1000	2.0584	1.9574	2.0147
8 (Ce)	0.0044	0.0045	0.0043	0.0043
9 (La)	0.0136	0.0145	0.0139	0.0138
10 (U)	0.0157	0.0172	0.0162	0.0159
11 (Cd)	2.9180	3.0035	2.9278	2.9320
12 (Sn)	2.9170	3.0034	2.9294	2.9318

Table 6.5.2.3. Ex-Vessel Source Terms – Debris Distribution Sensitivity Study

Class	Radionuclide Release (% Initial Inventory) Case 1 (100% to cav)	Case 2 (75% to cav)	Case 3 (15% to cav)	Case 4 (10% to cav)
1 (Xe)	0.5363	0.5824	0.4910	0.4464
2 (Cs)	0.5656	0.6158	0.5183	0.4709
3 (Ba)	9.3572	0.3114	0.2607	0.1758
4 (I)	0.0	0.0	0.0	0.0
5 (Te)	53.397	21.047	3.3867	2.0027
6 (Ru)	3×10^{-5}	2×10^{-8}	7×10^{-10}	3×10^{-10}
7 (Mo)	1.5298	1.3682	0.1915	0.1709
8 (Ce)	0.0012	0.0006	0.0002	0.0002
9 (La)	0.5413	0.0009	0.0003	0.0002
10 (U)	0.0030	0.0007	0.0003	0.0002
11 (Cd)	0.3926	0.0934	0.0030	0.0016
12 (Sn)	3.8647	0.8132	0.0280	0.0149

Table 6.5.2.4. Total Source Terms – Debris Distribution Sensitivity Study

Class	Radionuclide Release (% Initial Inventory) Case 1 (100% to cav)	Case 2 (75% to cav)	Case 3 (15% to cav)	Case 4 (10% to cav)
1 (Xe)	99.996	99.921	99.901	99.895
2 (Cs)	100.02	99.953	99.925	99.915
3 (Ba)	62.534	53.547	53.410	53.320
4 (I)	99.486	99.366	99.438	99.476
5 (Te)	98.609	66.310	48.614	47.272
6 (Ru)	2.8896	2.8953	2.8903	2.8901
7 (Mo)	23.485	23.281	22.004	22.040
8 (Ce)	0.0547	0.0542	0.0536	0.0536
9 (La)	1.1003	0.5608	0.5597	0.5594
10 (U)	0.5793	0.5785	0.5770	0.5768
11 (Cd)	89.589	89.375	89.209	89.212
12 (Sn)	93.059	90.094	89.234	89.224

pressurization in these figures and in the rest of the figures in this subsection are due to one set of calculations being run on a SUN Sparc2 workstation and the other pair of calculations being run on an IBM RISC-6000 Model 550 workstation, as discussed in more detail in Section 7.1, and is not due to any effect of varying debris characteristic interaction times.)

Figure 6.5.3.1 shows a very large increase in the magnitude of the pressure spike in the cavity control volume as the characteristic interaction times are shortened (*i.e.*, with more rapid oxidation of and heat transfer from airborne debris, in the two cases with most of the HPME debris deposited into the cavity atmosphere; the large effect was due to the relatively large amount of debris introduced into the relatively small volume of the cavity atmosphere. In contrast, Figure 6.5.3.2 shows a small increase in the magnitude of the pressure spike in the rest of containment as the characteristic interaction times are made longer; the longer settling times specified allowed more DCH interaction to occur between the airborne debris and the containment atmosphere, even though the longer oxidation and heat transfer characteristic interaction times caused that interaction to occur more slowly.

The long-term containment pressure history is presented in Figure 6.5.3.3. The major division into two curves is due to the different debris distribution assumed (as discussed in Section 6.5.2); varying the characteristic HPME/DCH interaction times had very little effect on the longterm containment response, as would be expected.

6.5.4 DCH-Driven Hydrogen Combustion

As reported in detail in [10], the hydrogen combustion behavior observed in the IET direct containment heating experiments done at 1:10-scale at Sandia and at 1:40-scale at Argonne could not be calculated using the default burn package input in MELCOR, because the default ignition criteria are never satisfied in these experiments. Instead, in the majority of our IET analysis calculations, the hydrogen mole fraction ignition criterion in the absence of igniters was set to 0.0, which (in the absence of CO) also gives a combustion completeness correlation value of 0.0; in addition, burn was suppressed in all control volumes except the vessel dome. This particular combination of input was found to produce reasonable agreement with test data in all cases. The combustion completeness being set to 0 prevents the burning of any pre-existing hydrogen, but allows burning of any additional hydrogen generated during the HPME. Suppressing burn except in the dome mimicked the experimental behavior of a jet flame burning at the outlet from the subcompartments to the dome; because little or no hydrogen was generated by debris oxidation in the dome in our analyses, only hydrogen advected into the dome from the subcompartments burned, and only on the time scale over which it was advected into the dome.

While these non-standard combustion criteria could be specified with the standard BUR package input for those experiment analyses, the same input modification could not be made conveniently in plant analyses such as the PWR TMLB' calculations, because the non-standard input could affect the results calculated both before and after the

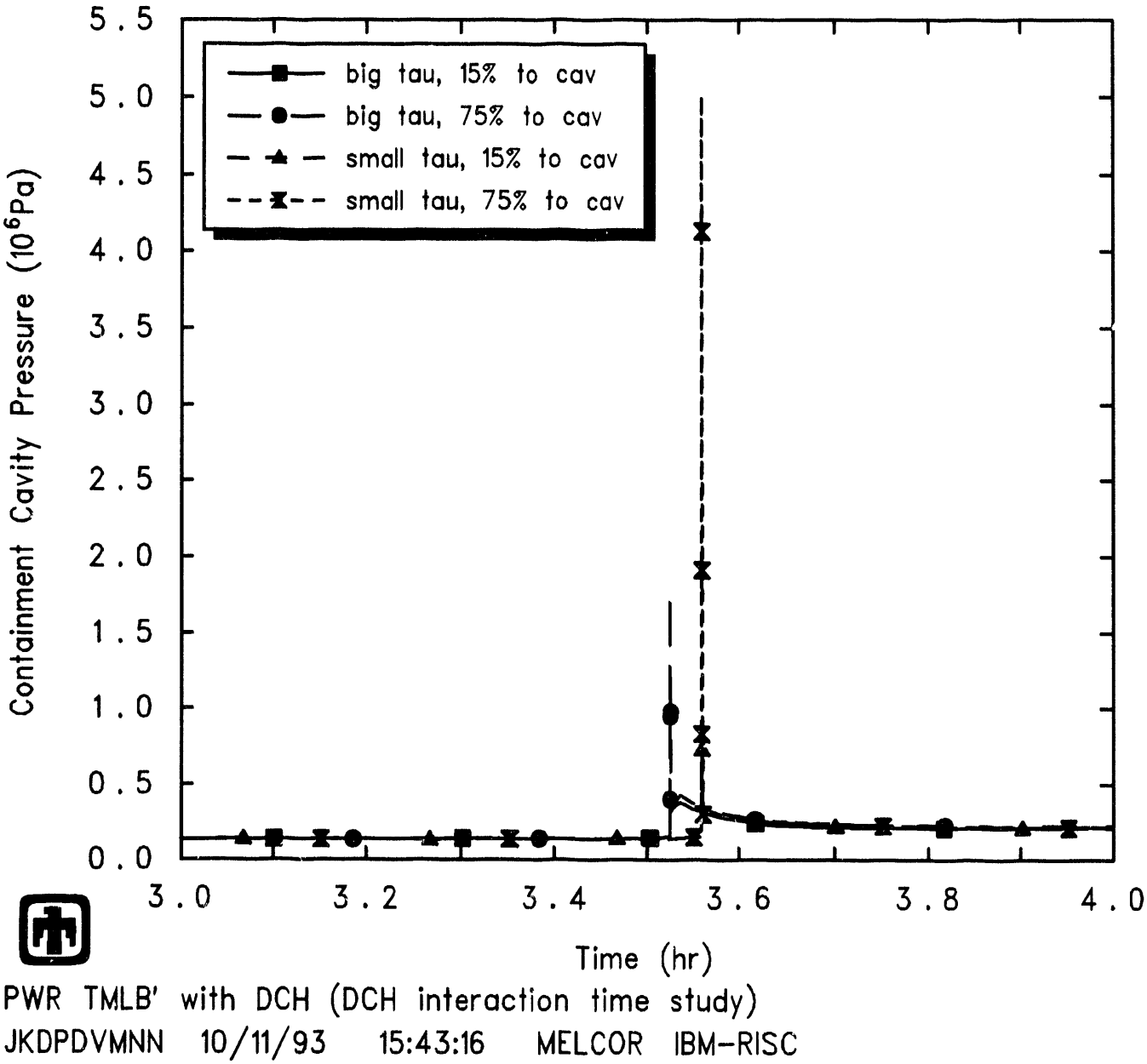

Figure 6.5.3.1. Cavity Pressure during HPME and DCH – HPME/DCH Debris Characteristic Interaction Times Sensitivity Study

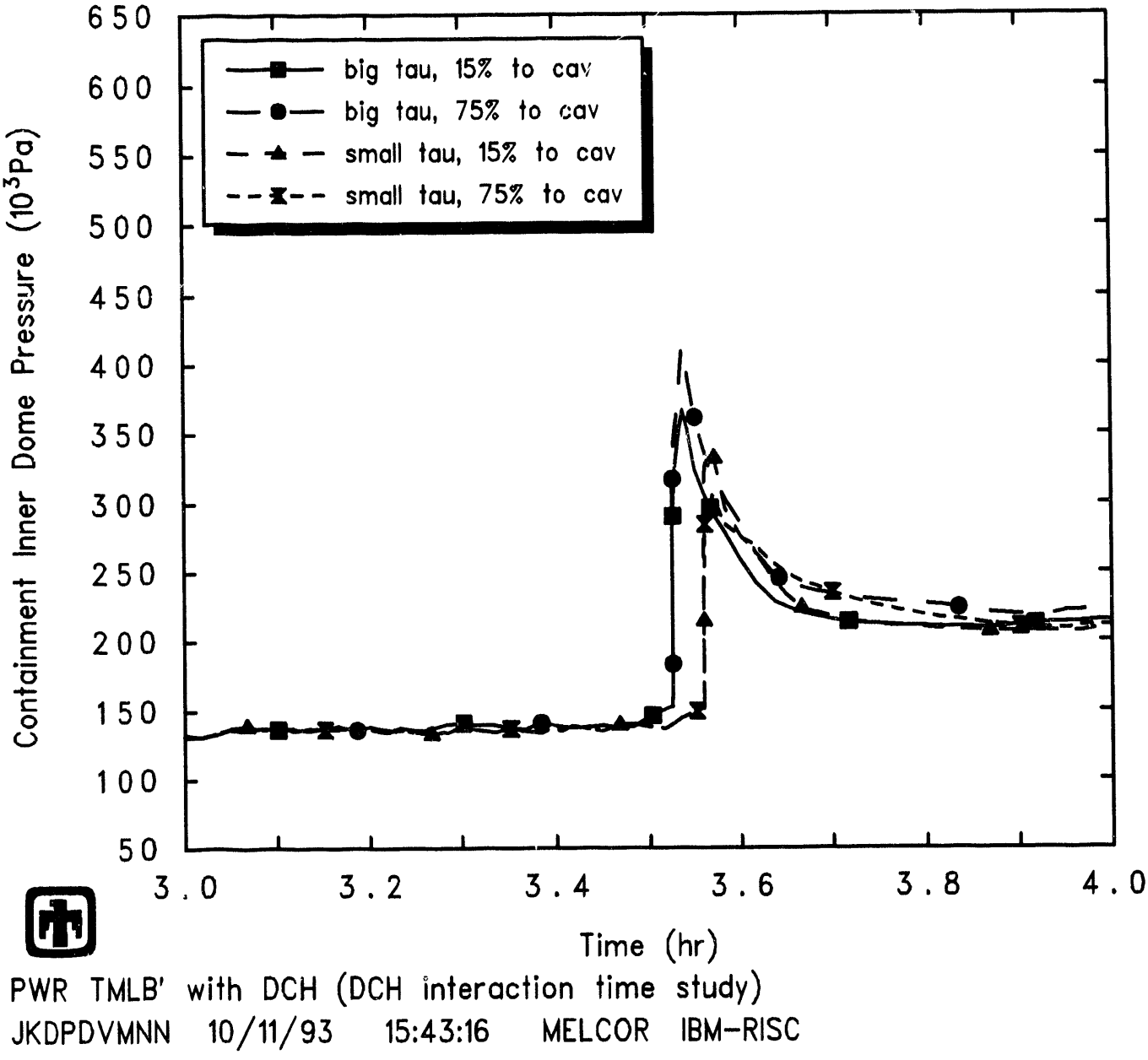

Figure 6.5.3.2. Containment Dome Pressure during HPME and DCH – HPME/DCH Debris Characteristic Interaction Times Sensitivity Study

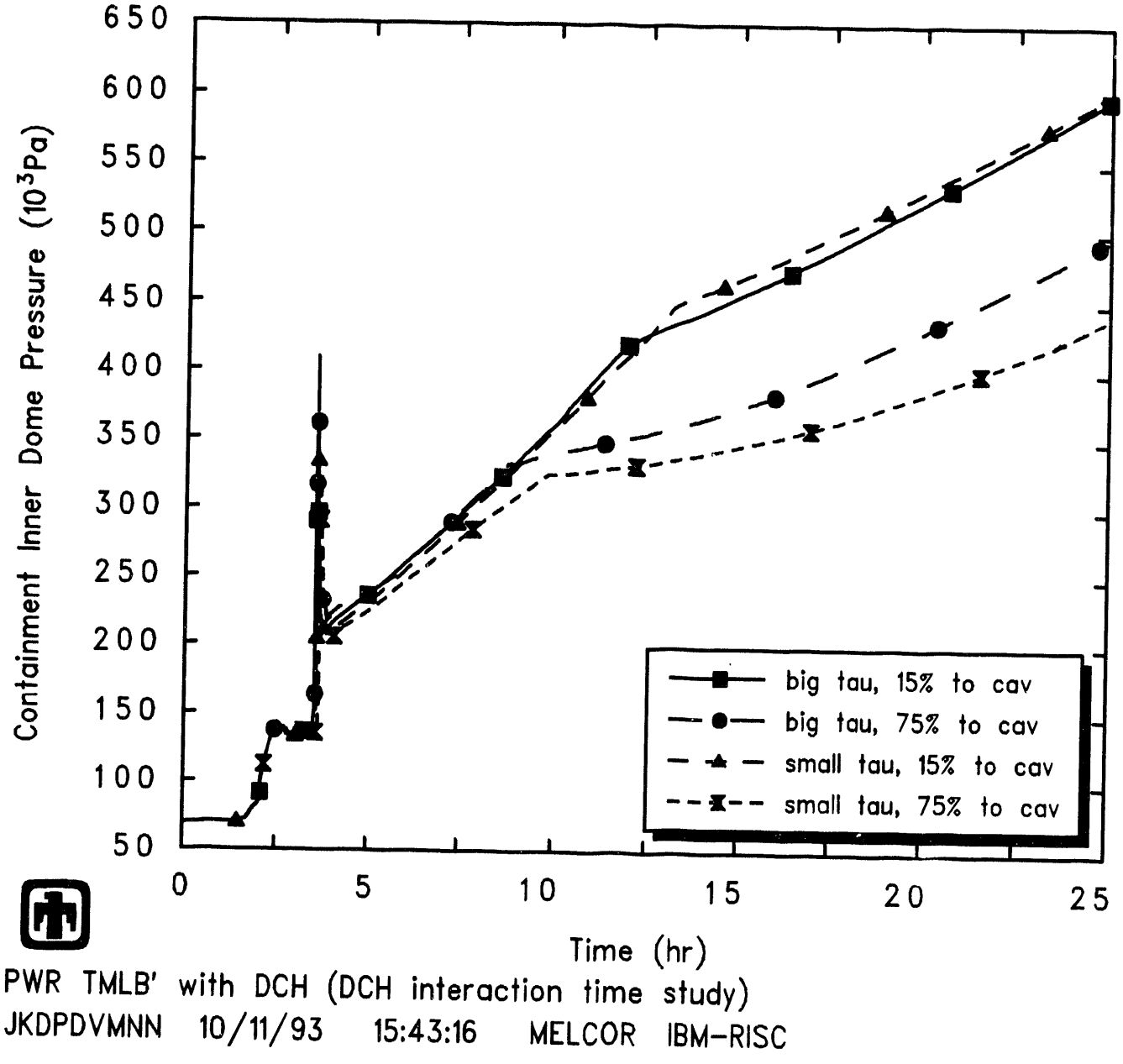

Figure 6.5.3.3. Containment Pressure – HPME/DCH Debris Characteristic Interaction Times Sensitivity Study

HPME period; these combustion input parameters can be changed upon restart, but this would require the user knowing exactly when HPME/DCH begins and ends, and doing several runs with different input. As a user convenience, new, optional input have been provided in the BUR package, allowing the user to specify one set of input parameters to be used only during periods of HPME and another set of input parameters to be used during other times.

The atmospheric pressures predicted during HPME in the cavity and inner containment dome control volumes are shown in Figures 6.5.4.1 and 6.5.4.2, for calculations with and without modified hydrogen combustion ignition parameters during the HPME/DCH period, and with the two sets of debris characteristic interaction times described in Section 6.5.3; the pressures in the other containment control volumes were very similar to the pressures shown for the inner dome volume. (The small differences in timing of vessel breach, HPME initiation and containment pressurization in these figures and in the rest of the figures in this subsection are due to one set of calculations being run on a SUN Sparc2 workstation and the other pair of calculations being run on an IBM RISC-6000 Model 550 workstation, as discussed in more detail in Section 7.1, and is not due to any effect of varying debris characteristic interaction times or hydrogen combustion.)

The cavity pressures were identical in the two calculations with different burn ignition criteria during HPME/DCH, for the larger characteristic interaction times. The cavity pressure in the case with the default burn and the shorter characteristic interaction times appears higher than the cavity pressure in the case with the enhanced burn ignition during HPME/DCH and the shorter characteristic interaction times; this is unexpected, and probably reflects numerical problems in the burn coding (discussed in more detail in Section 7) more than any actual effect of the enhanced burn during HPME/DCH.

The pressures in the rest of containment also were identical in the two calculations with different burn ignition criteria during HPME/DCH, for the larger characteristic interaction times. The containment dome pressures in the case with enhanced burn during HPME/DCH and shorter characteristic interaction times were slightly higher than the containment dome pressure in the case with the default burn and shorter characteristic interaction times; this is the expected result, but the effect appears quite small.

The long-term containment pressure history is presented in Figure 6.5.4.3. There was relatively little difference in the results in these various cases. Both sets of calculations, with larger and with smaller characteristic interaction times, showed higher late-time containment pressures with enhanced burn ignition during HPME/DCH than with default burn throughout the transient. While this would be expected during the HPME/DCH period, the late-time effect appears larger than might be expected, and is most likely due to accumulating small numerical differences rather than to differences in calculated hydrogen burn.

Further analysis of the effects of enhanced hydrogen ignition during HPME/DCH is severely hampered and prevented by the numerical problems in the burn coding (discussed in more detail in Section 7), which can be large enough to dominate and cover up the actual physical effect we want to study.

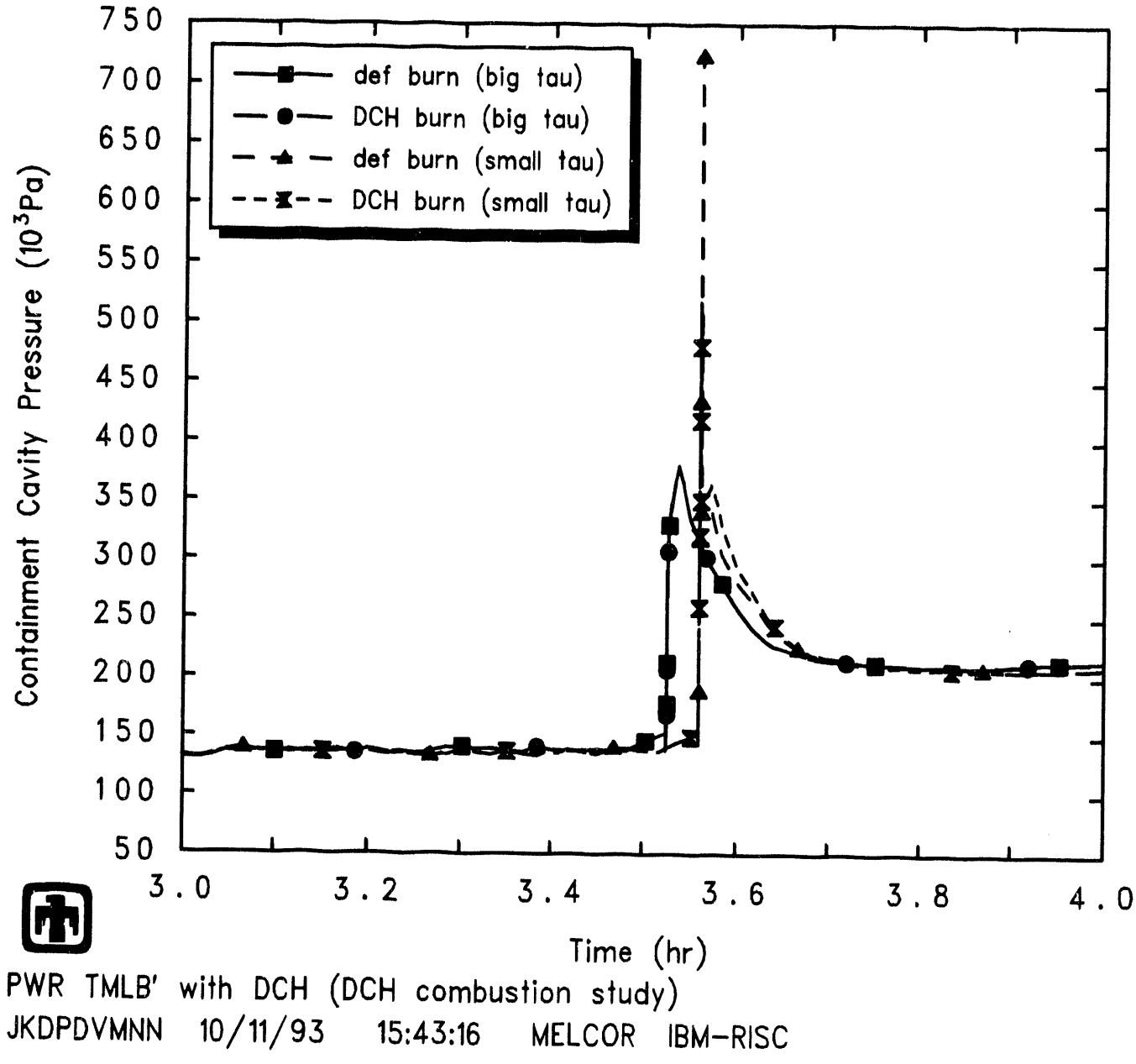

Figure 6.5.4.1. Cavity Pressure during HPME and DCH - DCH-Driven Hydrogen Combustion Sensitivity Study

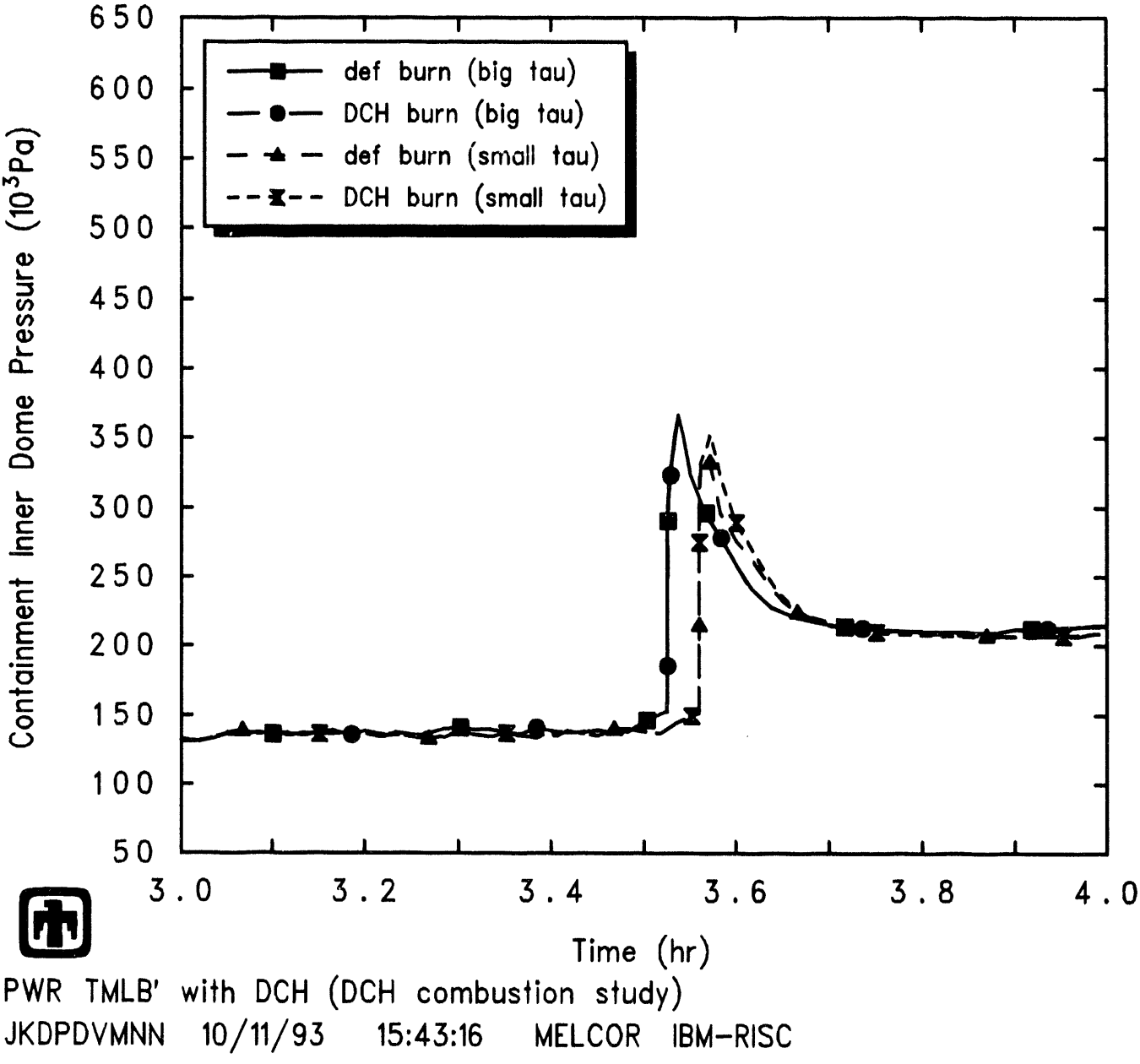

Figure 6.5.4.2. Containment Dome Pressure during HPME and DCH – DCH-Driven Hydrogen Combustion Sensitivity Study

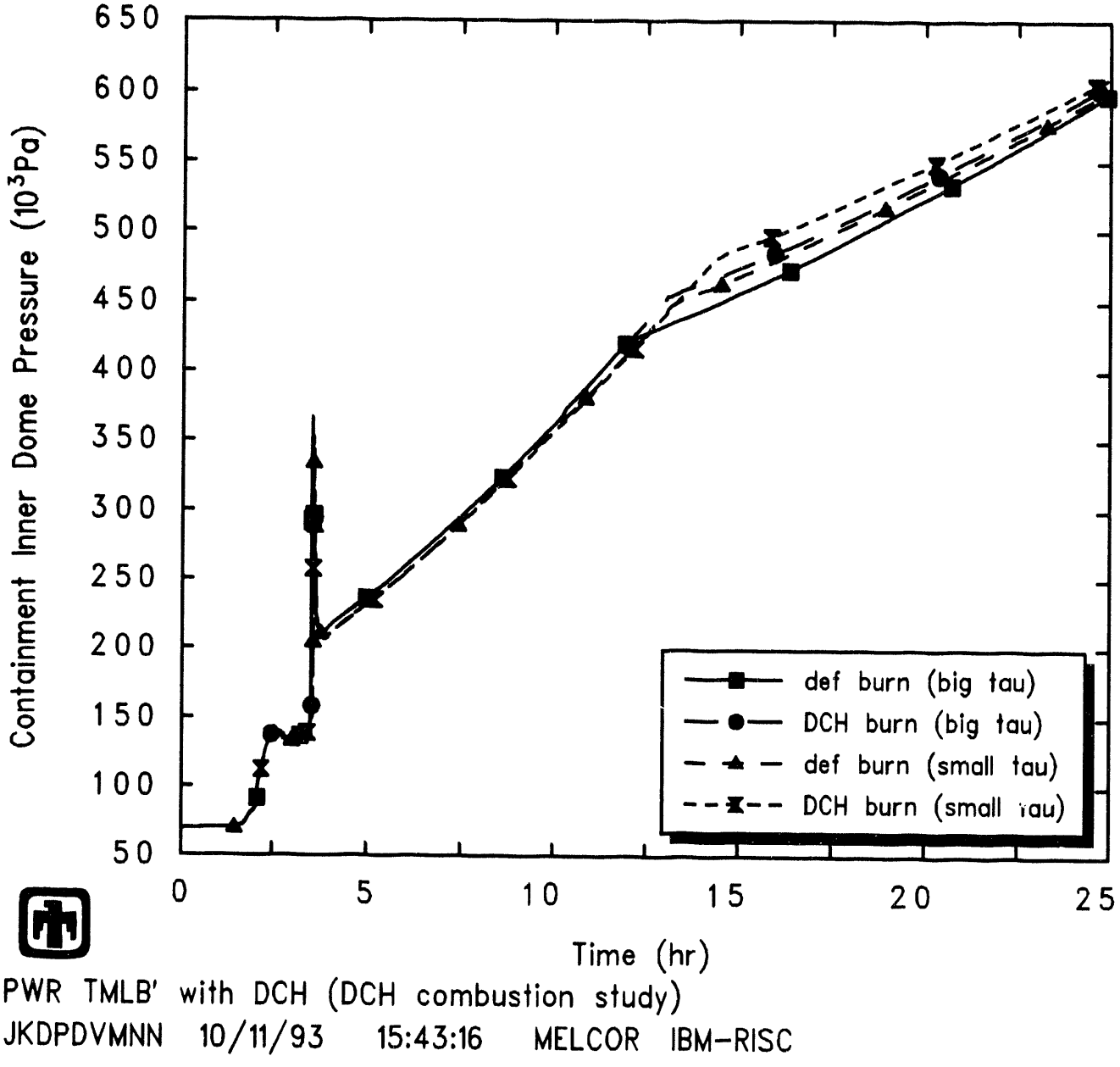

Figure 6.5.4.3. Containment Pressure – DCH-Driven Hydrogen Combustion Sensitivity Study

7 Numeric Effects

The MELCOR peer review (and a number of MELCOR users) have expressed concern about numeric effects seen in various MELCOR calculations [11], which produced either differences in results for the same input on different machines or differences in results when the time step used is varied. Several calculations have been done to identify whether any such effects existed in our Surry PWR TMLB' assessment analyses.

7.1 Machine Dependency

The calculation discussed in detail in Section 4 and the majority of our sensitivity study analyses were run on an IBM RISC-6000 Model 550 workstation. The reference calculation was rerun, using the same code version (1.8NM, the release version of MELCOR 1.8.2), on a SUN Sparc2 workstation, on an HP 755 workstation, on a CRAY Y-MP8/864, and on a 50MHz 486 PC, to check for machine dependencies. The user-allowed maximum time step was set to 10s in all these runs, as in the reference calculation discussed in Section 4.

Table 7.1.1 compares the timings of various key events predicted by MELCOR in this set of machine-dependency sensitivity study calculations. The differences are generally small, accumulating and growing somewhat as the transient progresses, but with no significant branching into different accident sequences. There was a $\leq$20s spread in clad-failure/gap-release times predicted in the various rings on the different hardware platforms used. Both the [illegible] plate and the lower head penetration failed first in the innermost, high-power [illegible] all cases, and the failure times were all within a 4min time span. Debris eject[illegible] e cavity began immediately upon lower head penetration failure in all cases, thus also within a 4min time window, and DCH always lasted about 30s.

The biggest timing difference found was in hydrogen deflagrations occurring in the cavity. Calculations on the five platforms showed one set of hydrogen burns occurring $\leq$0.5hr after vessel breach and the start of core-concrete interaction. Except for the IBM workstation, the time of this initial burn agreed within 2s on the other four platforms; the number and duration of burns were generally somewhat different, however. Calculations on each of the five platforms predicted a second period of hydrogen burns in the cavity later in the transient, but the timing and extent of that second burn period differed substantially among the various platforms; three of the five calculations (on the HP workstation, Cray and PC) showed a single, isolated burn at ~30,000s, while the other two (on the IBM and SUN workstations) showed a series of multiple burns starting somewhat later in the transient and lasting for a considerable length of time.

Comparing the calculations on these various hardware platforms, the first difference visible is in the boiloff of the secondary side inventory early in the transient. Figure 7.1.1 presents the SG secondary system pressures calculated on these various platforms, expanded to show the first few hours in detail. The pressures oscillate as the SRV cycles,

Table 7.1.1. Timing of Key Events – Machine Dependency Sensitivity Study

Event	Time (s) IBM	SUN	HP	Cray	PC
Gap Release					
Ring 1	10,235.0	10,226.4	10,244.6	10,235.1	10,233.3
Ring 2	10,334.4	10,326.4	10,334.6	10,335.1	10,323.3
Ring 3	10,667.9	10,666.4	10,680.1	10,665.1	10,663.3
Core Plate Fails					
Ring 1	11,177.9	11,280.3	11,329.0	11,100.6	11,323.9
Ring 2	11,906.3	11,980.0	12,775.2	11,832.6	12,029.7
Ring 3	13,062.9	13,120.5	11,864.3	13,042.5	13,350.8
LH Penetration Fails					
Ring 1	11,219.3	11,322.5	11,376.6	11,152.5	11,362.5
Ring 2	13,029.5	13,241.7	13,750.4	13,112.9	11,419.5
Ring 3	13,842.3	13,977.2	13,196.8	13,823.5	14,009.9
Debris to Cavity	11,219.3	11,322.5	11,376.6	11,152.5	11,362.5
HPME/DCH Starts	11,219.3	11,322.5	11,376.6	11,152.5	11,362.5
HPME/DCH Ends	11,251.7	11,353.8	11,406.8	11,177.9	11,392.7
Deflagrations Start	12,863.2	12,685.3	12,685.8	12,684.9	12,684.2
Deflagrations End	13,766.2	13,961.1	14,121.4	13,807.0	14,011.0
CORCON Layer Flip	~24,000	~24,000	~24,500	~24,500	~24,500
Cavity Dries Out	~28,200	~27,900	~28,200	~28,500	~28,800
Deflagrations Start	–	–	29,687.0	29,116.4	30,576.2
Deflagrations End	–	–	29,688.6	29,118.0	30,577.7
Deflagrations Start	32,970.0	44,958.5	–	–	–
Deflagrations End	44,778.9	47,209.6	–	–	–

venting steam. The pressures are initially identical on all platforms, but then gradually get slightly out of phase as small differences in SRV setpoint over- and undershoots accumulate. (Similar divergences in SG SRV cycling calculated on different platforms have been identified and reported in other analyses [6], also.) Figure 7.1.2 gives the cycling of the SRV and Figure 7.1.3 demonstrates the cumulative effect on the steam generator secondary pressure, later in the transient; note that, even in cases when the SRV cycles the same number of times (*i.e.*, "IBM" and "Cray", or "HP" and "SUN"), the resulting pressure history can diverge, due to small differences in amount of outflow and/or time that the SRV was open.

The predicted vessel pressures for the SUN, IBM and HP workstation, and Cray and PC, calculation sets are presented in Figure 7.1.4. In all cases, the primary system pressure initially dropped as decay heat was transferred to the secondary system and removed by vented steam; then after the loss of the secondary-side heat sink, the primary system pressure and temperature began to rise. The primary system pressure histories on all platforms are qualitatively identical and quantitatively very similar (as are the pressurizer liquid levels), with the major difference seen in the slight offsets in vessel failure time and associated primary system depressurization.

In all these calculations, the primary coolant pressure was sufficiently high to cause the PORV to open by ~5250s. As predicted earlier in the transient sequence for the SG secondary-side relief valve, the pressurizer PORV cycled rapidly and often, but with accumulating small differences in valve cycling and outflow in the calculations on different machines, as shown in Figures 7.1.5 and 7.1.6.

Figure 7.1.7 demonstrates that the accumulating small changes in valve cycling and inventory loss did not significantly change the core uncovery. There are some differences visible in liquid level oscillations, but these are minor. The very small differences found in clad-failure/gap-release times in Table 7.1.1 ($\leq$20s) reflect the very small differences in calculated core uncovery in all these cases.

Table 7.1.2 summarizes the amount of the various materials in the lower plenum debris bed at the time a lower head penetration first fails (*i.e.*, at vessel breach), for the calculations done on various machines, and also gives the average temperature of the debris in the lower plenum, the fraction of core material relocated in or from the active fuel region, and the fractions of zircaloy and steel oxidized by the time the vessel fails.

The fraction of core materials relocated and the amount of debris in the lower plenum at vessel failure varies in otherwise-identical calculations run on different hardware platforms, and there is no apparent direct correlation between differences in lower head failure time (given in Table 7.1.1) and in the amount of core damage at the time of vessel failure. Averaging these five results, the lower plenum debris mass at vessel failure is ~52,000kg$\pm$6,000kg; given that the initial total intact core mass in the active fuel region (*i.e.*, above the core support plate) is $\geq$100,000kg, this range corresponds to $\pm$6% of the total core mass in the active fuel region, not a large variation. The debris temperature in the lower plenum also varies somewhat, over a 200K range, and there is no obvious correlation between the debris temperatures and the amount of debris in the lower plenum

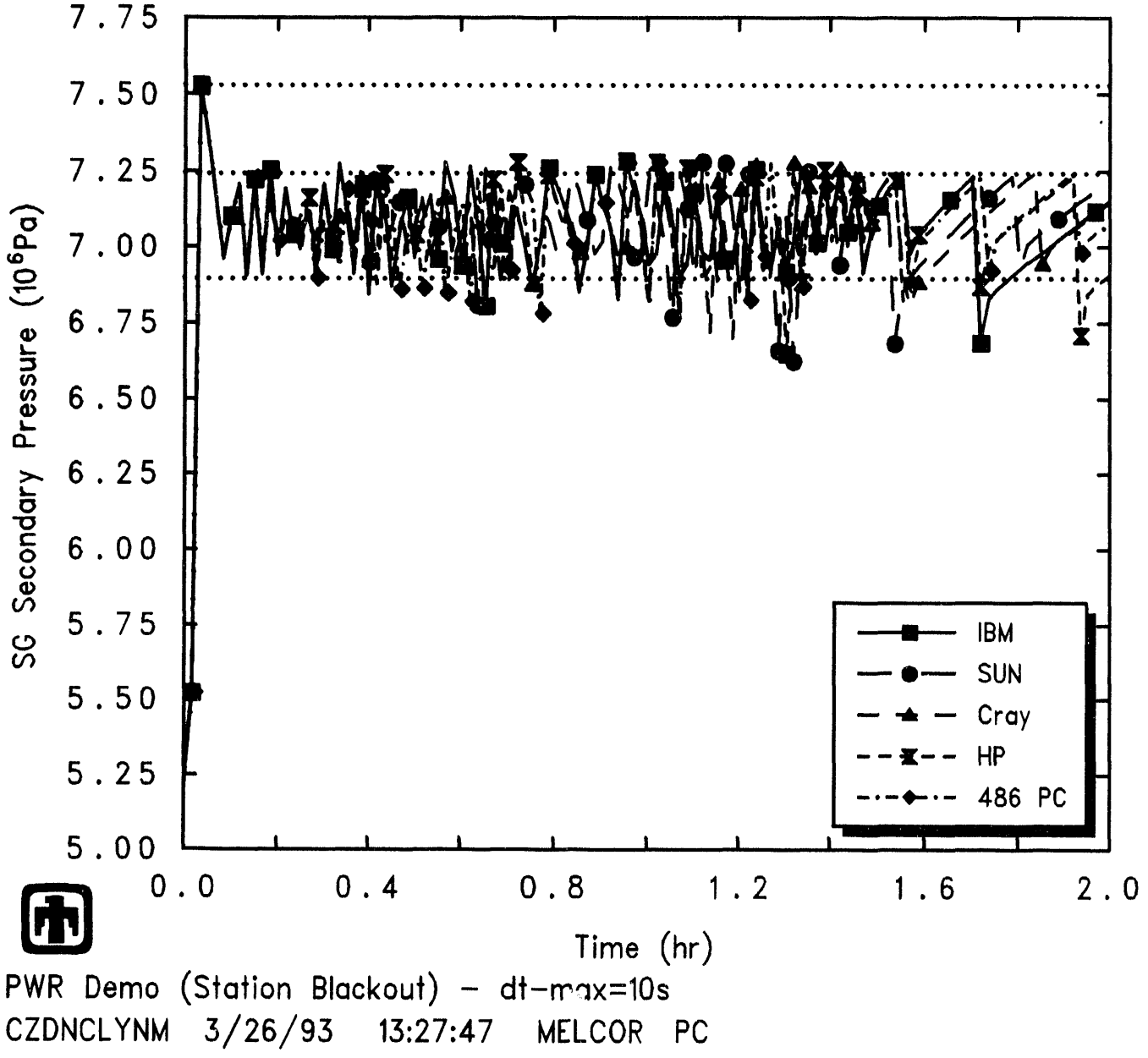

Figure 7.1.1. Early-Time SG Secondary-Side Pressures – Machine Dependency Sensitivity Study

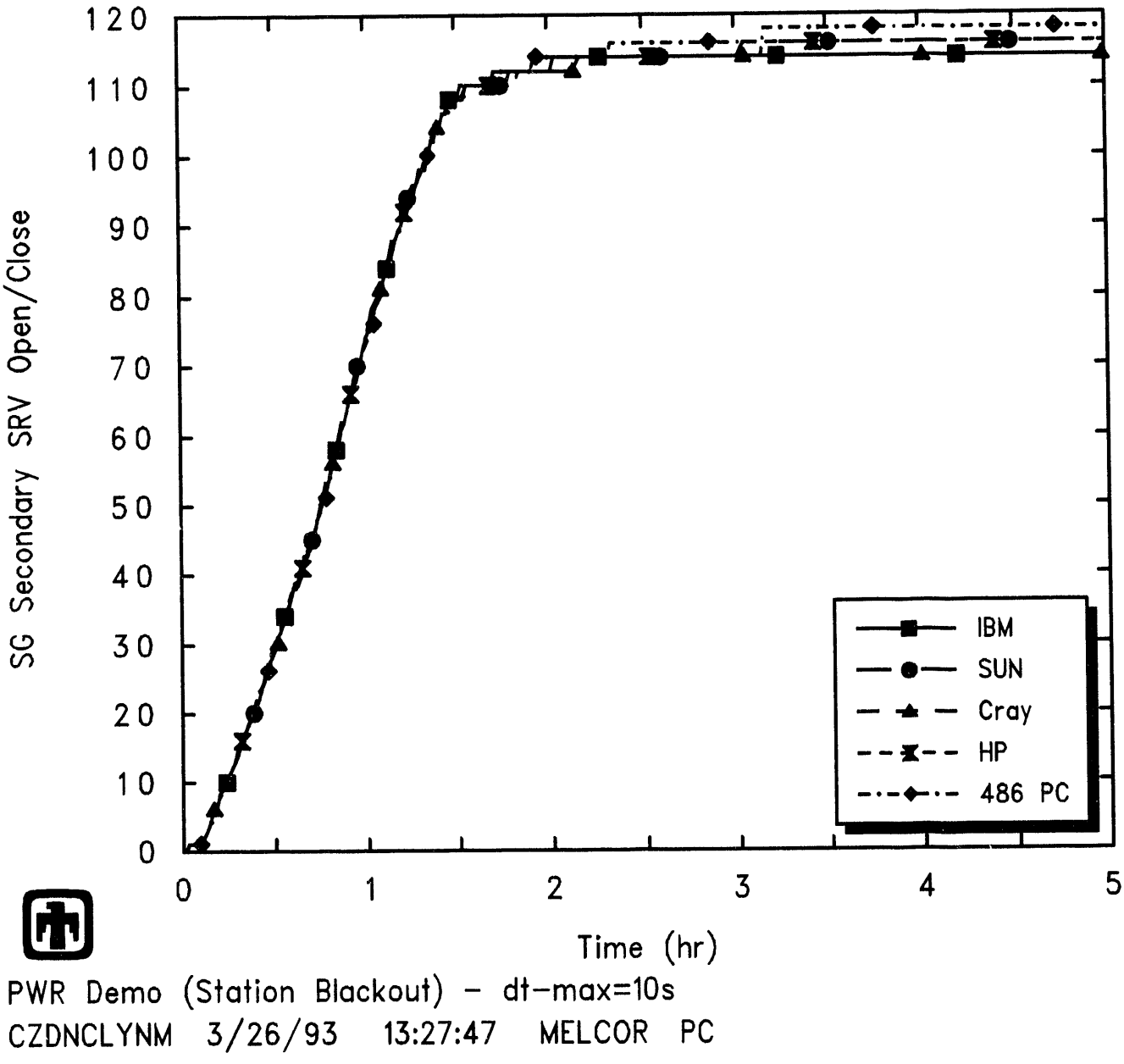

Figure 7.1.2. SG Secondary-Side SRV Cycling – Machine Dependency Sensitivity Study

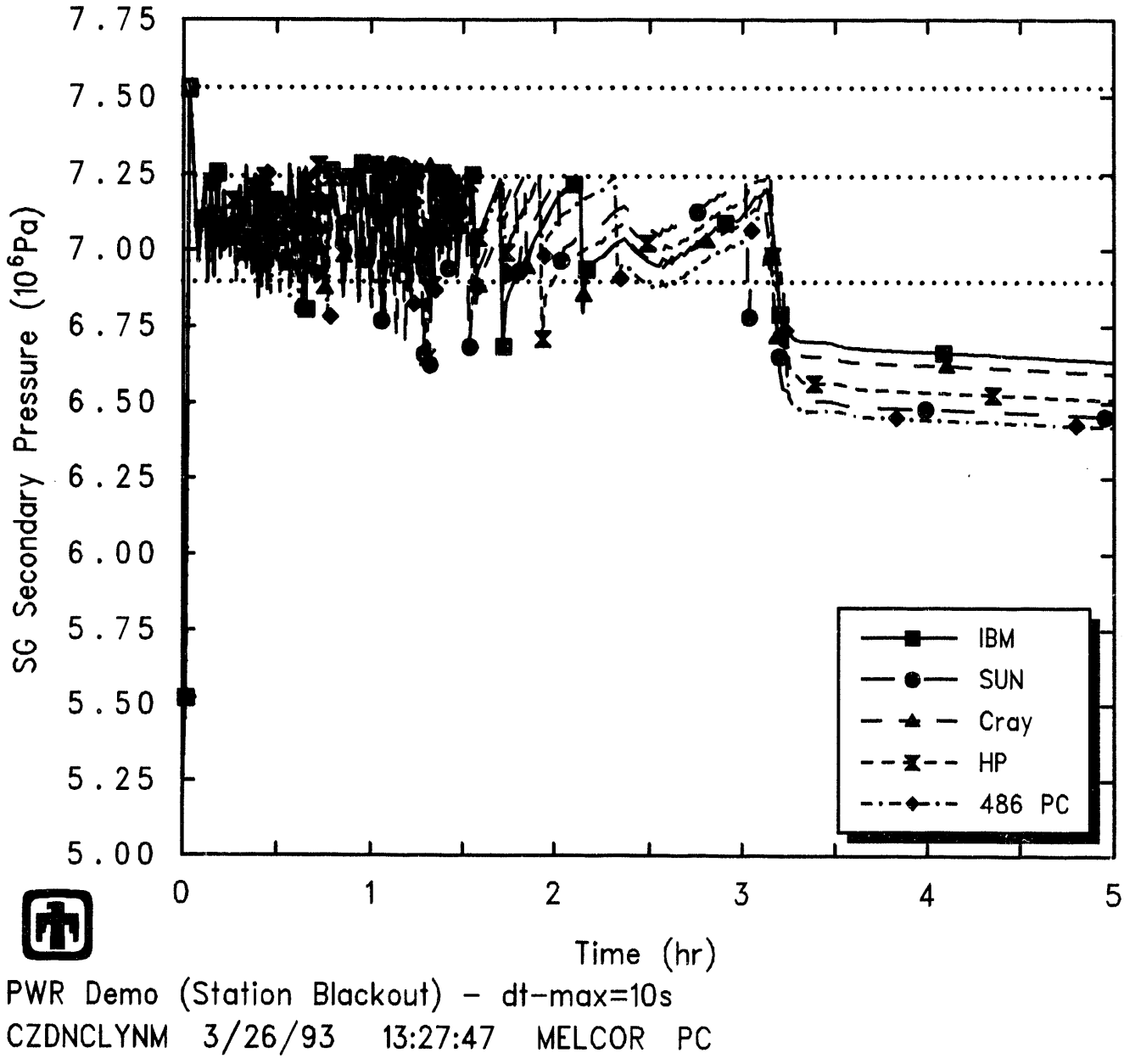

Figure 7.1.3. Later-Time SG Secondary-Side Pressures – Machine Dependency Sensitivity Study

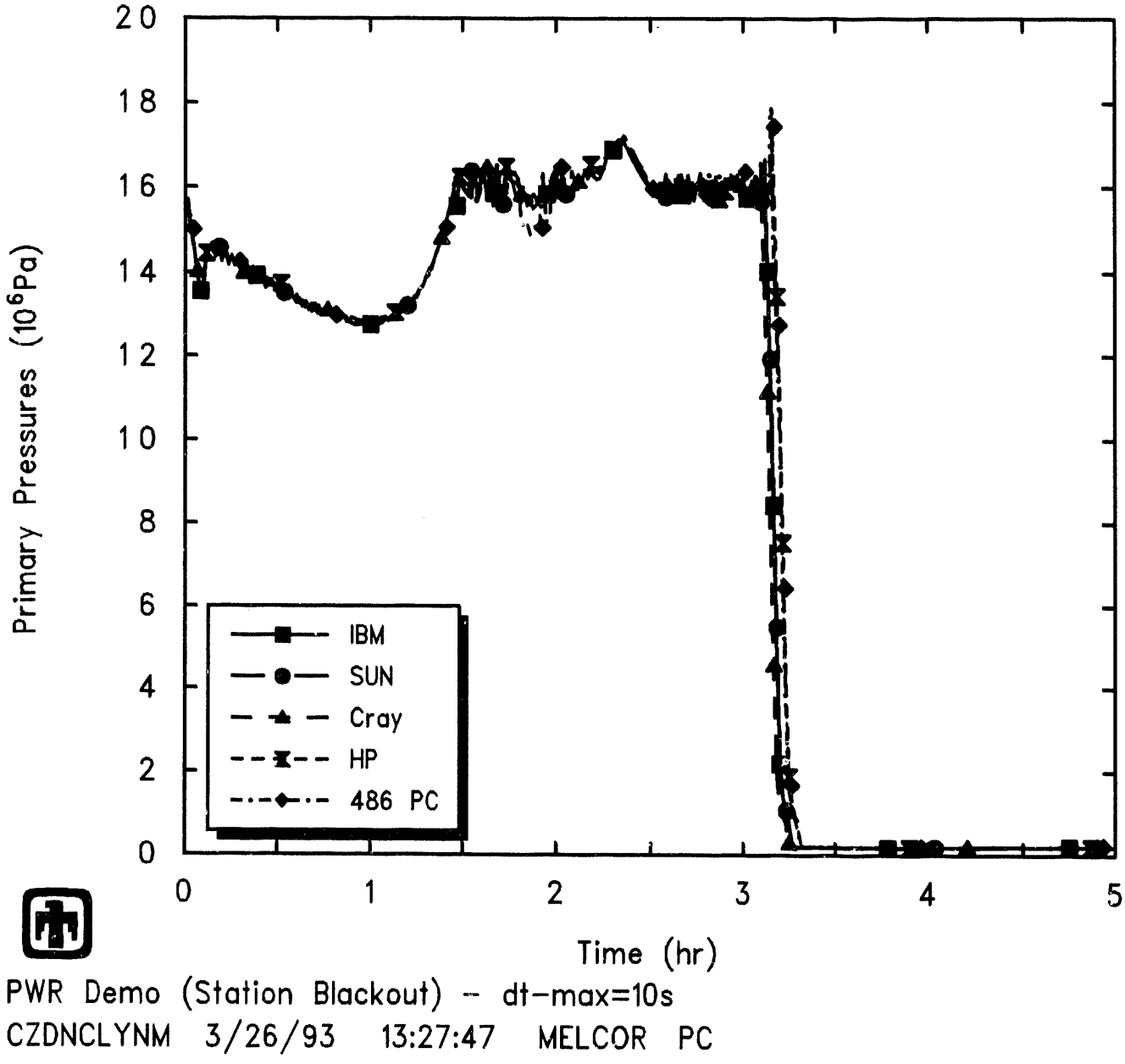

Figure 7.1.4. Vessel Pressures - Machine Dependency Sensitivity Study

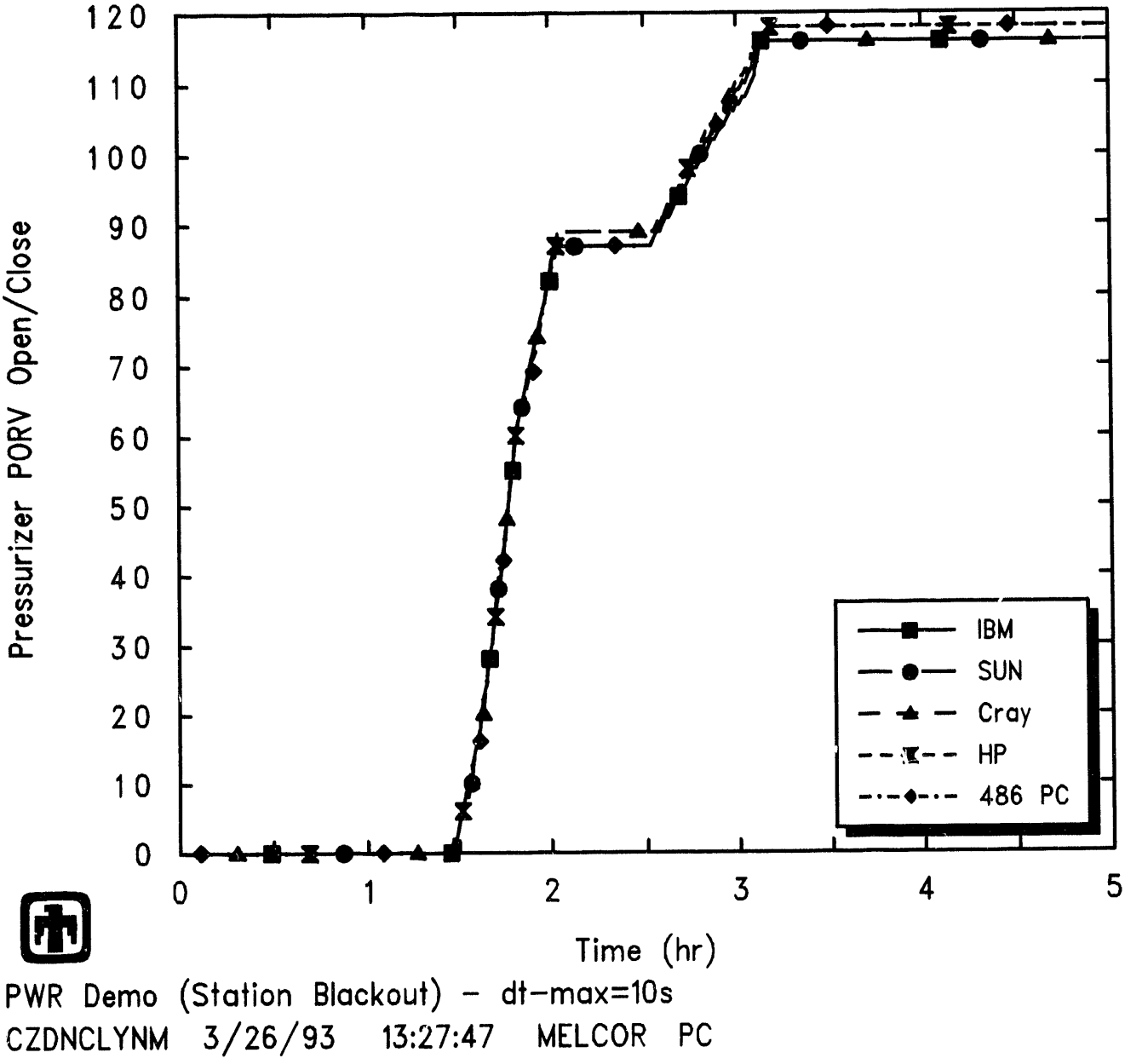

Figure 7.1.5. Pressurizer PORV Cycling – Machine Dependency Sensitivity Study

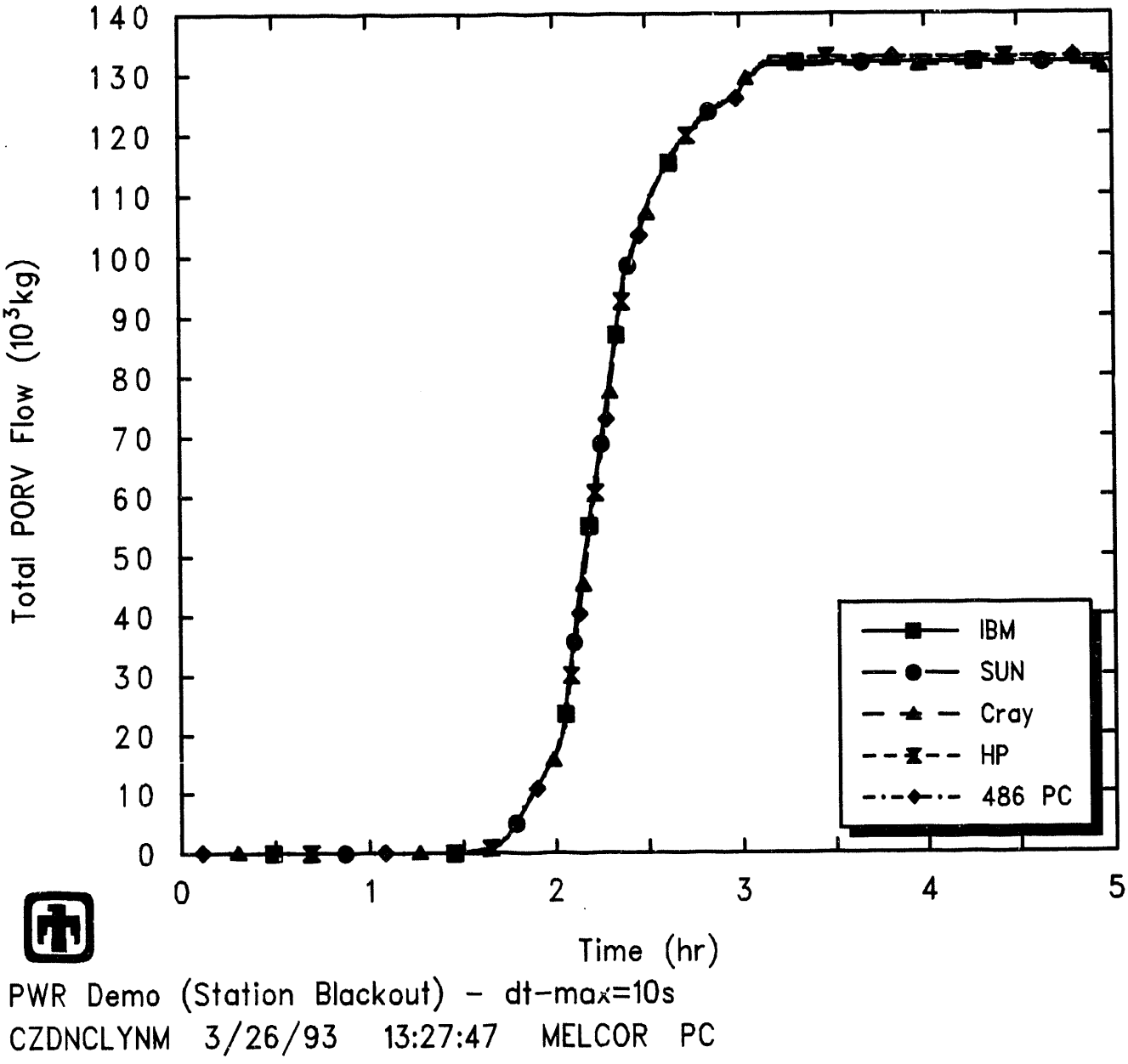

Figure 7.1.6. Pressurizer PORV Integral Flows - Machine Dependency Sensitivity Study

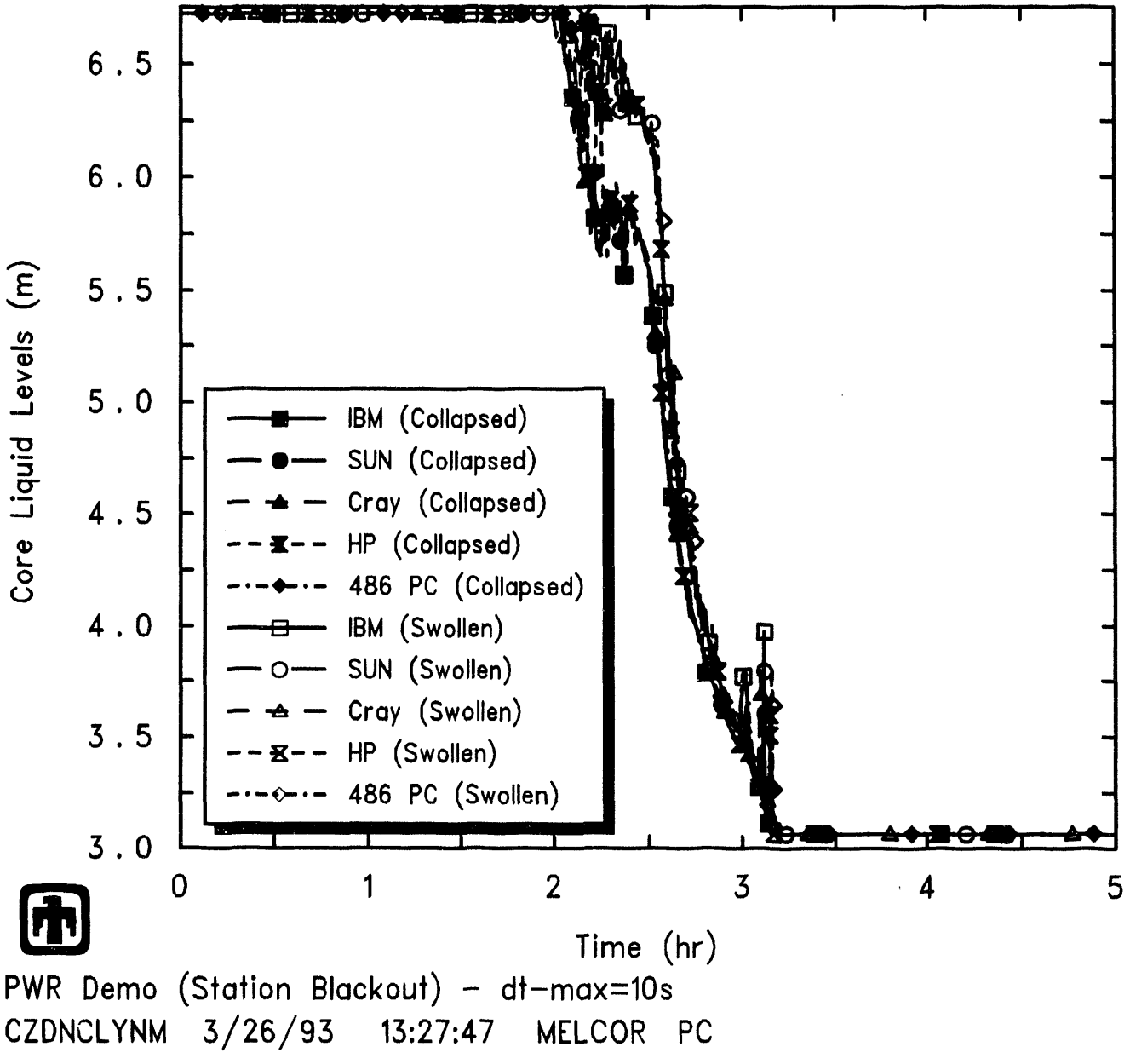

Figure 7.1.7. Core Liquid Levels – Machine Dependency Sensitivity Study

Table 7.1.2. Core State at Vessel Failure - Machine Dependency Sensitivity Study

	IBM	SUN	HP	Cray	PC
Lower Plenum Debris Masses (kg)					
UO_2	39,751	44,434	45,504	41,080	48,425
Zircaloy	2,450	2,825	3,262	2,950	3,200
Zirc Oxide	4,486	4,943	4,893	3,600	6,052
Steel	96	95	86	105	102
Steel Oxide	78	114	96	77	79
CRP	334	334	166	334	334
Total	47,195	52,745	54,008	48,147	58,192
Average Debris Temperature (K)	~2450	~2450	~2400	~2300	~2480
Fraction Material Relocated	~47%	~53%	~54%	~48%	~58%
Fraction Oxidized					
Zircaloy	~25%	~30%	~30%	~23%	~35%
Steel	~0.3%	~0.4%	~0.3%	~0.2%	~0.3%

at the time of vessel failure. The fraction of zircaloy oxidized by the time of vessel breach varies from 23% to 39%, with most of these machine-dependency sensitivity study calculations predicting $\leq$30%; the fraction of steel oxidized by the time of vessel breach also varies in these machine-dependency analyses, from 0.2% to 0.4% with most of these calculations predicting $\leq$0.3%.

Figure 7.1.8 shows the total masses of core materials (UO_2, Zircaloy and zirc oxide, stainless steel and steel oxide, and control rod poison) remaining in the vessel; the masses of fuel and of control rod poison remaining in the vessel are given in Figure 7.1.9, while the masses of Zircaloy and zirc oxide, and stainless steel and steel oxide, remaining in the vessel are presented in Figure 7.1.10. As noted in Table 7.1.1, debris ejection began immediately after lower head failure in all cases. Also, for all platforms tested, all the UO_2 was transferred to the cavity within a short period of time ($\leq$1hr), as was the unoxidized zircaloy, the associated zirc oxide and the control rod poison. There are, however, differences visible in how much material was lost in the initial high-pressure melt ejection *vs* how much mass left the vessel later, in a low-pressure melt pour. Some of the structural steel in the lower plenum (and associated steel oxide) was predicted to remain unmelted and in place even after vessel breach in all cases, although the amount remaining varies from ~85% to ~50% of the steel initially present in the core and lower plenum region.

The total mass of debris in the cavity and the mass of ablated concrete calculated in these machine-dependency sensitivity studies are illustrated in Figure 7.1.11; the mass of core debris in the cavity is basically an inversion of Figure 7.1.8. Before about 24,000s, the debris in the cavity was dominated by debris ejected from the vessel; after ~24,000s significant core-concrete interaction began and substantial masses of ablated and reacted concrete were added to the total cavity debris. While there is some spread among the various results shown, the same overall behavior was predicted in all cases, and the quantitative differences are generally small.

Figures 7.1.12, 7.1.13 and 7.1.14 show the masses and temperatures of the light oxide, metallic and heavy oxide debris layers in the cavity, respectively. In the calculations on all five hardware platforms, a CORCON layer flip occurred at around 24,000s, switching from an initial configuration with a metallic debris layer above a heavy oxide layer to a later configuration with a light oxide layer above a metallic debris layer. Very little difference was found in any of the layer temperature histories, or in the masses initially in the heavy-oxide layer and later in the light-oxide layer. There was a significant difference in the masses of the metallic layer predicted in the calculations on the different machines, directly reflecting the differences in predicted retention of lower plenum structural steel in the vessel.

The pressure calculated in the containment dome control volume is given in Figure 7.1.15. There is very little difference visible in the early-time containment response in either magnitude or timing, for any of the hardware platforms tested. The offset differences seen at later times in the transient sequence reflect different times needed to boil off water in the cavity, switching from more rapid containment pressurization due to that steam generation to a slower pressurization due primarily to continued core-

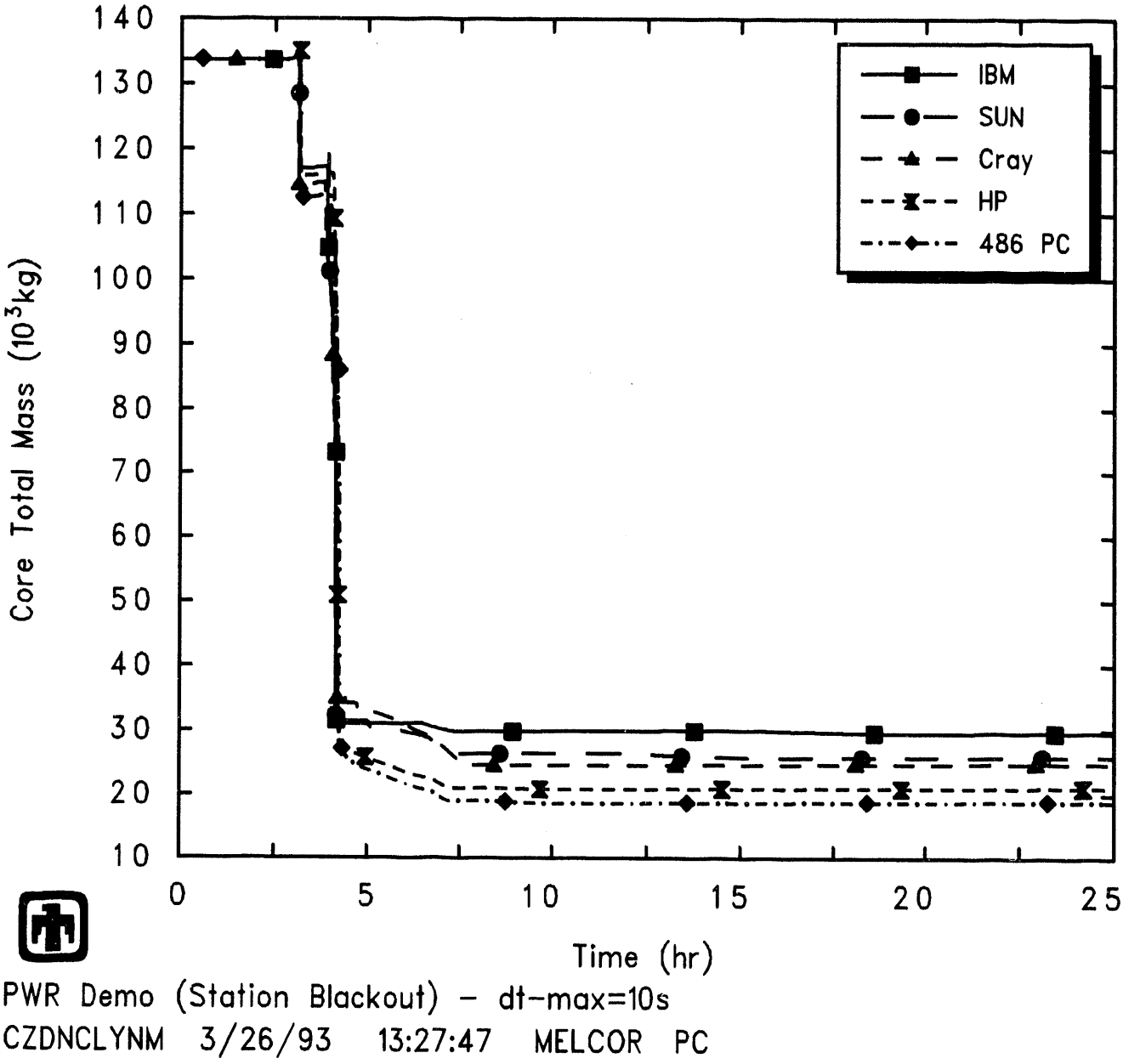

Figure 7.1.8. Total Core Masses – Machine Dependency Sensitivity Study

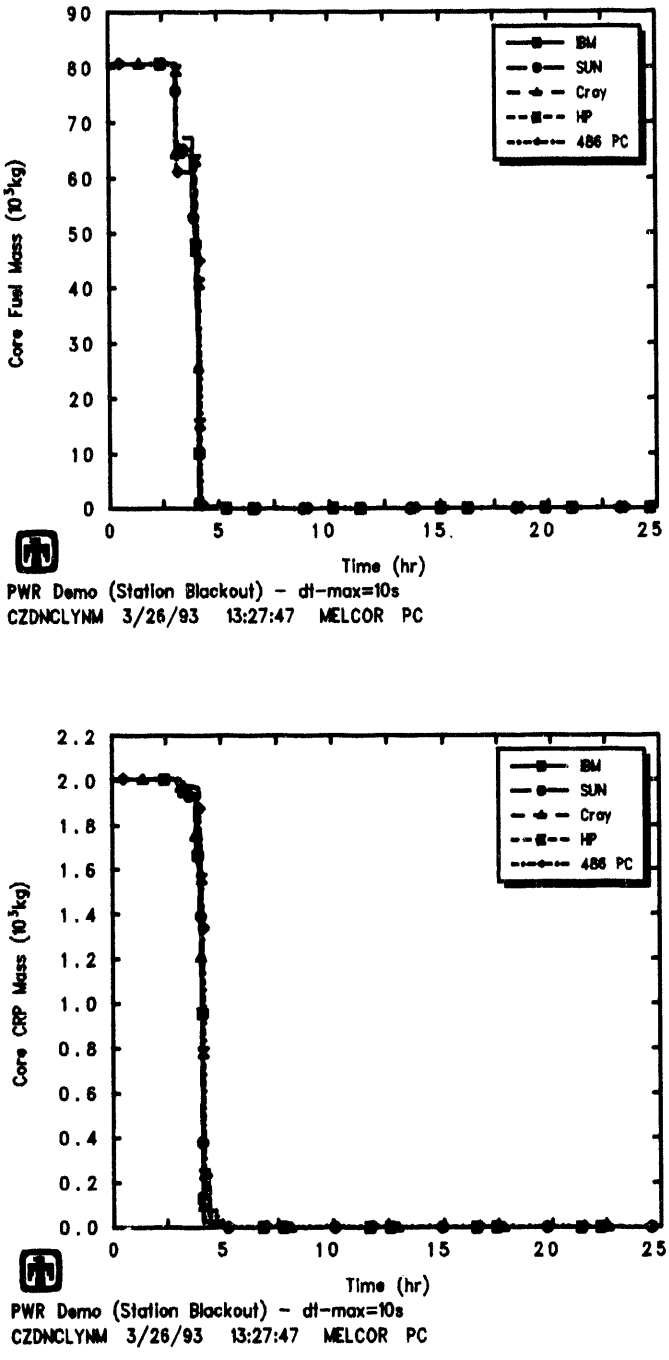

Figure 7.1.9. Total Fuel (top) and Control Rod Poison (bottom) Core Masses - Machine Dependency Sensitivity Study

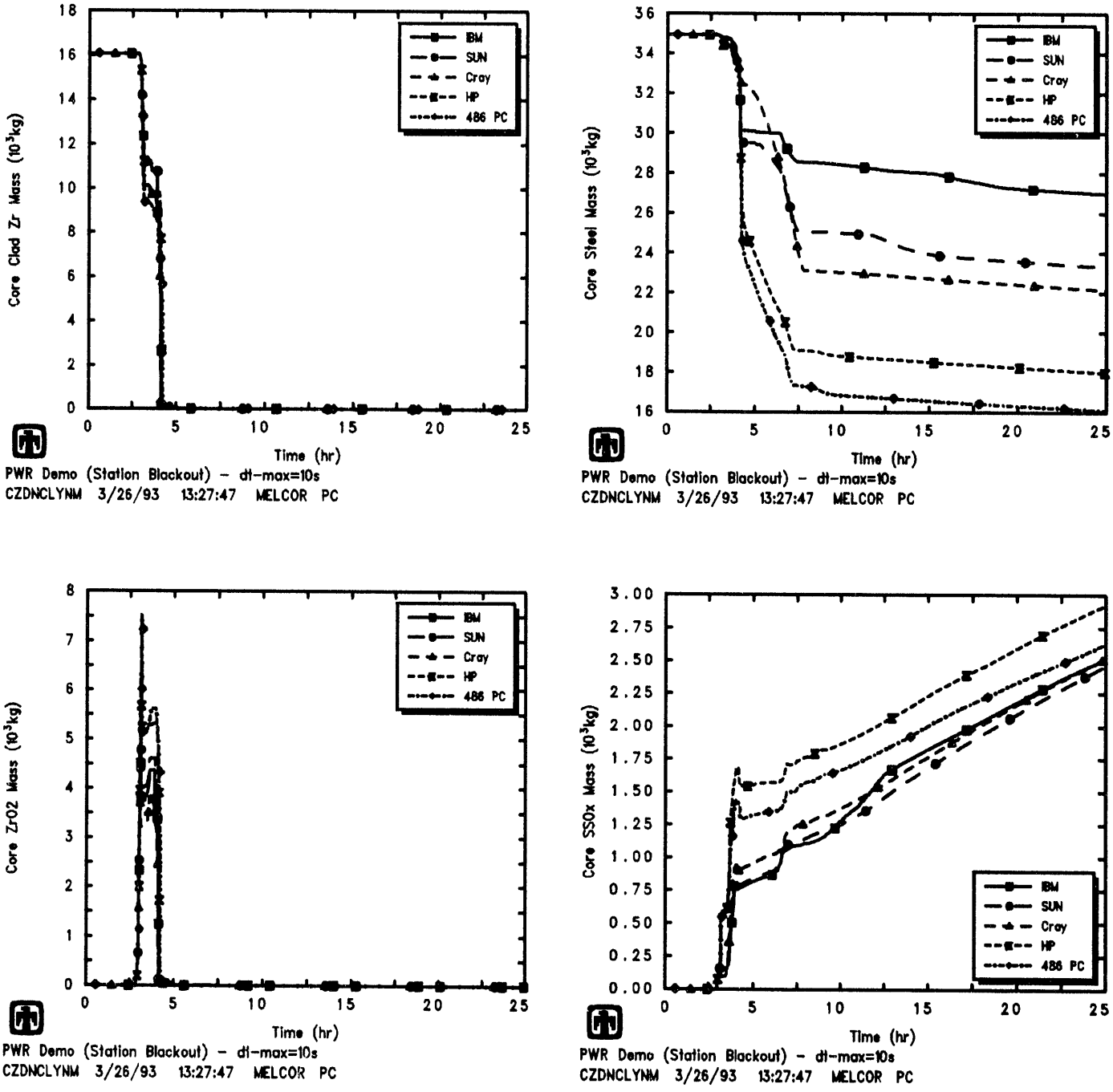

Figure 7.1.10. Total Zircaloy (upper left), Zirc Oxide (lower left), Stainless Steel (upper right) and Steel Oxide (lower right) Core Masses – Machine Dependency Sensitivity Study

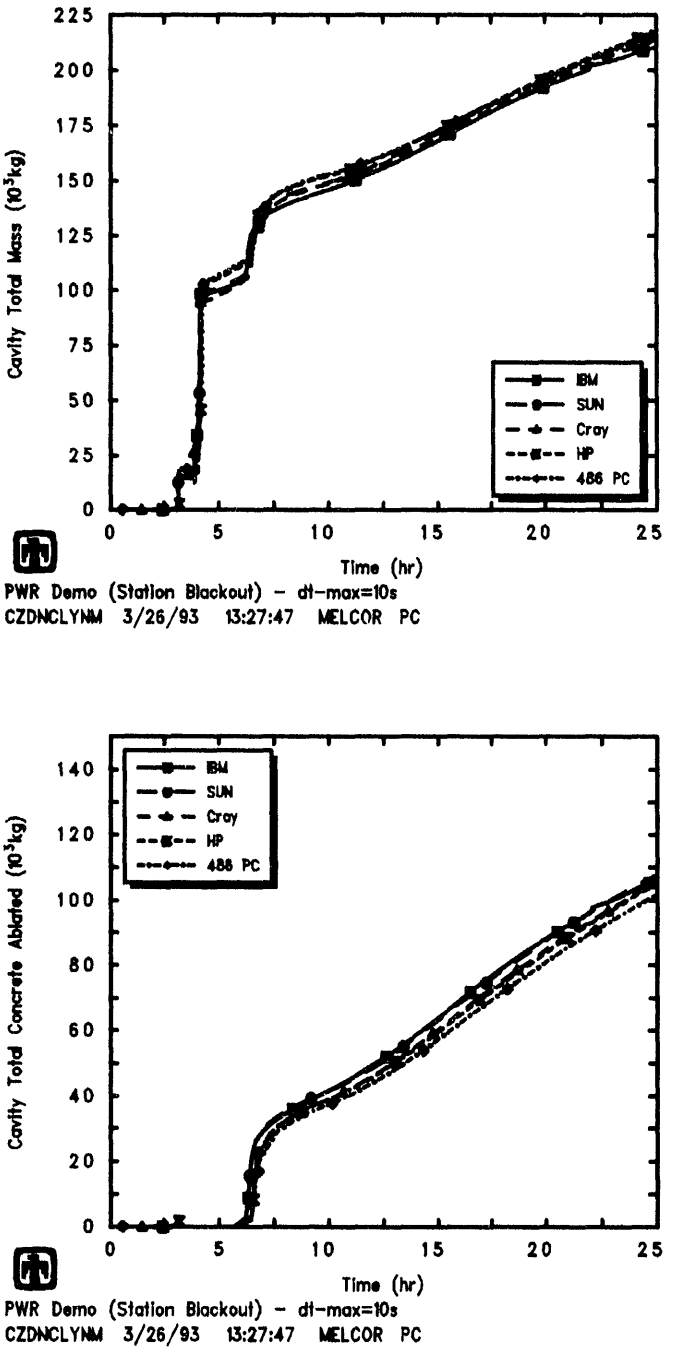

Figure 7.1.11. Total Cavity Masses (top) and Ablated Concrete Masses (bottom) - Machine Dependency Sensitivity Study

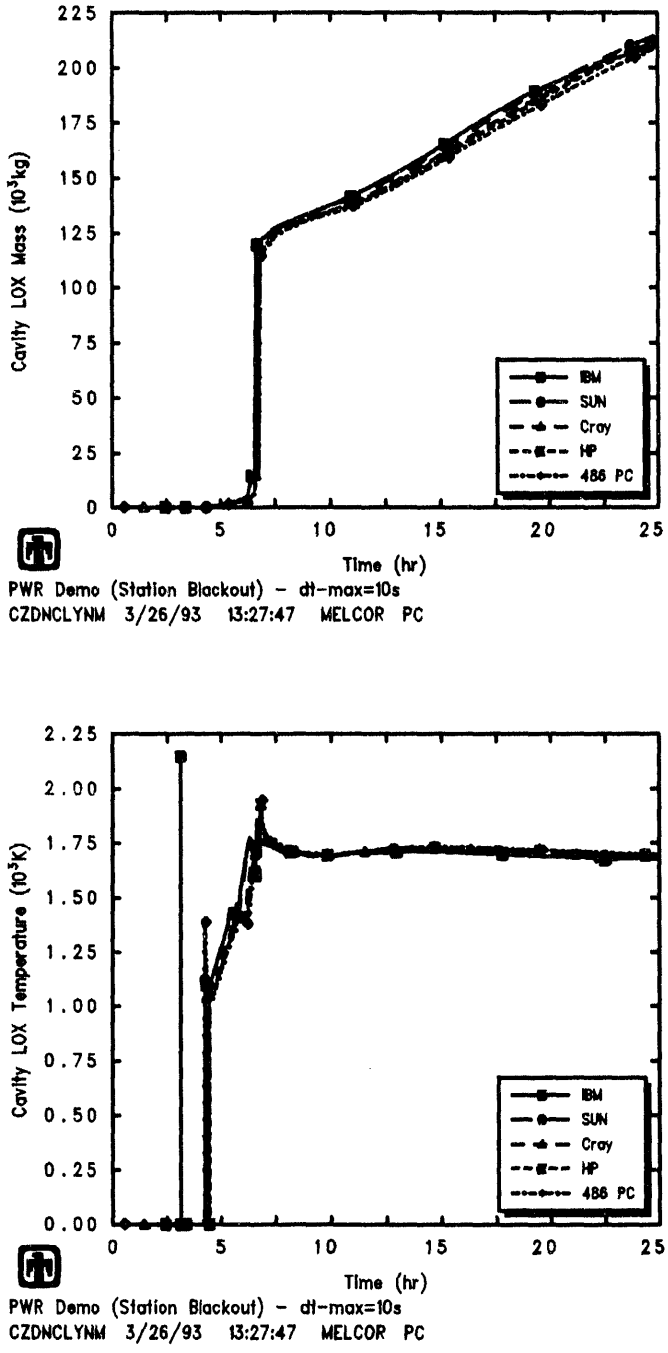

Figure 7.1.12. Cavity Light-Oxide Layer Masses (top) and Temperatures (bottom) - Machine Dependency Sensitivity Study

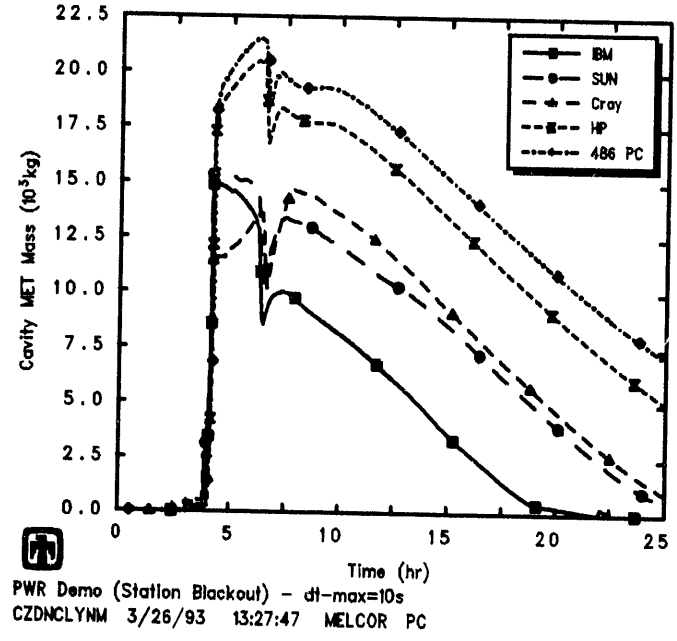

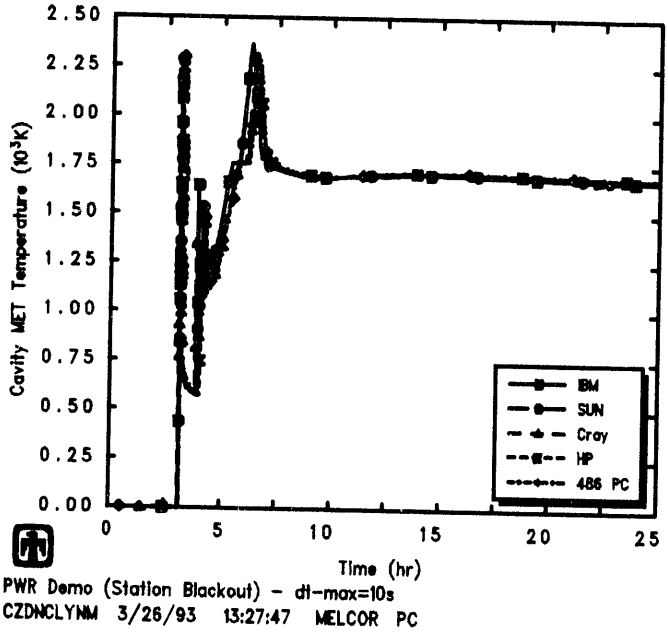

Figure 7.1.13. Cavity Metallic Layer Masses (top) and Temperatures (bottom) - Machine Dependency Sensitivity Study

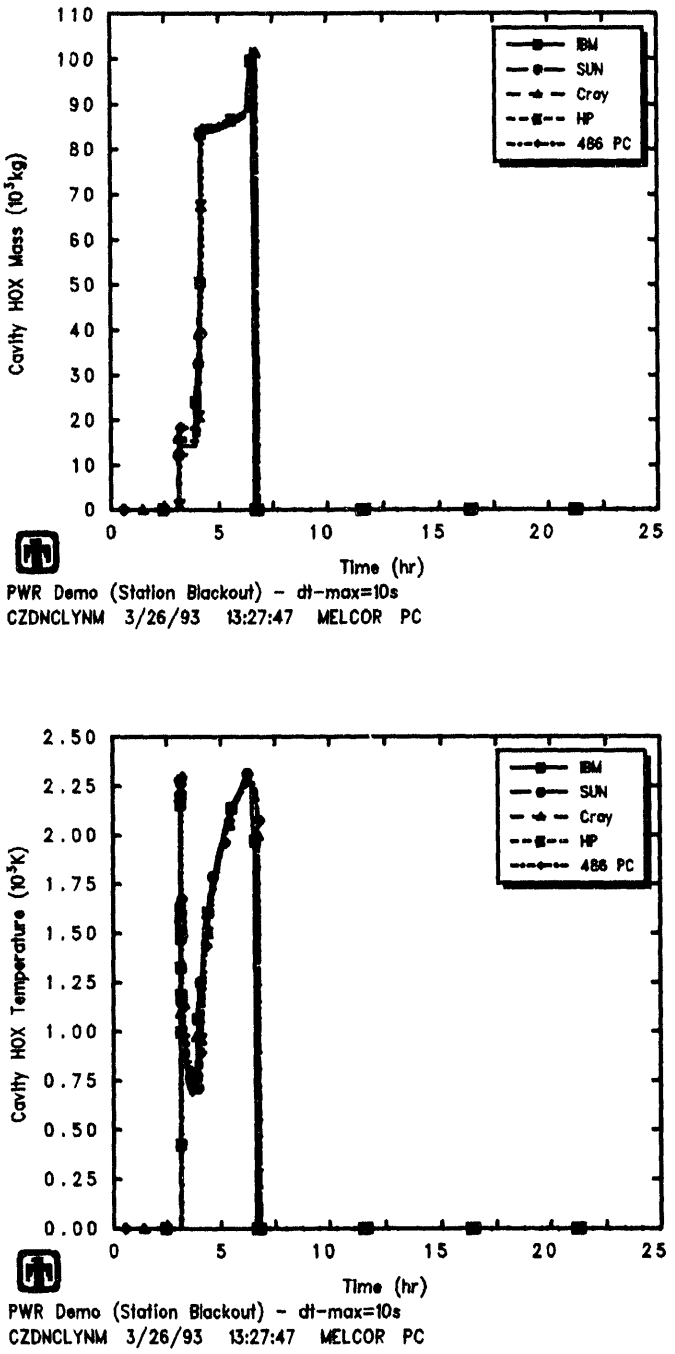

Figure 7.1.14. Cavity Heavy-Oxide Layer Masses (top) and Temperatures (bottom) – Machine Dependency Sensitivity Study

concrete interaction; the range in times at which the cavity water disappeared in turn reflects different amounts of core debris transferred to the cavity from the vessel.

The temperature behavior of the containment atmosphere was very similar to that of the pressure. Most of the containment remained saturated, except for the cavity. Slightly different temperature spikes in the cavity reflect the differences in hydrogen deflagrations in the cavity noted in Table 7.1.1, and the temperature of the cavity atmosphere eventually rose to that of the core debris materials at slightly different times, reflecting the different times when all the water in the cavity had boiled off.

Figure 7.1.16 shows a substantial difference in the number and timing of hydrogen burns in the cavity and in the amount of hydrogen burned in deflagrations in these various calculations; no hydrogen burns occurred in the containment outside the cavity during any of these calculations, because the other control volumes modelling containment remained steam/CO_2 inerted. Calculations on the five platforms used showed one set of hydrogen burns occurring $\leq$0.5hr after vessel breach and the start of core-concrete interaction. All these calculations also predicted a second period of hydrogen burns in the cavity later in the transient, but the timing and extent of that second burn period differed substantially among the various platforms; three of the five calculations showed a single, isolated burn at ~30,000s, while the other two showed a series of multiple burns starting somewhat later in the transient and lasting for a considerable length of time. The amount of hydrogen burned generally reflected the number of deflagrations occurring in these various machine-dependency sensitivity study calculations.

Figures 7.1.17 through 7.1.19 show mole fractions in the cavity control volume atmosphere as calculated on four of the hardware platforms used, the SUN Sparc2 and HP 755 workstations, a Cray supercomputer and a 486PC, compared to the default ignition limits used in MELCOR. (Corresponding results for the reference calculation run on an IBM RISC-6000 Model 550 workstation can be found in the upper left of Figures 7.2.17 through 7.2.19.)

Figure 7.1.17 presents a combined equivalent mole fraction of H_2 and CO (equal to $x_{H_2} + \frac{0.10}{0.167} x_{CO}$), which must be greater than 0.10 for detonation in the absence of igniters. Figure 7.1.18 presents the O_2 mole fraction which must be greater than 0.05 for detonation in the absence of igniters. Figure 7.1.19 presents a combined total mole fraction of H_2O and CO_2, which must be less than 0.55 for the mixture to not be assumed inert. [34]

The first period of hydrogen combustion occurred in all five machine-dependency sensitivity study calculations between $\geq$12,680s ($\geq$3.5hr) and $\leq$14,100s ($\leq$3.9hr); the timing was similar on all platforms, as were the number and total mass of hydrogen burned. In some calculations (*i.e.*, on the HP workstation, Cray supercomputer and 486 PC), a single burn was predicted sometime between ~29,100 (8hr) and ~30,600s (8.5hr); the mole fraction plots indicate that this burn corresponded to a spike up in combined H_2 and CO concentration, and in O_2 also, with a simultaneous spike down in total H_2O plus CO_2 concentration. The combined H_2 and CO concentration and the O_2 concentration both easily exceeded their ignition limits; the ignition was controlled by whether the

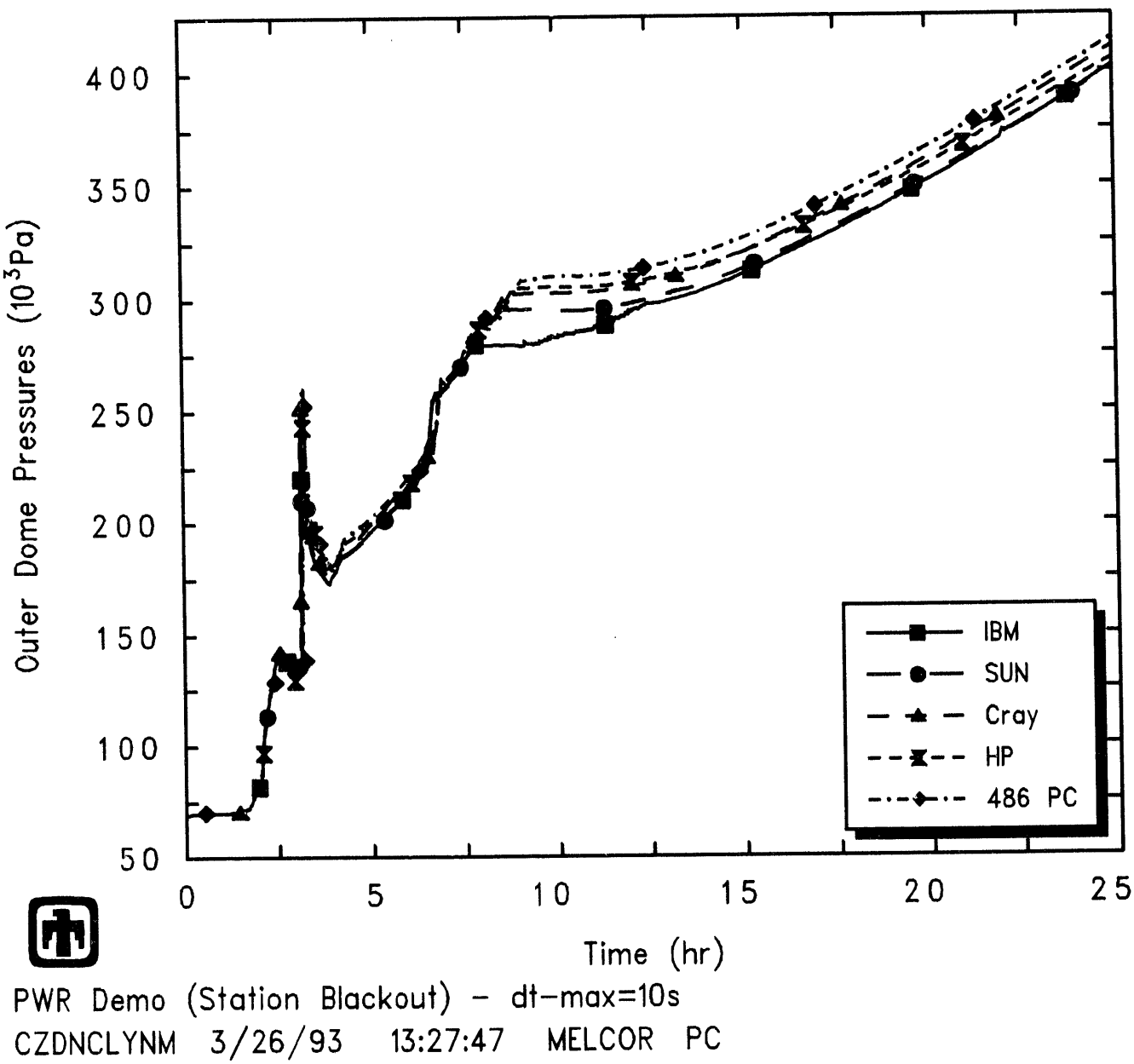

Figure 7.1.15. Containment Pressures - Machine Dependency Sensitivity Study

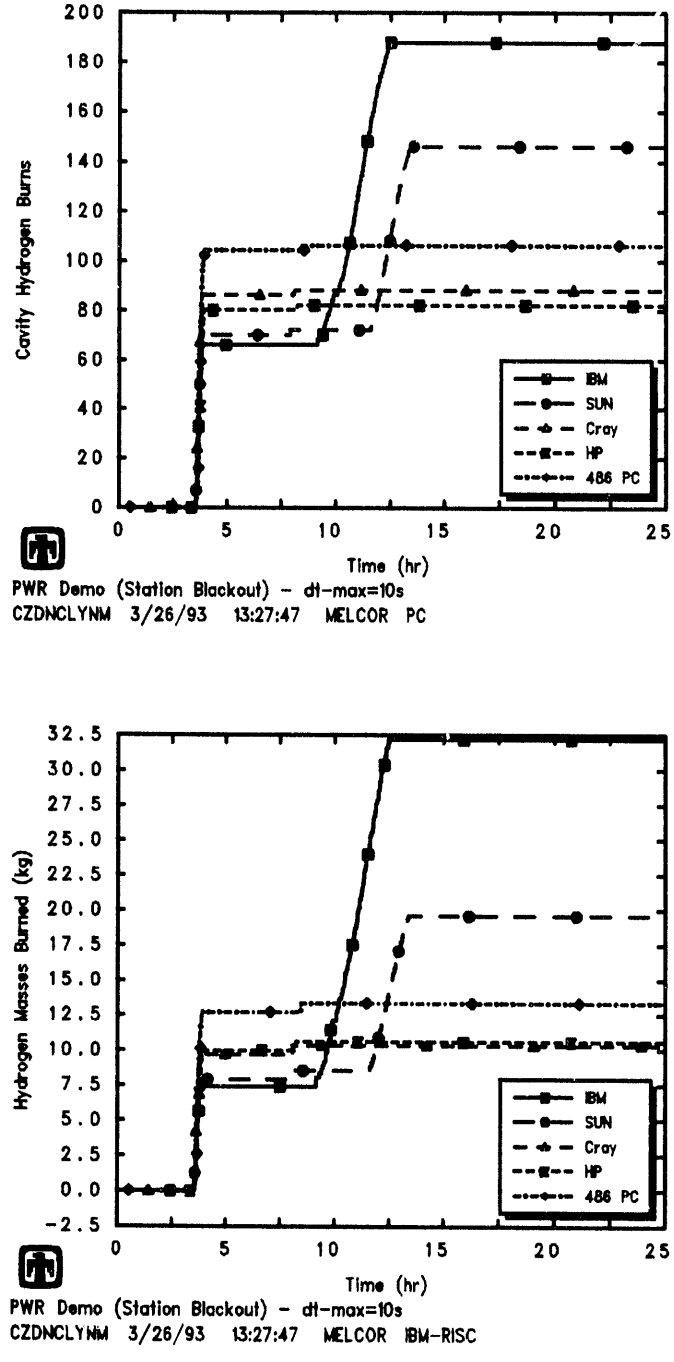

Figure 7.1.16. Number of (top) and Masses Burned in (bottom) Cavity Hydrogen Deflagrations – Machine Dependency Sensitivity Study

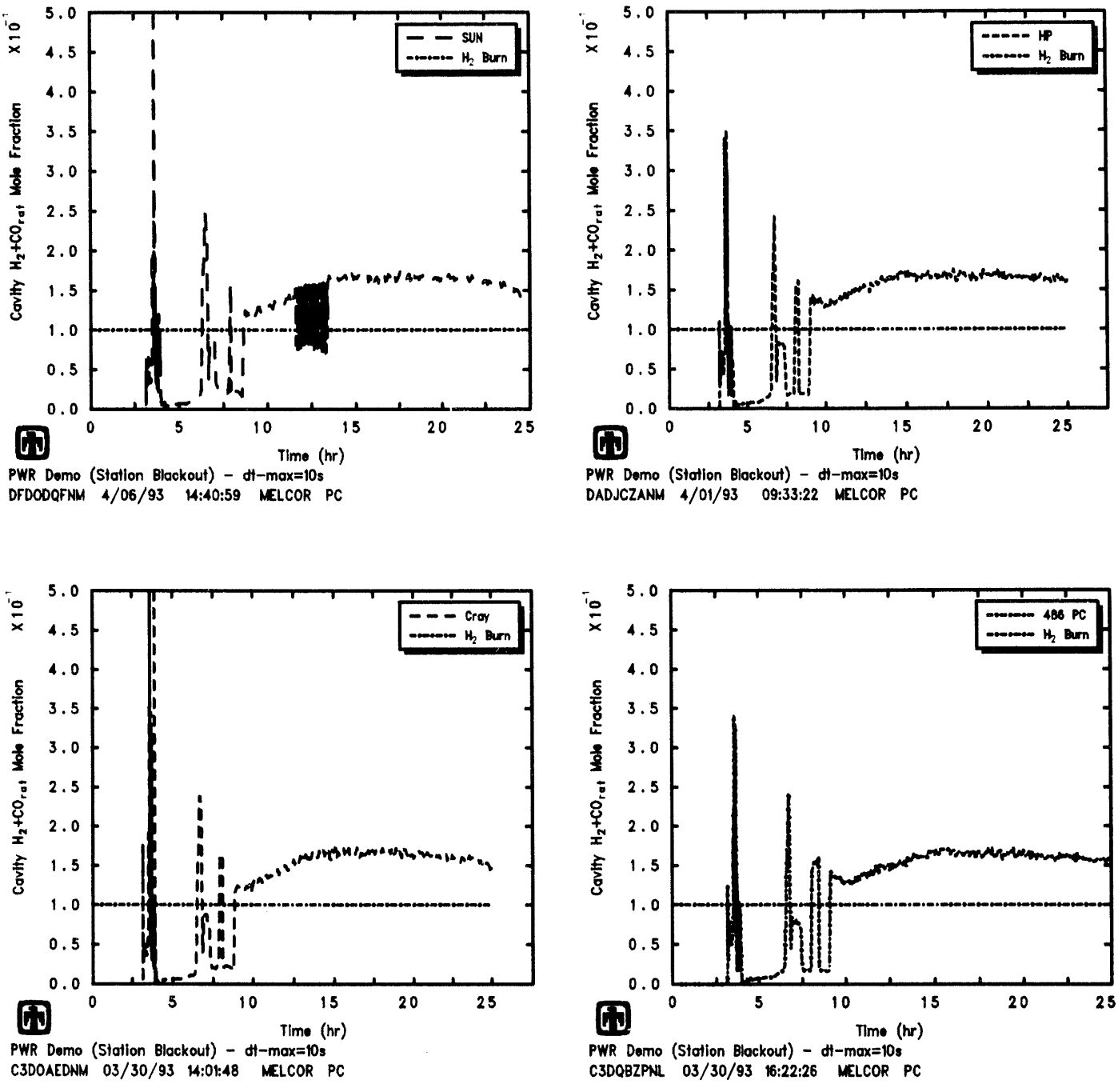

Figure 7.1.17. Combined H_2 and CO Mole Fraction in Cavity Calculated on SUN Sparc2 (upper left), HP 755 (upper right), Cray (lower left) and 486PC (lower right) - Machine Dependency Sensitivity Study

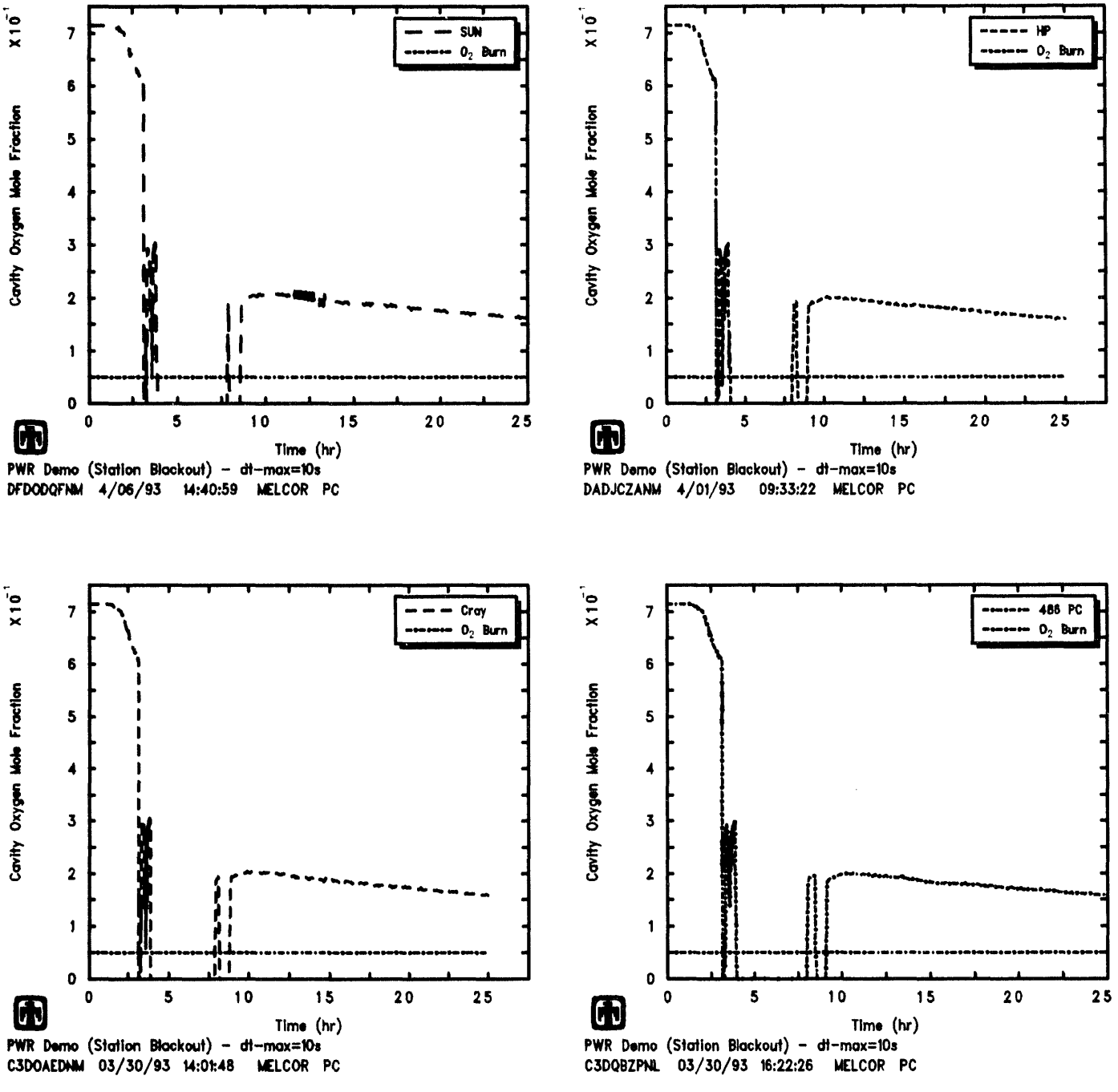

Figure 7.1.18. O_2 Mole Fraction in Cavity Calculated on SUN Sparc2 (upper left), HP 755 (upper right), Cray (lower left) and 486PC (lower right) – Machine Dependency Sensitivity Study

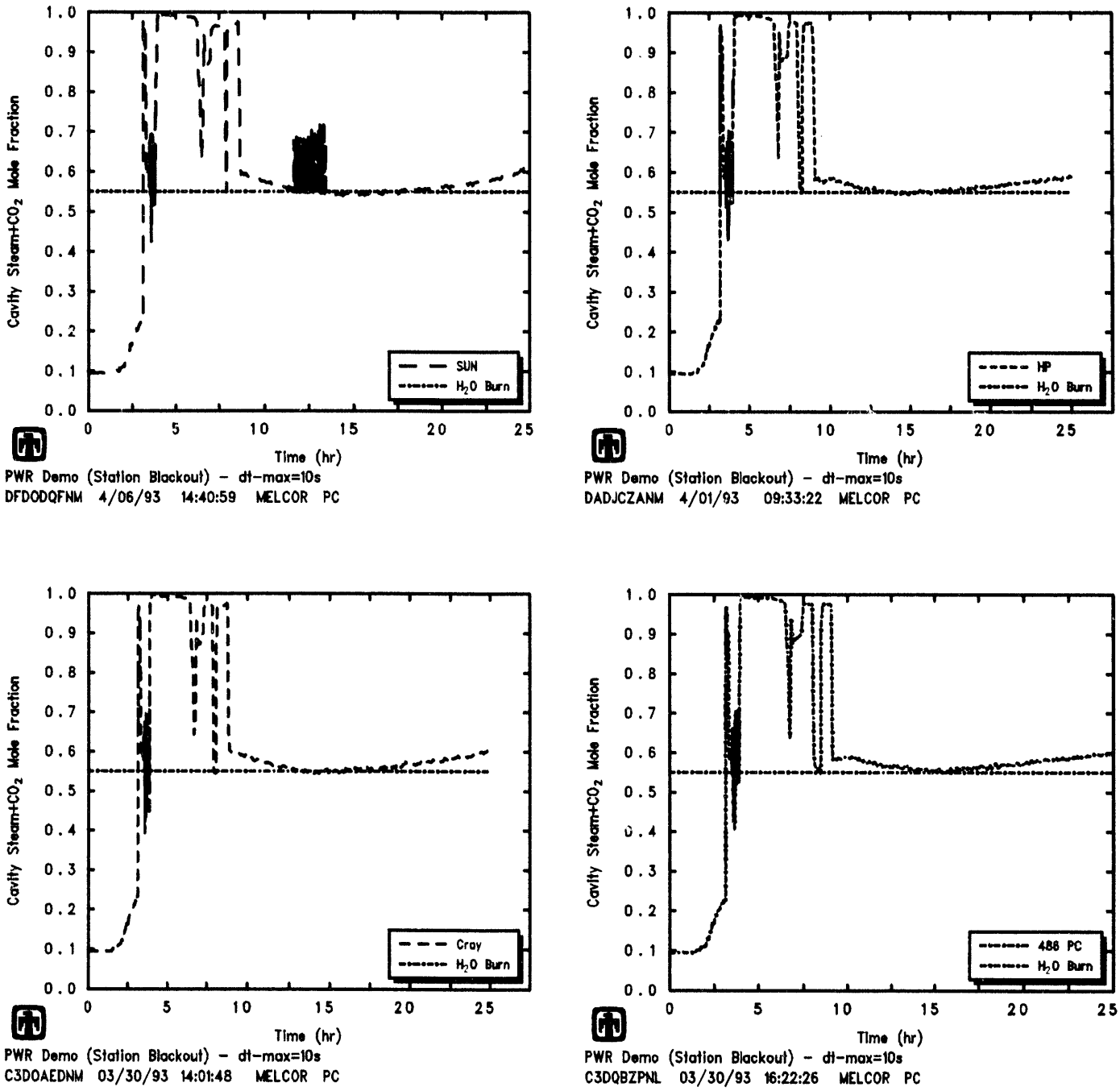

Figure 7.1.19. Combined H_2O and CO_2 Mole Fraction in Cavity Calculated on SUN Sparc2 (upper left), HP 755 (upper right), Cray (lower left) and 486PC (lower right) - Machine Dependency Sensitivity Study

total H_2O plus CO_2 concentration was reduced to below the inerting limit. The plot in the upper left of Figure 7.1.19 suggests that the SUN Sparc2 calculation approached this limit very closely, also.

In these machine-dependency studies, a separate, prolonged series of combustion events was seen only in the two calculations (on the IBM RISC-6000 Model 550 and SUN Sparc2) which did not show a single burn predicted sometime between ~29,100 (8hr) and ~30,600s (8.5hr); that third phase of hydrogen combustion was quite extensive in the IBM RISC-6000 calculation (as seen in Figures 4.3.7 and in the upper left of Figures 7.2.17 through 7.2.19) while it was smaller and briefer in the SUN Sparc2 calculation. Figures 7.1.17 through 7.1.19) indicate that in all cases the combined H_2 and CO concentration and the O_2 concentration both easily exceeded their ignition limits throughout most of the later portions of the transient, after ~8-9hr; as in the brief single burn predicted sometime between ~29,100s (8hr) and ~30,600s (8.5hr) only in some calculations, the combustion ignition at later times also seemed controlled by whether the total H_2O plus CO_2 concentration was reduced to below the inerting limit. Figure 7.1.19) also demonstrates how closely all the calculations approached the inerting limit for a long period of time between >12.5hr and <17.5hr. It is clear from Figure 7.1.19) that the potential for a prolonged period of hydrogen burn existed in all cases later in the transient, and it is not clear from Figure 7.1.19) why combustion was not predicted in more of the cases during that time (especially for the calculation done on the SUN Sparc2, which appears to remain below the inert concentration limit for some time after combustion was predicted to end).

The final amounts of each radionuclide class released by the end of the calculated transient period (90,000s or 25hr) in-vessel (in both the core active-fuel region and in the lower plenum), ex-vessel (in the cavity) and overall are given in Tables 7.1.3, 7.1.4 and 7.1.5, respectively, for analyses run on different hardware platforms. These releases are expressed as percent of inventory initially present in the core, and consider only the release of radioactive forms of these classes, not additional releases of nonradioactive aerosols from structural materials.

The ex-vessel source terms given in Table 7.1.4 for these machine-dependency sensitivity study calculations were affected by the different amounts of structural steel retained in the lower plenum and by the resulting differences in the size and eventual disappearance of the metallic debris layer, for reasons discussed in detail in Section 6.4. In summary, the VANESA code [22], which is used to calculate ex-vessel releases in MELCOR, has no provision for a disappearing metallic layer; therefore, as the metallic layer in the cavity goes to zero, the releases of radionuclide species associated with that layer (*i.e.*, Te, Ru, Cd and Sn) can begin growing exponentially, as shown in Figure 7.1.20 for several of these radionuclide species. The effect was not pronounced for Te, because most of that species mass had been released prior to the metallic layer vanishing, and also was not pronounced for Ru, because very little of that species mass was being released at all; however, the release of other species, such as Cd and Sn, is significantly in error. As noted in Section 6.4, this problem is inherent in the VANESA formulation itself, not in MELCOR, but is more likely to be encountered with MELCOR 1.8.2 than with

Table 7.1.3. In-Vessel Source Terms - Machine Dependency Sensitivity Study

Class	Radionuclide Release (% Initial Inventory) IBM	SUN	HP	Cray	PC
<u>In-Core</u>					
1 (Xe)	47.910	56.243	54.895	44.153	64.534
2 (Cs)	47.892	56.247	54.869	44.155	64.521
3 (Ba)	4.1330	6.2409	6.6245	2.6088	8.4150
4 (I)	47.871	56.235	54.869	44.144	64.504
5 (Te)	3.2899	4.9998	5.3303	2.2527	6.6664
6 (Ru)	0.1596	0.2441	0.2605	0.0958	0.3350
7 (Mo)	1.6993	2.5169	2.7380	1.2492	3.2504
8 (Ce)	0.0034	0.0051	0.0054	0.0021	0.0069
9 (La)	0.0109	0.0187	0.0207	0.0055	0.0282
10 (U)	0.0112	0.0192	0.0212	0.0056	0.0282
11 (Cd)	14.898	21.780	22.242	9.4772	28.535
12 (Sn)	14.896	21.784	22.248	9.4767	28.529
<u>In LP</u>					
1 (Xe)	12.409	12.306	11.363	24.311	12.682
2 (Cs)	12.547	12.356	11.506	24.624	12.715
3 (Ba)	3.0679	4.3090	2.6386	3.5315	4.4384
4 (I)	12.413	12.309	11.370	24.324	12.688
5 (Te)	2.6949	3.6060	2.2909	2.9384	3.7708
6 (Ru)	0.1169	0.1671	0.0913	0.1303	0.1719
7 (Mo)	1.3373	1.8267	1.2980	1.4799	1.8519
8 (Ce)	0.0024	0.0032	0.0019	0.0026	0.0033
9 (La)	0.0349	0.0496	0.0395	0.0344	0.0629
10 (U)	0.0368	0.0515	0.0409	0.0358	0.0654
11 (Cd)	10.195	13.605	10.071	13.526	13.989
12 (Sn)	10.195	13.605	10.071	13.526	13.988

Table 7.1.4. Ex-Vessel Source Terms - Machine Dependency Sensitivity Study

	Radionuclide Release (% Initial Inventory)				
Class	IBM	SUN	HP	Cray	PC
1 (Xe)	38.937	30.744	33.002	30.429	22.232
2 (Cs)	41.817	33.067	35.426	32.488	23.913
3 (Ba)	30.585	23.336	21.861	27.364	18.603
4 (I)	0.0	0.0	0.0	0.0	0.0
5 (Te)	84.122	53.210	51.674	66.431	45.473
6 (Ru)	4×10^{-6}	1×10^{-6}	2×10^{-6}	3×10^{-6}	1×10^{-6}
7 (Mo)	2.2436	1.2773	1.0752	1.8755	0.9002
8 (Ce)	0.0010	0.0010	0.0010	0.0010	0.0010
9 (La)	0.2845	0.1530	0.1771	0.2099	0.1475
10 (U)	0.0024	0.0018	0.0019	0.0020	0.0018
11 (Cd)	2.7877	0.3952	0.3707	0.8107	0.2486
12 (Sn)	27.097	3.4945	3.3711	6.8015	2.2954

Table 7.1.5. Total Source Terms - Machine Dependency Sensitivity Study

	Radionuclide Release (% Initial Inventory)				
Class	IBM	SUN	HP	Cray	PC
1 (Xe)	99.256	99.293	99.260	98.892	99.448
2 (Cs)	102.26	101.67	101.80	101.27	101.15
3 (Ba)	37.786	32.886	21.125	33.454	31.456
4 (I)	60.284	60.544	66.239	68.468	77.192
5 (Te)	90.106	61.816	59.295	71.623	55.910
6 (Ru)	0.2765	0.4112	0.3518	0.2260	0.5069
7 (Mo)	5.2802	5.6209	5.1113	4.6046	6.0025
8 (Ce)	0.0067	0.0093	0.0083	0.0058	0.0111
9 (La)	0.3303	0.2213	0.2373	0.2498	0.2386
10 (U)	0.0503	0.0724	0.0641	0.0434	0.0954
11 (Cd)	27.881	35.780	32.684	23.814	42.773
12 (Sn)	52.188	38.884	35.690	29.805	44.812

MELCOR 1.8.1 because of the increased likelihood of more retention of lower plenum structural steel in-vessel.

Figure 7.1.21 presents overall run times for calculations on the various platforms for these Surry PWR TMLB' simulations. The SUN and PC were slowest in run time required; the IBM, HP and Cray were all significantly faster, with the HP the fastest for this particular analysis.

7.2 Time Step Effects

The reference calculation used a user-specified maximum time step Δt_{MAX} of 10s throughout the entire transient period. As a time-step sensitivity study, otherwise identical MELCOR Surry TMLB' calculations were run on an IBM RISC-6000 Model 550 workstation with the user-input maximum allowed time step progressively set to 5s, 2.5s and 1s.

Table 7.2.1 compares the timings of various key events predicted by MELCOR in this set of time-step sensitivity study calculations. As in the similar comparison for the machine-dependency sensitivity study (Table 7.1.1), the differences are generally small, accumulating and growing somewhat as the transient progresses, but with no significant branching into different accident sequences. There is a ~1min spread in clad-failure/gap-release times predicted in the various rings with different maximum time steps allowed. Both the core plate and the lower head penetration failed first in the innermost, high-power ring in all cases, and the failure times were all within a 4min time span. Debris ejection to the cavity began immediately upon lower head penetration failure in all cases, thus also within a 4min time window, and DCH always lasted about 30s. The variation in various timings observed in this time-step numeric effects sensitivity study are very similar in magnitude to the differences found in our machine-dependency numeric effects sensitivity study (Table 7.1.1).

Again, as found in our machine-dependency numeric effects sensitivity study (Table 7.1.1), the biggest timing difference was in hydrogen deflagrations occurring in the cavity. All four time-step-study calculations showed one set of hydrogen burns initially occurring $\leq$0.5hr after vessel breach and the start of core-concrete interaction, lasting about 600-900s. One calculation (with Δt_{MAX}=5s) showed a single hydrogen burn at $\geq$29,160s and then a third period of burns late in the transient, between 47,200s and 47,750s; the other three time step study calculations showed a single, second set of hydrogen burns occurring later in the transient, but the timing and extent of that later burn period differed substantially among these various cases.

Figure 7.2.1 presents the SG secondary system pressures calculated with different maximum allowed time steps, expanded to show the first two hours in detail. Again, as found in our machine-dependency numeric effects sensitivity study (Figure 7.1.1), the pressures were initially identical with all maximum allowed time steps, but then gradually got slightly out of phase as small differences in SRV setpoint over- and undershoots accumulate. Figure 7.2.2 gives the cycling of the SRV and Figure 7.2.3 demonstrates the cumulative effect on the steam generator secondary pressure, later in the transient; note that,

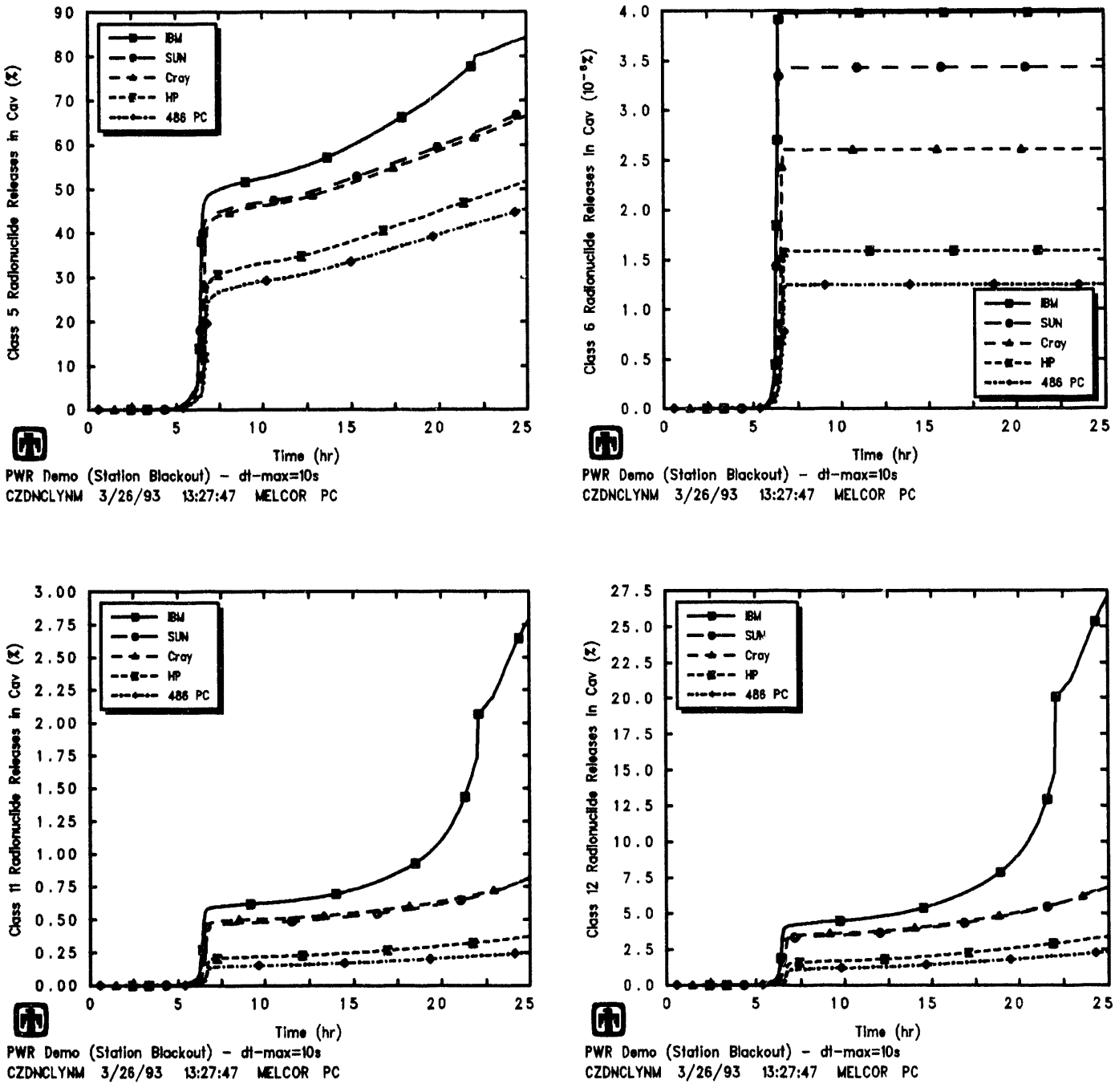

Figure 7.1.20. Ex-Vessel Class 5 (Te) Releases (upper left), Class 6 (Ru) Release (upper right), Class 11 (Cd) Releases (lower left) and Class 12 (Sn) Releases (lower right) for Surry TMLB' - Machine Dependency Sensitivity Studies

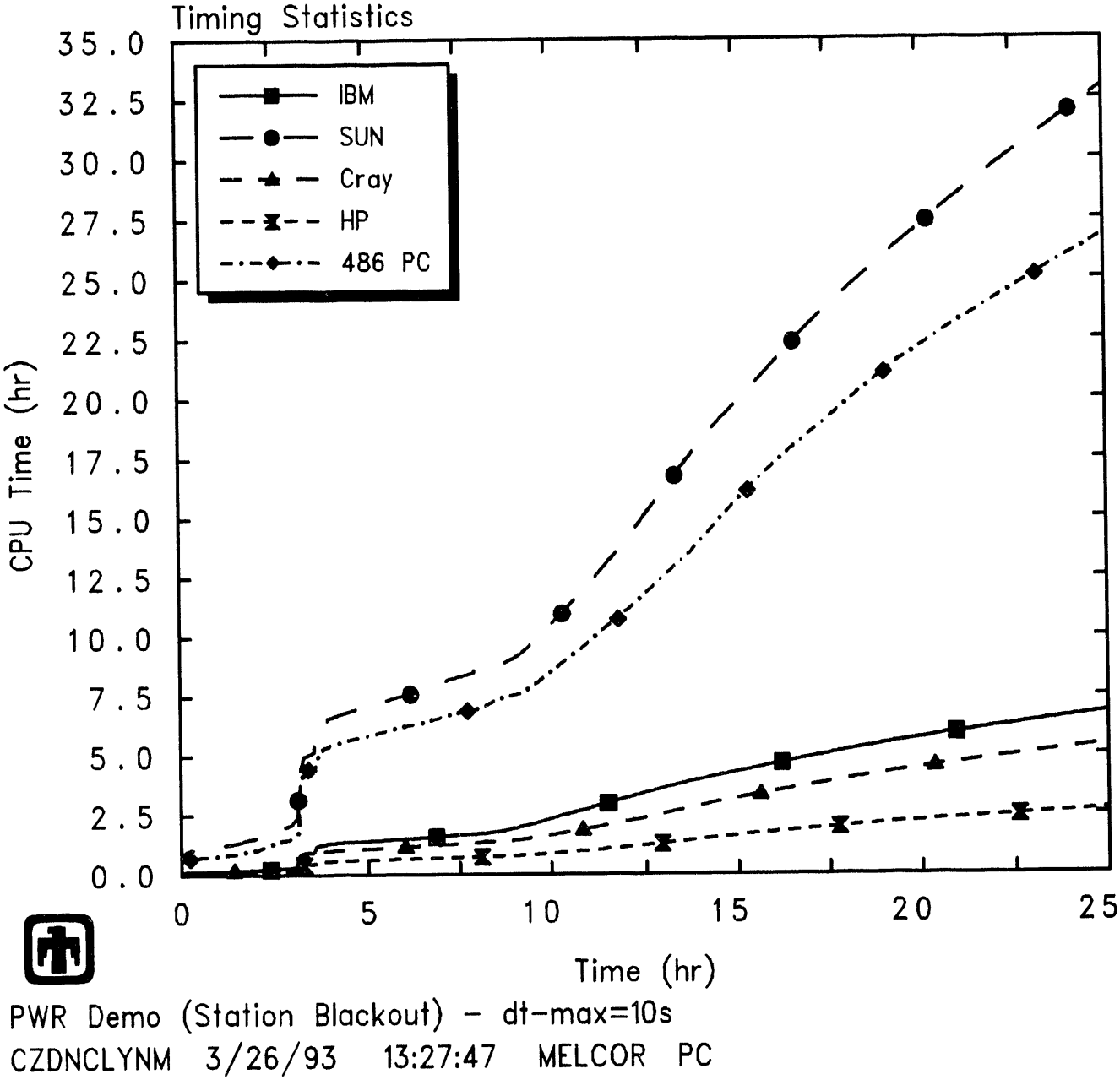

Figure 7.1.21. Total Run Times – Machine Dependency Sensitivity Study

Table 7.2.1. Timing of Key Events - Time Step Sensitivity Study

Event	Time (s) MELCOR Δt_{MAX} = 10s	5s	2.5s	1s
Gap Release				
Ring 1	10,235.0	10,237.2	10,211.8	10,170.2
Ring 2	10,334.4	10,342.2	10,315.2	10,269.2
Ring 3	10,667.9	10,687.2	10,660.2	10,608.2
Core Plate Fails				
Ring 1	11,177.9	11,215.9	11,422.7	11,318.2
Ring 2	11,906.3	11,962.7	12,172.5	12,104.5
Ring 3	13,062.9	13.131.6	11,870.4	11,834.4
LH Penetration Fails				
Ring 1	11,219.3	11,262.3	11,460.3	11,417.4
Ring 2	13,029.5	13,085.0	13,722.4	13,455.7
Ring 3	13,842.3	13,896.0	13,221.5	12,862.3
Debris to Cavity	11,219.3	11,262.3	11,460.3	11,417.4
HPME/DCH Starts	11,219.3	11,262.3	11,460.3	11,417.4
HPME/DCH Ends	11,251.7	11,301.8	11,491.7	11,447.5
Deflagrations Start	12,863.2	13,011.3	13,321.5	13,109.3
Deflagrations End	13,766.2	13,907.9	13,905.7	14,028.4
CORCON Layer Flip	~24,000	~24,750	~25,750	~22,750
Cavity Dries Out	~28,200	~28,500	~29,100	~28,500
Deflagrations Start	–	29,162.5	–	–
Deflagrations End	–	29,164.2	–	–
Deflagrations Start	32,970.0	47,214.2	37,986.7	33,963.9
Deflagrations End	44,778.9	47,751.7	45,565.5	40,461.1

unlike the results seen in the machine-dependency study (Figures 7.1.3 and 7.1.2), in the time step study cases when the SRV cycled the same number of times (*i.e.*, "dt_{MAX}=5s" and "dt_{MAX}=2.5s") the resulting pressure history remained the same, indicating little or no difference in amount of outflow and/or time that the SRV was open.

The predicted vessel pressures for this time step sensitivity study are presented in Figure 7.2.4. The primary system pressure histories were qualitatively identical and quantitatively very similar (as are the pressurizer liquid levels), with the major difference seen in the slight offsets in vessel failure time and associated primary system depressurization, also similar to the behavior noted in our machine-dependency numeric effects sensitivity study (Figure 7.1.4).

In all these calculations, the primary coolant pressure was sufficiently high to cause the PORV to open by ~5250s. As predicted earlier in the transient sequence for the SG secondary-side relief valve, the pressurizer PORV cycled rapidly and often. Reducing the maximum allowed time step significantly increased the valve cycling, as shown in Figure 7.2.5, but note that it did not result in much change in total outflow, as shown in Figure 7.2.6; the PORV cycled more frequently as the maximum allowed time step was reduced because there was less over- and undershooting the valve controller pressure setpoints, but the time the valve was opened shortened, so overall inventory loss was virtually unchanged.

Figure 7.2.7 demonstrates that the accumulating small changes in valve cycling and inventory loss did not significantly change the core uncovery. Again, as found in our machine-dependency numeric effects sensitivity study (Figure 7.1.7), there are some differences visible in liquid level oscillations, but these are minor. The small differences in calculated core uncovery in these cases are reflected in the small differences found in clad-failure/gap-release times in Table 7.2.1 (~60s).

Table 7.2.2 summarizes the amount of the various materials in the lower plenum debris bed at the time a lower head penetration first failed (*i.e.*, at vessel breach), for the calculations done with various user-specified maximum time steps, and also gives the average temperature of the debris in the lower plenum, the fraction of core material relocated in or from the active fuel region, and the fractions of zircaloy and steel oxidized by the time the vessel fails.

The fraction of core materials relocated and the amount of debris in the lower plenum generally increased as the user-specified time step was reduced, although not monotonically. Averaging these four results, the lower plenum debris mass at vessel failure is ~53,000kg±6,500kg; given that the initial total intact core mass in the active fuel region (*i.e.*, above the core support plate) is ≥100,000kg, this range corresponds to ±7% of the total core mass in the active fuel region, not a large variation. There was little or no change in the average temperature of the debris in the lower plenum, or the fractions of zircaloy and steel oxidized by the time the vessel fails, in these time step sensitivity study calculations.

Figures 7.2.8, 7.2.9 and 7.2.10 show the total and individual masses of core materials (UO_2, Zircaloy and zirc oxide, stainless steel and steel oxide, and control rod poison)

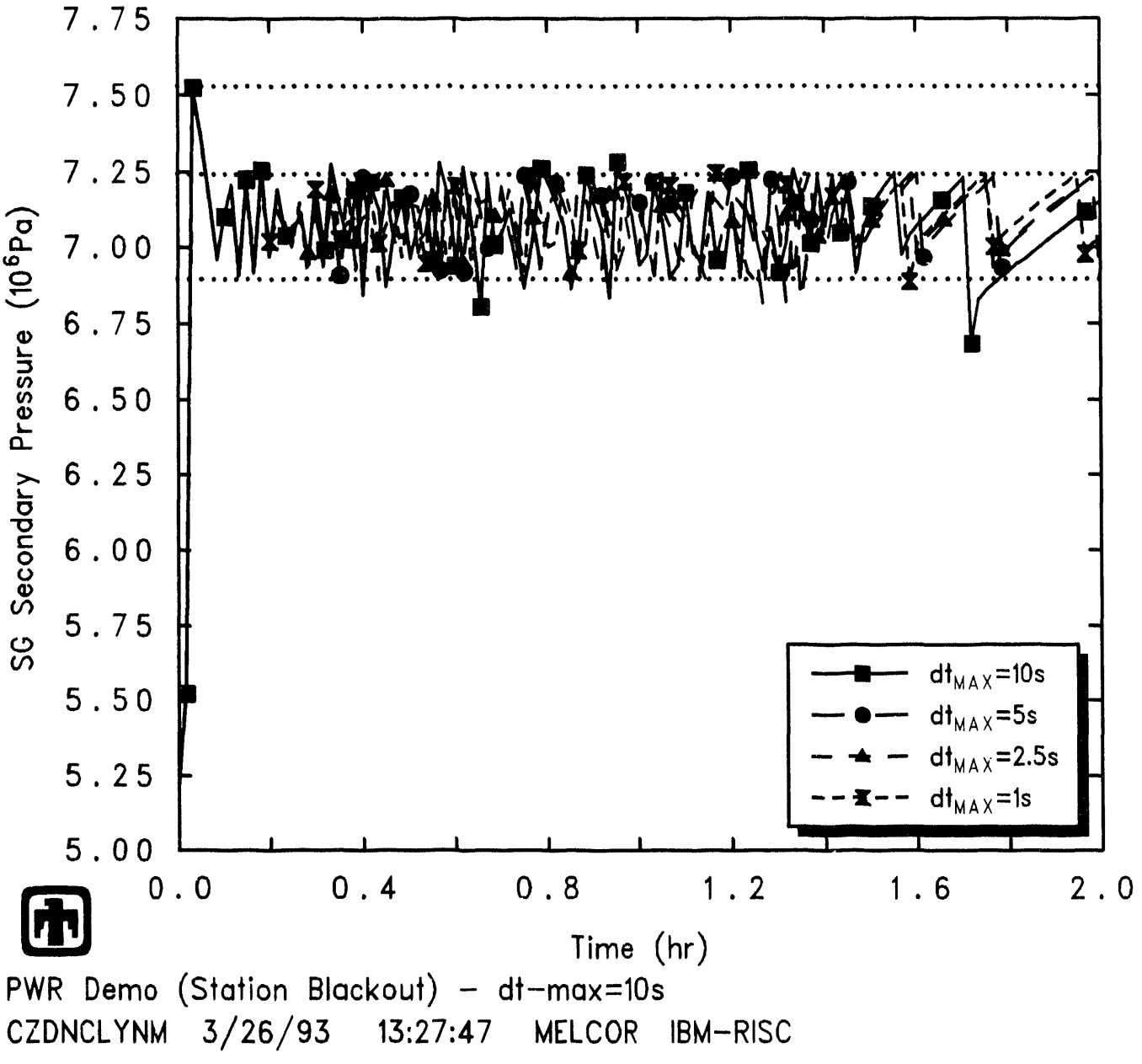

Figure 7.2.1. Early-Time SG Secondary-Side Pressures - Time Step Sensitivity Study

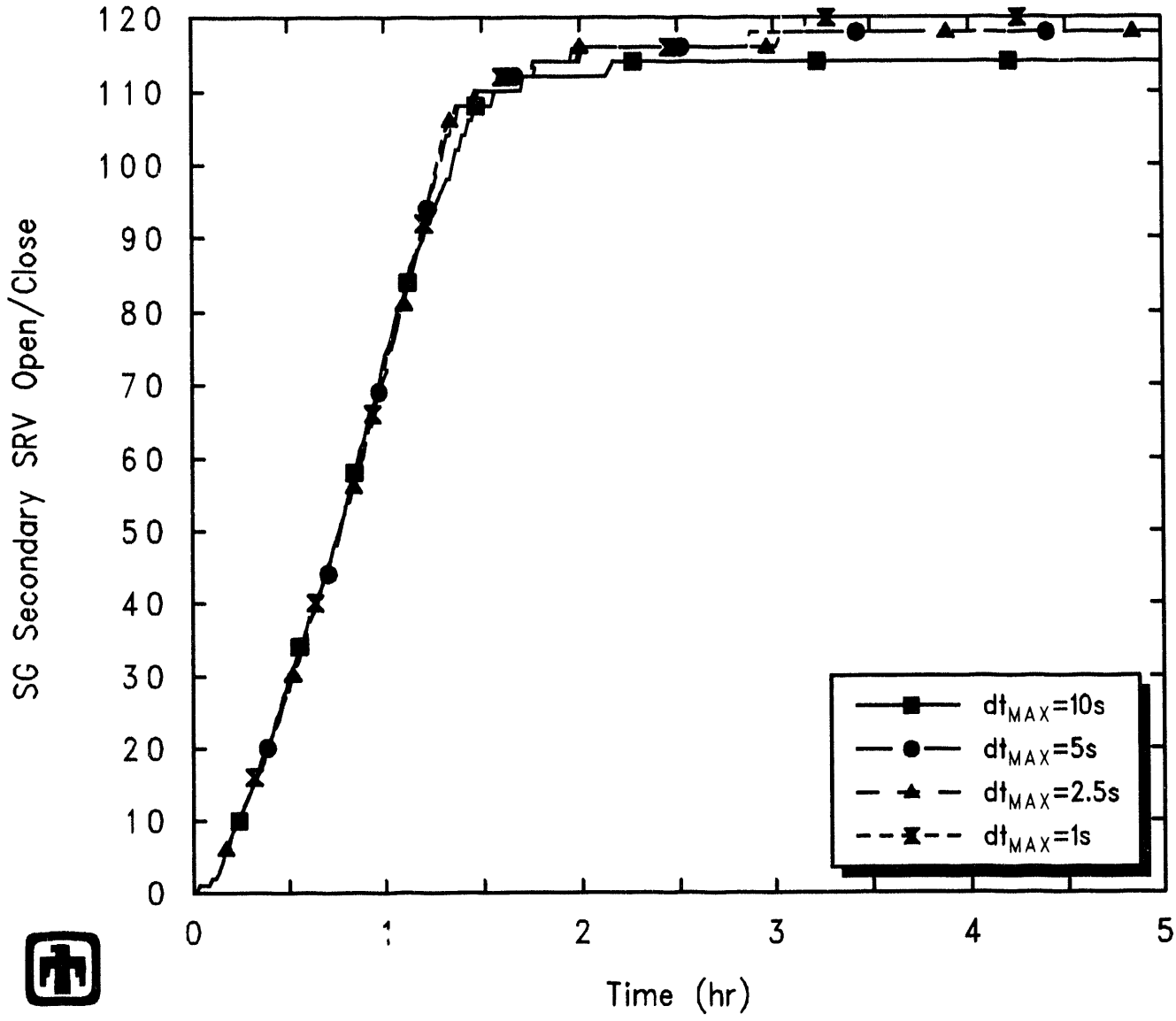

Figure 7.2.2. SG Secondary-Side SRV Cycling - Time Step Sensitivity Study

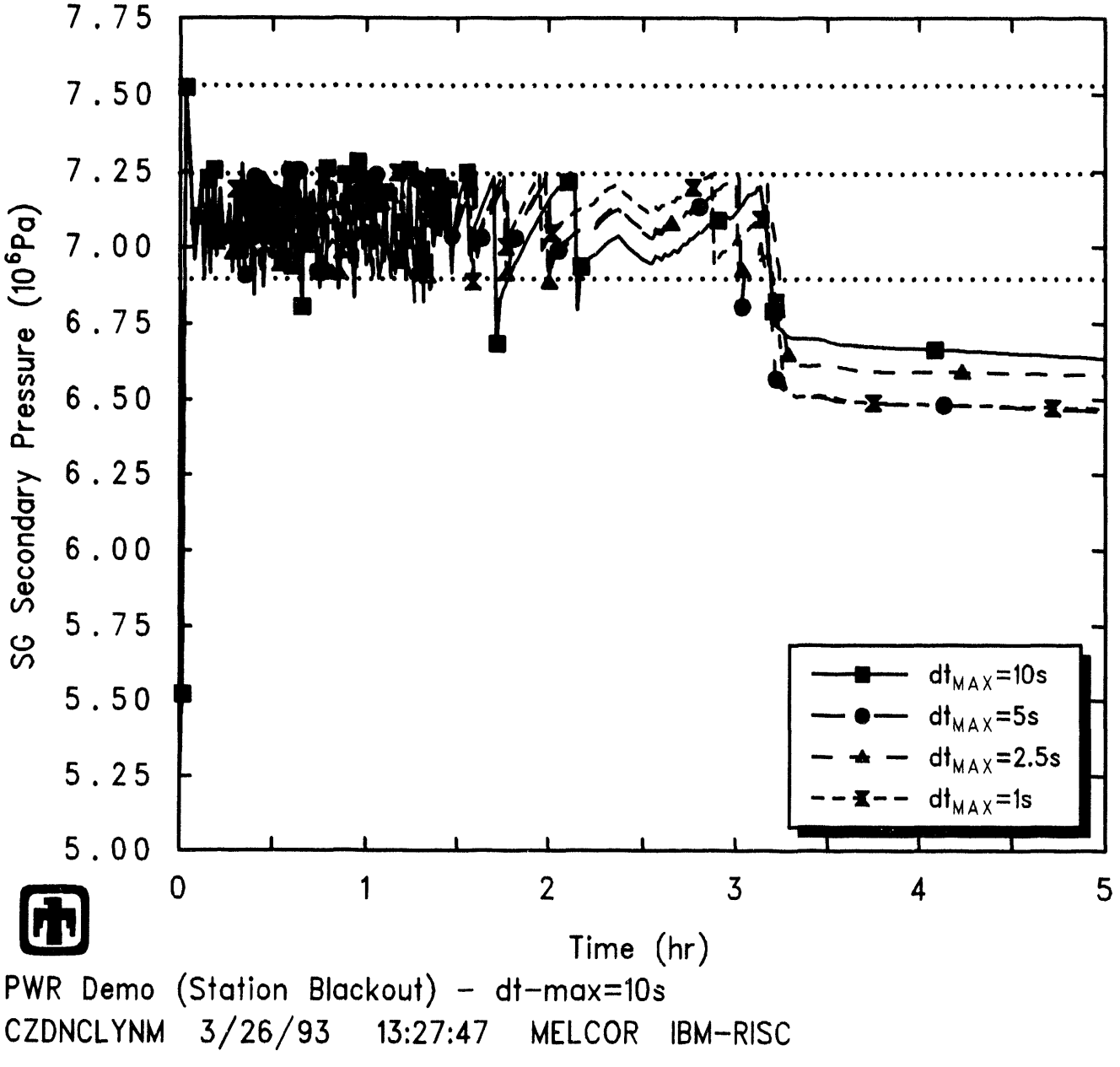

Figure 7.2.3. Later-Time SG Secondary-Side Pressures – Time Step Sensitivity Study

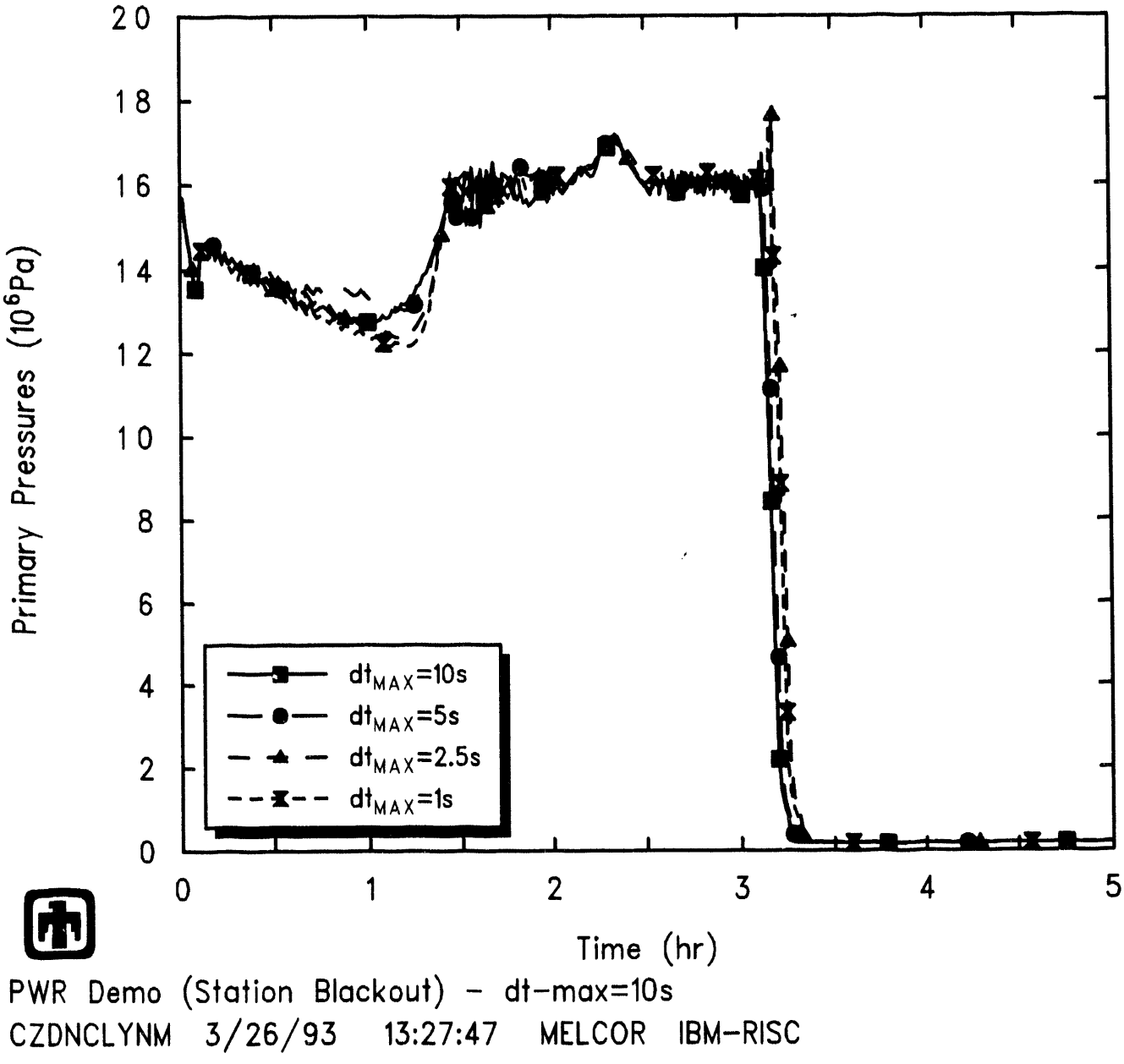

Figure 7.2.4. Vessel Pressures - Time Step Sensitivity Study

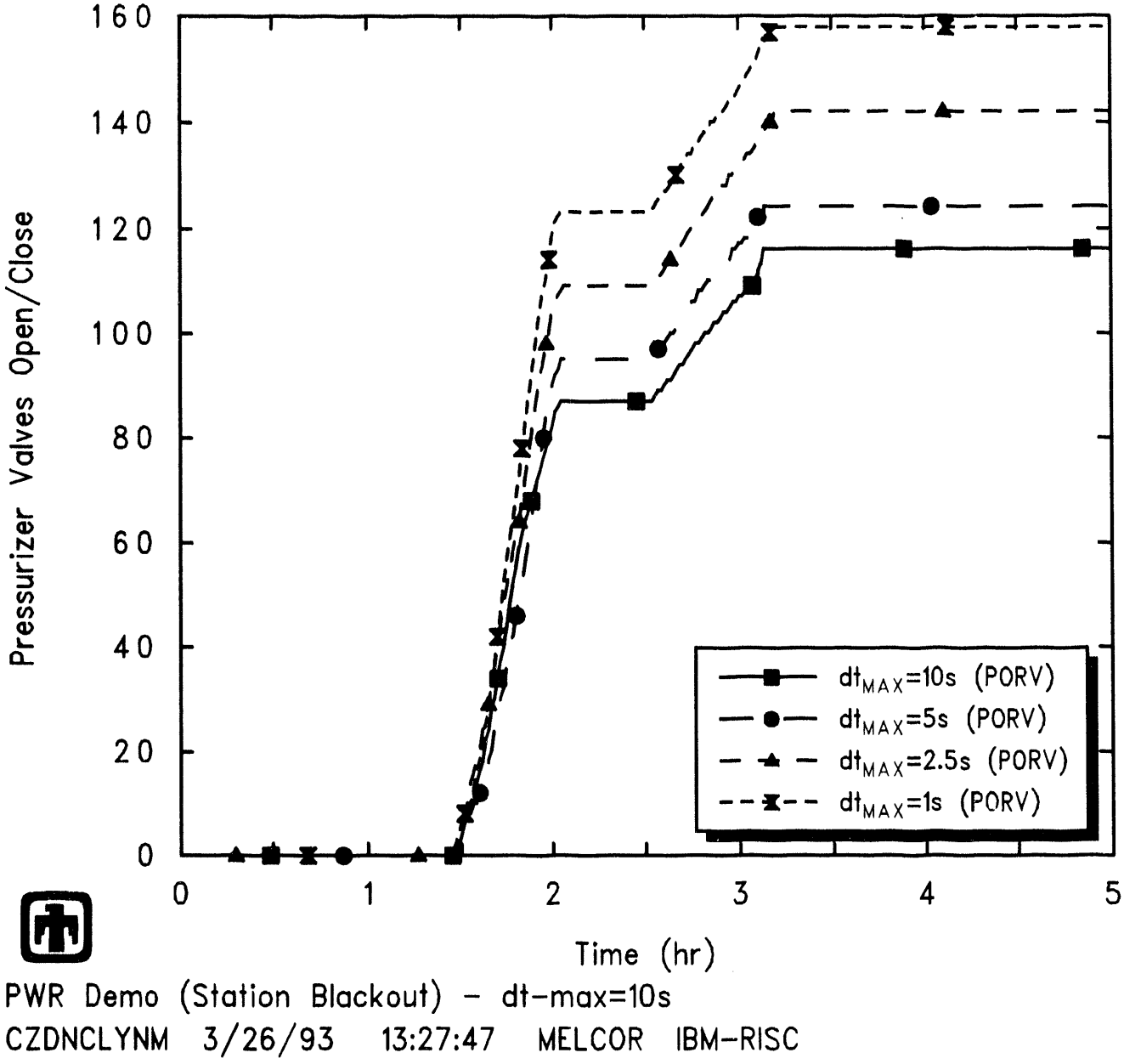

Figure 7.2.5. Pressurizer PORV Cycling – Time Step Sensitivity Study

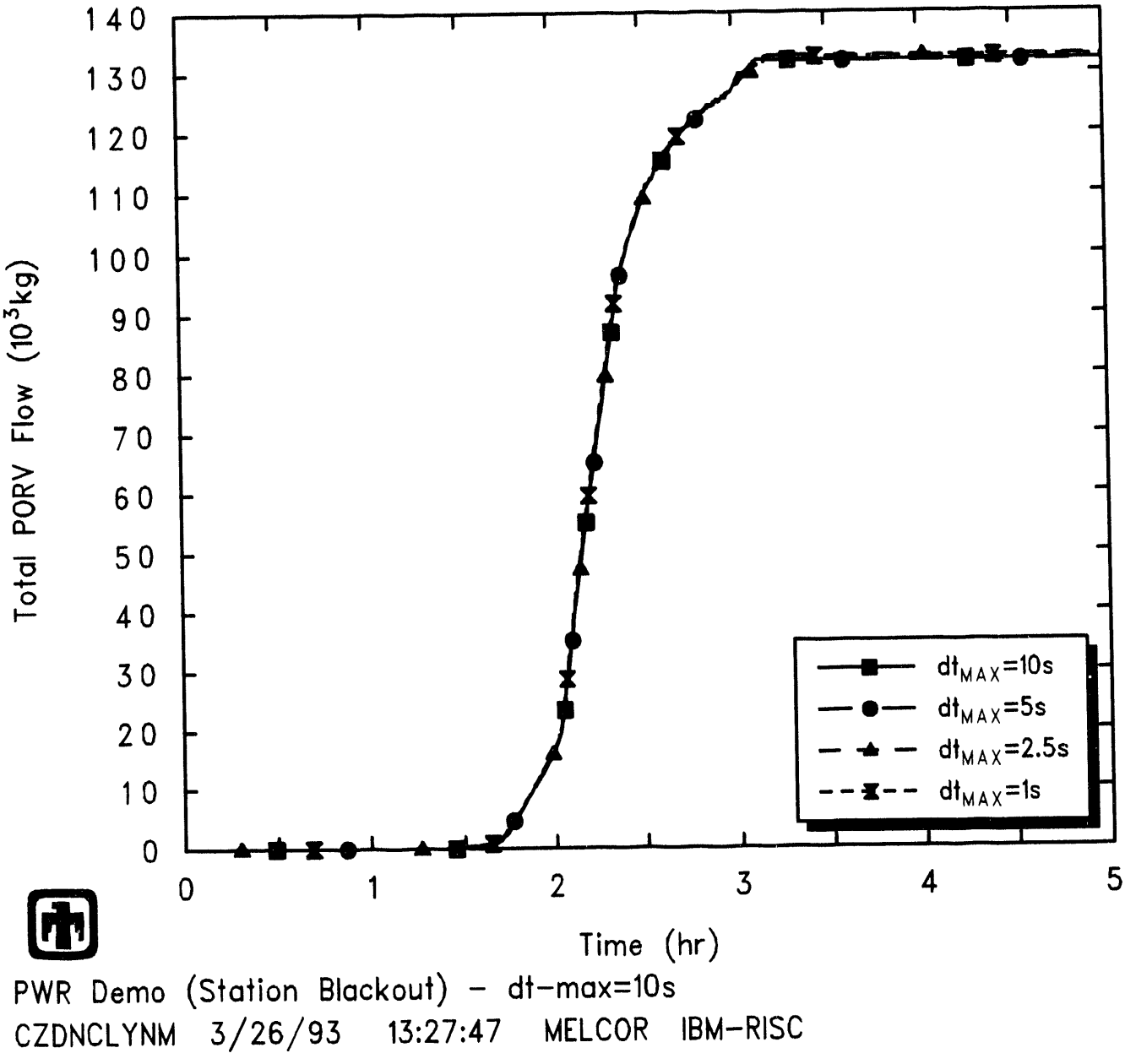

Figure 7.2.6. Pressurizer PORV Integral Flows - Time Step Sensitivity Study

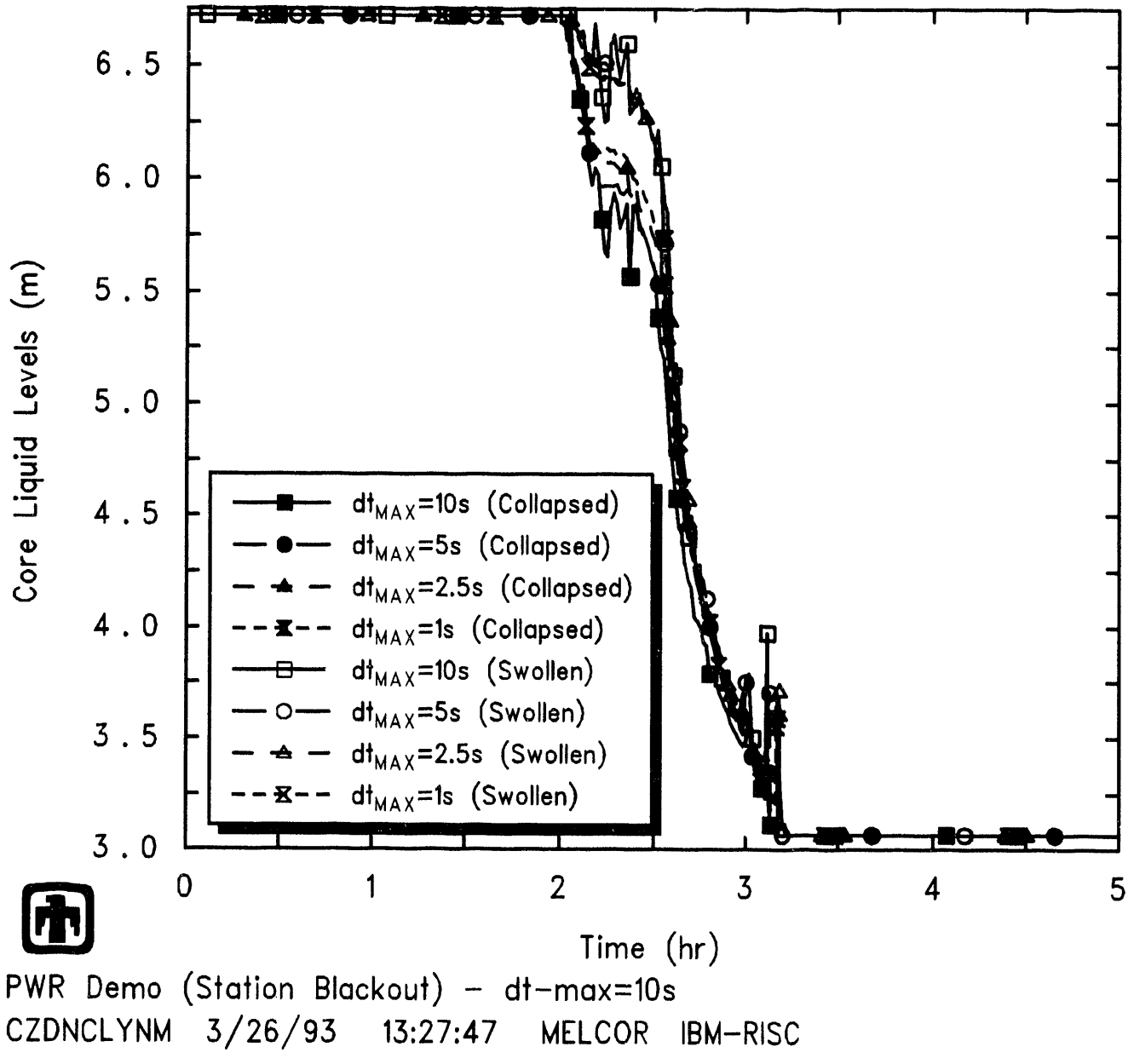

Figure 7.2.7. Core Liquid Levels – Time Step Sensitivity Study

Table 7.2.2. Core State at Vessel Failure – Time Step Sensitivity Study

	MELCOR Δt_{MAX} =			
	10s	5s	2.5s	1s
Lower Plenum Debris Masses (kg)				
UO_2	39,751	40,377	51,139	50,538
Zircaloy	2,450	2,329	3,237	2,644
Zirc Oxide	4,486	4,631	5,500	3,583
Steel	96	99	76	91
Steel Oxide	78	62	85	60
CRP	334	335	334	334
Total	47,195	47,834	60,371	57,249
Average Debris Temperature (K)	~2450	~2450	~2450	~2500
Fraction Material Relocated	~47%	~48%	~60%	~57%
Fraction Oxidized				
Zircaloy	~25%	~26%	~33%	~39%
Steel	~0.3%	~0.3%	~0.3%	~0.3%

remaining in the vessel, as predicted in the various time-step-study calculations. As noted in Table 7.2.1, debris ejection began immediately after lower head failure in all cases. The overall response is quite similar to that observed in our machine-dependency numeric effects sensitivity study (Figures 7.1.8, 7.1.9 and 7.1.10). Almost all of the UO_2 was transferred to the cavity within a short period of time ($\leq$1hr), as was the majority of the unoxidized zircaloy, the associated zirc oxide and the control rod poison, although there are differences visible in how much material was lost in the initial high-pressure melt ejection *vs* how much left the vessel later, in low-pressure melt pours between 5hr and 10hr. Some of the structural steel in the lower plenum (and associated steel oxide) was predicted to remain unmelted and in place even after vessel breach in all cases, although the amount remaining varied from ~85% to ~70% of the steel initially present in the core and lower plenum region.

The total mass of debris in the cavity and the mass of ablated concrete calculated using different maximum allowed time steps are illustrated in Figure 7.2.11, while the mass of core debris in the cavity is basically an inversion of Figure 7.2.8. The range of variation in results was generally small, and similar to that found in our machine-dependency numeric effects sensitivity study (Figure 7.1.11). Before about 24,000s, the debris in the cavity was primarily only debris ejected from the vessel; after ~24,000s significant core-concrete interaction began and substantial masses of ablated and reacted concrete were added to the total cavity debris.

Figures 7.2.12, 7.2.13 and 7.2.14 show the masses and temperatures of the light oxide, metallic and heavy oxide debris layers in the cavity, respectively. In all these time step study calculations, a CORCON layer flip occurred at around 24,000s, switching from an initial configuration with a metallic debris layer above a heavy oxide layer to a later configuration with a light oxide layer above a metallic debris layer. Very little difference was seen in any of the layer temperature histories, or in the masses initially in the heavy-oxide layer and later in the light-oxide layer. There was again a significant difference in the masses of the metallic layer predicted in the calculations with the different user-specified maximum time steps, directly reflecting the differences in predicted retention of lower plenum structural steel in the vessel, as noted in our machine-dependency numeric effects sensitivity study (Figure 7.1.13).

The pressure predicted in the containment dome control volume is given in Figure 7.2.15. There is very little difference visible in the early-time containment response in either magnitude or timing, for any of the cases shown. The offset differences seen at later times in the transient sequence reflect different times needed to boil off water in the cavity, switching from more rapid containment pressurization due to that steam generation to a slower pressurization due primarily to continued core-concrete interaction; the range in times at which the cavity water disappeared in turn reflects different amounts of core debris transferred to the cavity from the vessel.

The temperature behavior of the containment atmosphere was very similar to that of the pressure. Most of the containment remained saturated, except for the cavity. Slightly different temperature spikes in the cavity reflect the differences in hydrogen deflagrations in the cavity noted in Table 7.2.1, and the temperature of the cavity atmosphere even-

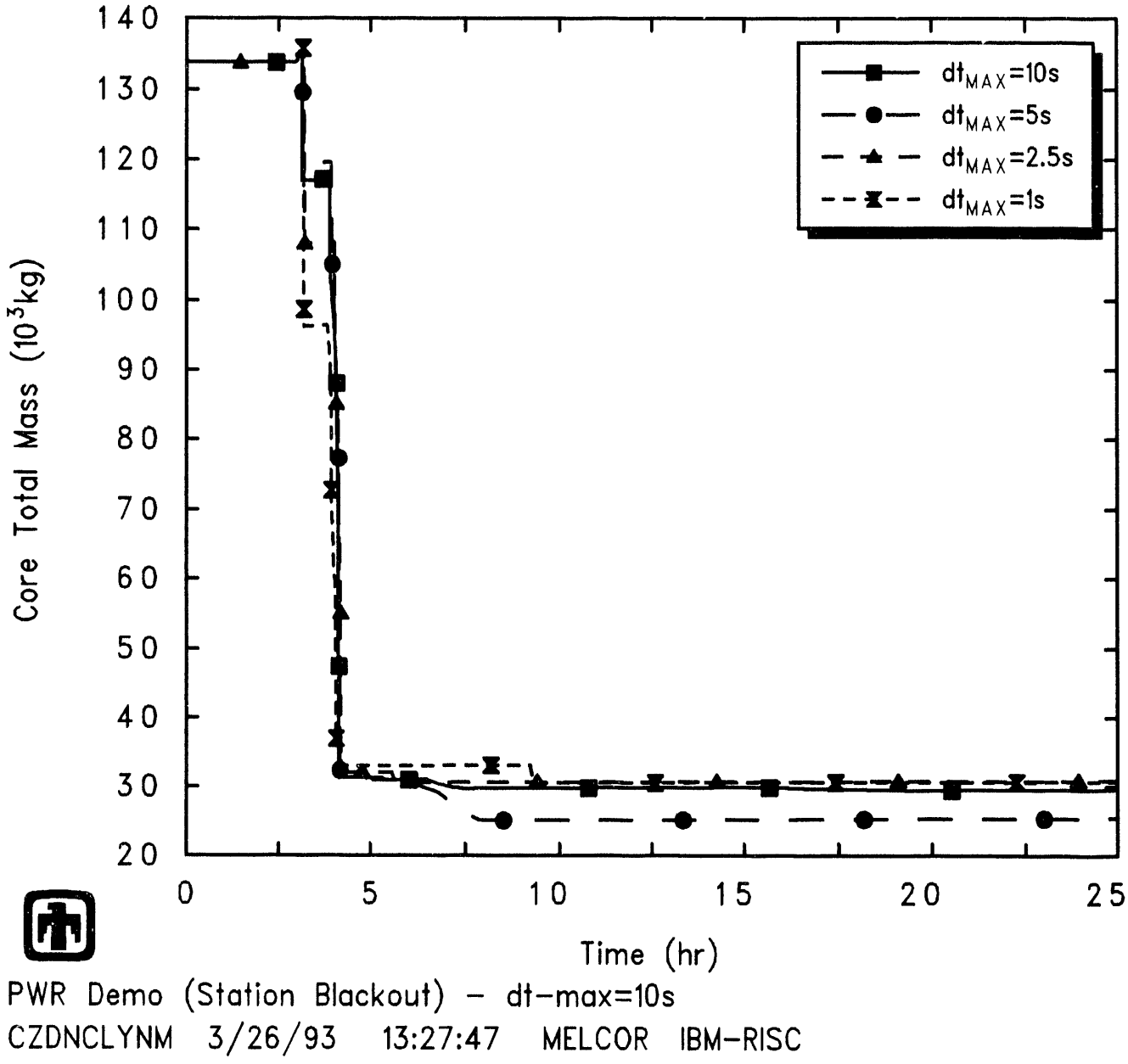

Figure 7.2.8. Total Core Masses – Time Step Sensitivity Study

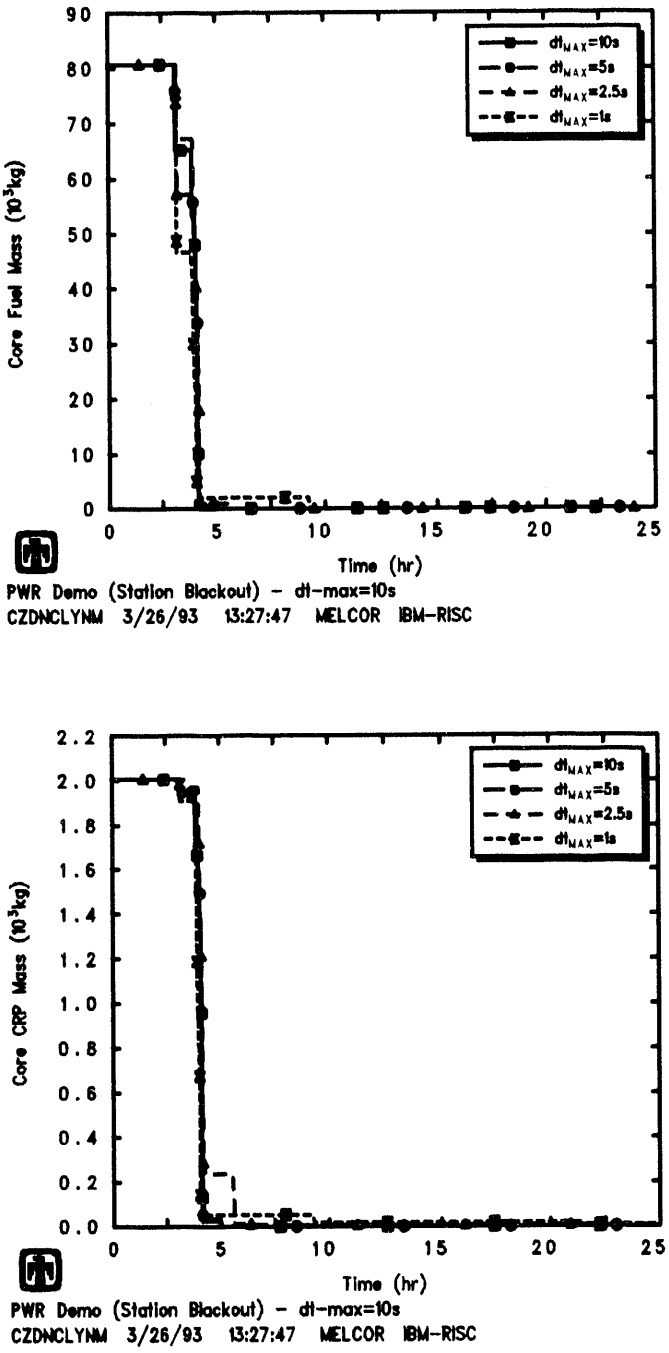

Figure 7.2.9. Total Fuel (top) and Control Rod Poison (bottom) Core Masses - Time Step Sensitivity Study

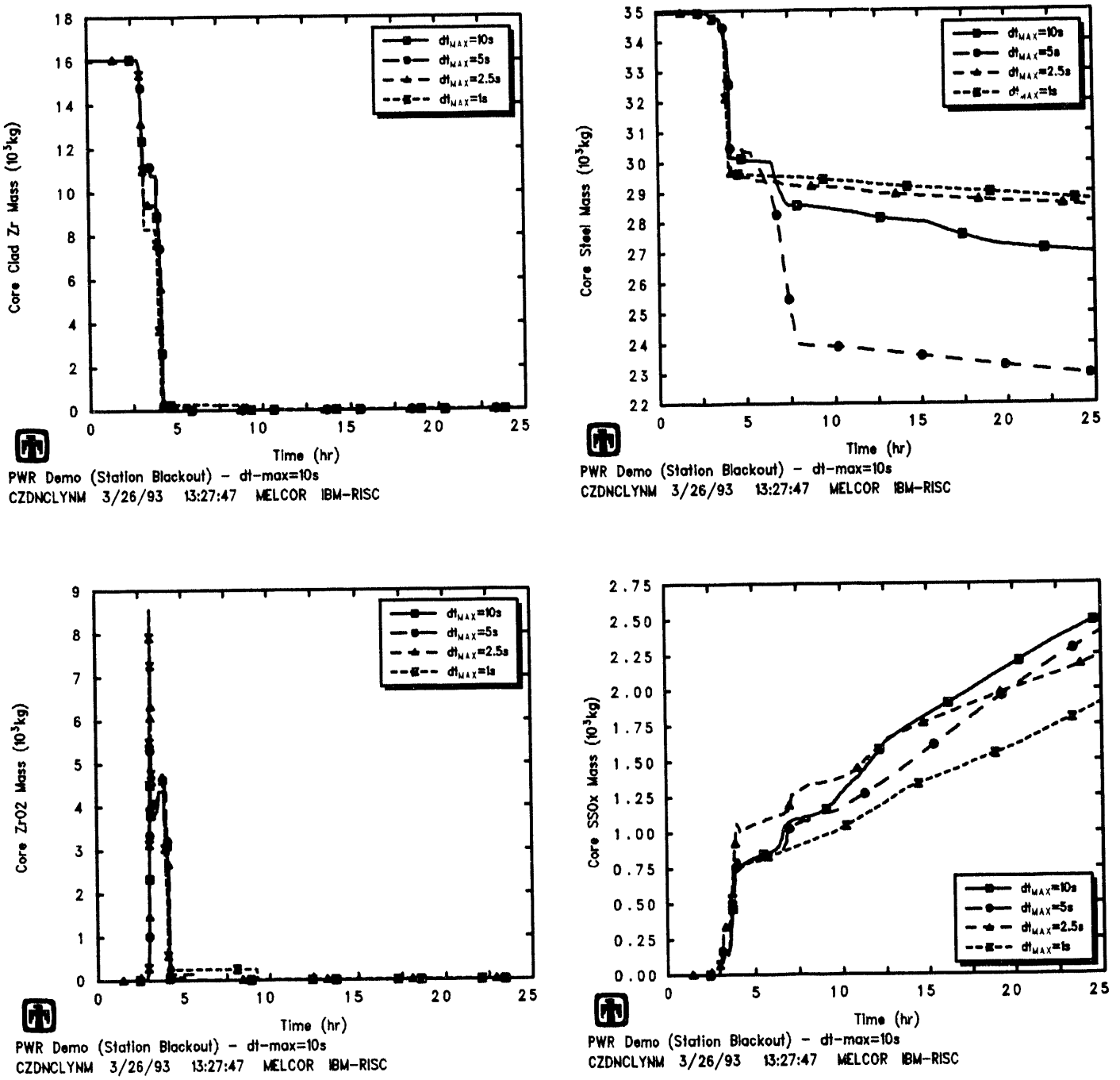

Figure 7.2.10. Total Zircaloy (upper left), Zirc Oxide (lower left), Stainless Steel (upper right) and Steel Oxide (lower right) Core Masses – Time Step Sensitivity Study

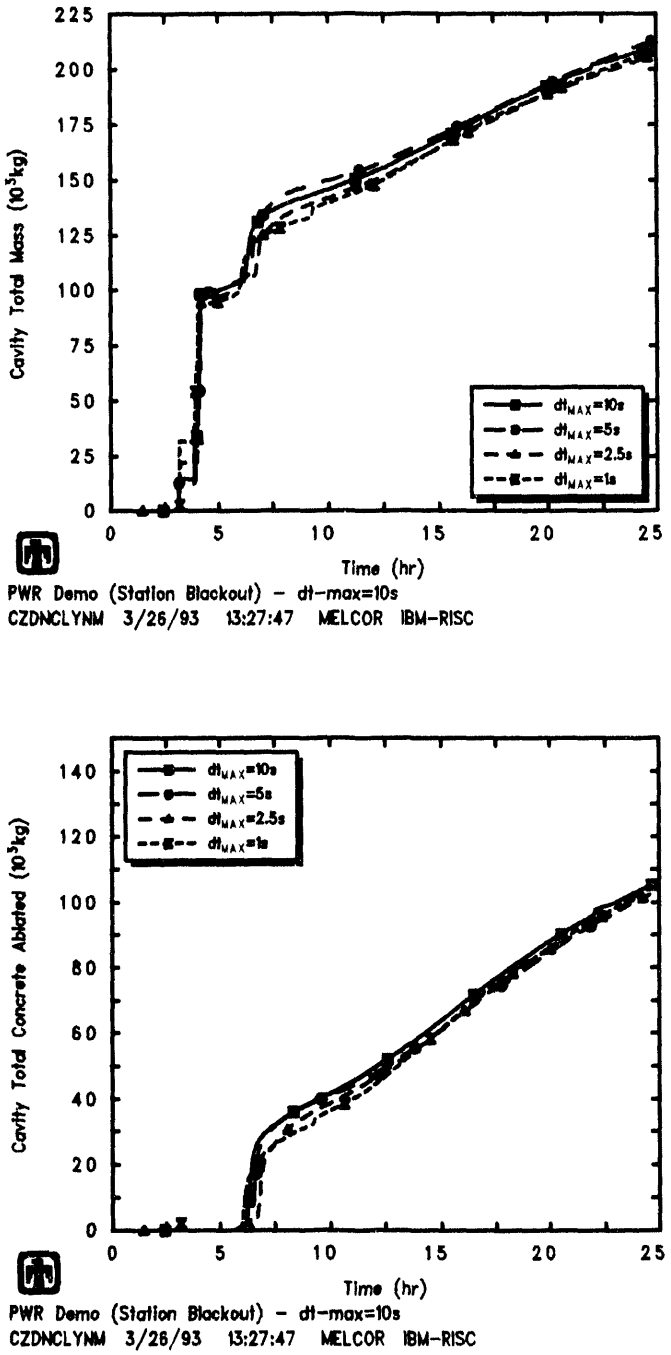

Figure 7.2.11. Total Cavity Masses (top) and Ablated Concrete Masses (bottom) - Time Step Sensitivity Study

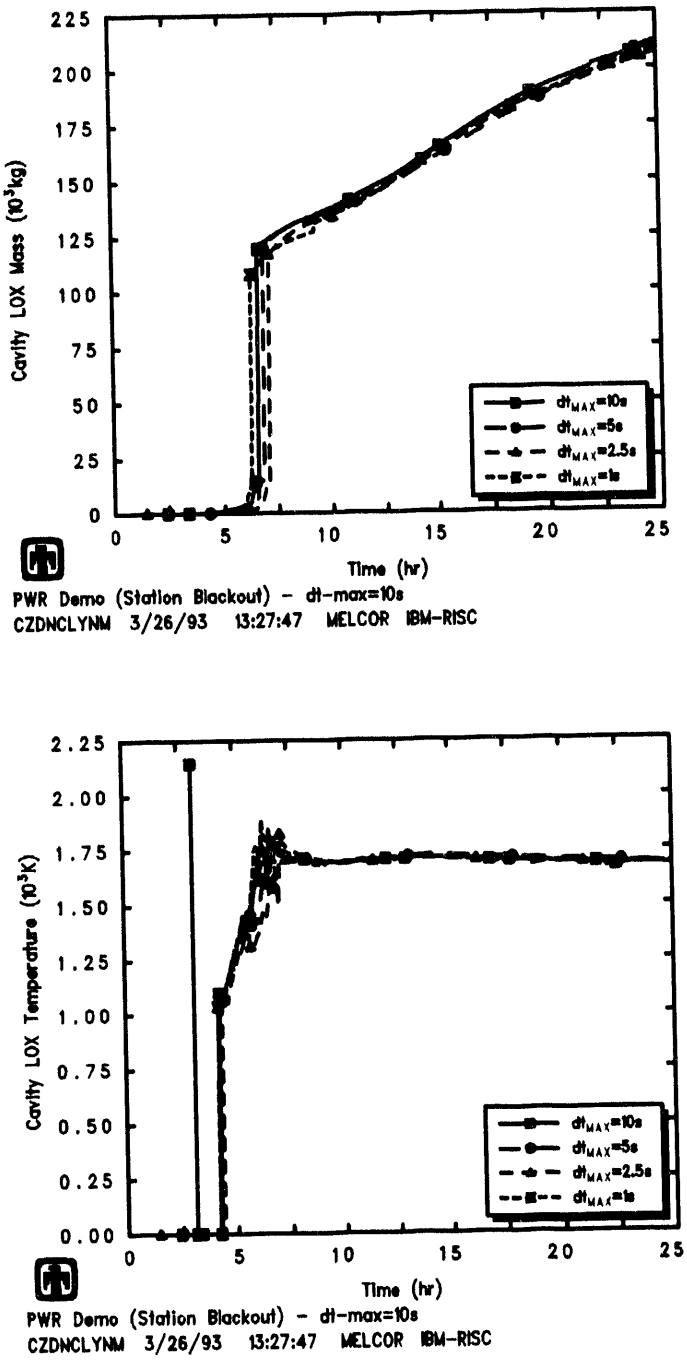

Figure 7.2.12. Cavity Light-Oxide Layer Masses (top) and Temperatures (bottom) – Time Step Sensitivity Study

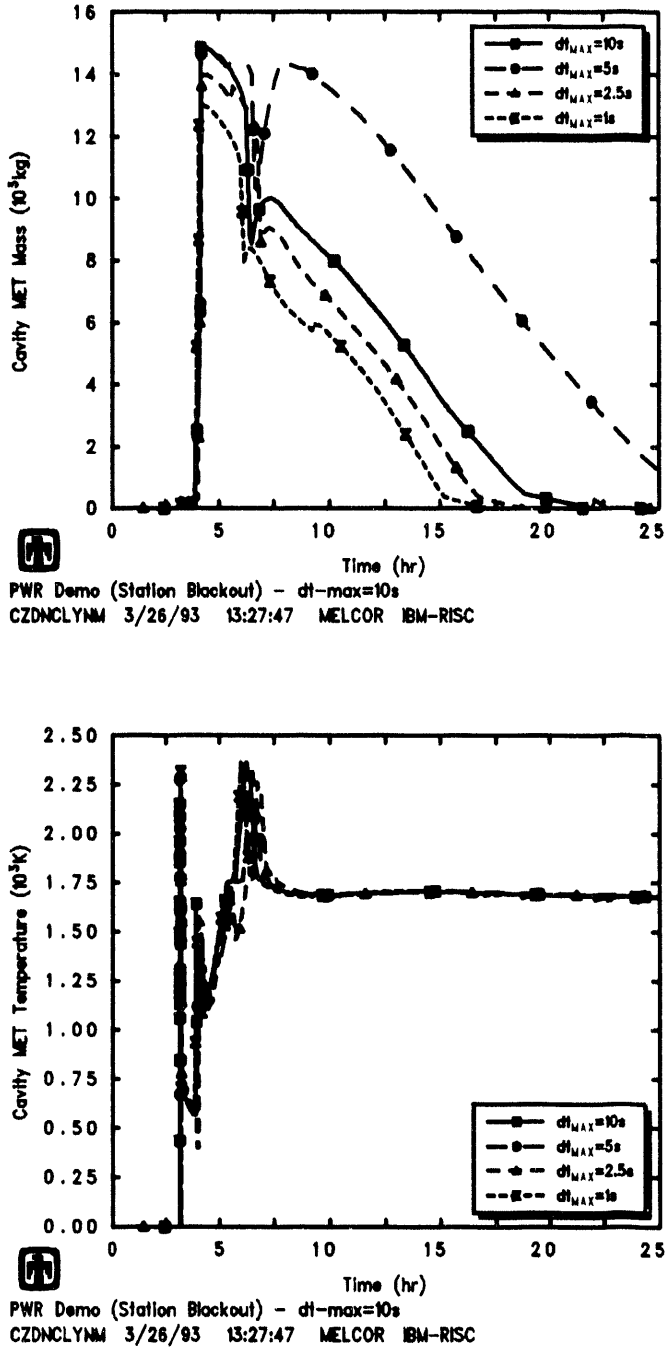

Figure 7.2.13. Cavity Metallic Layer Masses (top) and Temperatures (bottom) – Time Step Sensitivity Study

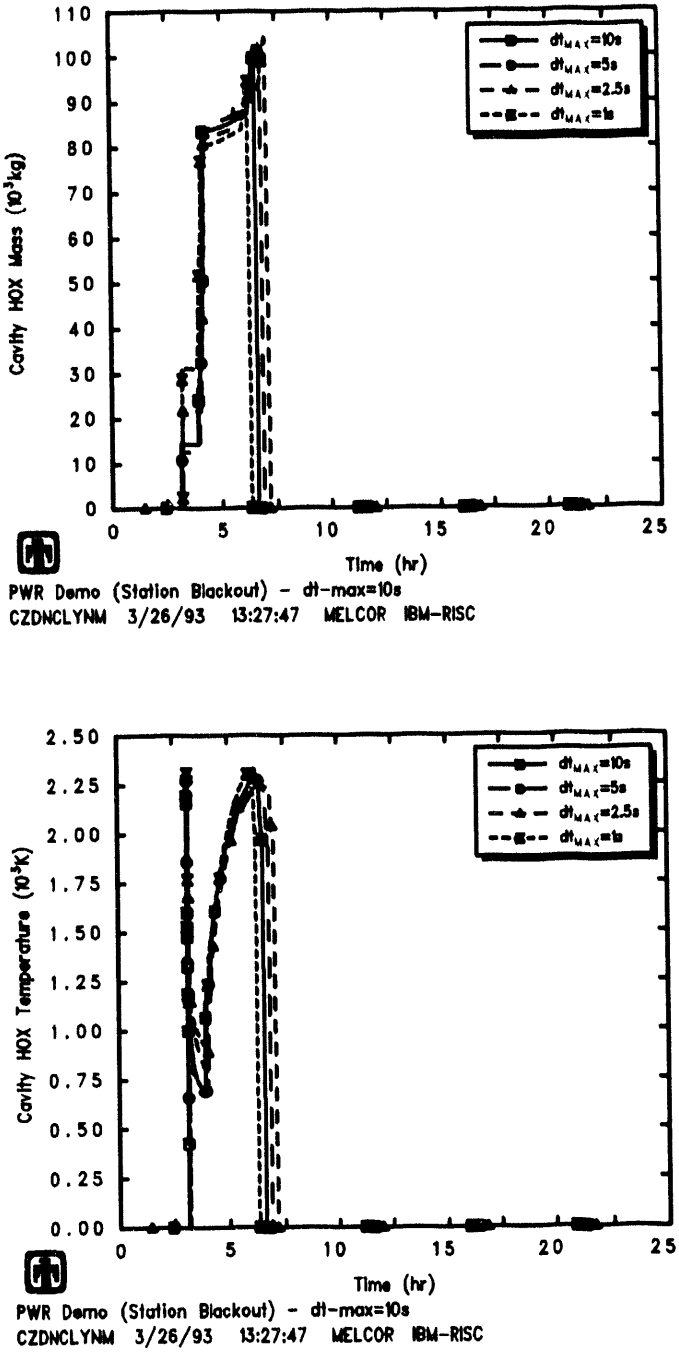

Figure 7.2.14. Cavity Heavy-Oxide Layer Masses (top) and Temperatures (bottom) – Time Step Sensitivity Study

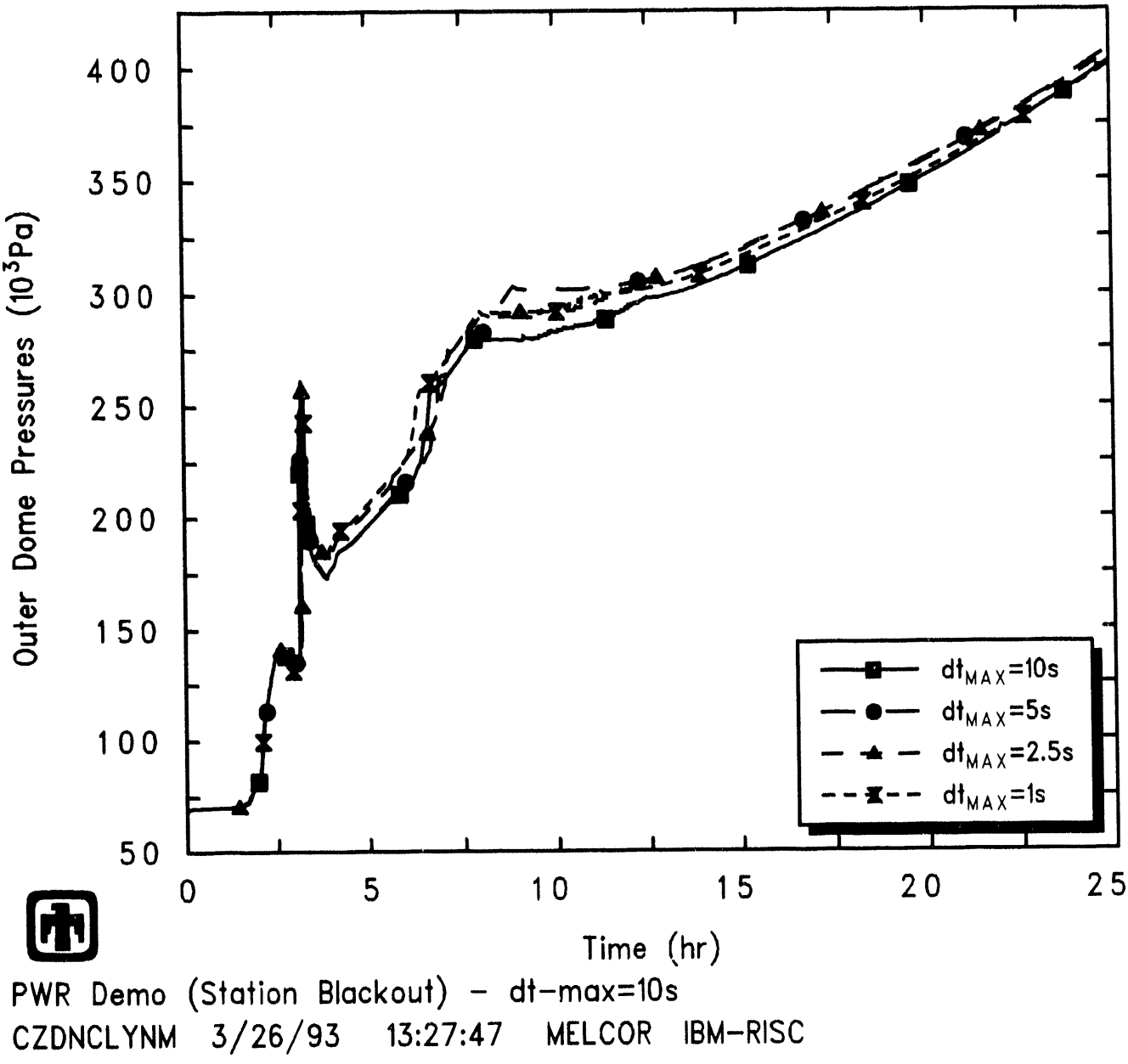

Figure 7.2.15. Containment Pressures - Time Step Sensitivity Study

tually rose to that of the core debris materials at slightly different times, reflecting the different times when all the water in the cavity has boiled off.

Figure 7.2.16 shows the number and timing of hydrogen burns in the cavity, and the amount of hydrogen burned, in these various calculations; no hydrogen burns occurred in the containment outside the cavity during any of these calculations, because the rest of containment generally remained inerted after the first ~3hr. As found in our machine-dependency numeric effects sensitivity study (Table 7.1.1), one of the biggest timing differences seen in this time-step sensitivity study was in hydrogen deflagrations occurring in the cavity. All four time-step-study calculations showed one set of hydrogen burns initially occurring ≤0.5hr after vessel breach and the start of core-concrete interaction. One calculation showed a single hydrogen burn at ~30,000s; the other three time-step-study calculations showed a second set of multiple hydrogen burns occurring later in the transient, but the timing and extent of that later burn period differed substantially among these various cases. As found for our machine-dependency numerics study (Figure 7.1.16), the amount of hydrogen burned generally tended to reflect the number of deflagrations occurring in these various time-step sensitivity study calculations.

Figures 7.2.17 through 7.2.19 show mole fractions in the cavity control volume atmosphere as calculated on an IBM RISC-6000 Model 550 workstation with different user-specified maximum time steps, compared to the default ignition limits used in MELCOR. Figure 7.2.17 presents a combined equivalent mole fraction of H_2 and CO (equal to $x_{H_2} + \frac{0.10}{0.167} x_{CO}$), which must be greater than 0.10 for detonation in the absence of igniters [34]. Figure 7.2.18 presents the O_2 mole fraction which must be greater than 0.05 for detonation in the absence of igniters [34]. Figure 7.2.19 presents a combined total mole fraction of H_2O and CO_2, which must be less than 0.55 for the mixture to not be assumed inert [34]. (Corresponding results for the machine-dependency study calculations were given in Figures 7.1.17 through 7.1.19).

The first period of hydrogen combustion occurred in all four time-step sensitivity study calculations between ≥12,860s (≥3.5hr) and ≤14,100s (≤3.9hr); the timing was similar for all four cases, as were the number and total mass of hydrogen burned. For a user-specified maximum time step of 5s, a single burn was predicted just after ~29,160s (8hr); the mole fraction plots indicate that this burn corresponded to a spike up in combined H_2 and CO concentration, and in O_2 also, with a simultaneous spike down in total H_2O plus CO_2 concentration. The combined H_2 and CO concentration and the O_2 concentration both easily exceeded their ignition limits; the ignition was controlled by whether the total H_2O plus CO_2 concentration was reduced to below the inerting limit.

A later, prolonged series of combustion events was seen in the other three time-step sensitivity study calculations which did not show that single burn at ~29,160s (8hr); in the calculation with a user-specified maximum time step of 5s and a single burn just after ~29,160s (8hr), a third, small series of combustion events was predicted between ~47,200s (13.1hr) and ~47,750s (13.3hr).

Figures 7.2.17 through 7.2.19) show that in all cases the combined H_2 and CO concentration and the O_2 concentration both easily exceeded their ignition limits throughout

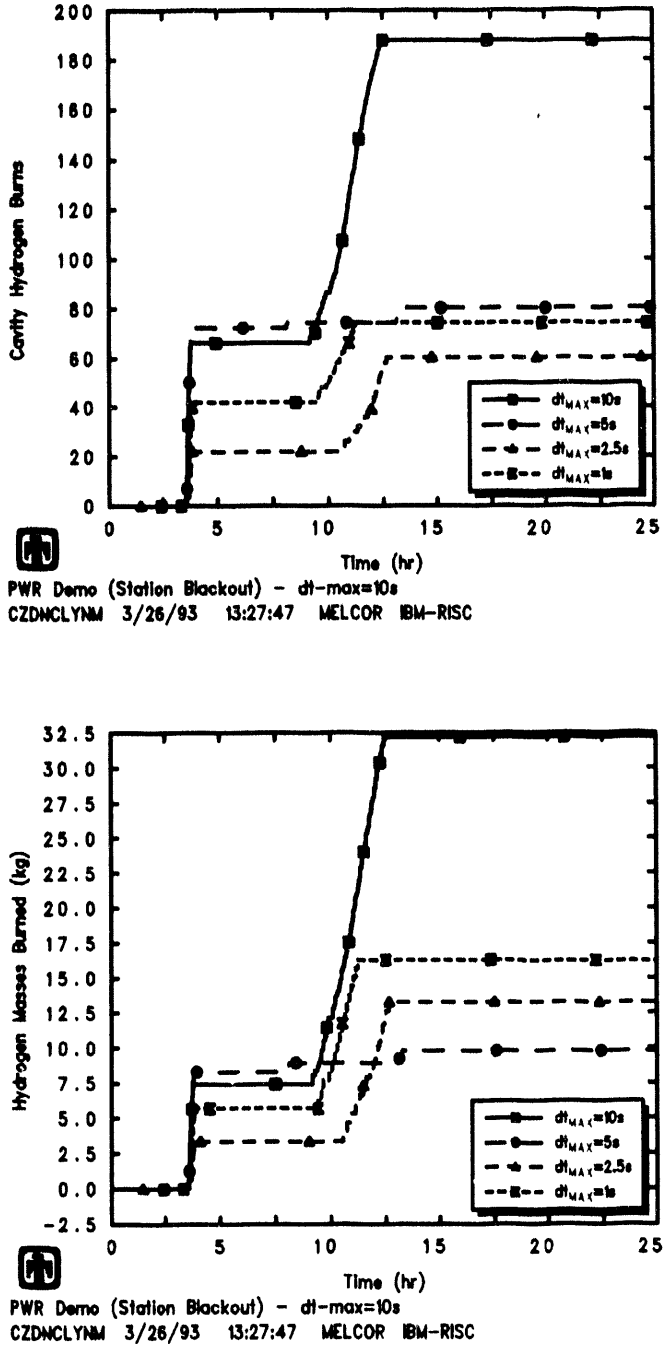

Figure 7.2.16. Number of (top) and Masses Burned in (bottom) Cavity Hydrogen Deflagrations – Time Step Sensitivity Study

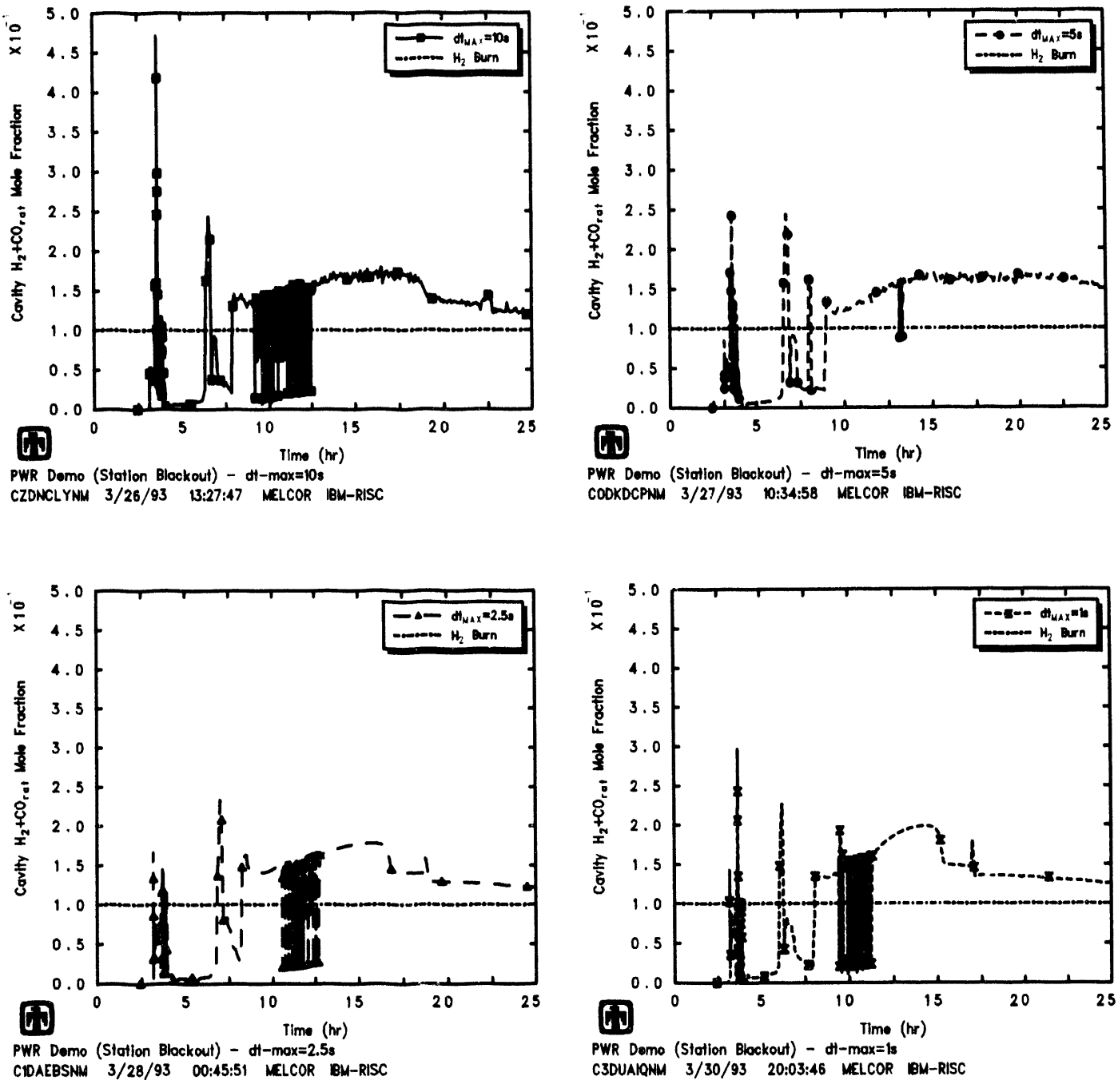

Figure 7.2.17. Combined H_2 and CO Mole Fraction in Cavity Calculated on IBM RISC-6000 Model 550 with Δt_{MAX}=10s (upper left), Δt_{MAX}=5s (upper right), Δt_{MAX}=2.5s (lower left), and Δt_{MAX}=1s (lower right) - Time Step Sensitivity Study

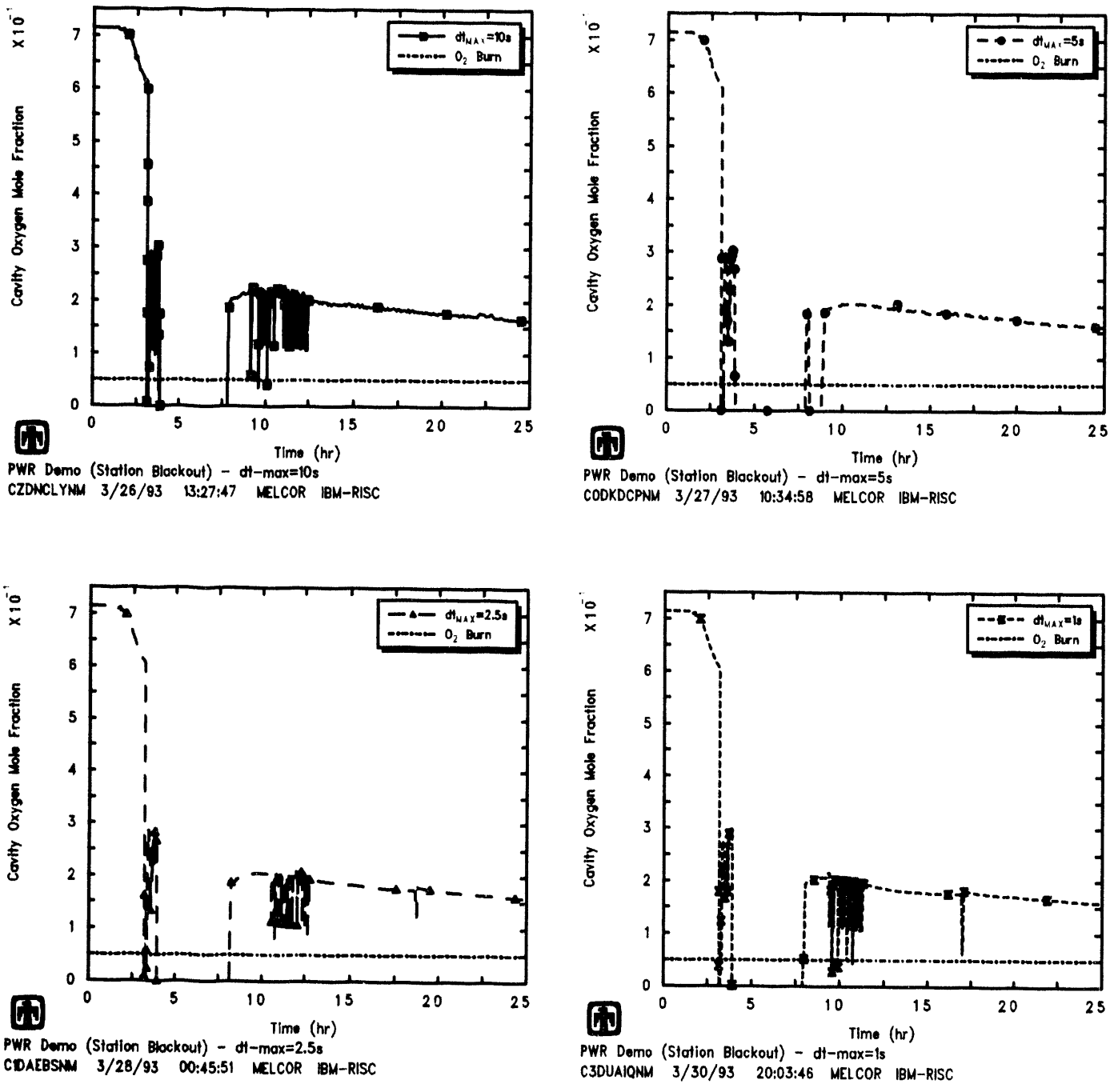

Figure 7.2.18. O_2 Mole Fraction in Cavity Calculated on IBM RISC-6000 Model 550 with Δt_{MAX}=10s (upper left), Δt_{MAX}=5s (upper right), Δt_{MAX}=2.5s (lower left), and Δt_{MAX}=1s (lower right) Time Step Sensitivity Study

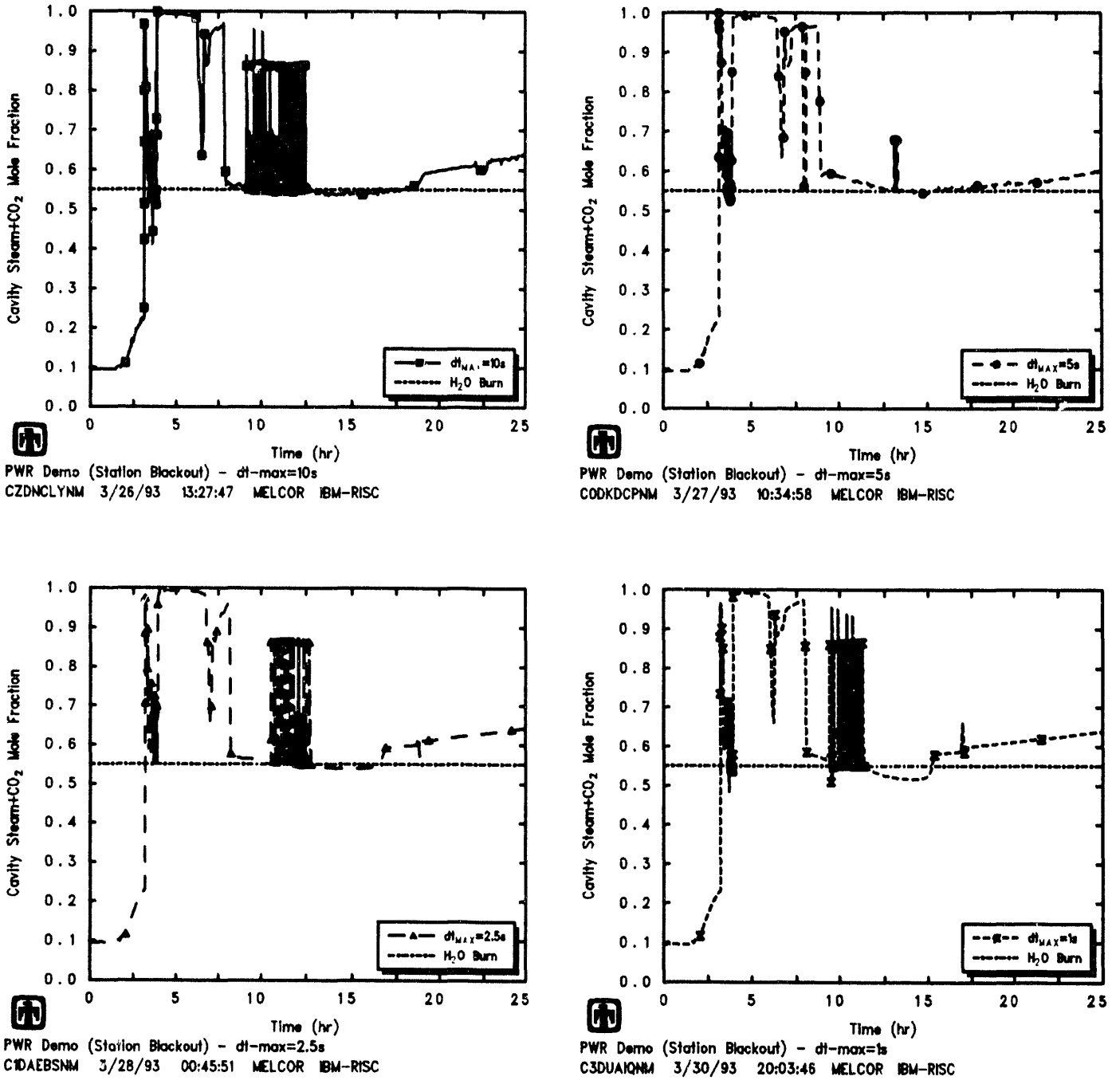

Figure 7.2.19. Combined H_2O and CO_2 Mole Fraction in Cavity Calculated on IBM RISC-6000 Model 550 with Δt_{MAX}=10s (upper left), Δt_{MAX}=5s (upper right), Δt_{MAX}=2.5s (lower left), and Δt_{MAX}=1s (lower right) – Time Step Sensitivity Study

most of the later portions of the transient, after ~8-9hr; the combustion ignition at later times again seemed controlled by whether the total H_2O plus CO_2 concentration was reduced to below the inerting limit. Figure 7.2.19) illustrates how closely all the calculations approached the inerting limit for a long period of time between >12.5hr and <17.5hr. It is clear from Figure 7.2.19) that the potential for a prolonged period of hydrogen burn existed in all cases later in the transient, and it is not clear from Figure 7.2.19) why combustion was not predicted in more of the cases during that time (especially for the calculation done with Δt_{MAX}=1s, which appears to remain significantly below the inert concentration limit for 2-3hr after combustion was predicted to end).

The final amounts of each radionuclide class released by the end of the calculated transient period (90,000s or 25hr) in-vessel (in both the core active-fuel region and in the lower plenum), ex-vessel (in the cavity) and overall are given in Tables 7.2.3, 7.2.4 and 7.2.5, respectively, for analyses using different maximum allowed time steps; these releases are expressed as percent of inventory initially present in the core. (Note that these amounts include only the release of radioactive forms of these classes, and not additional releases of nonradioactive aerosols from structural materials.)

As for the ex-vessel source terms for the machine-dependency sensitivity study analyses given in Table 7.1.4 and Figure 7.1.20, the ex-vessel source terms given in Table 7.2.4 for these time-step sensitivity study calculations were affected by the different amounts of structural steel retained in the lower plenum and by the resulting differences in the size and eventual disappearance of the metallic debris layer, for reasons discussed in detail in Section 6.4. In summary, the VANESA code [22], which is used to calculate ex-vessel releases in MELCOR, has no provision for a disappearing metallic layer; therefore, as the metallic layer in the cavity goes to zero, the releases of radionuclide species associated with that layer (*i.e.*, Te, Ru, Cd, and Sn) can begin growing exponentially, as shown in Figure 7.2.20 for several of these radionuclide species. The effect was not pronounced for Te, because most of that species mass had been released prior to the metallic layer vanishing, and also was not pronounced for Ru, because very little of that species mass was released at all; however, the release of other species, such as Cd and Sn, is significantly in error. As noted in Section 6.4, this problem is inherent in the VANESA formulation itself, not in MELCOR, but is more likely to be encountered with MELCOR 1.8.2 than with MELCOR 1.8.1 because of the increased likelihood of more retention of lower plenum structural steel in-vessel.

Figure 7.2.21 and 7.2.22 present run times and time step histories, respectively, for calculations using different allowed maximum time steps. There was generally little difference in overall run time required as the maximum allowed time step was reduced from 10s to 2.5s, but there was a substantial time penalty when the maximum allowed time step is reduced further, to 1s (Figure 7.2.21); with the larger allowed time steps, the code spent a greater fraction of time simply running at its own, internally determined time step (Figure 7.2.22).

Table 7.2.3. In-Vessel Source Terms – Time Step Sensitivity Study

Class	Radionuclide Release (% Initial Inventory) MELCOR Δt_{MAX} = 10s	5s	2.5s	1s
<u>In-Core</u>				
1 (Xe)	47.910	47.992	59.633	66.780
2 (Cs)	47.892	47.973	59.603	66.785
3 (Ba)	4.1330	4.1926	10.195	10.782
4 (I)	47.871	47.946	59.592	66.770
5 (Te)	3.2899	3.3993	8.3613	8.5798
6 (Ru)	0.1596	0.1606	0.4080	0.4332
7 (Mo)	1.6993	1.7548	3.8290	4.1837
8 (Ce)	0.0034	0.0034	0.0079	0.0088
9 (La)	0.0109	0.0114	0.0522	0.0410
10 (U)	0.0112	0.0116	0.0535	0.0412
11 (Cd)	14.898	15.137	32.431	35.094
12 (Sn)	14.896	15.131	32.428	35.093
<u>In LP</u>				
1 (Xe)	12.409	17.457	10.840	7.1559
2 (Cs)	12.547	17.581	10.949	7.2531
3 (Ba)	3.0679	3.6730	2.5027	3.0436
4 (I)	12.413	17.468	10.849	7.1578
5 (Te)	2.6940	3.2885	2.2865	2.6009
6 (Ru)	0.1169	0.1389	0.1020	0.1211
7 (Mo)	1.3373	1.7010	1.1903	1.3267
8 (Ce)	0.0024	0.0029	0.0021	0.0023
9 (La)	0.0349	0.0354	0.0308	0.0460
10 (U)	0.0368	0.0375	0.0321	0.0477
11 (Cd)	10.195	11.727	6.5536	9.0903
12 (Sn)	10.195	11.727	6.5547	9.0917

Table 7.2.4. Ex-Vessel Source Terms – Time Step Sensitivity Study

Class	Radionuclide Release (% Initial Inventory) MELCOR Δt_{MAX} = 10s	5s	2.5s	1s
1 (Xe)	38.937	34.027	28.771	25.581
2 (Cs)	41.817	36.533	30.897	27.460
3 (Ba)	30.585	28.211	24.468	25.213
4 (I)	0.0	0.0	0.0	0.0
5 (Te)	84.122	64.523	82.911	83.191
6 (Ru)	4×10^{-6}	2×10^{-6}	2×10^{-6}	4×10^{-6}
7 (Mo)	2.2436	1.9350	2.0304	1.9434
8 (Ce)	0.0010	0.0010	0.0010	0.0011
9 (La)	0.2845	0.2083	0.1308	0.2261
10 (U)	0.0024	0.0019	0.0020	0.0026
11 (Cd)	2.7877	0.7284	3.4324	3.4478
12 (Sn)	27.097	6.1105	32.008	33.637

Table 7.2.5. Total Source Terms – Time Step Sensitivity Study

Class	Radionuclide Release (% Initial Inventory) MELCOR Δt_{MAX} = 10s	5s	2.5s	1s
1 (Xe)	99.256	99.476	99.244	99.517
2 (Cs)	102.26	102.09	101.45	101.50
3 (Ba)	37.786	36.077	37.166	39.039
4 (I)	60.284	65.414	70.440	73.928
5 (Te)	90.106	71.211	93.569	94.371
6 (Ru)	0.2765	0.2994	0.5099	0.5543
7 (Mo)	5.2802	5.3908	7.0497	7.4537
8 (Ce)	0.0067	0.0072	0.0110	0.0122
9 (La)	0.3303	0.2551	0.2138	0.3131
10 (U)	0.0503	0.0510	0.0876	0.0915
11 (Cd)	27.881	27.592	42.417	47.633
12 (Sn)	52.188	32.968	70.991	77.822

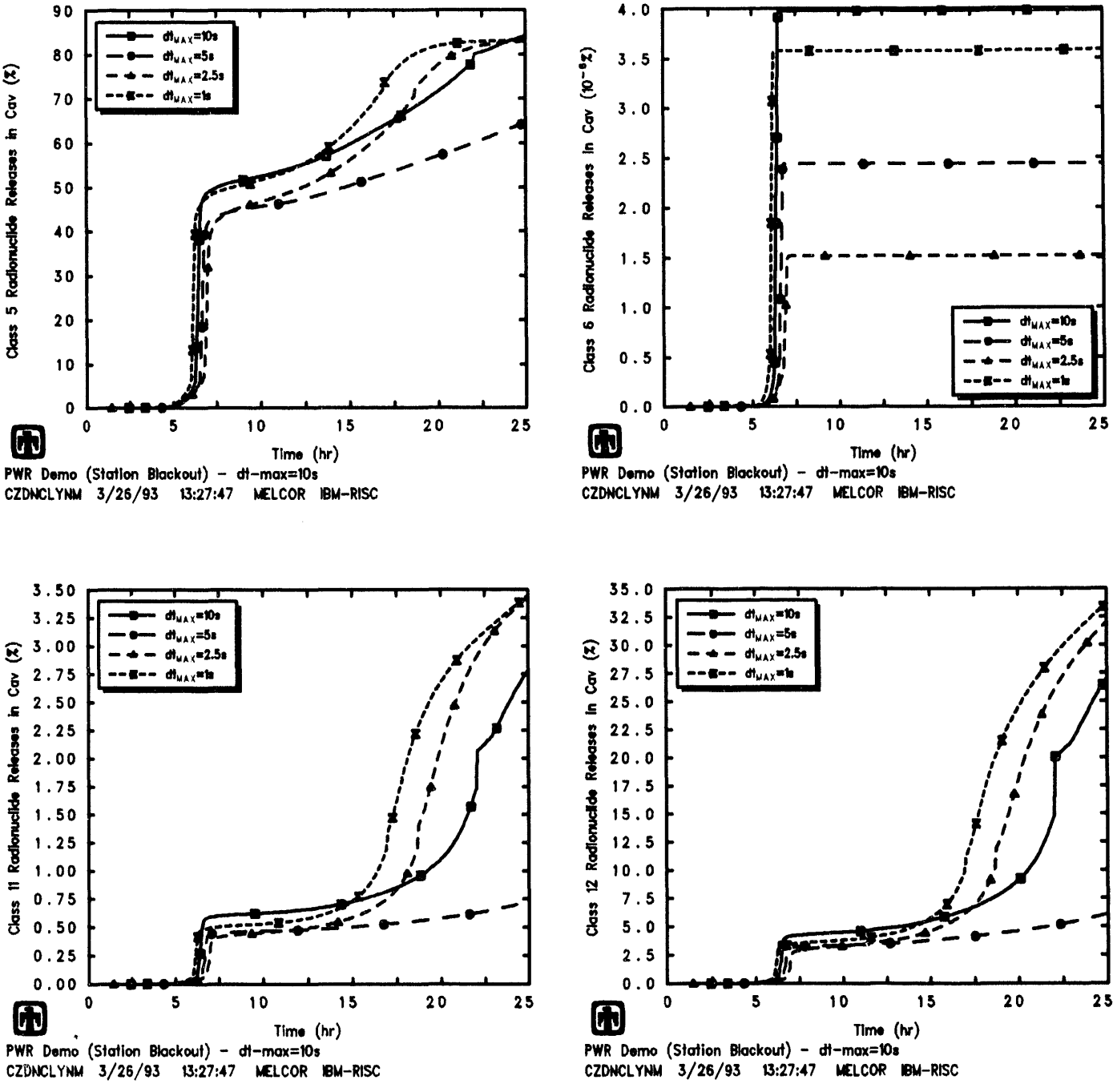

Figure 7.2.20. Ex-Vessel Class 5 (Te) Releases (upper left), Class 6 (Ru) Release (upper right), Class 11 (Cd) Releases (lower left) and Class 12 (Sn) Releases (lower right) for Surry TMLB' – Time Step Sensitivity Studies

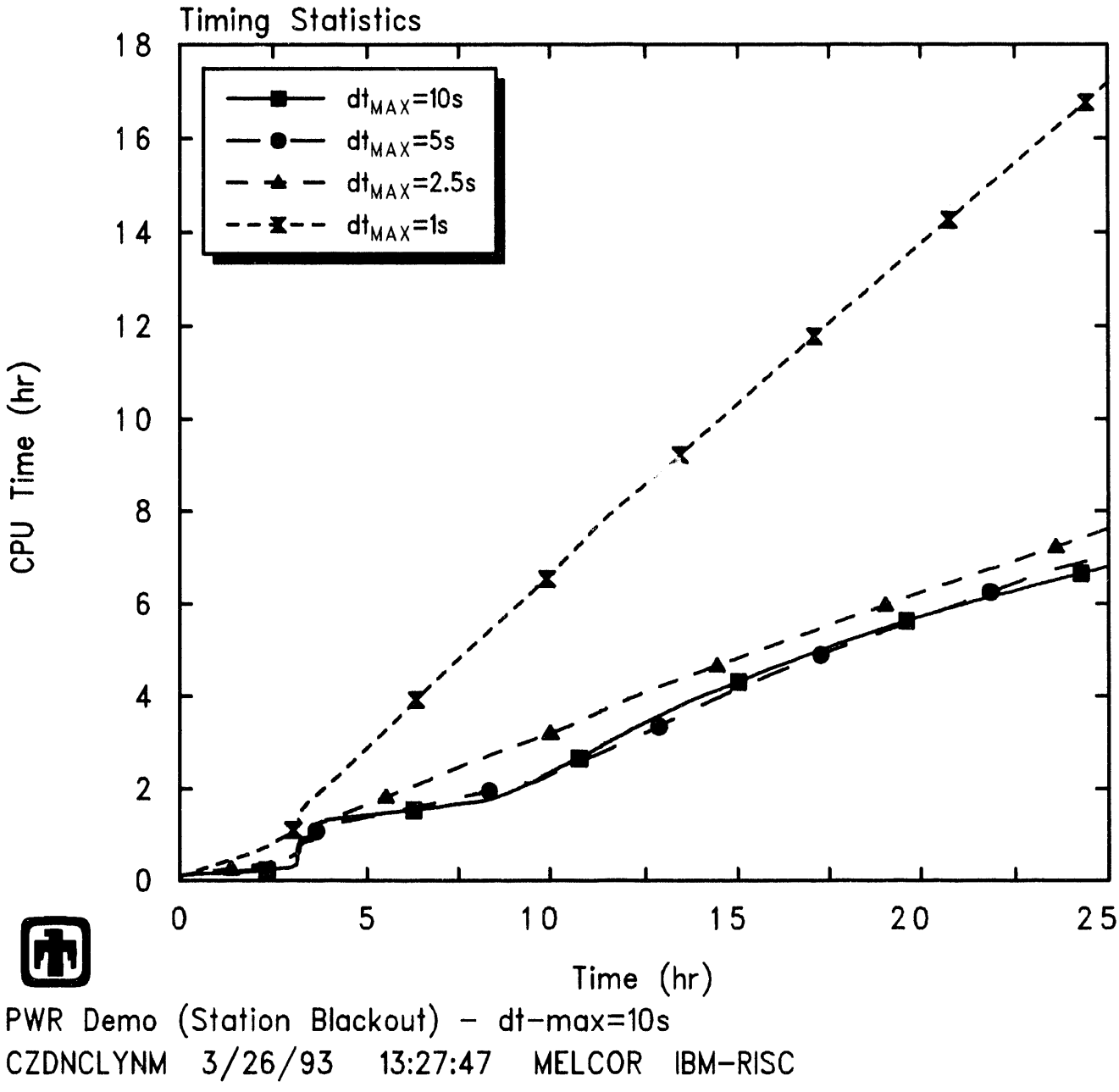

Figure 7.2.21. Total Run Times - Time Step Sensitivity Study

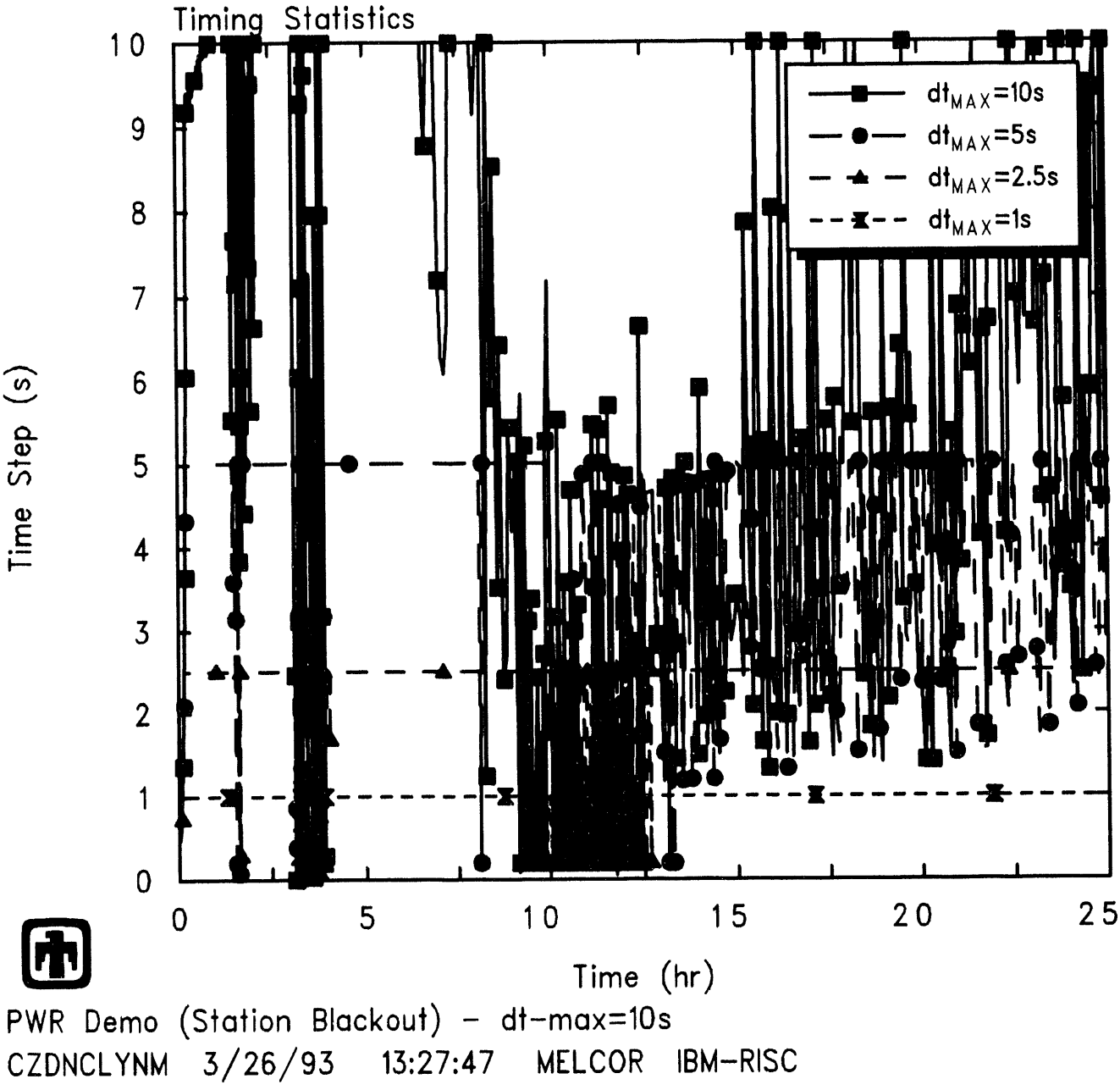

Figure 7.2.22. Time Steps Used – Time Step Sensitivity Study

7.3 Valve Controller

In both the machine-dependency and time-step studies discussed in Sections 7.1 and 7.2, a number of differences were noted early in the transient in the number of times that the steam generator SRV and, later, the pressurizer PORV cycled. Those differences were traced to differences in over- and undershooting the valve controller setpoint pressures with different time steps and/or different machine accuracies. The tabular function logic was modified to allow step function input, to minimize valves getting caught in a part-open state interpolating between table entries. A time-step controller is now being tested which is intended to limit the time step whenever a valve pressure setpoint is being approached in a control volume.

To evaluate this new valve-setpoint time-step controller, sensitivity study calculations were done with the maximum allowed time step set to 10s and to 1s, and with the new time-step controller told to limit pressure setpoint over- and undershoots for both the SG secondary relief valves and the pressurizer PORV and SRV to $\leq$1kPa ($\leq$0.01atm); early-time results from these calculations were then compared to results from equivalent calculations also done with the maximum allowed time step set to 10s and to 1s, but with no attempt to control valve pressure-setpoint over- and/or undershoots.

The early-time steam generator secondary side pressures presented in Figure 7.3.1 demonstrate that this addition to the code's time-step control algorithm significantly decreased the valve pressure-setpoint over- and undershoots, and helped keep the pressure oscillations in phase. (Note that the valve open and close pressure setpoints are included on these figures as dotted horizontal lines.) However, Figure 7.3.2 shows similar cumulative effects on (and offsets in) the steam generator secondary pressure, later in the transient, with and without the new valve-setpoint time step controller. The cycling of the SG relief valve in these various calculations is illustrated in Figure 7.3.3; the discrepancy in the number of valve cycles with the new valve-setpoint time step controller and different maximum time steps was not significantly reduced from the discrepancy in the number of valve cycles without the new valve-setpoint time step controller and different maximum time steps.

Figure 7.3.4 shows the primary system pressures calculated in these valve-controller sensitivity study analyses. There was a significantly greater delay in vessel failure and primary system depressurization as the maximum allowed time step was reduced from 10s to 1s in the pair of calculations using the new valve-setpoint time step controller ($\leq$1,000s) than was observed in the equivalent pair of calculations without it ($\leq$250s).

The corresponding PORV cycling comparison in Figure 7.3.5 demonstrates that the new valve-setpoint time step controller did succeed in maintaining identical PORV cycling for a significant period of time in calculations with different maximum allowed time steps, quite different from the behavior seen in the pair of calculations without it. However, after $\sim$3hr, the results diverge.

The results of this sensitivity study indicate that, while one source of numeric sensitivity affecting the early time period of this Surry TMLB' analysis (and in other analyses

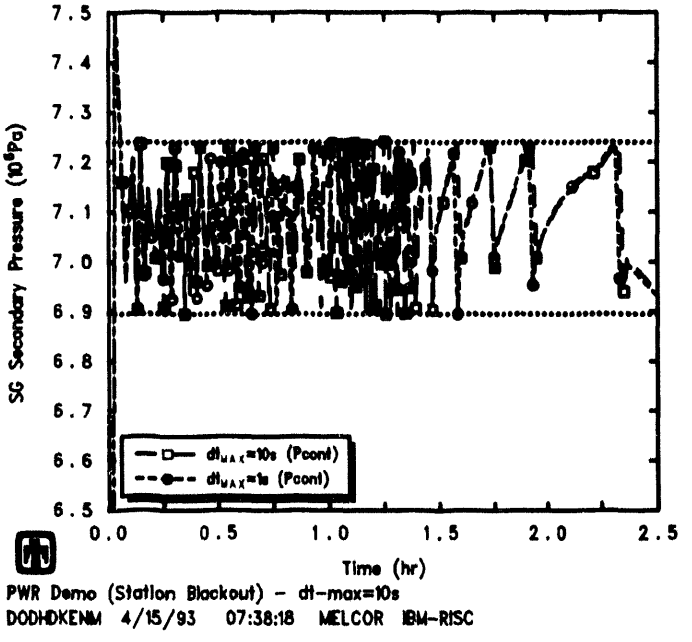

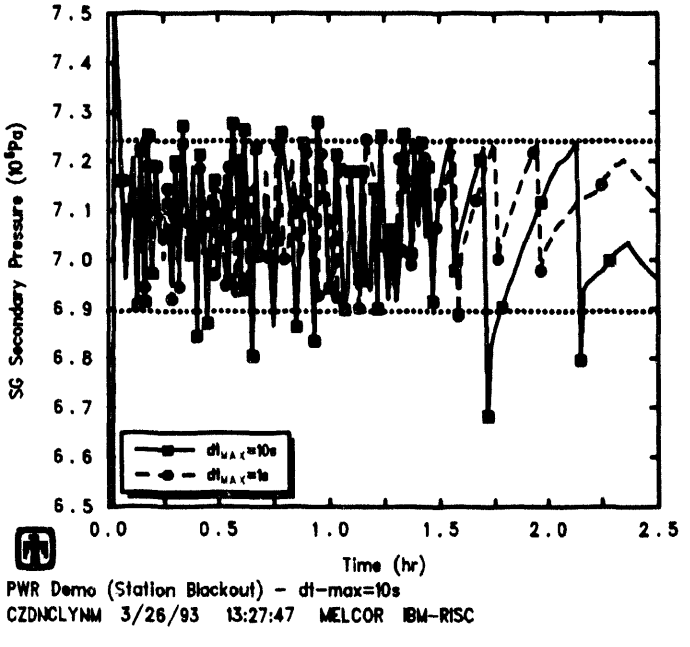

Figure 7.3.1. Early-Time SG Secondary-Side Pressures with (top) and without (bottom) Valve Pressure Setpoint Time-Step Controller – Valve Controller Sensitivity Study

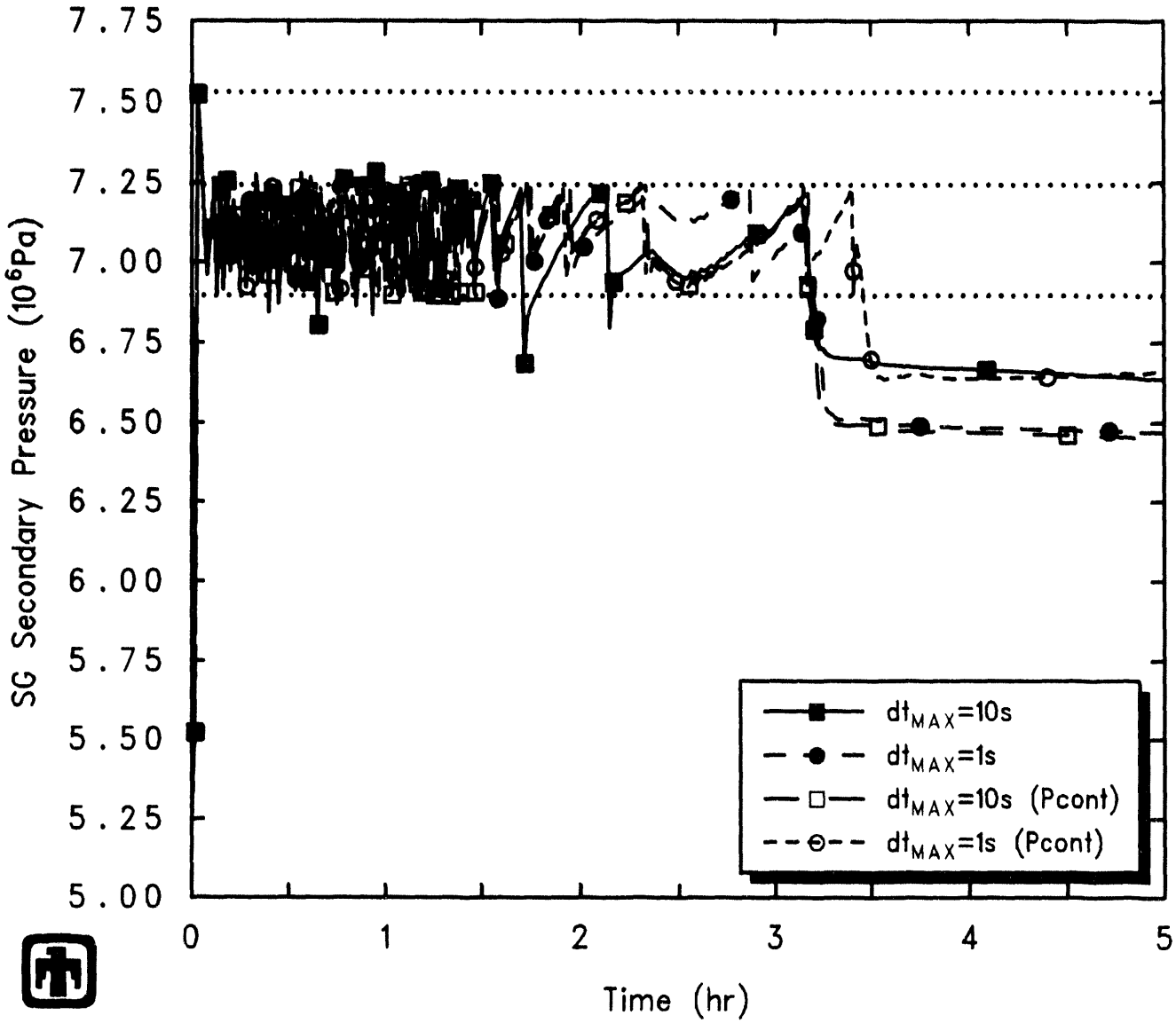

Figure 7.3.2. Later-Time SG Secondary-Side Pressures – Valve Controller Sensitivity Study

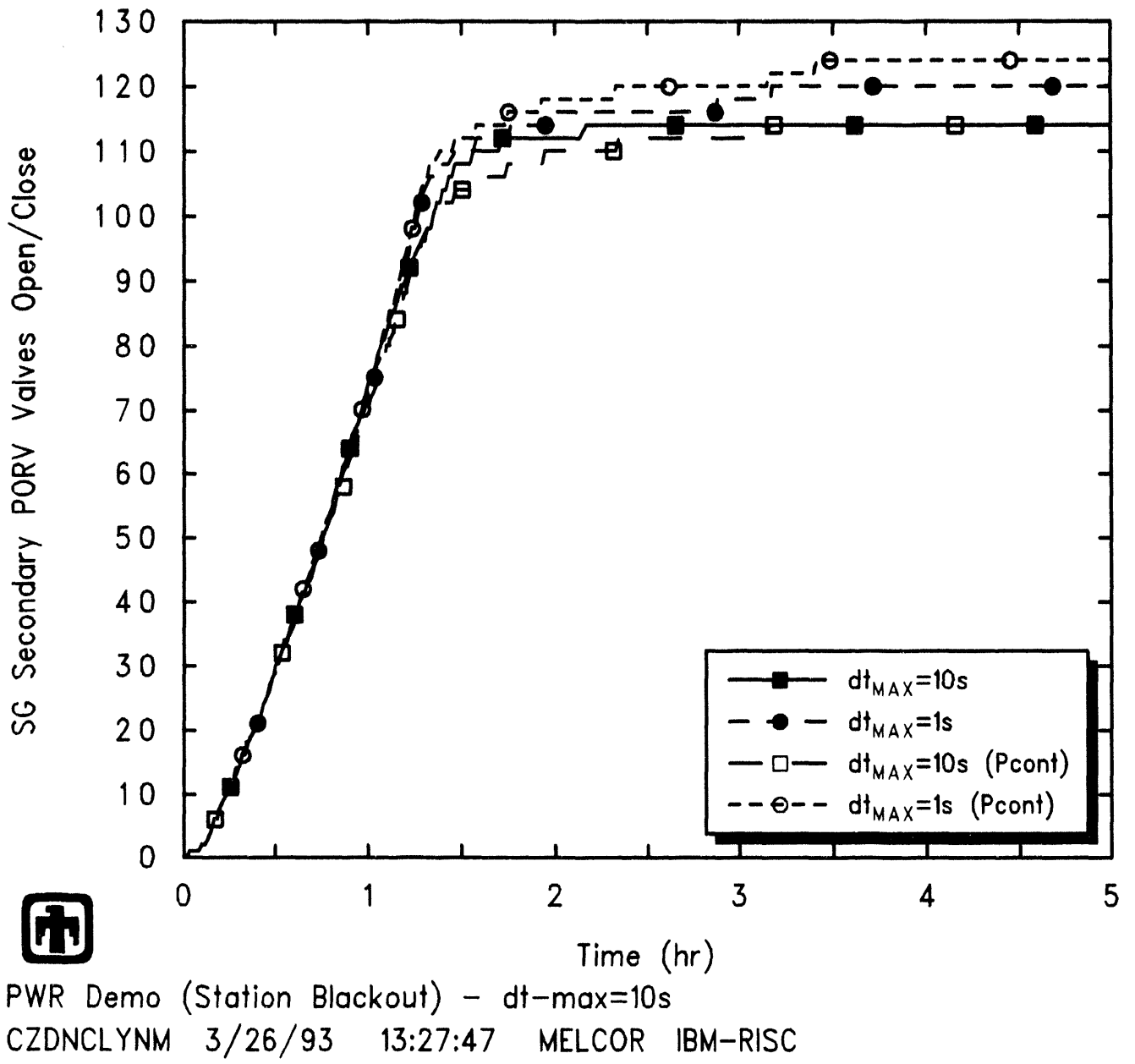

Figure 7.3.3. SG Secondary SRV Cycling Valve Controller Sensitivity Study

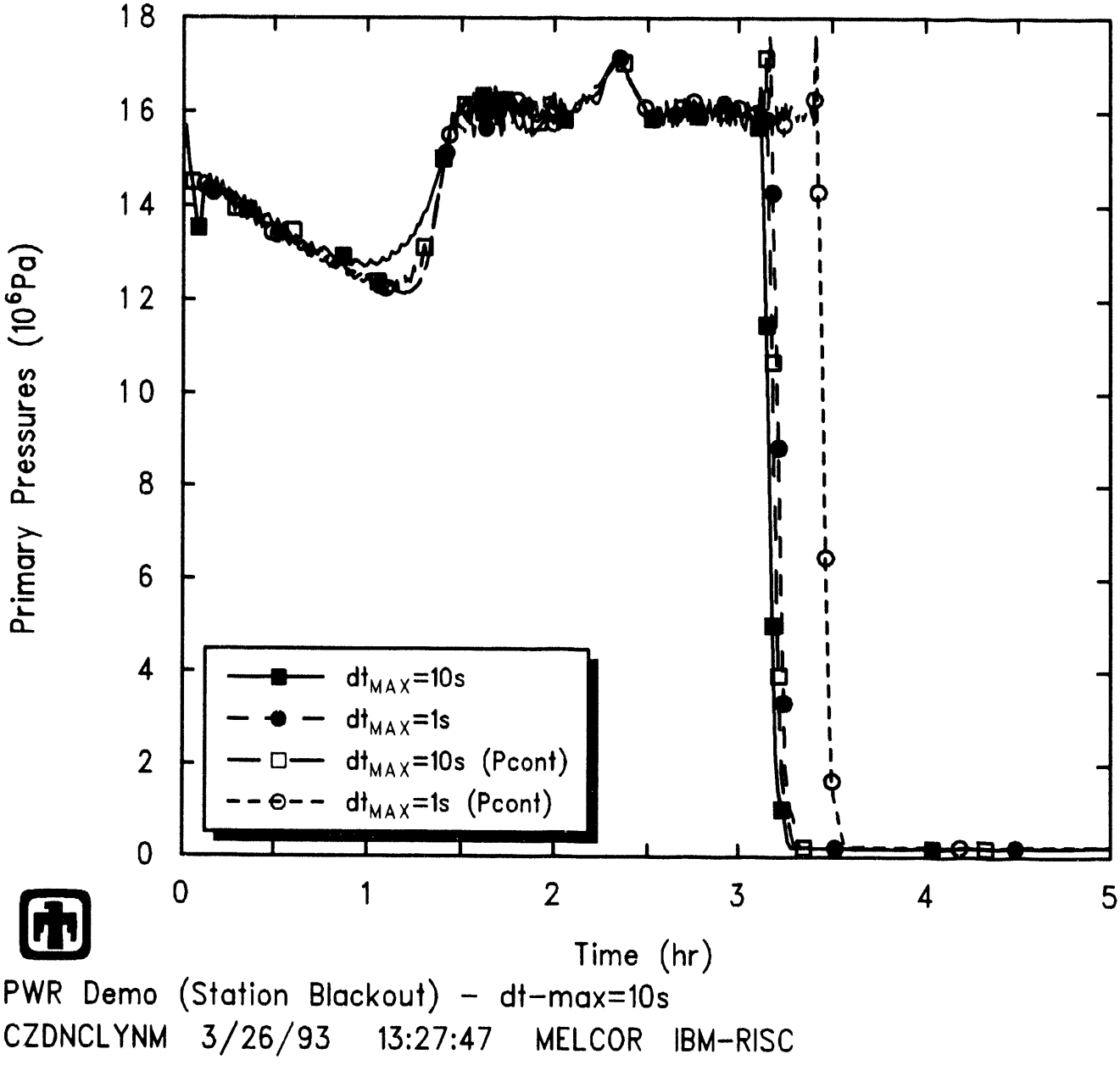

Figure 7.3.4. Vessel Pressures - Valve Controller Sensitivity Study

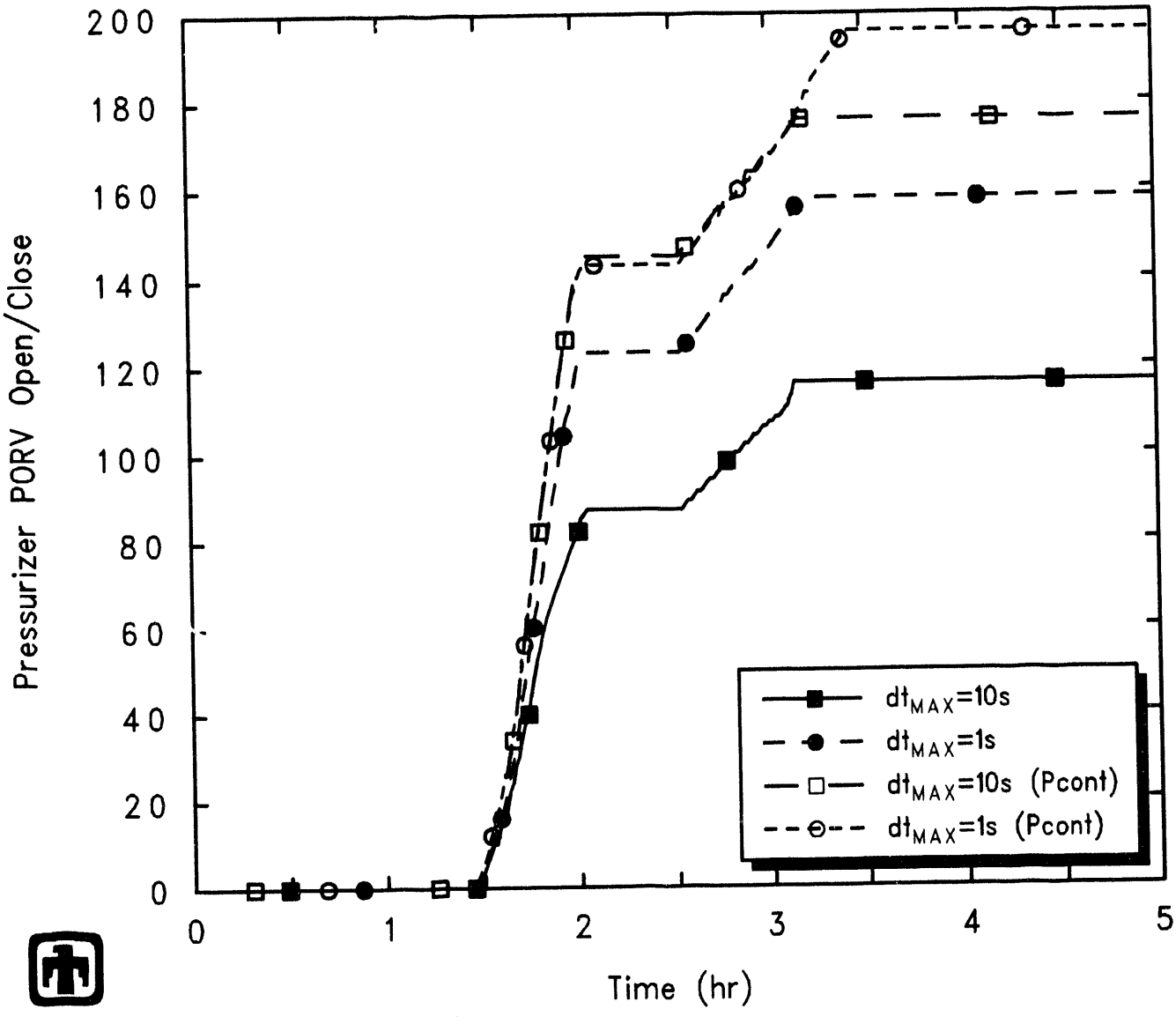

Figure 7.3.5. Pressurizer PORV Cycling - Valve Controller Sensitivity Study

[6]) has been identified and reduced or eliminated, discrepant results are still visible; therefore, other contributing effects still remain to be found.

7.4 Hydrogen Burns

In both the machine-dependency and time-step studies discussed in Sections 7.1 and 7.2, a number of differences were noted later in the transient in the timing and number of hydrogen deflagrations occurring in the cavity. All the machine-dependency and time-step sensitivity study calculations showed one set of hydrogen burns initially occurring $\leq$0.5hr after vessel breach and the start of core-concrete interaction; these calculations also all predicted a second period of hydrogen burns in the cavity later in the transient, but the timing and extent of that second burn period differed substantially among the various platforms. Some of the calculations showed a single, isolated burn at ~30,000s, while others showed a series of multiple burns starting somewhat later in the transient and lasting for a considerable length of time.

One possible cause of these numeric differences is over- and/or undershooting various combustion ignition criteria by different amounts in different calculations, just as over- and/or undershooting various valve controller pressure setpoints by different amounts in different calculations caused accumulating differences in predicted response (as just discussed in Section 7.3.

The default criteria for hydrogen combustion in the absence of igniters were used in these Surry TMLB' analyses: a hydrogen mole fraction $x_{H_2} \geq 0.10$ and/or a carbon monoxide mole fraction $x_{CO} \geq 0.167$, an oxygen mole fraction $x_{O_2} \geq 0.05$, and a combined steam plus carbon dioxide mole fraction $x_{H_2O+CO_2} \leq 0.55$. In the BUR package coding, a time advancement is rejected and repeated with a smaller time step if either the combustible fraction overshoots the ignition limit excessively while flammable or if the diluent or oxygen concentration overshoots the deinerting limit excessively while the combustible concentration is above the ignition limit. The default overshoot allowed on combustible gas concentration (H_2+CO) is a mole fraction difference of 0.005, while the default overshoot allowed on the deinerting limit for O_2 or H_2O+CO_2 is 0.01.

A set of sensitivity study calculations was done in which these default overshoots allowed were both reduced by an order of magnitude, to 0.0005 and 0.001, respectively, in calculations otherwise identical to the four used in the time-step sensitivity study described in detail in Section 7.2, for comparison.

Figure 7.4.1 shows the number and timing of hydrogen burns in the cavity, and the amount of hydrogen burned, in these various calculations; no hydrogen burns occurred in the containment outside the cavity during any of these calculation, because those other containment volumes remained inerted by sufficient steam and/or CO_2 in their atmospheres. As found in both our machine-dependency and time-step sensitivity studies (Table 7.1.1 and 7.2.1), one of the biggest timing differences found in these numeric effects studies is in hydrogen deflagrations occurring in the cavity. All five of our machine-dependency and all four of our time-step study calculations showed one set of hydrogen

burns initially occurring $\leq$0.5hr after vessel breach and the start of core-concrete interaction, lasting about 600-900s. Three of the machine-dependency studies and one time step study calculation showed a single hydrogen burn at ~30,000s; the other two machine-dependency and other three time-step study calculations showed a second set of multiple hydrogen burns occurring later in the transient, but the timing and extent of that later burn period differed substantially among these various cases.

Figures 7.4.2 through 7.4.4 show mole fractions in the cavity control volume atmosphere as calculated on an IBM RISC-6000 Model 550 workstation with different user-specified maximum time steps and the combustible concentration limit allowed overshoots reduced by an order of magnitude, together with the default ignition limits used in MELCOR, for the combined equivalent mole fraction of H_2 and CO (equal to $x_{H_2} + \frac{0.10}{0.167} x_{CO}$), the O_2 mole fraction and a combined total mole fraction of H_2O and CO_2, respectively. (The results in these plots should be compared to corresponding results for the corresponding time-step study calculations using the default combustible concentration limit allowed overshoots given in Figures 7.2.17 through 7.2.19).

Figures 7.4.2 through 7.4.4) demonstrate that, in all the cases with the reduced combustion limit allowed overshoots, the combined H_2 and CO concentration and the O_2 concentration both easily exceeded their ignition limits throughout most of the later portions of the transient, after ~8-9hr; as discussed in Sections 7.1 and 7.2, the late-time combustion ignition at later times always was controlled by whether the total H_2O plus CO_2 concentration was reduced to below the inerting limit.

Figure 7.4.4 illustrates how closely all these calculations approached the inerting limit for a long period of time between >12.5hr and <17.5hr. These results are very similar to those presented in Figure 7.2.19. Both figures indicate the potential for a prolonged period of hydrogen burn in all cases later in the transient. As was the case in Figure 7.2.19, it is not clear from Figure 7.4.4) why combustion was not predicted in more of the cases during that time. The calculations done with Δt_{MAX}=1s in particular, either with the default or with the reduced combustion limit allowed overshoots, appeared to remain significantly below the inert concentration limit, and above both the combined H_2 and CO, and O_2, ignition concentration limits, for a long period of time after combustion was predicted to end.

These results indicate both a particular problem in the BUR package coding, not predicting combustion to occur under conditions which obviously allow ignition (according to the MELCOR documentation [34]), and a more general problem of how to avoid "threshhold" effects (*i.e.*, burn *vs* no burn) when calculations approach and remain very near an ignition concentration threshhold; furthermore, the coding problem which is preventing ignition under conditions which should allow it may be causing these calculations to remain so close to the H_2O+CO_2 inert limit for so long.

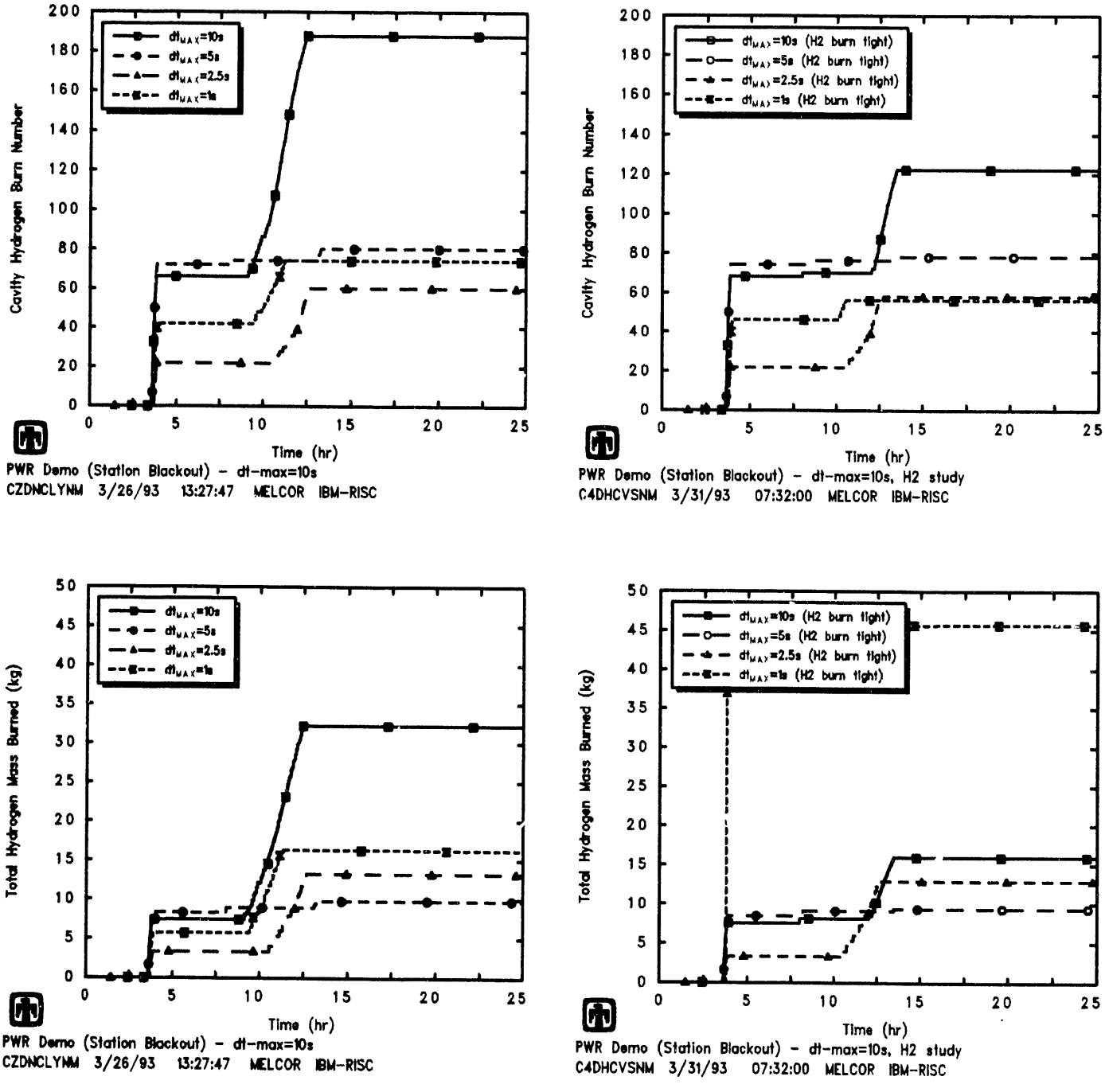

Figure 7.4.1. Number of (top) and Masses Burned in (bottom) Cavity Hydrogen Deflagrations in Calculations with Default (left) and Reduced (right) Combustion/Dilution Concentration Allowed Overshoots - Hydrogen Burns Sensitivity Study

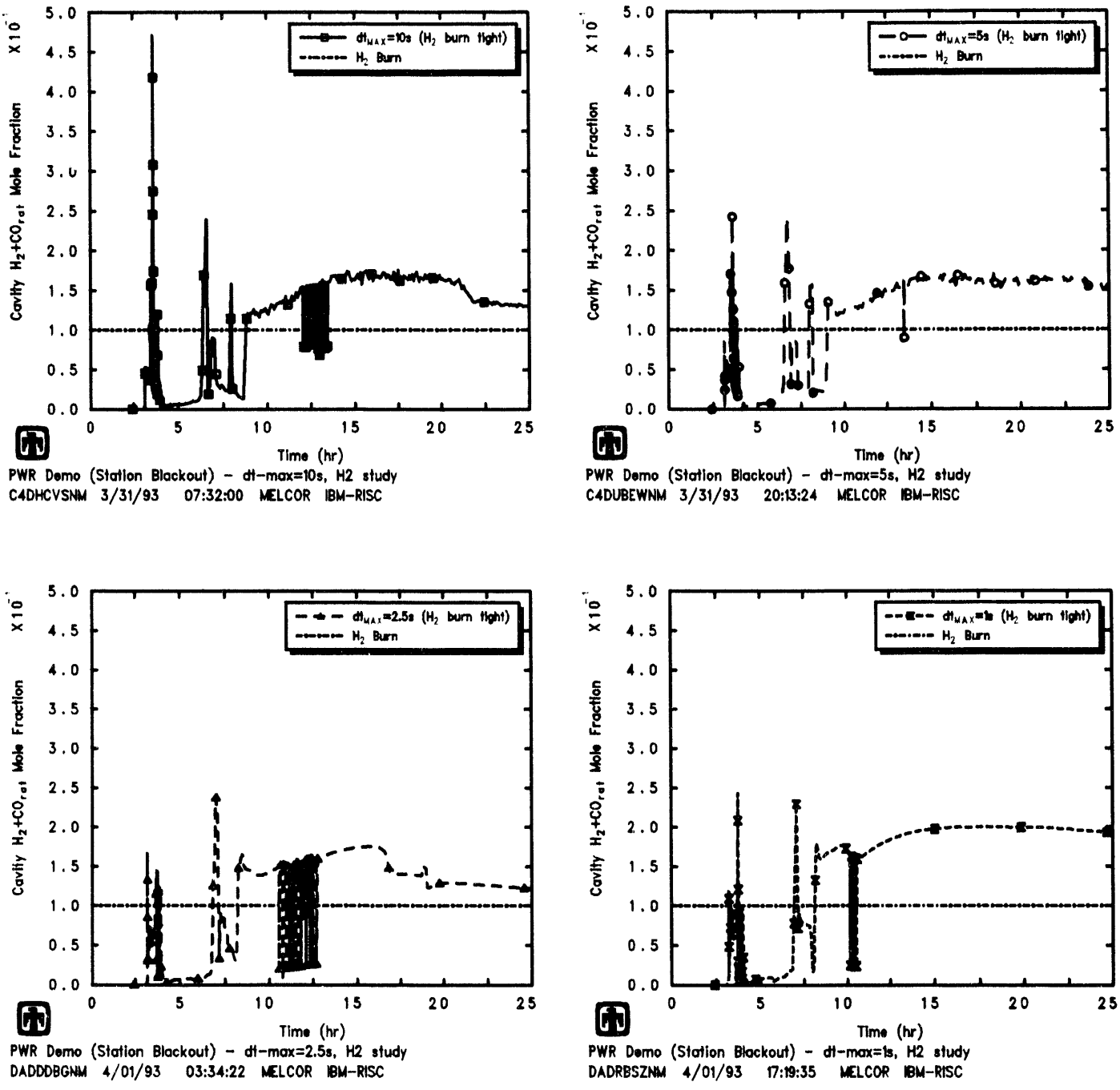

Figure 7.4.2. Combined H_2 and CO Mole Fraction in Cavity Calculated with Δt_{MAX}=10s (upper left), Δt_{MAX}=5s (upper right), Δt_{MAX}=2.5s (lower left), and Δt_{MAX}=1s (lower right) with Reduced Combustion/Dilution Concentration Allowed Overshoots – Hydrogen Burns Sensitivity Study

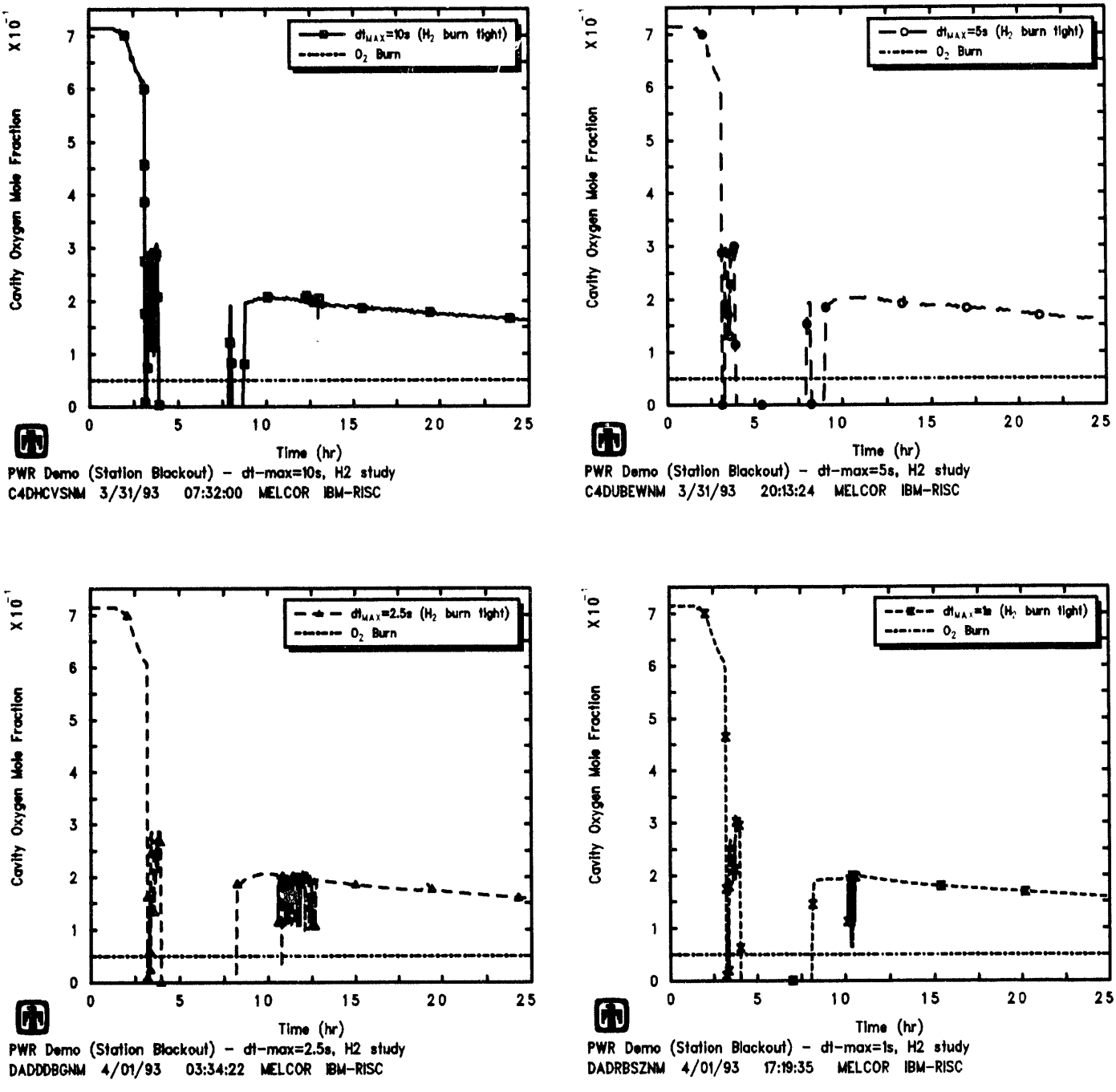

Figure 7.4.3. O_2 Mole Fraction in Cavity Calculated with Δt_{MAX}=10s (upper left), Δt_{MAX}=5s (upper right), Δt_{MAX}=2.5s (lower left), and Δt_{MAX}=1s (lower right) with Reduced Combustion/Dilution Concentration Allowed Overshoots – Hydrogen Burns Sensitivity Study

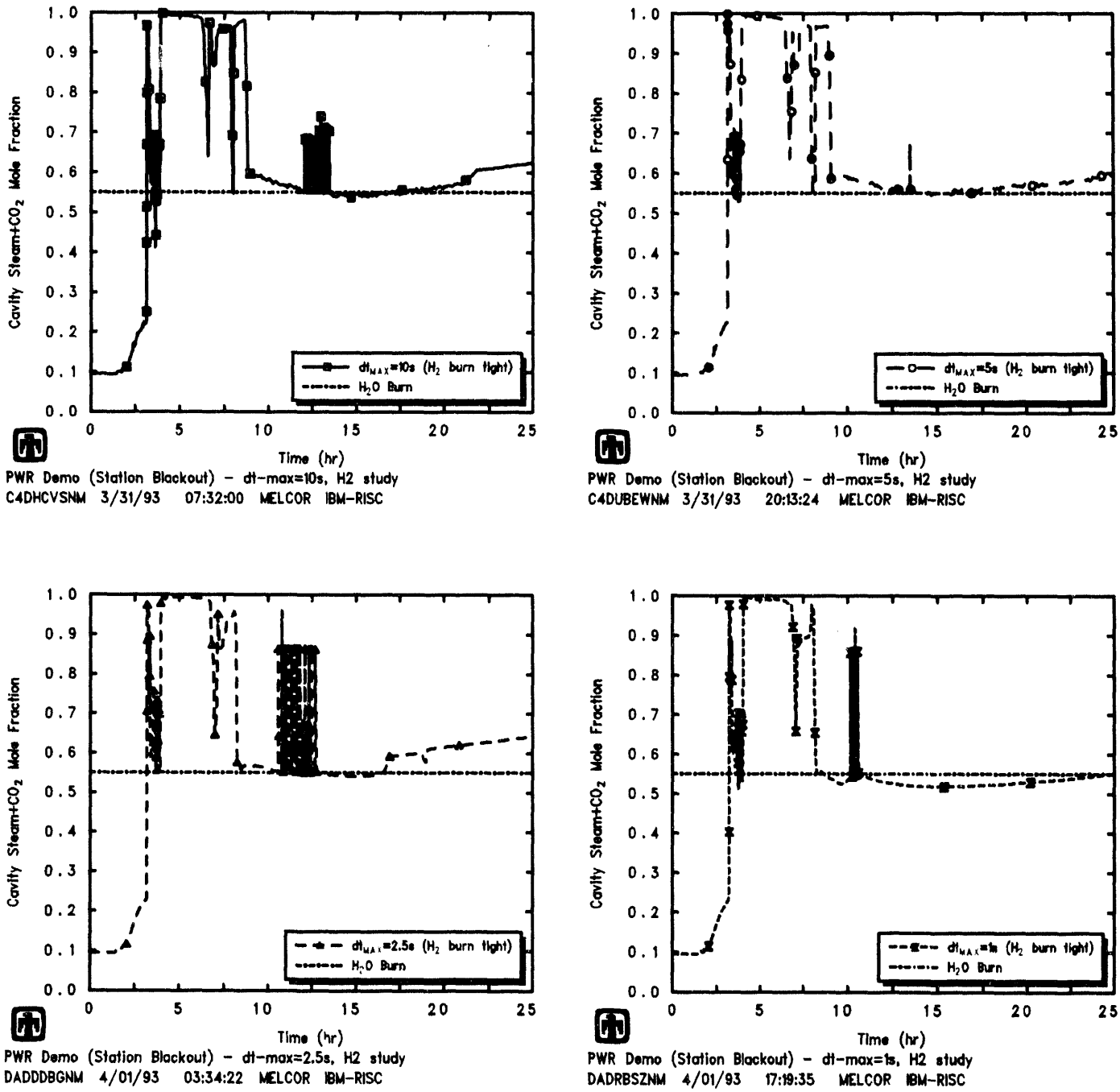

Figure 7.4.4. Combined H_2O and CO_2 Mole Fraction in Cavity Calculated with Δt_{MAX}=10s (upper left), Δt_{MAX}=5s (upper right), Δt_{MAX}=2.5s (lower left), and Δt_{MAX}=1s (lower right) with Reduced Combustion/Dilution Concentration Allowed Overshoots - Hydrogen Burns Sensitivity Study

8 Comparison to Other Codes

The reference MELCOR calculation for the Surry PWR TMLB' accident sequence described in Section 4 has been compared to similar calculations done for that sequence in that plant with other codes, when available. Note that, unlike experiment analyses, in these plant analysis comparisons there is no implied or tested guarantee that the input models and/or modelling and sequence assumptions are identical; the input decks are generally proprietary and not available for comparison, and the steady state conditions assumed may not always be the same. Further, analyses of this scenario may produce different, diverging sequences due to differences in basic code assumptions (such as vessel failure modes and criteria). Finally, some codes (*e.g.*, CONTAIN) do not perform an integrated calculation for the entire plant and beginning at full power but instead analyze later-time response of part of the plant (*e.g.*, cavity and containment) based upon assumed behavior earlier in the rest of the plant (*i.e.*, in the primary system and core); the sources used to drive such partial calculations may not be the same as the equivalent, internalized sources calculated by MELCOR. Also, the comparisons possible are limited to the relatively small amount of published figures and tables for these other code analyses.

8.1 Primary System and Core Response

The early-time behavior of the Surry PWR TMLB' accident has been calculated by several best-estimate codes, notably by SCDAP/RELAP5 [18], MELPROG/TRAC [35] and MELPROG-PWR/MOD1 [36].

The SCDAP/RELAP5 calculation was an integral calculation of the primary system thermal/hydraulics and the core behavior, beginning at full power steady state and terminated at 200min. The calculations selected for comparison to MELCOR in this section are "scoping Case 1" and "scoping Case 2" from [18]; these are best-estimate simulations with a once-through model of the core and upper plenum in "Case 1" (*i.e.*, without in-vessel and hot leg circulation flows modelled), chosen because that model most closely resembles the MELCOR representation, and with in-vessel natural circulation modelled in "Case 2" (*i.e.*, without hot leg circulation flows modelled), included to indicate how big an effect the lack of an in-vessel natural circulation model in MELCOR 1.8.2 could have.

The standalone MELPROG calculation was run from the point where the primary system saturates (taken as 6500s) to the point where the reactor vessel fails. The calculations selected for comparison to MELCOR in this section are "MELPROG-2D" and "MELPROG-1D" from [36]; as with the SCDAP/RELAP5 cases selected, these include calculations with and without in-vessel natural circulation simulated. The "front end" of the TMLB' transient, needed to begin the standalone MELPROG calculation at 6500s, was based on TRAC-PF1 calculations; the flow into the vessel then was terminated when boiling began. There was only one MELPROG/TRAC calculation in [35]; it was run from the accident initiator through disruption of the core region.

Table 8.1.1 compares the timing of various events in the first phase of the TMLB' transient, from accident initiation to vessel failure, as predicted to occur in the reference MELCOR 1.8.2 calculation and in the SCDAP/RELAP5, MELPROG/TRAC and MELPROG-PWR/MOD1 analyses.

Figure 8.1.1 compares the primary system pressures early in the TMLB' sequence predicted by MELCOR and by SCDAP/RELAP5. (Note that at these times the "Case 1" and "Case 2" SCDAP/RELAP5 would be virtually identical.) Qualitatively, both codes predict the same behavior – a small decrease in pressure over the first $\geq$1hr, followed by cycling at the pressurizer PORV setpoints after steam generator dryout. Quantitatively, MELCOR predicts a greater pressure drop during the first $\geq$1hr than seen in the SCDAP/RELAP5 calculation. The greater depressurization in MELCOR during the period when the decay heat is being transferred to the steam generators and the steam generator secondary sides are removing the decay heat by boiling dry and venting suggests some imbalance in the primary-to-secondary heat transfer modelling in MELCOR; in particular, the steady state conditions were established with such an older code version (pre- MELCOR 1.8.1) that accumulated code changes may have disturbed that steady state heat balance.

The collapsed liquid level in the pressurizer predicted in the MELCOR 1.8.2 reference calculation is compared to the corresponding result from SCDAP/RELAP5 in Figure 8.1.2. (There is no significant swelling predicted in the pressurizer, so the swollen liquid level appears the same.) Recall that Figure 6.1.1 shows the collapsed liquid level in the pressurizer predicted in the MELCOR 1.8.2 and 1.8.1 basecase calculations and in various momentum exchange length sensitivity study analyses, all compared to the pressurizer response predicted by SCDAP/RELAP5 for the same TMLB' accident sequence.

Comparing these MELCOR results to corresponding SCDAP/RELAP5 results for the same accident, there is an initial timing shift visible in pressurizer filling and venting due to a higher initial liquid level. The subsequent pressurizer drainage rate from SCDAP/RELAP5 appears somewhat faster than the MELCOR 1.8.2 reference calculation result (but somewhat slower than in the MELCOR sensitivity study analyses when the interfacial momentum exchange length specified in the pressurizer surge line is further reduced, as illustrated in Figure 6.1.1). The pressurizer was still ~25% full of liquid when the SCDAP/RELAP5 calculation was terminated at 200min; the lower pressurizer water inventory in the SCDAP/RELAP5 analysis is due to drainage occurring over a longer period than in any of the MELCOR calculations. Note that the pressurizer was predicted to drain more quickly in the SCDAP/RELAP5 calculation with in-vessel natural circulation ("Case 2") than in the SCDAP/RELAP5 calculation with once-through core and upper plenum flow ("Case 1"), reflecting slower core damage progression and reduced steam generation with in-vessel natural circulation.

Figure 8.1.3 shows the collapsed liquid levels in the various vessel control volumes calculated in the MELCOR 1.8.2 reference calculation, together with the vessel response predicted by SCDAP/RELAP5 for the same TMLB' accident sequence (Figure 8 in [18]), for comparison. (Results were given in [18] only for "Case 1".) There is not much difference in initial core uncovery time, but the MELCOR calculation uncovers the core

Table 8.1.1. Timing of Key Events from Accident Start to Vessel Failure – Code Comparison Study

Event	Time (s)					
	MELCOR	SCDAP/RELAP5		MELPROG		MELPROG/TRAC
	1.8.2	"Case 1"	"Case 2"	"1D"	"2D"	
Loss of Electrical Power	0.0	0.0	0.0	0.0	0.0	0.0
SG Secondary Side Dried Out	~5000	4524-4632	4524-4632	(4170	(4170)	
Pressurizer PORV First Open	~5250	4308	4308			
Core Uncovery	~7200	~7610	~7610		7070	7750
Natural Circulation Stopped	~7850	6582	6582			
Incipient Boiling				6500	6500	6430
Core Heatup		7776	7788			
Core Empty	~11,900	~10,225			8350	9450
Start of Zr Oxidation/H_2 Production	~10,000	8646	8778		9280	10400
Control Rods Fail/Relocate		9432	9972		9970	11310
Clad Melts/Fuel Rods Fail		9630	10020-10200		10156-10181	11635
Core Slumps					14877	
Core Support Plate Fails	11,181.5					
Lower Head Fails	11,225.5			12800	15928	
Calculation Stopped		12000	12000	12800	15928	

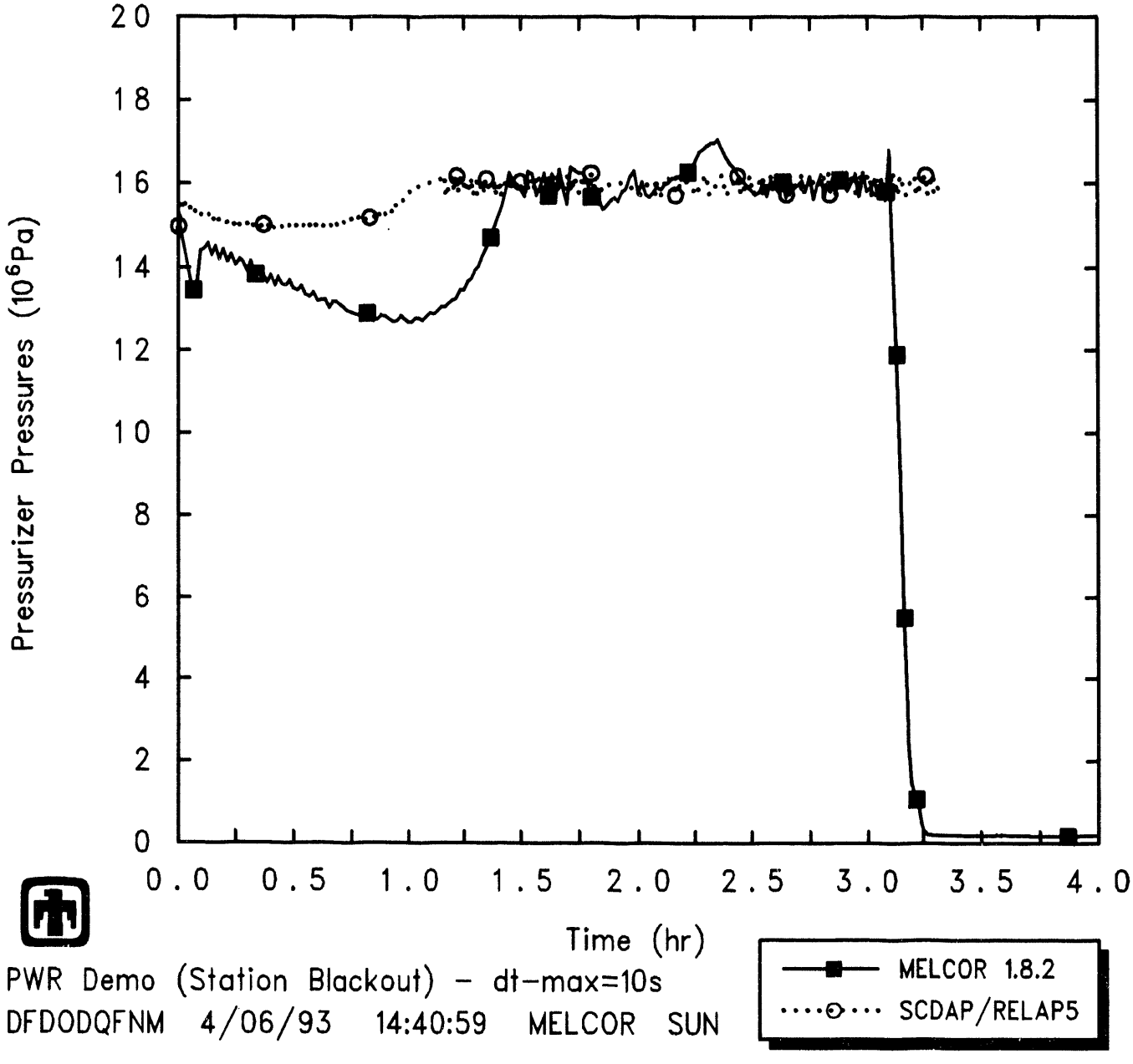

Figure 8.1.1. MELCOR Primary System Pressure, Compared to SCDAP/RELAP5 – Code Comparison Study

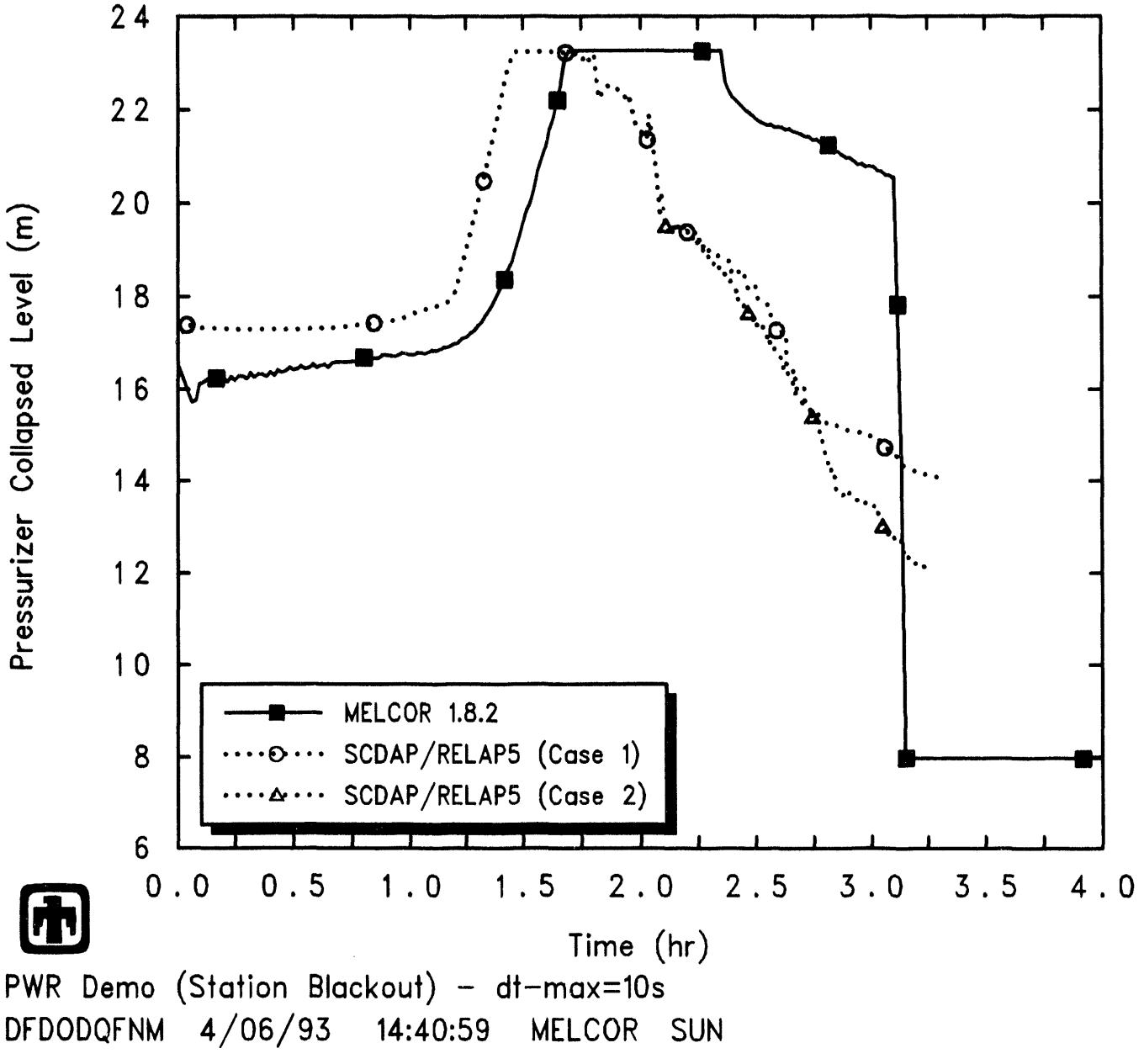

Figure 8.1.2. MELCOR Pressurizer Liquid Level, Compared to SCDAP/RELAP5 Code Comparison Study

more slowly than seen with SCDAP/RELAP5. The major difference appears to be the delay of ~0.5hr early in the core uncovery process, when MELCOR predicts significant water remaining in the upper plenum while the collapsed liquid level in the core region drops as steam bubbles appear in the saturated core water; once the upper plenum is completely drained, the rate of core uncovery in the MELCOR calculation appears similar to the SCDAP/RELAP5 result. There is not enough detail given in [18] to analyze this difference further.

This difference in predicted core uncovery is reflected in the subsequent core heatup behavior calculated by MELCOR and by SCDAP/RELAP5. Clad temperature comparisons at four core elevations are presented in Figures 8.1.4 through 8.1.7. A single set of clad temperatures were given in [18] (in Figure 5) for "Case 1", the SCDAP/RELAP5 calculation with once-through core and upper plenum flow, while two sets of clad temperatures, for the center and outer channels, were given in [18] (in Figures 12 and 14) for "Case 2", the SCDAP/RELAP5 calculation with in-vessel natural circulation. At all four levels, the initial heatup is offset by the timing difference in core uncovery but the subsequent heatup rates calculated by MELCOR and by SCDAP/RELAP5 generally agree very well. The SCDAP/RELAP5 calculations show somewhat slower core heatup with in-vessel natural circulation, but the differences are not very large.

Figures 8.1.8 and 8.1.9 show the major effect of including or neglecting the in-vessel natural circulation. These figures compare the temperatures in the upper plenum, hot leg, pressurizer surge line and steam generator tubes calculated by MELCOR and by SCDAP/RELAP5 without ("Case 1") and with ("Case 2") in-vessel natural circulation, respectively. Note that the MELCOR results for the temperatures in the hot leg, pressurizer surge line and steam generator tubes closely resemble those from the SCDAP/RELAP5 calculation with the once-through core and upper plenum, with all the temperatures generally at or near saturation, while the SCDAP/RELAP5 calculation with in-vessel natural circulation included exhibits much higher hot leg and surge line temperatures, increasing continually after core uncovery. The MELCOR calculation does show superheated steam in the upper plenum late in the core uncovery process, just before vessel breach, but these superheated steam temperatures are much lower and much later than in the "Case 2" SCDAP/RELAP5 calculation with in-vessel natural circulation, and do not persist in the hot leg or surge line, which remain at saturation. (Note that none of these calculations includes a hot leg countercurrent flow model, analyzed in [18] as "Case 3".)

Figure 8.1.10 shows the swollen liquid levels in the various vessel control volumes calculated in the MELCOR 1.8.2 reference calculation, together with the two-phase core levels predicted by MELPROG and MELPROG/TRAC for the same TMLB' accident sequence (Figure 2 in [35]), for comparison. The MELPROG calculation (the "2D" calculation in [36]) uncovers the core significantly earlier than MELCOR, SCDAP/RELAP5 or MELPROG/TRAC; MELPROG/TRAC uncovers the core later than MELCOR, and slightly later than SCDAP/RELAP5. As with the vessel level comparison to SCDAP/RELAP5 in Figure 8.1.3, there appears to be a ~0.5hr delay early in the core uncovery process in the MELCOR calculation, when MELCOR predicts significant

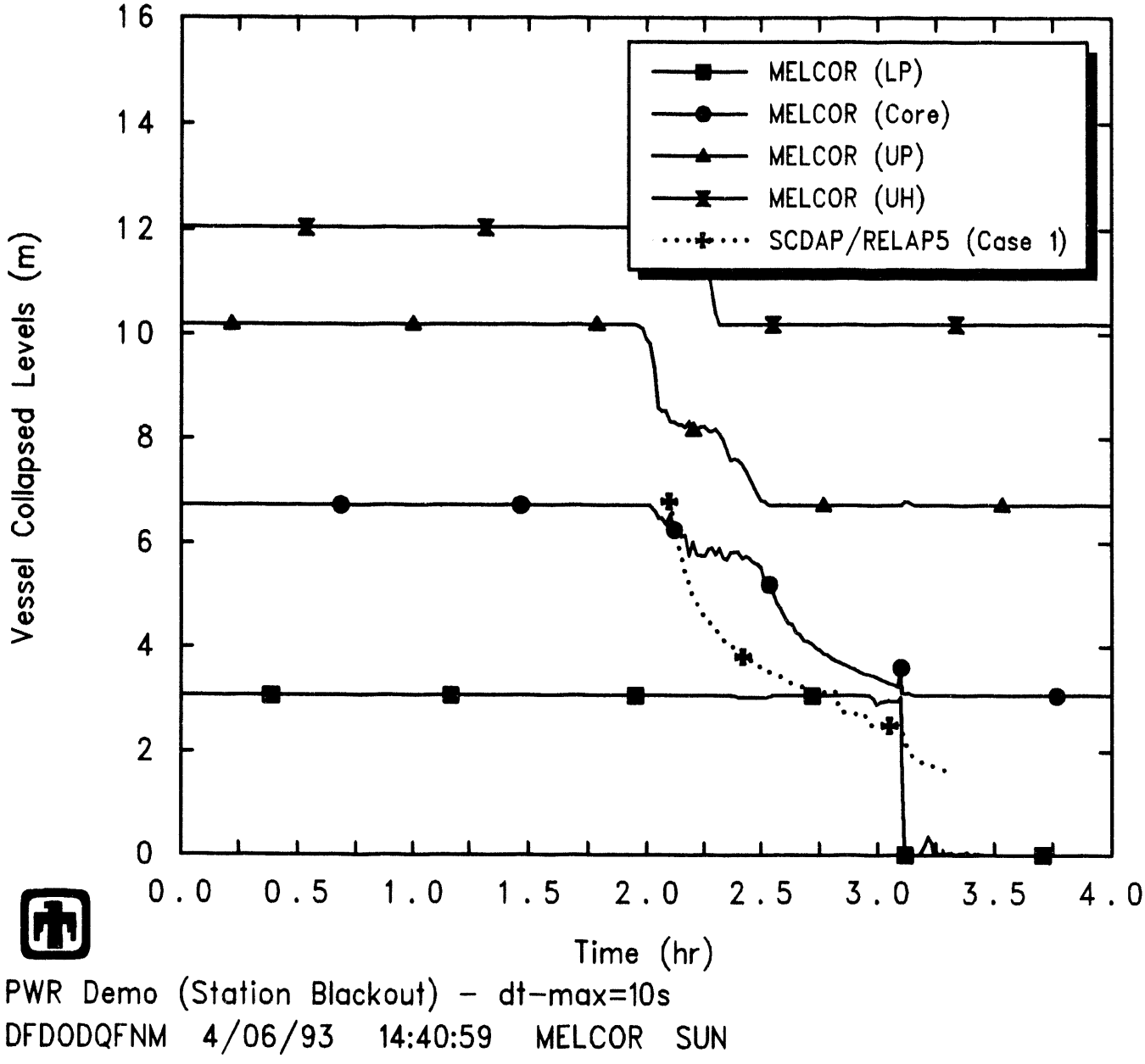

Figure 8.1.3. MELCOR Vessel Collapsed Liquid Levels, Compared to SCDAP/RELAP5 – Code Comparison Study

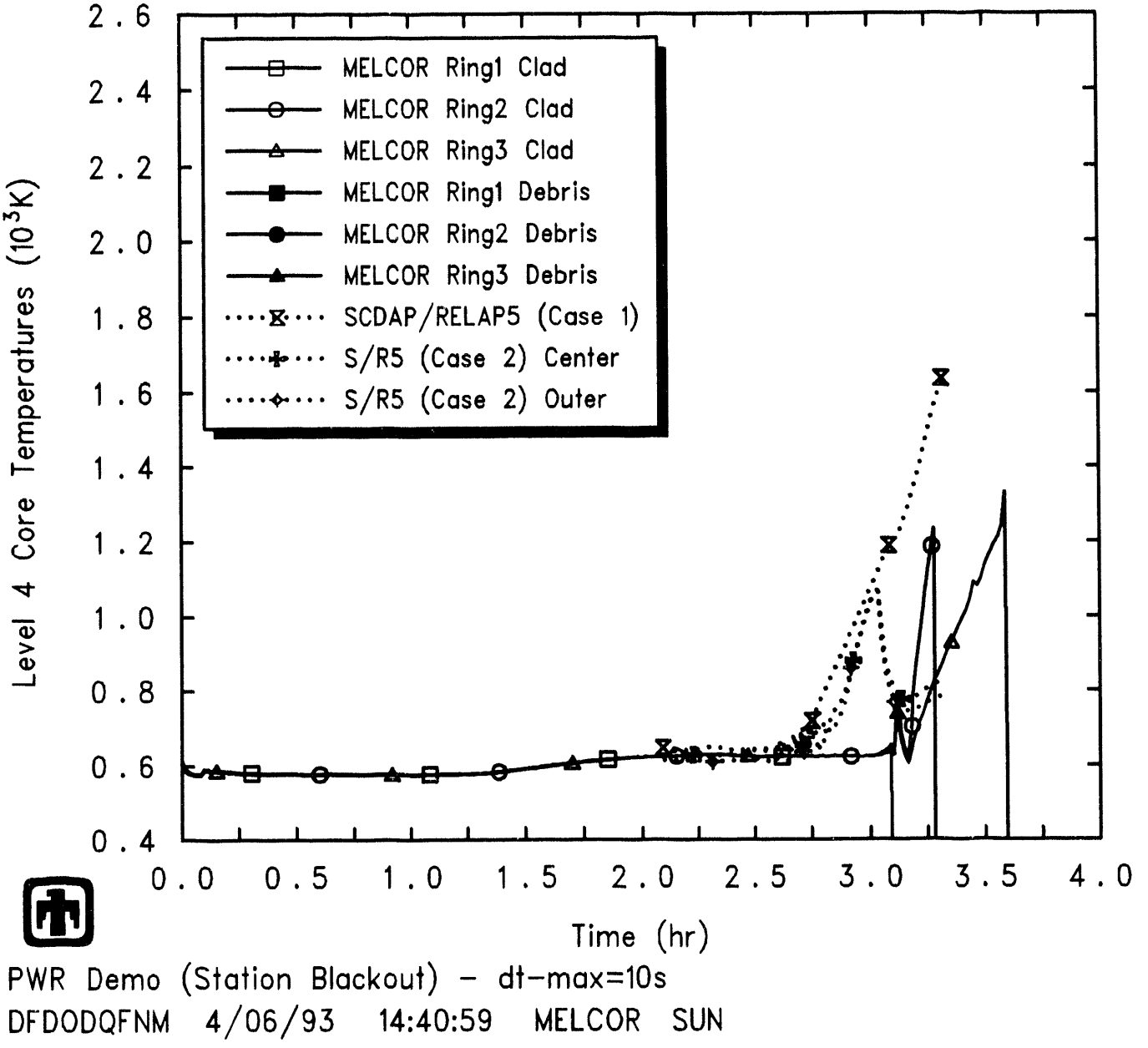

Figure 8.1.4. MELCOR Core Level 4 Clad Temperatures, Compared to SCDAP/RELAP5 Code Comparison Study

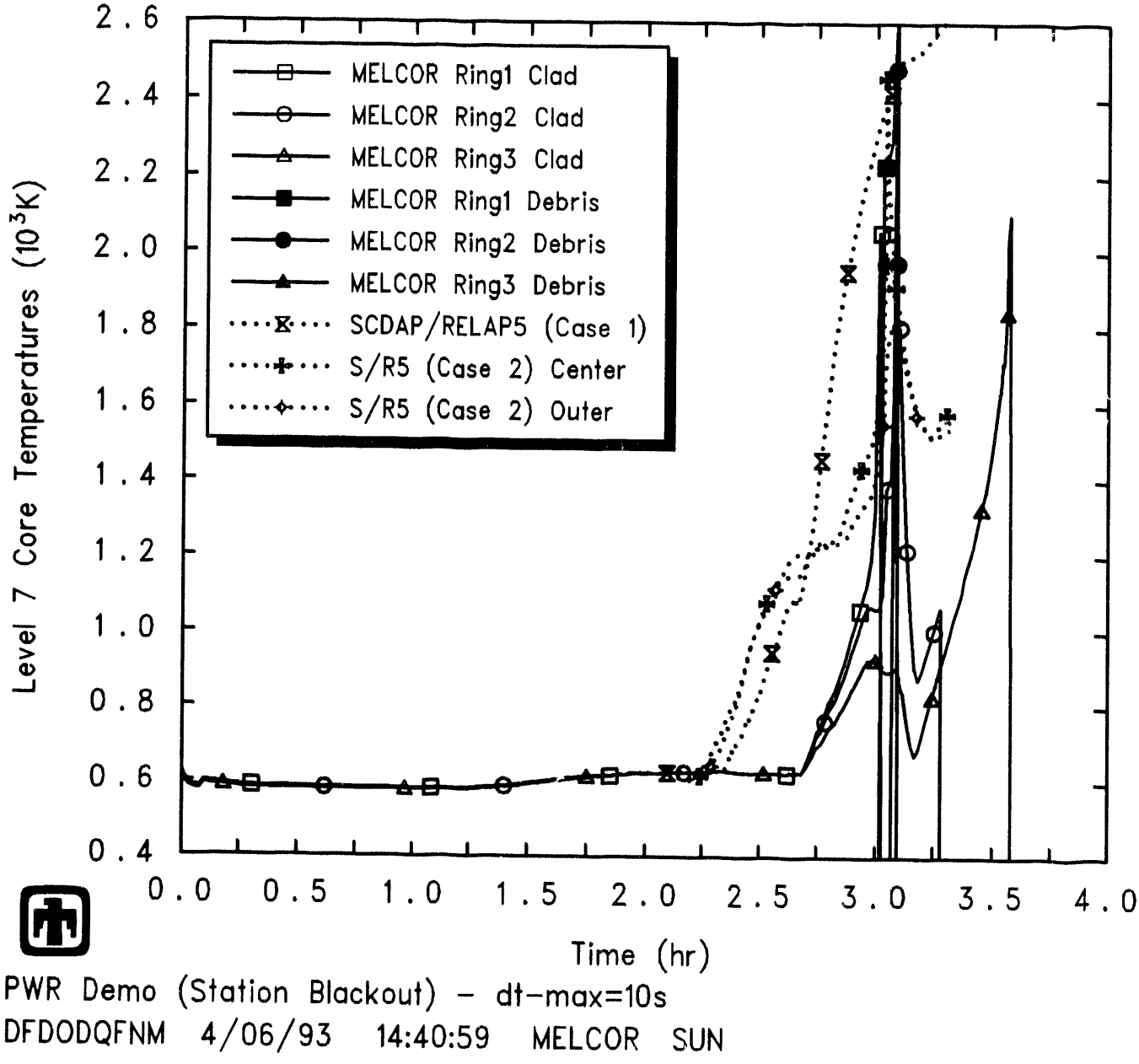

Figure 8.1.5. MELCOR Core Level 7 Clad Temperatures, Compared to SCDAP/RELAP5 Code Comparison Study

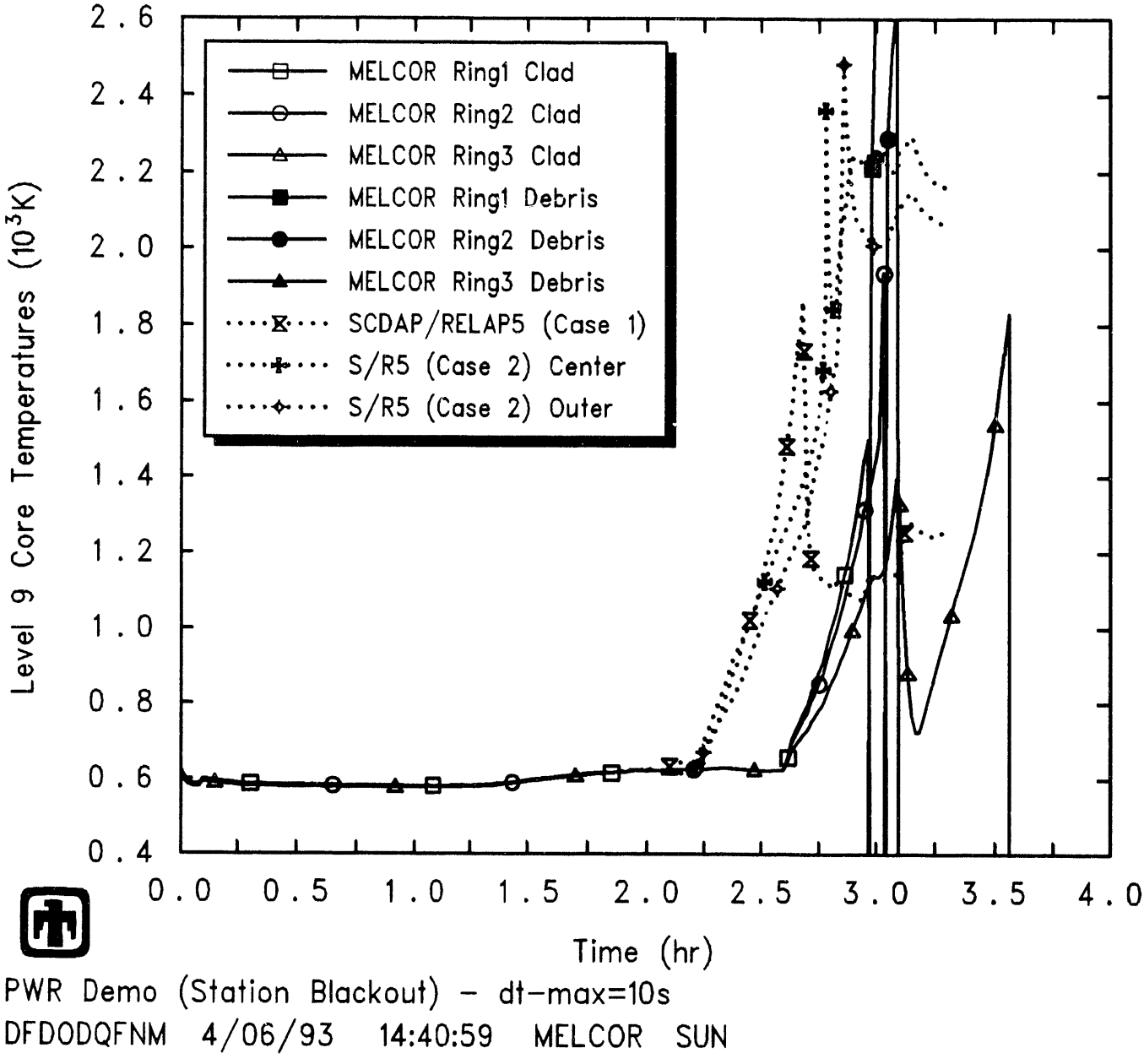

Figure 8.1.6. MELCOR Core Level 9 Clad Temperatures, Compared to SCDAP/RELAP5 - Code Comparison Study

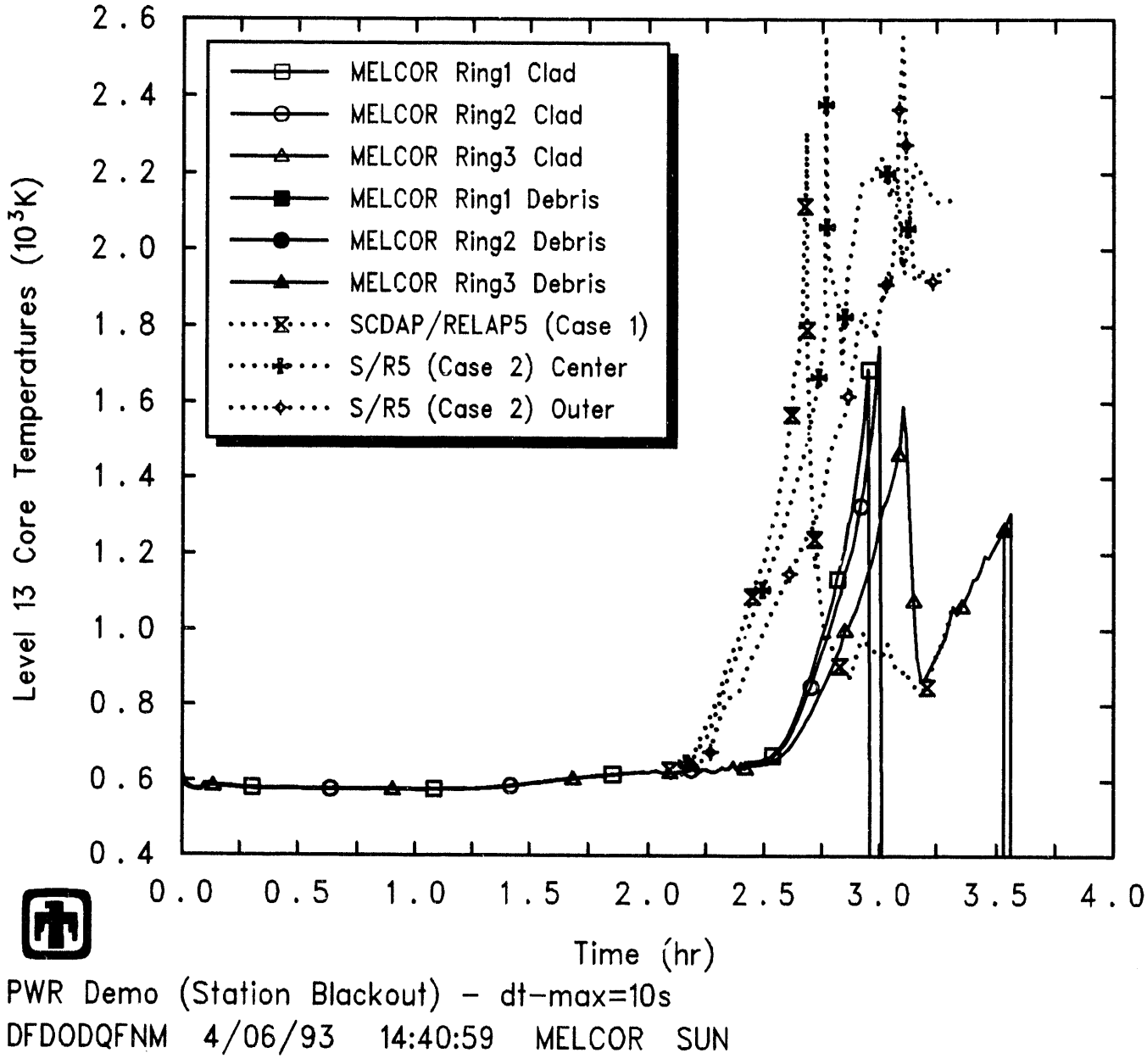

Figure 8.1.7. MELCOR Core Level 13 Clad Temperatures, Compared to SCDAP/RELAP5 – Code Comparison Study

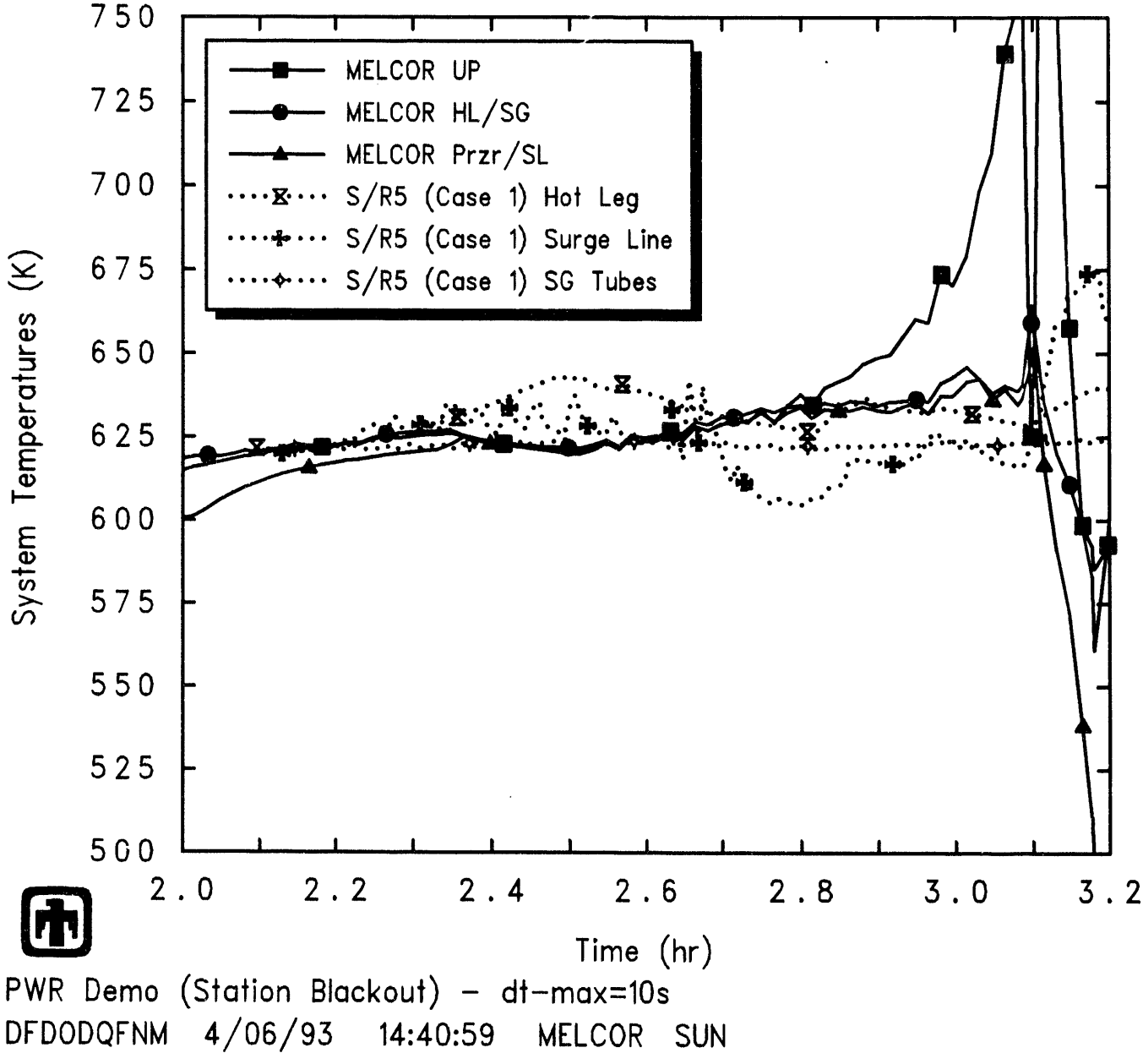

Figure 8.1.8. MELCOR Upper Plenum, Hot Leg, Surge Line and Steam Generator Tube Temperatures, Compared to SCDAP/RELAP5 with Once-Through Core and Upper Plenum Model - Code Comparison Study

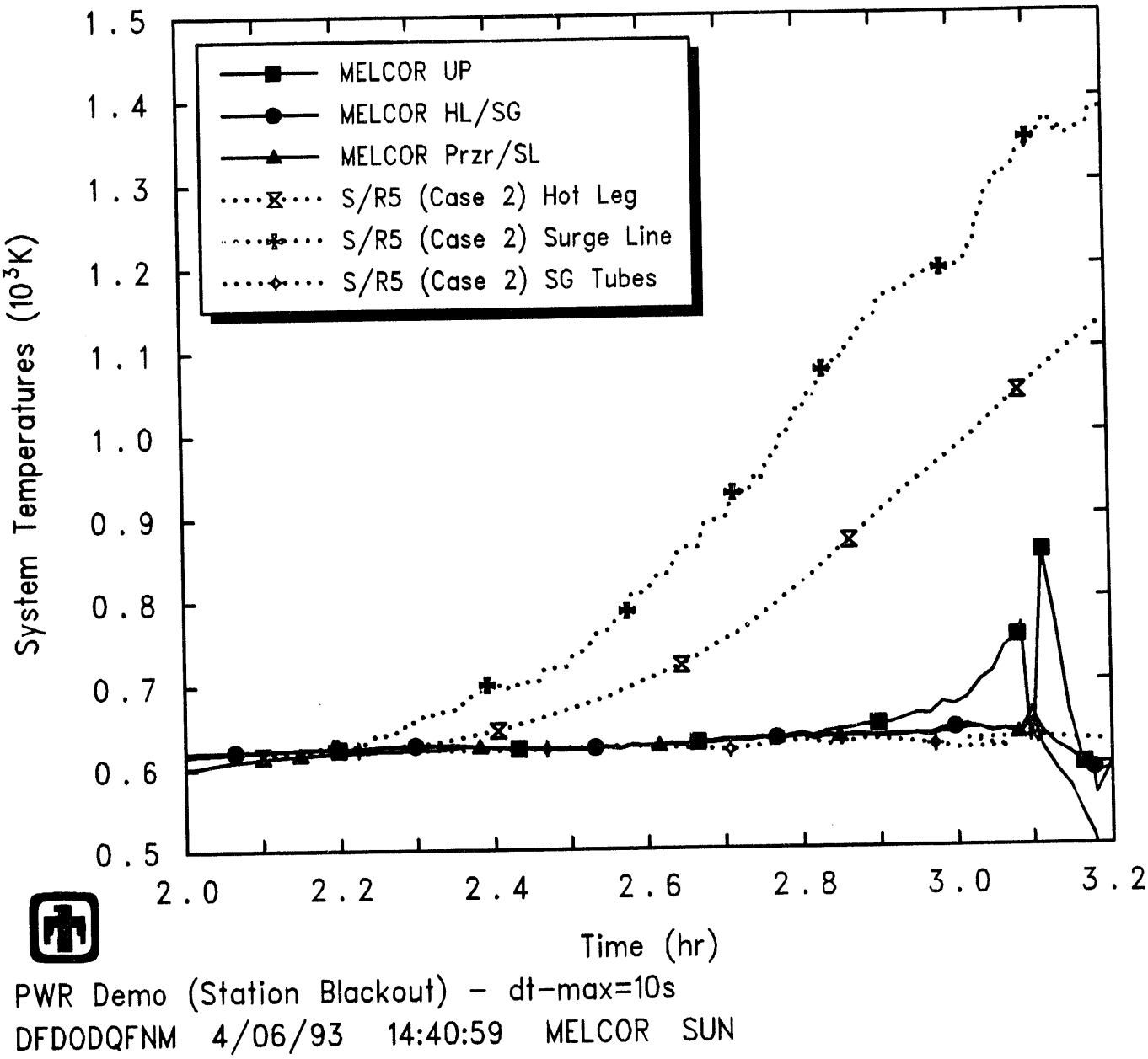

Figure 8.1.9. MELCOR Upper Plenum, Hot Leg, Surge Line and Steam Generator Tube Temperatures, Compared to SCDAP/RELAP5 with In-Vessel Natural Circulation Model – Code Comparison Study

water remaining in the upper plenum while the collapsed and swollen liquid levels in the core region drop slightly as steam bubbles appear in the saturated core water. Once the upper plenum is completely drained, the MELCOR calculation uncovers the core more slowly than seen with MELPROG or MELPROG/TRAC, which both uncover the core at the same rate after an initial timing offset. There is not enough detail given in [35] or [36] to analyze this difference further.

This difference in predicted core uncovery is reflected in the subsequent core heatup behavior calculated by MELCOR and by MELPROG and MELPROG/TRAC. Core maximum temperatures for these calculations are compared in Figure 8.1.11. Since Figure 3 in [35] and Figure 5.1 in [36] did not make clear what "maximum core temperature" was being plotted, we included comparisons to the maximum fuel, clad and debris temperatures in the MELCOR reference calculation; however, there was little or no difference in the maximum temperatures for the various MELCOR core components.

Again there are timing offsets due to the differences in predicted core uncovery. The subsequent core heatup rate calculated by MELCOR closely resembles the result from the MELPROG "1D" calculation, which did not include any in-vessel natural circulation; this is reasonable since MELCOR also does not include in-vessel natural circulation. As seen with SCDAP/RELAP5, the core heatup was visibly slower in the MELPROG "2D" and MELPROG/TRAC calculations (both of which included in-vessel natural circulation).

Figures 8.1.12 through 8.1.14 illustrate individual clad temperatures calculated by MELCOR and by MELPROG ("2D") throughout the core. Note that MELCOR used ten axial levels in the active fuel region, as described in Section 3, while the MELPROG input model had only six levels in the active core region (with clad temperatures shown for only five of those levels [36]). Also note that, while both MELCOR and MELPROG used three radial rings, the MELPROG calculation divided the core equally, while MELCOR had a large middle ring and smaller inner and outer rings. The results do suggest a smaller difference in behavior in upper and lower levels, and among radial rings, in the MELPROG analysis than seen in the MELCOR reference calculation.

The in-vessel hydrogen production for the MELCOR, MELPROG and MELPROG/TRAC calculations are compared in Figure 8.1.15. Despite timing shifts reflecting differences in beginning core uncovery and heatup, the total hydrogen produced in-vessel calculated by MELCOR closely resembles the corresponding final value from the MELPROG "1D" calculation, which did not include any in-vessel natural circulation; this is reasonable since that calculation agreed best with MELCOR on predicted core heatup rates. The total in-vessel hydrogen production in the MELPROG "2D" calculation (which included in-vessel natural circulation) is also only ~20% higher than the MELCOR result. The total in-vessel hydrogen production in the MELPROG/TRAC calculation is both significantly higher than any of the other results and qualitatively different in that the MELPROG/TRAC result does not show any slowdown in hydrogen production rate after the initial rapid generation. The higher hydrogen production in the MELPROG/TRAC calculation is due to setting the core failure temperature to 2500K [35] instead of to 2200K as in the MELPROG calculation used in this comparison; a MELPROG sensitivity study calculation using a failure temperature of 2500K instead

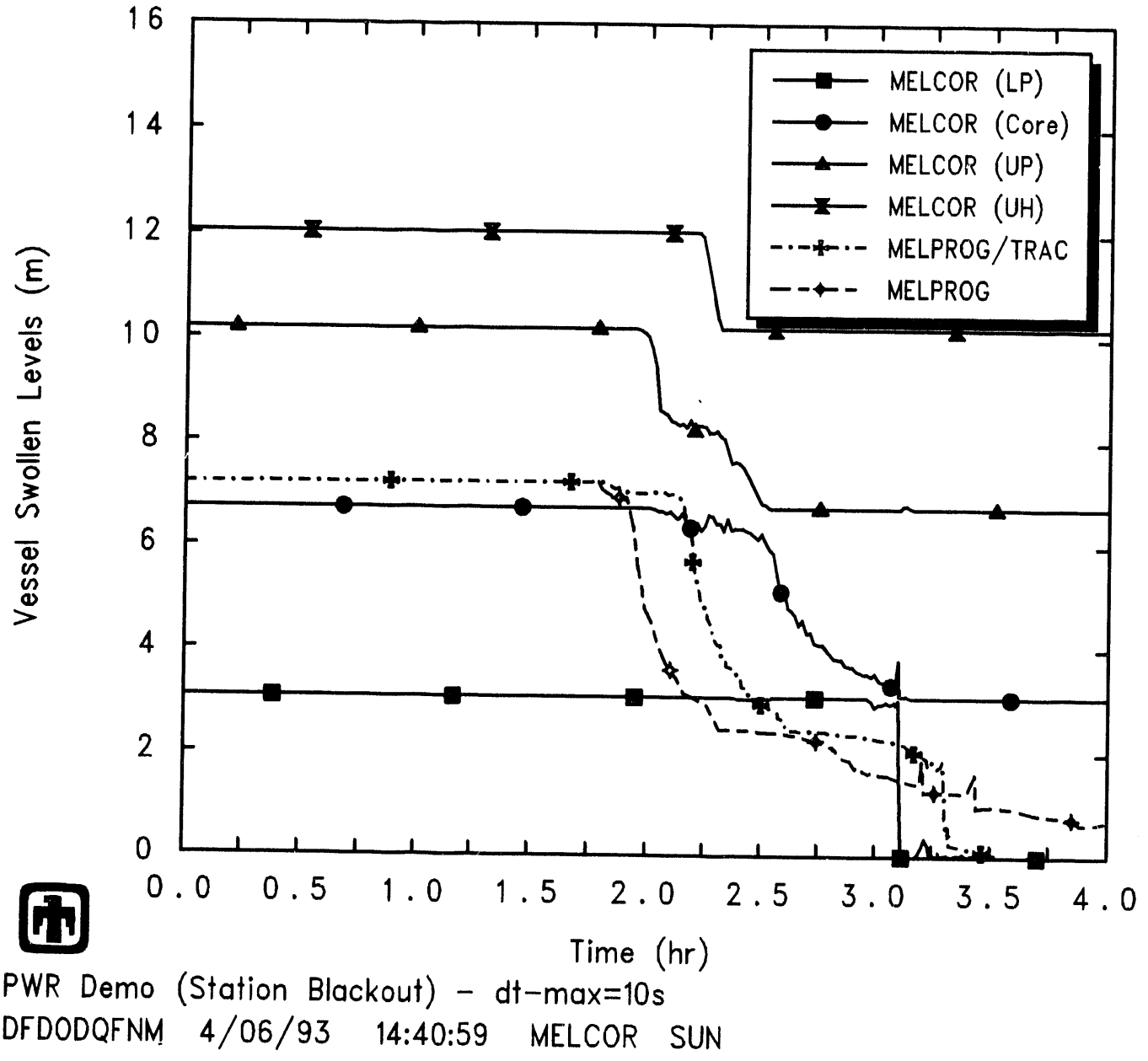

Figure 8.1.10. MELCOR Vessel Swollen (Two-Phase) Liquid Levels, Compared to MELPROG and MELPROG/TRAC – Code Comparison Study

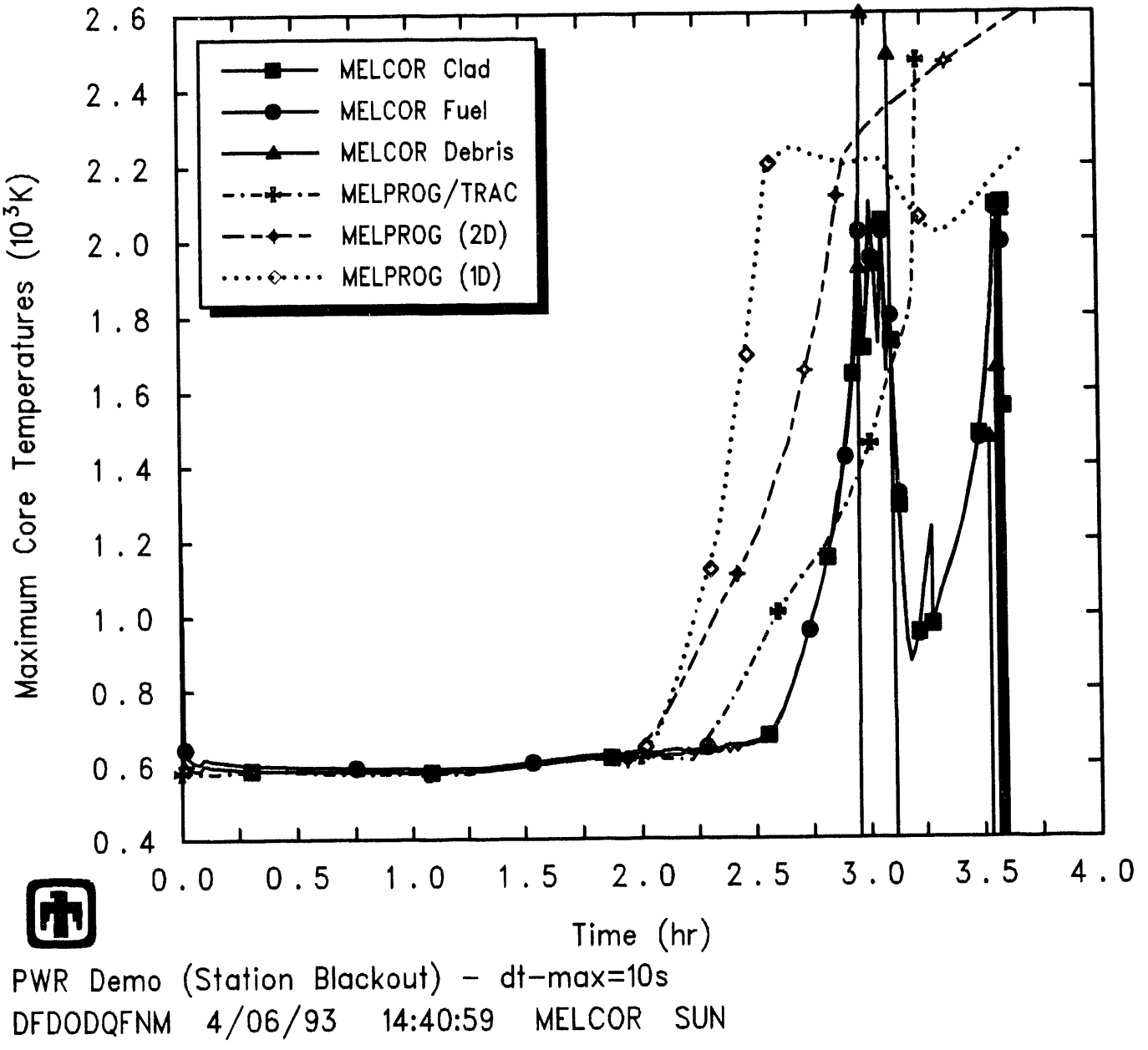

Figure 8.1.11. MELCOR Maximum Core Temperatures, Compared to MELPROG and MELPROG/TRAC - Code Comparison Study

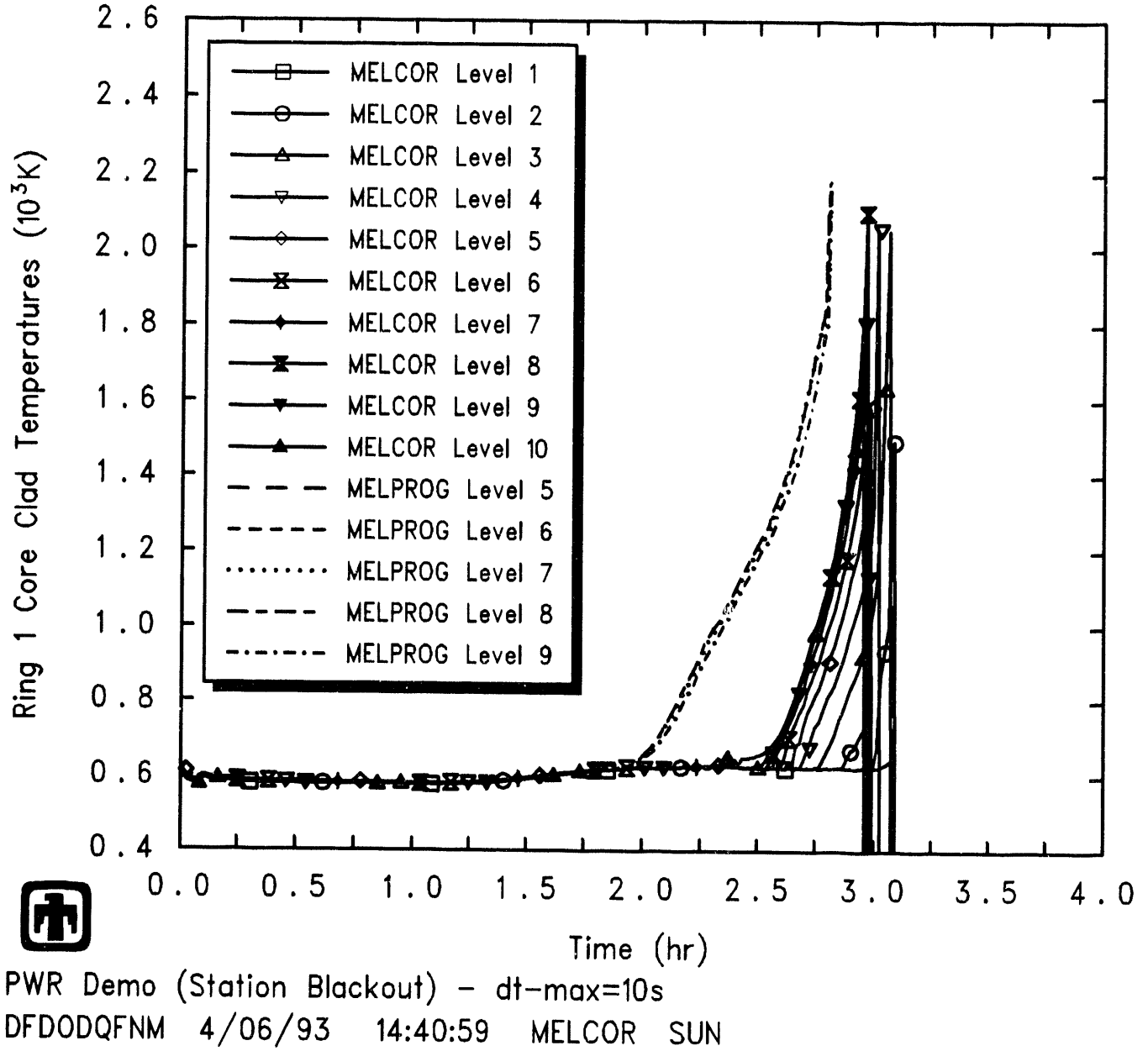

Figure 8.1.12. MELCOR Ring 1 Core Clad Temperatures, Compared to MELPROG - Code Comparison Study

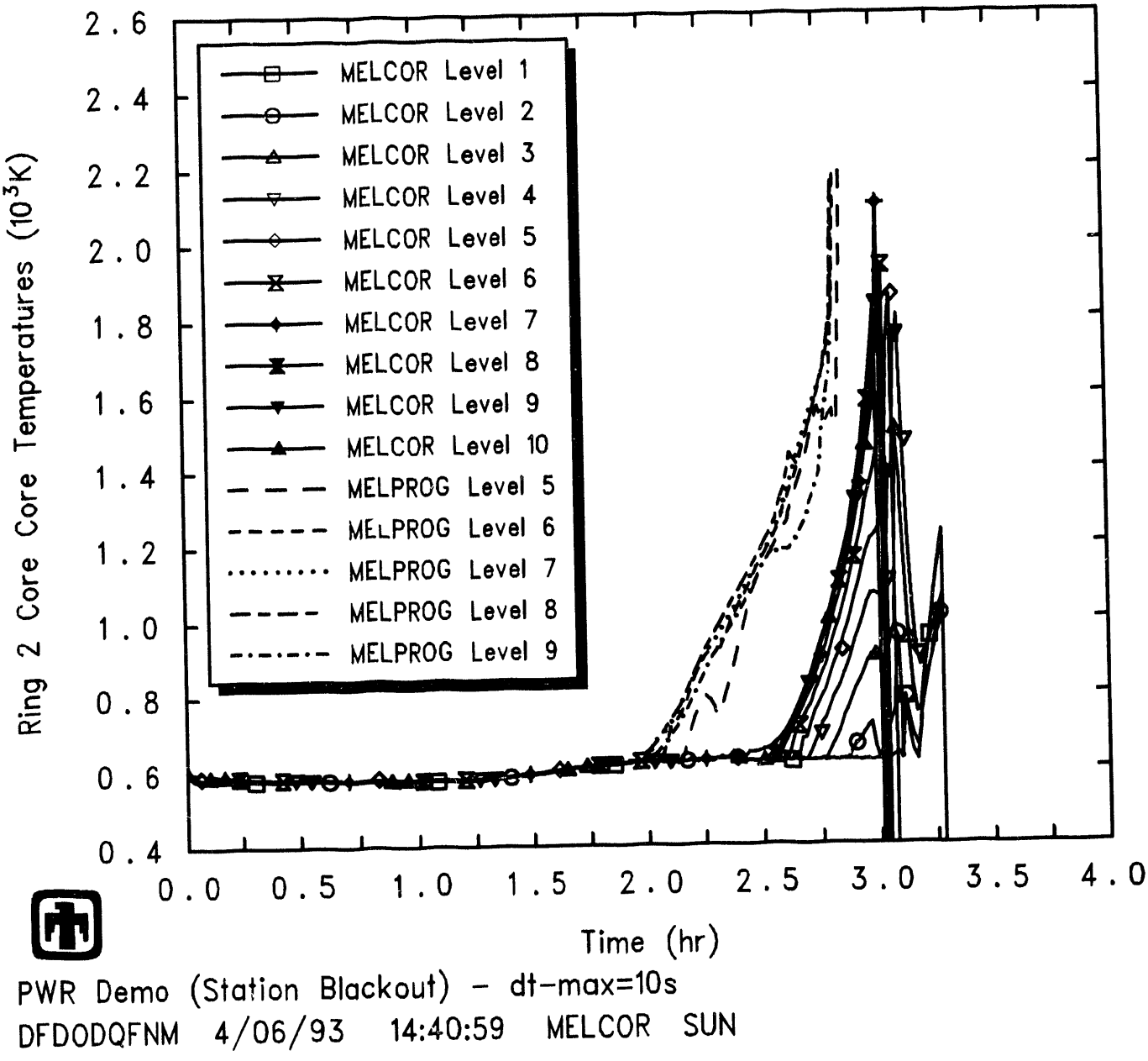

Figure 8.1.13. MELCOR Ring 2 Core Clad Temperatures, Compared to MELPROG - Code Comparison Study

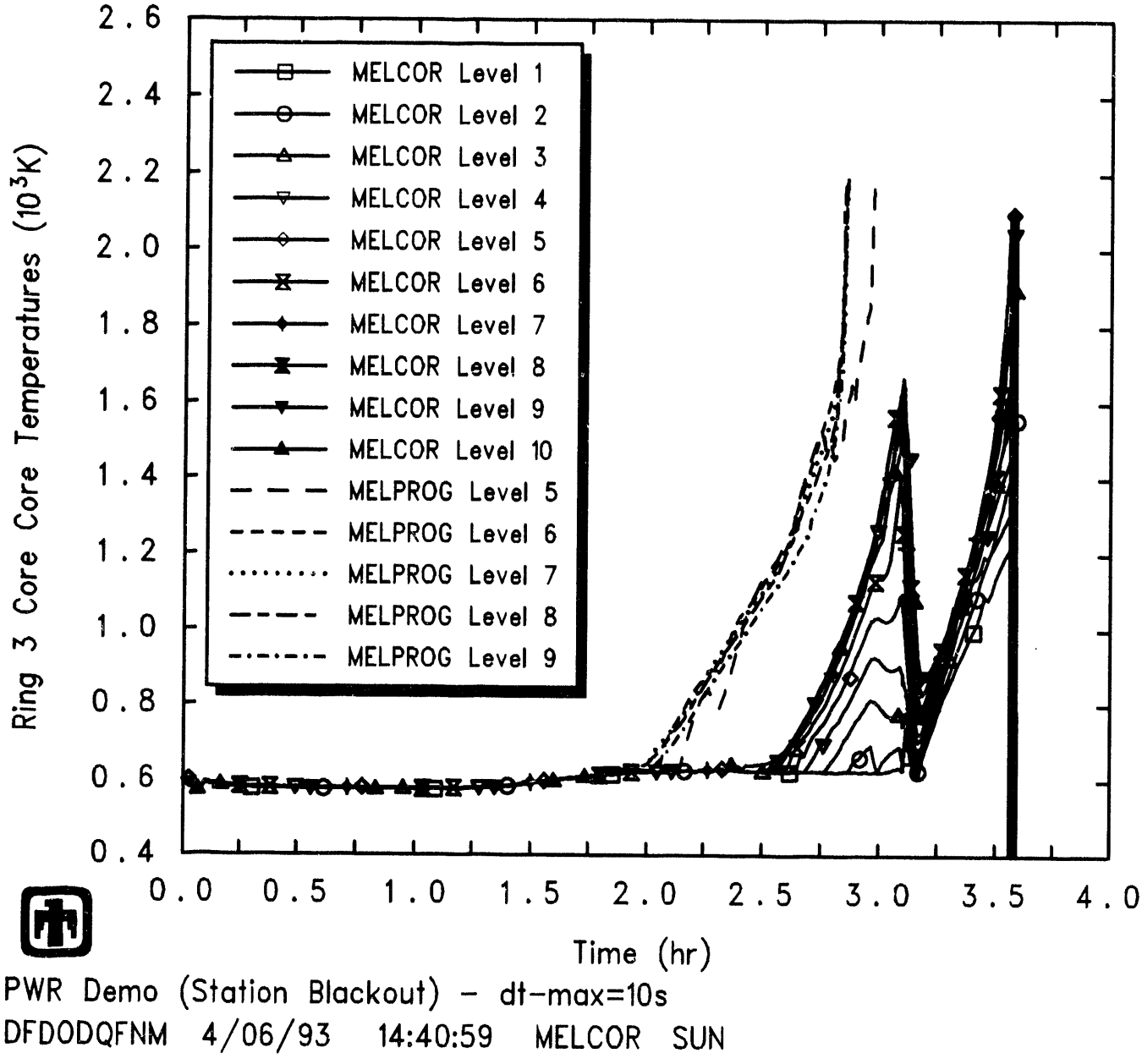

Figure 8.1.14. MELCOR Ring 3 Core Clad Temperatures, Compared to MELPROG - Code Comparison Study

of 2200K also showed higher in-vessel hydrogen production, quantitatively similar to the MELPROG/TRAC result, as described in [36]. Also, the MELPROG/TRAC calculation was not run to vessel failure, as were the MELPROG calculations, so the "plateau" in hydrogen production is not seen in that case.

Table 8.1.2 summarizes the state of materials in the core at vessel breach, as predicted by MELCOR and by MELPROG. It is assumed in this comparison that the values reported for debris states in [35] and [36] are for debris in the lower plenum at vessel failure, so the MELCOR values for the reference calculation are taken from Table 4.2.1 for debris in the lower plenum.

The results of comparisons for primary system response and core damage with detailed, best-estimate, state-of-the-art codes such as SCDAP/RELAP5, MELPROG and MELPROG/TRAC (and with older, engineering-level integrated codes such as STCP, as described later in Section 8.3) highlight the importance of continued assessment of MELCOR's ability to calculate the early-time thermal/hydraulics in the severe accident precursor. This portion of MELCOR (*i.e.*, the CVH/FL packages) is significantly different than the corresponding RELAP5 and/or TRAC modelling approach (and also significantly different than the corresponding MARCH modelling approach), and the biggest differences found in the results were in the predicted times to core uncovery, which then propagated throughout the remainder of the accident sequence. The maximum and average core heatup rates in the various calculations were generally similar, if best-estimate calculations without in-vessel natural circulation were used as the comparison values; including in-vessel natural circulation tends to slow the core heatup and degradation process somewhat.

The MELCOR calculations generally showed core damage and relocation at lower temperatures than the MELPROG, MELPROG/TRAC or STCP analyses using default failure temperature and other failure criteria, but the various failure criteria are adjustable through input. Because of this, MELCOR also generally seemed to have less debris in the lower plenum at the time of vessel failure (although there is some question of the exact definition of the quantities being compared). Since MELCOR can continue to lose debris from the vessel to the cavity throughout an integral transient calculation, this difference may not be as significant as appears. However, the amount of debris present in the lower plenum at vessel failure and the conditions in that debris (*i.e.*, temperature, composition, *etc.*) are very important parameters for DCH analyses. The variations in core state and lower plenum debris found in the various MELCOR sensitivity-study analyses done, and the differences seen between MELCOR results and corresponding results from other codes such as MELPROG, MELPROG/TRAC and STCP identify late-time vessel melt progression (and particularly core plate and lower head failure) as an area requiring further study.

8.2 Containment Response

The containment response of the Surry PWR to a TMLB' accident has been calculated by the best-estimate containment thermal/hydraulic code CONTAIN, both for the early-

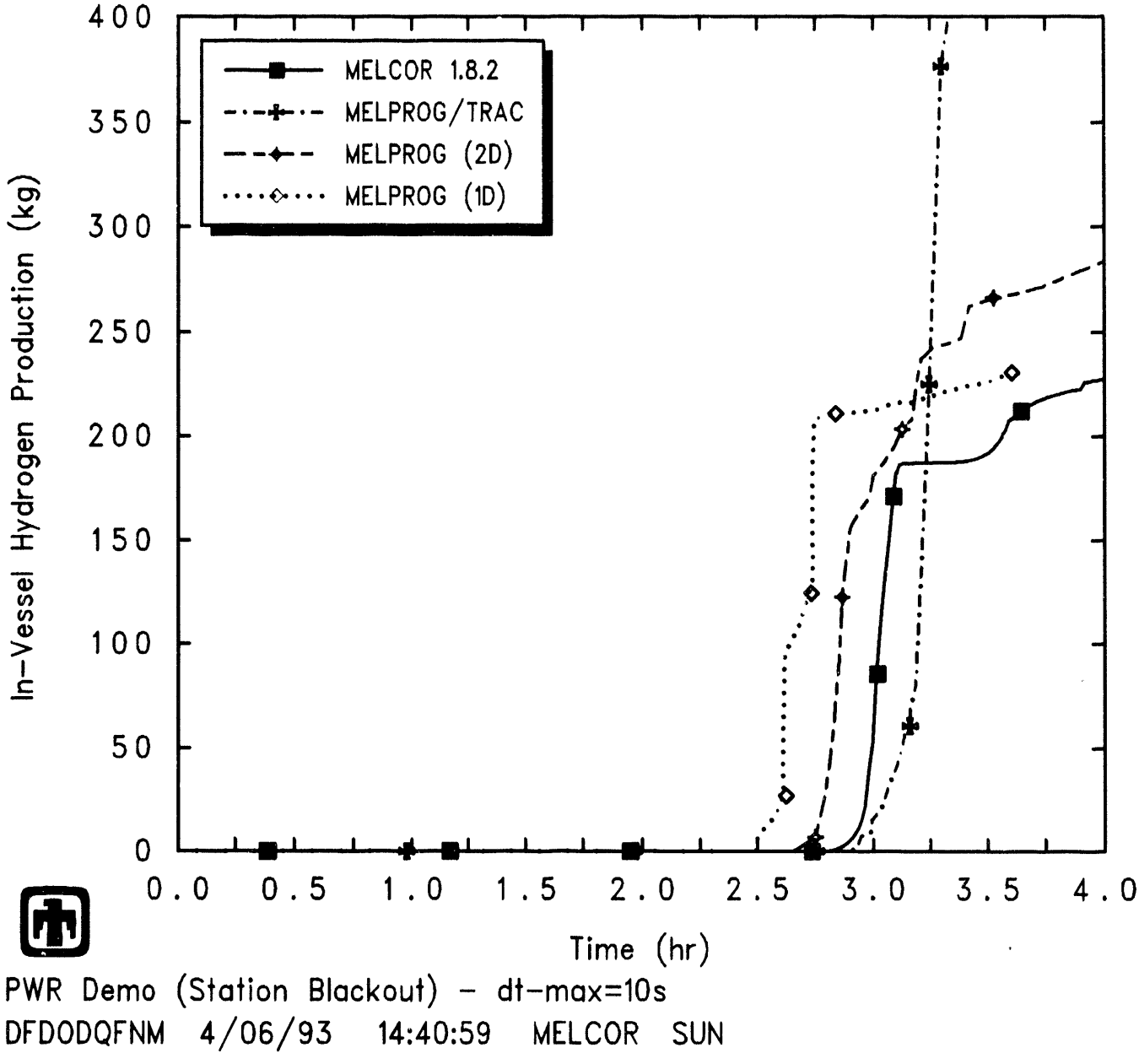

Figure 8.1.15. MELCOR In-Vessel Hydrogen Production, Compared to MELPROG and MELPROG/TRAC - Code Comparison Study

Table 8.1.2. MELCOR Core State at Vessel Failure, Compared to MELPROG – Code Comparison Study

Parameter	MELCOR 1.8.2	MELPROG "1D"	MELPROG "2D"
Mass of Debris			
UO_2	44,434		96,000
Zircaloy	2,825		9,600
Zirc Oxide	4,943		9,250
Steel	95	900	19,300
Steel Oxide	114		
CRP	334		2,850
Total	52,745	117,500	137,000
Average Debris Temperature	~2450	2600	2460
Fraction Debris Molten	~6%	34%	30%
Fraction Material Relocated	~50%		
Fraction Zircaloy Oxidized	~30%	31%	40%

time containment response at vessel failure including direct containment heating effects [37, 38, 39], and recently for the longterm containment response [40] with no direct containment heating.

Many of the DCH calculations documented were done with older versions of the CONTAIN code [37, 38], and are not used in this comparison. The most recent CONTAIN DCH calculations for Surry were done as part of an integrated program on DCH issue resolution [39]. The calculations selected for comparison were cases "SY11" and "SY12" in [39]. Both these calculations assumed the primary system at 16MPa at vessel failure; one calculation ("SY11") assumed an autoignition temperature of 950K, while the other ("SY12") assumed an autoignition temperature of 700K.

Figure 8.2.1 shows short-term containment dome pressures for a number of MELCOR HPME/DCH sensitivity study calculations, described in more detail in Section 6.5.1, together with CONTAIN results from Figure 3.20 in [39]. Vessel failure and high-pressure melt ejection were assumed to occur at 10,900s in the CONTAIN calculation, and containment was assumed to be at 200kPa at the start of HPME/DCH. CONTAIN results were presented for a 20s period following the start of HPME/DCH.

These results are difficult to compare graphically because of the short period for which CONTAIN results are available. The timing offsets are obviously due to differences in assumed (CONTAIN) or calculated (MELCOR) vessel failure times. More interestingly, the peak pressure excursions (*i.e.*, ΔP_{MAX}) for these CONTAIN DCH calculations are 0.35MPa for the calculation with an autoignition temperature of 950K ("SY11" in [39]), and 0.46MPa for the calculation with an autoignition temperature of 700K ("SY12" in [39]). The result for either value of autoignition temperature is substantially higher that the peak pressure rise of $\leq$0.20MPa in the MELCOR calculation with $\sim$60% initial debris ejection and with both high-pressure melt ejection and direct containment heating modelled. There are also several qualitative differences in the CONTAIN and MELCOR results. Unlike the CONTAIN result, little or no pressure increase was calculated by MELCOR using an enhanced burn ignition during HPME/DCH, as discussed in Section 6.5.4; this may reflect numerical problems in the burn coding in MELCOR (already discussed in Section 7) more than any actual effect of enhanced combustion during HPME/DCH. Also, the pressures in the CONTAIN calculations appear to drop more quickly from their peak values than the pressure decreases predicted in the MELCOR analyses; however, note that, since the CONTAIN results are only given for a 20s period, this comparison is quite limited.

CONTAIN calculations have also been done studying the late containment pressurization resulting from a station blackout in Surry, but with no DCH modelled [40]. Those results are compared to the long-term containment pressure response from the MELCOR reference calculation in Figure 8.2.2.

This CONTAIN calculation also assumed vessel failure at 10,900s, and a containment pressure of $\sim$130kPa at vessel failure. The amount of core debris sourced into CONTAIN was probably comparable to the MELCOR core debris ejected from the vessel. The starting pressure in the CONTAIN calculation is quite similar to the MELCOR containment

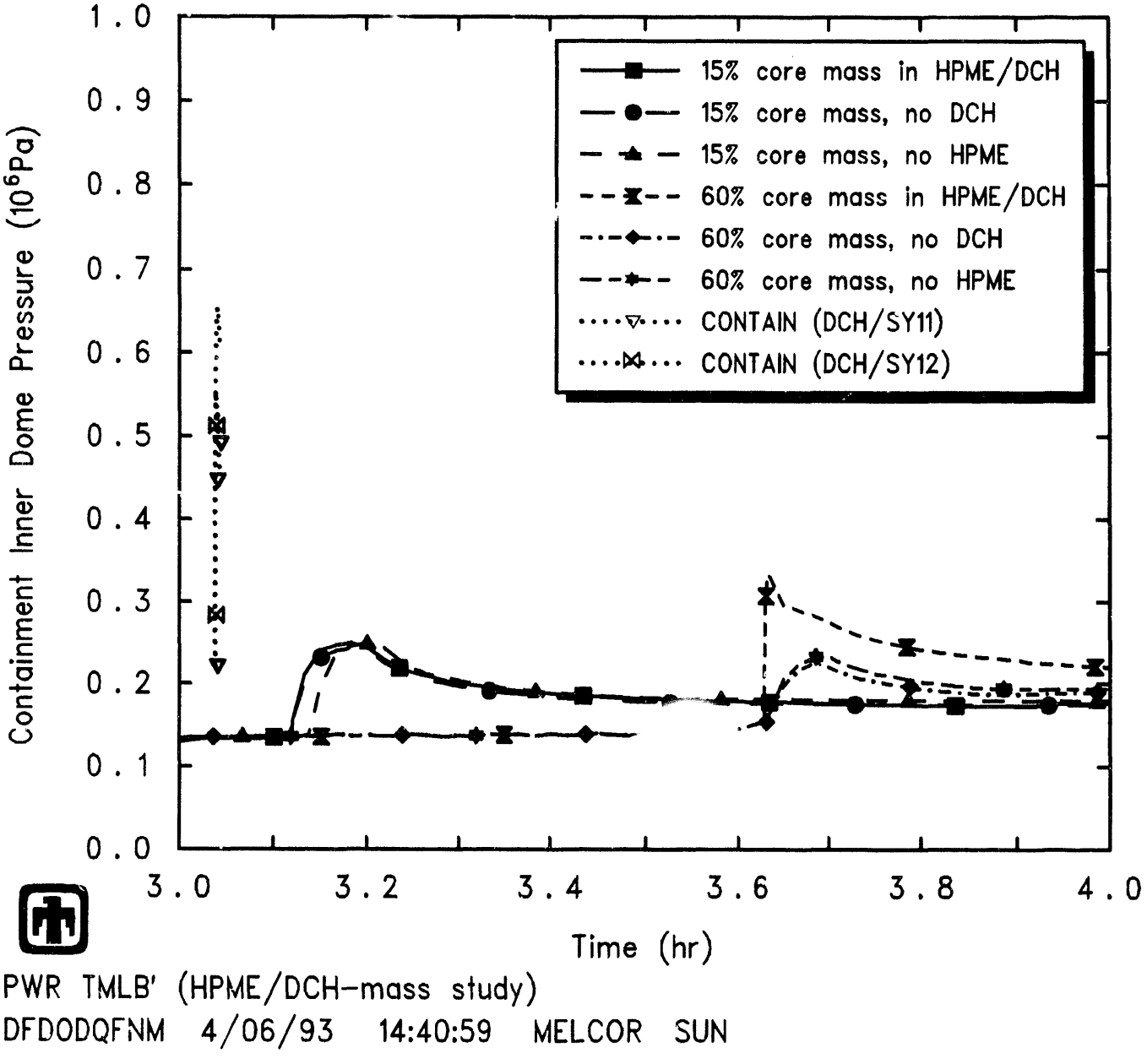

Figure 8.2.1. MELCOR Containment Dome Pressure during HPME and DCH for HPME/DCH Debris Mass Sensitivity Study, Compared to CONTAIN - Code Comparison Study

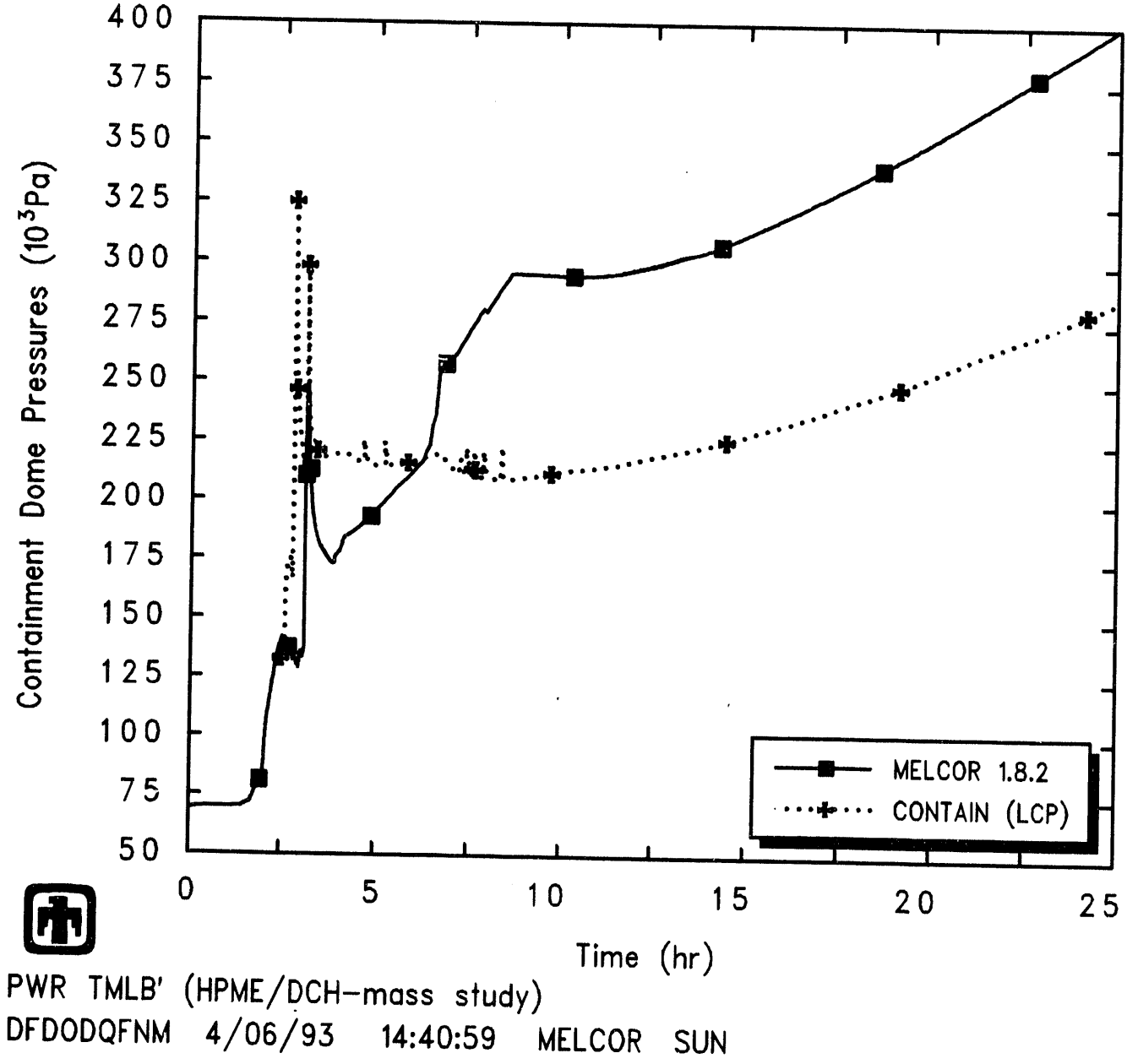

Figure 8.2.2. MELCOR Containment Dome Pressure, Compared to CONTAIN – Code Comparison Study

pressure just before vessel failure, with that early pressurization due to primary inventory loss out the pressurizer PORV. The initial pressure spikes in the CONTAIN calculation are due to hydrogen deflagrations in addition to debris ejection, and are larger than the corresponding MELCOR pressure spike; however, the CONTAIN calculation sources the core debris over a short period of time after vessel failure and calculation start, while the MELCOR calculation can lose debris from the vessel more gradually (as shown in Figure 4.2.12. The more rapid containment pressurization in MELCOR between ~4hr and ~8hr corresponds to the time when water in the cavity (from the lower plenum, accumulators and pressurizer) is being boiled away; the much slower containment pressurization in MELCOR after ~8hr corresponds to the time when significant core-concrete interaction is occurring. The CONTAIN calculation assumed a dry cavity, and thus began core-concrete interaction soon after vessel failure and debris introduction into the cavity. The long-term pressurization rate predicted by CONTAIN is very similar to the corresponding behavior predicted by MELCOR, neglecting the offset due to boiling off cavity water in the MELCOR analysis.

8.3 Overall Transient Response

The overall transient behavior of the Surry PWR TMLB' accident has been calculated several times by STCP, by various users [41, 42, 43, 44]. At the time they were done, these were best-estimate source term calculations, using a linked set of codes to analyze the entire accident sequence.

The NRC sponsored a large number of calculations for various accident sequences in a number of representative plants done at Battelle [41, 42]. For these analyses, overall thermal/hydraulic conditions on a time-dependent basis were calculated with the MARCH code, and detailed thermal/hydraulic conditions for the primary system estimated with the MERGE code; the resultant time-dependent core temperatures were used as input to CORSOR, which predicts time- and temperature-dependent mass releases of radionuclides from the fuel within the vessel, while releases during core-concrete interactions of radionuclides remaining with the melt were provided by VANESA. Using the MARCH/MERGE-predicted thermal/hydraulic conditions and the CORSOR-predicted radionuclide release rates as input, the TRAP-MELT2 code was used to predict vapor and particulate transport in the primary coolant system; transport and deposition of radionuclides in the containment were calculated using the NAUA-4 code.

Results are given in [41] for TMLB' sequences in the Surry plant with both early and late containment failure by overpressure (TMLB'-δ and TMLB'-ϵ, respectively) assumed; these were the first calculations done, and used early code versions such as MARCH1.1 for the thermal/hydraulic response and CORRAL-2 for radionuclide transport in the containment (as well as NAUA-4). These calculations were repeated with the thermal/hydraulic response calculated by MARCH2 and the radionuclide transport in the containment all by NAUA-4, with results given in [42]; again, variants with both early and late containment failure by overpressure were analyzed. (The MELCOR 1.8.2 analysis corresponds to the TMLB'-ϵ late containment failure case.)

An independent verification of the source term predicted by Battelle using STCP in selected accident sequences was performed by BNL [43], including the Surry TMLB' with early containment failure. Although in this case the containment fails very soon after vessel breach, the system response prior to that is identical to the case with late containment failure assumed. In this analysis, updated versions of several codes were used, notably MARCH3.

EPRI also sponsored a best-estimate recalculation of the source term and accident consequences for several different transient sequences in the Surry plant, using STCP [44]. In this set of calculations, a mixture of NRC and EPRI codes were linked to analyze the entire transient sequence. The overall thermal/hydraulic conditions on a time-dependent basis were calculated with the MARCH2 code, and detailed thermal/hydraulic conditions for the primary system estimated with the EPRI PTSAC code. Radioactivity and structural material releases from the core, both in-vessel and ex-vessel, were developed specifically for these analyses from reports of experimental studies and detailed analytical modelling results, with timing requirements provided by MARCH-2. Using the PTSAC-predicted primary system thermal/hydraulic conditions and the MARCH-2/CORCON-MOD1 containment thermal/hydraulic conditions and the CORSOR-predicted radionuclide release rates as input, the TRAPMELT-82 code was used to predict vapor and particulate transport in the primary coolant system; transport and deposition of radionuclides in the containment were calculated using the MATADOR code. Finally, the radioactivity releases to the environment were fed to the ex-plant consequence code CRAC-2.

Table 8.3.1 compares the timing of various events in the TMLB' transient as predicted to occur in the reference MELCOR 1.8.2 calculation and in the various STCP analyses.

Figure 8.3.1 compares the primary system pressures early in the TMLB' sequence predicted by MELCOR and by MARCH3 [43]. Qualitatively, both codes predict the same behavior – a decrease in pressure over the first hour, followed by cycling at the pressurizer PORV setpoints after steam generator dryout; quantitatively, MARCH predicts a greater pressure drop during the first hour than seen in the MELCOR calculation.

The total water inventory predicted in the MELCOR 1.8.2 reference calculation is compared to the corresponding result from MARCH3 [43] in Figure 8.3.2. As with the primary system pressure comparison given in Figure 8.3.1, the two results agree well qualitatively, but with some quantitative shifts in both magnitude and timing.

The earlier primary system water inventory loss seen in this STCP analysis is reflected in earlier core uncovery and core heatup behavior calculated by STCP compared to MELCOR. Core maximum temperatures for the STCP calculation [43] are compared to corresponding MELCOR results in Figure 8.3.3. Since it was not clear what "maximum core temperature" was being plotted, we included comparisons to the maximum fuel, clad and debris temperatures in the MELCOR reference calculation. There was little or no difference in the maximum temperatures for the fuel and clad MELCOR core components, but the maximum debris temperature obviously compares best to the STCP results just before vessel failure. The maximum heatup rates agree reasonably well given the timing

Table 8.3.1. Timing of Key Events for Overall Transient – Code Comparison Study

Event	Time (s)				
	MELCOR	STCP			
	1.8.2	[41]	[42]	[43]	[44]
Loss of Electrical Power	0.0	0.0	0.0	0.0	0.0
SG Secondary Side Dried Out	~5000	4980	4050	4782	4574-4632
Core Uncovery	~7200	10980	5730	6624	7740
Clad Melts/Fuel Rods Fail		7098		8610	
Core Slumps		16200	8778	9906	10200
Core Collapse		16380	8838	9936	10200
Core Support Plate Fails	11,181.5				
Lower Head Fails	11,225.5	16500	9168	10566	10500
Cavity Dried Out	~30,000	16638	12894		
Start Concrete Attack	~30,000	23394	17394		25152 (INTER)
Containment Fails	–	169848	44292		
Calculation Ended	90,000	169848	66000		

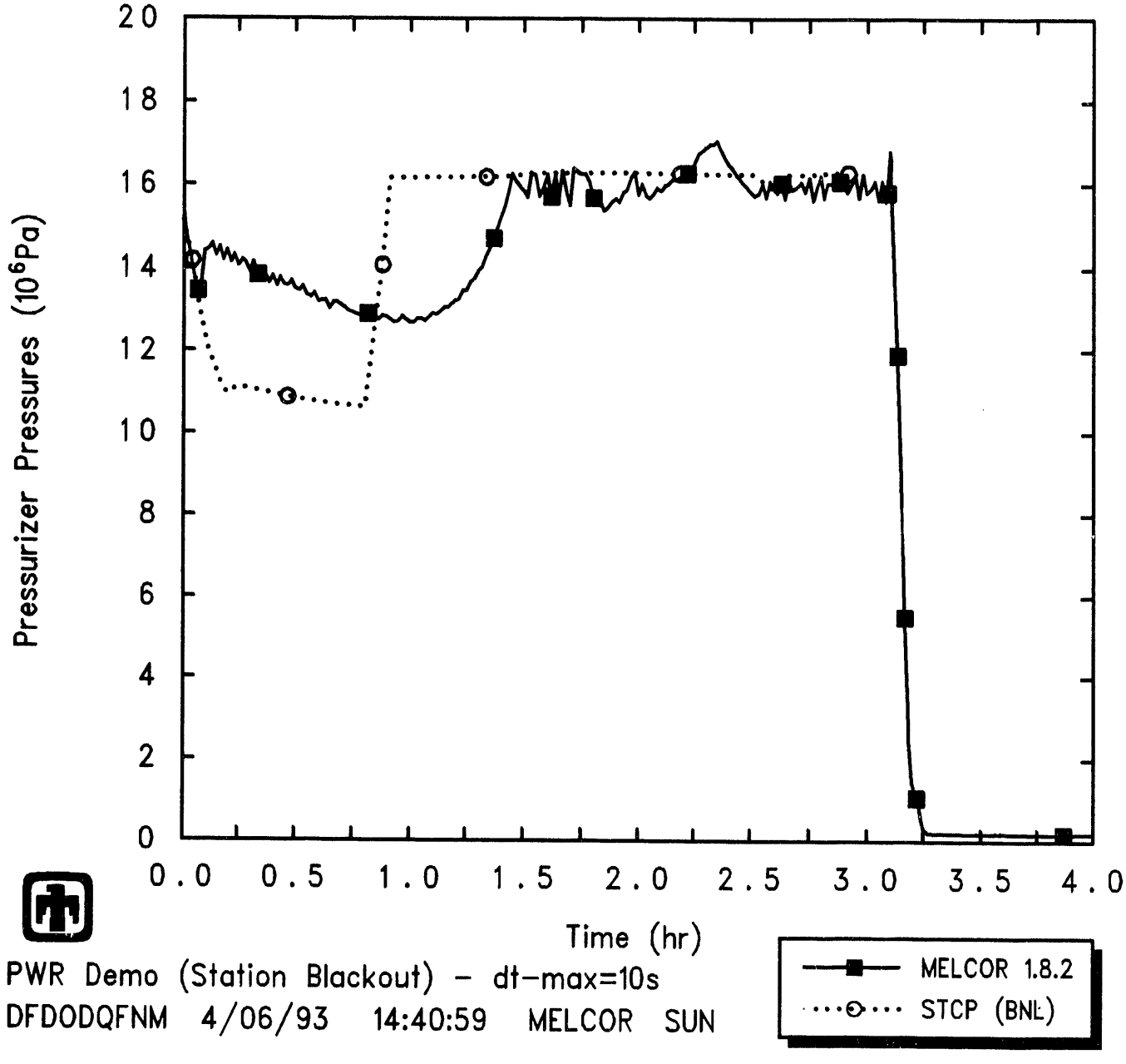

Figure 8.3.1. MELCOR Primary System Pressure, Compared to STCP – Code Comparison Study

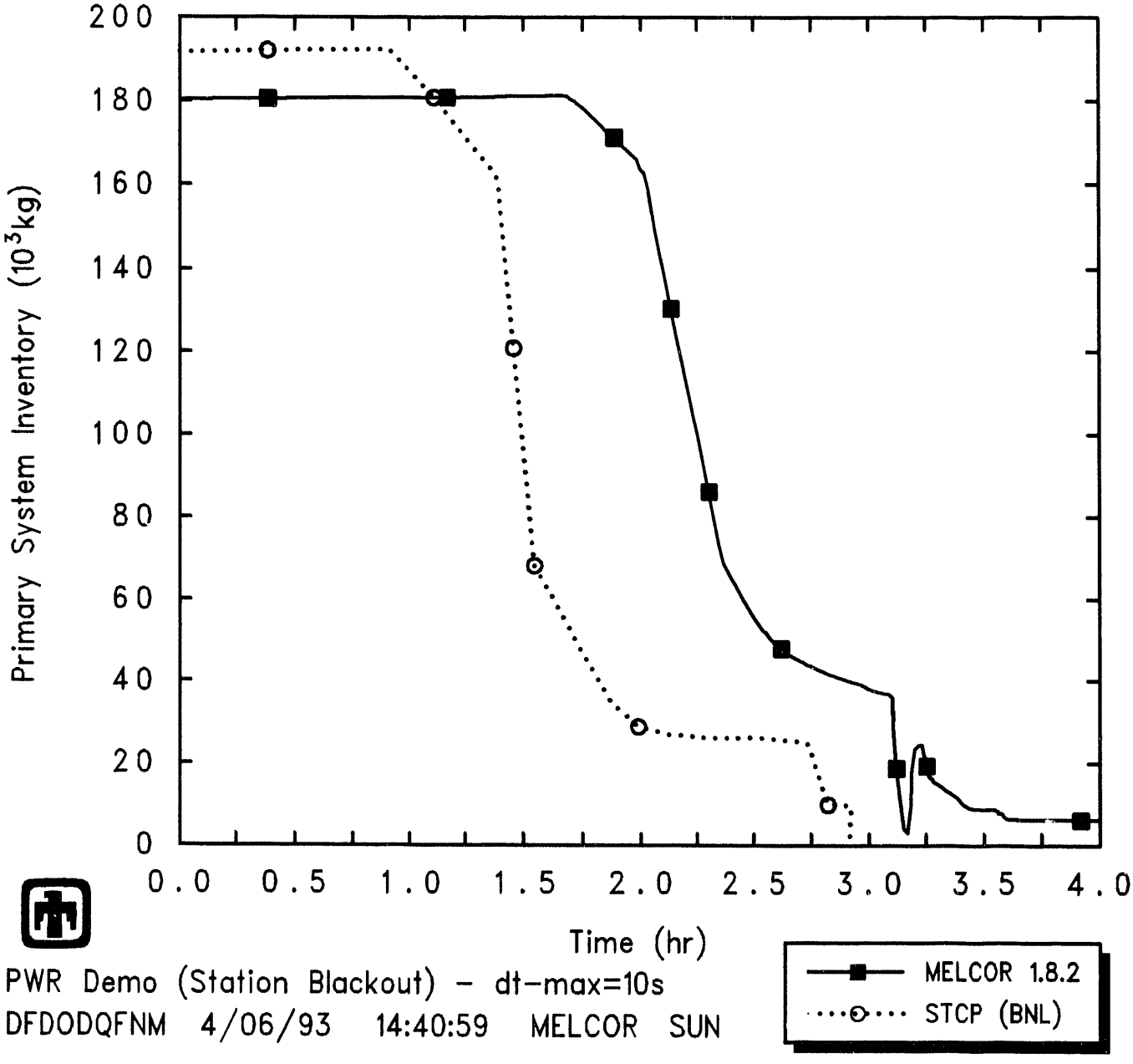

Figure 8.3.2. MELCOR Primary System Water Inventory, Compared to STCP – Code Comparison Study

difference in core uncovery, although the MELCOR core heatup appears slower at low temperatures, and the STCP core maintains high ($\geq$2500K) core temperatures longer before failing the vessel.

Figure 8.3.4 presents core average temperatures from two of the STCP calculations [43, 44], compared to corresponding results from the MELCOR reference analysis. Again, since it was not clear what "average core temperature" was being plotted, we included comparisons to the average fuel only, average fuel and debris, and average fuel, clad and debris temperatures in the MELCOR reference calculation. There was little or no difference in the average temperatures with and without the clad temperature included, but the average core temperature including both debris and intact fuel is generally higher than the average core temperature including intact fuel only, as might be expected. As with the maximum temperature comparison given in Figure 8.3.3, the average heatup rates agree reasonably well given the timing difference in core uncovery, although the MELCOR core heatup appears slower at low temperatures, and the STCP core reaches higher ($\geq$2000K) average core temperatures before failing the vessel than does the MELCOR analysis.

Clad temperature comparisons at four core elevations are presented in Figures 8.3.5 through 8.3.8, for MELCOR compared to the two earlier STCP analyses [41, 42]. The results in these figures once again show the effect of different core uncovery times being calculated (given in Table 8.3.1); the MARCH1.1 analysis in [41] predicts core uncovery significantly later than the corresponding MARCH2 analysis in [42].

Figure 8.3.9 compares the temperatures in the upper plenum, hot leg, pressurizer, surge line and steam generator tubes calculated by MELCOR and by STCP (using the PTSAC code) [44]. The MELCOR results for the temperatures in the hot leg, pressurizer surge line and steam generator tubes generally resemble those from the PTSAC calculation, given the earlier core uncovery and failure in that STCP analysis shifting results in time. Both calculations show the hottest temperatures in the upper plenum, as would be expected, and then lower temperatures farther from the core. The MELCOR calculation has superheated steam only in the upper plenum for a short time before vessel failure; the STCP/PTSAC calculation has superheated steam also in the hot leg and pressurizer surge line, with saturated conditions in the pressurizer. The saturated conditions in the MELCOR surge line and hot leg may reflect the incomplete pressurizer draining prior to vessel failure in our calculations (discussed in more detail in Sections 4 and 6.1).

Table 8.3.2 summarizes the state of materials in the core at vessel breach, as predicted by MELCOR and by STCP. We assumed in this comparison that the values reported for debris states in [41, 42, 43, 44] are for debris in the lower plenum at vessel failure, so the MELCOR values for the reference calculation are taken from Table 4.2.1 for debris in the lower plenum.

The atmospheric pressures calculated in the containment by MELCOR and by STCP are compared in Figure 8.3.10, divided into two displays for increased clarity; the upper plot in Figure 8.3.10 presents a comparison of the MELCOR reference calculation result to early STCP calculations [41, 42], while the lower plot in Figure 8.3.10 presents a comparison of the MELCOR reference calculation result to more recent STCP calculations

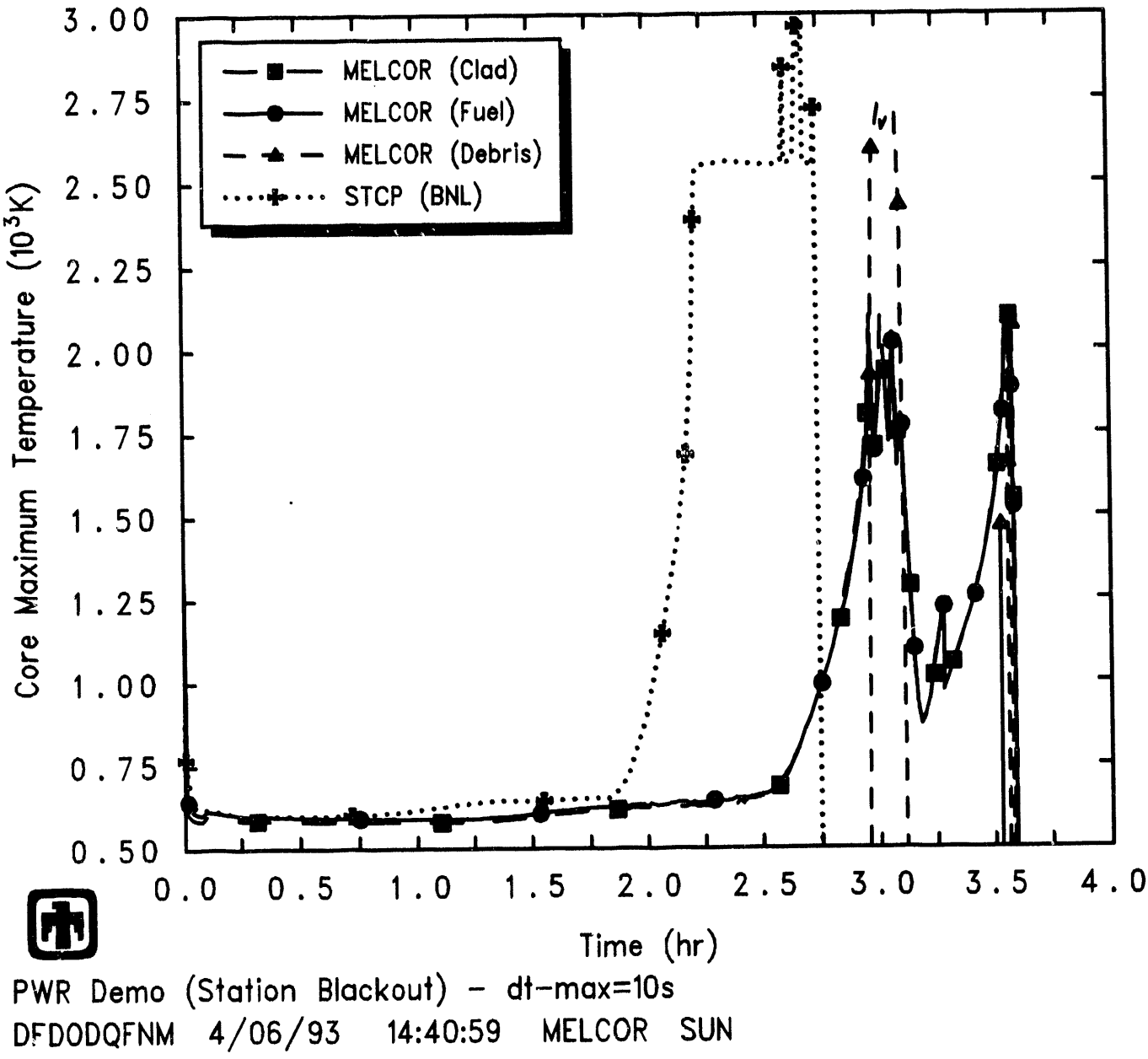

Figure 8.3.3. MELCOR Maximum Core Temperatures, Compared to STCP – Code Comparison Study

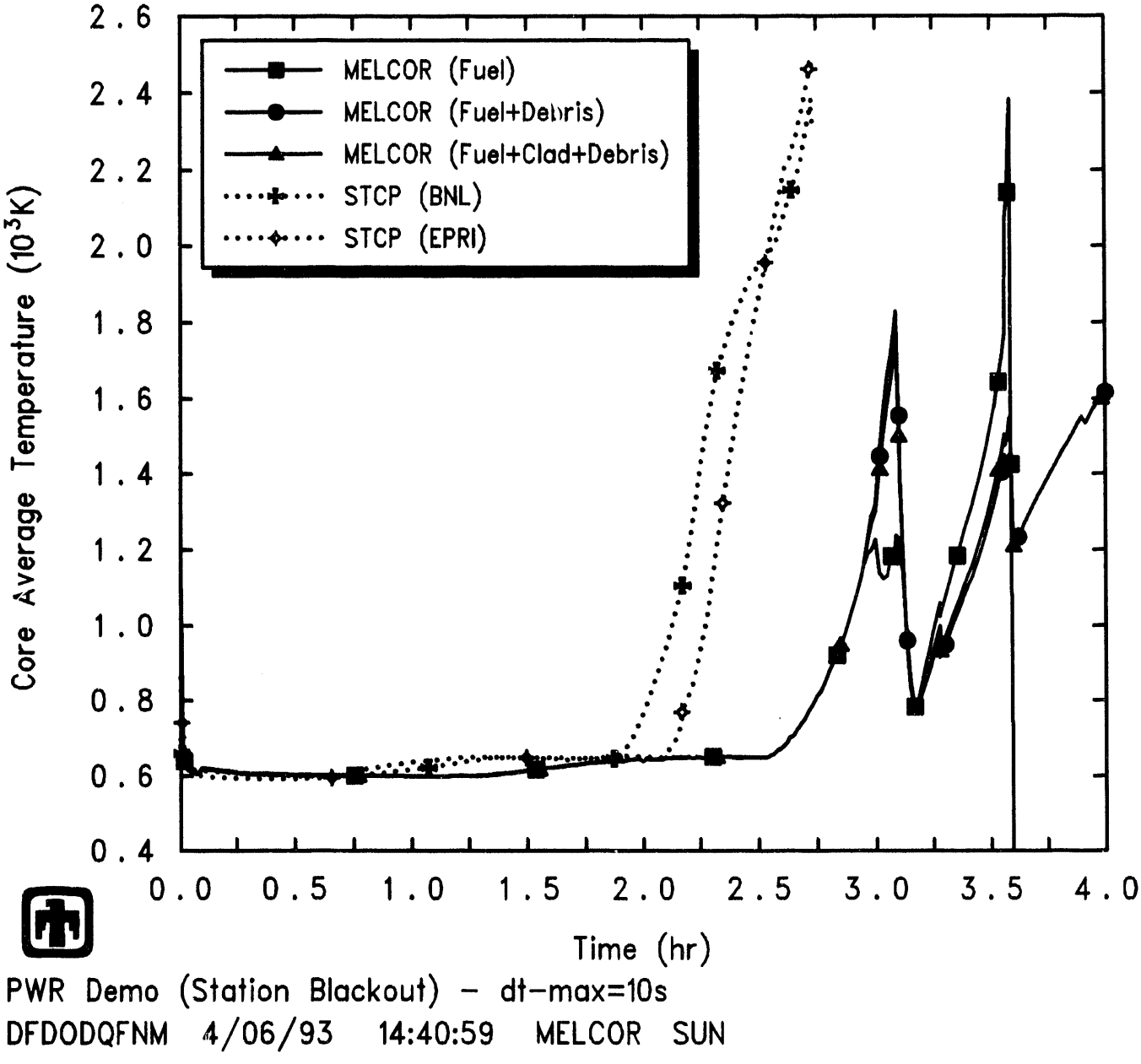

Figure 8.3.4. MELCOR Average Core Temperatures, Compared to STCP – Code Comparison Study

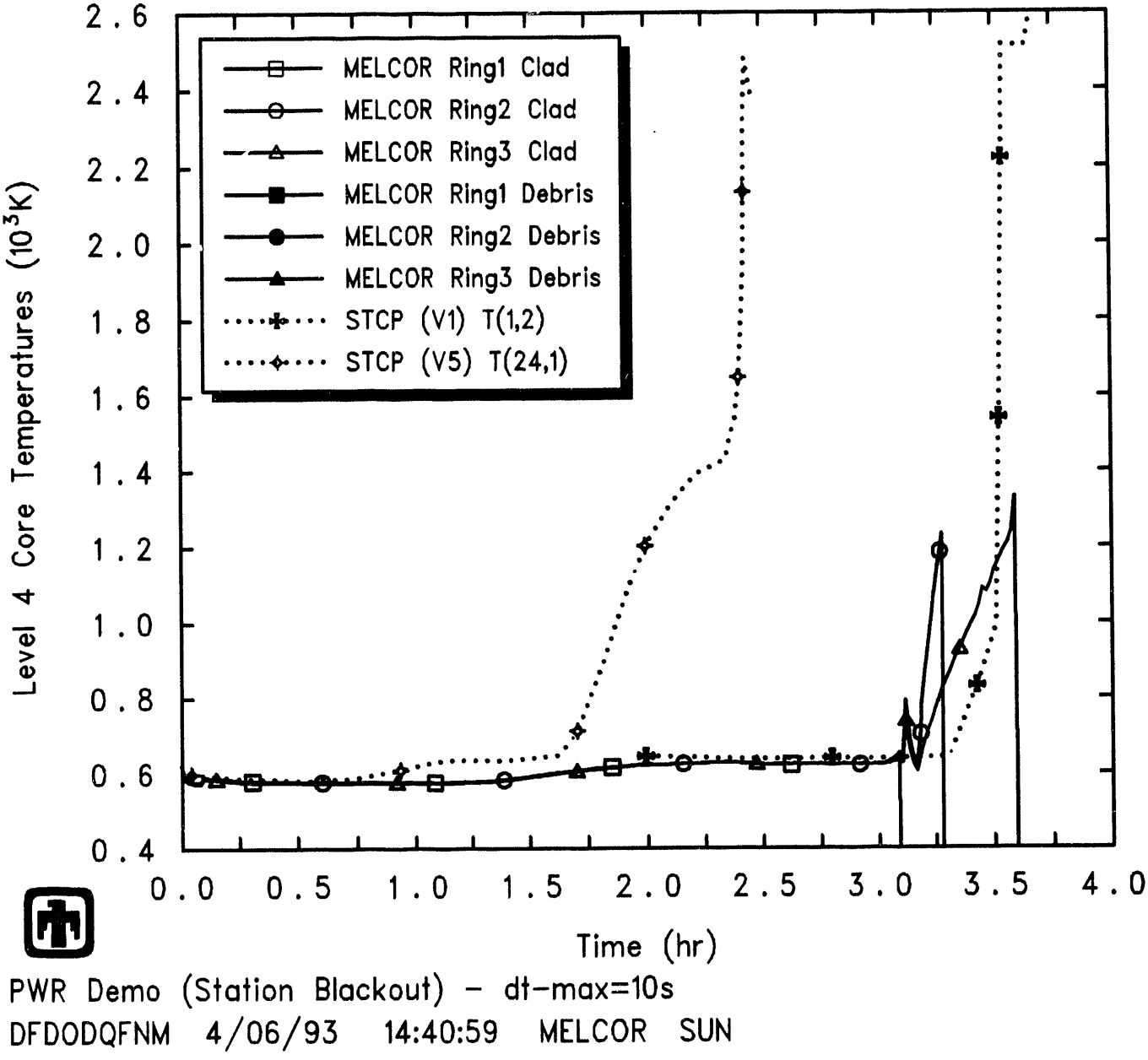

Figure 8.3.5. MELCOR Core Level 4 Clad Temperatures, Compared to STCP – Code Comparison Study

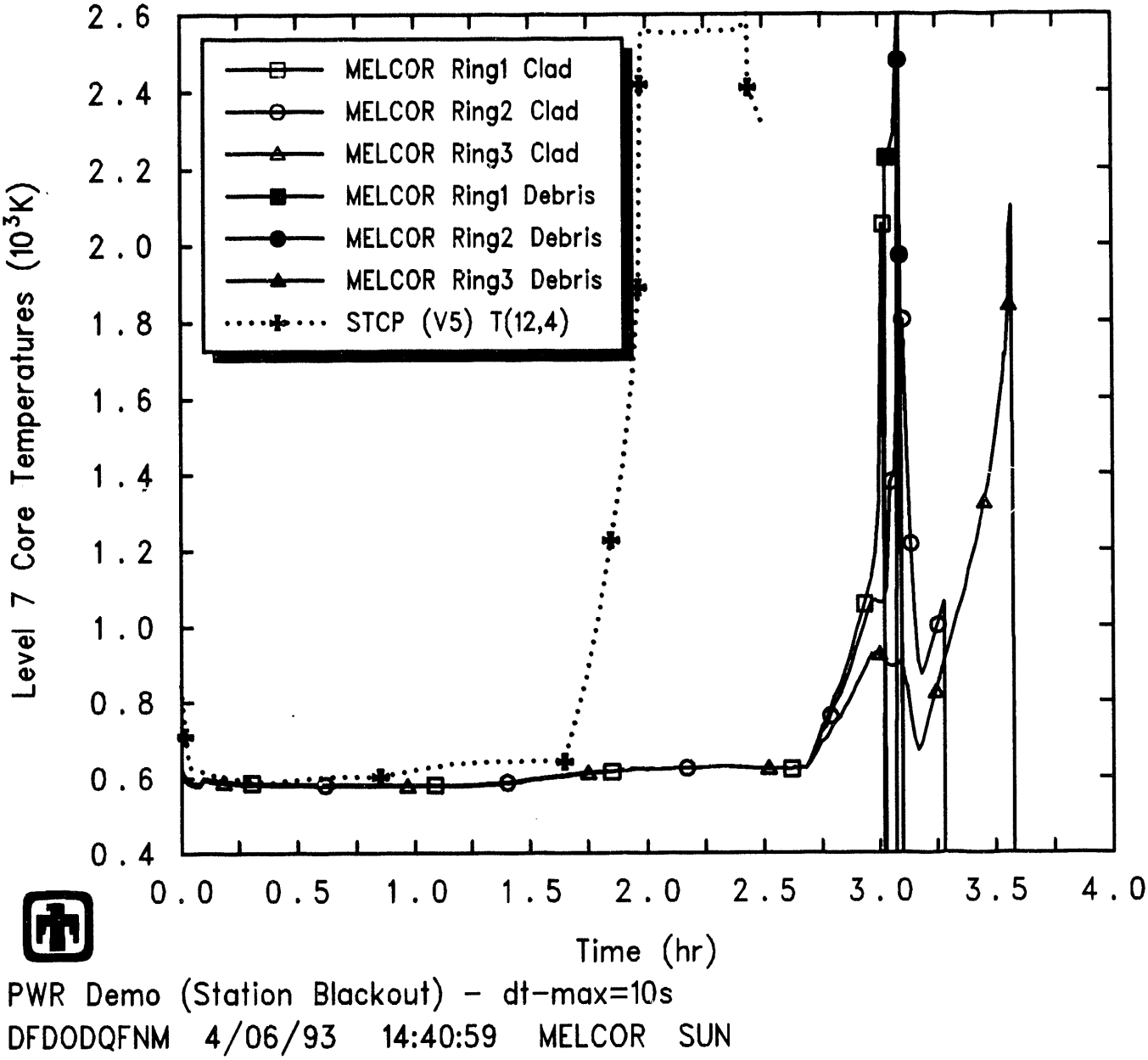

Figure 8.3.6. MELCOR Core Level 7 Clad Temperatures, Compared to STCP - Code Comparison Study

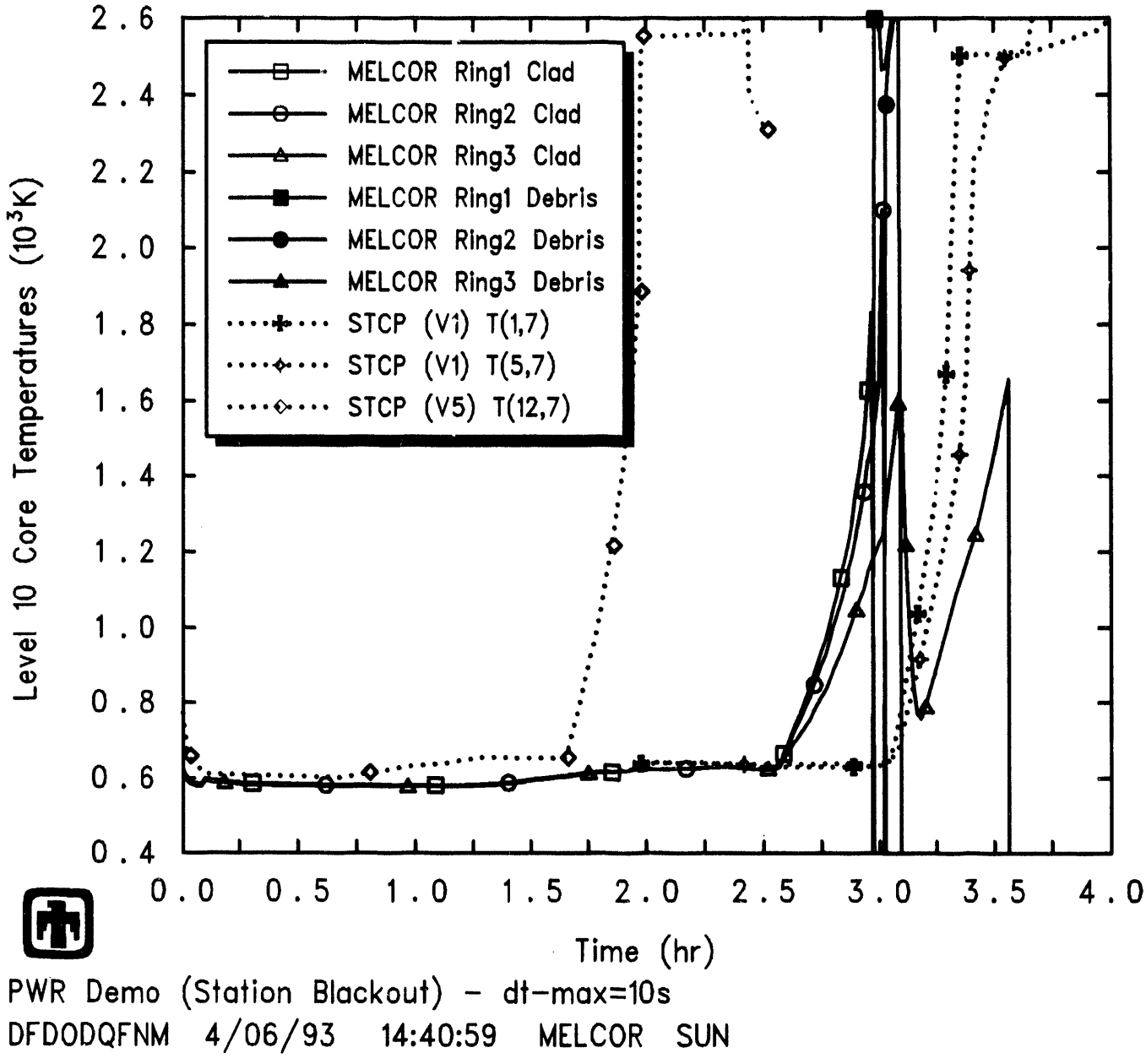

Figure 8.3.7. MELCOR Core Level 10 Clad Temperatures, Compared to STCP - Code Comparison Study

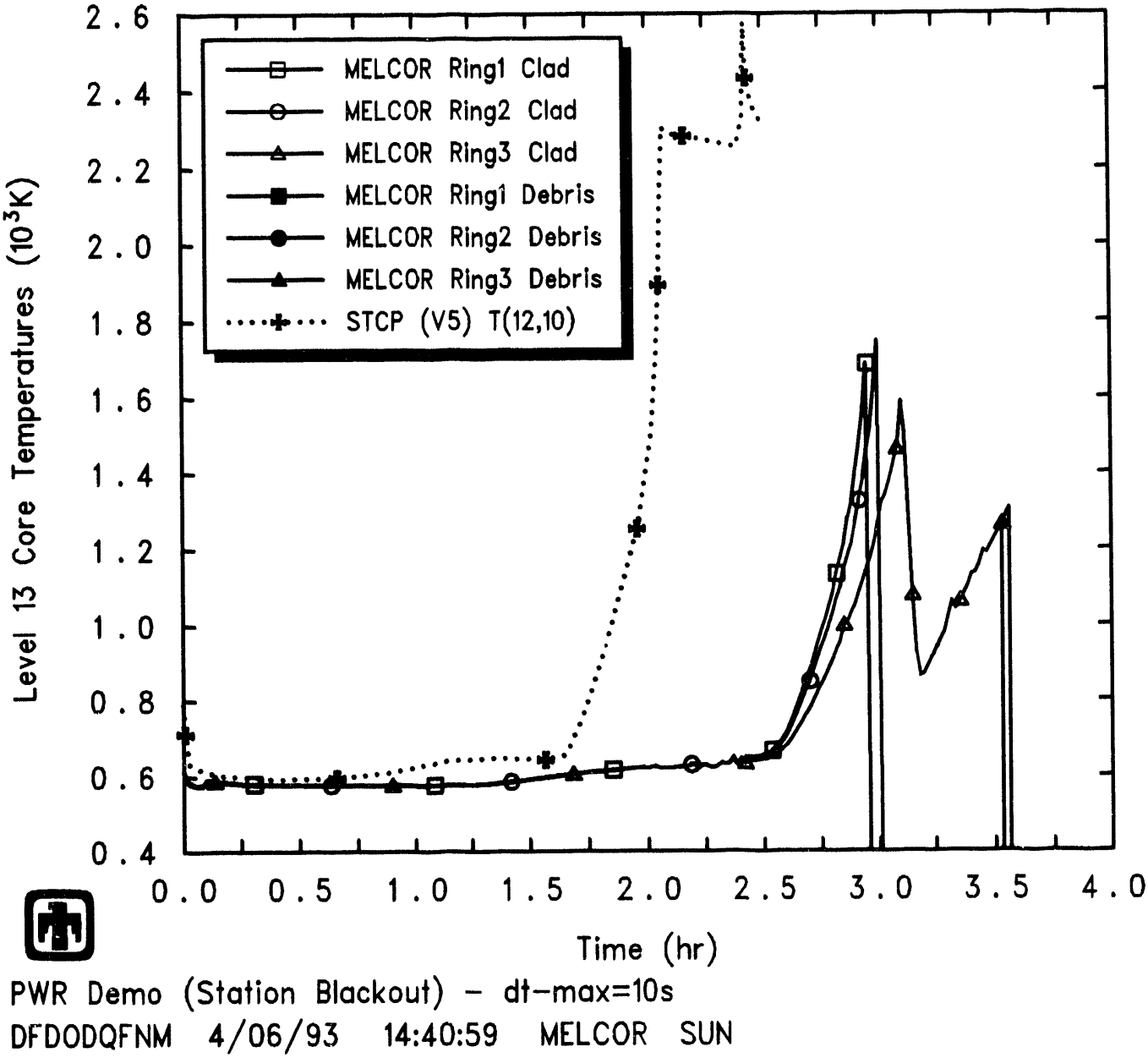

Figure 8.3.8. MELCOR Core Level 13 Clad Temperatures, Compared to STCP – Code Comparison Study

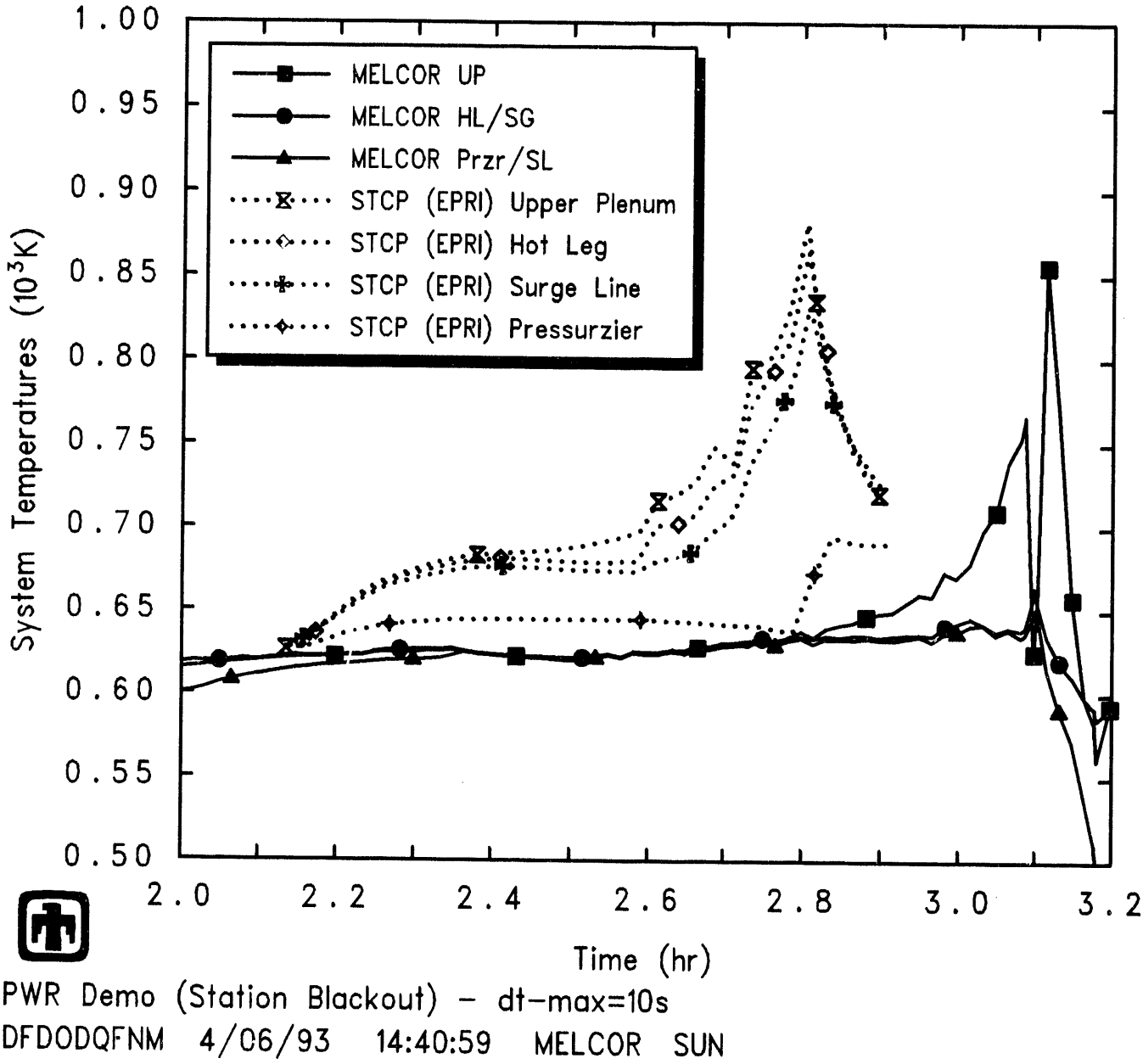

Figure 8.3.9. MELCOR Upper Plenum, Hot Leg, Surge Line, Pressurizer and Steam Generator Tube Temperatures, Compared to STCP – Code Comparison Study

Table 8.3.2. MELCOR Core State at Vessel Failure, Compared to STCP – Code Comparison Study

Parameter	MELCOR 1.8.2	STCP [41]	[42]	[43]	[44]
Mass of Debris (kg)					
UO_2	44,434	78,844	79,630	79,643	79,700
Zircaloy	2,825	16,455	6,690	7,368	9,320
Zirc Oxide	4,943		13,210	12,289	9,650
Steel	95	6,563	34,140	33,034	18,940
Steel Oxide	114				4,860
CRP	334		1,931	2,798	265
Total	52,745	101,862	135,601	135,132	122,735
Average Debris Temperature (K)	~2450	2550	2378		2130†(2890‡)
Fraction Debris Molten	~6%				
Fraction Material Relocated	~50%				
Fraction Core Melted		100%	85%	75%	
Fraction Zircaloy Oxidized	~30%	99.84%	59%	55.25%	42%

†at core slump
‡at head failure

[44]. (The STCP calculation in [43] was a TMLB'-δ sequence, with early containment failure immediately after vessel breach, so the containment response is not comparable.)

The ~2hr vessel failure timing difference in the two early STCP calculations [41, 42], given in Table 8.3.1, is reflected as a timing shift in the containment responses predicted in these two calculations in the upper plot in Figure 8.3.10. One of those early STCP calculations failed containment on basemat melt-through, at 738.2min [42], seen in Figure 8.3.10 as a sudden sharp drop in pressure to ambient, while the other reached the failure pressure of ~690kPa (100psia) at 2830.8min [41]. The STCP calculation which failed the vessel earlier also failed the containment earlier, so both in-vessel core damage and ex-vessel core-concrete interaction were accelerated in MARCH2 relative to MARCH1.1. However, other than the quantitative difference in vessel failure time, these two STCP analyses show qualitatively similar containment response. In both, an initial pressurization due to PORV outflow was followed by a much greater pressurization upon vessel failure; the containment pressure then drops somewhat until a slow pressurization is resumed, to eventual failure. The same qualitative behavior can be seen in the MELCOR containment response calculated. Even the change from rapid pressurization while boiling off cavity water to slower pressurization during core-concrete interaction can be seen in the STCP calculation [41] which did not fail the basemat early. The containment pressure in the MELCOR analysis is generally lower than the STCP results, especially during the first portion of the TMLB' transient analyzed, until after ~8hr when MELCOR begins significant core-concrete interaction.

Two containment-response calculations were included in the more recent STCP analysis [44], one using the INTER routines in MARCH for core-concrete interaction and the other coupling to CORCON-Mod1; both are shown in the lower plot in Figure 8.3.10. These calculations also show the initial pressurization due to PORV outflow followed by a much greater pressurization upon vessel failure; however, the containment pressure then rises gradually for some period before dropping until a rapid pressurization resumes (with INTER) or a slow pressurization (with CORCON) begins. The STCP behavior predicted with CORCON-MOD1 resembles the late-time containment behavior calculated in MELCOR much more than the INTER analysis result. As with the comparison in the upper plot in Figure 8.3.10, the comparison in the lower plot also shows the containment pressure in the MELCOR analysis generally lower than the STCP results, especially during the first portion of the TMLB' transient analyzed, until after ~8hr when MELCOR begins significant core-concrete interaction. Qualitatively, the initial pressurization due to PORV outflow followed by a much greater pressurization upon vessel failure are the same with MELCOR as with this STCP analysis, but there is no counterpart in the MELCOR result to the subsequent continued slow pressurization for some time after vessel breach in this STCP calculation.

The calculated release of fission products from the fuel is summarized in Table 8.3.3. In-vessel fractional releases are given, and both total in-vessel releases and releases prior to vessel breach are presented.

The greater core damage predicted before vessel failure in the STCP calculations resulted in significantly higher in-vessel releases of most fission products than in the ref-

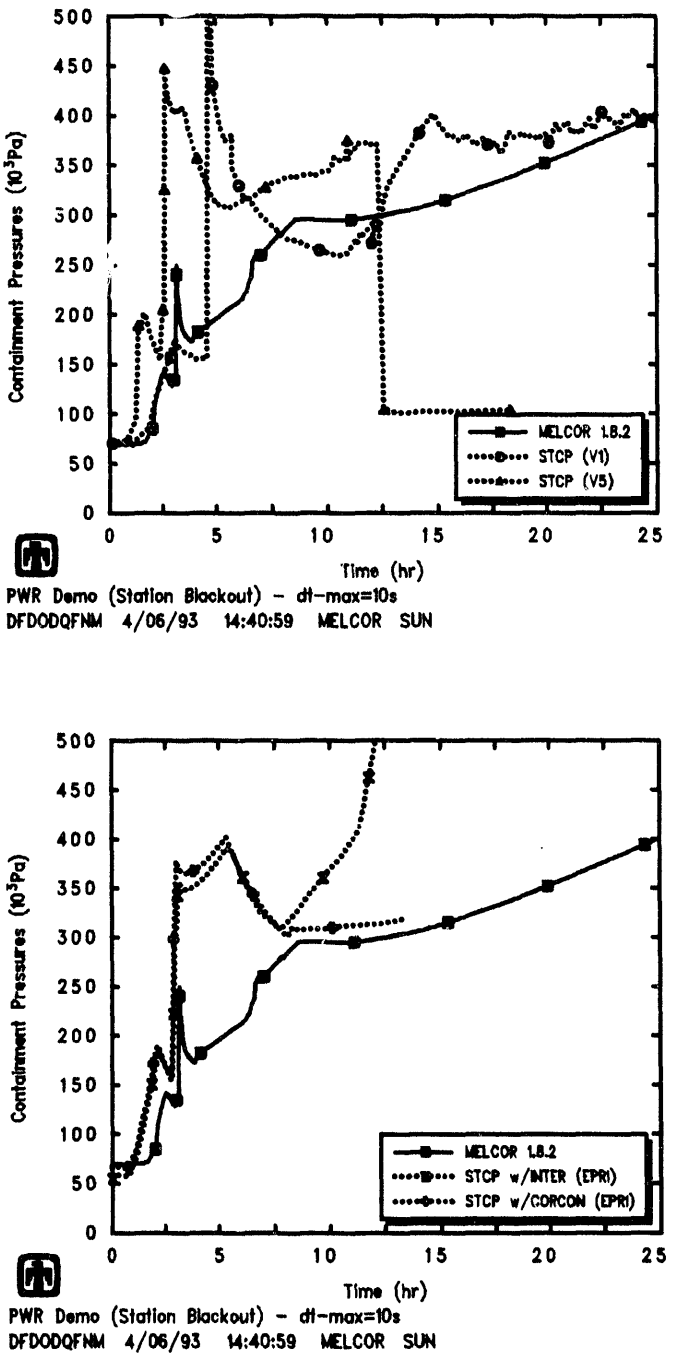

Figure 8.3.10. MELCOR Containment System Pressure, Compared to STCP – Code Comparison Study

Table 8.3.3. Fission Product Release – MELCOR 1.8.2 Reference Calculation

Class	In-Vessel Release (% Initial Inventory) MELCOR		STCP			
	Before Vessel Failure	by 90,000s	[41]	[42]	[43]	[44]
1 (Xe)	51.68	59.69	99.5	99.3	98.4	
2 (Cs)	51.69	59.89	99.5	99.3	98.2	95.9
3 (Ba)	4.32	8.04	43.9	19.8	1.26	
(Sr)			28.2	8.2	0.067	11.0
4 (I)	51.68	59.70	99.4	99.2	98.4	98.4
5 (Te)	3.50	6.68	94.4	34.6	46.5	
6 (Ru)	0.17	0.31	11.2	4.53	$\sim 10^{-4}$	
7 (Mo)	1.89	3.44				
8 (Ce)	0.0036	0.0064	–	–	0	
9 (La)	0.01	0.05	0.04	0.029	$\sim 10^{-5}$	
10 (U)	0.01	0.05				
11 (Cd)	15.27	27.33				(50.8)†
12 (Sn)	15.27	27.33				(6.0)†

†Nonradioactive release from control rods

erence MELCOR 1.8.2 calculation (although similar to the results from some sensitivity study calculations, notably calculations with the debris radial relocation model disabled). However, the added ex-vessel release of the volatiles in MELCOR produced similar total releases of noble gases, Cs, I and Te; the release fractions for more refractory species such as Ba, Ru and La varied greatly in the various STCP analyses with the MELCOR result somewhere in the range found.

(More comparisons of MELCOR 1.8.2 to STCP results are presented in [21], for the AG, S2D and S3D accident sequences in Surry.)

9 Summary and Conclusions

As part of the MELCOR Peer Review process [11], Sandia performed and presented a demonstration calculation of a Surry station blackout (TMLB') accident with MELCOR. This was the first fully-integrated PWR severe accident calculation performed with the code (since the earlier TMI analysis only included in-vessel phenomena). That calculation was done using the release version of MELCOR 1.8.1. The calculation has been rerun with the release version of MELCOR 1.8.2, allowing direct comparison of predicted results for the same problem. That analysis also has been used as a standard test problem to investigate problems identified by the Peer Review (*e.g.*, lack of pressurizer draining prior to vessel breach) and to evaluate the impact on the results of model improvements and extensions in MELCOR 1.8.2 (for example, adding the CORSOR-Booth fission product release model) and of new models (such as radial debris relocation, material eutectics interactions, and direct containment heating due to high pressure melt ejection).

No input changes were required between running with the release versions of MELCOR 1.8.1 and 1.8.2. Input changes made in the basecase model to take advantage of new models and/or upgraded models included using step functions in valve area-*vs*-time tables, and enabling the new eutectics model (not used by default); the new debris radial relocation model is enabled by default. Other input changes for various sensitivity studies included specifying high-pressure melt ejection debris distribution and interactions, varying the fission product release model option, varying the interfacial momentum exchange length in some flow paths, and changing in-vessel falling debris heat transfer parameters.

The results of the same transient run with MELCOR 1.8.1 and 1.8.2 show generally very similar early-time behavior, for the steam generator secondary inventory boiloff, for the pressurizer filling and venting through the PORV, and for the core uncovery and initial clad failure and gap release. The vessel was calculated to fail ~1hr earlier by MELCOR 1.8.2 than by 1.8.1; of that difference, $\geq$0.5hr was due to correcting the "levitating water" problem diagnosed and corrected during our LOFT LP-FP-2 MELCOR assessment [6], while $\leq$0.5hr was due to incorrect failure of the blocked core plate in the MELCOR 1.8.1 analysis (corrected in 1.8.2). More hydrogen was generated in-vessel in the MELCOR 1.8.2 analysis than in the MELCOR 1.8.1 analysis, but the total hydrogen generated (adding together in-vessel and in-cavity production) by the two code versions was within 5%. There was very little change in calculated containment response, with a pressure spike at vessel breach shifted in time due to the different vessel failure times, but the same long-term pressure and temperature response predicted by both MELCOR 1.8.1 and 1.8.2. (Note that this direct comparison did not use the new direct containment heating model added in MELCOR 1.8.2, but even with that model enabled there was simply an increase in the containment pressure spike at vessel failure, and no other significant long-term differences in predicted system response, since the mass of debris initially ejected was relatively small.)

During the MELCOR peer review [11], questions were raised concerning the failure of the pressurizer to drain until the time of vessel failure and subsequent primary system depressurization in the MELCOR 1.8.1 Surry TMLB' demonstration calculation; there

was general agreement that this appeared to violate physical intuition, and might reflect a code problem. In particular, concern was expressed by members of the peer review committee that the failure of the pressurizer to drain was a result of the inadequacy of the momentum exchange model in MELCOR, leading to an incorrect two-phase countercurrent flow limit (CCFL). In response to this problem (and to other concerns), a number of modifications were made to the code including treating the momentum exchange length as a separate variable from the inertial length, defaulted to the buoyancy force characteristic dimension; user input can be used to override the default if desired. As part of evaluating the current momentum exchange model, the Surry TMLB' analysis which originally highlighted the pressurizer drainage problem was rerun with input appropriate to the new interfacial momentum exchange model in MELCOR, in a number of sensitivity study calculations. The results of this sensitivity study indicate that the ability of the user to change the interfacial momentum exchange length through input added in MELCOR 1.8.2 obviously allows wide variation in countercurrent flow limits and associated pressurizer drainage rates, but the question of the "correct" value to use remains open.

Another code model added in MELCOR 1.8.2 is a debris radial relocation model. Previous versions of MELCOR would show each radial ring in the core package model responding independently, with artificial "stacking" of debris columns often observed. This new model was added to relocate molten and/or particulate debris between rings (and axial levels), based upon hydrostatic head equilibration. Sensitivity study results for the Surry TMLB' sequence show more coherent behavior among rings when the debris radial relocation model is enabled. There is no effect on early core heatup or initial clad failure and gap release, but a slightly faster core damage progression and earlier lower head penetration failure (at 11,219s with the debris radial relocation model, *vs* 12,531s with that model disabled).

The core state at vessel failure is also greatly affected by the new debris radial relocation model. With the debris radial relocation model disabled, there is much less debris in the lower plenum at the time a lower head penetration first fails; in particular, the amount of debris in the lower plenum corresponds quite well to the mass of material initially present in the active fuel region in the ring whose core plate failed just previously (*i.e.*, the first, inner, high-powered ring). In the reference calculation with the debris radial relocation model enabled, the mass of debris in the lower plenum at the time a lower head penetration first fails is much greater, about half the total mass initially present in the active fuel region. Also, in the reference calculation with the debris radial relocation model enabled, most of the material remaining in the active fuel region is "intact" (either still in its initial location or refrozen onto intact components). However, in the sensitivity-study calculation with the debris radial relocation model disabled, almost all of the material still in the active fuel region (*i.e.*, above the core support plate) is predicted to be particulate debris. This is the old problem of "stacking" of debris in separate columns, seen in MELCOR 1.8.1 calculations; without the debris radial relocation model, debris in the outer two rings cannot move sideways to the empty inner ring and move down to fall through the failed core plate in that innermost ring.

The capability to model a variety of material eutectics interactions (such as inconel and zircaloy, zircaloy and stainless steel, B_4C and stainless steel, zircaloy and Ag-In-Cd, UO_2 and ZrO_2, and B_4C and zircaloy) was also added to the core package modelling in MELCOR 1.8.2. Earlier versions of MELCOR treated melting materials individually, although there was coding for a specified fraction of solid material to be relocated by molten Zr or steel, to represent dissolution of UO_2 and/or ZrO_2 in melts; the new model has a better treatment of the dissolution of solid material by eutectics melts, based on phase equilibrium and dissolution rate limits, proceeding sequentially as determined by a solid dissolution material hierarchy.

Using the new material eutectic interactions model generally had only a small effect on the results for the Surry TMLB' station blackout sequence. Both earlier core support plate failure (11,178s *vs* 11,675s) and earlier vessel lower head penetration failure (11,219s *vs* 11,685s) were calculated when the model was enabled, but the difference is quite small ($\leq$500s). The biggest difference found was in the lower plenum structural response. Without the eutectic interactions modelled, most ($\sim$80%) of the steel structure in the lower plenum melted and fell into the cavity. The behavior predicted by MELCOR 1.8.2 with the eutectic interactions not modelled was very similar to the results previously obtained using MELCOR 1.8.1. With the eutectic interactions model enabled, Zr and stainless steel debris in the lower plenum melted at lower temperatures and flowed to the cavity somewhat sooner, with less heating of the lower plenum steel structure due to the lower melt temperature and shorter residence time of the debris; thus, most ($\sim$70%) of the lower plenum structure remained in the vessel throughout the entire transient period analyzed. The larger amount of stainless steel transferred to the cavity in the case without the eutectic interactions modelled resulted in a thicker metallic layer in CORCON existing for a longer time period, and the increased concrete ablation then resulted in slightly higher ($\leq$5%) containment pressures at late times.

A set of MELCOR Surry TMLB' assessment analyses was run with different fission product release model options enabled in MELCOR, as a sensitivity study on fission product source term. These include the CORSOR and CORSOR-M models, each with and without a surface/volume correction term, and the new CORSOR-Booth model with low- and high-burnup coefficient sets, for a total of six possible variations (although obviously only the high-burnup version of the CORSOR-Booth model should apply to most plant analyses). In-vessel, the CORSOR and CORSOR-M options result in similar releases of the Xe, Cs and I volatiles. The CORSOR expression and constants give higher releases for many classes (Ba, Ru, Mo, Ce, La, Cd and Sn), while the CORSOR-M expression and constants produce significantly higher release of Te, with no release at all of Mo, La or Cd. The new CORSOR-Booth model predicts lower releases for the most volatile species (Xe, Cs and I), as well as for Ba, Te and U, than either of the older CORSOR options, while the releases of some other species are intermediate between the higher CORSOR and lower CORSOR-M predictions. The effects of using various CORSOR options are less evident in the total-release comparisons, because the later ex-vessel release can somewhat compensate for in-vessel differences.

A number of our MELCOR 1.8.2 Surry TMLB' calculations predicted increased retention of steel mass in the lower plenum, which results in a smaller, thinner metallic layer in the cavity, that can then be completely oxidized by the end of the transient. The VANESA code, which is used to calculate ex-vessel releases in MELCOR, has no provision for a disappearing metallic layer; therefore, as the metallic layer in the cavity goes to zero, the releases of radionuclide species associated with that layer (*i.e.*, Te, Ru, Cd and Sn) can begin growing exponentially. This problem is inherent in the VANESA formulation itself, not in MELCOR, but is more likely to be encountered with MELCOR 1.8.2 than with MELCOR 1.8.1 because of the increased likelihood of more retention of lower plenum structural steel in-vessel with the new eutectics model enabled. That increased retention of lower plenum structural steel (together with the increased robustness of MELCOR 1.8.2, which makes it easier to run long transients to completion without code failure) results in an increased likelihood of oxidizing the entire cavity metallic layer before the end of the transient period of interest. Code users can check for this potential problem easily: if a vanishing metallic layer in CORCON is predicted, the time-dependent release of radionuclides in the cavity should be inspected to determine if significant releases are occurring ex-vessel and are increasing exponentially with time. Users sometimes could extrapolate the releases occurring prior to the metallic layer disappearing to estimate the degree of error. However, the problem is significant and needs to be addressed within CORCON/VANESA.

The new direct containment heating model added in MELCOR 1.8.2, which models high pressure melt ejection from the vessel into containment, also has been used in these PWR TMLB' analyses. These Surry TMLB' DCH analyses relied heavily on modelling insights and code improvements from the earlier MELCOR DCH assessment analyses of the IET experiments [10].

Initial calculations showed a rapid, brief pressure and temperature spike in containment immediately upon high-pressure melt ejection and direct containment heating. The effect was not extremely pronounced, because only ~15% of the available core material was predicted to be ejected during the high-pressure melt ejection phase in our reference Surry TMLB' calculation.

The amount of melt in the lower plenum at failure is a concatenation of early-time core damage, core plate failure criteria, falling debris heat transfer and possible quench in the lower plenum, and lower head penetration heat transfer and failure criteria. The core plate and bottom head penetration failure temperatures, and the falling debris and lower head penetration heat transfer coefficients were all set to their default values in the MELCOR reference calculation. Some studies were done varying these parameters, but there is little data available for these phenomena, either for evaluation of the MELCOR models' adequacy or for guidance on the values to use for the various input parameters controlling predicted response. Sensitivity study calculations were done in which ~60% of the available core material was predicted to be ejected during the high-pressure melt ejection phase; this was not to represent "correct" values for HPME masses , but simply to allow a comparison of DCH behavior in otherwise similar calculations with different amounts of high-pressure melt ejection.

Sensitivity studies also have been done varying the relative amounts of melt deposited directly in the cavity, in the various containment volume atmospheres, and on various heat structures in the cavity, basement and containment dome. As would be expected, depositing more debris directly into the cavity or onto heat structures reduces the magnitude of the pressure/temperature excursion, while increasing the amount of debris deposited in the containment atmosphere increases the magnitude of the pressure/temperature excursion. In addition, varying the relative amounts of debris deposited into various containment control volume atmospheres changes the relative magnitude of the pressure/temperature excursion predicted: specifying more debris into the cavity atmosphere (a relatively small volume) results in a very large pressure and temperature spike in that local volume, but much smaller pressure/temperature excursions throughout the rest of containment, while specifying more debris into the containment dome atmosphere (a relatively large volume) results in a significantly smaller pressure and temperature spike more uniformly throughout the containment.

Including DCH in the Surry TMLB' analysis also affects the amount of material in the cavity (because some debris settled onto heat structures outside the cavity) and hence the amount of concrete ablated, and affects the source term because release of fission products from air-borne debris and from debris settled onto heat structures (instead of into the cavity) is neglected in the MELCOR model. This may or may not be a reasonable assumption. Debris dispersed throughout containment is quickly cooled and quenched, and because fission product release is generally a strong function of temperature, this may inhibit further release of radionuclides over the long term. However, the dispersal of debris into relatively small fragments during the HPME/DCH process, fragments which then undergo rapid oxidation and heating, could conceivably facilitate fission product release from the greatly increased debris surface area. Further model development may be needed in this area.

In response to concerns raised on numeric effects seen in various MELCOR calculations, producing either differences in results for the same input on different machines or differences in results when the time step used is varied, several calculations have been done to identify whether any such effects exist in our Surry PWR TMLB' assessment analyses, and to evaluate their impact on the accident sequence prediction. The reference analysis has been run on a Cray, SUN Sparc2, HP Model 755 and IBM RISC-6000 Model 550 workstations, and on a 50MHz 486 PC, and with the code-selected time step and then the maximum allowable time step set by user input to 5, 2.5 and 1s. Similar, minor differences were found in both numeric studies, including: 1) accumulating offsets in both steam generator secondary and pressurizer relief valve cycling early in the transient; 2) timing shifts in clad failure and gap release, and core support plate and lower head penetration failure; 3) variations in amounts of radionuclides released; 4) magnitude and timing offsets in cavity and containment response; and 5) variations in hydrogen burn frequency and duration. However, despite the number of small differences observable, no significant branching into different response modes was found in the time-step or machine-dependency studies.

The differences seen in timing of key events such as clad failure, core plate failure, lower head penetration failure, *etc.*, in these machine-dependency and time-step studies vary by much smaller times (on the order of 10-100s) than the timestep-variation results observed by BNL for their Peach Bottom station blackout analysis with MELCOR 1.8.1 (which often varied by 1,000-10,000s) [45]. The fraction of core materials relocated and the amount of debris in the lower plenum at vessel failure vary in otherwise-identical calculations run on different hardware platforms and with different time steps, but the range found ±6-7% of the total core mass in the active fuel region, not a large variation; the debris temperature in the lower plenum also varies somewhat, over a ≤200K range. The fraction of zircaloy oxidized by the time of vessel breach varies from ≥20% to ≤40%, with most of the numeric-effects sensitivity study calculations predicting ≤30%; the fraction of steel oxidized by the time of vessel breach also varies in these analyses, from 0.2% to 0.4%, with most of these calculations predicting ≤0.3%. A large part of this reduction in numeric sensitivity represents the significant efforts of the code developers since the Peer Review in identifying and eliminating numeric sensitivities in MELCOR. BNL has seen similar significant reduction in time step sensitivity rerunning their Peach Bottom station blackout analysis with MELCOR 1.8.2 [45].

In both the machine-dependency and time-step studies, differences were noted early in the transient in the number of times that the steam generator secondary relief valve and, later, the pressurizer PORV cycled. Those differences were traced to differences in over- and undershooting the valve controller setpoint pressures with different time steps and/or different machine accuracies. The tabular function logic was modified to allow step function input, to minimize valves getting caught in a part-open state interpolating between table entries. A time-step controller has been developed to limit the time step whenever a valve pressure setpoint is being approached, through control function input. Based on prototype testing, this addition to the code's time-step control algorithm will decrease the numeric sensitivity significantly, but some other contributing effects still remain to be identified.

Another numeric effect recently identified in these Surry TMLB' demonstration analyses (in our machine-dependency and time-step sensitivity studies) are differences in the time that hydrogen burns occur in containment, and in the amount of hydrogen burned, which in turn can significantly impact containment failure times and releases to environment. A set of sensitivity study calculations was done in which the default overshoots allowed in the combustion ignition mole fractions were both reduced by an order of magnitude, with no visible improvement in the scatter of results calculated. This numerical sensitivity severely hampered and essentially prevented any substantive analysis of the effects of enhanced hydrogen ignition during HPME/DCH, because the numerical sensitivities in the burn coding can be large enough to dominate and cover up the actual physical effect we want to study.

The results from the MELCOR TMLB' analysis have been compared to results from similar analyses by other codes. The early-time behavior of the Surry PWR TMLB' accident has been calculated by several best-estimate codes, notably by SCDAP/RELAP5, MELPROG/TRAC and MELPROG-PWR/MOD1. The containment response of the

Surry PWR to a TMLB' accident has been calculated by the best-estimate containment thermal/hydraulic code CONTAIN, both for the early-time containment response at vessel failure including direct containment heating effects, and recently for the long-term containment response with no direct containment heating. The overall transient behavior of the Surry PWR TMLB' accident has been calculated several times by STCP, by various users; at the time they were done, these were best-estimate source term calculations, using a linked set of codes to analyze the entire accident sequence.

The results of comparisons for primary system response and core damage both with detailed, best-estimate, state-of-the-art codes such as SCDAP/RELAP5, MELPROG and MELPROG/TRAC, and with older, engineering-level integrated codes such as STCP, highlight the importance of continued assessment of MELCOR's ability to calculate the early-time thermal/hydraulics in the severe accident precursor. This portion of MELCOR (*i.e.*, the CVH/FL packages) is significantly different than the corresponding RELAP5 and/or TRAC modelling approach (and also significantly different than the corresponding MARCH modelling approach), and the biggest differences found in the results were in the predicted times to core uncovery, which then propagated throughout the remainder of the accident sequence. The maximum and average core heatup rates in the various calculations were generally similar, if best-estimate calculations without in-vessel natural circulation were used as the comparison values; including in-vessel natural circulation tends to slow the core heatup and degradation process somewhat.

The MELCOR calculations generally showed core damage and relocation at lower temperatures than the MELPROG, MELPROG/TRAC or STCP analyses using default failure temperature and other failure criteria, but the various failure criteria are adjustable through input. Because of this, MELCOR also generally seemed to have less debris in the lower plenum at the time of vessel failure (although there is some question of the exact definition of the quantities being compared), but since MELCOR can continue to lose debris from the vessel to the cavity throughout an integral transient calculation, this difference may not be as significant as it first appears. However, the amount of debris present in the lower plenum at vessel failure and the conditions in that debris (*i.e.*, temperature, composition, *etc.*) are very important parameters for DCH analyses. The variations in core state and lower plenum debris found in the various MELCOR sensitivity-study analyses done, and the differences seen between MELCOR results and corresponding results from other codes such as MELPROG, MELPROG/TRAC and STCP identify late-time vessel melt progression (and particularly core plate and lower head failure) as an area requiring further study.

The greater core damage predicted before vessel failure in the STCP calculations resulted in significantly higher in-vessel releases of most fission products than in the reference MELCOR 1.8.2 calculation (although those releases were similar to the results from some sensitivity study calculations, notably calculations with the debris radial relocation model disabled). However, the added ex-vessel release of the volatiles in MELCOR produced similar total releases of noble gases, Cs, I and Te; the release fractions for more refractory species such as Ba, Ru and La varied greatly in the various STCP analyses with the MELCOR result somewhere in the range found.

The pressures calculated in the containment by MELCOR and by STCP have also been compared. Differences in vessel failure timing are reflected as timing shifts in the early-phase containment responses predicted. Two of the STCP analyses available show qualitatively similar containment response to each other and to MELCOR. An initial pressurization due to PORV outflow was followed by a much greater pressurization upon vessel failure; the containment pressure then dropped somewhat until a slow pressurization is resumed, to eventual failure. Even the change from rapid pressurization while boiling off cavity water to slower pressurization during core-concrete interaction can be seen in one of the STCP calculations. Quantitatively, the containment pressure in the MELCOR analysis is generally lower than the STCP results, especially during the first portion of the TMLB' transient analyzed, until after ~8hr when MELCOR begins significant core-concrete interaction.

Comparisons with CONTAIN are complicated by the fact that the vessel failure timing and debris ejection, as well as the steam and hydrogen outflow and the containment conditions at vessel failure, may not be the same in the integral (internally-calculated) MELCOR analysis as in the (externally-defined) source(s) assumed to begin a CONTAIN calculation. However, given this uncertainty, the peak pressure rise predicted during DCH by CONTAIN is higher than that calculated by MELCOR in a comparison with no additional pressurization from enhanced hydrogen burn during DCH; the numeric problems found in the burn logic in MELCOR precluded quantitative comparison with a calculation including enhanced hydrogen burn during DCH. CONTAIN calculations have also been done studying the late containment pressurization resulting from a station blackout in Surry, with no DCH modelled. Those results when compared to the long-term containment pressure response from the MELCOR reference calculation demonstrate that the long-term pressurization rate predicted by CONTAIN is very similar to the corresponding behavior predicted by MELCOR, neglecting the offset due to boiling off cavity water in the MELCOR analysis.

In summary, the effects of new models added in MELCOR 1.8.2 have been investigated, both individually and collectively, for a TMLB' transient scenario in the Surry plant. Results obtained are considered reasonable, based upon comparison to other codes. Significant reduction in numeric sensitivity and significant improvement in code robustness was found, compared to MELCOR 1.8.1. Some numeric effects still remain, in valve cycling, in core material damage and relocation, and in hydrogen combustion, but no significant branching into different response modes was found in any of our numerous sensitivity studies.

Bibliography

[1] R. M. Summers *et al.*,"MELCOR 1.8.0: A Computer Code for Severe Nuclear Reactor Accident Source Term and Risk Assessment Analyses", NUREG/CR-5531, SAND90-0364, Sandia National Laboratories, January 1991.

[2] C. D. Leigh, ed.,"MELCOR Validation and Verification - 1986 Papers", NUREG/CR-4830, SAND86-2689, Sandia National Laboratories, March 1987.

[3] L. N. Kmetyk, "MELCOR 1.8.1 Assessment: LACE Aerosol Experiment LA4", SAND91-1532, Sandia National Laboratories, September 1991.

[4] L. N. Kmetyk, "MELCOR 1.8.1 Assessment: FLECHT SEASET Natural Circulation Experiments", SAND91-2218, Sandia National Laboratories, December 1991.

[5] L. N. Kmetyk, "MELCOR 1.8.1 Assessment: ACRR Source Term Experiments ST-1/ST-2", SAND91-2833, Sandia National Laboratories, April 1992.

[6] L. N. Kmetyk, "MELCOR 1.8.1 Assessment: LOFT Integral Experiment LP-FP-2", SAND92-1273, Sandia National Laboratories, December 1992.

[7] R. J. Gross, "MELCOR 1.8.1 Assessment: PNL Ice Condenser Experiments", SAND92-2165, Sandia National Laboratories, August 1993.

[8] L. N. Kmetyk, "MELCOR 1.8.1 Assessment: Marviken-V Aerosol Transport Tests Att-2b/Att-4", SAND92-2243, Sandia National Laboratories, January 1993.

[9] T. J. Tautges, "MELCOR 1.8.2 Assessment: the DF-4 BWR Fuel Damage Experiment", SAND93-1377, Sandia National Laboratories, October 1993.

[10] L. N. Kmetyk, "MELCOR 1.8.2 Assessment: IET Direct Containment Heating Tests", SAND93-1475, Sandia National Laboratories, October 1993.

[11] B. E. Boyack, V. K. Dhir, J. A. Gieseke, T. J. Haste, M. A. Kenton, M. Khatib-Rahbar, M. T. Leonard, R. Viskanta, "MELCOR Peer Review", LA-12240, Los Alamos National Laboratory, March 1992.

[12] P. N. Smith, P. L. Mason, "AEA Assessment of MELCOR 1.8.1 Using Calculations for TMLB' Accident Sequences", AEA RS 5484, UK AEA Winfrith Technology Centre, March 1993.

[13] "Reactor Risk Reference Document", NUREG-1150, Office of Nuclear Regulatory Research, U. S. Nuclear Regulatory Commission, February 1987.

[14] R. J. Breeding *et al.*, "Evaluation of Severe Accident Risks; Vol. 3, Rev.1, Pt. 1: Surry Unit 1", NUREG/CR-4551, SAND86-1309, Sandia National Laboratories, October 1990.

[15] Internal Memorandum from R. J. Dallman to R. D. Copp, "MELCOR Preliminary Evaluation", RJD-50-87, Idaho National Engineering Laboratory, December 28, 1987.

[16] Letter from C. A. Dobbe, INEL, to J. E. Kelly, SNL, "Transmittal of Calculational Workbooks for the MELCOR Input Decks of the Surry PWR", CAD-1-88, May 6, 1988.

[17] Letter from C. A. Dobbe, INEL, to J. E. Kelly, SNL, "Transmittal of Floppy Disk Containing the MELCOR Input Decks of the Surry PWR", CAD-2-88, May 17, 1988.

[18] P. D. Bayless, "Analyses of Natural Circulation During a Surry Station Blackout Using SCDAP/RELAP5", NUREG/CR-5214, EGG-2547, Idaho National Engineering Laboratory, October 1988.

[19] "Flow of Fluids through Valves, Fittings and Pipe", Technical Paper No. 410, Crane Co., NY, 1981.

[20] I. E. Idel'chik, "Handbook of Hydraulic Resistance: Coefficients of Local Resistance and of Friction", Gosudarstvennoe Energeticheskoe Izdatel'stvo, Moskva-Leningrad, 1960 (translated from the Russian by the Israel Program for Scientific Translation, Jerusalem, 1966).

[21] L. N. Kmetyk, L. N. Smith, "Summary of MELCOR 1.8.2 Calculations for Three LOCA Sequences (AG, S2D, and S3D) at the Surry Plant", NUREG/CR-6107, SAND93-2042, Sandia National Laboratories, to be published.

[22] D. A. Powers, J. E. Brockmann, A. W. Shiver, "VANESA: A Mechanistic Model of Radionuclide Release and Aerosol Generation during Core Debris Interactions with Concrete", NUREG/CR-4308, SAND85-1370, Sandia National Laboratories, July 1986.

[23] Private communication, D. A. Powers to R. K. Cole, October 7, 1993.

[24] E. A. Boucheron and J. E. Kelly, "MELCOR Analysis of the Three Mile Island Unit 2 Accident", Nuclear Technology 87, December 1989.

[25] R. K. Cole, "Interfacial Momentum Exchange Model", Sandia National Laboratories, letter report to R. B. Foulds, NRC, November 11, 1992.

[26] L. N. Kmetyk, R. K. Cole, "MELCOR Assessment: Gedanken Problems, Volume 2", SAND92-0965, Sandia National Laboratories, to be published.

[27] R. M. Summers, R. C. Smith, R. S. Longenbaugh, "Core Package Radial Relocation Model", Sandia National Laboratories, letter report to R. B. Foulds, NRC, September 30, 1992.

[28] R. M. Summers, "The Core Package Eutectic Model", Sandia National Laboratories, letter report to R. B. Foulds, NRC, November 11, 1992.

[29] "Technical Basis for Estimating Fission Product Behavior During LWR Accidents", NUREG-0772, U. S. Nuclear Regulatory Commission, June 1981.

[30] M. Ramamurthi, M. R. Kuhlman, "Final Report on Refinement of CORSOR - An Empirical In-Vessel Fission Product Release Model", Battelle Memorial Institute, October 31, 1990.

[31] R. C. Smith, "MELCOR CORSOR-Booth Fission Product Release Model", letter report to R. B. Foulds, NRC, April 15, 1992.

[32] I. K. Madni, X. D. Guo, "MELCOR Simulation of the Full-Length High-Temperature 4 Experiment", Brookhaven National Laboratories letter report to R. Foulds, NRC, November 26, 1991.

[33] R. C. Smith, "MELCOR Direct Containment Heating Model", letter report to R. B. Foulds (NRC), Sandia National Laboratories, February 10, 1992.

[34] S. E. Dingman, R. S. Longenbaugh, S. W. Webb, "Burn (BUR) Package Reference Manual", Sandia National Laboratories, draft dated March 6, 1993.

[35] R. J. Henninger, J. E. Kelly, "MELPROG/TRAC: Update and Applications" in Proceedings, 14th Water Reactor Safety Information Meeting, Gaithersburg MD, October 27-31, 1986, NUREG/CP-0082 (Vol. 6), published February 1987.

[36] J. E. Kelly, R. J. Henninger, J. F. Dearing, "MELPROG-PWR/MOD1 Analysis of a TMLB' Accident Sequence", NUREG/CR-4742, SAND86-2175, Sandia National Laboratories, January 1987.

[37] D. C. Williams *et al.*, "Containment Loads Due to Direct Containment Heating and Associated Hydrogen Behavior: Analysis and Calculations with the CONTAIN Code", NUREG/CR-4896, SAND87-0633, Sandia National Laboratories, May 1987.

[38] D. C. Williams, D. L. Y. Louie, "CONTAIN Analyses of Direct Containment Heating in the Surry Plant", Proceedings of the Thermal/Hydraulics Division, 1988 ANS/ENS Winter Meeting, Washington DC, October 31-November 4, 1988.

[39] DCH Working Group, "Integrated Report on DCH Issue Resolution for PWRs", NUREG/CR-6109, SAND93-2078, Sandia National Laboratories (Draft for Peer Review, August 31,1993).

[40] R. G. Gido *et al.*, "PWR Dry Containment Parametric Studies", NUREG/CR-5630, SAND90-2339, Sandia National Laboratories, April 1991.

[41] J. A. Gieseke *et al.*, "Radionuclide Release Under Specific LWR Accident Conditions; Volume I: PWR Large, Dry Containment Design", BMI-2104, Battelle Columbus Laboratories, July 1983.

[42] J. A. Gieseke *et al.*, "Radionuclide Release Under Specific LWR Accident Conditions; Volume V: PWR Large, Dry Containment Design (Surry Plant Recalculations)", BMI-2104, Battelle Columbus Laboratories, July 1984.

[43] E. Cazzoli *et al.*, "Independent Verification of Radionuclide Release Calculations for Selected Accident Scenarios", NUREG/CR-4629, BNL-NUREG-51998, Brookhaven National Laboratory, July 1986.

[44] R. L. Ritzman *et al.*, "Surry Source Term and Consequence Analysis", EPRI NP-4096, Science Applications International Corporation, June 1985.

[45] I. K. Madni, "Analyses of Long-Term Station Blackout Without Automatic Depressurization at Peach Bottom Using MELCOR (Version 1.8)", NUREG/CR-5850, BNL-NUREG-52319, Brookhaven National Laboratory, to be published.

External Distribution:

U. S. Nuclear Regulatory Commission (18)
Attn: S. Acharya, NLS-372
Y. S. Chen, NLN-344
M. A. Cunningham, NLS-372
F. Eltawila, NLN-344
R. B. Foulds, NLN-344
S. Basu, NLN-344
C. Gingrich, NLN-344
C. G. Tinkler, NLN-344
L. E. Lancaster, NLS-372
R. O. Meyer, NLS-007
J. A. Mitchell, NLS-314
C. P. Ryder, NLS-372
L. Soffer, NLS-324
B. Sheron, NLS-007
J. A. Murphy, NLS-007
L. M. Shotkin, NLN-353
N. Lauben, NLN-353
R. Landry, NLN-344
Washington, DC 20555

S. Y. Chen
Argonne National Laboratory
9700 South Cass Avenue
Argonne, IL 60439

Battelle Columbus Laboratories (3)
Attn: P. Cybulskis
M. Carmel
R. S. Denning
505 King Avenue
Columbus, OH 43201

Brookhaven National Laboratory (2)
Attn: I. K. Madni
T. Pratt
Bldg. 130
32 Lewis
Upton, NY 11973

Idaho National Engineering Laboratory (5)
Attn: A. Brown
R. J. Dallman
D. W. Golden
S. E. Reed
G. W. Johnsen
EG&G Idaho
P. O. Box 1625
Idaho Falls, ID 83404

D. Jones
EI International
P. O. Box 50736
Idaho Falls, ID 83405

Electric Power Research Institute (3)
Attn: E. Fuller
R. N. Oehlberg
B. R. Sehgal
P. O. Box 10412
Palo Alto, CA 94303

Los Alamos National Laboratory (2)
Attn: B. E. Boyack, K-551
D. R. Liles, K-553
P. O. Box 1663
Los Alamos, NM 87545

Oak Ridge National Laboratory (11)
P. O. Box 2009
Oak Ridge, TN 37831-8057
Attn: S. R. Greene, MS-8057
R. H. Morris, MS-8057
S. E. Fisher, MS-8057
R. Sanders, MS-8057
T. L. Heatherly, MS-8057
S. A. Hodge, MS-8057
C. R. Hyman, MS-8057
B. W. Patton, MS-8057
D. B. Simpson, MS-8057
R. P. Taleyarkhan, MS-8057
M. L. Tobias, MS-8088

Andrzej Drozd
Nuclear Regulatory Commission
OWFN, MS 8E1
11555 Rockville Pike
Rockville, MD 20852

W. P. Barthold
Barthold & Associates
132 Seven Oaks Drive
Knoxville, TN 37922

K. C. Wagner
Science Applications Intl. Corp.
2109 Air Park Rd. SE
Albuquerque, NM 87106

Savannah River Laboratory (2)
Attn: B. DeWald
D. Allison
Westinghouse Savannah River Co.
Bldg. 773-41A
Aiken, SC 29808-0001

Westinghouse Hanford Co. (2)
Attn: D. Ogden
O. Wang
P. O. Box 1970
Richland, WA 99352

General Electric Company (3)
Knolls Atomic Pwer Laboratory
Attn: D. F. McMullan
G. H. Epstein
E. Mennard
Bldg. F3, Room 8
P. O. Box 1072
Schenectady, NY 12301-1072

Bettis Atomic Power Laboratory (3)
Attn: Mark Riley
Jow Semanchik
Vincent Baiamonte
P. O. Box 79
West Mifflin, PA 15122

Mohsen Khatib-Rahbar
Energy Research Inc.
P. O. Box 2034
Rockville, MD 20852

V. K. Dhir
2445 22nd Street
Santa Monica, CA 90403

R. Viskanta
Purdue University
Heat Transfer Laboratory
School of Mechanical Engineering
West Lafayette, IN 47907

Dr. Jim Gieseke
Battelle Memorial Institute
505 King Ave.
Columbus, Ohio 43201

M. A. Kenton
Gabor, Kenton & Associates
770 Pasquinelli Drive
Suite 426
Westmont, IL 60559

University of California (2)
Attn: W. H. Amarasooriya
T. Theofanous
ERC-CRSS
Santa Barbara, CA 93106

Professor K. B. Cady
Nuclear Science and Engineering
Cornell Universioty
Ward Laboratory
Ithaca, NY 14853-7701

F. E. Haskin
University of New Mexico
Department of Chemical and Nuclear Engineering
Albuquerque, NM 87131

J. C. Lee
University of Michigan
Dept. of Nuclear Engineering
Cooley Building, North Campus
College of Engineering
Ann Arbor, MI 48109-2104

University of Wisconsin (2)
Dept. of Nuclear Engineering
Attn: M. L. Corradini
G. A. Moses
Engineering Research Building
1500 Johnson Drive
Madison, WI 53706

Ramu K. Sundaram
Manager, LOCA Analysis Group
Nuclear Engineering
Yankee Atomic Electric Company
580 Main Street
Bolton, MA 01740

John Bolin
CEGA
P. O. Box 85608
San Diego, CA 92186-9784

M. Plys
Fauske & Associates
16W070 West 83rd Street
Burr Ridge, IL 60521

Nick Trikouros
GPU Nuclear Corporation
One Upper Pond Road
Parsippany, NJ 07054

B. Raychaudhuri
Nebraska Public Power District
PRA & Engineering Review Group
P. O. Box 499
Columbus, NE 68601

Frank Elia
Stone & Webster Engineering Corp.
245 Summer Street
Boston, MA 02210

Prof. Dr. Johann Korkisch
Institute of Analytical Chemistry
University of Vienna
A-1090 Vienna, Währingerstrasse 38
AUSTRIA

Samir S. Girgis
Atomic Energy of Canada Limited
CANDU Operations
Sheridan Park Research Community
Mississagua, Ontario
CANADA L5K1B2

Paul J. Fehrenbach
Chalk River Nuclear Laboratories
Fuel Engineering Branch, RSR Division
Chalk River, Ontario
CANADA KOJ1J0

Dr. Bohumír Kujal
Department of Reactor Technology
Nuclear Research Institute Řež plc
250 68 Řež
CZECH REPUBLIC

Andrej Mitro
Institute of Radioecology and Applied Nuclear Techniques
Garbiarska 2
P. O. Box A-41
040 61 Košice
CHECHOSLOVAKIA

Shih-Kuei Cheng
Institute of Nuclear Energy Research
P. O. Box 3-3
Lung-Tan, Taiwan
REPUBLIC OF CHINA

Mr. Yi-Bin Chen
Department of Nuclear Technology
Atomic Energy Council
67, Lane 144.
Keelung Road, Section 4
Taipei, Taiwan 106
REPUBLIC OF CHINA

Technical Research Centre of Finland (3)
Nuclear Engineering Laboratory
Attn: Lasse Mattila
Ilona Lindholm
Esko Pekkarinen
P. O. Box 208 (Tekniikantie 4)
SF-002151 Espoo
FINLAND

Jorma V. Sandberg
Finnish Center Radiation & Nucl. Safety,
Dept. of Nuclear Safety
P. O. Box 268
SF-00101 Helsinki
FINLAND

Akihide Hidaka
Safety Research Department
Reactor Accident Studies and Modelling Branch
DRS/SEMAR
Cadarache Nuclear Center
13108 Saint-Paul-Lez-Durance Cedex
FRANCE

Dr. Lothar Wolf
Battelle Institute EV
AM Romerhof 35
D-6000
Frankfurt/Main90
GERMANY

Gesellschaft fur Anlagen- und Reaktorsicherheit (3)
Attn: Ulrich Erven
Walter Erdmann
Manfred Firnhaber
Schwertnergasse 1
D-5000 Koln 1
GERMANY

Kernforschungzentrum, Karlsruhe (3)
Attn: P. Hofmann
Werner Scholtyssek
Philipp Schmuck
P. O. Box 3640
D-7500 Karlsruhe 1
GERMANY

Udo Brockmeier
University of Bochum
Energietechnik
IB-4-128
D-4630 Bochum
GERMANY

György Gyenes
Central Research Institute for Physics
Institute for Atomic Energy Research
H-1525 Budapest, P. O. Box 49
HUNGARY

Joint Research Center
Commission of the European Communities
Attn: Alan Jones
Iain Shepherd
Safety Technology Institute
21020 Ispra (Va)
ITALY

Giovanni Saponaro
ENEA
Natl. Comm. for R&D of Nuclear Energy
Via Vitaliano Brancati, 48
00144 Rome
ITALY

Japan Atomic Energy Research Institute (3)
Attn: Kunihisa Soda
Jun Sugimoto
Norihiro Yamano
Tokai-mura, Naka-gun, Ibaraki-ken
319-11, JAPAN

Dr. Masayoshi Shiba, Director General
Institute of Nuclear Safety
Nuclear Power Engineering Corporation
Fujita Kankou Toranoman Bldg. 7F
3-17-1, Toranoman
Minato-Ku, Tokyo, 105
JAPAN

Masao Ogino
Mitsubishi Atomic Power Industries
4-1 Shibakoen 2-Chome
Minatoku Tokyo
JAPAN

Hidetoshi Okada
Nuclear Power Engineering Corporation
3-17-1, Toranomon Bldg. 5F
Minato-ku, Tokyo 105
JAPAN

Hirohide Oikawa
Toshiba Corporation
8, Shin-Sugita, Isogo-ku
Yokohama
JAPAN

Korea Atomic Energy Research Inst. (3)
Attn: Kun-Joong Yoo
Song-Won Cho
Dong-Ha Kim
P. O. Box 7, Daeduk Danji
Taejon
SOUTH KOREA 305-353

Jae Hong Park
Safety Assessment Department
Korea Atomic Energy Research Institute
P. O. Box 16, Daeduk-Danji
Taejon
SOUTH KOREA 305-353

Netherlands Energy Research Foundation (2)
Attn: Karel J. Brinkmann
E. J. Velema
P. O. Box 1
1755 ZG Petten
THE NETHERLANDS

Dr. Valery F. Strizhov
Russian Academy of Science
Institute of Nuclear Safety
Moscow, G. Tulsky, 52
113191, RUSSIA

Dr. B. Mavko
Institut Josef Stepan
Odsek za Reaktorsko Tehniko
61111 Ljubljana
Jamova 39
P. O. Box 100
SLOVENIA

Universidad Politecnica de Madrid (2)
Attn: Augustin Alonzo Santos
Francisco Martin
E.T.S. Ingenieros Industriales
Jose Gutierrez Abascal, 2
28006 Madrid
SPAIN

Juan Bagues
Consejo de Seguridad Nuclear
Justo Dorado, 11
28040, Madrid
SPAIN

Oddbjörn Sandervåg
Statens Kärnkraftinspektion
Swedish Nuclear Power Inspectorate
Box 27106 102 52 Stockholm
SWEDEN

L. Hammar, Director
Division of Research
Swedish Nuclear Power Inspectorate
Statens Karnkraftinspektion
Sehlstedtsgatan 11
Box 27106
S-102-50 Stockholm
SWEDEN

Swiss Federal Nuclear Safety Inspectorate (4)
Attn: S. Chakraborty
Sang Lung Chan
U. Schmocker
H. P. Isaak
CH-5232 Villigen-HSK
SWITZERLAND

United Kingdom Atomic Energy Agency (3)
Winfrith Technology Center
Attn: T. Haste
S. R. Kinnersley
D. W. Sweet
Winfrith, Dorchester, Dorset
UNITED KINGDOM, DTS 8DH

United Kingdom Atomic Energy Authority (2)
Safety & Reliability Directorate
Attn: M. I. Robertson
C. Wheatley
Wigshaw Lane, Culcheth, Warrington
Cheshire, WA3 4NE
UNITED KINGDOM

Internal Distribution:

MS1328 R. S. Longenbaugh, 6342
MS0736 N. R. Ortiz, 6400
MS0744 W. A. von Riesemann, 6403
MS0744 D. A. Powers, 6404
MS0747 A. L. Camp, 6412
MS0747 S. E. Dingman, 6412
MS0748 F. T. Harper, 6413
MS0742 J. E. Kelly, 6414
MS0745 S. L. Thompson, 6418 (10 copies)
MS0745 R. K. Cole, 6418
MS0745 A. A. Elsbernd, 6418
MS0745 L. N. Kmetyk, 6418 (10 copies)
MS0745 R. C. Smith, 6418
MS0745 D. S. Stuart, 6418
MS0745 R. M. Summers, 6418
MS0745 T. J. Tautges, 6418
MS0739 K. E. Washington, 6429
MS0899 Technical Library, 7141 (5 copies)
MS0619 Technical Publications, 7151
MS0100 Document Processing for DOE/OSTI, 7613-2 (10 copies)
MS9018 Central Technical Files, 8523-2

*U.S. GOVERNMENT PRINTING OFFICE 1994-0-573-026/80019

DATE
FILMED
4/20/94
END